

**NASA**  
**Technical**  
**Report**  
**3527**

Army Research  
Laboratory  
Technical Report  
ARL-TR-333

June 1995

**Laser Anemometer Measurements of  
the Three-Dimensional Rotor Flow  
Field in the NASA Low-Speed  
Centrifugal Compressor**

**Michael D. Hathaway,  
Randall M. Chriss,  
Anthony J. Strazisar,  
and Jerry R. Wood**

(NASA-TP-3527) LASER ANEMOMETER  
MEASUREMENTS OF THE  
THREE-DIMENSIONAL ROTOR FLOW FIELD  
IN THE NASA LOW-SPEED CENTRIFUGAL  
COMPRESSOR (NASA. Lewis Research  
Center) 297 p

N-07  
68494  
7-297

N95-31985

Unclass

HI/07 0058494



National Aeronautics and  
Space Administration





**NASA  
Technical  
Paper  
3527**

Army Research  
Laboratory  
Technical Report  
ARL-TR-333

1995

**Laser Anemometer Measurements of  
the Three-Dimensional Rotor Flow  
Field in the NASA Low-Speed  
Centrifugal Compressor**

Michael D. Hathaway  
*Vehicle Propulsion Directorate  
U.S. Army Research Laboratory  
Lewis Research Center  
Cleveland, Ohio*

Randall M. Chriss, Anthony J. Strazisar, and Jerry R. Wood  
*National Aeronautics and Space Administration  
Lewis Research Center  
Cleveland, Ohio*



National Aeronautics and  
Space Administration

**Office of Management**

Scientific and Technical  
Information Program

1995



# Laser Anemometer Measurements of the Three-Dimensional Rotor Flow Field in the NASA Low-Speed Centrifugal Compressor

Michael D. Hathaway  
Vehicle Propulsion Directorate  
U.S. Army Research Laboratory  
Lewis Research Center  
Cleveland, Ohio

Randall M. Chriss, Anthony J. Strazisar, and Jerry R. Wood  
National Aeronautics and Space Administration  
Lewis Research Center  
Cleveland, Ohio

## Summary

A laser fringe anemometer was used to survey the NASA low-speed centrifugal compressor (LSCC) rotor flow field. Measurements of the three-dimensional velocity field were acquired at several measurement planes upstream, within, and downstream of the rotor. Most of the data were collected at the design flow rate; a few selected additional measurements were made at a lower flow rate.

The experimental configuration consisted of a backswept impeller followed by a vaneless diffuser. The rotor was designed for axial inlet flow, so there were no inlet guide vanes. This rotor-only configuration enabled the laser anemometer data to be compared with results from numerical flow analysis codes that assume the flow is steady in the reference frame of the rotor. In addition, the large size and low speed of the compressor generated large viscous regions, thus enabling near-wall details to be measured with laser anemometry. The resulting data provide an experimental data base with which to compare the results from three-dimensional viscous analysis codes.

The laser anemometer surveys were conducted along axisymmetric surfaces of revolution that were constructed by a computational fluid dynamics (CFD) grid-generation routine so as to be approximately orthogonal to the casing and hub flow paths. Data were acquired at nominally 20 survey planes upstream, within, and downstream of the rotor. Within each survey plane, data were acquired, nominally, at 15 spanwise locations in intervals of 5-percent-of-span from the shroud. At each survey point within a measurement plane, the axial, radial, and relative tangential velocity components were resolved at 1000 points across the rotor blade pitch. However, for presentation purposes and to provide more manageable data sets, the results were routinely averaged to a resolution of 200 points across a rotor pitch. The laser anemometer survey data at fixed span locations are presented in the form of blade-to-blade plots of axial, radial, and relative tangential velocity, all normalized by the rotor exit tip speed. In addition, for all measurement planes there are wire-frame and contour plots of

throughflow velocity and vector plots of secondary velocity, all normalized by the rotor exit tip speed.

Spanwise pneumatic probe surveys of the total and static pressures, the total temperature, and the flow yaw and pitch angles were also performed at stations upstream and downstream of the rotor. These probe survey data were used to calculate overall compressor performance. Both the survey data and performance data are included herein in tabular form and can be used to set boundary conditions for computational codes.

Detailed descriptions of the blade and flow path geometry, as well as a complete set of the laser anemometer survey data, are available on magnetic medium upon request.

## Introduction

Centrifugal compressors traditionally have not performed as well as their axial flow counterparts, partly because of our inability to predict their inherently complex three-dimensional viscous flow fields. With the development of three-dimensional Navier-Stokes codes for turbomachinery flow-field analysis, it became possible to predict such viscous flow fields. However, detailed experimental measurements with which to assess the limitations of the computational analyses are largely lacking.

Several previous investigators have measured flow fields within unshrouded centrifugal compressor impellers. Eckardt's laser anemometer measurements in a radial-outflow impeller (1976) provided the first experimental evidence that in high-speed impellers a "wake" of low momentum fluid develops. At the impeller exit, the wake appears near the suction surface-shroud corner of the blade passage. However, Krain (1988), Krain and Hoffman (1989), Ahmed and Elder (1990), Sipos (1991), and Rohne and Banzhaf (1991) acquired laser anemometer measurements in backswept impellers which indicated that, at the impeller exit, the wake appears near the shroud at midpitch.

Because of the small passage size and limited optical access in these previous investigations, few experimental details were available about the development of secondary flow inside high-speed impeller passages. Krain (1988) and Sipos (1991), therefore, used vortex models to infer the vortical nature of the secondary flow from the flow angle measurements that they acquired on blade-to-blade stream surfaces.

Several investigations of low-speed compressors have also provided some insight into secondary flows. Nishi, Senoo, and Yamaguchi (1968) used dye in a water-flow experiment to visualize the tip clearance flow. Farge, Johnson, and Maksoud (1989) used five-hole pressure probes to obtain measurements in a 1-m-diameter shrouded impeller that rotated at 500 rpm. A clearance gap was left between the blade tip and the impeller shroud in order to generate a tip clearance flow. However, as the authors point out, there was no relative motion between the blade and the shroud, so the physics of the tip clearance flow in their investigation is not the same as it would be in an unshrouded impeller. Fagan and Fleeter (1991) used laser anemometry to measure all three velocity components in a low-speed, shrouded, mixed-flow compressor.

NASA Lewis Research Center's low-speed centrifugal compressor (LSCC) was built so that detailed experimental measurements suitable for assessing the capabilities of three-dimensional Navier-Stokes codes could be made within an unshrouded centrifugal compressor impeller. The experimental configuration consisted of a backswept impeller followed by a vaneless diffuser. The rotor was designed for axial inlet flow, so inlet guide vanes were not required. The resulting rotor-only configuration enabled us to compare the laser anemometer data with results from numerical flow analysis codes that assume a steady flow in the reference frame of the rotor. In addition, the large size and low speed of the compressor generated large viscous regions, which enabled us to measure near-wall details with laser anemometry. The result was an excellent experimental data base with which to compare the results of three-dimensional viscous flow analysis codes.

A conventional pneumatic probe surveyed the spanwise distributions of total and static pressures, total temperature, and flow yaw angle at stations upstream and downstream of the rotor. These probe survey data were used to calculate overall compressor performance. Both the pneumatic probe data and performance data are included in tables herein and can be used to set boundary conditions for computational codes.

Laser anemometer surveys were conducted along axisymmetric surfaces of revolution that were constructed from a CFD grid-generation routine so as to be approximately orthogonal to the casing and hub flow paths. There were nominally 20 survey planes upstream, within, and downstream of the rotor. At each survey plane the data were acquired, nominally, at 15 spanwise locations in intervals of 5-percent-of-span from the shroud. At each survey point, the axial, radial, and relative tangential velocity components were measured and recorded on a magnetic medium at a resolution of 1000 points

per rotor blade pitch. However, for presentation purposes and to provide more manageable data sets, the data were routinely averaged to a resolution of 200 points per rotor blade pitch.

To keep the size of this report manageable, all laser data are presented in plotted form. For all measurement planes, the pitchwise distributions of axial, radial, and relative tangential velocity were normalized by the rotor exit tip speed, as were the wire-frame and contour plots of throughflow velocity and the vector plots of secondary velocity.

Detailed descriptions of the blade and flow path geometry, as well as a complete set of the laser anemometer survey data, are available on magnetic medium upon request. A complete description of the data format is given in appendix A. Symbols used in this report are defined in appendix B.

This report describes in detail the data acquired and also discusses measurement uncertainty. No attempt was made herein to compare our data to computational results or to use the data to study detailed flow physics. An experimental and computational investigation of the development of the characteristic throughflow momentum wake in centrifugal compressors is available in the literature (Hathaway et al. (1993) and Chriss, Hathaway, and Wood (1994)).

## Apparatus

### Low-Speed Centrifugal Compressor Facility

The LSCC is designed to duplicate the flow fields of a high-speed subsonic centrifugal compressor in a large low-speed machine. Thus the essential flow physics of the flow field can be investigated in detail. A schematic diagram of the LSCC facility is shown in figure 1.

Air is drawn into the facility room through a filtered vent in the roof and then past a bank of steam pipes and louvers designed to control the air temperature to within  $\pm 1$  °F for mass flows up to 45 kg/sec. The facility room air is then drawn into the plenum through a bank of air straighteners contained between two mesh screens. Next, the air passes through a specially designed bellmouth with a 10:1 area contraction. From there it flows into the compressor and exits through a specially designed throttle valve at the entrance to the collector. The throttle valve consists of two concentric overlapping rings with holes that have been drilled in each ring and that slide relative to each other to produce a throttle. This valve design was chosen to minimize circumferential asymmetry in the static pressure distribution at the exit, such as is typically found in scroll-type collectors. The bellmouth, inlet transition piece, and shroud flow path were machined together to minimize any boundary layer disturbance that might be caused by a step in the flow path. A complete description of the facility is provided by Wood, Adam, and Buggele (1983) and Hathaway, Wood, and Wasserbauer (1992).

## Test Rotor

The test impeller (see fig. 2) is a backswept impeller with a design tip speed of 153 m/sec. The impeller is followed by a vaneless diffuser that generates an axisymmetric outflow boundary condition, which is desirable for CFD analysis of an isolated blade row. The original vaneless diffuser was modified to eliminate a region of reverse flow that occurred on the back wall of the diffuser (Hathaway, Wood, and Wasserbauer (1992)). This modification ensured that there would be no backflow at stations downstream of the impeller. The impeller has 20 full blades with a backsweep of 55°. The inlet diameter is 0.870 m and the inlet blade height is 0.218 m. The exit diameter is 1.524 m and the exit blade height is 0.141 m. The clearance between the impeller blade tip and the shroud is a constant 2.54 mm from the impeller inlet to the impeller exit. This clearance is 1.8 percent of the blade height at the exit of the impeller. The blade surfaces are composed of straight-line elements from hub to tip. This feature allowed the laser anemometer optical axis to be directed parallel to the blade surface, thereby facilitating laser anemometer measurement of velocities close to the blade surfaces. The impeller surface finish is 64  $\mu\text{m}$ . rms and the fillet radii are 9.525 mm.

Blade coordinates at the design speed operating condition are given in table I for six blade sections (surfaces of revolution) from hub to tip (i.e., blade section six is the physical blade tip). The nomenclature used in table I is shown in figure 3. The origin of all blade geometry  $z$ -coordinates is at the intersection of the blade leading edge with the hub. The blade surface coordinates provided in table I are given at 75 points for each blade section and include definition of the blade leading and trailing edges.

Figure 4 shows profiles of three actual (as inspected) blade tips: one for the LSCC and two from high-speed impellers scaled to the same dimensions.

## Flow Path

A meridional view of the LSCC flow path, which includes the locations of the aerodynamic probe survey stations and the vaneless diffuser hub and shroud contractions, is shown in figure 5; the coordinates of the hub and shroud contours are provided in table II. The origin of both the blade and the flow path  $z$ -coordinates is at the intersection of the blade leading edge with the hub flow path.

Figure 6 shows the spanwise and streamwise locations at which laser anemometer data were acquired, with arrows denoting the locations where such measurements were made at both design and off-design conditions. The station numbers are the streamwise indices of a body-fitted measurement grid that was used to position the laser measurement point within the impeller. The measurement grid used in this investigation divided the streamwise blade length into a series of quasi-orthogonal, or near-normal, cross-channel planes.

## Instrumentation

**Pneumatic probes.**—Spanwise probe traverses were available at stations upstream and downstream of the rotor (see fig. 5). Five-hole probes with self-nulling yaw capability (fig. 7) were used for all standard pneumatic probe surveys. These probes were calibrated in a steady flow duct in which the pressure and temperature could be accurately controlled. During calibration, the probe pitch angle was varied over a range of Mach numbers, and the results were used together with the five-hole probe measurements acquired in the compressor to extract total and static pressures and the pitch angle. Before a probe was installed in the compressor test rig, a check on the pitch and swirl aerodynamic zero angle was performed in a calibration jet.

**Surface static pressure taps.**—Static pressure taps were provided along the shroud and rotor blade surfaces. Those on the rotor surface (see fig. 8) measured the rotor blade pressure distribution and provided the opportunity for ammonia-ozalid flow visualization. They were located along quasi-orthogonal measurement planes at nominally 5, 20, 50, 80, 93, and 97 percent of blade span from the hub. The quasi-orthogonal measurement planes were located at approximately 2.5, 5, 15, 30, 50, 70, 90, 95, and 98 percent of meridional distance. Table III gives the  $r, z$  coordinates of the center of each static pressure tap on the rotor blade surfaces. The  $r, z$  coordinates of the centers of each shroud static pressure tap are given in table IV.

**Laser anemometer system.**—The laser anemometer system used for the present investigation was a two-component laser fringe anemometer operating in on-axis backscatter mode. An argon-ion laser produced the 514.5-nm (green) and 488-nm (blue) wavelengths for the two orthogonal fringe systems. Frequency shifting was used in both fringe systems to provide directional sensitivity for all velocity measurements. Because of the size of the compressor, a relatively long focal length of 733 mm was needed. The final focusing lens aperture was 155 mm. Beam expansion (3.75 $\times$ ) enhanced the system signal-to-noise ratio. The fringe spacing was 8.2 nm for the blue component and 8.6 nm for the green component.

Optical access to the flow field was provided by three 3-mm-thick glass windows that conformed to the flow path in both the circumferential and streamwise directions (see fig. 9). The windows covered the inlet, knee, and exit regions of the impeller and the inlet of the vaneless diffuser. The window mounting frames prevented laser anemometer measurements from being made in four areas: ahead of station 18; between stations 95 and 110; between stations 135 and 156; and downstream of station 188 (see fig. 6).

Polystyrene latex (PSL) spheres, used as seed particles, were introduced into the flow stream via four spray nozzles located in the plenum. During the development of the seeding system, an aerodynamic particle sizer was used to ensure that the seeding system could deliver mono-disperse particles and that the liquid carrier was fully evaporated by the time the seed

material arrived at the compressor inlet. In each batch of PSL seed solution produced, the seed particles were near-perfect spheres, varying by less than 0.1 percent of diameter. All tests were conducted with PSL particles no larger than 1.1  $\mu\text{m}$  nor smaller than 0.8  $\mu\text{m}$ . Figure 10 shows a typical particle size distribution acquired by the aerodynamic particle sizer at the inlet of the rotor. Further details of the instrumentation, laser anemometer system, and seeding system can be found in Hathaway et al. (1993) and Wasserbauer and Hathaway (1993).

## Test Procedure

The research operating point (flow rate and rotor speed) selected for the data presented herein was the National Advisory Committee on Aeronautics (NACA) standard-day sea-level-corrected condition of 30.0 kg/sec and 1862 rpm, which is near the design point condition. Additional data were acquired at the same rotor speed but a lower flow rate (off-design condition) of 23.6 kg/sec (i.e., 78.7-percent  $\dot{m}_d$ ).

The corrected mass flow and rotor rotational speed were continually monitored and adjusted as required to maintain a constant operating point. As data were acquired, the results were corrected to account for any changes in plenum conditions due to changes in atmospheric conditions.

## Performance Measurements

The plenum total temperature was calculated from the area average of measurements from 10 thermocouples located along the leading edge of an aerodynamically shaped horizontal strut that spanned the plenum. The plenum total pressure was measured by a pitot probe located at approximately midspan of the strut leading edge; it was checked against the average of four static pressure taps equally spaced around the circumference of the plenum. Mass flow was determined from a calibration curve of actual bellmouth mass flow (based on integrated pressure probe surveys at the bellmouth throat) versus theoretical mass flow (based on the average of eight static pressure taps equally spaced around the circumference of the bellmouth throat), together with the plenum total pressure and temperature.

Spanwise surveys of total and static pressures, total temperature, swirl (yaw) angle, and pitch angle were conducted at survey stations 1 and 2 (upstream and downstream of the rotor, respectively), as shown in figure 5. All spanwise surveys were conducted with self-nulling-yaw five-hole pressure probes with attached thermocouples (see fig.7). At stations 1 and 2, measurements were acquired at approximately 20 spanwise locations, and the endwall boundary layers were resolved to within 1-percent-of-span from the endwalls. Inner- and outer-wall static pressures were also measured at stations 1 and 2.

The overall pressure ratio was calculated from the plenum total pressure and the energy-average of the spanwise distribution of total pressure at survey station 2. Efficiency was calcu-

lated from torque measurements since the small temperature rise of the LSCC impeller caused a significant uncertainty in temperature-based efficiency. For some surveys, efficiency calculations were based on the plenum total temperature and the mass-average of the spanwise distribution of total temperature at survey station 2. Details of the averaging procedures used for overall total pressure and total temperature, as well as the calculation of efficiency, are given in the subsequent **Calculations Procedures** section.

## Laser Anemometer Measurements

Laser anemometer measurement locations are specified in  $r, \theta, z$  and  $W_n$  coordinates (see fig.3). The  $r, \theta, z$  coordinates are locations in the laboratory frame of reference, whereas the  $W_n$  coordinate is in the rotor frame of reference according to coordinates of a body-fitted measurement grid. The measurement grid used in this investigation divided the streamwise blade length into a series of quasi-orthogonal, or near-normal, cross-channel planes.

The circumferential location of each individual velocity measurement acquired by the laser anemometer was determined by using two digital shaft angle encoders (one for each laser anemometer channel) to generate a fixed number of pulses for each rotor revolution. The encoders were frequency agile pulse generators whose frequency was digitally phase-locked to a multiple of the frequency of a once-per-revolution signal from the rotor. The encoder pulses were accumulated in a counter that was zeroed at the start of each rotor revolution. When a laser velocity measurement occurred, the concurrent encoder count was recorded along with the velocity data. The encoder count thus indicated the circumferential location of the measurement relative to the once-per-revolution timing mark on the impeller. Measurements that occurred anywhere between two adjacent encoder counts were assigned to the same measurement window  $W_n$ . Here  $W_n$  denotes, in the rotor frame of reference, the circumferential measurement location in window counts relative to the local blade suction surface. Further details of this process are described by Strazisar et al. (1989) and Wood, Strazisar, and Hathaway (1990).

The width of a window defined the minimum spatial resolution of the data in the circumferential direction. It was, therefore, advantageous to select the smallest window width possible while maintaining a reasonable total number of windows. In the present investigation, the encoders were set to generate 20 000 pulses for each rotor revolution. The circumferential location of the center of each laser anemometer measurement window was therefore known to a resolution of 1000 windows across each of the 20 impeller blade channels. However, to produce a data set that would be more manageable and meet the needs of most users, the data were routinely averaged across adjacent windows to produce a resolution of 200 measurement windows per blade channel. These velocity data were then passage-averaged (see **Calculation Procedures**) across the 20 blade channels to yield a single velocity profile that was

representative of the velocity profile across each individual blade passage (all the passages were assumed to be identical). All of the data presented in this report are based on passage-averaged velocity distributions.

All of the laser anemometer measurements were acquired in coincidence mode with a coincidence window width of 8  $\mu$ sec, which ensured that velocity data were recorded only if a velocity measurement occurred in both the blue and green fringe systems within 8  $\mu$ sec of one another. Since the time interval between each of the 200 pitchwise measurement points was also 8  $\mu$ sec, we are confident that all measured velocity components occurred in the same circumferential measurement interval.

An inhibiting circuit driven by the shaft angle encoders was used to interrupt the laser anemometer signal processor while an impeller blade was in the measurement volume. This was done so that light scattered from the blade surface would not trigger a laser anemometer measurement. Without the inhibiting circuit, approximately 80 percent of the acquired data would have been triggered by light scattered from the blade surface.

In most regions of the flow field, 50 000 velocity measurements were acquired at each of the laser anemometer locations shown in figure 6. This would yield an average of 250 measurements at each of the 200 points in the ensemble-averaged velocity distribution if the measurements were evenly distributed across the blade pitch. In reality, since the rate at which the seed particles arrive at the laser anemometer volume measurement location is directly tied to the streamwise momentum, the number of measurements acquired per unit time can vary considerably across the pitch. In order to acquire at least 100 to 200 measurements at each of the 200 pitchwise points in the ensemble-averaged velocity distributions that cut across low-momentum regions, we had to acquire as many as 200 000 measurements for a given spanwise and streamwise measurement location.

At each measurement point in the flow field, the laser anemometer optical axis was directed into the compressor at an azimuth angle  $\zeta$  (see fig. 11). The angle  $\zeta$  ranged from 90° at the impeller inlet to 0° at the impeller exit. Although the blades were designed as straight-line elements from hub to tip, there was considerable blade-lean away from the meridional plane in some regions of the impeller. In order to obtain velocity measurements near the blade surfaces at any azimuth angle  $\zeta$ , the optical axis could be deflected out of the meridional plane by a declination angle  $\eta$  (see fig. 12). The probe volume  $x, y, z$ -location and the optical axis orientation angles  $\zeta$  and  $\eta$  could all be varied independently.

For a given ( $\zeta, \eta$ ) orientation of the laser anemometer optical axis, two velocity components were measured in a plane perpendicular to the optical axis by the blue and green fringe systems. In order to determine all three components of the total velocity at a point in the flow field, measurements were acquired at two different  $\zeta$  orientations of the optical axis for each measurement point. At each  $\zeta$ , the  $\eta$  was oriented such

that the optical axis was tangent to the blade surface, thus minimizing optical blockage. In order to maintain measurement accuracy, the two optical axis orientations used at each point were generally separated by 20° to 30°. As a result, four measurements were available (blue and green optical axes at each of two ( $\zeta, \eta$ ) orientations) for use in calculating the three orthogonal components of the total velocity vector. However, since only three measurements were needed, the calculated total vector was over-specified. We chose to use the information from all four measurements and applied a least-squares fit to all four velocity component measurements to calculate the three-components of the total velocity vector (see **Calculation Procedures**).

The aforementioned measurement technique was developed in order to measure the spanwise velocity at any point in the flow field, since the spanwise velocity had not been measured by most previous laser anemometer investigations in centrifugal compressors. The accuracy of this technique in measuring the spanwise velocity component was verified at the upstream aerodynamic survey station (station 23 in fig. 6) by comparing axisymmetric-averaged pitch angles derived from the laser anemometer measurements to those derived from five-hole probe measurements. The pitch angle is defined as  $\alpha = \tan^{-1}(V_r/V_z)$ , where  $V_r$  and  $V_z$  are the radial and axial velocity components respectively. Note that the spanwise velocity component must be accurately measured in order to accurately measure the pitch angle, but it cannot be measured when the laser anemometer optical axis is directed along the span. The results of this exercise are shown in figure 13. The five-hole probe measurements of pitch angle vary smoothly in the spanwise direction from 0° at the shroud to 21° at the hub, which is the pitch angle of the rotor spinner surface. The laser measurements tend to depart from the five-hole probe measurements at lower spans; this is probably due to the curved window altering the laser beam paths and thereby distorting the laser measurement volume. However, the agreement between the laser and the five-hole-probe measurements of the pitch angle is better than 2° over the outer 70 percent of the span (20 cm immersion). These results indicate that the laser measurement technique is capable of accurately measuring the relatively small pitch angles near the shroud, and they give us confidence that with this technique we can accurately measure the spanwise velocity component.

## Flow Visualization

Flow direction on the blade surfaces was visualized by the ammonia-Ozalid technique described by Joslyn and Dring (1987). Ammonia gas was leaked into the flow stream through existing static pressure taps on the blade surfaces via a pneumatic slip ring. A remotely actuated pressure regulator controlled the rate of ammonia leakage into the flow stream, and a strobe light and camera monitored the process through the laser windows. Wherever the ammonia contacted a 25.4-mm-wide strip of 0.001-mm-thick Ozalid paper taped immediately

adjacent to and downstream of the static tap, a blue streak marking the flow direction resulted. The Ozalid paper was taped parallel to quasi-orthogonal lines scribed on the blade surfaces. Knowing the orientation of the scribe lines, we could determine the pitch orientation of the resultant ammonia traces.

## Calculation Procedures

All of the data presented herein were corrected to NACA standard-day sea-level conditions ( $t_{std} = 288.2$  K;  $p_{std} = 101\,325$  N/m<sup>2</sup>) at the plenum.

### Performance Measurements

Rotor overall performance was based on plenum total pressure, bellmouth mass flow, torque, and the five-hole probe measurements acquired at station 2, downstream of the rotor. The bellmouth mass flow was corrected to standard-day conditions at the plenum. The spanwise distributions of total temperature were mass-averaged across the span. The spanwise distributions of total pressure were energy-averaged by converting them to their enthalpy equivalents and then mass-averaging them across the span. The formulas used were

$$\left. \begin{aligned}
 \bar{T}_j &= \frac{\sum_{i=1}^{NS_j} T_{j,i} \rho_{j,i} (V_n)_{j,i} (\Delta A)_{j,i}}{\sum_{i=1}^{NS_j} \rho_{j,i} (V_n)_{j,i} (\Delta A)_{j,i}} \\
 \frac{\bar{P}_j}{P_o} &= \left[ \frac{\sum_{i=1}^{NS_j} \left( \frac{P_{j,i}}{P_o} \right)^\gamma \rho_{j,i} (V_n)_{j,i} (\Delta A)_{j,i}}{\sum_{i=1}^{NS_j} \rho_{j,i} (V_n)_{j,i} (\Delta A)_{j,i}} \right]^{\frac{\gamma}{(\gamma-1)}} \\
 \eta_{ad} &= \frac{\left[ \left( \frac{\bar{P}_2}{P_o} \right)^\gamma - 1 \right]}{\frac{\bar{T}_2}{T_o} - 1} \\
 \eta_\Gamma &= \frac{mR\gamma T_o \left[ \left( \frac{\bar{P}_2}{P_o} \right)^\gamma - 1 \right]}{N(\Gamma - \Gamma_{tare})(\gamma - 1)}
 \end{aligned} \right\} \quad (1)$$

$$\left. \begin{aligned}
 T_{2,i} &= T_o \frac{\left[ \left( \frac{P_{2,i}}{P_o} \right)^\gamma + (\eta_{2,i} - 1) \right]}{\eta_{2,i}} \\
 V_{2,i} &= \sqrt{2c_p T_{2,i} \left[ 1 - \left( \frac{P_{2,i}}{P_{2,i}} \right)^\gamma \right]} \\
 V_{\theta_{2,i}} &= V_{2,i} \cos(\alpha_{2,i}) \sin(\beta_{2,i}) \\
 T_{2,i} &= T_o + \frac{U_{2,i} V_{\theta_{2,i}}}{c_p} \\
 \eta_{2,i} &= \frac{\left[ \left( \frac{P_{2,i}}{P_o} \right)^\gamma - 1 \right]}{\frac{T_{2,i}}{T_o} - 1}
 \end{aligned} \right\} \quad (2)$$

where  $i$  refers to the  $i$ th spanwise measurement location from the hub;  $j$  refers to the station number (1 is upstream of the rotor, 2 is downstream);  $\Delta A$  is the incremental flow area;  $V_n$  is the velocity component normal to  $\Delta A$  ( $V_n = V_z$  upstream of the rotor and  $V_n = V_r$  downstream of the rotor);  $P_o$  and  $T_o$  are the plenum total pressure and temperature, respectively; and  $NS$  is the number of survey locations across the span. Typically, measurements were acquired at 20 or more survey locations across the span, and the endwall boundary layers were resolved to within 1 percent of the span.

The tare torque  $\Gamma_{tare}$  that was used to calculate the torque-based efficiency  $\eta_\Gamma$  was determined from torque measurements with a bare aluminum rotor (smooth rotor hub contour without blades) operating at 1862 rpm without a shroud. The tare torque represents the torque required to overcome all drag forces not associated with the aerodynamic blade pressure loading (e.g., bearing friction, rotor drum windage, etc.). The tare torque was subtracted from the measured torque in order to determine the actual torque required to drive the compressor against the aerodynamic blade pressure loading.

After aerodynamic testing was completed, we discovered that the downstream total temperature sensor was broken and thus provided a false total temperature. The total temperature was, therefore, determined iteratively by using the Euler energy equation and assuming adiabatic flow conditions:

Here axial inlet flow is assumed;  $T_o$  is the plenum total temperature; and  $\eta_{2,i} = 1.0$  was initially assumed. No attempt was made to account for the loss in the vaneless space up to the measurement station. The accuracy of this estimated total temperature at the rotor exit was checked against measurements acquired (Hathaway, Wood, and Wasserbauer (1992)) before the diffuser hub contour was modified (see fig. 14). Figure 14, which compares the Euler-based temperature with the measured temperature, indicates that the Euler temperature is within  $\pm 0.4$  percent of the measured temperature, and thus within the measurement uncertainty, except near the hub.

### Rotor Blade Static Pressure Measurements

The rotor blade static pressures were measured in the rotating frame of reference by piezoelectric pressure sensors located near the rotor centerline. The pressure sensors were connected by pneumatic tubing to their corresponding static pressure taps on the blade surface. Since the column of air in the pneumatic tubing was subjected to centrifugal head effects, the pressure measured by the pressure sensor had to be corrected to account for the "head" term. The pressure for each static pressure tap was corrected as follows (Fagan and Fleeter (1991)):

$$\frac{p_i}{p_{sen}} = \exp\left[\frac{\omega^2}{2Rt_i}(r_i^2 - r_{sen}^2)\right] \quad (3)$$

where  $\omega$  is the rotational speed in radians per second;  $r_i$  is the radius of  $i$ th static tap;  $r_{sen}$  is the radius of the pressure sensor located near the rotor centerline;  $p_{sen}$  is the pressure measured by the pressure sensor;  $p_i$  is the pressure at the radius of the  $i$ th static tap;  $t_i$  is the temperature of the air in the pneumatic tubing corresponding to the  $i$ th static tap; and  $R$  is the universal gas constant for air. The temperature of the air in the pneumatic tubing was assumed equal to the temperature of the air in the rotor channel at the static tap location. And the temperature of the air at the static tap location was estimated as the temperature that would be calculated from isentropic energy addition:

$$t_i = T_o \left(\frac{p_i}{P_o}\right)^{\frac{(\gamma-1)}{\gamma}} \quad (4)$$

The preceding two equations were iterated until  $t_i$  changed by less than 0.001 percent.

The assumed temperature of the air in the pneumatic tubing (taken to be equal to the temperature of the air in the rotor channel at the static tap location) was compared with various estimated linear and quadratic temperature distributions along the tube. The differences in  $p_i$  as determined with the assumed temperature were estimated to be less than  $\pm 0.5$  percent.

### Laser Anemometer Measurements

The laser anemometer velocity measurements acquired along a line that passes through a given axial and radial ( $z, r$ ) location can be represented by the following array:

$$V_f(i, j) \quad (5)$$

for  $i = 1, 2, \dots, NM(j)$  and  $j = 1, 2, \dots, NWN * NP$  and where  $V_f(i, j)$  is the  $i$ th measurement of the velocity component in the fringe normal direction in window  $j$ , and  $NM(j)$  is the number of measurements acquired in window  $j$ . The total number of measurement windows is  $NWN * NP$ , where  $NWN$  is the number of measurement windows across one rotor pitch, and  $NP$  is the number of rotor blade passages that were surveyed. As mentioned previously, for all of the data reported herein,  $NWN = 200$  and  $NP = 20$ .

The velocities can be corrected to standard-day conditions by using the relation

$$V_{fc}(i, j) = V_f(i, j) \sqrt{\frac{t_{std}}{T_o}} \quad (6)$$

where  $V_{fc}$  and  $V_f$  are the corrected and uncorrected velocities, respectively, and  $t_{std}$  and  $T_o$  are the standard-day and plenum total temperatures, respectively. The  $c$  subscript notation will be dropped in the following discussion for simplicity; however, all velocities should be understood to be standard-day corrected.

**Ensemble-averaging.**—The mean and standard deviation of the velocity measurements acquired within each measurement window were calculated as follows:

$$\bar{V}_f(j) = \frac{1}{NM(j)} \sum_{i=1}^{NM(j)} V_f(i, j) \quad (7)$$

for  $j = 1, 2, \dots, NWN * NP$

$$V_f'(j) = \left[ \frac{1}{NM(j) - 1} \sum_{i=1}^{NM(j)} (V_f(i, j) - \bar{V}_f(j))^2 \right]^{1/2}$$

for  $j = 1, 2, \dots, NWN * NP$ , where  $\bar{V}_f(j)$  and  $V_f'(j)$  are, respectively, the circumferential distributions of the ensemble-averaged velocity component and the rms unsteadiness in the fringe normal direction across each of the  $NP$  blade passages surveyed. The ensemble-averaging period was one rotor revolution.

**Least-squares fit.**—As mentioned in the **Test Procedure** section, measurements obtained at four different fringe orientations were used to calculate the axial, radial, and tangential components of velocity. The measured ensemble-averaged fringe normal velocity components were least-squares fit to the total ensemble-averaged velocity vector as follows:

$$\begin{aligned}\epsilon_n(j) &= \vec{\bar{V}}(j) \cdot \hat{f}_n - \bar{V}_{f_n}(j) \\ &= \bar{u}(j)f_{x_n} + \bar{v}(j)f_{y_n} + \bar{w}(j)f_{z_n} - \bar{V}_{f_n}(j)\end{aligned}\quad (8)$$

for  $j = 1, 2, \dots, \text{NWN} \cdot \text{NP}$ . Here  $\epsilon_n(j)$  is the error between the projection of the least-squares estimate of the total ensemble-averaged velocity vector  $\vec{\bar{V}}(j) = (\bar{u}(j), \bar{v}(j), \bar{w}(j))$  in the fringe normal direction  $\hat{f}_n = (\hat{f}_{x_n}, \hat{f}_{y_n}, \hat{f}_{z_n})$  and the measured ensemble-averaged velocity component in the fringe normal direction  $\bar{V}_{f_n}(j)$ , where  $n$  denotes the  $n$ th fringe orientation, and  $j$  denotes the  $j$ th window number. The least-squares estimate of the total ensemble-averaged velocity vector was then determined by minimizing the sum of the square of the errors between the total ensemble-averaged velocity component in the fringe normal direction and the measured ensemble-averaged velocity component in the fringe normal direction as follows:

$$\begin{aligned}\frac{\partial \sum_{n=1}^4 \epsilon_n^2(j)}{\partial \vec{\bar{V}}(j)} &= \frac{\partial \left[ \sum_{n=1}^4 \left( \vec{\bar{V}}(j) \cdot \hat{f}_n - \bar{V}_{f_n}(j) \right)^2 \right]}{\partial \vec{\bar{V}}(j)} \\ &= \begin{bmatrix} \frac{\partial \sum_{n=1}^4 \epsilon_n^2(j)}{\partial \bar{u}(j)} \\ \frac{\partial \sum_{n=1}^4 \epsilon_n^2(j)}{\partial \bar{v}(j)} \\ \frac{\partial \sum_{n=1}^4 \epsilon_n^2(j)}{\partial \bar{w}(j)} \end{bmatrix} = 0, \quad j = 1, 2, \dots, \text{NWN} \cdot \text{NP}\end{aligned}\quad (9)$$

This results in the following three equations, which can be solved simultaneously for the three unknowns  $(\bar{u}(j), \bar{v}(j), \bar{w}(j))$  that describe the least-squares estimate of the total ensemble-averaged velocity vector in window  $j$ :

$$\begin{bmatrix} \sum_{n=1}^4 f_{x_n}^2 & \sum_{n=1}^4 f_{x_n} f_{y_n} & \sum_{n=1}^4 f_{x_n} f_{z_n} \\ \sum_{n=1}^4 f_{x_n} f_{y_n} & \sum_{n=1}^4 f_{y_n}^2 & \sum_{n=1}^4 f_{y_n} f_{z_n} \\ \sum_{n=1}^4 f_{x_n} f_{z_n} & \sum_{n=1}^4 f_{y_n} f_{z_n} & \sum_{n=1}^4 f_{z_n}^2 \end{bmatrix} \begin{bmatrix} \bar{u}(j) \\ \bar{v}(j) \\ \bar{w}(j) \end{bmatrix} = \begin{bmatrix} \sum_{n=1}^4 \bar{V}_{f_n} f_{x_n} \\ \sum_{n=1}^4 \bar{V}_{f_n} f_{y_n} \\ \sum_{n=1}^4 \bar{V}_{f_n} f_{z_n} \end{bmatrix}\quad (10)$$

The ensemble-averaged velocity components in cylindrical coordinates were determined as follows:

$$\left. \begin{aligned}\bar{V}_r(j) &= \bar{u}(j) * \cos(\theta) + \bar{v}(j) * \sin(\theta) \\ \bar{V}_\theta(j) &= \bar{v}(j) * \cos(\theta) - \bar{u}(j) * \sin(\theta) \\ \bar{V}_z(j) &= \bar{w}(j)\end{aligned}\right\} \quad (11)$$

As a check of the least-squares method, the least-squares estimate of the calculated total ensemble-averaged velocity vector was projected in each of the four measured fringe normal directions and compared to the measured components in each of the respective fringe normal directions. The difference was generally less than 2 percent of the measured component.

**Passage-averaging.**—The circumferential distributions of  $\bar{V}_r$ ,  $\bar{V}_\theta$ , and  $\bar{V}_z$  across each rotor blade passage can be used to assess passage-to-passage variations in the ensemble-averaged flow field. However, our data set was quite large since there were  $\text{NWN} \cdot \text{NP} = 200 \cdot 20 = 4000$  data points along the measurement line through each  $(r, z)$  survey point shown in figure 6. NASA Lewis will provide this unaveraged-passage data in ASCII format upon request.

To arrive at a more compact data set that would meet the needs of most users, the measurements acquired in each of the NP blade passages surveyed were averaged across all the measured blade passages to yield a passage-averaged circumferential velocity distribution. The passage-average was formulated as follows:

$$\left. \begin{aligned}\bar{\bar{V}}_r(k) &= \frac{1}{\text{NP} - \text{NZ}} \sum_{j=1}^{\text{NP}} \bar{V}_r[k + (j-1) * \text{NWN}] \\ \bar{\bar{V}}_\theta(k) &= \frac{1}{\text{NP} - \text{NZ}} \sum_{j=1}^{\text{NP}} \bar{V}_\theta[k + (j-1) * \text{NWN}] \\ \bar{\bar{V}}_z(k) &= \frac{1}{\text{NP} - \text{NZ}} \sum_{j=1}^{\text{NP}} \bar{V}_z[k + (j-1) * \text{NWN}]\end{aligned}\right\} \quad (12)$$

for  $k = 1, 2, \dots, \text{NWN}$ , where NZ is the number of blade passages in which no measurements were acquired in window  $k$ .

After looking at the normalized difference

$$\frac{\tilde{V}(k) - \bar{V}[k + (j-1) * \text{NWN}]}{\tilde{V}(k)} \quad (13)$$

where  $\tilde{V}(k)$  is the passage-averaged velocity at any pitchwise location  $k$ , and  $\bar{V}[k + (j-1) * \text{NWN}]$  is the ensemble-averaged velocity in blade passage  $j$  at the same pitchwise location, we found this difference to be a maximum of 1 percent. This indicates that the passage-averaging process does not appreciably alter any details of the blade-to-blade velocity profile.

**Velocity triangle components.**—Values of  $\tilde{V}_r$ ,  $\tilde{V}_\theta$ , and  $\tilde{V}_z$  were used as follows to calculate passage-averaged absolute, relative, and meridional velocities, and swirl and pitch angles:

$$\left. \begin{aligned} \tilde{V}(k) &= \sqrt{[\tilde{V}_r(k)]^2 + [\tilde{V}_\theta(k)]^2 + [\tilde{V}_z(k)]^2} \\ \tilde{W}(k) &= \sqrt{[\tilde{V}_r(k)]^2 + [\tilde{V}_\theta(k) - r\omega]^2 + [\tilde{V}_z(k)]^2} \\ \tilde{V}_m(k) &= \sqrt{[\tilde{V}_r(k)]^2 + [\tilde{V}_z(k)]^2} \\ \beta_{\text{rel}}(k) &= \arctan \left[ \frac{\tilde{V}_\theta(k) - r\omega}{\tilde{V}_m(k)} \right] \\ \alpha(k) &= \arctan \left[ \frac{\tilde{V}_r(k)}{\tilde{V}_z(k)} \right] \end{aligned} \right\} \quad (14)$$

for  $k = 1, 2, \dots, \text{NWN}$ , where  $r$  is the local radius and  $\omega$  is the rotor rotational speed in radians per second.

Hereafter, all velocity components will be assumed to be the passage-average of ensemble-averaged results, and therefore, the overbar and tilde will be dropped from subsequent velocity component designations.

**Throughflow and secondary velocity calculations.**—In order to visualize secondary flow, we must view the total relative velocity vector along the streamwise direction. However, in a geometrically complex channel such as a centrifugal impeller blade passage, the streamwise direction can be defined in several different ways, each of which yields a slightly different result for the secondary flow. This problem has been pointed out by many previous authors. The following discussion will document the procedure used to generate the secondary flow field results presented in this report.

The secondary flows presented herein are defined as the departure of the local relative velocity vector from the local streamwise grid direction as defined by a body-fitted measure-

ment grid (refer to fig. 15). The measurement grid used in this investigation divided the streamwise blade length into a series of quasi-orthogonal, or near-normal, cross-channel planes. The secondary velocity vector  $\vec{W}_s(k)$  for any given window  $k$  (hereafter we shall drop the  $k$  denoting window number) is given by  $\vec{W}_s = \vec{W} - \vec{W}_{st}$ , where  $\vec{W}$  is the total relative velocity vector and  $\vec{W}_{st} = (\vec{W} \cdot \hat{g}_{st}) * \hat{g}_{st}$  is the projection of  $\vec{W}$  in the local streamwise grid direction  $\hat{g}_{st}(r, \theta, z)$ . The spanwise and pitchwise components of the secondary velocity vector,  $W_{sp}$  and  $W_p$ , respectively, are the projections of the secondary velocity vector in the local spanwise and pitchwise grid directions:

$$\begin{aligned} W_{sp} &= \vec{W}_s \cdot \hat{g}_{sp} \\ W_p &= \vec{W}_s \cdot \hat{g}_p \end{aligned} \quad (15)$$

where  $\hat{g}_{sp}$  and  $\hat{g}_p$  are unit vectors in the local spanwise and pitchwise grid directions. When secondary flow results are presented in the form of vector plots in a quasi-orthogonal plane,  $W_{sp}$  and  $W_p$  are used to determine the magnitude and direction of the plotted secondary velocity vectors.

The procedure just described was applied at each measurement grid node. Thus, in a cross-channel vector plot of secondary velocity components, a flow field with no secondary flow components appears as a point at each grid node, indicating that the flow is following the streamwise grid direction. Since the local streamwise grid direction was parallel to the blade, hub, and shroud surfaces, the aforementioned definition of secondary flow also ensured that the secondary velocity was zero at all solid surfaces.

The throughflow velocity component  $V_T$  is the vector projection of the meridional velocity vector  $\vec{V}_m$  in the local streamwise meridional-plane grid direction:  $V_T = \vec{V}_m \cdot \hat{g}_m$ . Since a quasi-orthogonal plane is nearly normal to the streamwise grid direction at any station in the impeller,  $V_T$  is a close approximation to the throughflow velocity that crosses a quasi-orthogonal plane. It is also a close approximation to the streamwise velocity component measured by Krain (1988), Ahmed and Elder (1990), and Fagan and Fleeter (1991) in laser anemometer investigations. In these investigations, the streamwise velocity component was defined as the velocity component normal to the azimuthal angle  $\zeta$  of the laser anemometer optical axis, where  $\zeta$  was chosen to be normal to the local shroud direction.

## Results and Discussion

### Performance Measurements

Figure 16 is a plot of the impeller inlet axial velocity distributions normalized by the impeller exit tip speed  $U_t$  at design and off-design conditions. The distributions of impeller inlet total and static pressures (normalized by the reference pressure

$p_{std}$ ), along with pitch and yaw angles and Euler-based temperatures (normalized by the reference temperature  $t_{std}$ ), are provided in tables V and VI for the design and off-design conditions, respectively. These tables provide the necessary inlet boundary conditions for computational analyses of the LSCC flow field.

In this report aerodynamic performance data are presented for two operating conditions at 1862 rpm: at the design mass flow rate and at a lower flow rate. The location of these two points on the rotor operating line are shown in figure 17 along with additional aerodynamic performance measurements not reported in detail herein. The data shown in figure 17 are based on plenum total pressure, bellmouth mass flow, and aerodynamic survey measurements acquired at survey station 2 downstream of the rotor. The aerodynamic survey results obtained at station 2 for the design and off-design conditions are presented in tables VII and VIII, respectively. The overall rotor aerodynamic performance based on the energy-averaged total pressure ratio and the mass-averaged total temperature ratio at station 2, as well as the temperature- and torque-based performance, is shown at the bottom of each table.

### Surface Static Pressure Measurements

The rotor blade surface static pressures measured at design and off-design conditions are provided in tables IX and X, respectively, and they are plotted in figures 18 and 19 as a function of percent of meridional distance for each spanwise location. The static pressures shown in these tables and figures have been normalized by the reference pressure  $p_{std}$ . Figures 20 and 21 show contour plots of the blade surface static pressures normalized by  $p_{std}$  for design and off-design conditions, respectively. The locations of the static pressure taps (see table VIII) are indicated on the contour plots to aid in interpretation of the contours.

The shroud surface static pressures measured over a range of mass flows were normalized by the reference pressure  $p_{std}$  and are given in table XI. Figure 22 is a contour plot of these data. The locations where the shroud static pressures were measured are provided in table IV.

### Flow Visualization

Figure 23 shows the ammonia-Ozalid flow traces on the blades' pressure and suction surfaces at the design flow condition. The traces are arrows depicting the direction of flow. They were computer-generated from measurements of the orientation of the actual flow traces acquired in the experiment. Also noted in figure 23 are the laser anemometer survey stations and corresponding spanwise measurement locations nearest to the ammonia-Ozalid flow traces. The measured pitch angles of the ammonia-Ozalid flow traces are provided in table XII, and the method for determining them is described in the Flow Visualization subsection of the **Test Procedure** section.

### Laser Anemometer Measurements

Several features of the velocity measurements should be kept in mind when the laser anemometer data are being interpreted. First, the average of all the velocity measurements in a given window was often considered as a single velocity measurement at a point located in the center of the measurement window. It is important to remember that these measurements did not actually occur at a single point, but rather in a region centered about the plotted point. Second, although each individual velocity measurement was an instantaneous measurement of the unsteady velocity field, the measurements acquired in each measurement window were acquired over thousands of separate rotor revolutions. The average of all velocity measurements acquired in a given window was, therefore, the ensemble-averaged velocity at the window location (with the averaging period being one rotor revolution). Furthermore, the ensemble-averaged laser anemometer measurements for the same relative window location in each blade passage were averaged for all blade passages to produce a blade-to-blade distribution of passage-averaged velocities in each blade passage. Last, the three-dimensional velocity measurements were a result of combining measurements acquired independently for two separate orientations of the laser beam optical axis; therefore these measurements were not acquired concurrently, although they were acquired during the same run session.

Figures 24 to 46 and 47 to 51 are, respectively, plots of the pitchwise distributions of laser anemometer measurements, at design and off-design conditions, for selected stations through the impeller. Typically these data are plotted at 5-percent-of-span increments at a resolution of 200 points per pitch, proceeding from suction to pressure surface. For results acquired within the impeller, the blade is indicated by the cross-hatched region to the right of each plot.

Figures 52 to 74 and 75 to 79 are contour plots of laser-anemometer-measured throughflow velocity distributions for all stations through the impeller at design and off-design conditions, respectively.

Likewise, figures 80 to 102 and 103 to 107 are wire-frame plots of laser-anemometer-measured throughflow velocity distributions for all stations through the impeller at design and off-design conditions. These data are typically plotted at 5-percent-of-span increments at a resolution of 200 points per pitch.

Figures 108 to 130 and 131 to 135 are vector plots of laser-anemometer-measured secondary velocity distributions at design and off-design conditions, respectively. Data are plotted at 5-percent-of-span increments for all stations through the impeller. The page numbers of figures 24 to 135 are given in table XIII.

### Data Uncertainty and Reproducibility

*Aerodynamic probe measurements.*—The uncertainty of the aerodynamic probe measurements is indicated in table XIV.

The uncertainties are a best estimate based on precision, bias, and measurement repeatability. The precision of the measurement instruments is, of course, better than table XIV indicates. Nonrepeatability is the greatest contributor to the estimated uncertainties. Thus, the relative uncertainties are much smaller in the measurements comprising individual spanwise profiles, which were acquired at a particular operating condition without interruption of testing. However, the absolute level of the profile is less certain.

**Laser anemometer measurements.**—The uncertainty of the individual velocity component measurements was estimated from the least-squares calculation to be, on the average, approximately  $\pm 1.5$  m/sec throughout most of the impeller passage. Through much of the impeller passage, the throughflow velocity magnitude was on the order of 75 m/sec. Thus, the uncertainty of the measured velocity components is generally less than 2 percent of the throughflow component (except in regions of high unsteadiness, such as the throughflow wake).

The measured velocity components are subject to the uncertainties arising from window curvature, which distorts the laser anemometer probe volume. The uncertainties of the measured velocity components, in turn, propagate into the calculated velocity components. The spanwise velocity component and flow pitch angle are very susceptible to uncertainty propagation and most sensitive to window curvature. The uncertainty in pitch angle, which directly indicates the ability to resolve the spanwise velocity component, is estimated from figure 13 to be less than  $\pm 2^\circ$  for measurement locations in the outer 70 percent of blade span (i.e., for all measurement stations up to and in-

cluding station 135). Because window curvature and blade span both decrease in the rear of the impeller, the uncertainty in the pitch angle for measurement stations 165 to 178 should be less than  $\pm 2^\circ$  over the entire blade span (except in regions of high unsteadiness, such as the throughflow wake).

## Summary of Results

A laser anemometer system was used to provide detailed surveys of the three-dimensional velocity field within a low-speed centrifugal impeller operating with a vaneless diffuser. Both laser anemometer and aerodynamic performance data were acquired at the design flow rate and at a lower flow rate.

Flow path coordinates, detailed blade geometry, and pneumatic probe survey results are presented in tabular form. The laser anemometer data are presented in the form of pitchwise distributions of axial, radial, and relative tangential velocity on blade-to-blade stream surfaces at 5-percent-of-span increments, starting at 95-percent-of-span from the hub. The laser anemometer data are also presented as contour and wire-frame plots of throughflow velocity and vector plots of secondary velocities at all measurement stations through the impeller.

Lewis Research Center  
National Aeronautics and Space Administration  
Cleveland, Ohio, February 22, 1995

## Appendix A

### Description of Data on Magnetic Medium

Blade and flowpath geometries, as well as a complete set of laser anemometer measurements acquired at the design and off-design conditions, are available as formatted ASCII files. The blade and flowpath geometry files reflect the data shown in tables I and II. The contents of the laser anemometer data files are described in the following section.

#### Master Grid File Describing Laser Survey Points

The Master Grid File contains the coordinates of the body-fitted measurement grid which was used to define the laser anemometer survey points. The Master Grid File was also used to define the throughflow and secondary velocity components presented in this document and in prior publications (Hathaway et al. (1993) and Chriss, Hathaway, and Wood (1994)). The Master Grid File, file name *mgf.dat*, is available on disk as an ASCII formatted file that contains the following information:

<i>itip,ile,ite</i>	indices of the tip, leading, and trailing edge grid points
<i>ni,nj,nk</i>	number of grid points in the pitchwise, streamwise, and spanwise directions
<i>nb</i>	number of impeller blades
<i>rpm</i>	tested rotational speed of the impeller
<i>r(ni,nj,nk)</i>	array of <i>r</i> -coordinates of each grid point
<i>t(ni,nj,nk)</i>	array of $\theta$ -coordinates of each grid point
<i>z(ni,nj,nk)</i>	array of <i>z</i> -coordinates of each grid point

In order to keep the size of the Master Grid File manageable, only the coordinates of the blade surfaces and mean camberline are provided. The 200 pitchwise points resolved from the laser anemometer measurements can be generated from the blade geometry information. The pitchwise indices of the Master Grid File are arranged across the blade passage, from suction, to mean camberline, to pressure surface. Points upstream and downstream of the blade leading and trailing edges are extensions of the blade mean camberline. The following FORTRAN program can be used to read the Master Grid File:

```

real*4 r(3,221,106),t(3,221,106),z(3,221,106),rpm
integer*2 itip,ile,ite,ni,nj,nk,nb
C
read(unit,10) itip,ile,ite
read(unit,10) ni,nj,nk
read(unit,10) nb
10 format(3i8)
read(unit,20) rpm
20 format(f13.2)
read(unit,30) (((r(i,j,k),i=1,ni),j=1,nj),k=1,nk)
read(unit,30) (((t(i,j,k),i=1,ni),j=1,nj),k=1,nk)

```

```

read(unit,30) (((z(i,j,k),i=1,ni),j=1,nj),k=1,nk)
30 format(8f10.4)
C
stop
end

```

#### Laser Anemometer Data

The laser anemometer measurements are stored as formatted ASCII files of the passage-averaged results at a pitchwise resolution of 200 points. The files are named according to the streamwise *J*-index of the body-fitted measurement grid that was used to position the laser anemometer within the impeller. The measurement grid used in this investigation divided the streamwise blade length into a series of quasi-orthogonal or near-normal, cross-channel planes. Therefore, each *J*-index, and thus each file, corresponds to a particular quasi-orthogonal measurement plane within the impeller. The data in each file are organized in order of increasing percent-of-span from the hub. For each span, the percent-of-span and the *r,z* location of the measurement point are provided, followed by the measured radial, relative tangential, and axial velocities for each of the 200 pitchwise measurement points across an average rotor passage (expressed in SI units throughout). For relative tangential velocities, positive is in the direction of rotor rotation. Each file consists of the following:

- A file header block 20 lines long
- The file creation date and time, *datetime*
- The *J*-index of the current quasi-orthogonal measurement station and the blade leading and trailing edges, *j, jle, jte*
- The number of spanwise survey locations for the current quasi-orthogonal survey plane, *nk*
- The number of pitchwise measurement windows per blade passage, *ni*
- The operating condition, massflow and speed for the current data set, *wc, rpm*
- For each spanwise survey, *k*, at the current quasi-orthogonal measurement station
  - (a) *rn1, rn2* are laser anemometer run numbers.
  - (b) *ps, r, z* are nominal percent span, radius, and axial position of survey data at current spanwise location.
  - (c) *wn, vr, vt, vz* are a tabulation of window number and radial, relative tangential, and axial velocities for each pitchwise window number.

Window number 1 lies on the suction surface and window 200 is one window away from the suction surface of the adjacent passage. The window number increases in the direction opposite of rotor rotation.

The following FORTRAN program can be used to read the data files:

```
real*4wc,rpm,r(20),z(20),vr(200,20),vt(200,20),vz(200,20)
integer*2 j,jle,jte,nk,ni,rn1,rn2,ps(20),wn(200)

character*24 adum,datetime
C
do i=1,20
  read(unit,10) adum
enddo
10 format(a24)
  read(unit,20) datetime
20 format(25x,a24)
  read(unit,30) j,jle,jte
30 format(32x,i4,28x,i2,1x,i3)
  read(unit,40) nk
40 format(i4)
  read(unit,40) ni
  read(unit,10) adum
  read(unit,10) adum
  read(unit,50) wc,rpm
50 format(43x,f2.0,7x,f5.0)
```

```
do k=1,nk
  read(unit,10) adum
  read(unit,60) rn1,rn2
60 format(43x,i5,1x,i5)
  read(unit,70) ps(k),r(k),z(k)
70 format(i4,26x,f8.5,4x,f8.5)
  read(unit,10) adum
  read(unit,10) adum
  read(unit,10) adum
  rni = float(ni)/2.
  do i=1,rni
    read(unit,80) wn(i),vr(i,k),vt(i,k),vz(i,k),
1 wn(i+rni),vr(i+rni,k),vt(i+rni,k),vz(i+rni,k)
80 format(i3,3f8.2,5x,i3,3f8.2)
  enddo
  if(rni-ni gt 0.) read(unit,80) wn(rni),
1 vr(rni,k),vt(rni,k),vz(rni,k)
  enddo
C
stop
end
```

## Appendix B Symbols

$\Delta A$	incremental spanwise flow area, $\text{cm}^2$	$r$	radial coordinate, cm
$c_p$	specific heat of air at constant pressure	$r/r_t$	radius nondimensionalized by exit tip radius
$\hat{f}_n$	unit vector in the $n$ th measured velocity component direction	SS	suction surface
$\hat{g}_m$	unit vector in local meridional grid direction	$s$	surface distance
$\hat{g}_p$	unit vector in local pitchwise grid direction, $\theta$	$T$	total temperature
$\hat{g}_{sp}$	unit vector in local spanwise grid direction	$t$	static temperature
$\hat{g}_{st}$	unit vector in local streamwise grid direction	$t_{\text{std}}$	temperature at standard-day sea-level conditions; 288.15 K
$i$	$i$ th static tap	$U$	impeller tip speed, m/sec
$J$	streamwise measurement grid index	$u, v, w$	velocity components in x-, y-, and z-coordinate directions, m/sec
$\dot{m}$	mass flow rate, kg/sec	$V$	absolute velocity, m/sec
$\dot{m}_d$	design mass flow rate; 30.0 kg/sec	$V_f$	velocity component measured in direction $\hat{f}_n$ , m/sec
$m/m_s$	nondimensional shroud meridional distance	$V_m$	meridional velocity component, m/sec; $\sqrt{V_z^2 + V_r^2}$
$N$	rotor rotational speed, rad/sec	$V_r$	radial velocity component, m/sec
NM	number of laser anemometer measurement realizations at a given window	$V_T$	throughflow velocity component, m/sec; $\vec{V}_m \cdot \hat{g}_m$
NP	number of impeller blade passages	$V_z$	axial velocity component, m/sec
NS	number of spanwise survey locations	$V_\theta$	tangential velocity component, m/sec
NWN	number of rotor relative pitchwise measurement windows	$W$	relative velocity, m/sec
NZ	number of rotor blade passages with zero measurements	$W_n$	$n$ th rotor relative pitchwise laser anemometer measurement window
$P$	total pressure	$W_p$	pitchwise secondary velocity component, m/sec
PS	pressure surface	$\vec{W}_s$	secondary velocity vector, m/sec; $\vec{W} - \vec{W}_{st}$
$p$	static pressure	$W_{sp}$	spanwise secondary velocity component (positive towards the shroud), m/sec
$p_{\text{std}}$	pressure at standard-day sea-level conditions; 101 325 N/m <sup>2</sup>	$\vec{W}_{st}$	vector projection of $\vec{W}$ in the local streamwise direction $\hat{g}_{st}$ , m/sec
$R$	universal gas constant for air	$W_\theta$	relative tangential velocity component, m/sec

$x,y$	x- and y-axis coordinates, cm	$f$	laser anemometer fringe normal direction
$z$	axial coordinate along rig centerline (positive in direction of impeller exit), cm	$m$	component in meridional direction
$\alpha$	flow pitch angle, deg; $\alpha = \tan^{-1} (V_r/V_z)$	$o$	plenum condition
$\beta$	absolute flow angle, deg; $\beta = \tan^{-1} [V_\theta/V_m]$	$p$	component in pitchwise direction
$\Gamma$	compressor torque, N-m	$r$	component in radial or $r$ -axis direction
$\Gamma_{tare}$	compressor tare torque, N-m	sen	at pressure sensor
$\gamma$	ratio of specific heats for air	$sp$	component in spanwise direction
$\varepsilon$	difference between least square estimate and laser anemometer measurement of fringe normal velocity, m/sec	$st$	component in streamwise direction
$\zeta$	azimuthal orientation of laser anemometer optical axis, rad	$T$	component in throughflow direction
$\eta$	declination angle of laser anemometer optical axis, rad	$x$	component in $x$ -axis direction
$\eta_{ad}$	adiabatic, temperature-based efficiency	$y$	component in $y$ -axis direction
$\eta_T$	torque-based efficiency	$z$	component in axial or $z$ -axis direction
$\theta$	tangential coordinate, rad	$\theta$	component in tangential or $\theta$ -axis direction
$\rho$	density of air	1	impeller inlet survey station
$\omega$	compressor speed, rad/sec	2	impeller exit survey station
<u>Subscripts</u>		<u>Superscripts</u>	
$c$	corrected to standard-day sea-level dry condition	–	ensemble- or mass-average
$d$	design condition	~	passage-average
		^	unit vector
		→	vector quantity
		'	rms unsteadiness level

## References

- Ahmed, N.A.; and Elder, R.L.: Flow Investigation in a Small High Speed Impeller Passage Using Laser Anemometry. ASME Paper 90-GT-233, 1990.
- Chriss, R.M.; Hathaway, M.D.; and Wood, J.R.: Experimental and Computational Results From the NASA Lewis Low-Speed Centrifugal Impeller at Design and Part Flow Conditions. ASME Paper 94-GT-213, 1994.
- Eckardt, D.: Detailed Flow Investigations Within a High-Speed Centrifugal Compressor Impeller. *J. Fluid Eng. Trans. ASME*, vol. 98, Sept. 1976, pp. 390-402.
- Fagan, J.R.; and Fleeter, S.: Impeller Flow Field Measurement and Analysis. *J. Turbomachinery Trans. ASME*, vol. 113, no. 4, Oct. 1991, pp. 670-679.
- Farge, T.Z.; Johnson, M.W.; and Maksoud, T.M.A.: Tip Leakage in a Centrifugal Impeller. *J. Turbomachinery Trans. ASME*, vol. 111, July, 1989, pp. 244-249.
- Hathaway, M.D.; Wood, J.R.; Wasserbauer, C.A.: NASA Low-Speed Centrifugal Compressor for Three-Dimensional Viscous Code Assessment and Fundamental Flow Physics Research. *J. Turbomachinery Trans. ASME*, vol. 114, Apr. 1992, pp. 295-303.
- Hathaway, M.D., et al.: Experimental and Computational Investigation of the NASA Low-Speed Centrifugal Compressor Flow Field. *J. Turbomachinery Trans. ASME*, vol. 115, no. 3, July 1993, pp. 527-542.
- Joslyn, H.D., and Dring, R.P.: Surface Indicator and Smoke Flow Visualization Techniques in Rotating Machinery. *Heat Transfer and Fluid Flow in Rotating Machinery, Proceedings of the First International Symposium on Transport Phenomena*, Hemisphere Publishing Corp., 1987, pp. 156-169.
- Krain, H.: Swirling Impeller Flow. *J. Turbomachinery Trans. ASME*, vol. 110, Jan. 1988, pp. 122-128.
- Krain, H.; and Hoffmann, W.: Verification of an Impeller Design by Laser Measurements and 3D-Viscous Flow Calculations. ASME Paper 89-GT-159, 1989.
- Rohne, K.-H.; and Banzhaf, M.: Investigation of the Flow at the Exit of an Unshrouded Centrifugal Impeller and Comparison With the "Classical" Jet-Wake Theory. *J. Turbomachinery Trans. ASME*, vol. 113, no. 4, Oct. 1991, pp. 654-659.
- Nishi, M.; Senoo, Y.; and Yamaguchi, M.: A Photographic Study of Three-Dimensional Flow in a Radial Compressor. ASME Paper 68-GT-2, 1968.
- Sipos, G.: Secondary Flow and Loss Distribution in a Radial Compressor with Untwisted Backswept Vanes. *J. Turbomachinery Trans. ASME*, vol. 113, no. 4, Oct. 1991, pp. 686-695.
- Strazisar, A.J., et al.: Laser Anemometer Measurements in a Transonic Axial-Flow Fan Rotor. NASA TP-2879, 1989.
- Wasserbauer, C.W.; and Hathaway, M.D.: Development of the Seeding System Used for Laser Velocimeter Surveys of the NASA Low-Speed Centrifugal Compressor Flow Field. NASA TM-4485, 1993.
- Wood, J.R., Adam, P.W.; and Buggele, A.E.: NASA Low-Speed Centrifugal Compressor for Fundamental Research. NASA TM-83398, 1983.
- Wood, J.R.; Strazisar, A.J.; and Hathaway, M.D.: Test Case E/C0-2 Single Transonic Fan Rotor. AGARD-AR-275, 1990, pp. 165-171.

TABLE I.—BLADE SURFACE COORDINATES ON SURFACES OF REVOLUTION OF NASA LOW-SPEED CENTRIFUGAL COMPRESSOR

Surface number 1	hub.	Number of impeller blades . . . . .	20
Surface number 6	tip of the blade (not the casing or shroud)	Backsweep from radial, deg . . . . .	55
$z$	axial distance, cm	Tested rpm . . . . .	1862
$r$	radial distance, cm	Tested mass flow rates, kg/sec	
$\theta_1$	tangential coordinate of lower surface, rad	At 100-percent $\dot{m}_d$ . . . . .	30
$\theta_2$	tangential coordinate of upper surface, rad	At 78.7-percent $\dot{m}_d$ . . . . .	23.6
		Clearance between impeller tip and stationary casing, cm . . . . .	0.254

Rotation is such that surface 1 is the leading or pressure side of the blade and surface 2 is the trailing or suction side of the blade. With the blade tangential coordinates defined as in figure 3, the rotation rate will have a positive sign to be algebraically consistent.

A gap of approximately 0.635 cm existed between the impeller disk at exit and the stationary diffuser hub back wall. This gap was sealed with a rope seal to reduce or eliminate any leakage into the flow.

Surface number 1 from the hub									
J	$z$ (cm)	$r$ (cm)	$\theta_1$ (radians)	$\theta_2$ (radians)	J	$z$ (cm)	$r$ (cm)	$\theta_1$ (radians)	$\theta_2$ (radians)
1	0.00000	21.47011	-0.00828	-0.00828	39	4.09346	22.97643	-0.09283	-0.16142
2	0.00366	21.47164	-0.00599	-0.01076	40	4.50647	23.13219	-0.10347	-0.17148
3	0.00732	21.47285	-0.00512	-0.01187	41	4.94995	23.30044	-0.11442	-0.18187
4	0.01097	21.47438	-0.00447	-0.01272	42	5.42635	23.48240	-0.12567	-0.19257
5	0.01463	21.47560	-0.00395	-0.01347	43	5.93811	23.67961	-0.13723	-0.20354
6	0.01829	21.47712	-0.00351	-0.01414	44	6.48736	23.89388	-0.14905	-0.21473
7	0.02195	21.47834	-0.00309	-0.01474	45	7.07654	24.12675	-0.16105	-0.22609
8	0.02560	21.47987	-0.00274	-0.01531	46	7.70900	24.37973	-0.17322	-0.23759
9	0.02926	21.48108	-0.00241	-0.01585	47	8.38718	24.65558	-0.18547	-0.24919
10	0.03292	21.48261	-0.00213	-0.01637	48	9.11443	24.95672	-0.19776	-0.26081
11	0.03658	21.48413	-0.00186	-0.01685	49	9.89411	25.28560	-0.21001	-0.27239
12	0.04023	21.48535	-0.00159	-0.01732	50	10.72926	25.64618	-0.22213	-0.28383
13	0.04359	21.48688	-0.00136	-0.01777	51	11.62355	26.04181	-0.23406	-0.29509
14	0.04724	21.48809	-0.00115	-0.01821	52	12.58062	26.47676	-0.24573	-0.30608
15	0.05273	21.49023	-0.00087	-0.01884	53	13.60383	26.95621	-0.25705	-0.31672
16	0.06066	21.49328	-0.00050	-0.01973	54	14.69715	27.48564	-0.26794	-0.32695
17	0.07041	21.49693	-0.00011	-0.02074	55	15.86423	28.07177	-0.27836	-0.33674
18	0.08443	21.50212	0.00033	-0.02211	56	17.10873	28.72191	-0.28830	-0.34605
19	0.10516	21.51004	0.00084	-0.02399	57	18.43369	29.44398	-0.29773	-0.35491
20	0.13564	21.52132	0.00135	-0.02654	58	19.84278	30.24805	-0.30673	-0.36341
21	0.17922	21.53778	0.00178	-0.02986	59	21.33844	31.14507	-0.31544	-0.37167
22	0.24018	21.56064	0.00199	-0.03404	60	22.92309	32.14726	-0.32406	-0.37996
23	0.32339	21.59173	0.00179	-0.03920	61	24.59736	33.26922	-0.33297	-0.38865
24	0.43647	21.63348	0.00096	-0.04552	62	26.36124	34.52744	-0.34266	-0.39828
25	0.57638	21.68500	-0.00067	-0.05261	63	28.21229	35.94080	-0.35390	-0.40965
26	0.72695	21.73986	-0.00294	-0.05957	64	30.14502	37.53216	-0.36768	-0.42375
27	0.88910	21.79869	-0.00580	-0.06647	65	32.14939	39.32865	-0.38523	-0.44175
28	1.06345	21.86147	-0.00929	-0.07338	66	34.20770	41.36166	-0.40796	-0.46496
29	1.25090	21.92914	-0.01338	-0.08027	67	36.29315	43.66900	-0.43740	-0.49471
30	1.45237	22.00168	-0.01815	-0.08715	68	38.36304	46.29424	-0.47511	-0.53237
31	1.66878	22.07971	-0.02365	-0.09405	69	40.35735	49.28372	-0.52262	-0.57919
32	1.90134	22.16414	-0.02994	-0.10121	70	42.19590	52.68072	-0.58111	-0.63641
33	2.15128	22.25528	-0.03710	-0.10872	71	43.78726	56.51602	-0.65151	-0.70523
34	2.41981	22.35342	-0.04526	-0.11660	72	45.04609	60.79846	-0.73423	-0.78618
35	2.70845	22.45949	-0.05400	-0.12483	73	45.91660	65.51737	-0.82842	-0.87830
36	3.01843	22.57410	-0.06315	-0.13344	74	46.39117	70.65447	-0.93164	-0.97882
37	3.35158	22.69815	-0.07267	-0.14241	75	46.51766	76.20000	-1.04014	-1.08385
38	3.70911	22.83196	-0.08258	-0.15173					

TABLE I.—Continued.  
Surface number 2 from the hub

J	z (cm)	r (cm)	$\theta_1$ (radians)	$\theta_2$ (radians)	J	z (cm)	r (cm)	$\theta_1$ (radians)	$\theta_2$ (radians)
1	0.00000	25.82770	-0.00610	-0.00610	39	3.88664	27.04543	-0.09134	-0.14286
2	0.00335	25.82892	-0.00441	-0.00799	40	4.27828	27.17310	-0.10134	-0.15254
3	0.00701	25.82989	-0.00377	-0.00883	41	4.69921	27.31145	-0.11175	-0.16264
4	0.01037	25.83111	-0.00331	-0.00950	42	5.15125	27.46156	-0.12254	-0.17311
5	0.01403	25.83209	-0.00293	-0.01008	43	5.63654	27.62482	-0.13368	-0.18393
6	0.01738	25.83331	-0.00261	-0.01060	44	6.15721	27.80276	-0.14518	-0.19508
7	0.02104	25.83428	-0.00233	-0.01107	45	6.71630	27.99705	-0.15697	-0.20650
8	0.02440	25.83550	-0.00208	-0.01152	46	7.31603	28.20889	-0.16905	-0.21821
9	0.02775	25.83648	-0.00185	-0.01194	47	7.95902	28.44099	-0.18136	-0.23016
10	0.03141	25.83769	-0.00166	-0.01235	48	8.64869	28.69553	-0.19388	-0.24231
11	0.03477	25.83891	-0.00146	-0.01273	49	9.38785	28.97493	-0.20653	-0.25460
12	0.03843	25.83989	-0.00130	-0.01311	50	10.17973	29.28283	-0.21928	-0.26698
13	0.04178	25.84111	-0.00114	-0.01347	51	11.02713	29.62250	-0.23207	-0.27940
14	0.04544	25.84208	-0.00100	-0.01381	52	11.93411	29.99805	-0.24484	-0.29181
15	0.05032	25.84379	-0.00082	-0.01431	53	12.90395	30.41449	-0.25753	-0.30413
16	0.05825	25.84623	-0.00059	-0.01503	54	13.93999	30.87712	-0.27009	-0.31634
17	0.06740	25.84916	-0.00035	-0.01584	55	15.04527	31.39238	-0.28246	-0.32839
18	0.08082	25.85330	-0.00010	-0.01694	56	16.22347	31.96750	-0.29465	-0.34026
19	0.10034	25.85964	0.00018	-0.01846	57	17.47783	32.61039	-0.30665	-0.35197
20	0.12931	25.86867	0.00042	-0.02053	58	18.81083	33.33087	-0.31849	-0.36357
21	0.17109	25.88184	0.00052	-0.02326	59	20.22466	34.13971	-0.33030	-0.37520
22	0.22934	25.90019	0.00037	-0.02673	60	21.72107	35.04912	-0.34224	-0.38703
23	0.30863	25.92506	-0.00021	-0.03104	61	23.30054	36.07362	-0.35460	-0.39938
24	0.41598	25.95854	-0.00142	-0.03639	62	24.96143	37.22923	-0.36779	-0.41270
25	0.54895	25.99982	-0.00337	-0.04245	63	26.70160	38.53497	-0.38242	-0.42761
26	0.69199	26.04380	-0.00587	-0.04848	64	28.51429	40.01268	-0.39930	-0.44495
27	0.84571	26.09100	-0.00888	-0.05451	65	30.38882	41.68818	-0.41948	-0.46569
28	1.01103	26.14144	-0.01242	-0.06058	66	32.30804	43.59126	-0.44409	-0.49089
29	1.18854	26.19585	-0.01654	-0.06672	67	34.24563	45.75592	-0.47443	-0.52170
30	1.37949	26.25417	-0.02124	-0.07291	68	36.16250	48.22160	-0.51189	-0.55935
31	1.58478	26.31701	-0.02660	-0.07926	69	38.00404	51.02881	-0.55780	-0.60498
32	1.80561	26.38511	-0.03267	-0.08594	70	39.69891	54.21472	-0.61331	-0.65976
33	2.04290	26.45878	-0.03956	-0.09296	71	41.16630	57.80560	-0.67934	-0.72480
34	2.29787	26.53819	-0.04721	-0.10035	72	42.33071	61.80977	-0.75642	-0.80068
35	2.57176	26.62414	-0.05527	-0.10810	73	43.14097	66.21909	-0.84393	-0.88663
36	2.86608	26.71719	-0.06369	-0.11621	74	43.58621	71.01820	-0.93981	-0.98037
37	3.18236	26.81814	-0.07252	-0.12470	75	43.70590	76.19909	-1.04087	-1.07862
38	3.52183	26.92728	-0.08173	-0.13358					

TABLE I.—Continued.  
Surface number 3 from the hub

J	z (cm)	r (cm)	$\theta_1$ (radians)	$\theta_2$ (radians)	J	z (cm)	r (cm)	$\theta_1$ (radians)	$\theta_2$ (radians)
1	0.00000	30.18528	-0.00466	-0.00466	39	3.67004	31.11391	-0.09029	-0.12890
2	0.00336	30.18620	-0.00336	-0.00614	40	4.04005	31.21344	-0.09984	-0.13828
3	0.00672	30.18693	-0.00289	-0.00680	41	4.43723	31.32176	-0.10981	-0.14810
4	0.00977	30.18784	-0.00255	-0.00734	42	4.86403	31.43986	-0.12022	-0.15834
5	0.01313	30.18858	-0.00228	-0.00780	43	5.32225	31.56904	-0.13103	-0.16901
6	0.01648	30.18949	-0.00203	-0.00822	44	5.81377	31.71050	-0.14225	-0.18005
7	0.01984	30.19022	-0.00185	-0.00861	45	6.34134	31.86595	-0.15387	-0.19148
8	0.02320	30.19114	-0.00167	-0.00898	46	6.90771	32.03643	-0.16585	-0.20328
9	0.02625	30.19187	-0.00152	-0.00932	47	7.51467	32.22453	-0.17819	-0.21545
10	0.02961	30.19278	-0.00138	-0.00964	48	8.16593	32.43218	-0.19085	-0.22794
11	0.03296	30.19370	-0.00125	-0.00997	49	8.86367	32.66176	-0.20381	-0.24072
12	0.03632	30.19443	-0.00114	-0.01027	50	9.61114	32.91654	-0.21702	-0.25377
13	0.03938	30.19534	-0.00103	-0.01056	51	10.41146	33.19993	-0.23047	-0.26704
14	0.04274	30.19607	-0.00094	-0.01084	52	11.26775	33.51565	-0.24410	-0.28052
15	0.04762	30.19735	-0.00083	-0.01126	53	12.18329	33.86851	-0.25788	-0.29413
16	0.05495	30.19918	-0.00068	-0.01184	54	13.16121	34.26369	-0.27178	-0.30788
17	0.06380	30.20138	-0.00054	-0.01252	55	14.20457	34.70754	-0.28576	-0.32171
18	0.07631	30.20449	-0.00040	-0.01343	56	15.31659	35.20712	-0.29982	-0.33565
19	0.09493	30.20924	-0.00027	-0.01470	57	16.49998	35.77009	-0.31396	-0.34969
20	0.12240	30.21601	-0.00023	-0.01644	58	17.75699	36.40629	-0.32825	-0.36389
21	0.16177	30.22589	-0.00034	-0.01874	59	19.08949	37.12630	-0.34275	-0.37835
22	0.21671	30.23973	-0.00073	-0.02170	60	20.49862	37.94244	-0.35760	-0.39322
23	0.29149	30.25839	-0.00154	-0.02539	61	21.98387	38.86875	-0.37305	-0.40876
24	0.39312	30.28358	-0.00299	-0.03001	62	23.54373	39.92168	-0.38942	-0.42533
25	0.51887	30.31464	-0.00516	-0.03529	63	25.17423	41.11937	-0.40719	-0.44342
26	0.65378	30.34770	-0.00781	-0.04057	64	26.86815	42.48301	-0.42700	-0.46370
27	0.79907	30.38328	-0.01095	-0.04590	65	28.61469	44.03753	-0.44971	-0.48695
28	0.95506	30.42137	-0.01457	-0.05129	66	30.39630	45.81050	-0.47624	-0.51404
29	1.12295	30.46251	-0.01873	-0.05676	67	32.18824	47.83310	-0.50767	-0.54596
30	1.30305	30.50660	-0.02344	-0.06238	68	33.95380	50.13960	-0.54519	-0.58376
31	1.49690	30.55424	-0.02879	-0.06833	69	35.64394	52.76470	-0.58996	-0.62849
32	1.70540	30.60598	-0.03485	-0.07460	70	37.19675	55.74027	-0.64305	-0.68123
33	1.92945	30.66215	-0.04159	-0.08123	71	38.54170	59.08776	-0.70538	-0.74298
34	2.17030	30.72279	-0.04872	-0.08821	72	39.61317	62.81527	-0.77749	-0.81429
35	2.42884	30.78858	-0.05624	-0.09556	73	40.36433	66.91676	-0.85889	-0.89455
36	2.70661	30.86002	-0.06415	-0.10329	74	40.78100	71.37999	-0.94784	-0.98183
37	3.00515	30.93779	-0.07246	-0.11142	75	40.89414	76.19878	-1.04159	-1.07338
38	3.32568	31.02220	-0.08117	-0.11995					

TABLE I.—Continued.

Surface number 4 from the hub

J	z (cm)	r (cm)	$\theta_1$ (radians)	$\theta_2$ (radians)	J	z (cm)	r (cm)	$\theta_1$ (radians)	$\theta_2$ (radians)
1	0.00000	34.54287	-0.00345	-0.00345	39	3.44251	35.18180	-0.08950	-0.11772
2	0.00306	34.54348	-0.00246	-0.00461	40	3.78969	35.25304	-0.09867	-0.12684
3	0.00611	34.54396	-0.00211	-0.00515	41	4.16224	35.33119	-0.10829	-0.13642
4	0.00917	34.54457	-0.00185	-0.00557	42	4.56263	35.41711	-0.11837	-0.14646
5	0.01222	34.54506	-0.00166	-0.00595	43	4.99263	35.51201	-0.12890	-0.15696
6	0.01558	34.54567	-0.00149	-0.00629	44	5.45417	35.61679	-0.13989	-0.16790
7	0.01864	34.54616	-0.00136	-0.00661	45	5.94931	35.73316	-0.15133	-0.17929
8	0.02169	34.54677	-0.00125	-0.00691	46	6.48088	35.86196	-0.16323	-0.19113
9	0.02475	34.54726	-0.00114	-0.00719	47	7.05124	36.00579	-0.17555	-0.20342
10	0.02780	34.54787	-0.00105	-0.00747	48	7.66263	36.16612	-0.18830	-0.21614
11	0.03086	34.54847	-0.00097	-0.00772	49	8.31806	36.34548	-0.20148	-0.22928
12	0.03392	34.54896	-0.00090	-0.00798	50	9.02032	36.54671	-0.21505	-0.24283
13	0.03697	34.54957	-0.00083	-0.00823	51	9.77210	36.77319	-0.22901	-0.25676
14	0.04002	34.55006	-0.00078	-0.00847	52	10.57688	37.02852	-0.24333	-0.27105
15	0.04460	34.55092	-0.00072	-0.00880	53	11.43764	37.31721	-0.25798	-0.28569
16	0.05133	34.55214	-0.00064	-0.00930	54	12.35689	37.64429	-0.27297	-0.30067
17	0.05958	34.55360	-0.00058	-0.00986	55	13.33791	38.01602	-0.28829	-0.31598
18	0.07150	34.55567	-0.00053	-0.01063	56	14.38329	38.43923	-0.30393	-0.33162
19	0.08891	34.55884	-0.00052	-0.01170	57	15.49572	38.92148	-0.31992	-0.34762
20	0.11458	34.56335	-0.00061	-0.01319	58	16.67689	39.47257	-0.33630	-0.36402
21	0.15155	34.56994	-0.00088	-0.01515	59	17.92841	40.10291	-0.35315	-0.38093
22	0.20317	34.57927	-0.00145	-0.01770	60	19.25080	40.82491	-0.37059	-0.39846
23	0.27344	34.59172	-0.00246	-0.02091	61	20.64312	41.65240	-0.38881	-0.41681
24	0.36847	34.60861	-0.00411	-0.02494	62	22.10265	42.60169	-0.40806	-0.43626
25	0.48640	34.62943	-0.00646	-0.02958	63	23.62526	43.69087	-0.42871	-0.45721
26	0.61319	34.65159	-0.00927	-0.03424	64	25.20271	44.94037	-0.45130	-0.48017
27	0.74946	34.67553	-0.01253	-0.03895	65	26.82332	46.37376	-0.47643	-0.50573
28	0.89582	34.70124	-0.01628	-0.04372	66	28.46978	48.01693	-0.50487	-0.53461
29	1.05319	34.72911	-0.02055	-0.04871	67	30.11780	49.89726	-0.53750	-0.56765
30	1.22247	34.75894	-0.02540	-0.05402	68	31.73414	52.04490	-0.57532	-0.60573
31	1.40430	34.79136	-0.03093	-0.05964	69	33.27532	54.48894	-0.61933	-0.64982
32	1.59956	34.82671	-0.03692	-0.06560	70	34.68806	57.25506	-0.67052	-0.70086
33	1.80978	34.86534	-0.04327	-0.07190	71	35.91269	60.36088	-0.72972	-0.75977
34	2.03530	34.90716	-0.05000	-0.07856	72	36.89291	63.81338	-0.79745	-0.82701
35	2.27793	34.95274	-0.05709	-0.08559	73	37.58635	67.60912	-0.87330	-0.90203
36	2.53858	35.00251	-0.06458	-0.09301	74	37.97549	71.73945	-0.95571	-0.98319
37	2.81879	35.05704	-0.07247	-0.10083	75	38.08238	76.19877	-1.04232	-1.06814
38	3.11949	35.11661	-0.08077	-0.10906					

TABLE I.—Continued.

Surface number 5 from the hub									
J	z (cm)	r (cm)	$\theta_1$ (radians)	$\theta_2$ (radians)	J	z (cm)	r (cm)	$\theta_1$ (radians)	$\theta_2$ (radians)
1	0.00000	38.90045	-0.00234	-0.00234	39	3.20153	39.24892	-0.08882	-0.10820
2	0.00275	38.90076	-0.00161	-0.00324	40	3.52441	39.29169	-0.09766	-0.11707
3	0.00581	38.90100	-0.00137	-0.00367	41	3.87179	39.33953	-0.10696	-0.12643
4	0.00856	38.90131	-0.00119	-0.00401	42	4.24457	39.39306	-0.11675	-0.13626
5	0.01132	38.90155	-0.00106	-0.00431	43	4.64490	39.45342	-0.12702	-0.14660
6	0.01438	38.90185	-0.00096	-0.00459	44	5.07498	39.52122	-0.13779	-0.15742
7	0.01714	38.90210	-0.00087	-0.00484	45	5.53656	39.59821	-0.14906	-0.16874
8	0.02019	38.90240	-0.00080	-0.00509	46	6.03221	39.68498	-0.16083	-0.18058
9	0.02295	38.90265	-0.00074	-0.00532	47	6.56396	39.78404	-0.17312	-0.19294
10	0.02570	38.90295	-0.00069	-0.00554	48	7.13461	39.89665	-0.18593	-0.20582
11	0.02875	38.90326	-0.00065	-0.00575	49	7.74634	40.02524	-0.19924	-0.21922
12	0.03151	38.90350	-0.00062	-0.00597	50	8.40192	40.17229	-0.21308	-0.23314
13	0.03427	38.90381	-0.00059	-0.00617	51	9.10463	40.34132	-0.22743	-0.24757
14	0.03732	38.90405	-0.00057	-0.00637	52	9.85642	40.53544	-0.24230	-0.26253
15	0.04160	38.90448	-0.00054	-0.00664	53	10.66099	40.75908	-0.25767	-0.27800
16	0.04772	38.90509	-0.00053	-0.00705	54	11.52106	41.01725	-0.27357	-0.29398
17	0.05537	38.90582	-0.00052	-0.00752	55	12.43882	41.31583	-0.28999	-0.31051
18	0.06639	38.90686	-0.00056	-0.00818	56	13.41719	41.66169	-0.30698	-0.32759
19	0.08260	38.90844	-0.00065	-0.00908	57	14.45834	42.06214	-0.32455	-0.34527
20	0.10646	38.91070	-0.00086	-0.01034	58	15.56380	42.52705	-0.34277	-0.36358
21	0.14073	38.91399	-0.00127	-0.01202	59	16.73507	43.06674	-0.36169	-0.38261
22	0.18876	38.91881	-0.00200	-0.01420	60	17.97145	43.69353	-0.38142	-0.40248
23	0.25393	38.92503	-0.00319	-0.01698	61	19.27202	44.42124	-0.40213	-0.42333
24	0.34233	38.93364	-0.00504	-0.02047	62	20.63320	45.26626	-0.42401	-0.44538
25	0.45216	38.94421	-0.00761	-0.02450	63	22.04977	46.24622	-0.44735	-0.46893
26	0.56996	38.95545	-0.01062	-0.02853	64	23.51320	47.38125	-0.47250	-0.49432
27	0.69662	38.96774	-0.01412	-0.03271	65	25.01043	48.69335	-0.49995	-0.52203
28	0.83277	38.98107	-0.01813	-0.03716	66	26.52425	50.20662	-0.53028	-0.55263
29	0.97902	38.99563	-0.02275	-0.04190	67	28.03131	51.94521	-0.56419	-0.58678
30	1.13631	39.01118	-0.02774	-0.04694	68	29.50110	53.93450	-0.60250	-0.62527
31	1.30522	39.02833	-0.03308	-0.05229	69	30.89570	56.19798	-0.64607	-0.66892
32	1.48696	39.04727	-0.03873	-0.05798	70	32.17096	58.75586	-0.69579	-0.71862
33	1.68248	39.06831	-0.04473	-0.06400	71	33.27781	61.62179	-0.75240	-0.77511
34	1.89238	39.09127	-0.05109	-0.07037	72	34.16921	64.80209	-0.81634	-0.83876
35	2.11791	39.11656	-0.05784	-0.07713	73	34.80680	68.29512	-0.88715	-0.90903
36	2.36026	39.14457	-0.06496	-0.08427	74	35.16954	72.09545	-0.96342	-0.98443
37	2.62069	39.17574	-0.07249	-0.09182	75	35.27061	76.19904	-1.04306	-1.06290
38	2.90070	39.21038	-0.08044	-0.09979					

TABLE I.—Concluded.

Surface number 6 from the hub

J	z (cm)	r (cm)	$\theta_1$ (radians)	$\theta_2$ (radians)	J	z (cm)	r (cm)	$\theta_1$ (radians)	$\theta_2$ (radians)
1	0.00000	43.25804	-0.00133	-0.00133	39	2.94325	43.31496	-0.08810	-0.09943
2	0.00274	43.25804	-0.00085	-0.00198	40	3.24092	43.32910	-0.09661	-0.10807
3	0.00523	43.25804	-0.00069	-0.00230	41	3.56077	43.34632	-0.10561	-0.11719
4	0.00796	43.25804	-0.00060	-0.00256	42	3.90477	43.36722	-0.11509	-0.12681
5	0.01042	43.25804	-0.00053	-0.00280	43	4.27397	43.39272	-0.12509	-0.13695
6	0.01317	43.25804	-0.00049	-0.00301	44	4.67079	43.42314	-0.13563	-0.14763
7	0.01591	43.25804	-0.00045	-0.00321	45	5.09707	43.46031	-0.14670	-0.15885
8	0.01840	43.25804	-0.00042	-0.00339	46	5.55497	43.50455	-0.15833	-0.17064
9	0.02113	43.25804	-0.00041	-0.00358	47	6.04661	43.55830	-0.17053	-0.18300
10	0.02359	43.25804	-0.00040	-0.00376	48	6.57451	43.62249	-0.18332	-0.19596
11	0.02636	43.25804	-0.00040	-0.00393	49	7.14078	43.69958	-0.19671	-0.20952
12	0.02882	43.25804	-0.00040	-0.00409	50	7.74845	43.79170	-0.21073	-0.22371
13	0.03155	43.25804	-0.00041	-0.00425	51	8.39983	43.90226	-0.22536	-0.23852
14	0.03432	43.25804	-0.00042	-0.00441	52	9.09779	44.03429	-0.24065	-0.25399
15	0.03802	43.25804	-0.00043	-0.00463	53	9.84495	44.19180	-0.25660	-0.27013
16	0.04382	43.25804	-0.00048	-0.00496	54	10.64409	44.37972	-0.27325	-0.28696
17	0.05087	43.25804	-0.00054	-0.00534	55	11.49759	44.60386	-0.29061	-0.30450
18	0.06098	43.25804	-0.00065	-0.00587	56	12.40825	44.87097	-0.30874	-0.32281
19	0.07570	43.25804	-0.00086	-0.00660	57	13.37767	45.18814	-0.32768	-0.34192
20	0.09776	43.25804	-0.00122	-0.00763	58	14.40763	45.56546	-0.34749	-0.36189
21	0.12931	43.25804	-0.00181	-0.00902	59	15.49859	46.01281	-0.36825	-0.38281
22	0.17316	43.25835	-0.00277	-0.01082	60	16.65013	46.54304	-0.39006	-0.40475
23	0.23319	43.25835	-0.00423	-0.01310	61	17.86050	47.16968	-0.41303	-0.42786
24	0.31441	43.25865	-0.00642	-0.01599	62	19.12544	47.90932	-0.43732	-0.45227
25	0.41497	43.25896	-0.00943	-0.01948	63	20.43855	48.77917	-0.46312	-0.47819
26	0.52315	43.25927	-0.01297	-0.02318	64	21.79065	49.79891	-0.49071	-0.50587
27	0.63960	43.25989	-0.01680	-0.02712	65	23.16819	50.98967	-0.52037	-0.53561
28	0.76465	43.26081	-0.02092	-0.03132	66	24.55288	52.37305	-0.55255	-0.56786
29	0.89918	43.26205	-0.02533	-0.03579	67	25.92259	53.97024	-0.58780	-0.60316
30	1.04355	43.26328	-0.03002	-0.04056	68	27.24964	55.80211	-0.62677	-0.64216
31	1.19892	43.26513	-0.03502	-0.04563	69	28.50148	57.88649	-0.67020	-0.68562
32	1.36598	43.26760	-0.04034	-0.05103	70	29.64280	60.23791	-0.71886	-0.73430
33	1.54562	43.27098	-0.04601	-0.05678	71	30.63537	62.86677	-0.77339	-0.78882
34	1.73845	43.27499	-0.05203	-0.06288	72	31.44081	65.77770	-0.83410	-0.84943
35	1.94597	43.27991	-0.05842	-0.06937	73	32.02502	68.97202	-0.90043	-0.91548
36	2.16911	43.28606	-0.06522	-0.07625	74	32.36303	72.44700	-0.97096	-0.98551
37	2.40882	43.29375	-0.07241	-0.08354	75	32.45885	76.19990	-1.04379	-1.05766
38	2.66638	43.30328	-0.08003	-0.09126					

TABLE II.—INNER AND OUTER FLOW PATH COORDINATES

J	z hub (cm)	r hub (cm)	z casing (cm)	r casing (cm)	Location
1	-117.05911	0.00000	-57.91200	43.51200	
2	-37.79520	0.00000	-51.81600	43.51200	
3	-36.57600	0.00000	-30.48000	43.51200	
4	-35.56102	0.00000	-22.86000	43.51200	
5	-35.47262	2.22809	-15.24000	43.51200	Hub spinner
6	-35.14344	4.43179	-9.14400	43.51200	
7	-34.41192	6.53491	-6.09600	43.51200	
8	-33.07080	8.31799	-3.04800	43.51200	
9	-31.23590	9.57986	-2.28600	43.51200	
10	-29.20898	10.50341	-1.52400	43.51200	
11	-27.12872	11.30656	-0.76200	43.51200	
12	-25.04176	12.08928	0.00006	43.51200	Casing leading edge
13	-22.95875	12.87963	1.32210	43.52096	
14	-20.87880	13.68034	2.63932	43.55641	
15	-18.80098	14.48562	3.95319	43.62493	
16	-16.72194	15.28816	5.26280	43.73075	
17	-5.08010	19.65960	6.56695	43.87745	
18	-1.27010	21.04644	7.86424	44.06783	
19	-0.73286	21.20338	9.15275	44.30426	
20	0.00000	21.47011	10.43041	44.58889	Hub leading edge
21	1.83163	22.13829	11.69493	44.92340	
22	3.66047	22.81410	12.94373	45.30931	
23	5.48387	23.50444	14.17418	45.74783	
24	7.29929	24.21548	15.38335	46.23981	
25	9.10438	24.95233	16.56841	46.78570	
26	10.89687	25.71942	17.72625	47.38579	
27	12.67459	26.52010	18.85389	48.04005	
28	14.43539	27.35723	19.94815	48.74779	
29	16.17735	28.23280	21.00608	49.50805	
30	17.89868	29.14851	22.02482	50.31968	
31	19.59748	30.10540	23.00167	51.18107	
32	21.27190	31.10414	23.93415	52.09035	
33	22.92017	32.14555	24.82002	53.04520	
34	24.54042	33.23003	25.65733	54.04308	
35	26.13063	34.35815	26.44451	55.08135	
36	27.68846	35.53047	27.18023	56.15711	
37	29.21148	36.74778	27.86360	57.26747	
38	30.69671	38.01078	28.49411	58.40934	
39	32.14089	39.32072	29.07149	59.57953	
40	33.54010	40.67855	29.59584	60.77526	
41	34.88991	42.08541	30.06767	61.99348	
42	36.18537	43.54239	30.48777	63.23140	
43	37.42118	45.05038	30.85704	64.48614	
44	38.59152	46.60989	31.17680	65.75545	
45	39.69032	48.22037	31.44865	67.03695	
46	40.71223	49.88089	31.67439	68.32830	
47	41.65193	51.58920	31.85605	69.62754	
48	42.50524	53.34219	31.99601	70.93336	

TABLE II.—Concluded.

J	z hub (cm)	r hub (cm)	z casing (cm)	r casing (cm)	Location
49	43.26950	55.13603	32.09699	72.24412	
50	43.94350	56.96553	32.16225	73.55775	
51	44.52799	58.82561	32.19611	74.87537	
52	45.02518	60.71086	32.20477	76.19976	Casing trailing edge
53	45.43894	62.61619	32.20477	76.97959	
54	45.77435	64.53649	32.20477	77.75948	
55	46.03748	66.46834	32.20477	79.24800	
56	46.23487	68.40779	32.20477	80.77200	
57	46.37364	70.35269	32.20477	82.29600	
58	46.46133	72.29883	32.20477	85.34400	
59	46.50596	74.24587	32.20477	91.44000	
60	46.51751	76.04760	32.20477	97.53600	
61	46.51751	76.20000	32.20477	103.63200	Hub trailing edge
62	46.51751	76.86050	32.20477	106.68000	Hub contraction
63	46.35094	77.47010	32.20477	107.89920	
64	46.18634	78.07970	32.20477	108.81360	
65	46.02480	78.68930	32.20477	109.72800	
66	45.68342	80.01000	32.32709	112.77600	Casing contraction
67	45.36643	81.28010	32.51667	114.30000	
68	44.75988	83.82000	32.70077	115.82400	
69	43.65041	88.90010	32.87999	117.34800	
70	42.20566	96.52010	33.05495	118.87200	
71	41.36136	101.59999	33.39145	121.92000	
72	38.69131	121.92000	33.71149	124.96800	
73	38.05428	128.01600	34.01629	128.01600	
74	37.75862	131.06400	34.30676	131.06400	
75	37.20694	137.16000	34.84931	137.16000	

TABLE III.—COORDINATES OF BLADE SURFACE STATIC PRESSURE TAPS

0.0 % Meridional Distance				
%Span From Hub	Pressure Surface		Suction Surface	
	<i>r</i> (cm)	<i>z</i> (cm)	<i>r</i> (cm)	<i>z</i> (cm)
4.9	22.55827	0.04216	22.55833	0.04216
19.7	25.77645	0.04064	25.77642	0.04064
49.3	32.21179	0.03353	32.21182	0.03353
78.8	38.64764	0.02286	38.64768	0.02286
93.6	41.86631	0.01600	41.86631	0.01600
97.6	42.72484	0.01397	42.72475	0.01397
2.6 % Meridional Distance				
%Span From Hub	Pressure Surface		Suction Surface	
	<i>r</i> (cm)	<i>z</i> (cm)	<i>r</i> (cm)	<i>z</i> (cm)
4.9	23.36844	2.28448	23.11369	1.57963
19.7	26.45877	2.00889	26.24419	1.38100
49.2	32.63961	1.45745	32.50496	0.98323
78.8	38.82013	0.90627	38.76590	0.58572
93.6	41.91053	0.63068	41.89640	0.38684
97.5	42.73471	0.55702	42.73122	0.33376
5.0 % Meridional Distance				
%Span From Hub	Pressure Surface		Suction Surface	
	<i>r</i> (cm)	<i>z</i> (cm)	<i>r</i> (cm)	<i>z</i> (cm)
4.9	23.82261	3.61061	23.82252	3.61061
19.7	26.84811	3.46075	26.84816	3.46075
49.3	32.89921	3.16103	32.89919	3.16103
78.8	38.95032	2.86131	38.95042	2.86131
93.5	41.97569	2.71145	41.97581	2.71145
97.5	42.78250	2.67157	42.78254	2.67157

TABLE III.—Continued.

15.0 % Meridional Distance				
%Span From Hub	Pressure Surface		Suction Surface	
	<i>r</i> (cm)	<i>z</i> (cm)	<i>r</i> (cm)	<i>z</i> (cm)
4.9	26.60857	10.74979	26.60861	10.74979
19.7	29.27612	10.30884	29.27614	10.30884
49.2	34.61127	9.42696	34.61107	9.42696
78.6	39.94635	8.54507	39.94636	8.54507
93.4	42.61359	8.10412	42.61379	8.10412
97.3	43.32521	7.98652	43.32517	7.98652
30.0 % Meridional Distance				
%Span From Hub	Pressure Surface		Suction Surface	
	<i>r</i> (cm)	<i>z</i> (cm)	<i>r</i> (cm)	<i>z</i> (cm)
4.9	31.83466	20.98878	31.83463	20.98878
19.6	34.02617	20.13966	34.02613	20.13966
49.0	38.40928	18.44142	38.40915	18.44142
78.4	42.79240	16.74317	42.79232	16.74317
93.1	44.98390	15.89380	44.98388	15.89380
97.0	45.56815	15.66748	45.56823	15.66748
50.0 % Meridional Distance				
%Span From Hub	Pressure Surface		Suction Surface	
	<i>r</i> (cm)	<i>z</i> (cm)	<i>r</i> (cm)	<i>z</i> (cm)
5.0	41.22898	33.08020	41.22884	33.08020
19.9	42.88066	31.70072	42.88063	31.70072
49.5	46.18430	28.94203	46.18452	28.94203
78.7	49.48813	26.18308	49.48788	26.18308
93.2	51.13982	24.80361	51.13987	24.80361
97.0	51.58020	24.43582	51.58030	24.43582

TABLE III.—Concluded.

70.0 % Meridional Distance				
%Span From Hub	Pressure Surface		Suction Surface	
	<i>r</i> (cm)	<i>z</i> (cm)	<i>r</i> (cm)	<i>z</i> (cm)
5.0	53.70255	41.88587	53.70255	41.88587
19.9	54.78479	40.02888	54.78469	40.02888
49.5	56.94925	36.31489	56.94926	36.31489
78.7	59.11350	32.60090	59.11349	32.60090
93.2	60.19594	30.74391	60.19585	30.74391
97.1	60.48447	30.24861	60.48430	30.24861
90.0 % Meridional Distance				
%Span From Hub	Pressure Surface		Suction Surface	
	<i>r</i> (cm)	<i>z</i> (cm)	<i>r</i> (cm)	<i>z</i> (cm)
4.9	69.21487	45.60291	69.21487	45.60291
19.5	69.21480	43.51503	69.21465	43.51503
48.9	69.21458	39.33952	69.21460	39.33952
78.2	69.21467	35.16401	69.21466	35.16401
92.9	69.21443	33.07613	69.21458	33.07613
96.8	69.21452	32.51937	69.21455	32.51937
95.0 % Meridional Distance				
%Span From Hub	Pressure Surface		Suction Surface	
	<i>r</i> (cm)	<i>z</i> (cm)	<i>r</i> (cm)	<i>z</i> (cm)
4.9	72.29748	45.77131	72.29748	45.77131
19.5	72.29738	43.70324	72.29739	43.70324
48.9	72.29745	39.56710	72.29729	39.56710
78.2	72.29728	35.43097	72.29739	35.43097
92.9	72.29723	33.36290	72.29733	33.36290
96.8	72.29726	32.81121	72.29737	32.81121
98.0 % Meridional Distance				
%Span From Hub	Pressure Surface		Suction Surface	
	<i>r</i> (cm)	<i>z</i> (cm)	<i>r</i> (cm)	<i>z</i> (cm)
4.9	74.42174	45.82058	74.42174	45.82058
19.5	74.42168	43.75835	74.42178	43.75835
48.9	74.42165	39.63390	74.42152	39.63390
78.2	74.42162	35.50971	74.42149	35.50971
92.9	74.42139	33.44748	74.42150	33.44748
96.8	74.42155	32.89757	74.42154	32.89757

TABLE IV.—COORDINATES OF SHROUD STATIC PRESSURE TAPS

Normalized meridional distance, $m/m_s$ , percent	Axial distance, $z$ , cm	Radial distance, $r$ , cm	Location
-435.6	-227.584	130.175	Plenum
-144.2	-75.364	43.512	Bellmouth Throat
-38.9	-20.373	43.512	Survey Station 1.0
-28.1	-14.732	43.512	
-9.7	-5.080	43.512	
-4.9	-2.540	43.512	
-2.4	-1.270	43.512	
-1.2	-0.635	43.512	
0.0	0.0	43.512	
2.0	1.057	43.531	
5.0	2.639	43.556	
15.1	7.864	44.066	
30.1	15.382	46.238	
50.0	23.935	52.090	
69.9	29.596	60.777	
86.6	31.811	69.215	
95.0	32.162	73.558	
100.0	32.205	76.200	
104.9	32.205	78.740	
109.7	32.205	81.280	Survey Station 2.0
111.3	32.205	82.118	
114.6	32.205	83.820	
117.0	32.205	85.090	
119.4	32.205	86.360	
121.8	32.205	87.630	
274.7	32.205	167.640	Station 3.0

TABLE V.—IMPELLER INLET AERODYNAMIC SURVEY DATA AT STATION 1  
 UPSTREAM OF ROTOR AT DESIGN FLOW  $\dot{m}_d$   
 [ $p_{std} = 101\,325\text{ N/m}^2$ ;  $t_{std} = 288.15\text{ K}$ .]

	$z$ , cm	$r$ , cm	$p/p_{std}$	
Hub	-20.373	13.905	-	
Shroud	-20.373	43.512	0.98381	
IMMERSION %	$P/p_{std}$ (total)	$p/p_{std}$ (static)	Absolute flow angle, deg	Pitch angle, deg
0.6	0.99367	0.98503	-1.1	3.9
1.0	0.99449	0.98503	-1.0	3.6
2.0	0.99585	0.98510	-1.0	2.7
3.0	0.99680	0.98503	-0.6	2.5
5.0	0.99803	0.98517	-0.8	2.7
7.0	0.99891	0.98510	-0.6	1.8
9.0	0.99925	0.98510	-0.6	1.5
11.0	0.99952	0.98517	-0.6	1.3
13.0	0.99966	0.98517	-0.6	1.4
15.0	0.99973	0.98523	-0.7	1.2
20.0	0.99986	0.98523	-0.7	2.0
30.0	0.99986	0.98557	-1.1	3.3
40.0	0.99993	0.98591	-1.0	4.8
50.0	0.99993	0.98625	-0.9	6.3
60.0	0.99986	0.98680	-1.0	8.1
70.0	0.99986	0.98734	-1.0	10.2
80.0	0.99980	0.98830	-1.4	12.5
85.0	0.99973	0.98911	-1.4	13.9
90.0	0.99966	0.98979	-1.6	15.6
93.0	0.99966	0.99020	-1.6	16.8
94.0	0.99966	0.99047	-1.6	17.2
95.0	0.99959	0.99061	-1.6	17.7
96.0	0.99959	0.99095	-1.6	18.2
97.0	0.99952	0.99122	-1.6	18.8
98.0	0.99952	0.99170	-1.7	19.5
98.5	0.99932	0.99170	-1.7	19.8

TABLE VI.—IMPELLER INLET AERODYNAMIC SURVEY DATA AT STATION 1  
 AT OFF-DESIGN OPERATING POINT (78.7 PERCENT  $\dot{m}_d$ )

[ $p_{std} = 101\,325\text{ N/m}^2$ ;  $t_{std} = 288.15\text{ K.}$ ]

	$z$ , cm	$r$ , cm	$p/p_{std}$	
Hub	-20.373	13.905	-	
Shroud	-20.373	43.512	0.99007	
IMMERSION %	$P/p_{std}$ (total)	$p/p_{std}$ (static)	Absolute flow angle, deg	Pitch angle, deg
0.6	0.99605	0.99109	-0.5	4.2
1.0	0.99660	0.99088	-0.5	3.7
2.0	0.99748	0.99095	-0.5	2.8
3.0	0.99796	0.99102	-0.6	2.7
5.0	0.99878	0.99095	-0.7	2.9
7.0	0.99918	0.99109	-0.5	2.0
9.0	0.99959	0.99109	-0.6	1.7
11.0	0.99966	0.99109	-0.5	1.5
13.0	0.99973	0.99115	-0.8	1.5
15.0	0.99986	0.99109	-0.6	1.2
20.0	1.00000	0.99105	-0.5	1.9
30.0	1.00000	0.99118	-0.6	3.3
40.0	1.00000	0.99142	-0.6	4.9
50.0	1.00000	0.99170	-0.6	6.6
60.0	1.00000	0.99211	-0.6	8.3
70.0	1.00000	0.99262	-0.9	10.2
80.0	0.99993	0.99323	-0.9	12.3
85.0	0.99993	0.99353	-1.0	12.9
90.0	0.99986	0.99406	-1.1	15.2
93.0	0.99986	0.99437	-1.1	16.3
94.0	0.99980	0.99442	-1.1	16.6
95.0	0.99986	0.99454	-1.1	16.8
96.0	0.99980	0.99469	-1.2	17.6
97.0	0.99973	0.99481	-1.1	17.7
98.0	0.99973	0.99498	-1.1	17.9
98.5	0.99966	0.99501	-1.2	18.2

TABLE VII.—IMPELLER EXIT AERODYNAMIC SURVEY DATA AT STATION 2  
AT DESIGN FLOW  $\dot{m}_d$

	$z$ , cm	$r$ , cm	$p/p_{std}$		
Hub	45.367	81.280	1.09839		
Shroud	32.205	81.280	1.09547		
IMMERSION %	$P/p_{std}$ (total)	$T/t_{std}$ (based on Euler work)	$p/p_{std}$ (static)	Absolute flow angle, deg	Pitch angle, deg
1.0	1.12840	1.04091	1.09002	-84.4	113.2
2.0	1.13391	1.04403	1.08907	-82.5	103.9
3.0	1.13745	1.04548	1.08921	-81.0	100.6
5.0	1.14208	1.04716	1.08921	-78.2	96.0
7.0	1.14548	1.04781	1.08996	-75.6	93.3
10.0	1.14895	1.04814	1.09043	-72.1	90.4
15.0	1.15140	1.04799	1.09050	-68.4	87.7
20.0	1.14997	1.04683	1.09050	-66.6	86.5
25.0	1.14643	1.04513	1.09091	-66.2	85.2
30.0	1.14296	1.04349	1.09139	-66.1	85.6
40.0	1.13820	1.04066	1.09213	-64.8	86.7
50.0	1.13752	1.03964	1.09275	-63.4	87.1
60.0	1.13909	1.03973	1.09336	-62.6	87.5
70.0	1.14031	1.03997	1.09384	-62.2	86.6
80.0	1.13909	1.03946	1.09431	-62.9	85.9
85.0	1.13759	1.03902	1.09445	-63.8	84.3
90.0	1.13568	1.03852	1.09465	-65.2	82.4
93.0	1.13487	1.03852	1.09458	-66.3	78.8
95.0	1.13487	1.03914	1.09377	-67.1	69.5
96.0	1.13514	1.03916	1.09418	-67.6	71.1
97.0	1.13562	1.03921	1.09486	-67.9	82.0
98.0	1.13616	1.03879	1.09635	-68.3	-
ENERGY AVERAGED TOTAL PRESSURE RATIO ACROSS IMPELLER					1.141
MASS AVERAGED TOTAL TEMPERATURE RATIO ACROSS IMPELLER					1.042
IMPELLER ADIABATIC EFFICIENCY			TEMPERATURE BASED		0.922
			TORQUE BASED		0.922

TABLE VIII.—IMPELLER EXIT AERODYNAMIC SURVEY DATA AT STATION 2  
AT OFF-DESIGN FLOW (78.7 percent  $m_d$ )

	z, cm	r, cm	$p/p_{std}$		
Hub	45.367	81.280	1.11343		
Shroud	32.205	81.280	1.11330		
IMMERSION %	$P/p_{std}$ (total)	$T/t_{std}$ (based on Euler work)	$p/p_{std}$ (static)	Absolute flow angle, deg	Pitch angle, deg
1.0	1.15406	1.04041	1.10207	-82.6	100.2
2.0	1.16120	1.04324	1.10112	-80.9	98.9
3.0	1.16522	1.04457	1.10159	-80.0	97.6
5.0	1.17032	1.04644	1.10261	-77.8	95.7
7.0	1.17386	1.04789	1.10377	-76.2	93.6
10.0	1.17774	1.04945	1.10513	-74.2	90.8
15.0	1.18141	1.05213	1.10595	-72.8	88.2
20.0	1.18053	1.05377	1.10629	-72.3	87.3
25.0	1.17794	1.05454	1.10635	-73.1	87.9
30.0	1.17433	1.05441	1.10649	-74.4	91.3
40.0	1.16814	1.05209	1.10778	-76.2	95.0
50.0	1.16345	1.04933	1.10867	-74.7	97.0
60.0	1.16290	1.04827	1.10976	-72.3	98.3
70.0	1.16522	1.04887	1.11078	-71.4	98.4
80.0	1.16501	1.04901	1.11078	-72.1	97.3
85.0	1.16392	1.04887	1.11044	-73.2	94.2
90.0	1.16249	1.04851	1.11057	-74.6	89.8
93.0	1.16181	1.04835	1.11044	-75.3	80.5
95.0	1.16202	1.04847	1.11023	-75.7	-25.1
96.0	1.16236	1.04858	1.11056	-75.8	-68.2
97.0	1.16249	1.04868	1.11091	-75.9	-61.6
98.0	1.16168	1.04849	1.11112	-76.2	-
ENERGY AVERAGED TOTAL PRESSURE RATIO ACROSS IMPELLER					1.169
MASS AVERAGED TOTAL TEMPERATURE RATIO ACROSS IMPELLER					1.050
IMPELLER ADIABATIC EFFICIENCY			TEMPERATURE BASED		0.907
			TORQUE BASED		0.931

TABLE IX.—NORMALIZED MEASURED BLADE STATIC PRESSURES AT DESIGN FLOW  $\dot{m}_d$

		NORMALIZED STATIC PRESSURE, $p/p_{std}$						
		Percent Meridional Distance	Percent Span From Hub					
			5	20	49	79	94	98
P R E S S U R E	S U R F A C E	0.0	a	a	a	a	a	a
		2.5	0.96879	0.96602	0.95502	0.93757	0.92892	0.92870
		5.0	0.97474	0.97177	0.96375	0.95162	0.94303	0.94041
		15.0	0.98056	0.97687	0.96942	0.95758	0.94963	0.94779
		30.0	0.97921	0.97765	0.97120	0.96134	0.95609	0.95368
		50.0	0.97957	0.97723	0.97098	0.96581	0.96524	0.96566
		70.0	0.97886	0.97666	0.97077	0.96715	0.96857	0.97049
		90.0	0.97602	0.97531	0.97382	0.97063	0.97013	0.97212
		95.0	0.97169	0.97184	0.97091	0.96815	0.96751	0.97006
		98.0	0.96297	0.96481	0.96673	0.96425	0.96261	0.96559
S U C T I O N	S U R F A C E	0.0	0.99659	a	0.99135	0.99844	a	a
		2.5	0.95978	0.95318	0.93927	0.93026	0.94225	0.92643
		5.0	0.96325	0.95772	0.94502	0.93339	0.92750	0.92558
		15.0	0.96609	0.96148	0.94828	0.93211	0.92033	0.91827
		30.0	0.96907	0.96276	0.95297	0.94190	0.92906	0.92686
		50.0	0.97091	0.96793	0.95878	0.94566	0.93977	0.93920
		70.0	0.97013	0.96552	0.96354	0.94977	0.94388	0.96467
		90.0	0.95566	0.95389	0.94970	0.94537	0.94396	0.94417
		95.0	0.95410	0.95318	0.95006	0.94694	0.94509	0.94530
		98.0	0.95474	0.95282	0.95041	0.94956	0.94949	0.94963

<sup>a</sup>No data because of plugged static pressure tap.

TABLE X.—NORMALIZED MEASURED BLADE STATIC PRESSURES AT OFF-DESIGN FLOW (78.7 percent  $m_d$ )

		NORMALIZED BLADE STATIC PRESSURE, $p/p_{std}$						
		Percent Meridional Distance	Percent Span From Hub					
			5	20	49	79	94	98
P R E S S U R E	S U R F A C E	0.0	a	a	a	a	a	a
		2.5	0.98240	0.98049	0.97439	0.96452	0.95814	0.95452
		5.0	0.98531	0.98283	0.97722	0.96821	0.96275	0.96140
		15.0	0.98872	0.98609	0.98098	0.97197	0.96630	0.96495
		30.0	0.98730	0.98602	0.98198	0.97566	0.97261	0.97141
		50.0	0.98680	0.98524	0.98141	0.97517	0.97332	0.97375
		70.0	0.98659	0.98496	0.98091	0.97701	0.97602	0.97694
		90.0	0.98652	0.98645	0.98503	0.98411	0.98389	0.98432
		95.0	0.98318	0.98368	0.98290	0.98177	0.98205	0.98177
		98.0	0.97666	0.97808	0.97744	0.97772	0.97744	0.97772
S U C T I O N	S U R F A C E	0.0	0.98716	a	0.99283	0.97247	a	a
		2.5	0.96935	0.96183	0.94487	0.92848	0.93919	0.92089
		5.0	0.97481	0.96956	0.95729	0.94359	0.93394	0.93167
		15.0	0.97808	0.97424	0.96509	0.95182	0.94388	0.94182
		30.0	0.97978	0.97488	0.96786	0.96027	0.95055	0.94934
		50.0	0.97886	0.97651	0.96985	0.96048	0.95445	0.95580
		70.0	0.97630	0.97325	a	0.96090	0.95750	0.97609
		90.0	0.96701	0.96523	0.96247	0.95998	0.95906	0.95885
		95.0	0.96687	0.96538	0.96296	0.96183	0.96076	0.96055
		98.0	0.96821	0.96658	0.96310	0.96289	0.96254	0.96240

<sup>a</sup>No data because of plugged static pressure tap.

TABLE XI.—NORMALIZED SHROUD STATIC PRESSURES FOR A RANGE OF MASS FLOW RATES

$m/m_s$ , percent	NORMALIZED SHROUD STATIC PRESSURE, $p/p_{std}$										
	$m/m_d$ , percent										
	38.45	51.34	57.08	62.45	68.04	76.01	83.37	90.22	99.94	115.93	132.40
-500.0	1.00000	1.00000	1.00000	1.00000	1.00000	1.00000	1.00000	1.00000	1.00000	1.00000	1.00000
-487.0	1.00009	1.00010	1.00010	1.00009	1.00005	1.00012	1.00006	1.00007	1.00010	1.00000	0.99989
-38.9	0.99846	0.99724	0.99659	0.99591	0.99514	0.99392	0.99268	0.99141	0.98944	0.98573	0.98129
-28.1	0.99819	0.99598	0.99500	0.99393	0.99271	0.99097	0.98909	0.98721	0.98429	0.97878	0.97221
-9.7	0.99826	0.99523	0.99428	0.99271	0.99107	0.98879	0.98653	0.98422	0.98066	0.97392	0.96592
-4.9	0.99826	0.99489	0.99352	0.99257	0.98973	0.98710	0.98492	0.98273	0.97884	0.97170	0.96294
-2.4	1.00069	0.99586	0.99369	0.99206	0.98997	0.98730	0.98465	0.98195	0.97878	0.96978	0.96046
-1.2	1.00108	0.99604	0.99376	0.99204	0.98989	0.98711	0.98514	0.98362	0.98114	0.96867	0.95874
0.0	1.00138	0.99626	0.99403	0.99233	0.99012	0.98713	0.98409	0.98087	0.97586	0.96607	0.95409
2.0	1.00235	0.99707	0.99507	0.99284	0.99067	0.98724	0.98417	0.98012	0.97547	0.95985	0.94173
5.0	1.00395	1.00131	1.00026	0.99967	0.99771	0.99237	0.98574	0.98066	0.97560	0.95692	0.93565
15.1	1.00792	1.00926	1.00895	1.01000	1.00632	0.99962	0.99269	0.98563	0.97666	0.95545	0.93429
30.1	1.01556	1.01800	1.01806	1.01922	1.01600	1.00976	1.00323	0.99639	0.98587	0.96594	0.94136
50.0	1.03369	1.03479	1.03462	1.03538	1.03265	1.02700	1.02134	1.01622	1.00842	0.99142	0.96971
69.9	1.06031	1.06066	1.06030	1.06060	1.05810	1.05270	1.04785	1.04295	1.03523	1.01883	0.99877
86.6	1.08765	1.08836	1.08837	1.08878	1.08693	1.08210	1.07658	1.07080	1.06400	1.04981	1.03174
95.0	1.10257	1.10343	1.10326	1.10372	1.10194	1.09766	1.09275	1.08751	1.08011	1.06665	1.04932
100.0	1.11020	1.11115	1.11067	1.11120	1.10939	1.10527	1.10085	1.09634	1.08948	1.07659	1.05963
104.9	1.11556	1.11676	1.11625	1.11688	1.11490	1.11054	1.10571	1.10069	1.09303	1.07960	1.06271
109.7	1.11894	1.12080	1.12027	1.12130	1.11932	1.11487	1.11010	1.10472	1.09665	1.08206	1.06479
111.3	1.11951	1.12135	1.12060	1.12168	1.11978	1.11537	1.11064	1.10525	1.09742	1.08262	1.06514
114.6	1.12124	1.12291	1.12167	1.12289	1.12106	1.11672	1.11196	1.10663	1.09908	1.08389	1.06612
117.0	1.12290	1.12390	1.12214	1.12320	1.12132	1.11689	1.11184	1.10665	1.09983	1.08512	1.06652
119.4	1.12456	1.12534	1.12295	1.12401	1.12213	1.11777	1.11273	1.10754	1.10099	1.08641	1.06736
121.8	1.12599	1.12694	1.12397	1.12517	1.12364	1.11951	1.11468	1.10954	1.10268	1.08745	1.06845
274.7	1.13576	1.13393	1.13054	1.12942	1.12765	1.12300	1.11791	1.11226	1.10514	1.09251	1.07396

TABLE XII.—MEASURED PITCH ANGLES OF AMMONIA-OZALID FLOW TRACES  
AT DESIGN FLOW  $m_d$

		Pitch Angle Measured from Axial, deg						
		Percent Meridional Distance	Percent Span From Hub					
			5	20	49	79	94	98
P R E S S U R E	S U R F A C E	0.0	a	a	a	a	a	a
		2.5	a	a	12.1	a	1.1	1.0
		5.0	7.8	11.8	14.8	a	a	a
		15.0	19.3	21.3	24.3	22.3	27.3	30.3
		30.0	26.1	42.1	47.1	48.1	46.1	44.1
		50.0	52.8	a	71.8	63.8	51.8	a
		70.0	93.7	99.7	107.7	50.7	49.7	66.7
		90.0	89.9	264.0	109.0	91.0	64.0	86.0
		95.0	a	93.0	105.0	257.0	57.0	a
	98.0	90.0	268.0	259.0	256.0	77.0	79.9	
S U C T I O N	S U R F A C E	0.0	12.0	9.0	a	1.1	1.1	a
		2.5	14.6	11.6	3.6	a	2.3	3.3
		5.0	15.8	a	7.8	5.8	2.1	2.1
		15.0	59.3	38.3	19.3	13.3	31.3	15.3
		30.0	a	56.1	54.1	a	54.1	62.1
		50.0	59.8	73.8	83.8	86.8	75.8	67.8
		70.0	a	90.7	a	105.7	99.7	83.7
		90.0	a	271.0	91.0	a	268.0	83.0
		95.0	269.9	270.0	a	96.0	93.0	a
	98.0	90.9	93.0	268.0	a	95.0	90.9	

<sup>a</sup>No data because of plugged static pressure tap.

TABLE XIII.—FIGURE AND PAGE NUMBERS OF PLOTTED LASER ANEMOMETER RESULTS

Streamwise grid station index, J	Velocity				Contour		Wire-frame		Vector	
	Fig #	Page #			Fig #	Page #	Fig #	Page #	Fig #	Page #
		Radial <sup>a</sup>	Rel. Tan. <sup>b</sup>	Axial <sup>c</sup>						
Design flow										
23	24	49	53	57	52	280	80	284	108	289
48	25	61	64	67	53	280	81	285	109	289
51	26	70	74	78	54	280	82	285	110	290
71	27	82	84	86	55	280	83	285	111	290
73	28	88	91	94	56	281	84	285	112	290
74	29	97	99	101	57	281	85	285	113	290
85	30	103	106	109	58	281	86	285	114	291
95	31	112	114	116	59	281	87	286	115	291
110	32	118	121	124	60	281	88	286	116	291
118	33	127	130	133	61	282	89	286	117	291
126	34	136	140	144	62	282	90	286	118	291
135	35	148	152	156	63	282	91	286	119	291
156	36	160	163	166	64	282	92	286	120	292
160	37	169	171	173	65	282	93	287	121	292
163	38	175	176	177	66	282	94	287	122	292
165	39	178	181	184	67	283	95	287	123	292
167	40	187	190	193	68	283	96	287	124	292
170	41	196	199	202	69	283	97	287	125	292
172	42	205	208	211	70	283	98	287	126	293
173	43	214	217	220	71	283	99	288	127	293
175	44	223	226	229	72	283	100	288	128	293
177	45	232	234	236	73	283	101	288	129	293
178	46	238	241	244	74	283	102	288	130	293
Off design flow										
118	47	247	249	251	75	284	103	288	131	293
126	48	253	255	257	76	284	104	288	132	294
135	49	259	261	263	77	284	105	289	133	294
165	50	265	268	271	78	284	106	289	134	294
172	51	274	276	278	79	284	107	289	135	294

<sup>a</sup>Part (a) of figure.

<sup>b</sup>Part (b) of figure.

<sup>c</sup>Part (c) of figure.

TABLE XIV.—AERODYNAMIC SURVEY PROBE MEASUREMENT UNCERTAINTIES

Measureand	Uncertainty	
	Dimensional	Dimensionless
Pressure, $P, p$	68.95 N/m <sup>2</sup>	0.0007
Temperature, $T$	0.6 K	0.0019
Flow angle, $\beta$	1.5°	-----
Mass flow rate, $\dot{m}$	0.091 kg/sec	0.0030

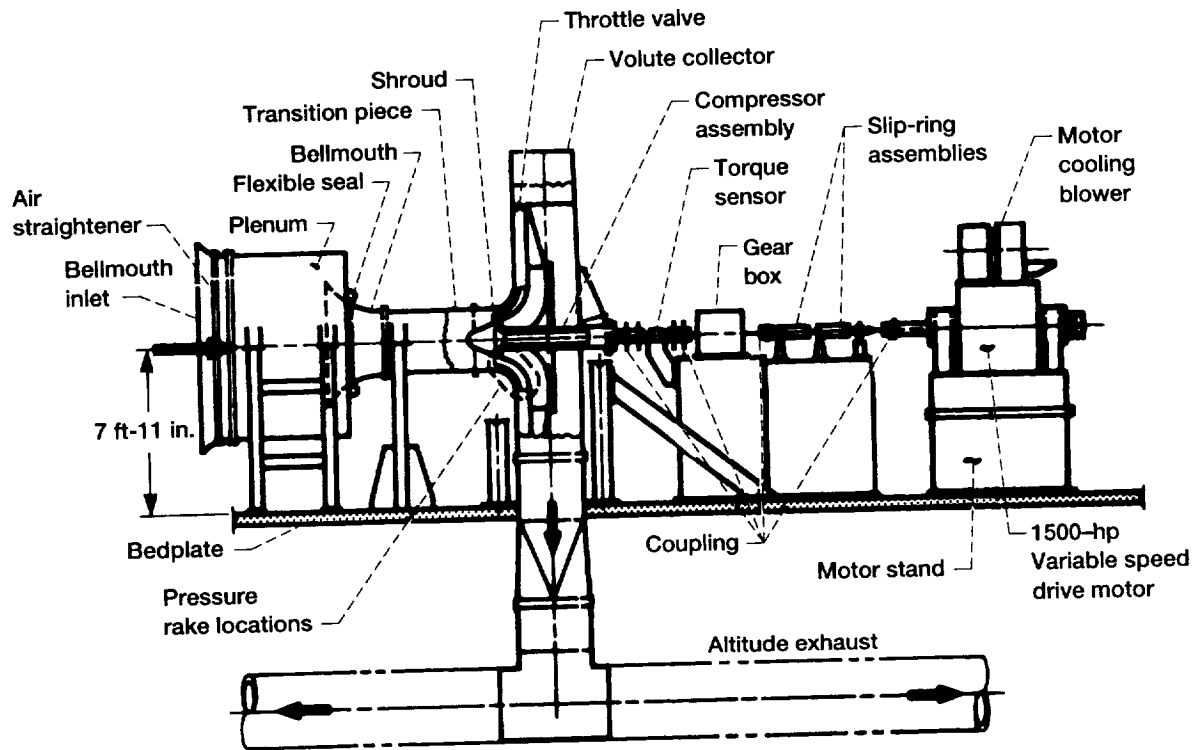


Figure 1.—Schematic of NASA Lewis low-speed centrifugal compressor test facility.

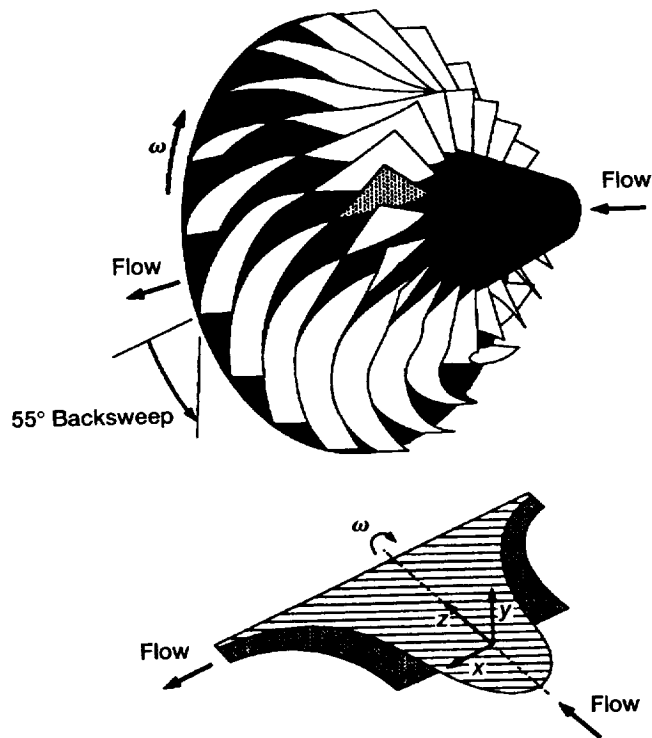


Figure 2.—Test impeller.

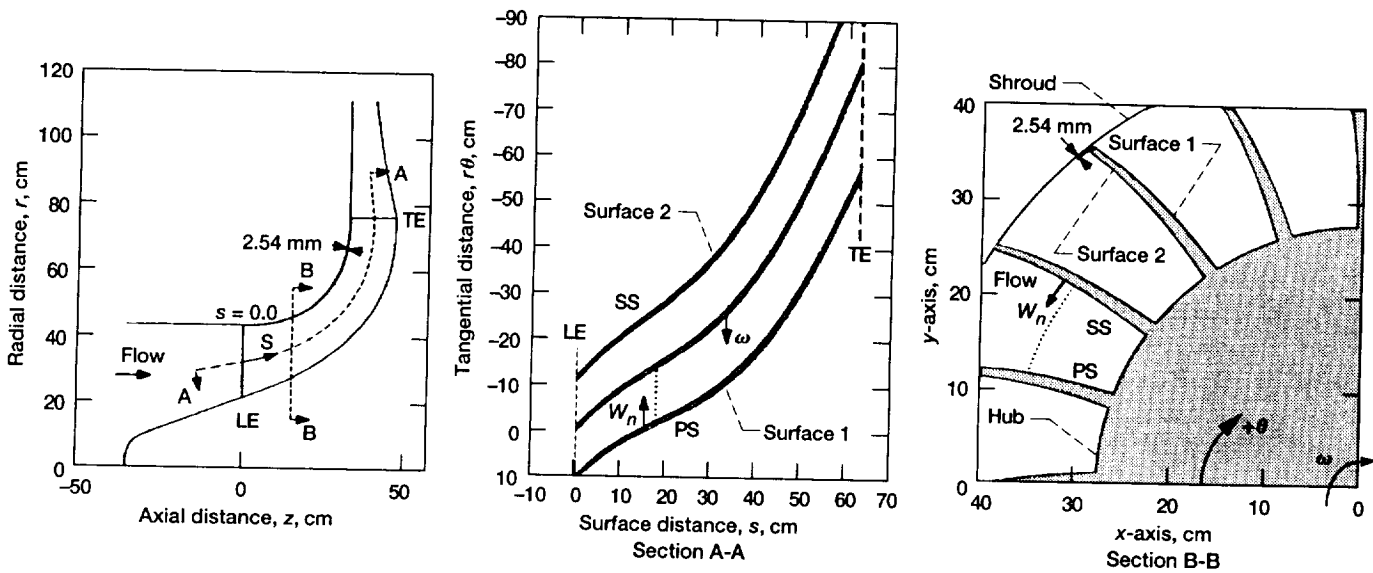


Figure 3.—Illustration of blade coordinate nomenclature (TE = trailing edge; LE = leading edge; SS = suction surface; PS = pressure surface). Although the blades are comprised of straight line elements from hub to tip along a quasi-orthogonal section, they appear curved for a constant  $z$ -section cut, as in section B-B.

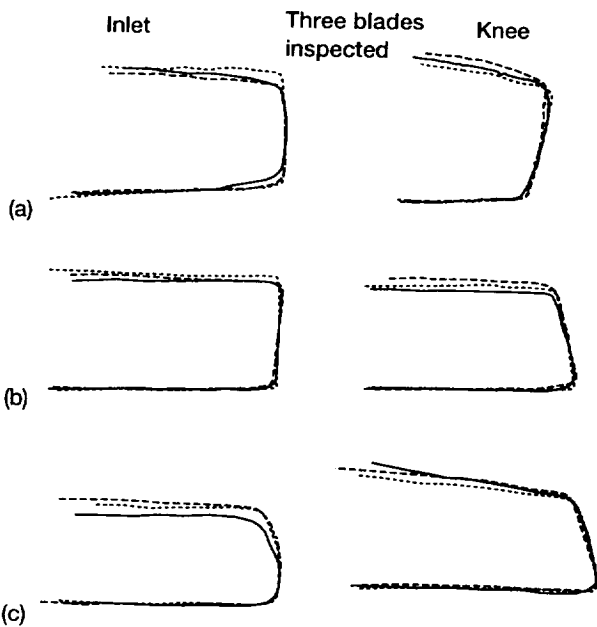


Figure 4.—Profiles of three inspected blade tips: one from the LSCC and two from high-speed impellers scaled to the same dimensions. (a) LSCC blade tips. (b) 6:1 Ti blade tips. (c) 4:1 Al blade tips. The lower side is the pressure side in all cases.

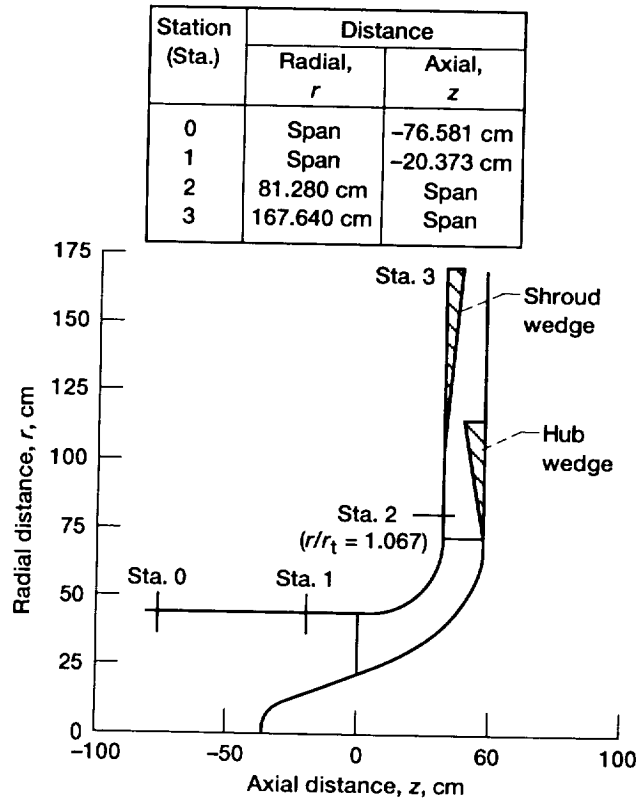


Figure 5.—Meridional view of LSCC flow path.

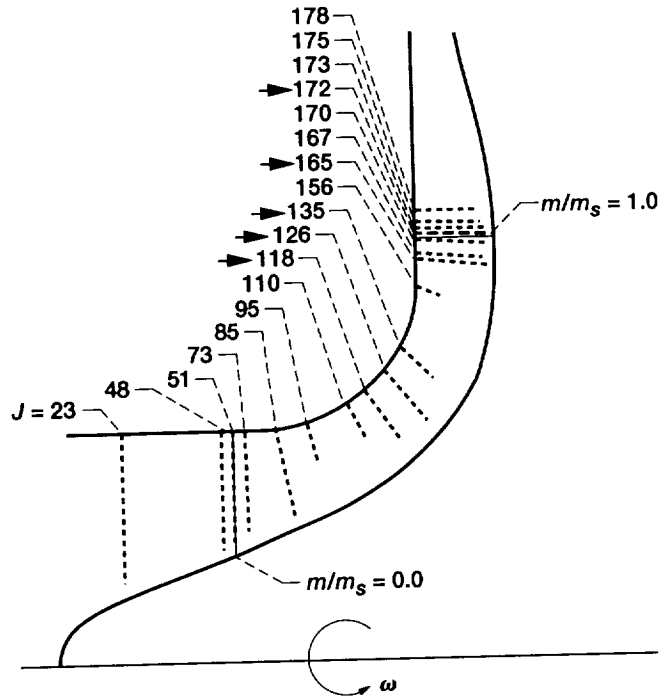


Figure 6.—Meridional view of LSCC impeller showing laser anemometer measurement locations. Arrows denote locations where measurements were acquired at both design and off-design conditions.

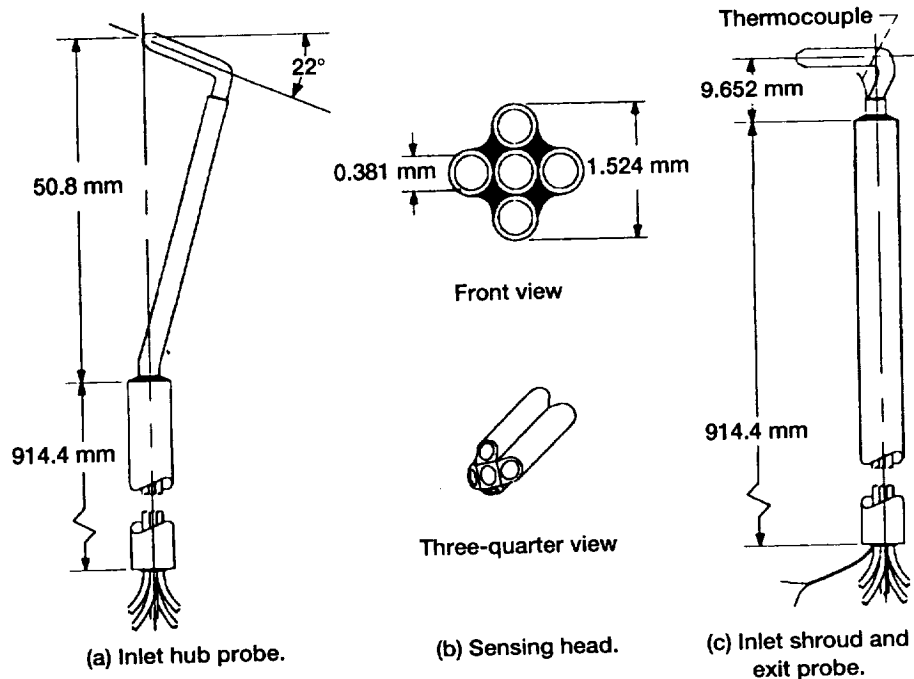


Figure 7.—Schematic of five-hole pressure probes.

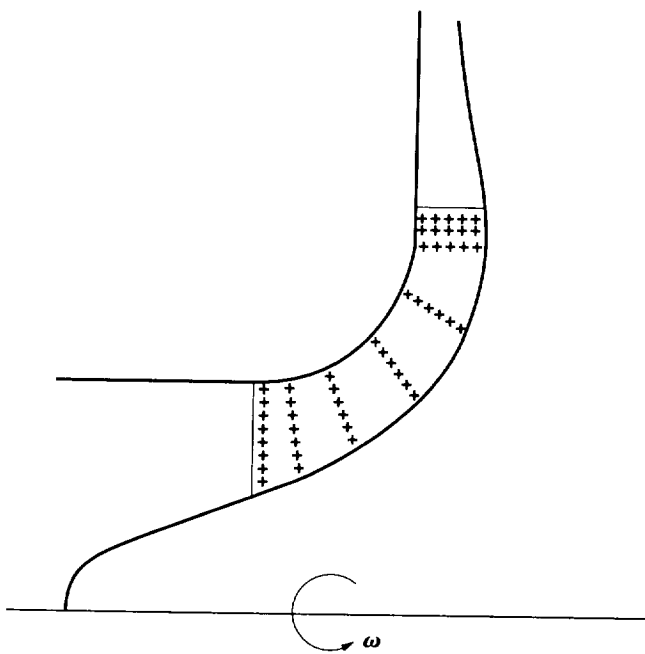


Figure 8.—Meridional view of LSCC showing location of blade static taps.

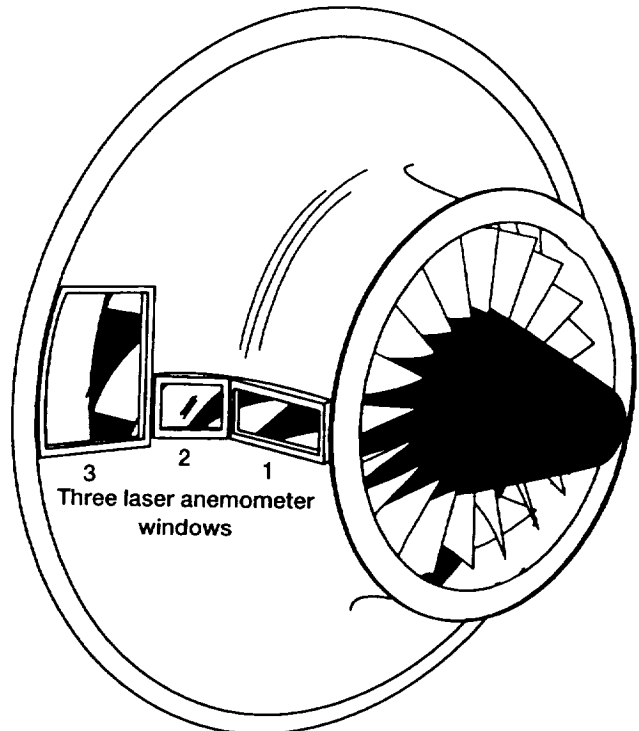
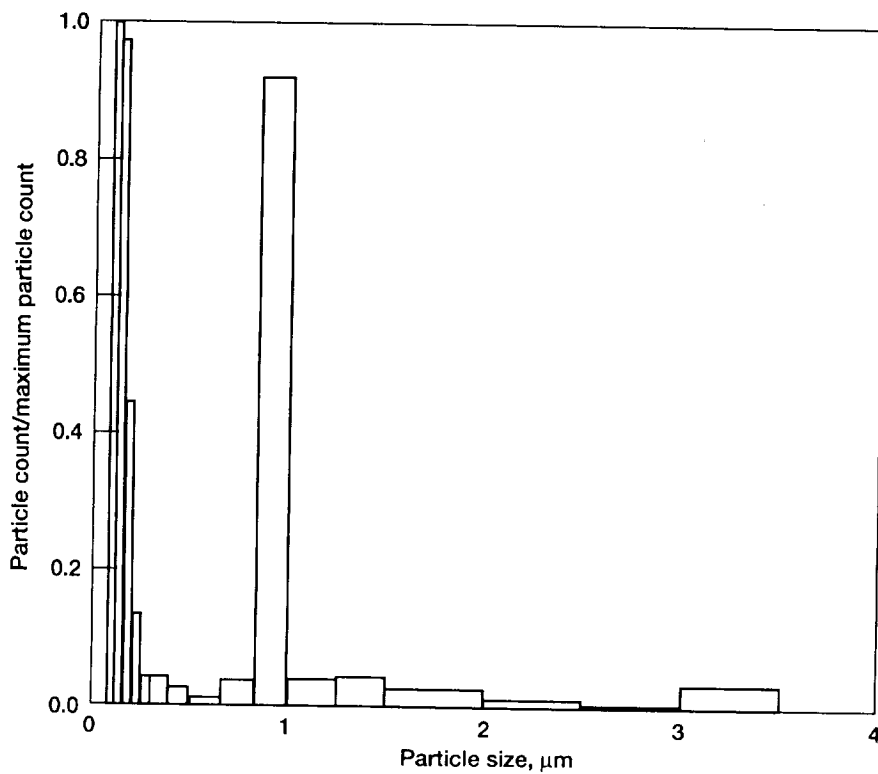


Figure 9.—Laser anemometer optical access to LSCC.



Sample duration 30 sec		
Bin number	Size, $\mu\text{m}$	Counts
1	0.1000	4606
2	0.1300	4464
3	0.1750	2014
4	0.2250	608
5	0.2750	190
6	0.3500	188
7	0.4500	135
8	0.5750	46
9	0.7250	172
10	0.9000	4261
11	1.1250	183
12	1.3750	207
13	1.7500	136
14	2.2500	27
15	2.7500	18
16	3.2500	156

Figure 10.—Seed particle measurement distribution sampled ahead of impeller.

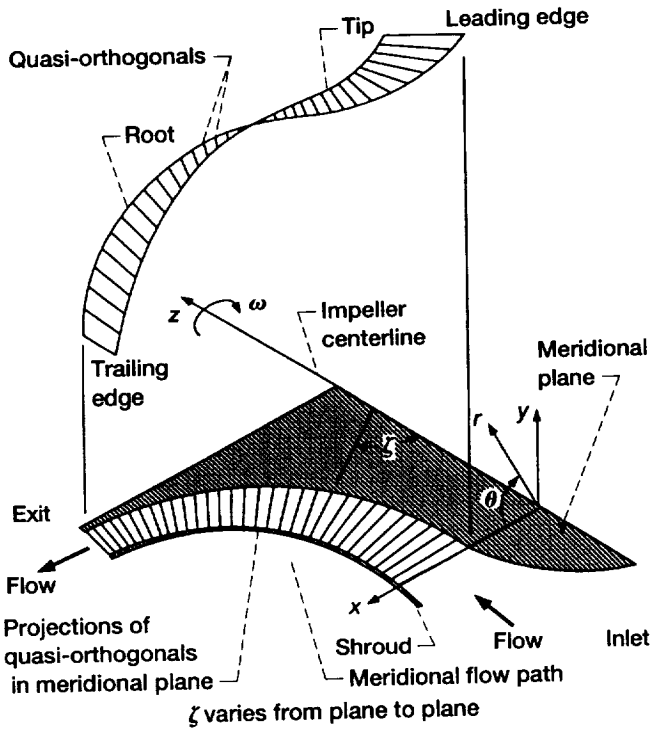


Figure 11.—Definition of azimuthal angle  $\zeta$ , which allows orientation of laser beam so as to view along a quasi-orthogonal surface.

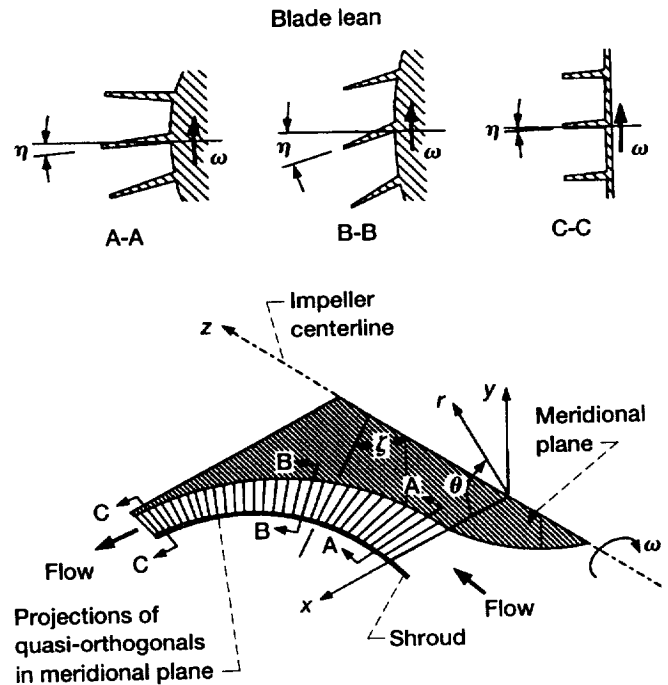


Figure 12.—Definition of declination angle  $\eta$ , which allows orientation of laser beam so as to view along blade surface.

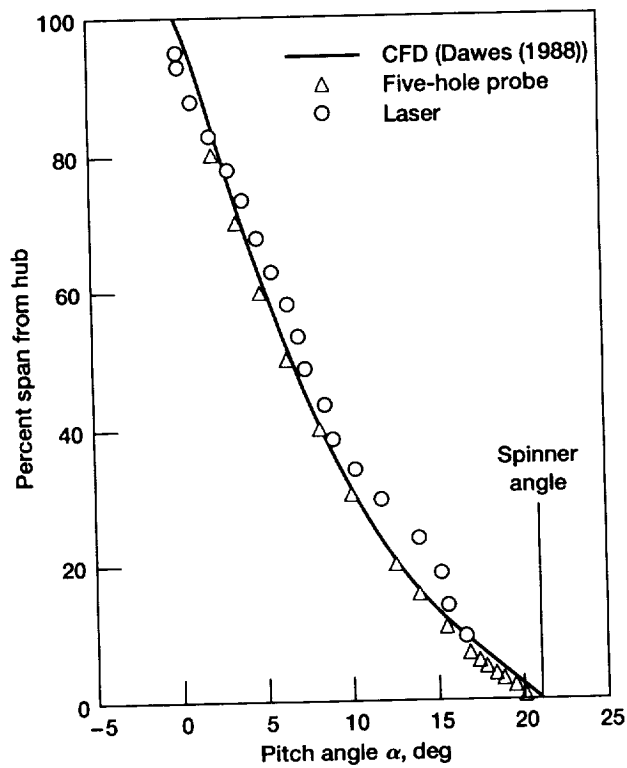


Figure 13.—Impeller inlet pitch angle distribution illustrating laser anemometer capability for resolving spanwise velocity (span = 0.294 m).

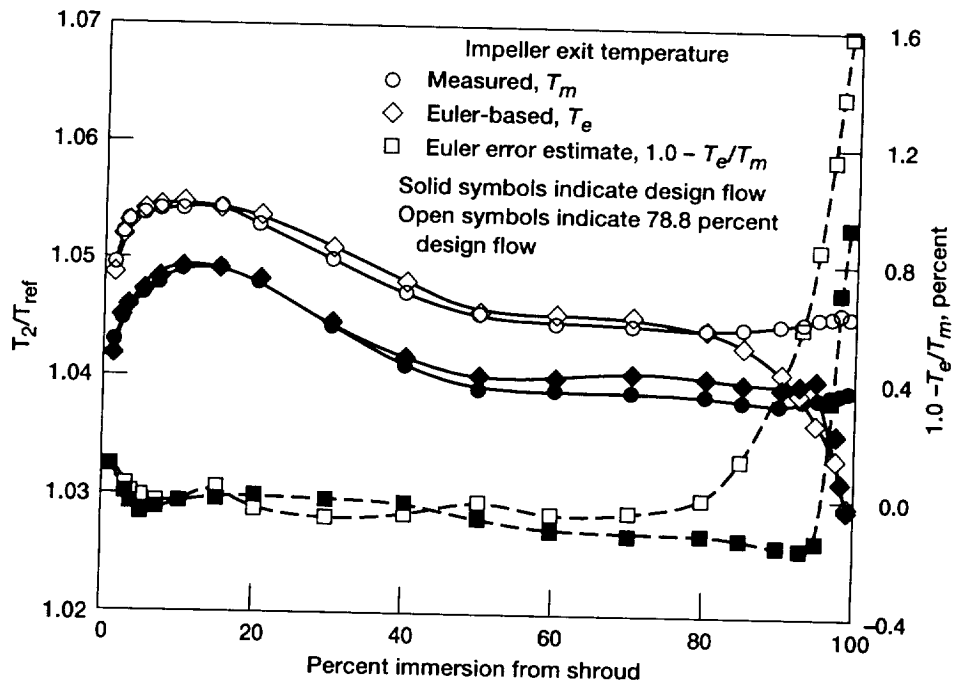


Figure 14.—Measured and Euler-based spanwise temperature distributions and error in Euler temperature estimate at impeller exit for design and higher loaded mass flow conditions.

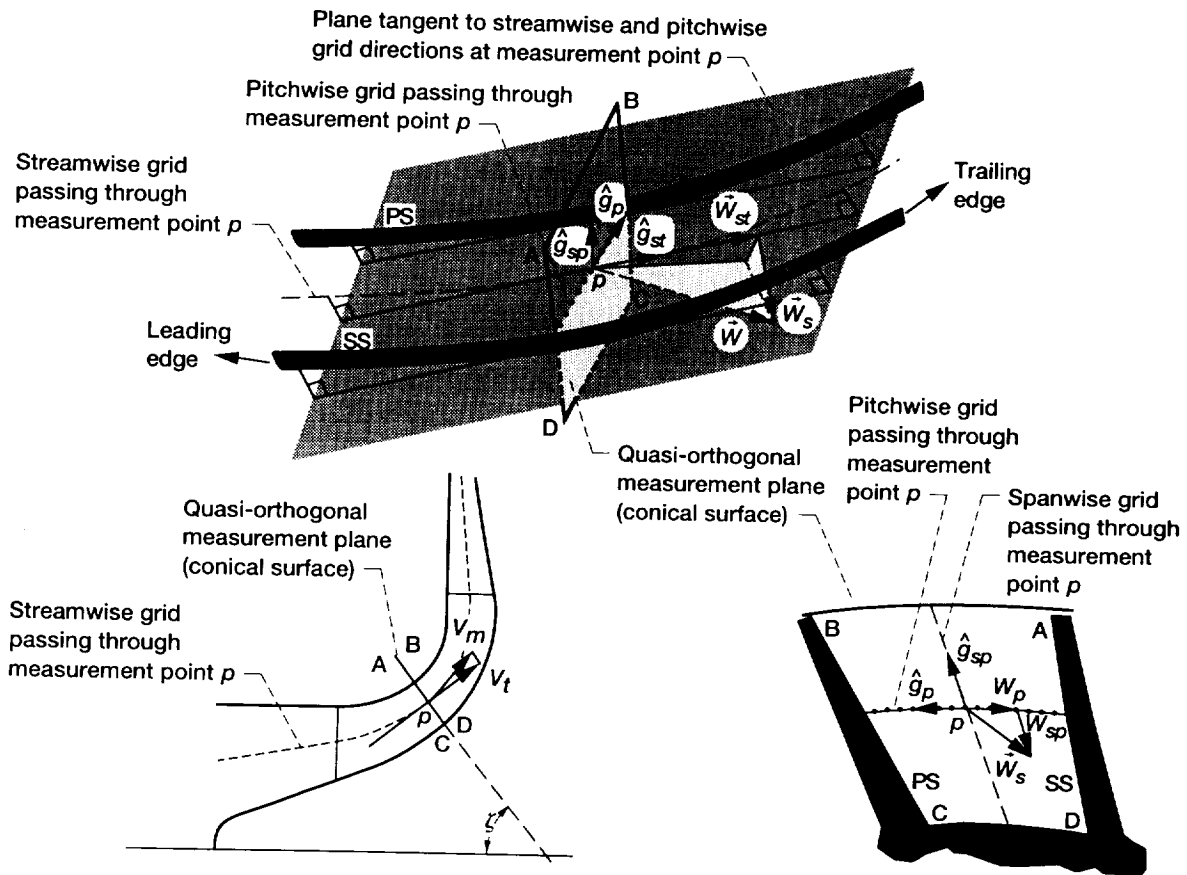


Figure 15.—Relationship of secondary and throughflow velocity components to total relative velocity vector and body-fitted measurement grid.

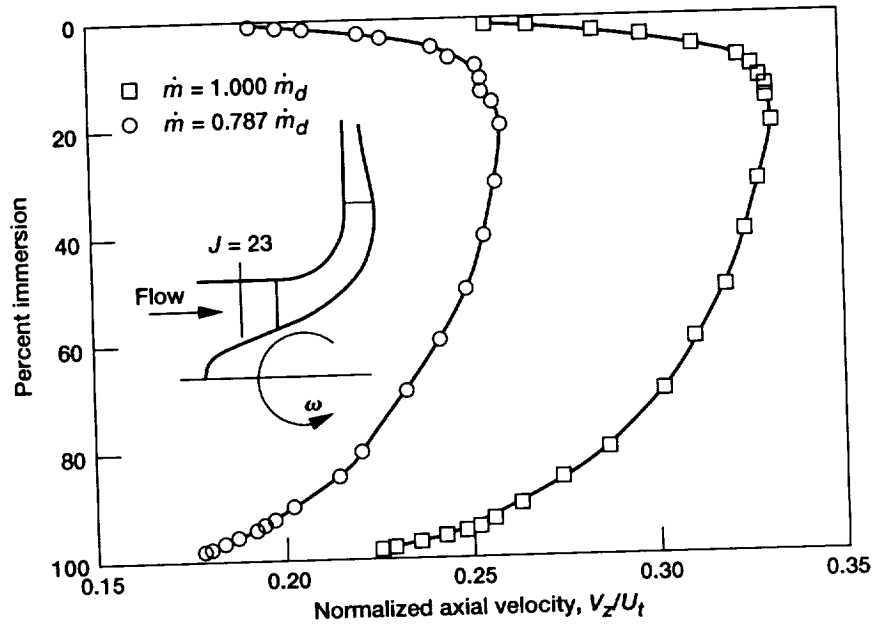


Figure 16.—Impeller inlet distribution of axial velocity normalized by impeller exit tip speed at station  $J = 23$ .

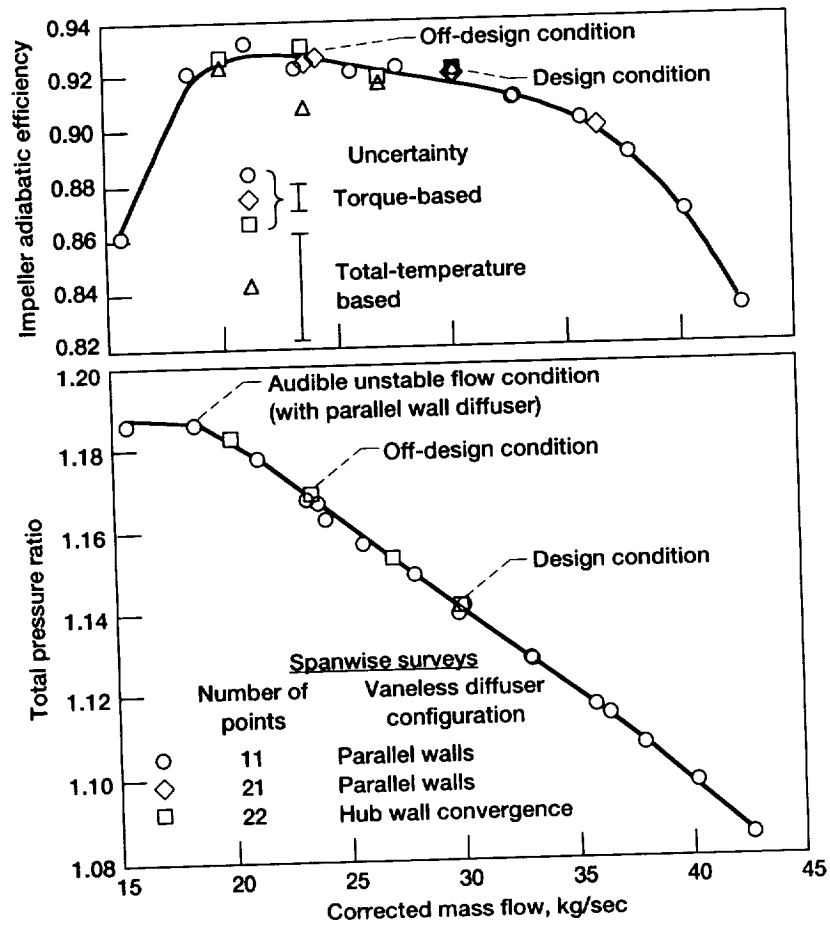


Figure 17.—Impeller performance characteristic at test speed of 1862 rpm.

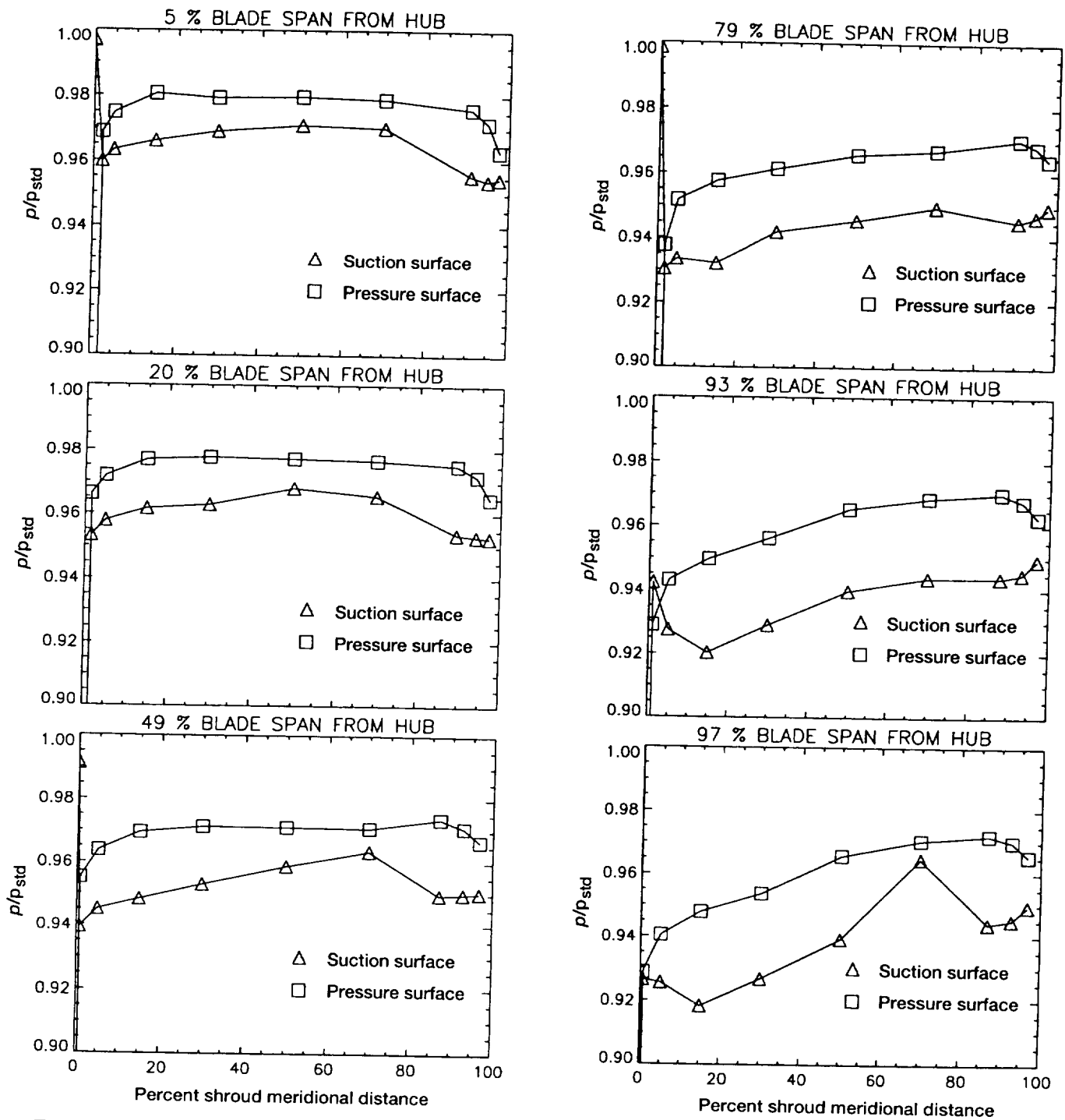


Figure 18.—Normalized blade surface pressure distributions for each spanwise location for design condition  $m_d$ .

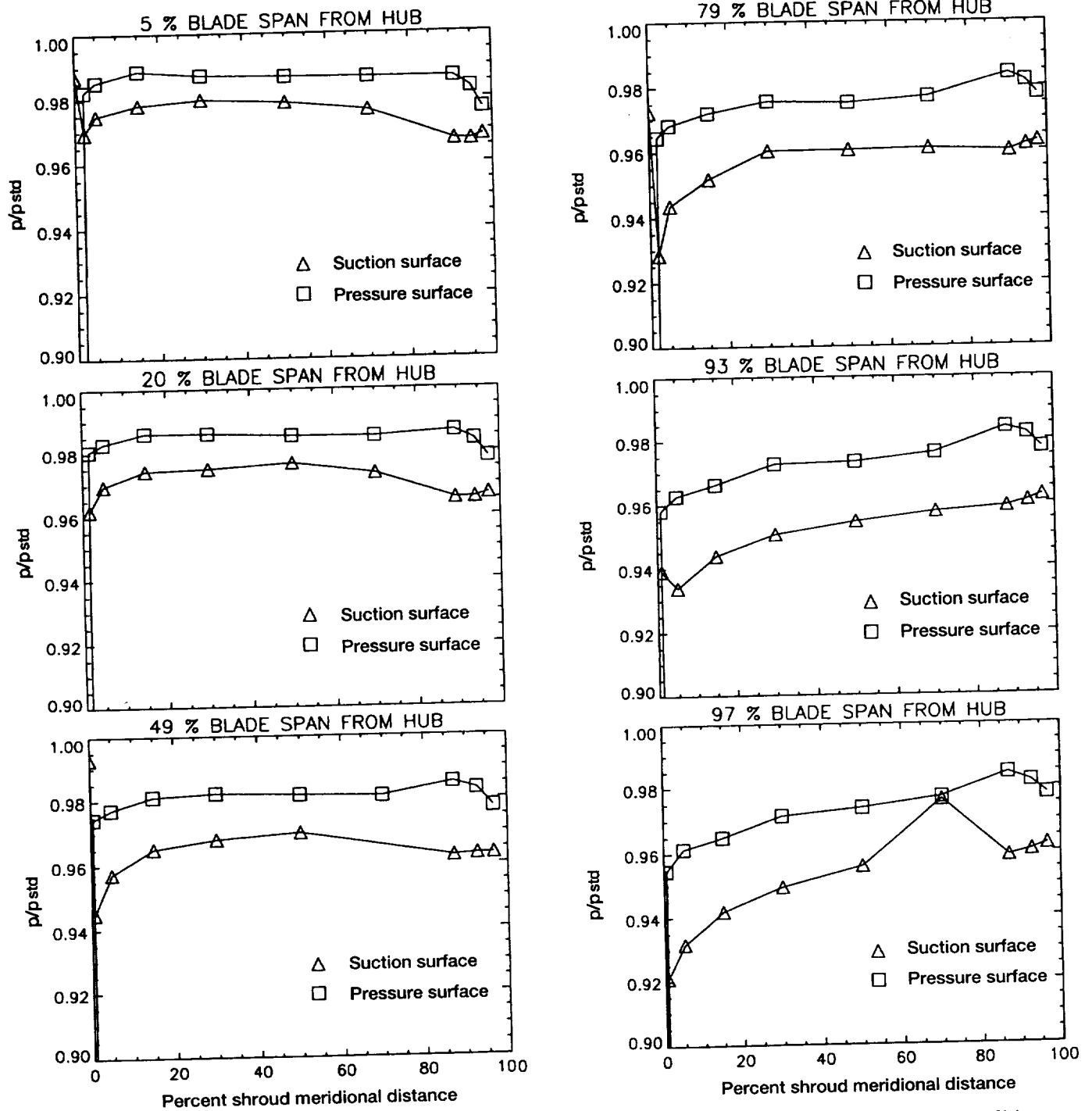
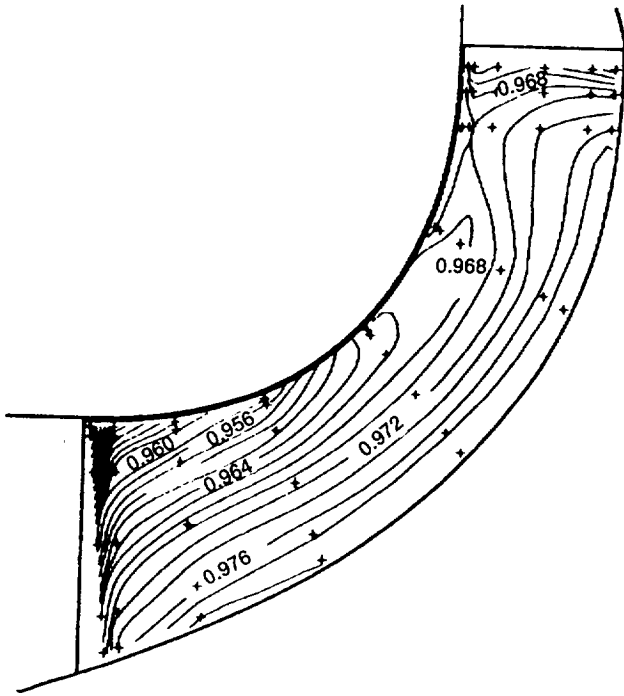
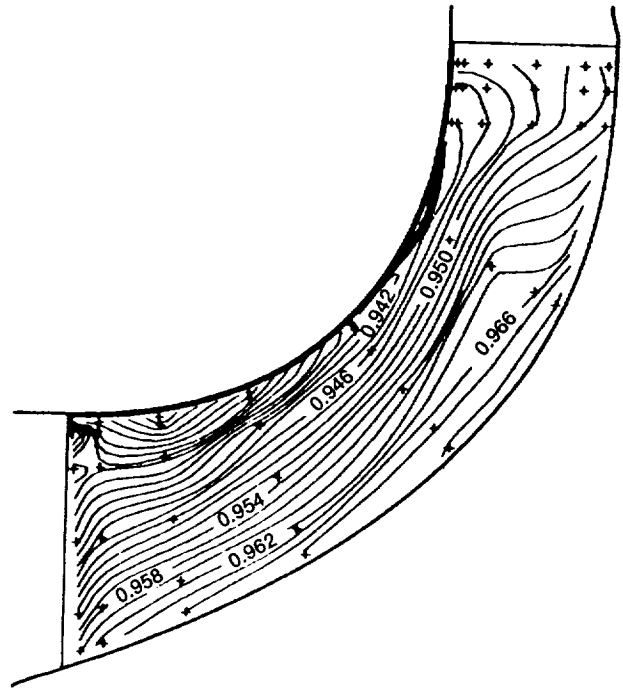


Figure 19.—Normalized blade surface pressure distributions for each spanwise location for off-design condition (78.7 percent  $\dot{m}_d$ ).

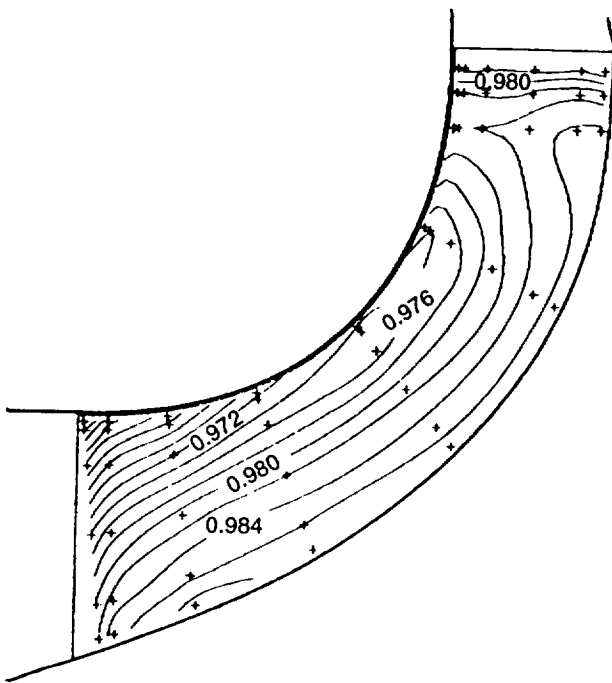


(a) Pressure surface.

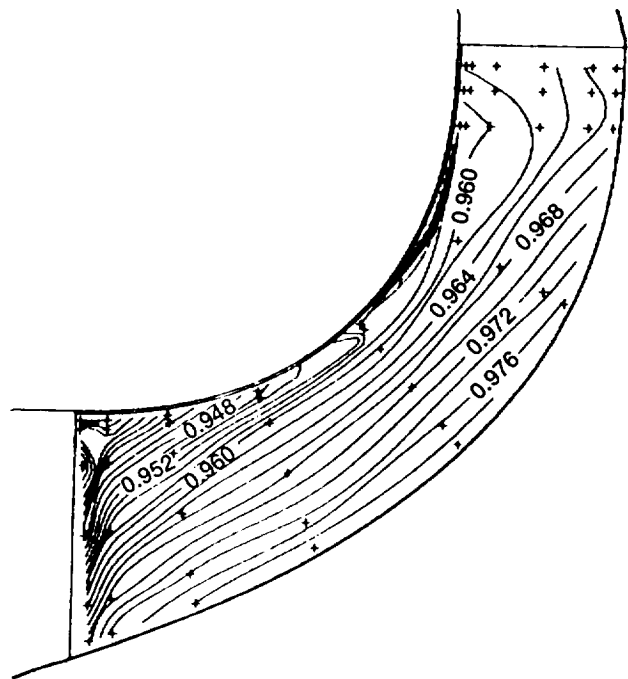


(b) Suction surface.

Figure 20.—Contour plots of pressure and suction surface static pressures normalized by  $p_{std}$  for design condition  $\dot{m}_d$  (+ denotes static pressure measurement location).



(a) Pressure surface.



(b) Suction surface.

Figure 21.—Contour plots of pressure and suction surface static pressures normalized by  $p_{std}$  for off-design condition, 78.7-percent  $\dot{m}_d$  (+ denotes static pressure measurement location).

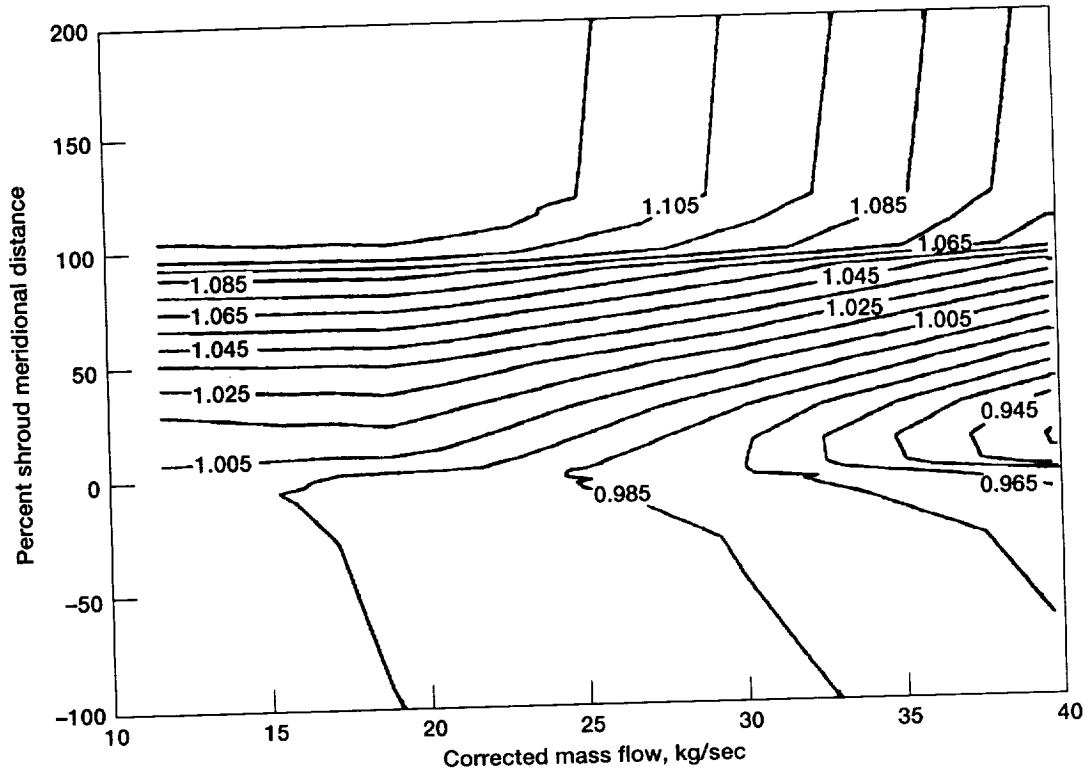
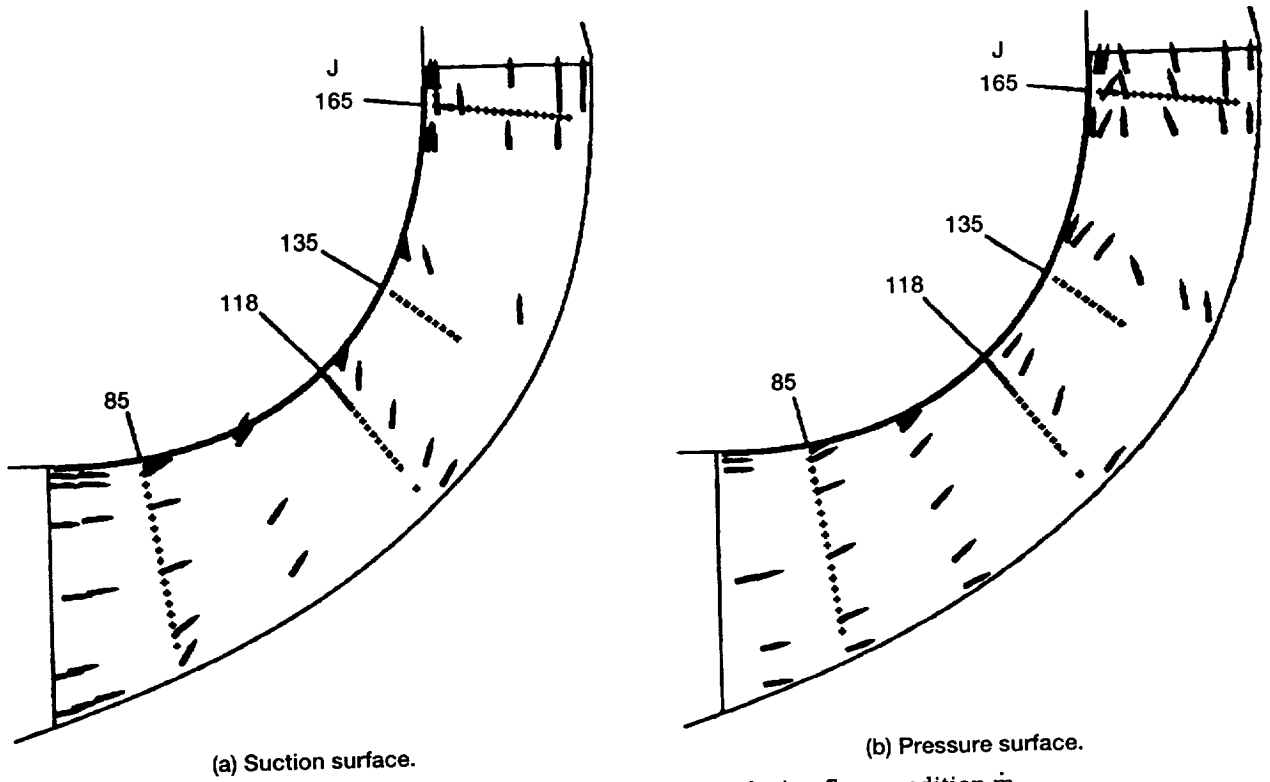


Figure 22.—Contour plots of distribution of shroud static pressures normalized by  $P_{std}$  over a range of mass flow rates.

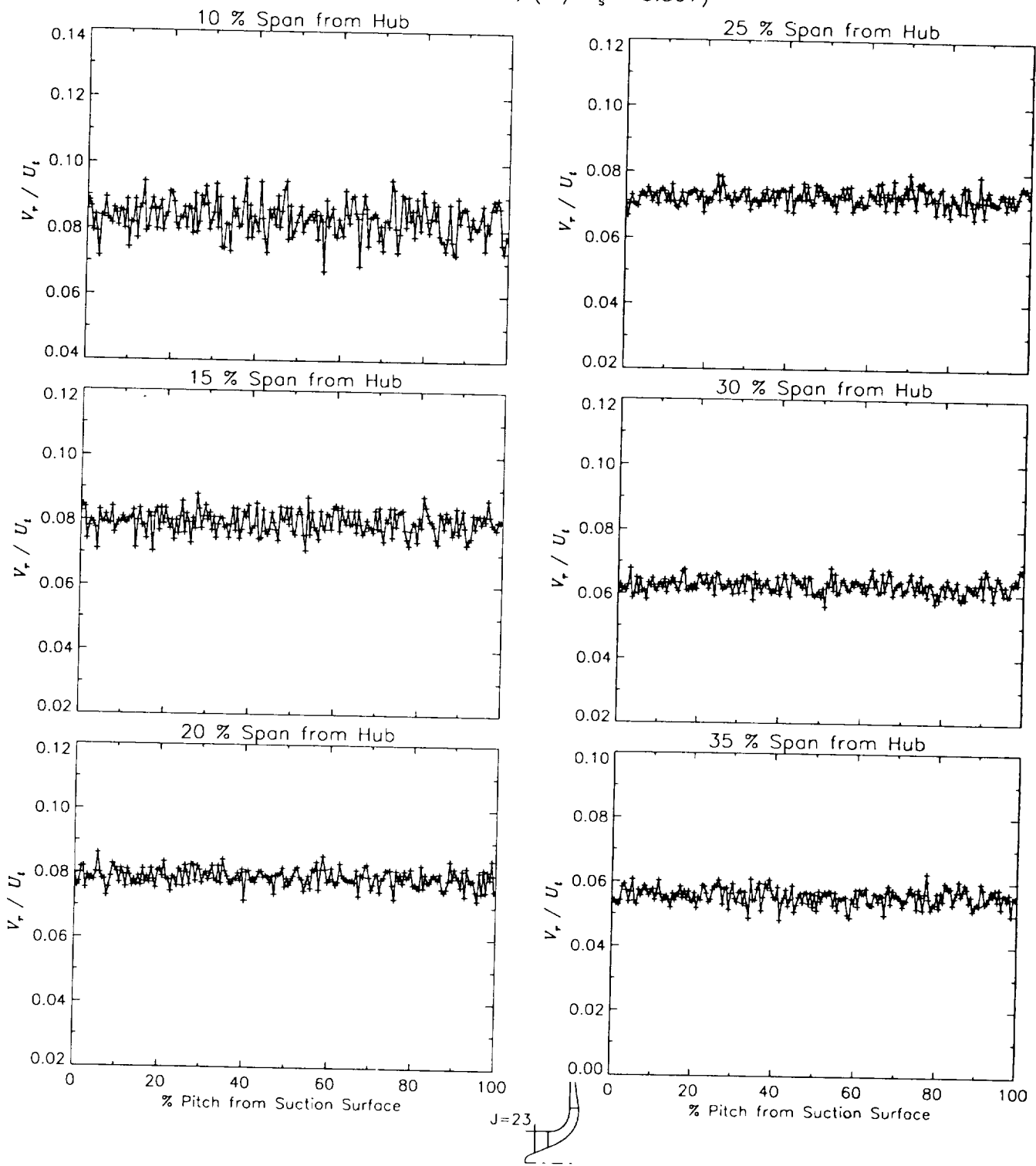


(a) Suction surface.

(b) Pressure surface.

Figure 23.—Ammonia-Ozalid flow traces at design flow condition  $\dot{m}_d$ .

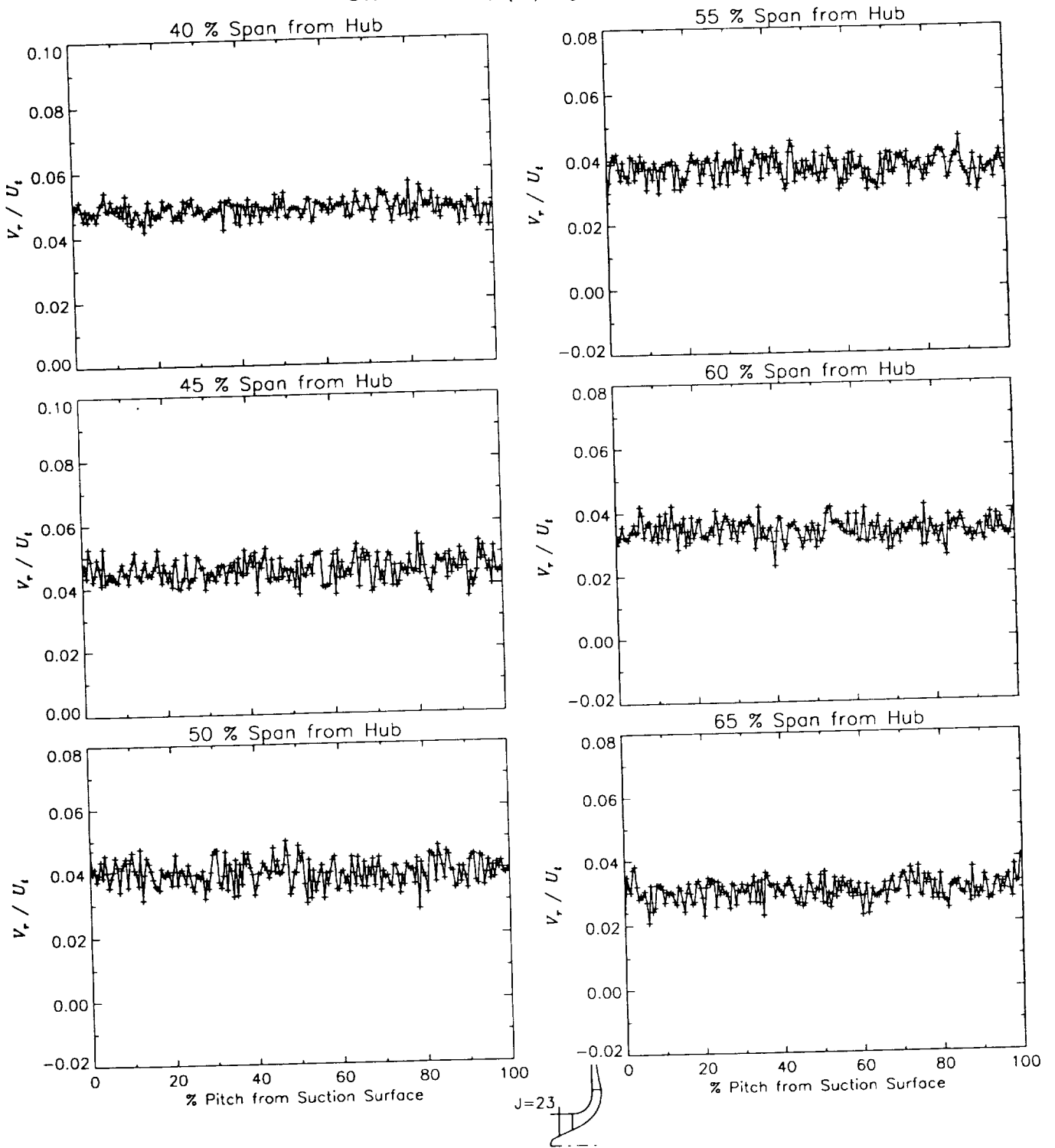
Station J=23, ( $m/m_s = -0.397$ )



(a) Radial velocity normalized by impeller tip speed.

Figure 24.—Laser velocimeter results of axial, radial, and relative tangential velocities normalized by impeller tip speed for the design flow condition,  $m_d$ , at station J=23, ( $m/m_s = -0.397$ ).

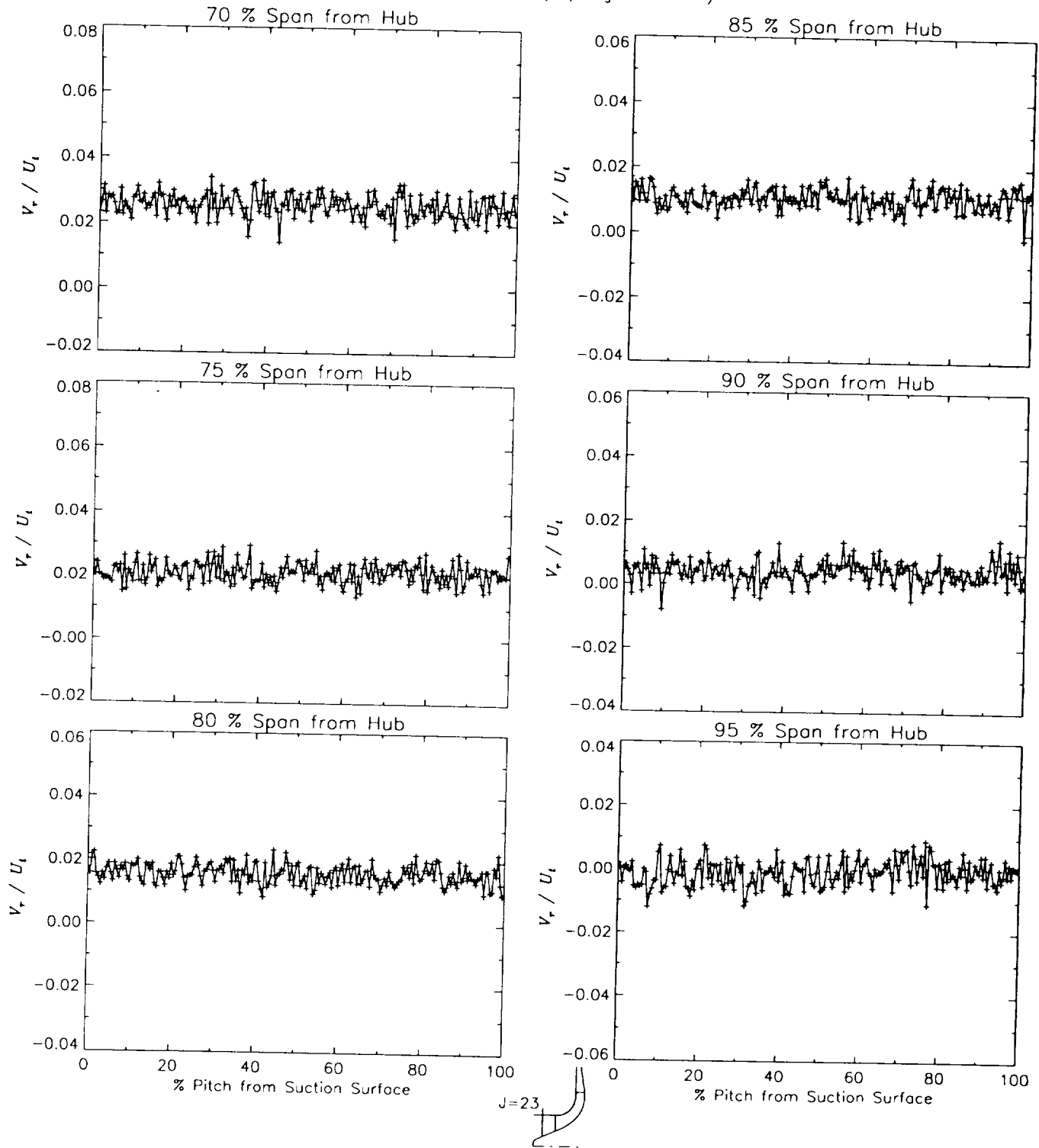
Station J=23, ( $m/m_s = -0.397$ )



(a) Radial velocity normalized by impeller tip speed.

Figure 24.-Continued.

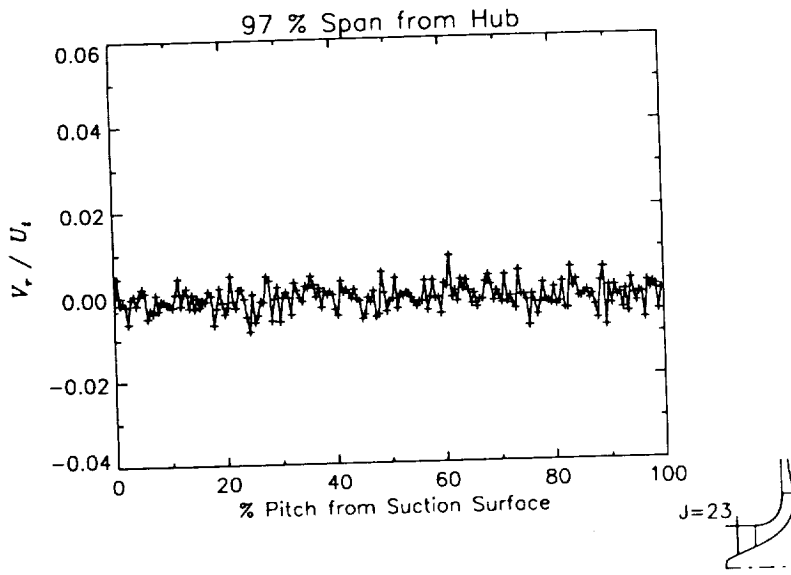
Station J=23, ( $m/m_s = -0.397$ )



(a) Radial velocity normalized by impeller tip speed.

Figure 24.—Continued.

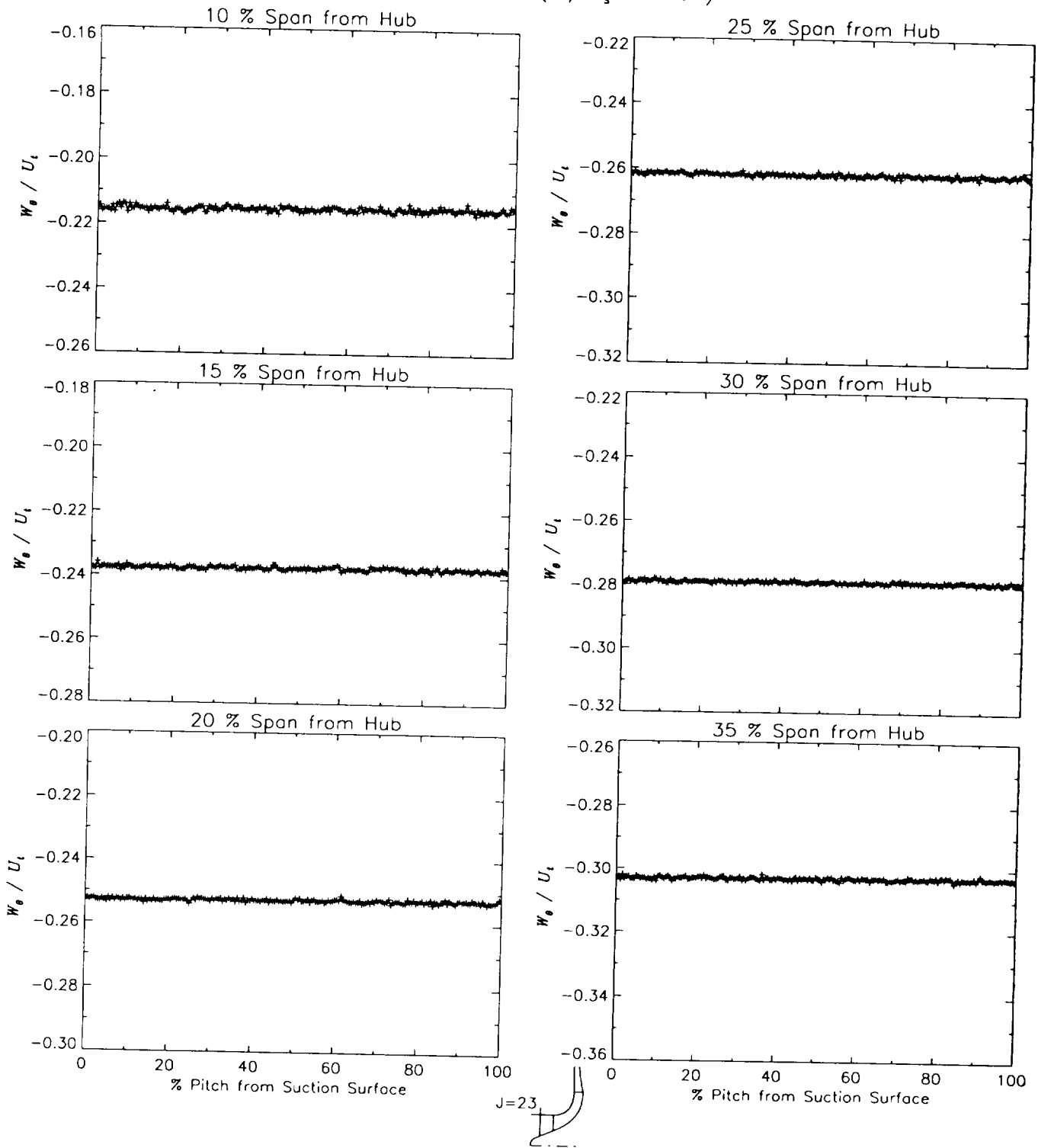
Station J=23, ( $m/m_s = -0.397$ )



(a) Radial velocity normalized by impeller tip speed.

Figure 24.-Continued.

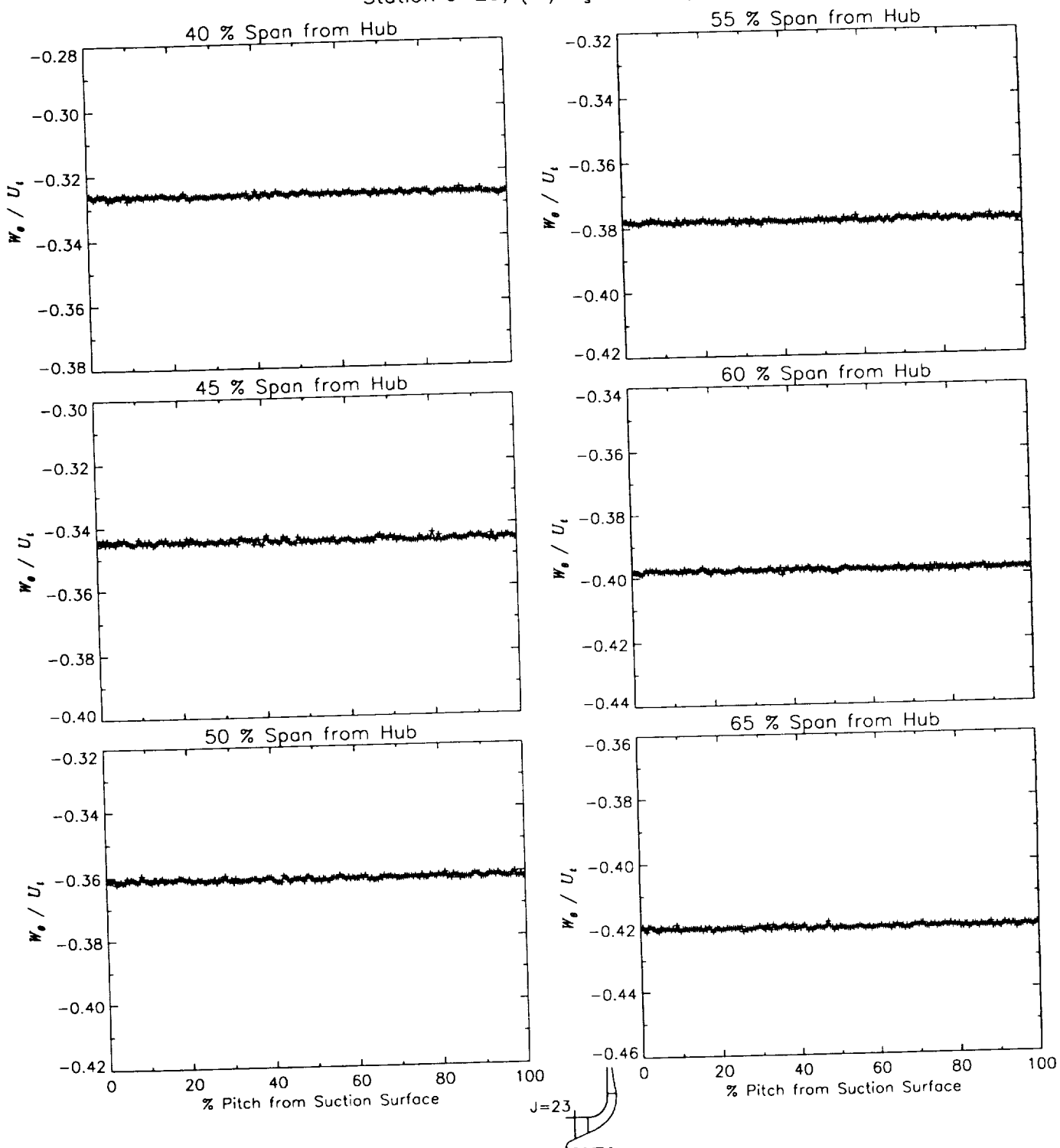
Station J=23, ( $m/m_s = -0.397$ )



(b) Relative tangential velocity normalized by impeller tip speed.

Figure 24.-Continued.

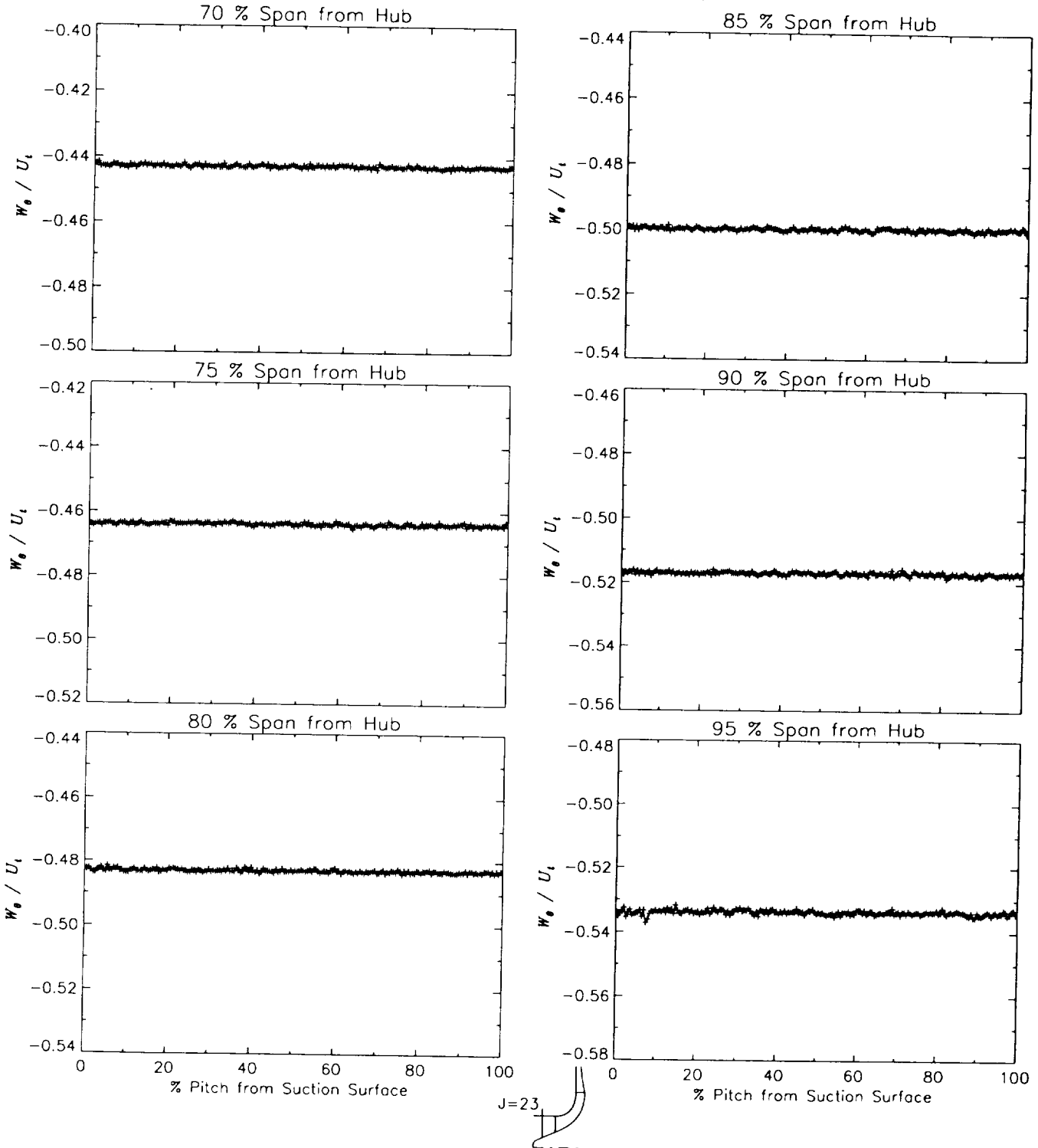
Station J=23, ( $m/m_s = -0.397$ )



(b) Relative tangential velocity normalized by impeller tip speed.

Figure 24.-Continued.

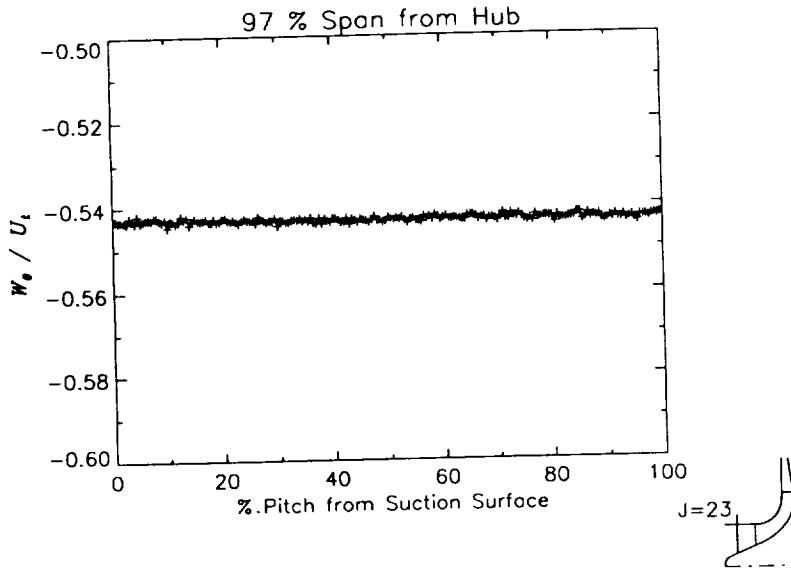
Station J=23, ( $m/m_s = -0.397$ )



(b) Relative tangential velocity normalized by impeller tip speed.

Figure 24.—Continued.

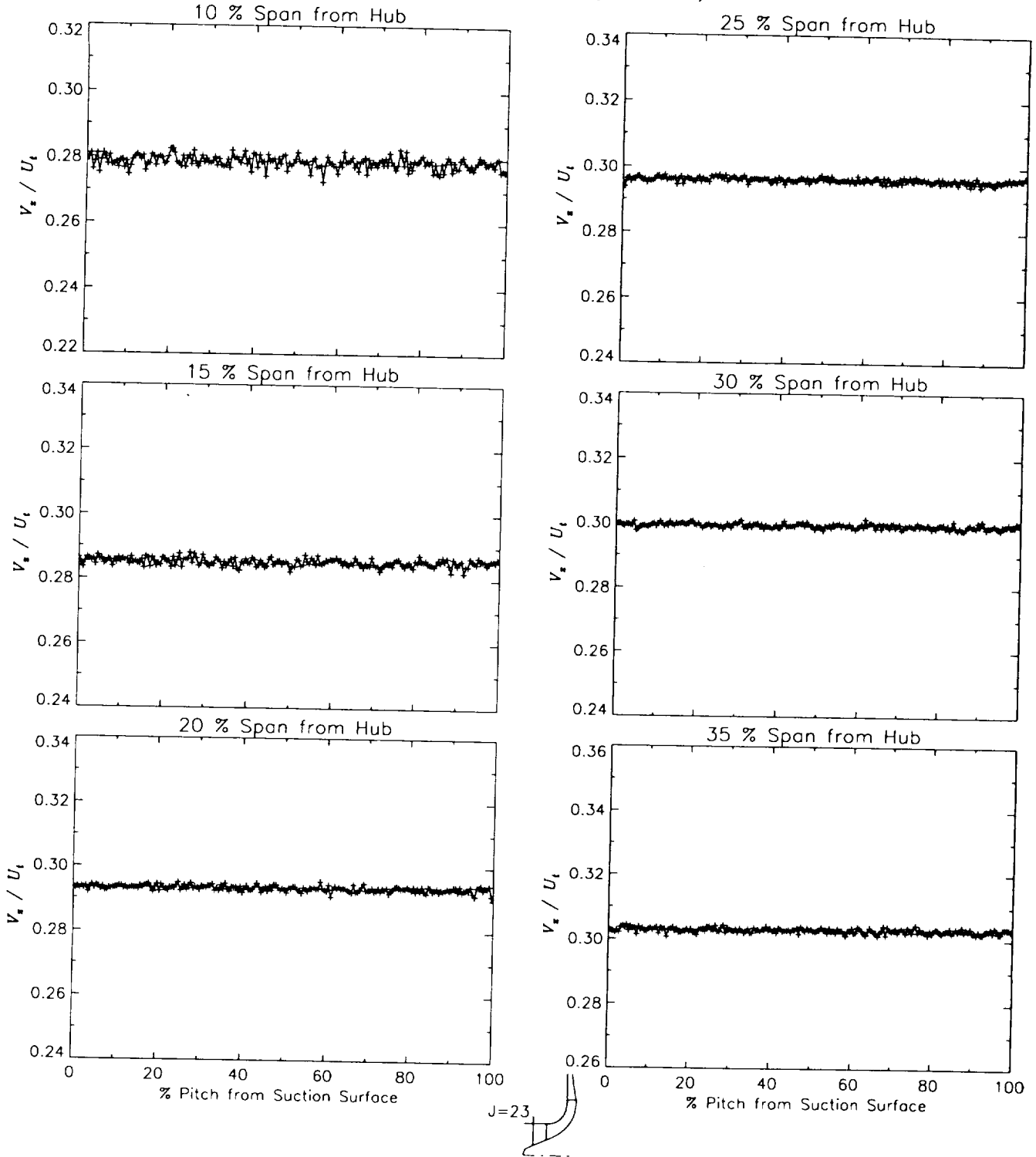
Station J=23, ( $m/m_s = -0.397$ )



(b) Relative tangential velocity normalized by impeller tip speed.

Figure 24.-Continued.

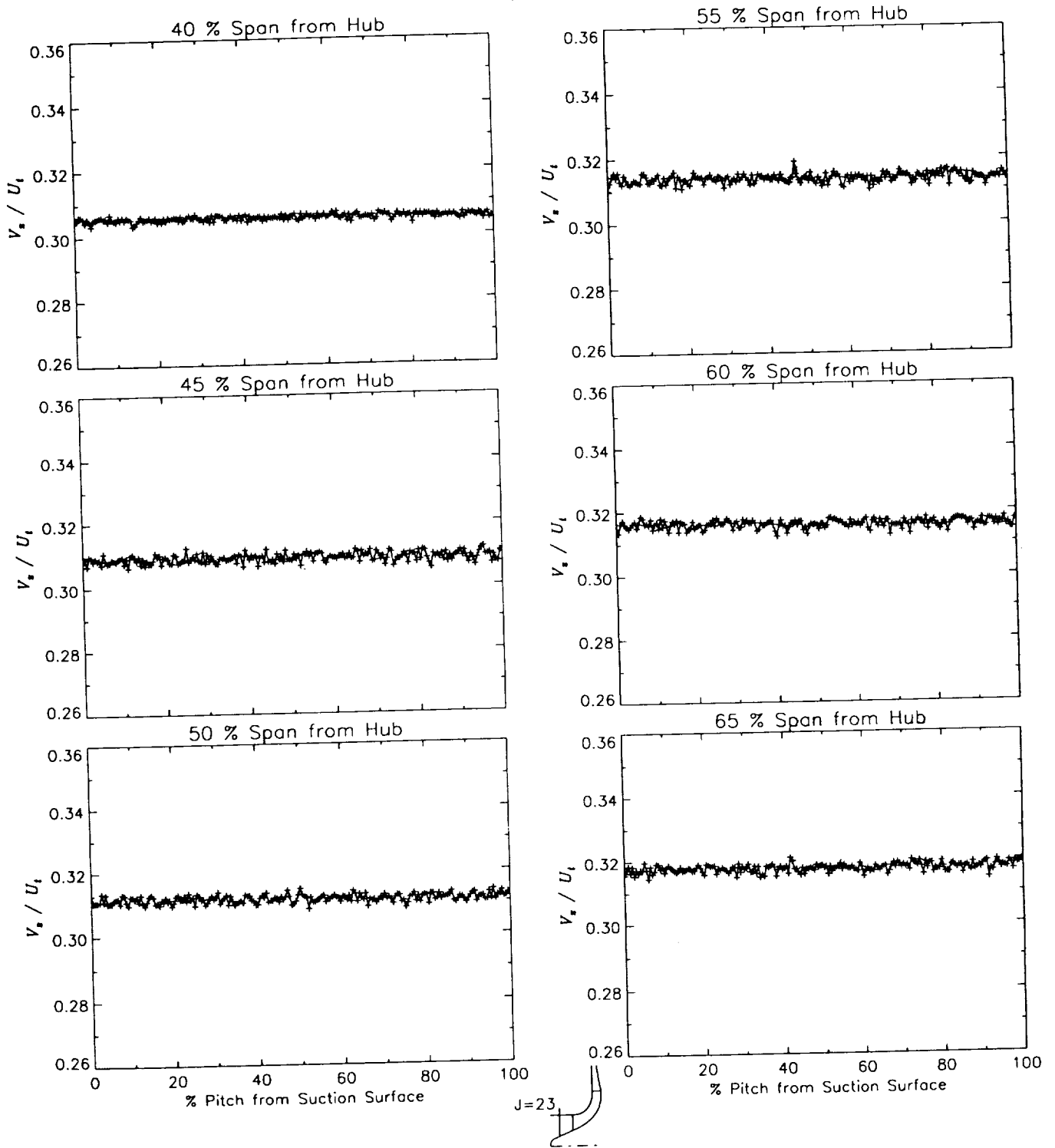
Station J=23, ( $m/m_s = -0.397$ )



(c) Axial velocity normalized by impeller tip speed.

Figure 24.-Continued.

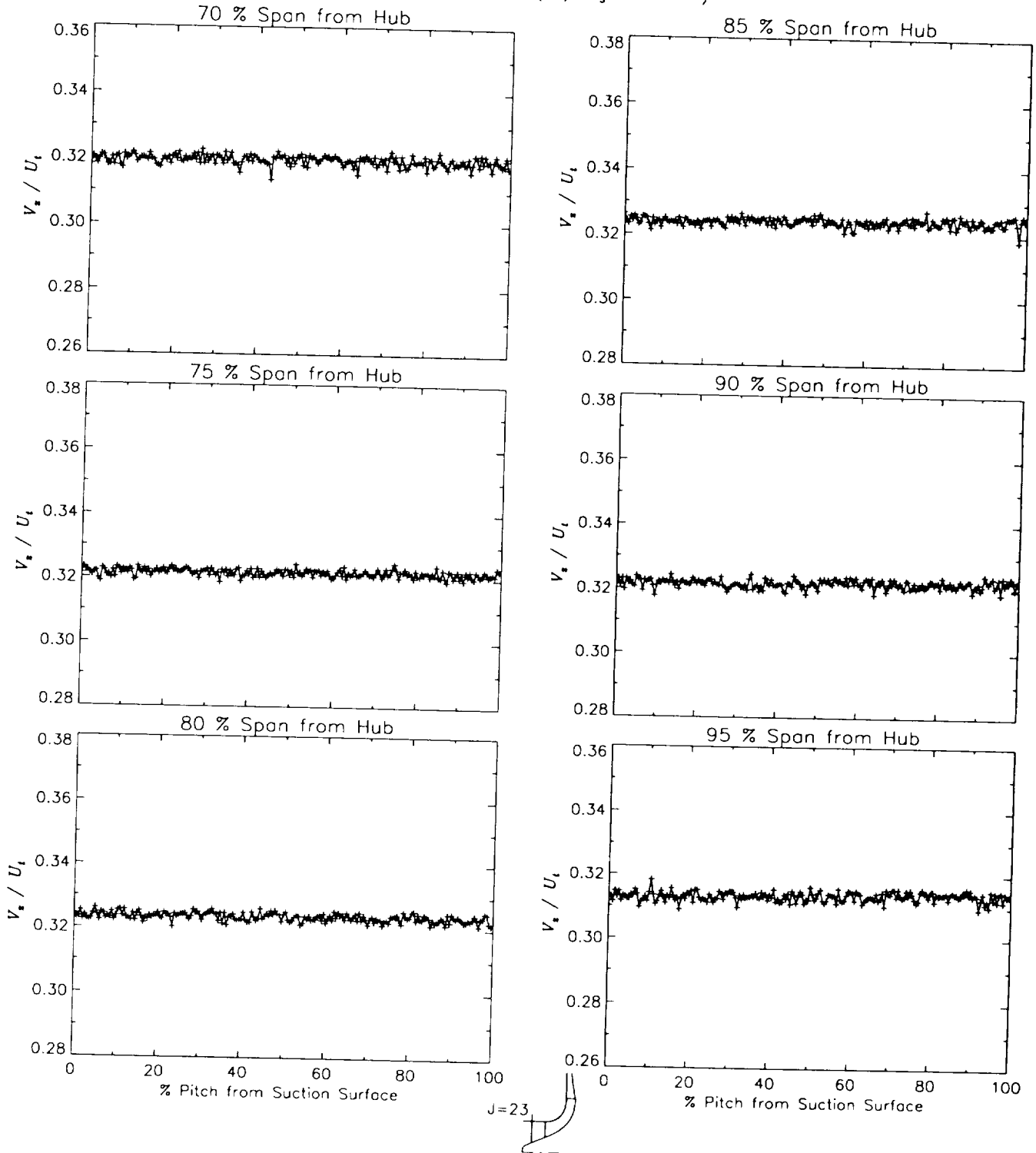
Station J=23, ( $m/m_s = -0.397$ )



(c) Axial velocity normalized by impeller tip speed.

Figure 24.-Continued.

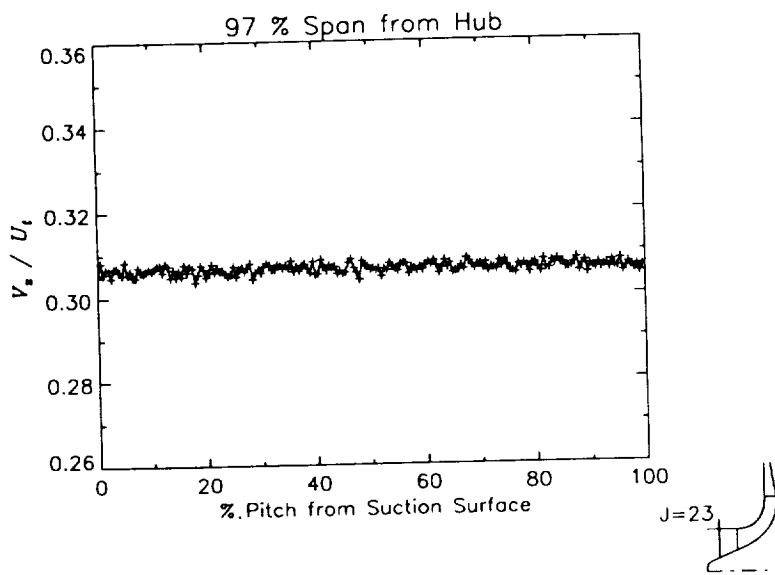
Station J=23, ( $m/m_s = -0.397$ )



(c) Axial velocity normalized by impeller tip speed.

Figure 24.-Continued.

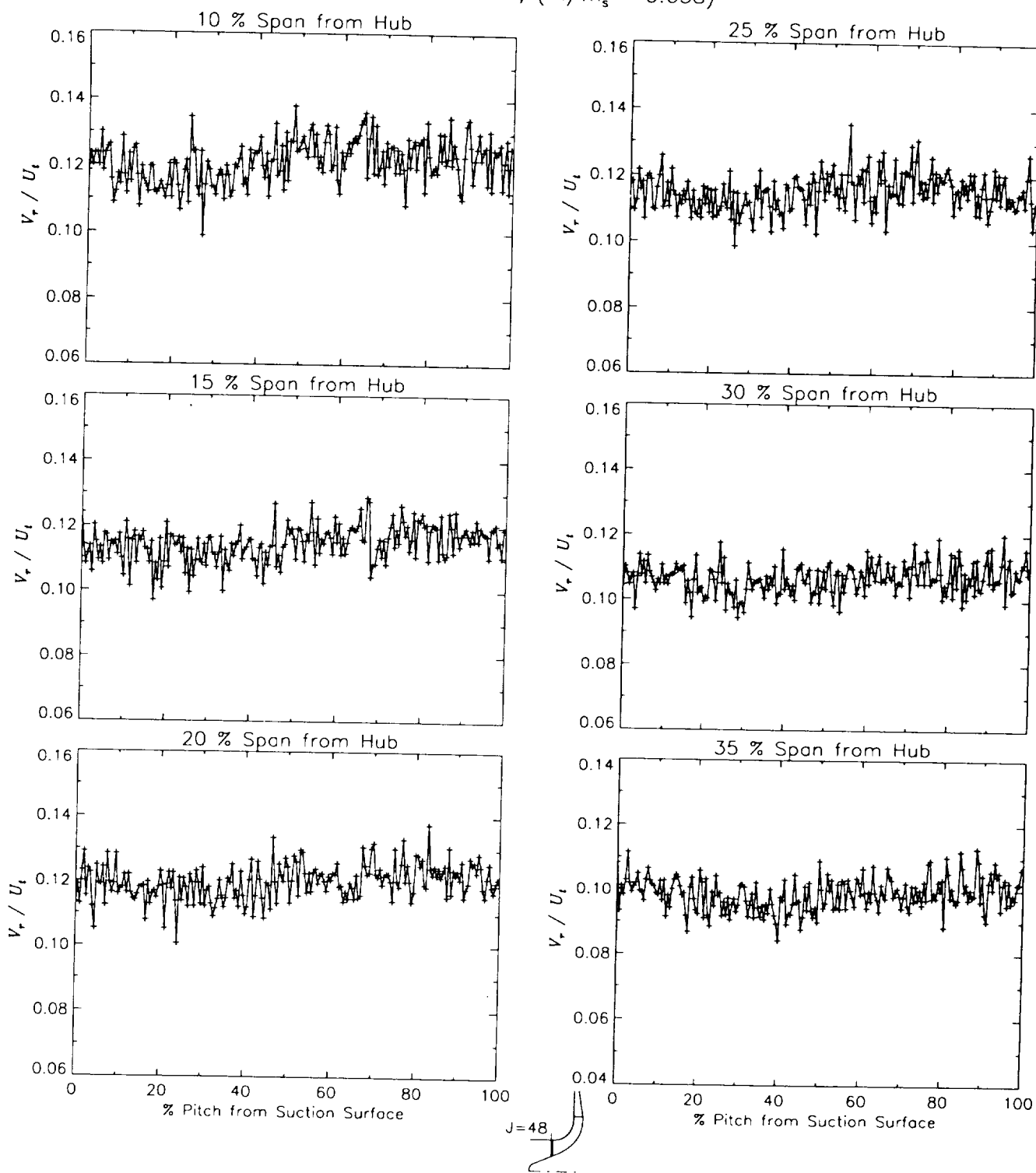
Station J=23, ( $m/m_s = -0.397$ )



(c) Axial velocity normalized by impeller tip speed.

Figure 24.—Concluded.

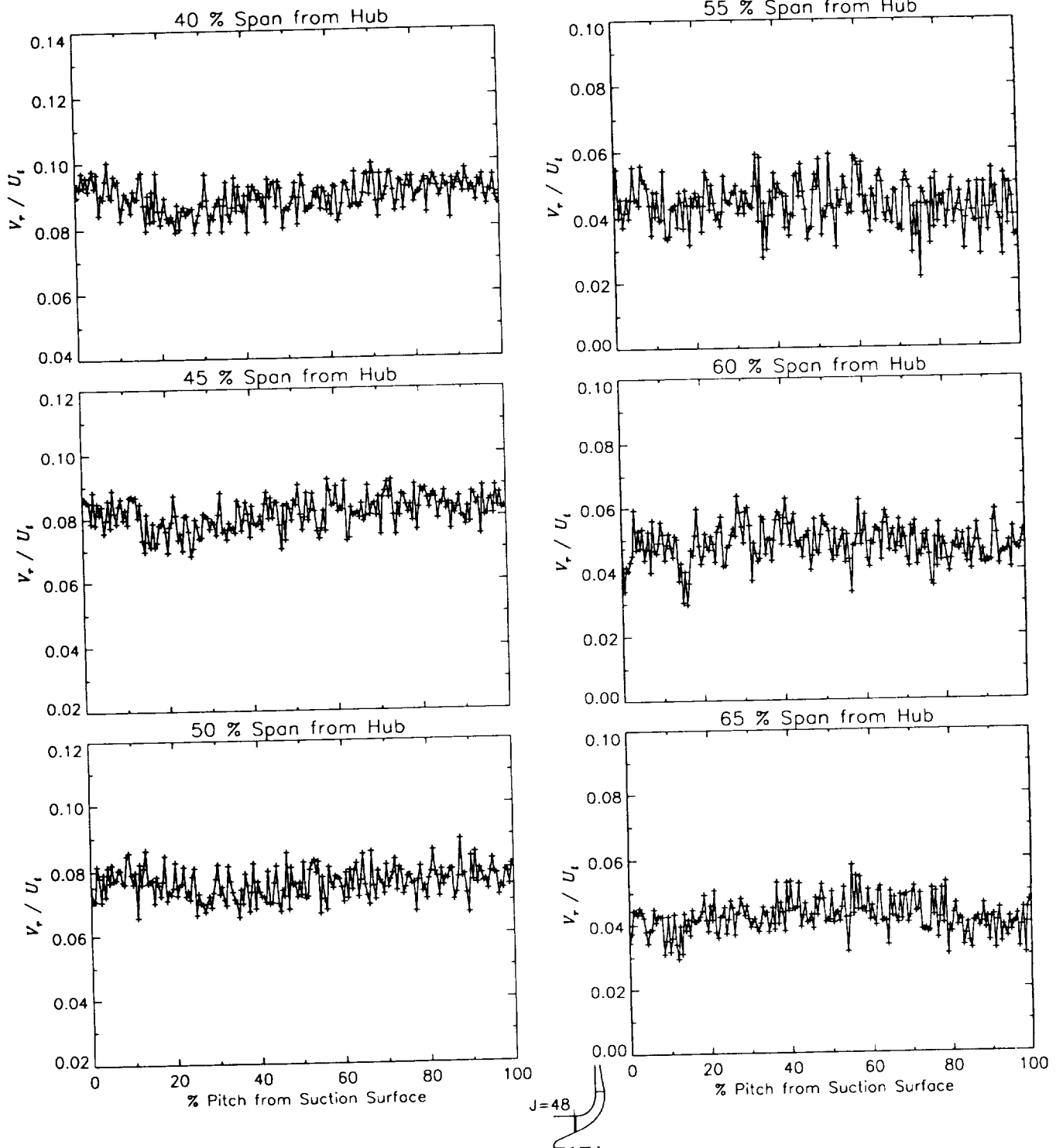
Station J=48, ( $m/m_s = -0.038$ )



(a) Radial velocity normalized by impeller tip speed.

Figure 25.-Laser velocimeter results of axial, radial, and relative tangential velocities normalized by impeller tip speed for the design flow condition,  $m_d$ , at station J=48, ( $m/m_s = -0.038$ ).

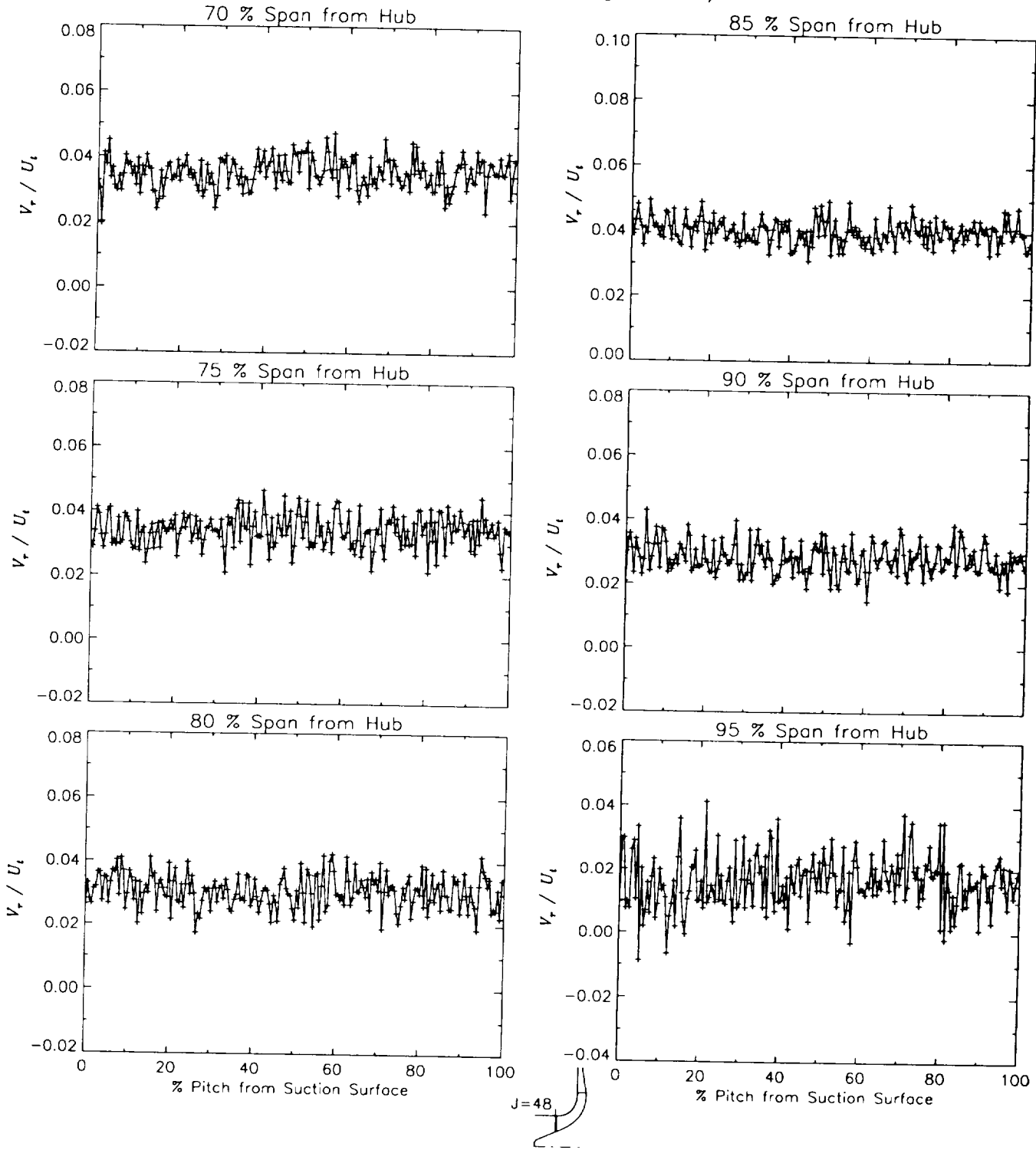
Station J=48, ( $m/m_s = -0.038$ )



(a) Radial velocity normalized by impeller tip speed.

Figure 25.-Continued.

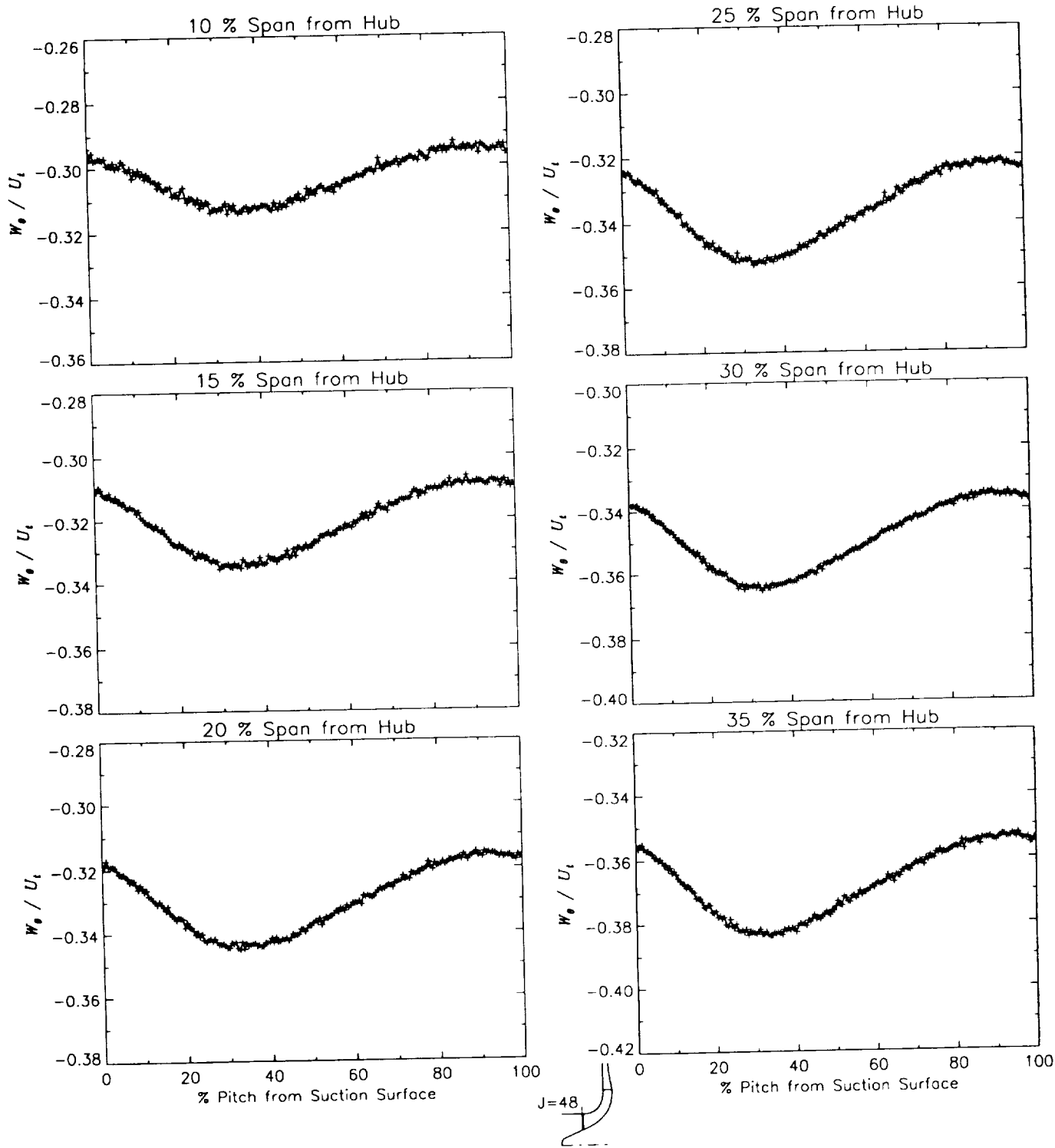
Station J=48, ( $m/m_s = -0.038$ )



(a) Radial velocity normalized by impeller tip speed.

Figure 25.-Continued.

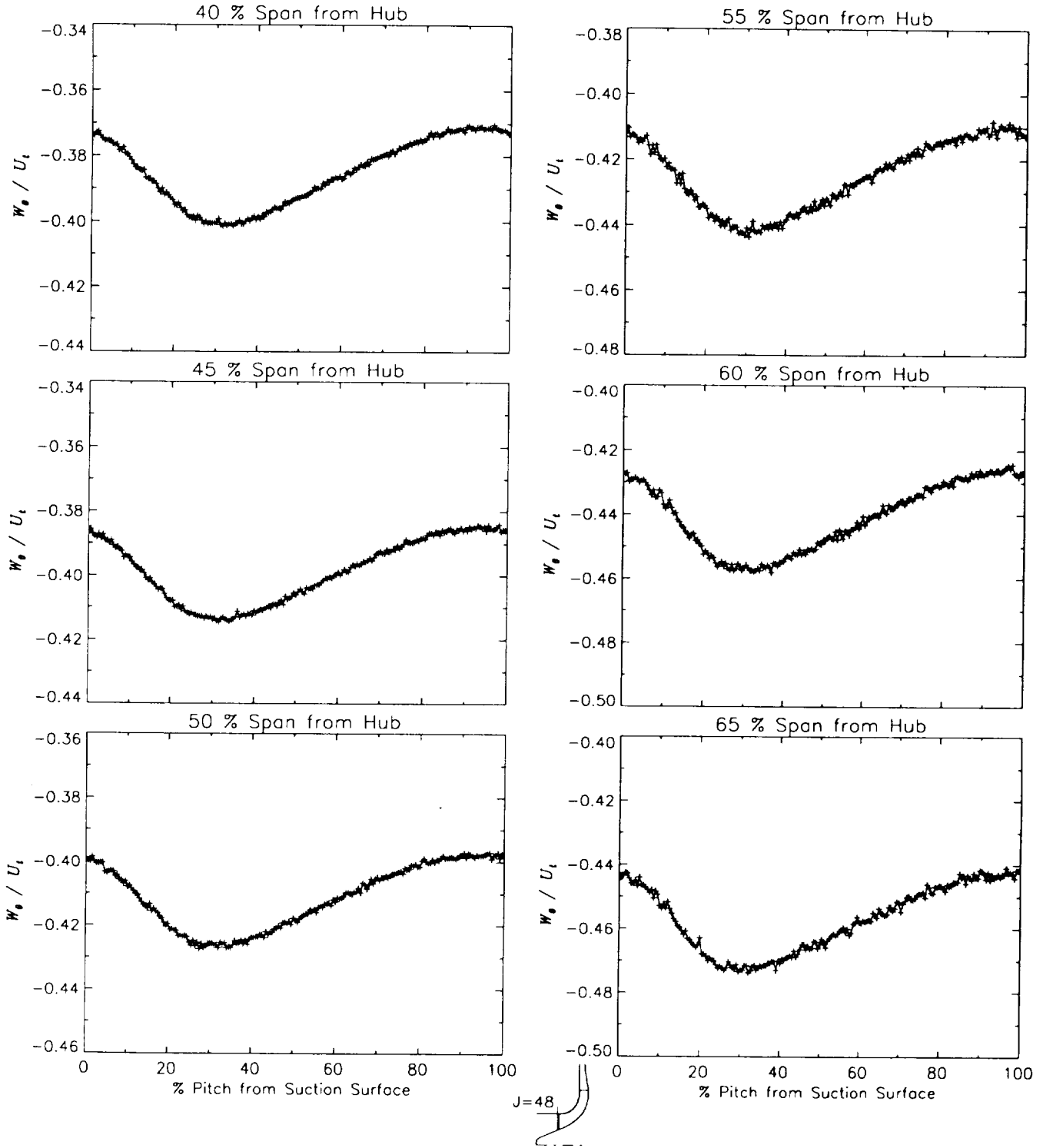
Station J=48, ( $m/m_s = -0.038$ )



(b) Relative tangential velocity normalized by impeller tip speed.

Figure 25.-Continued.

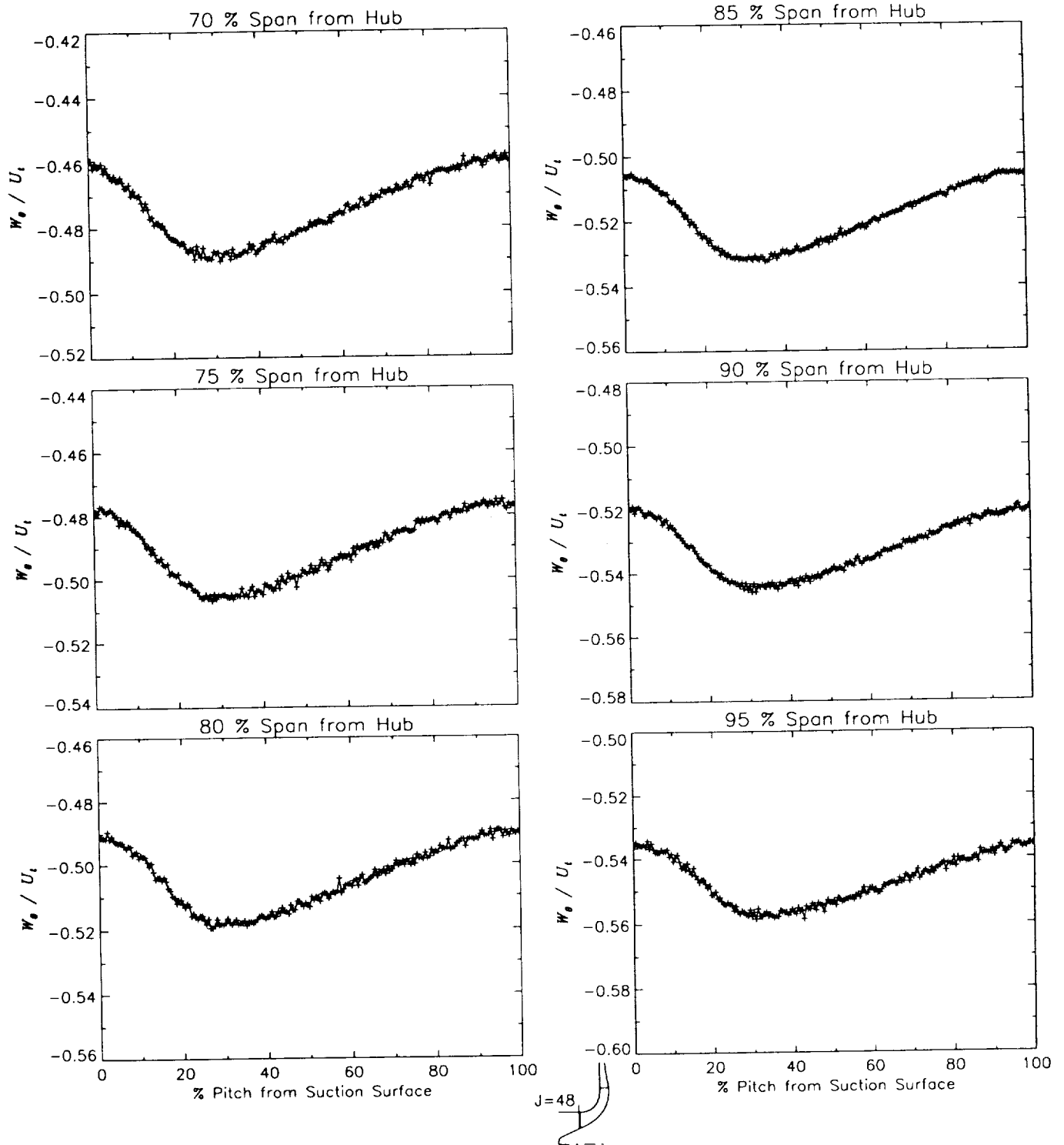
Station J=48, ( $m/m_s = -0.038$ )



(b) Relative tangential velocity normalized by impeller tip speed.

Figure 25.--Continued.

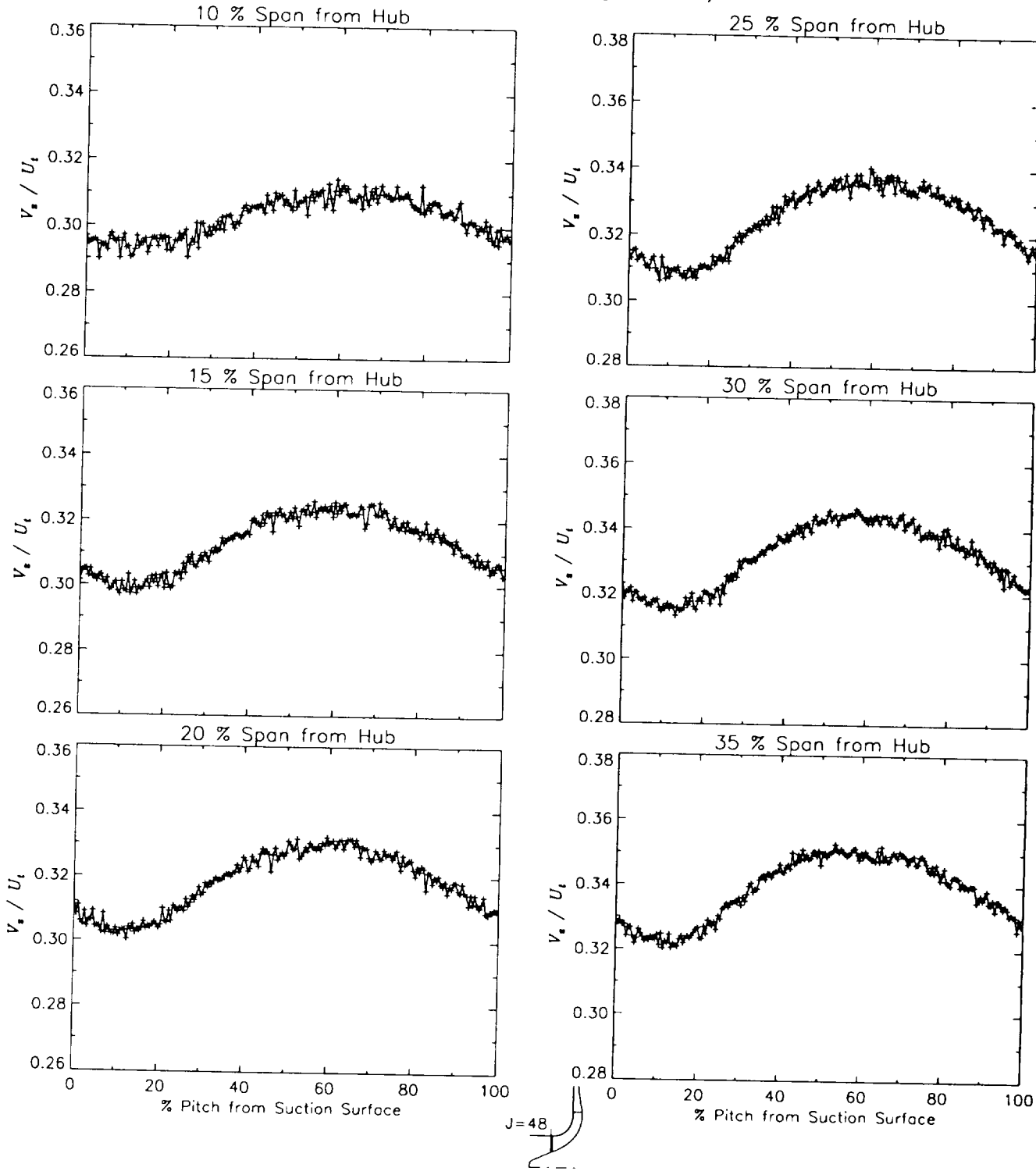
Station J=48, ( $m/m_s = -0.038$ )



(b) Relative tangential velocity normalized by impeller tip speed.

Figure 25.-Continued.

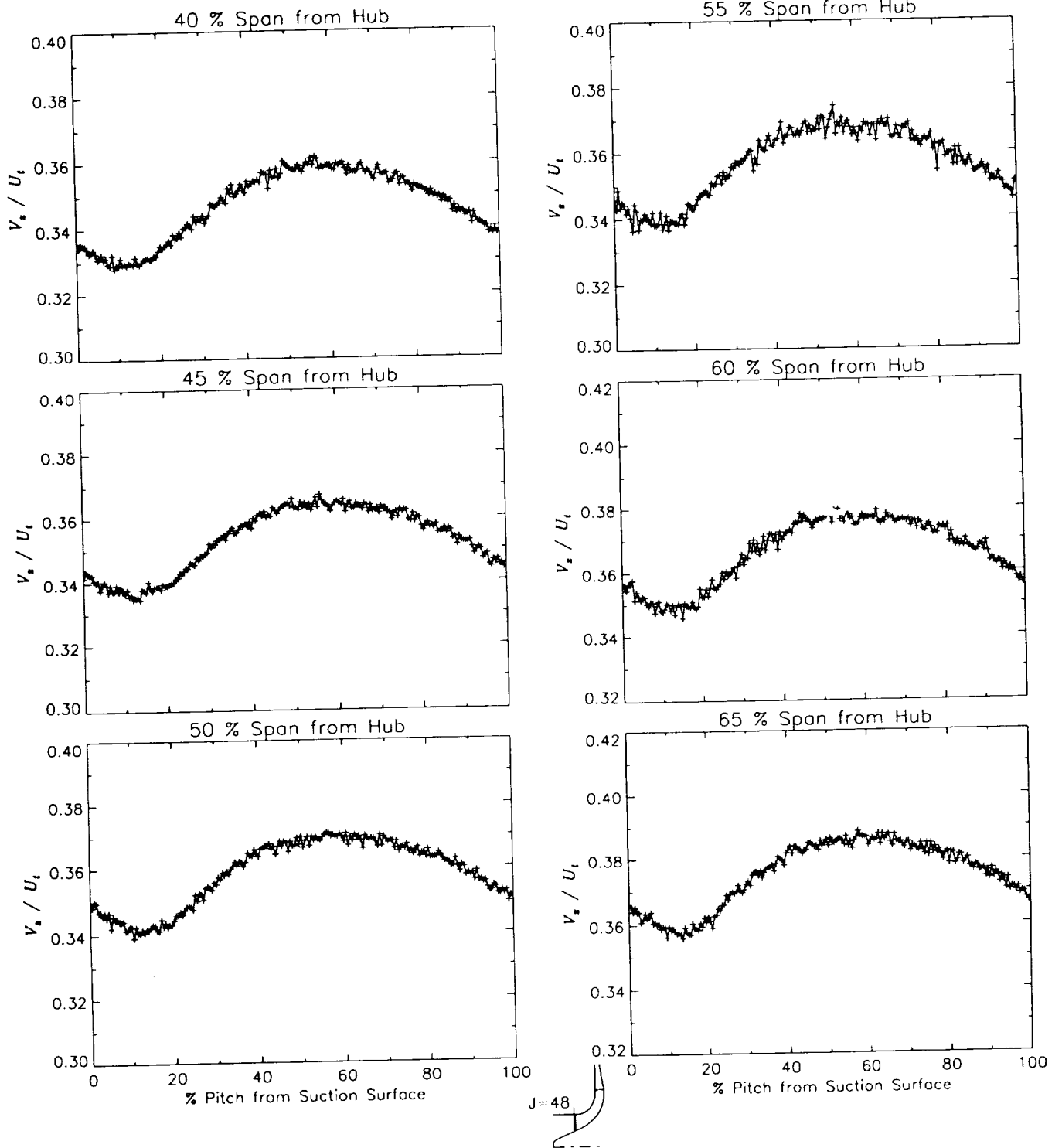
Station J=48, ( $m/m_s = -0.038$ )



(c) Axial velocity normalized by impeller tip speed.

Figure 25.-Continued.

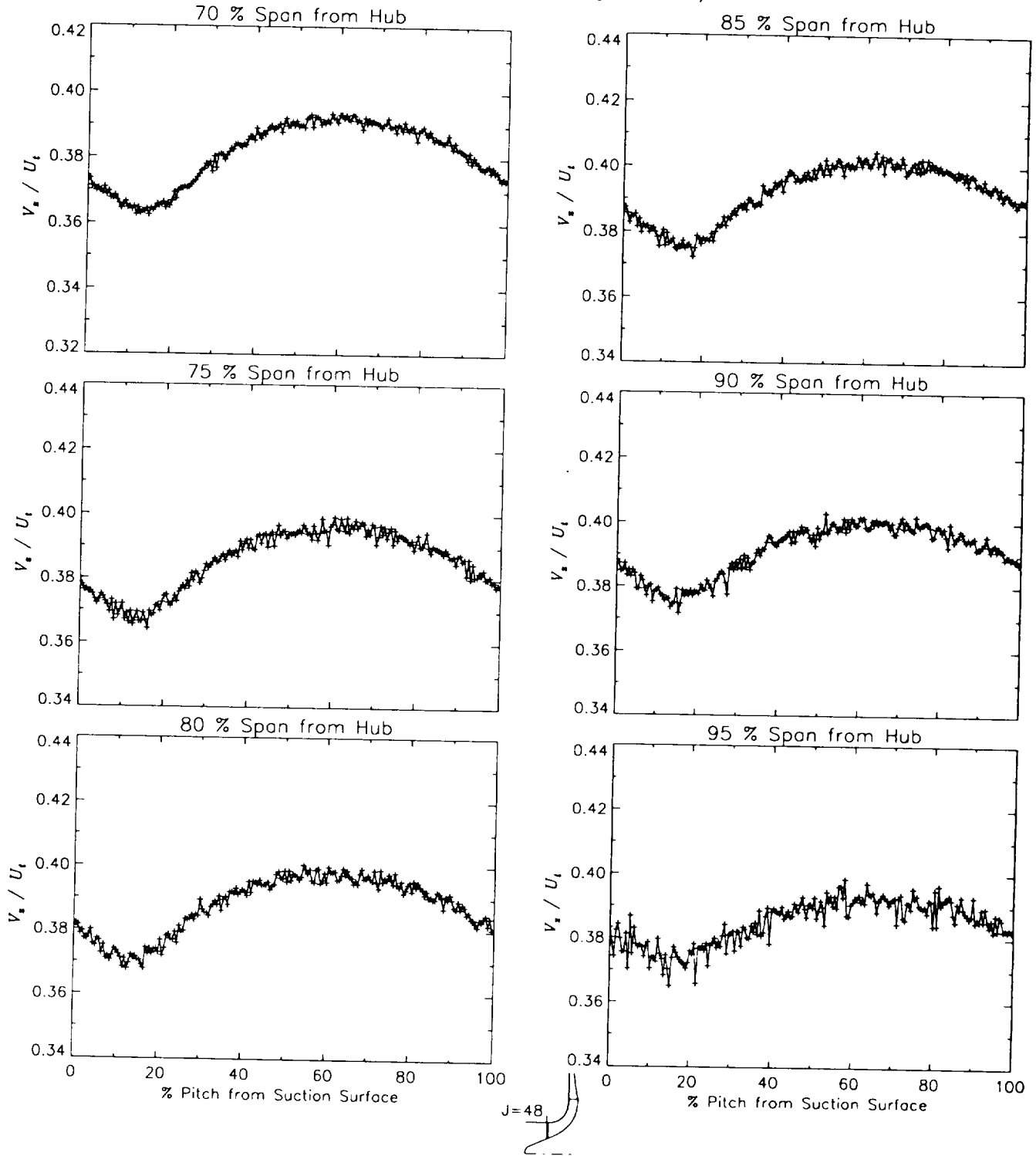
Station J=48, ( $m/m_s = -0.038$ )



(c) Axial velocity normalized by impeller tip speed.

Figure 25.-Continued.

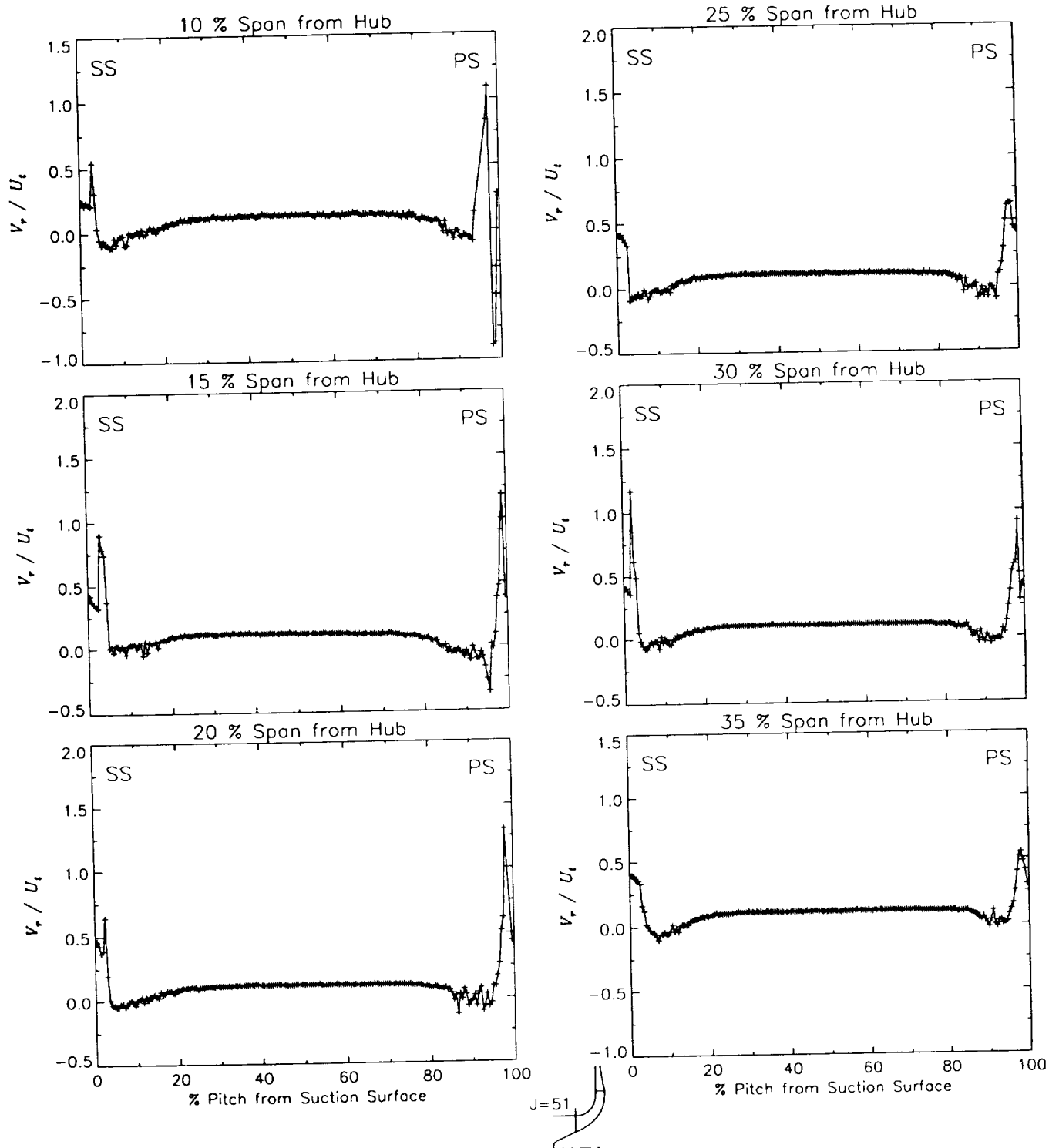
Station J=48, ( $m/m_s = -0.038$ )



(c) Axial velocity normalized by impeller tip speed.

Figure 25.-Concluded.

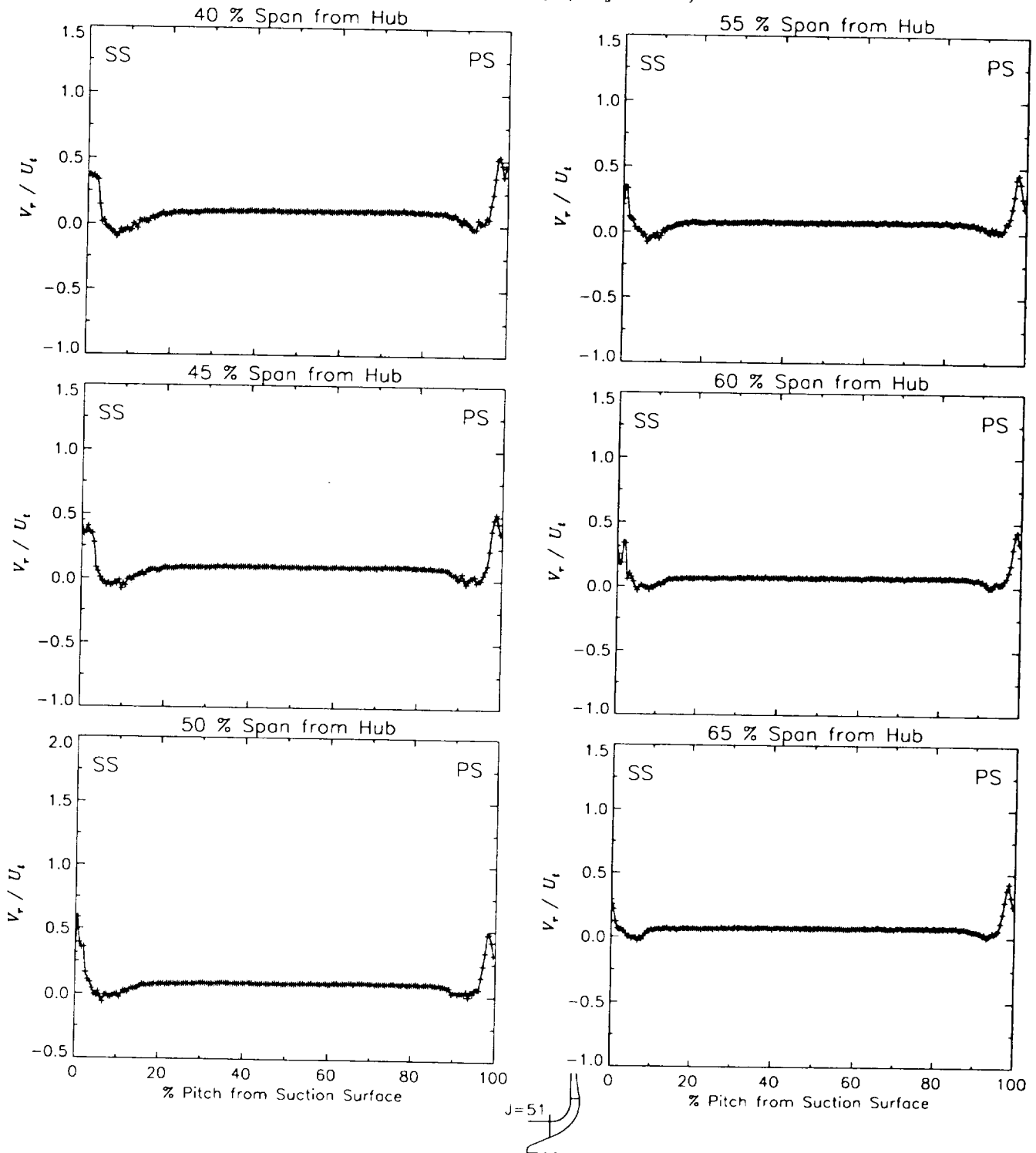
Station J=51, ( $m/m_s=0.000$ )



(a) Radial velocity normalized by impeller tip speed.

Figure 26.-Laser velocimeter results of axial, radial, and relative tangential velocities normalized by impeller tip speed for the design flow condition,  $m_d$ , at station J=51, ( $m/m_s=0.000$ ). The shaded region to the right of each plot represents the physical blade width.

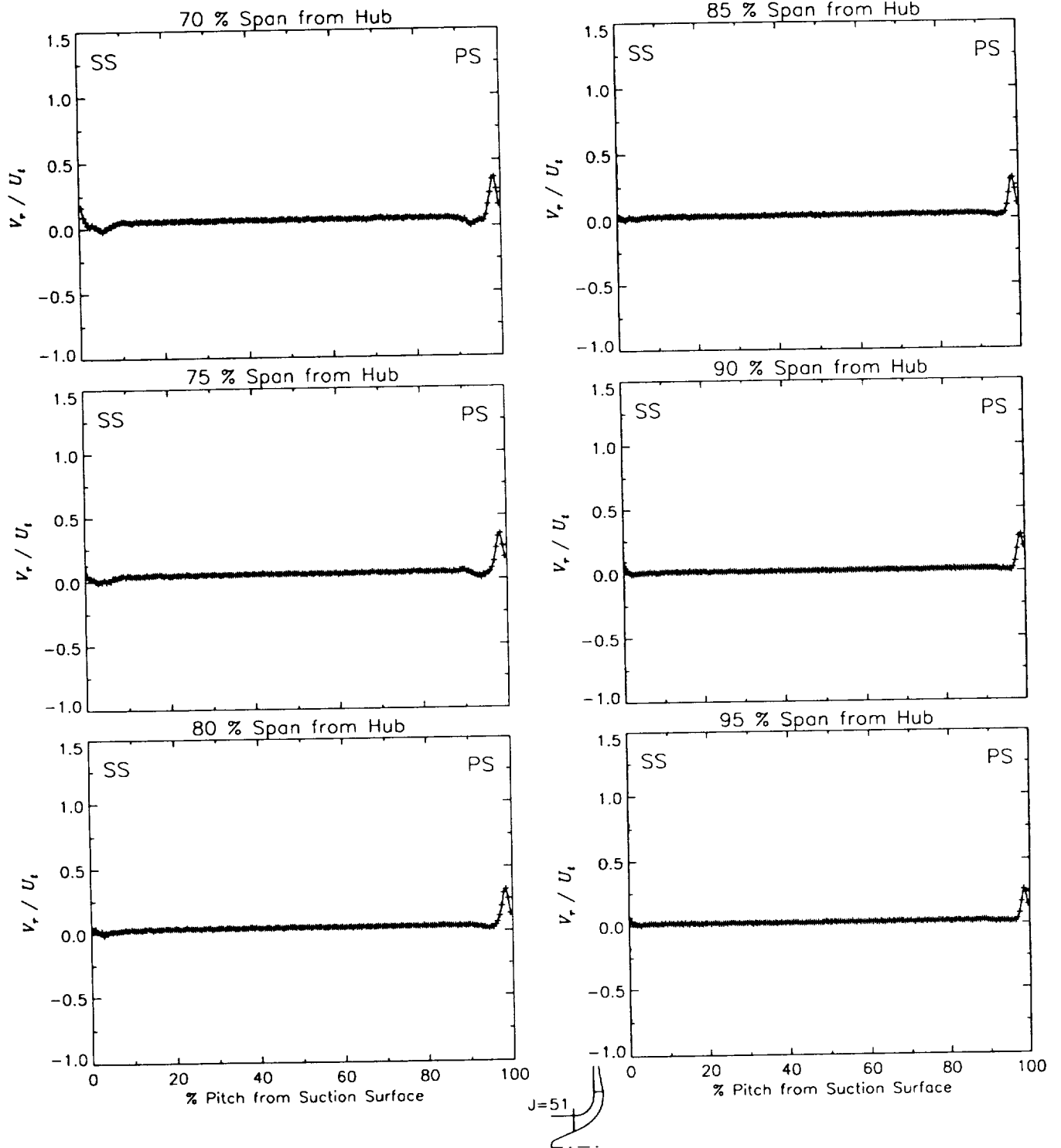
Station J=51, ( $m/m_s=0.000$ )



(a) Radial velocity normalized by impeller tip speed.

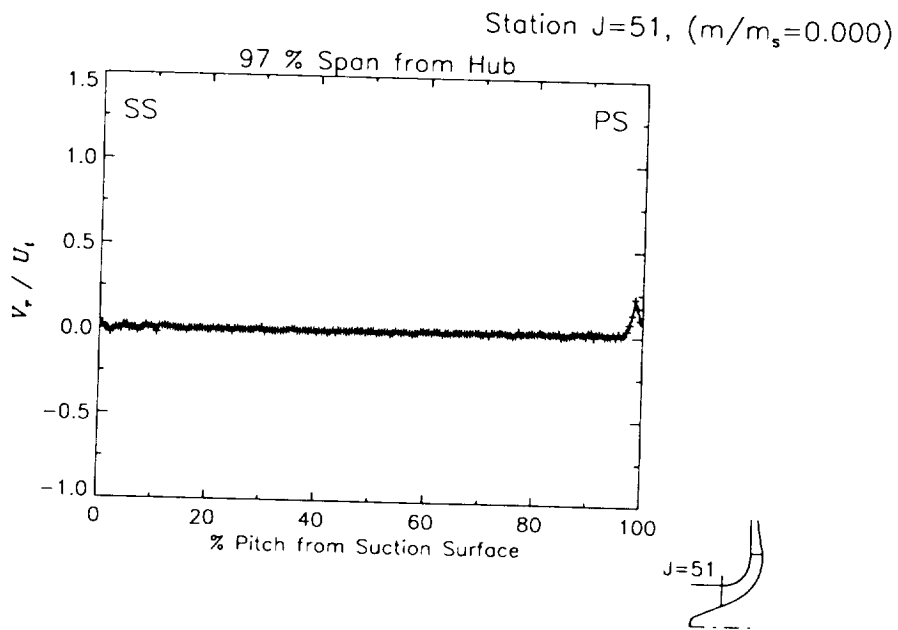
Figure 26.—Continued.

Station J=51, ( $m/m_s=0.000$ )



(a) Radial velocity normalized by impeller tip speed.

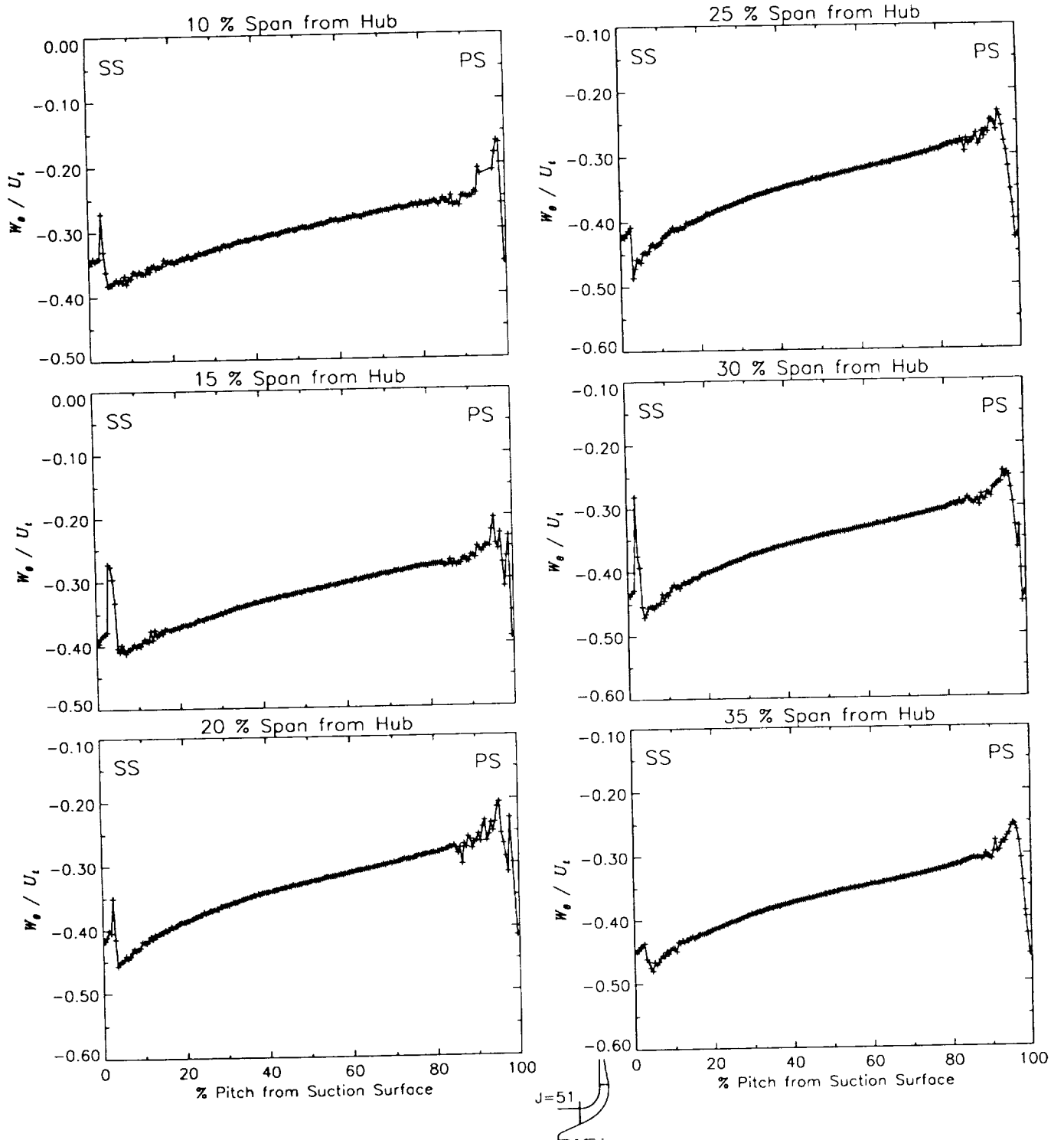
Figure 26.—Continued.



(a) Radial velocity normalized by impeller tip speed.

Figure 26.-Continued.

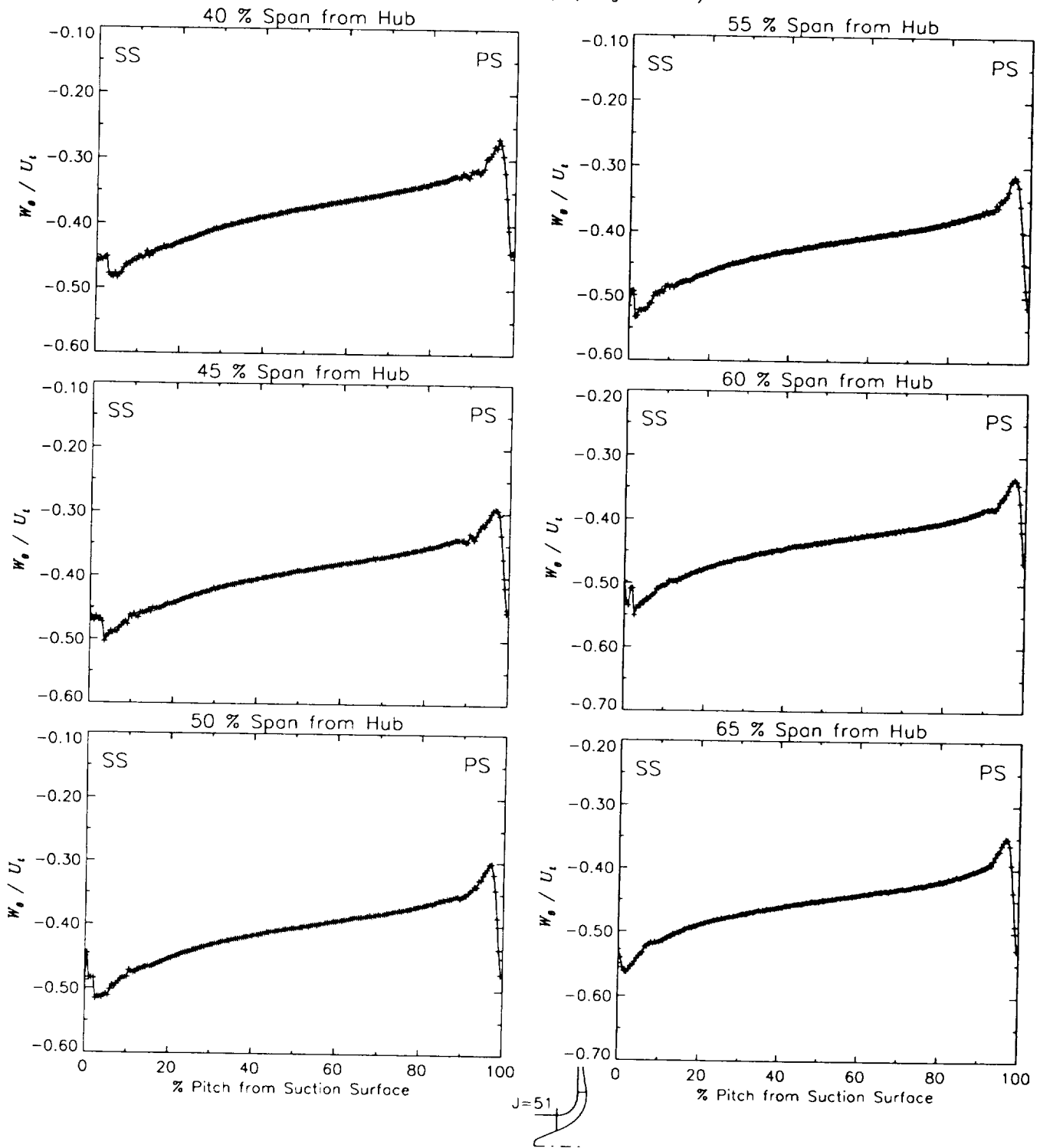
Station J=51, ( $m/m_s=0.000$ )



(b) Relative tangential velocity normalized by impeller tip speed.

Figure 26.-Continued.

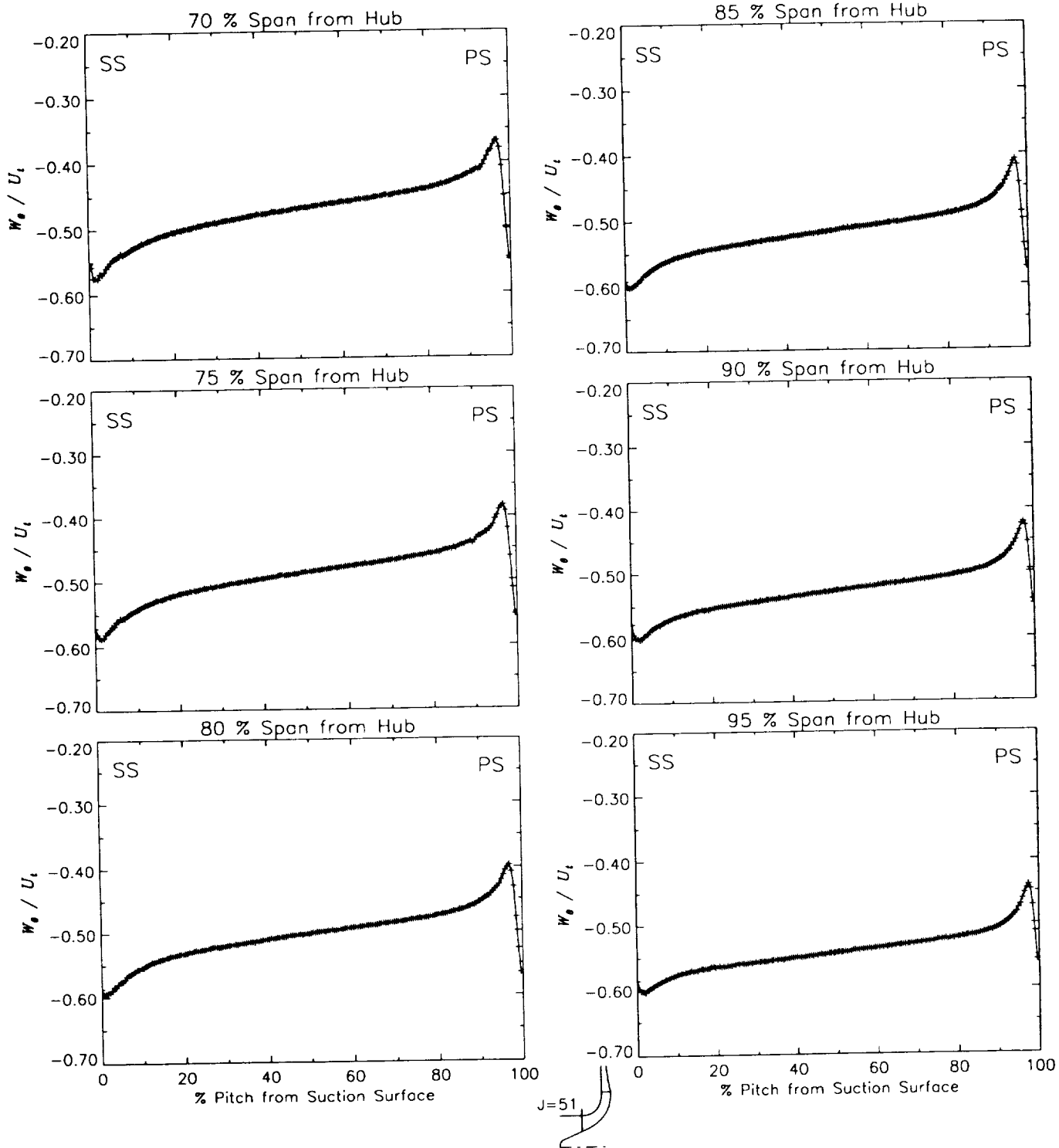
Station J=51, ( $m/m_s=0.000$ )



(b) Relative tangential velocity normalized by impeller tip speed.

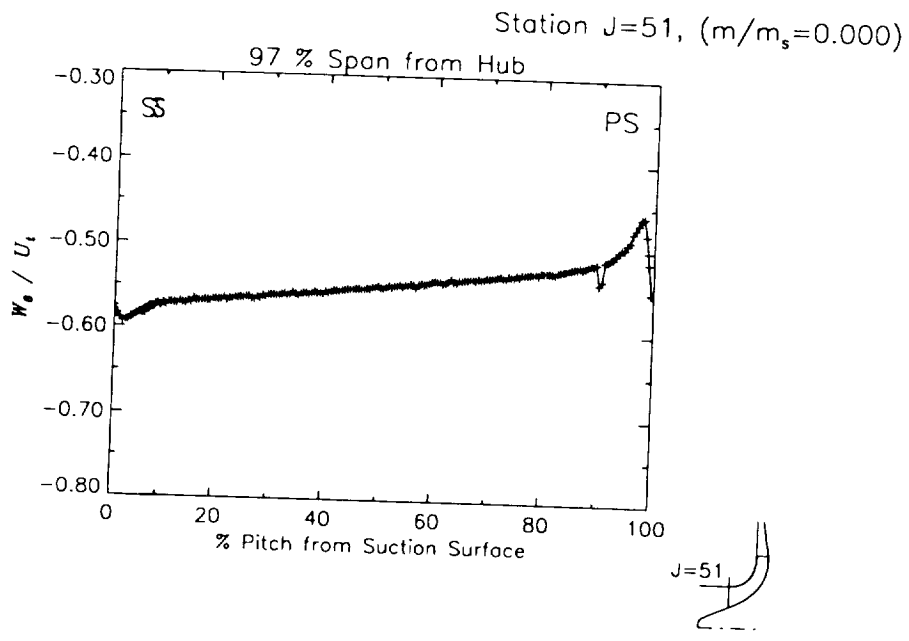
Figure 26.-Continued.

Station J=51, ( $m/m_s=0.000$ )



(b) Relative tangential velocity normalized by impeller tip speed.

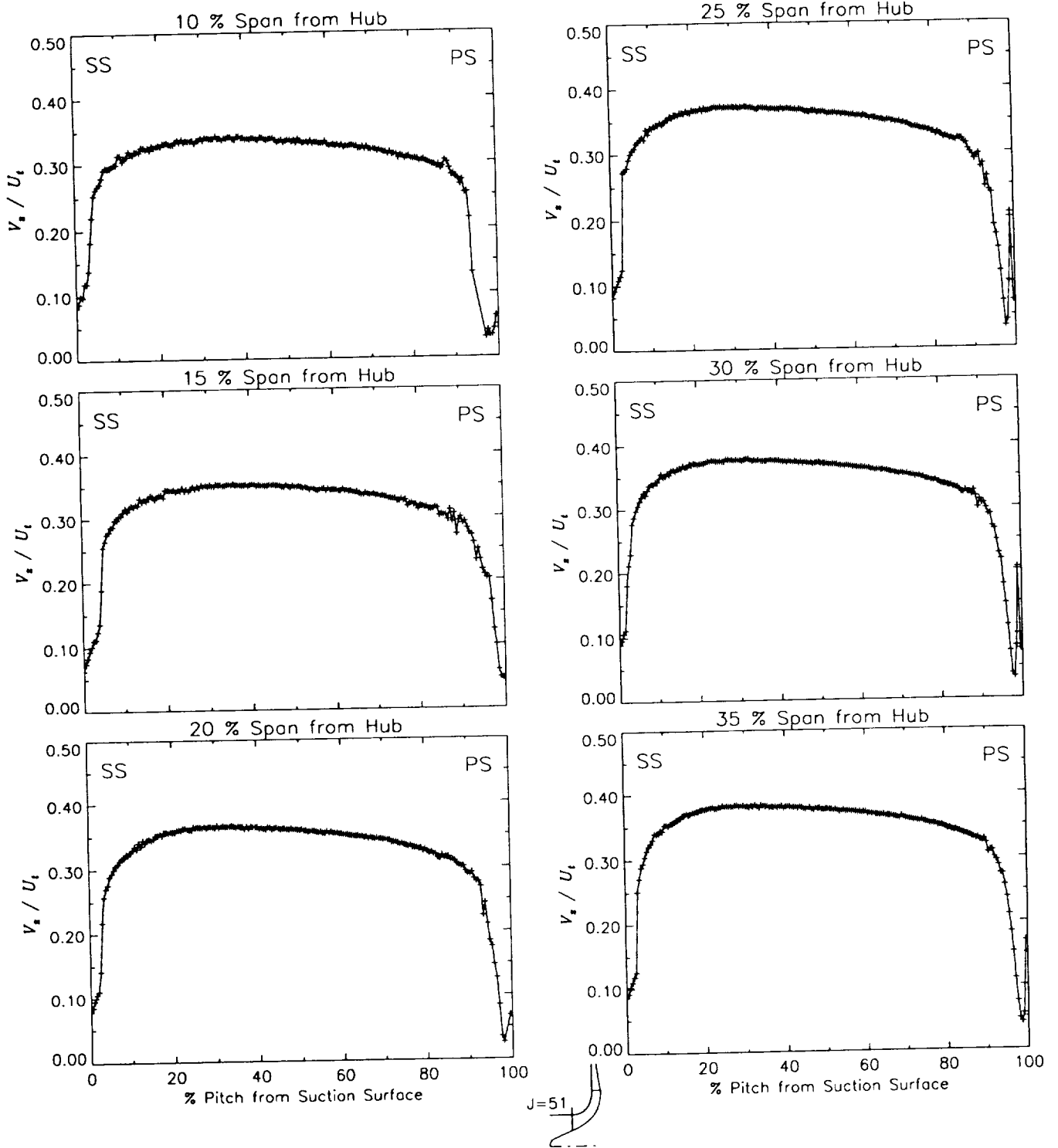
Figure 26.-Continued.



(b) Relative tangential velocity normalized by impeller tip speed.

Figure 26.-Continued.

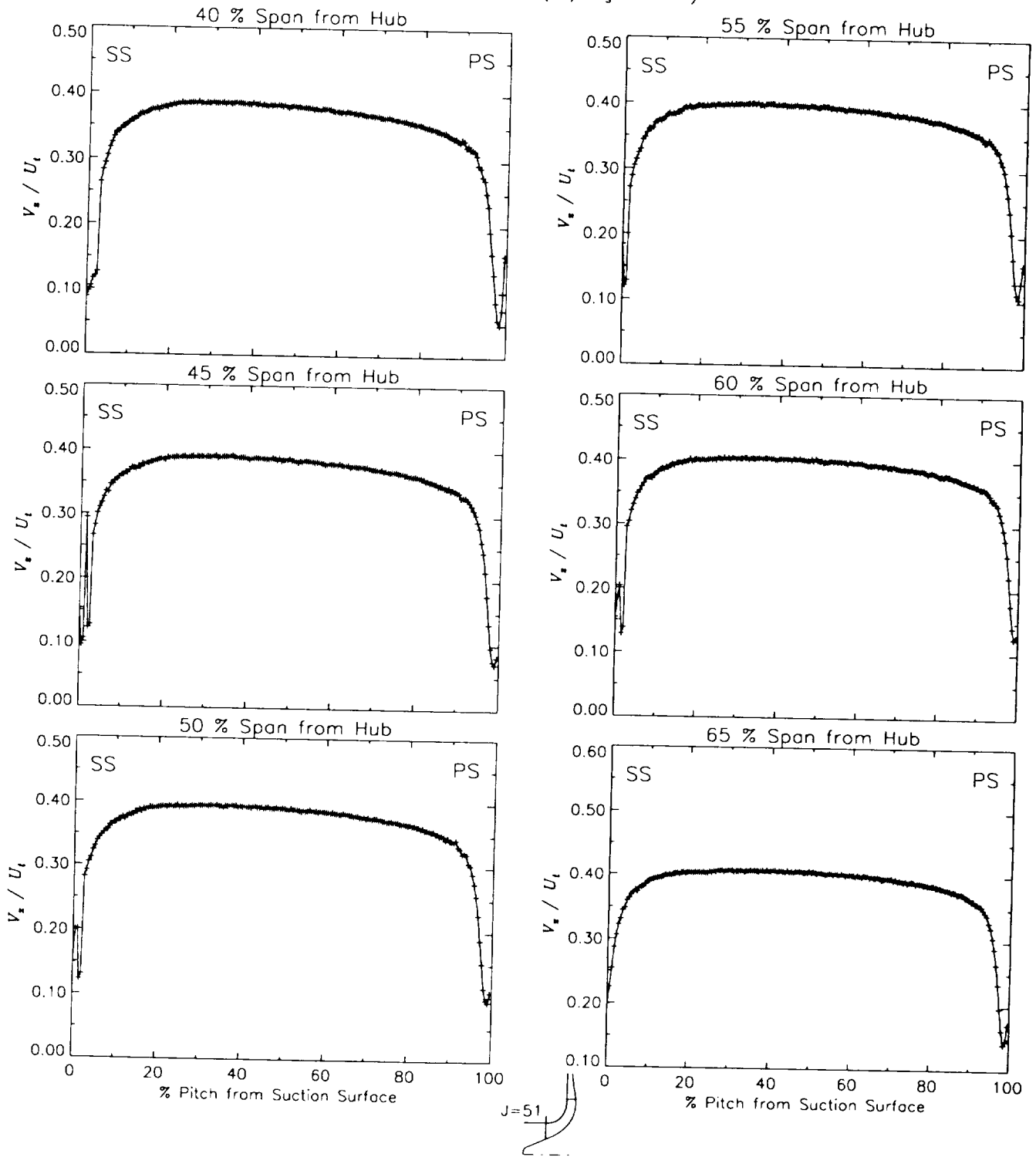
Station J=51, ( $m/m_s=0.000$ )



(c) Axial velocity normalized by impeller tip speed.

Figure 26.-Continued.

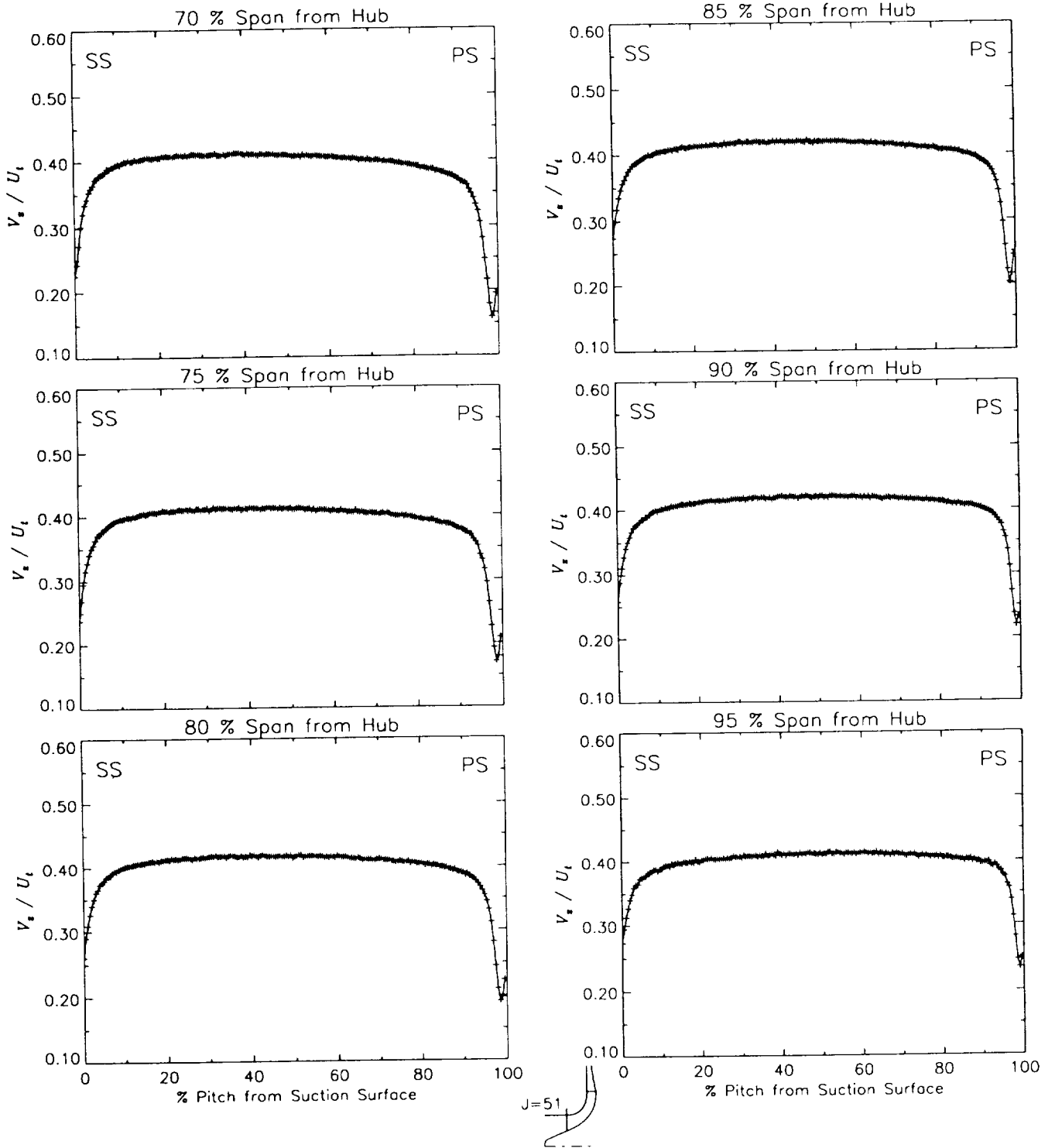
Station J=51, ( $m/m_s=0.000$ )



(c) Axial velocity normalized by impeller tip speed.

Figure 26.-Continued.

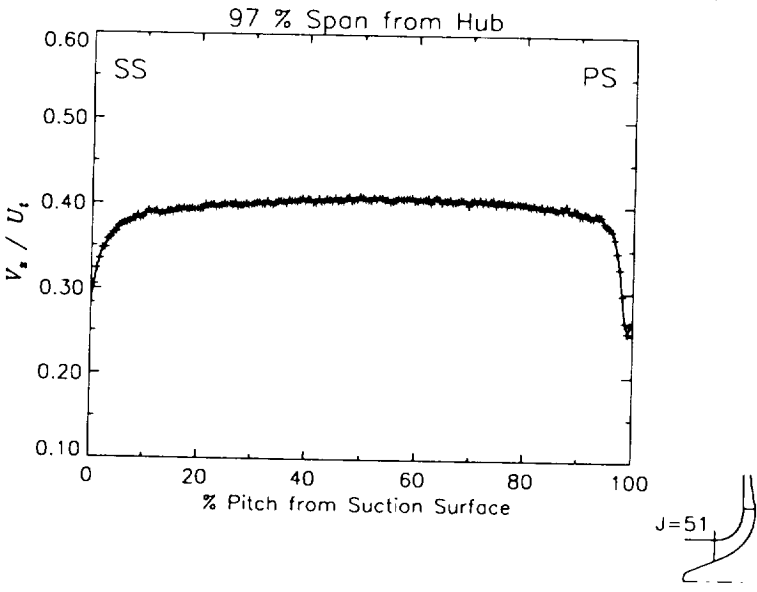
Station J=51, ( $m/m_s=0.000$ )



(c) Axial velocity normalized by impeller tip speed.

Figure 26.-Continued.

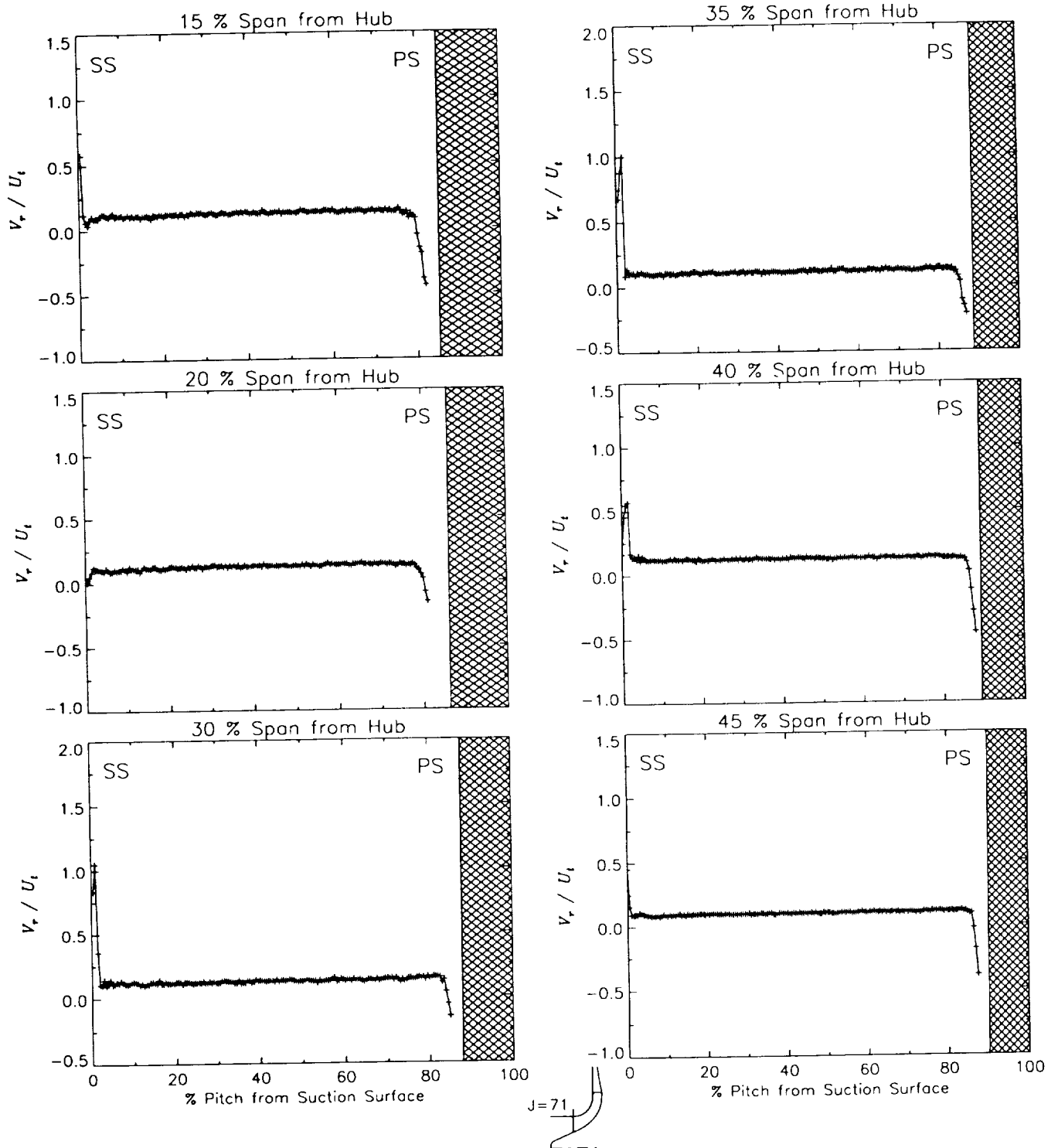
Station J=51, ( $m/m_s=0.000$ )



(c) Axial velocity normalized by impeller tip speed.

Figure 26.-Concluded.

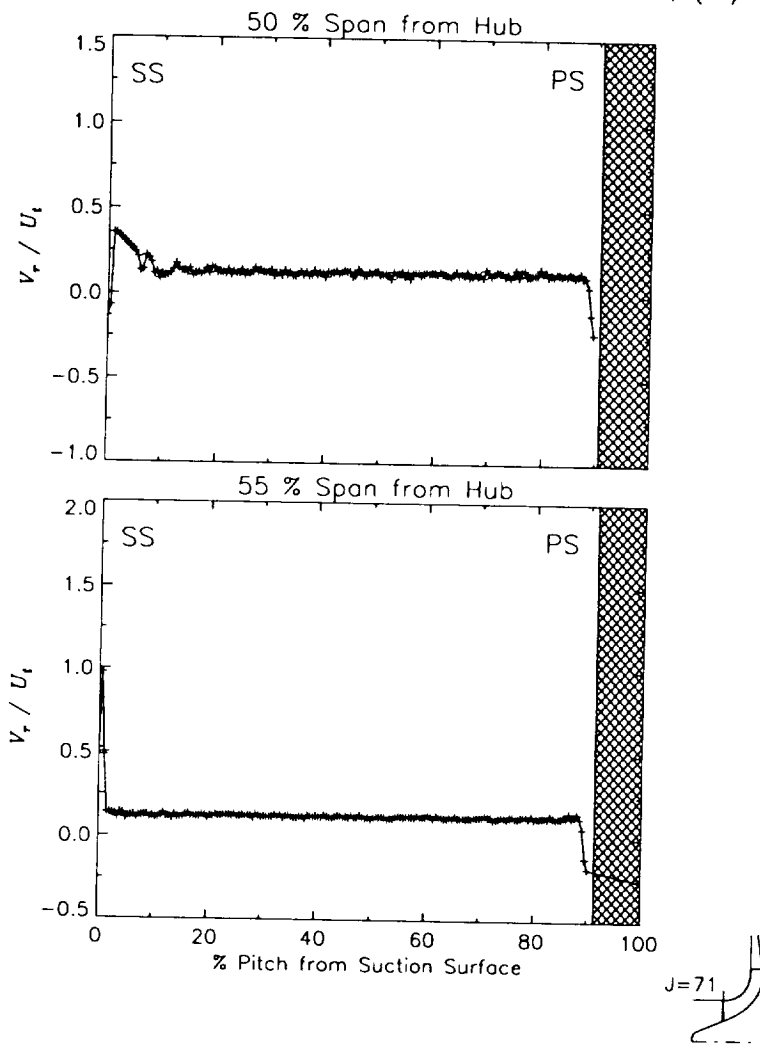
Station J=71, ( $m/m_s=0.010$ )



(a) Radial velocity normalized by impeller tip speed.

Figure 27.—Laser velocimeter results of axial, radial, and relative tangential velocities normalized by impeller tip speed for the design flow condition,  $m_d$ , at station J=71, ( $m/m_s=0.010$ ). The shaded region to the right of each plot represents the physical blade width.

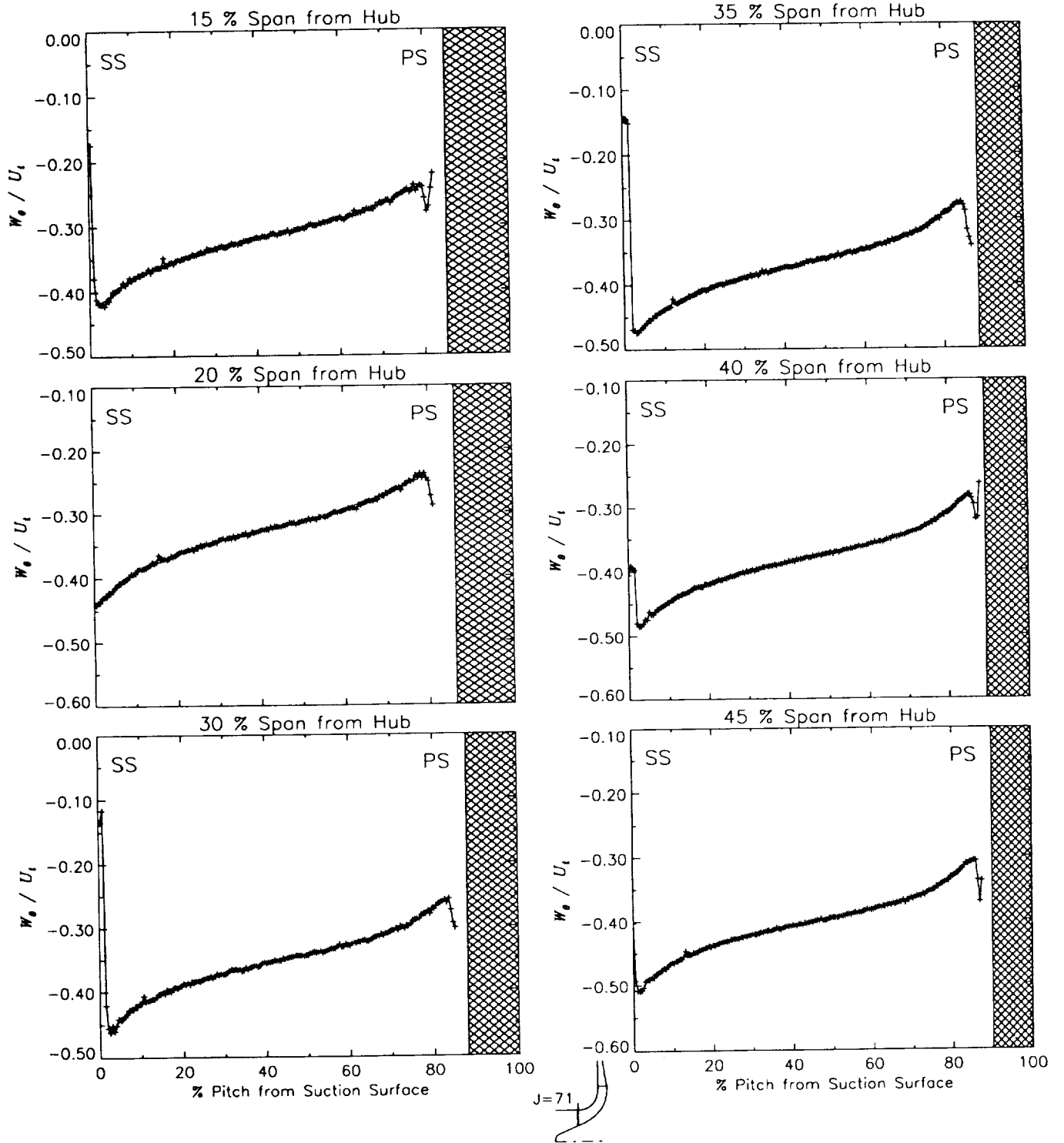
Station J=71, ( $m/m_s=0.010$ )



(a) Radial velocity normalized by impeller tip speed.

Figure 27.-Continued.

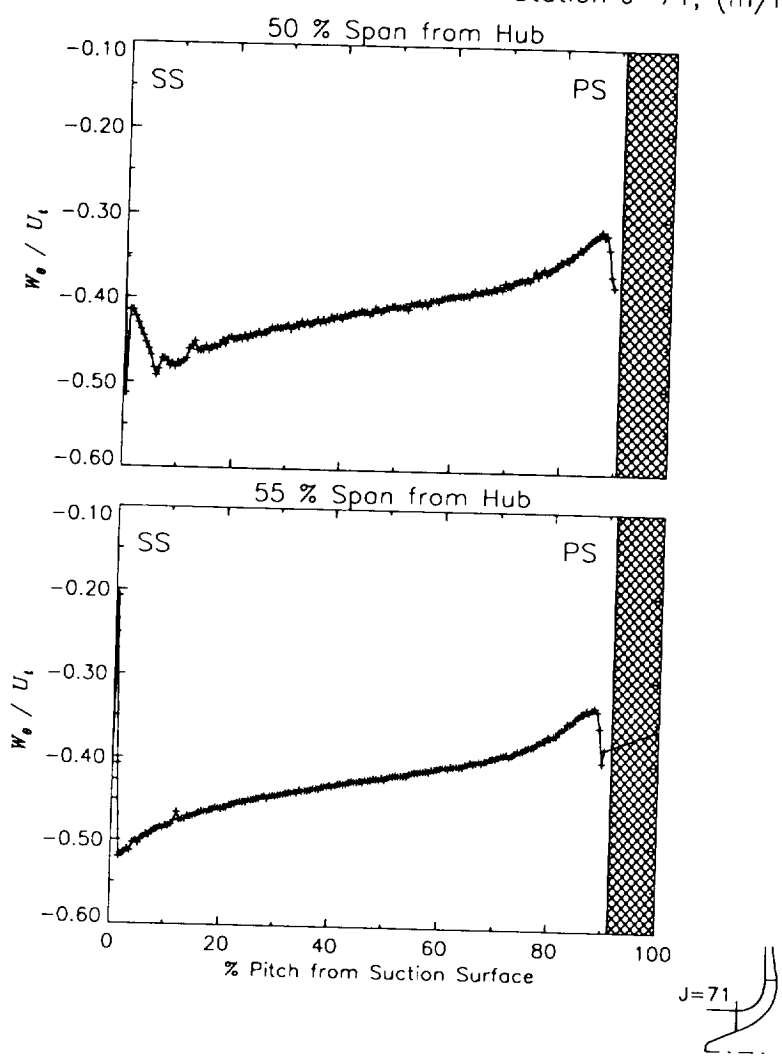
Station J=71, ( $m/m_s=0.010$ )



(b) Relative tangential velocity normalized by impeller tip speed.

Figure 27.—Continued.

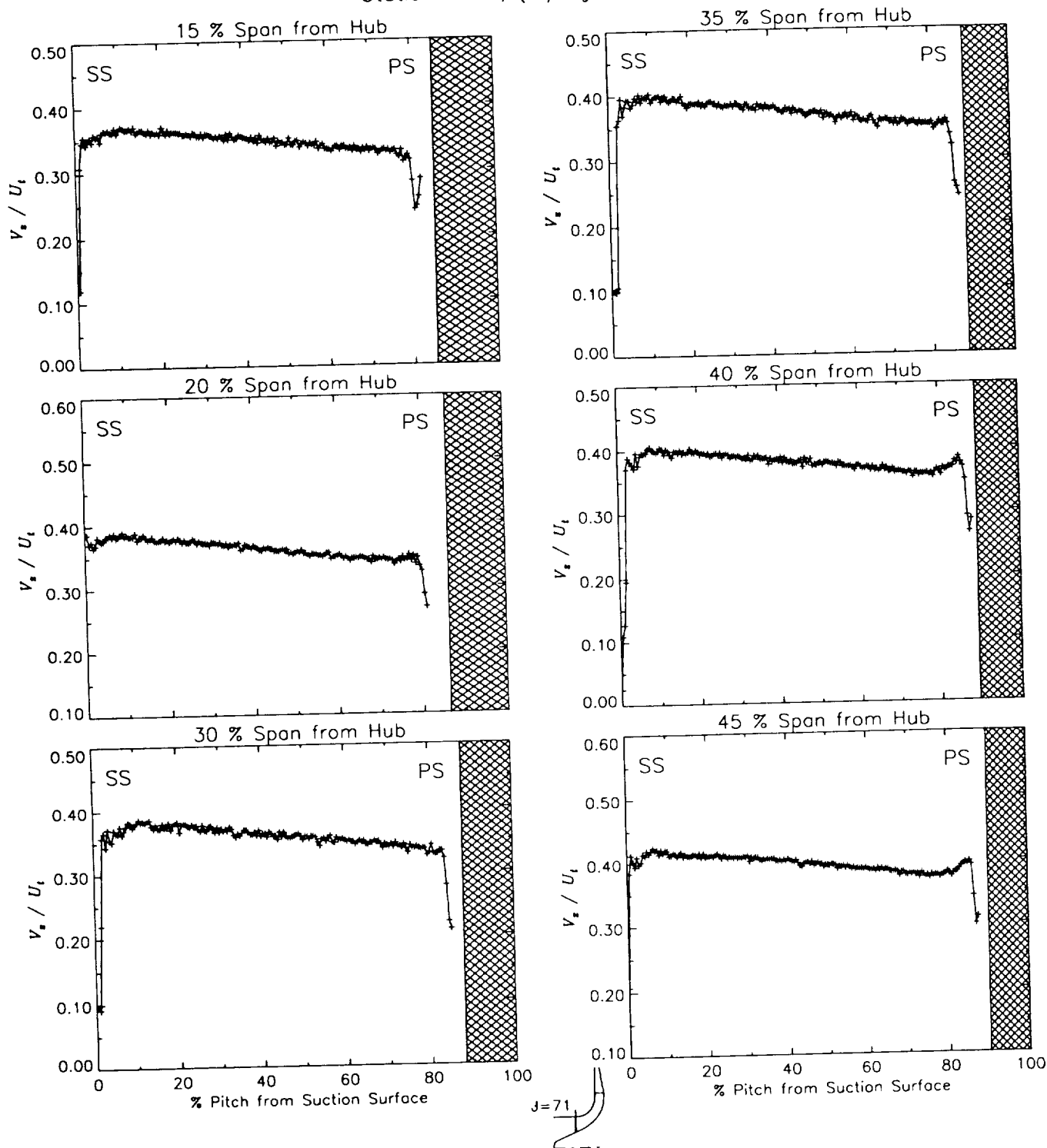
Station J=71, ( $m/m_s=0.010$ )



(b) Relative tangential velocity normalized by impeller tip speed.

Figure 27.—Continued.

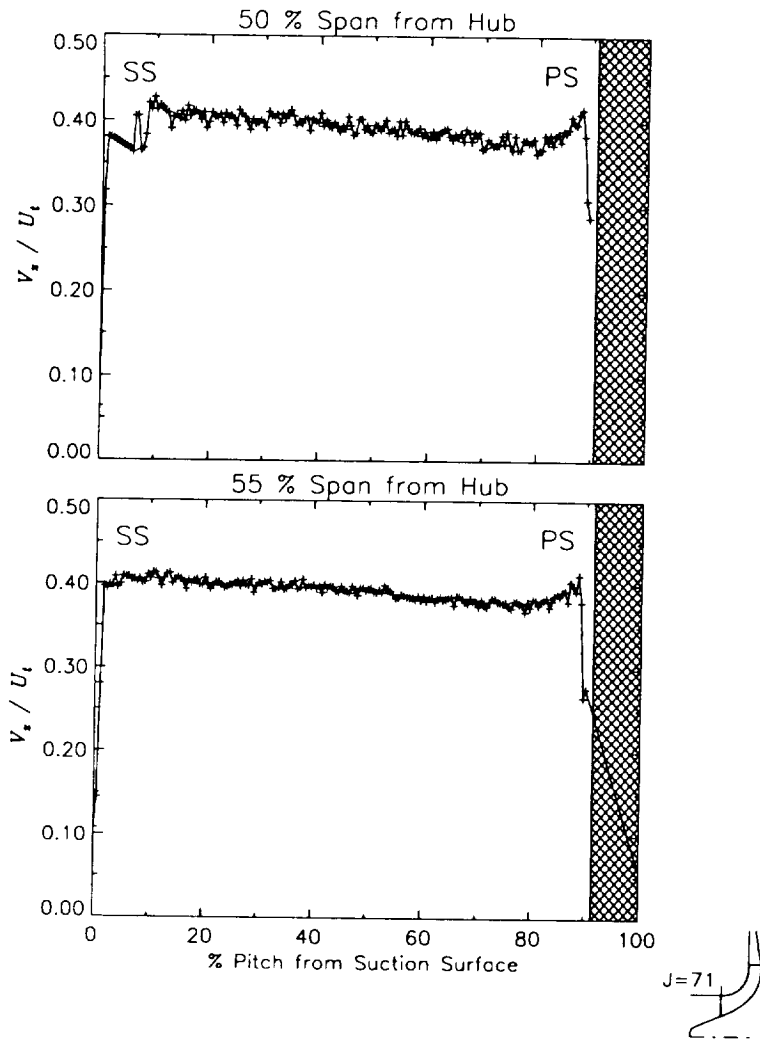
Station J=71, ( $m/m_s=0.010$ )



(c) Axial velocity normalized by impeller tip speed.

Figure 27.-Continued.

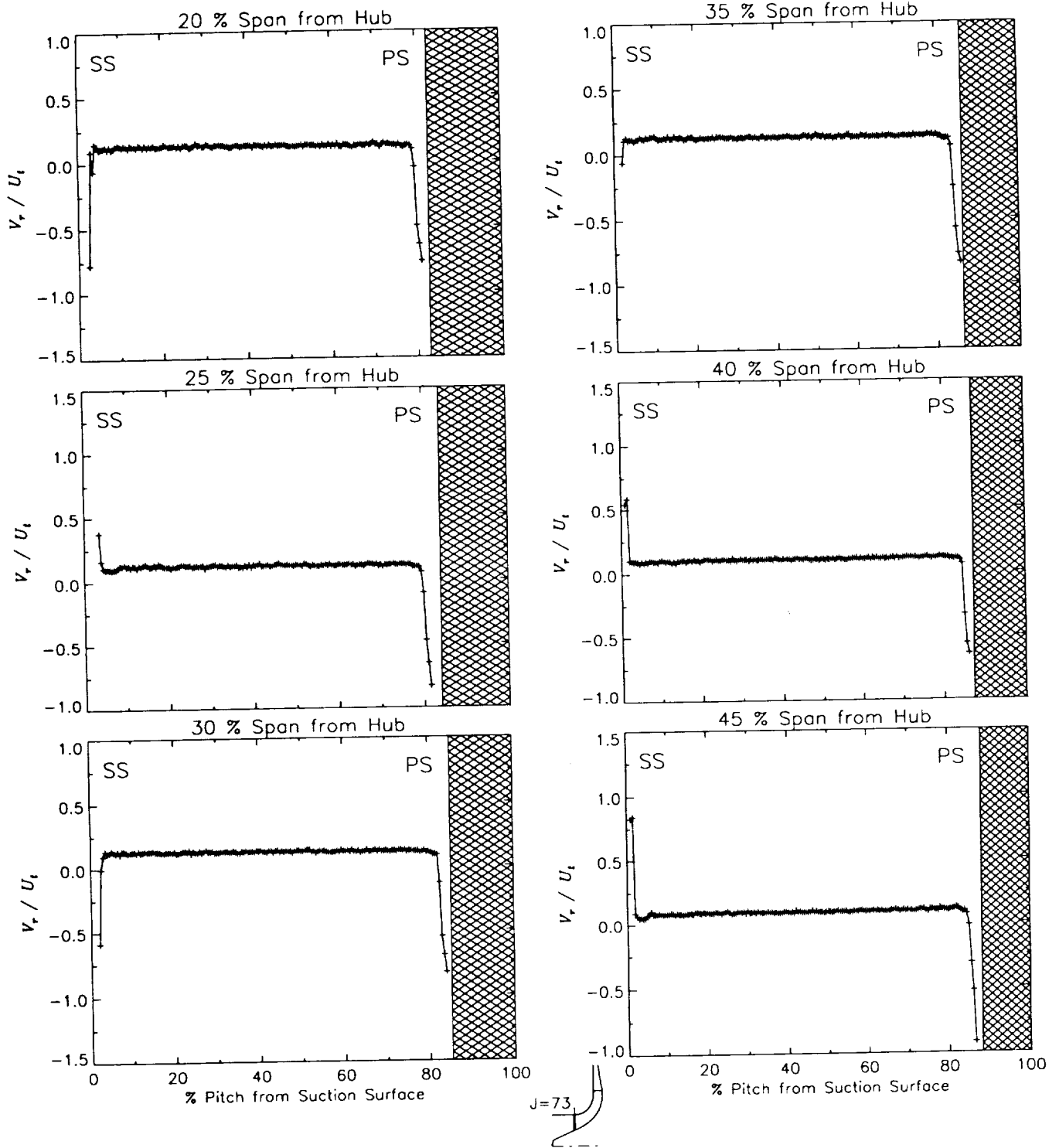
Station J=71, ( $m/m_s=0.010$ )



(c) Axial velocity normalized by impeller tip speed.

Figure 27.-Concluded.

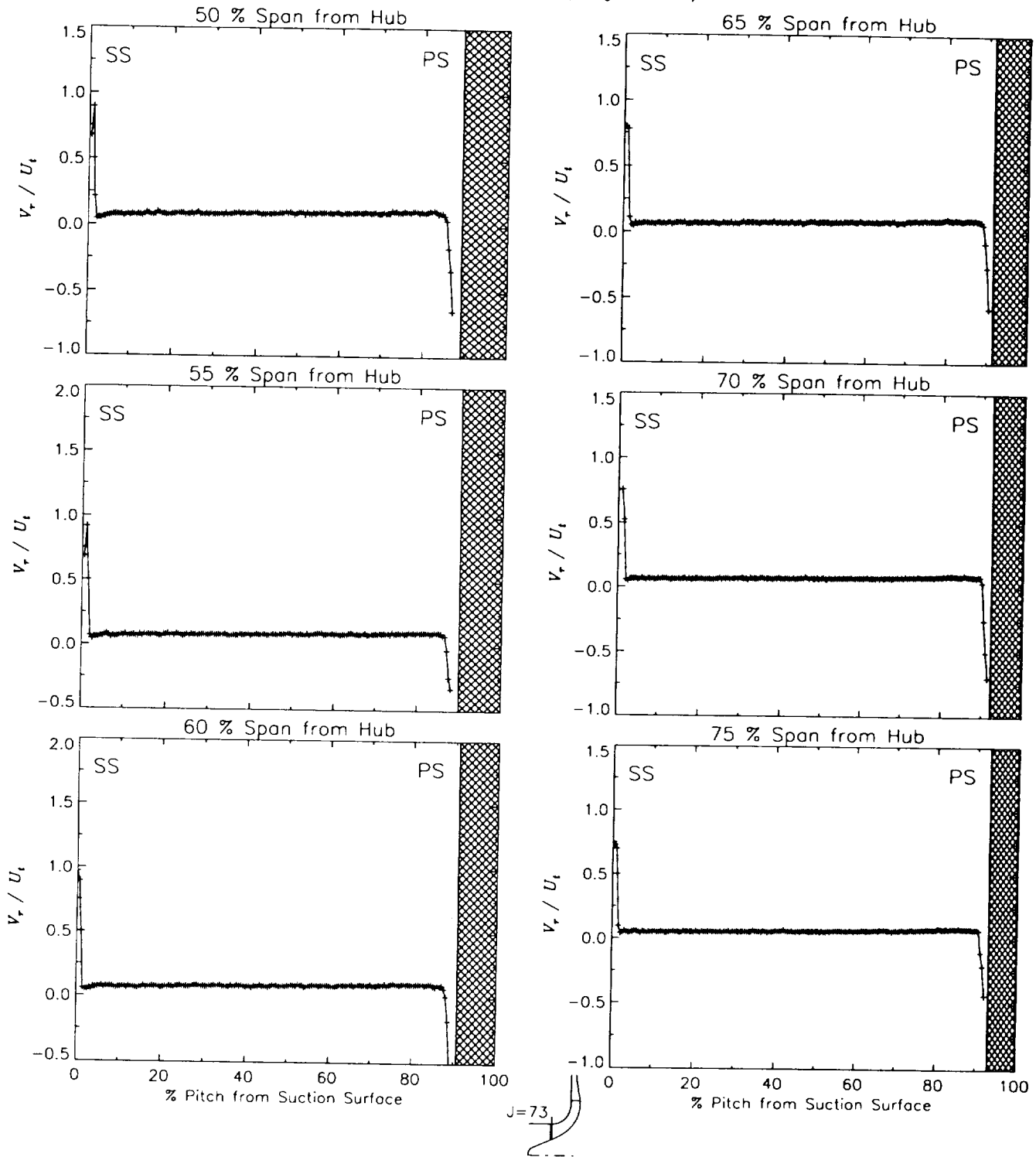
Station J=73, ( $m/m_s=0.030$ )



(a) Radial velocity normalized by impeller tip speed.

Figure 28.—Laser velocimeter results of axial, radial, and relative tangential velocities normalized by impeller tip speed for the design flow condition,  $m_d$ , at station J=73, ( $m/m_s=0.030$ ). The shaded region to the right of each plot represents the physical blade width.

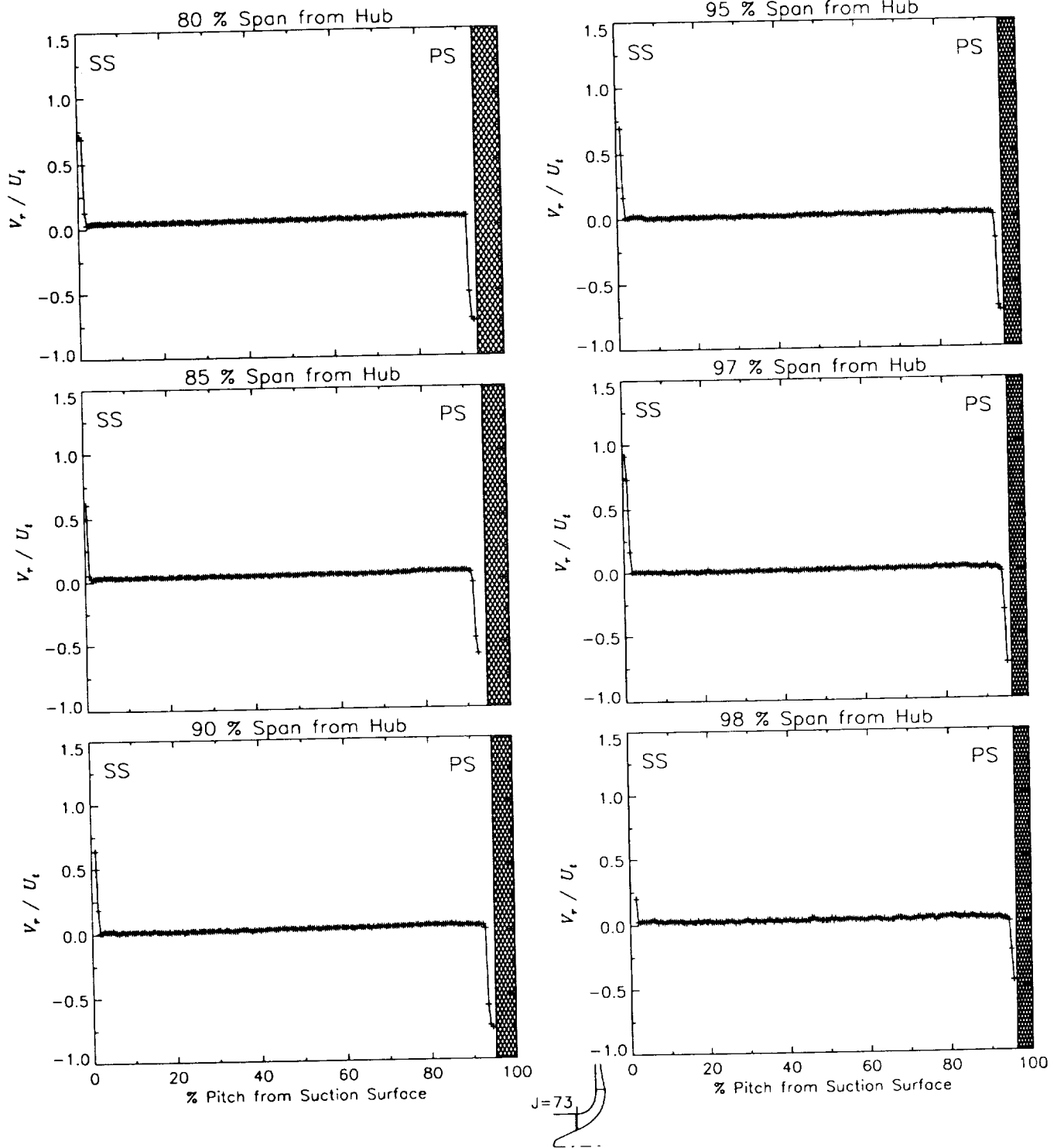
Station J=73, ( $m/m_s=0.030$ )



(a) Radial velocity normalized by impeller tip speed.

Figure 28.-Continued.

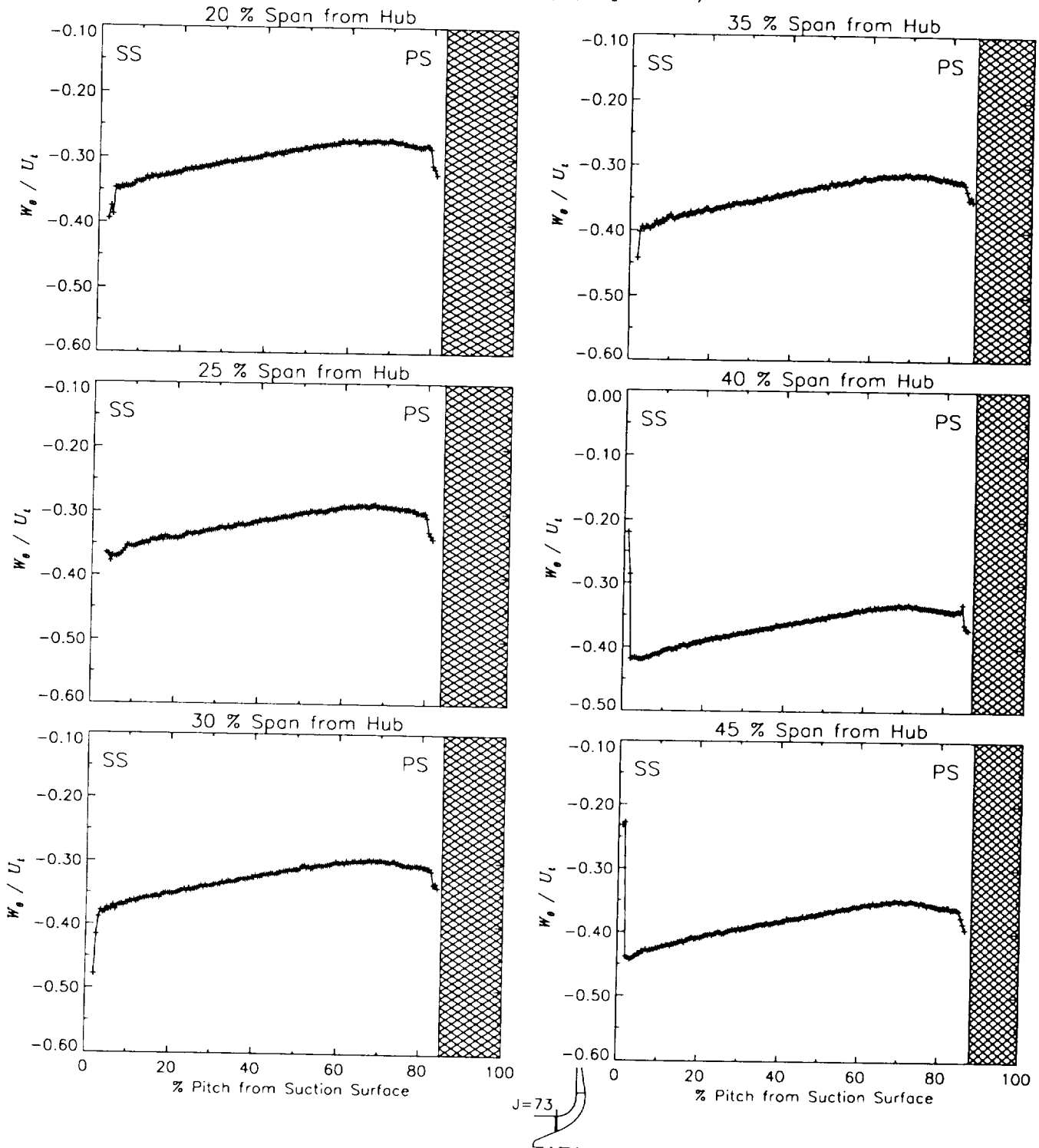
Station J=73, ( $m/m_s=0.030$ )



(a) Radial velocity normalized by impeller tip speed.

Figure 28.-Continued.

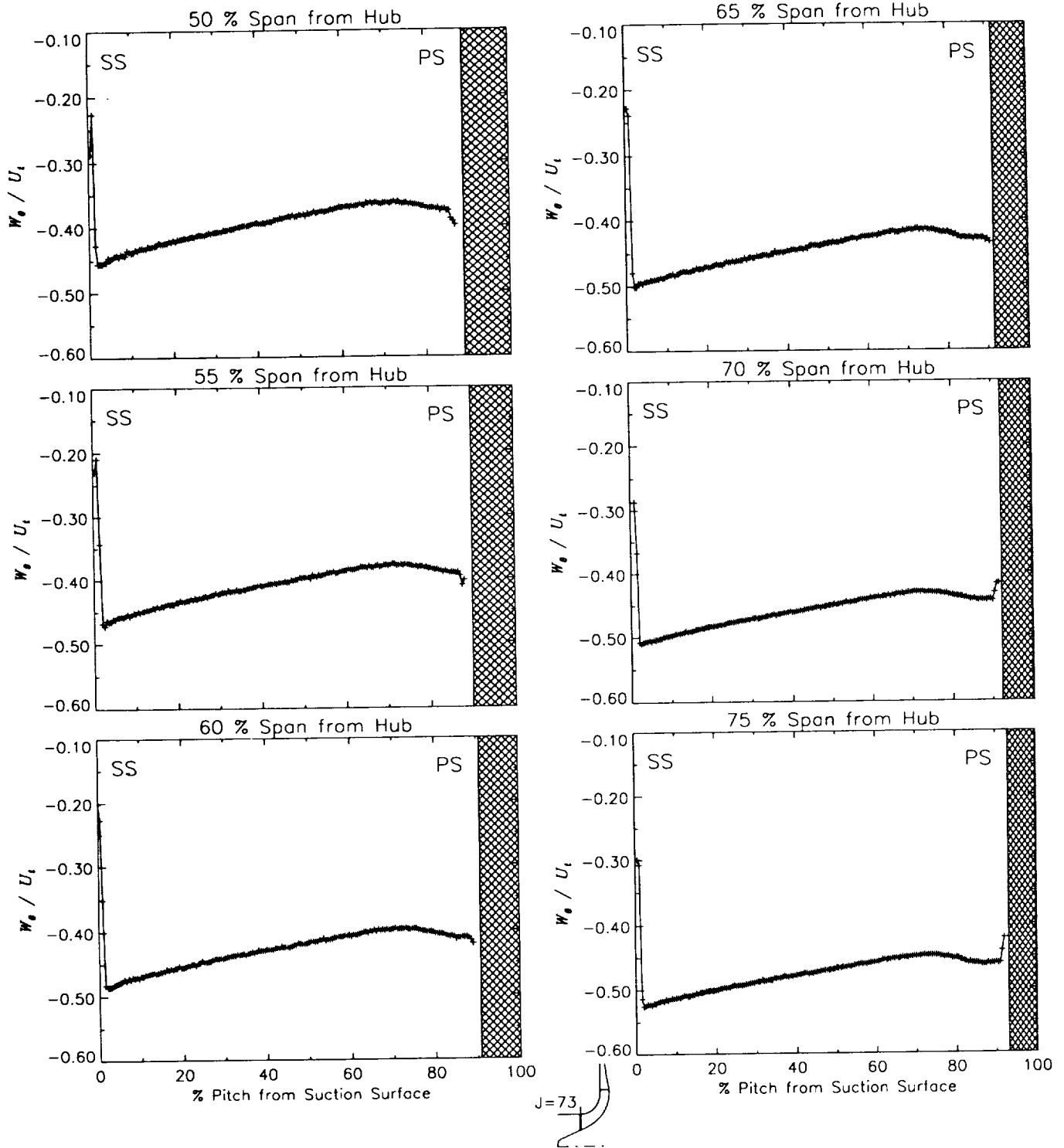
Station J=73, ( $m/m_s=0.030$ )



(b) Relative tangential velocity normalized by impeller tip speed.

Figure 28.—Continued.

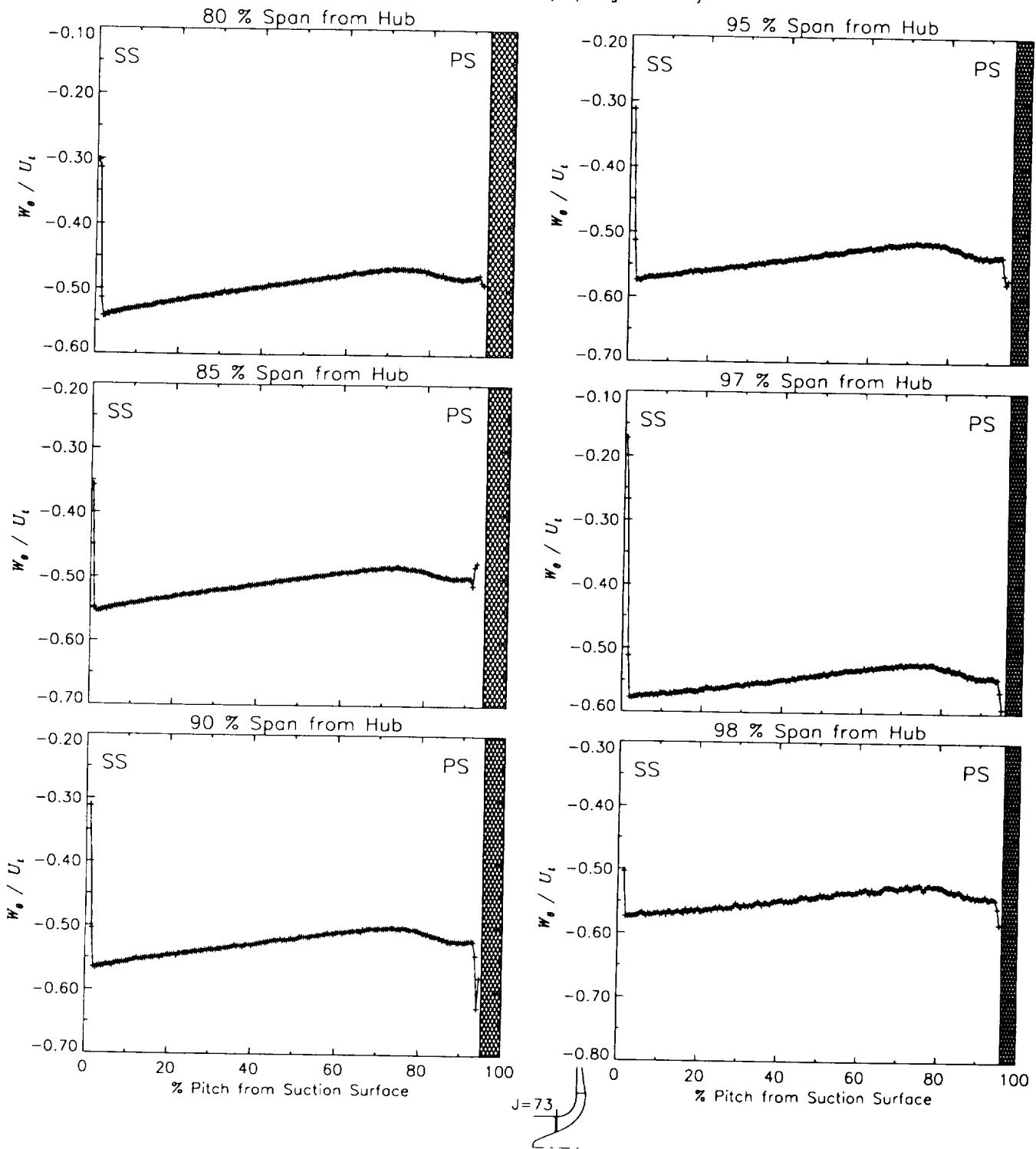
Station J=73, ( $m/m_s=0.030$ )



(b) Relative tangential velocity normalized by impeller tip speed.

Figure 28.-Continued.

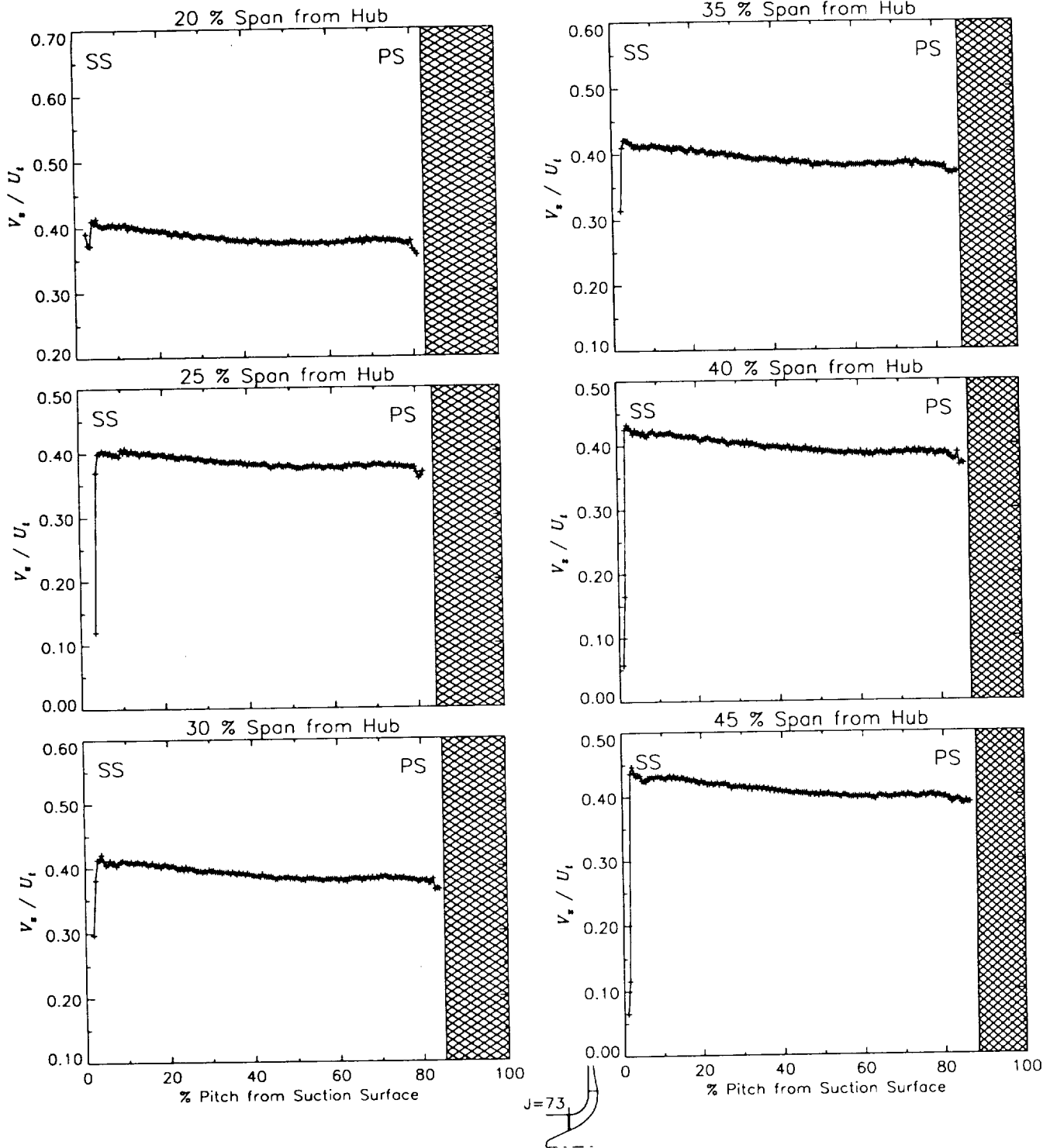
Station J=73, ( $m/m_s=0.030$ )



(b) Relative tangential velocity normalized by impeller tip speed.

Figure 28.--Continued.

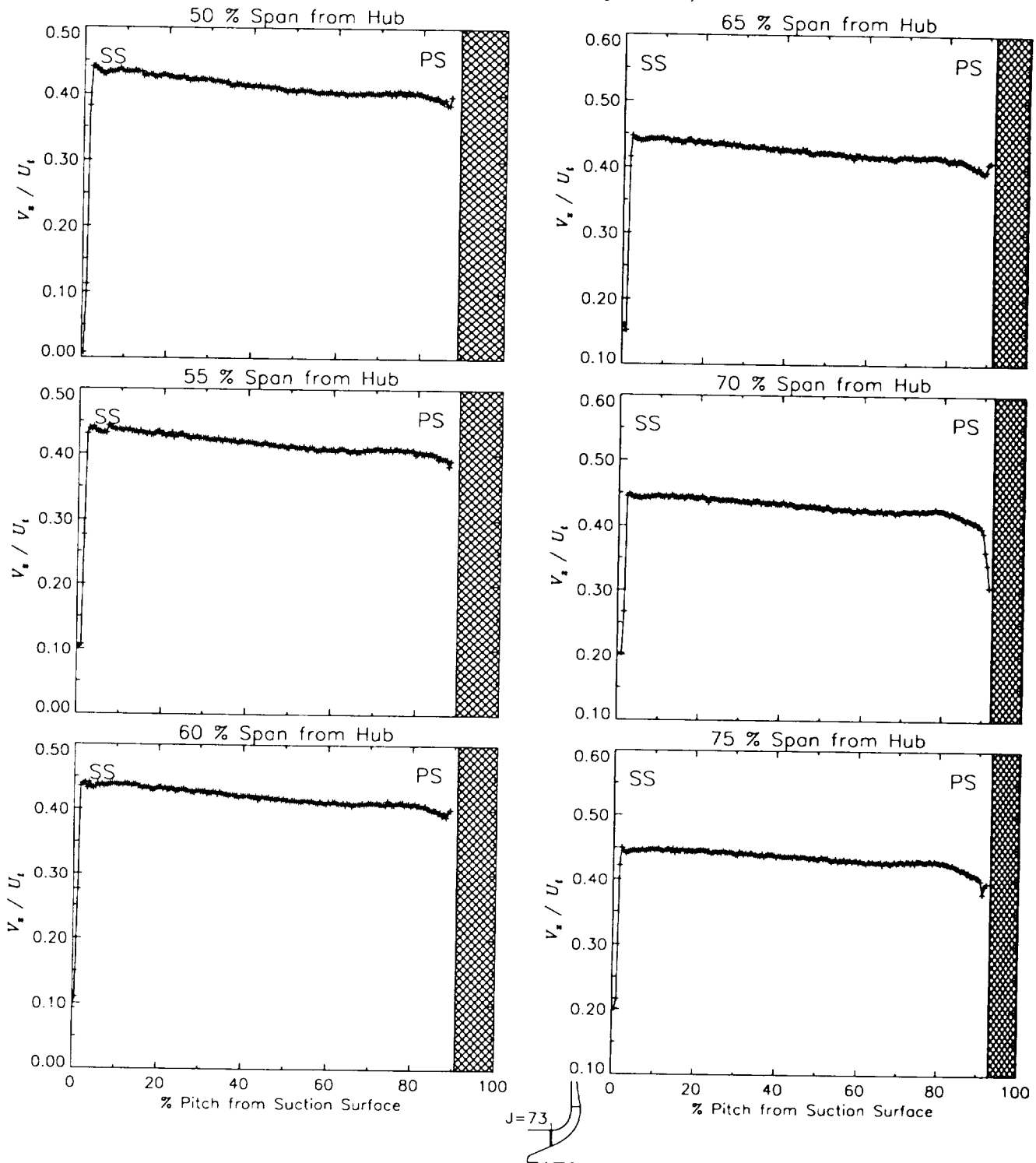
Station J=73, ( $m/m_s=0.030$ )



(c) Axial velocity normalized by impeller tip speed.

Figure 28.-Continued.

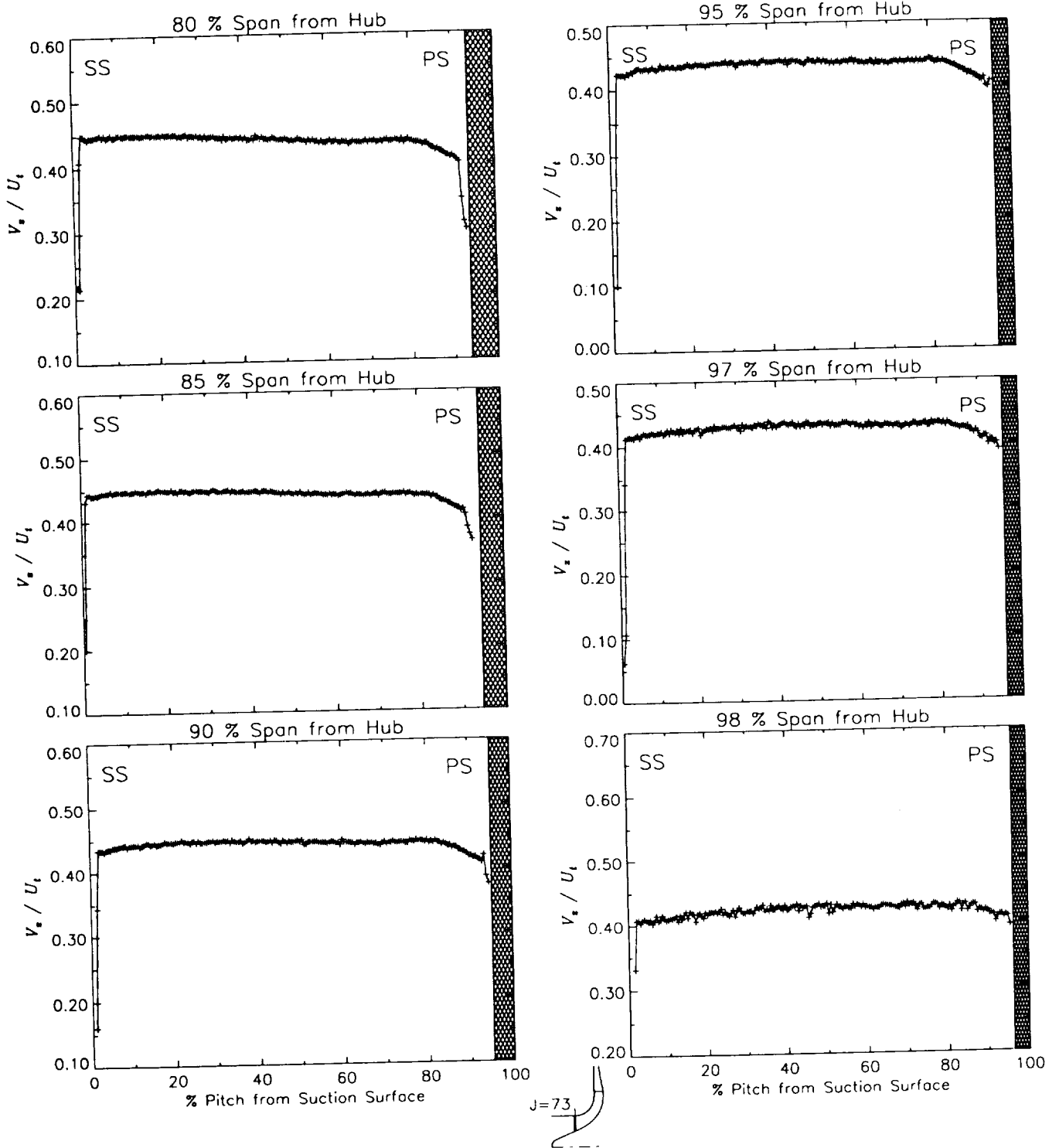
Station J=73, ( $m/m_s=0.030$ )



(c) Axial velocity normalized by impeller tip speed.

Figure 28.-Continued.

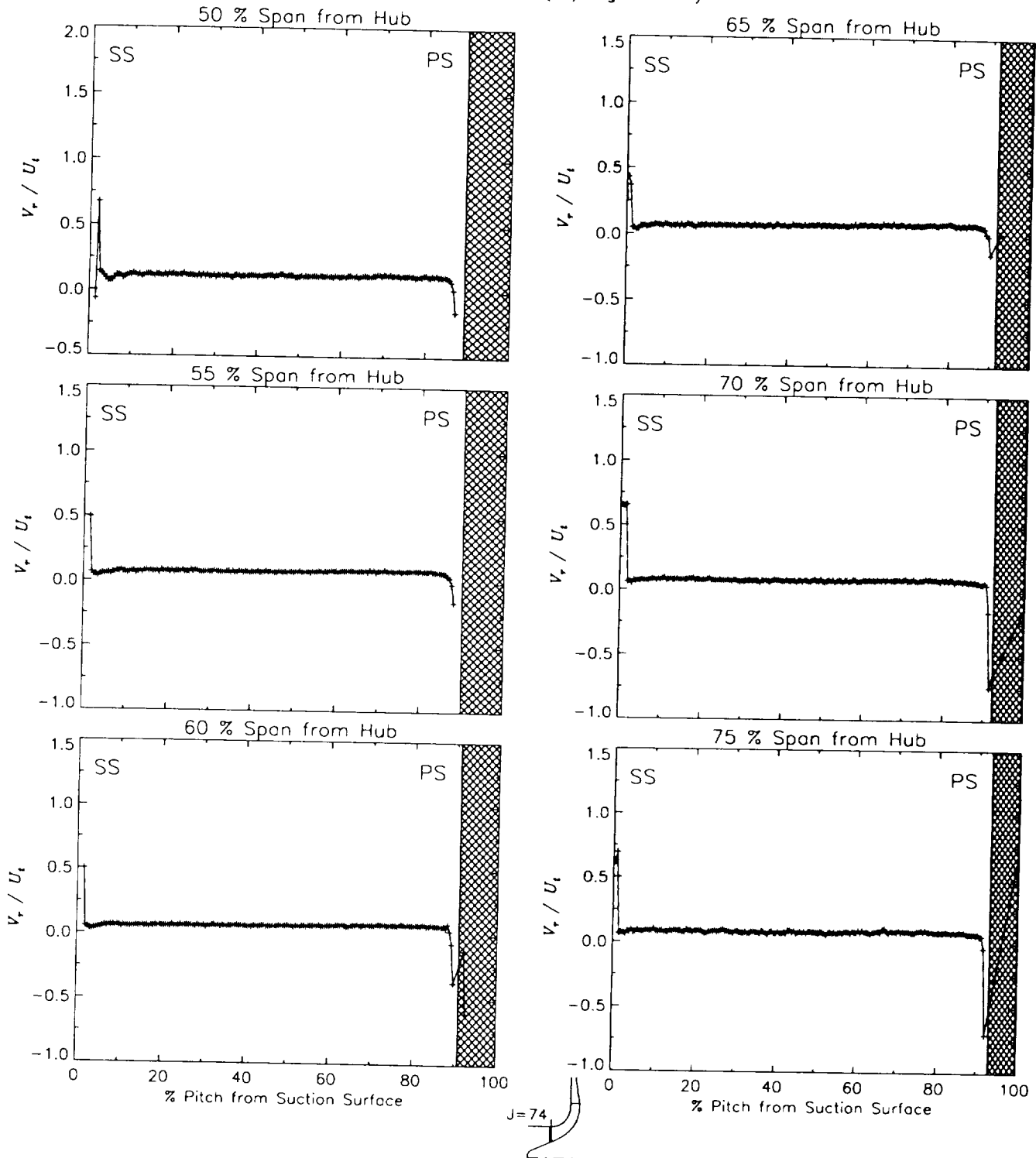
Station J=73, ( $m/m_s=0.030$ )



(c) Axial velocity normalized by impeller tip speed.

Figure 28.-Concluded.

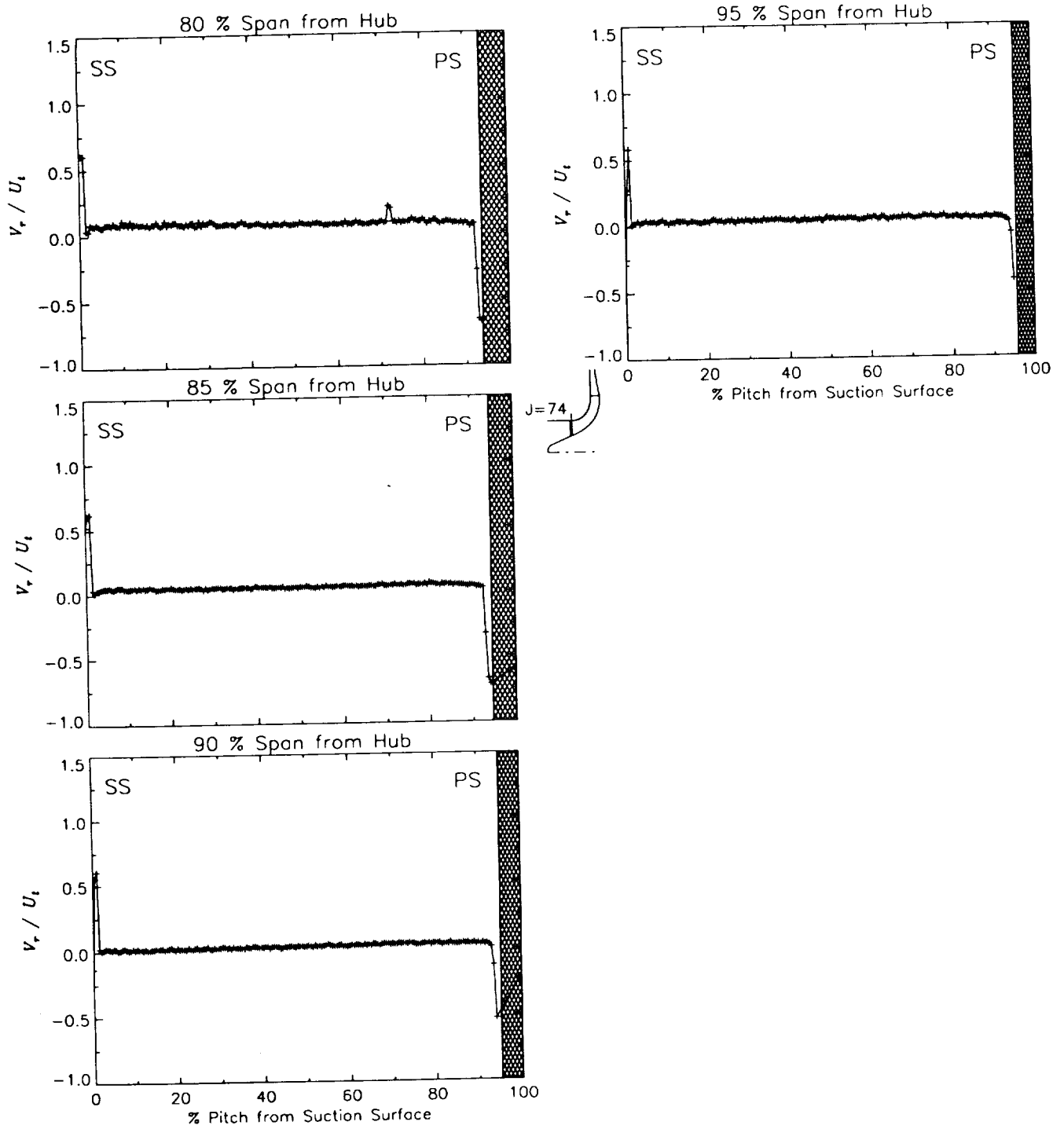
Station J=74, ( $m/m_s=0.040$ )



(a) Radial velocity normalized by impeller tip speed.

Figure 29.—Laser velocimeter results of axial, radial, and relative tangential velocities normalized by impeller tip speed for the design flow condition,  $m_d$ , at station J=74, ( $m/m_s=0.040$ ). The shaded region to the right of each plot represents the physical blade width.

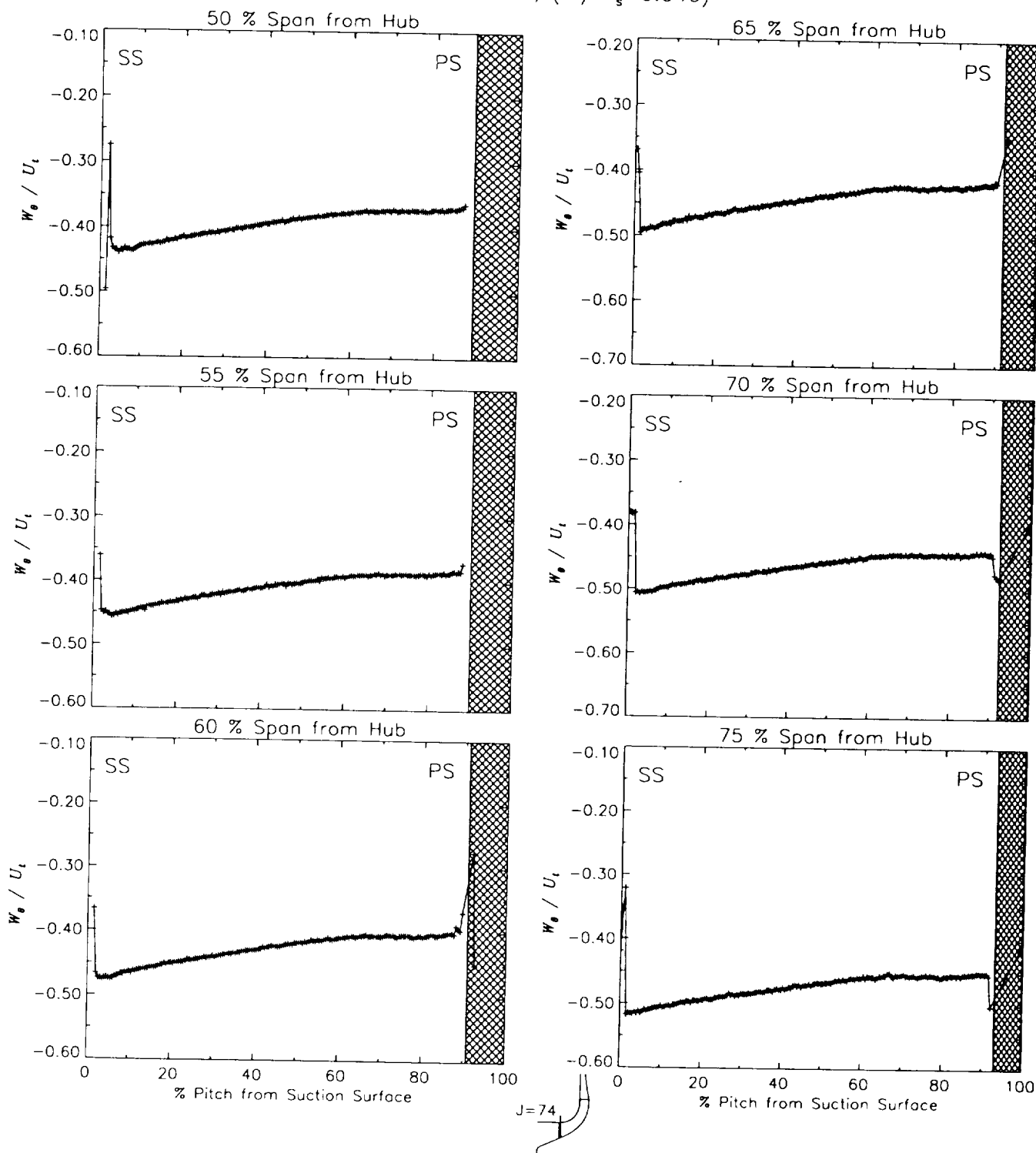
Station J=74, ( $m/m_s=0.040$ )



(a) Radial velocity normalized by impeller tip speed.

Figure 29.-Continued.

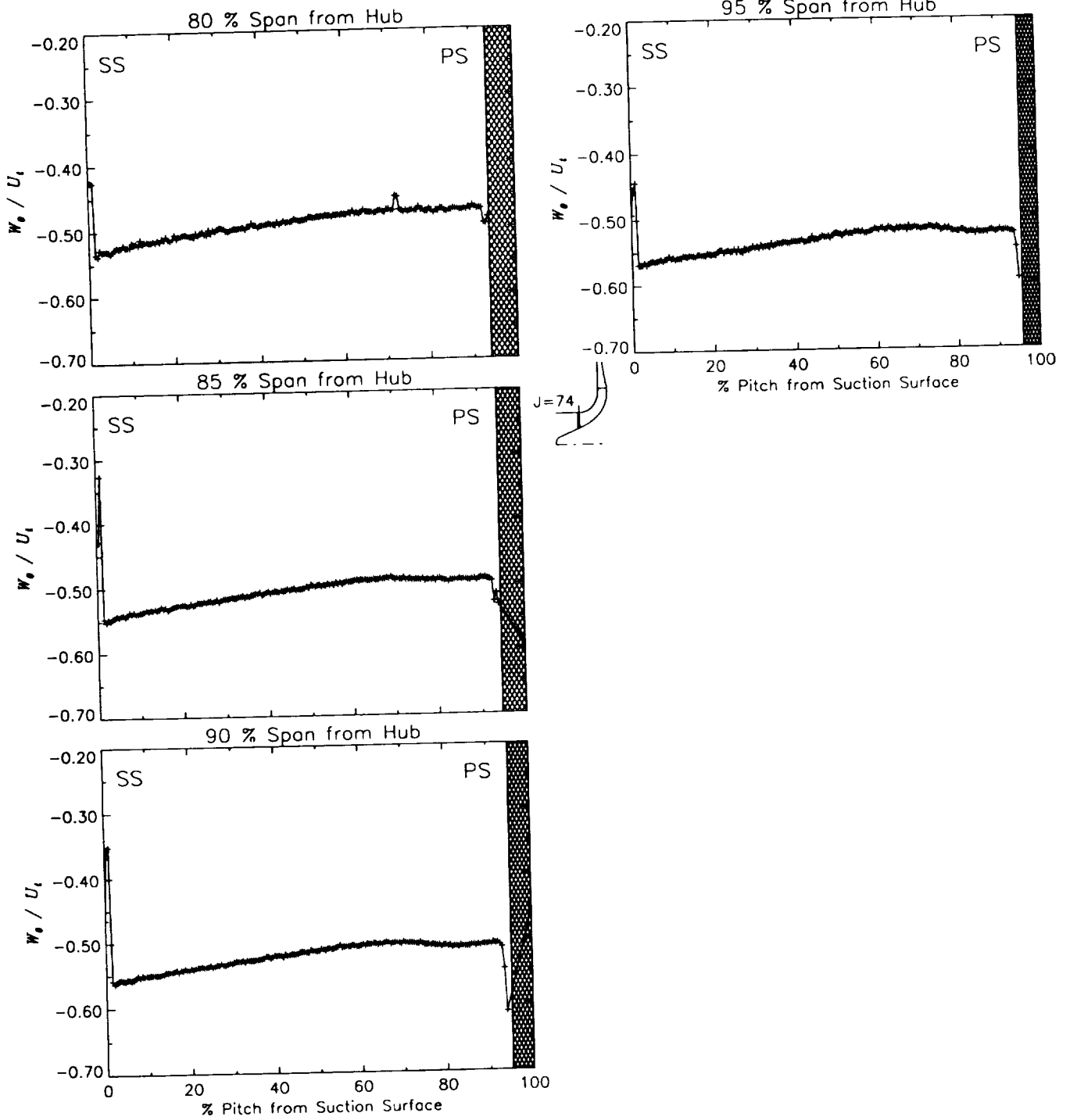
Station J=74, ( $m/m_s=0.040$ )



(b) Relative tangential velocity normalized by impeller tip speed.

Figure 29.-Continued.

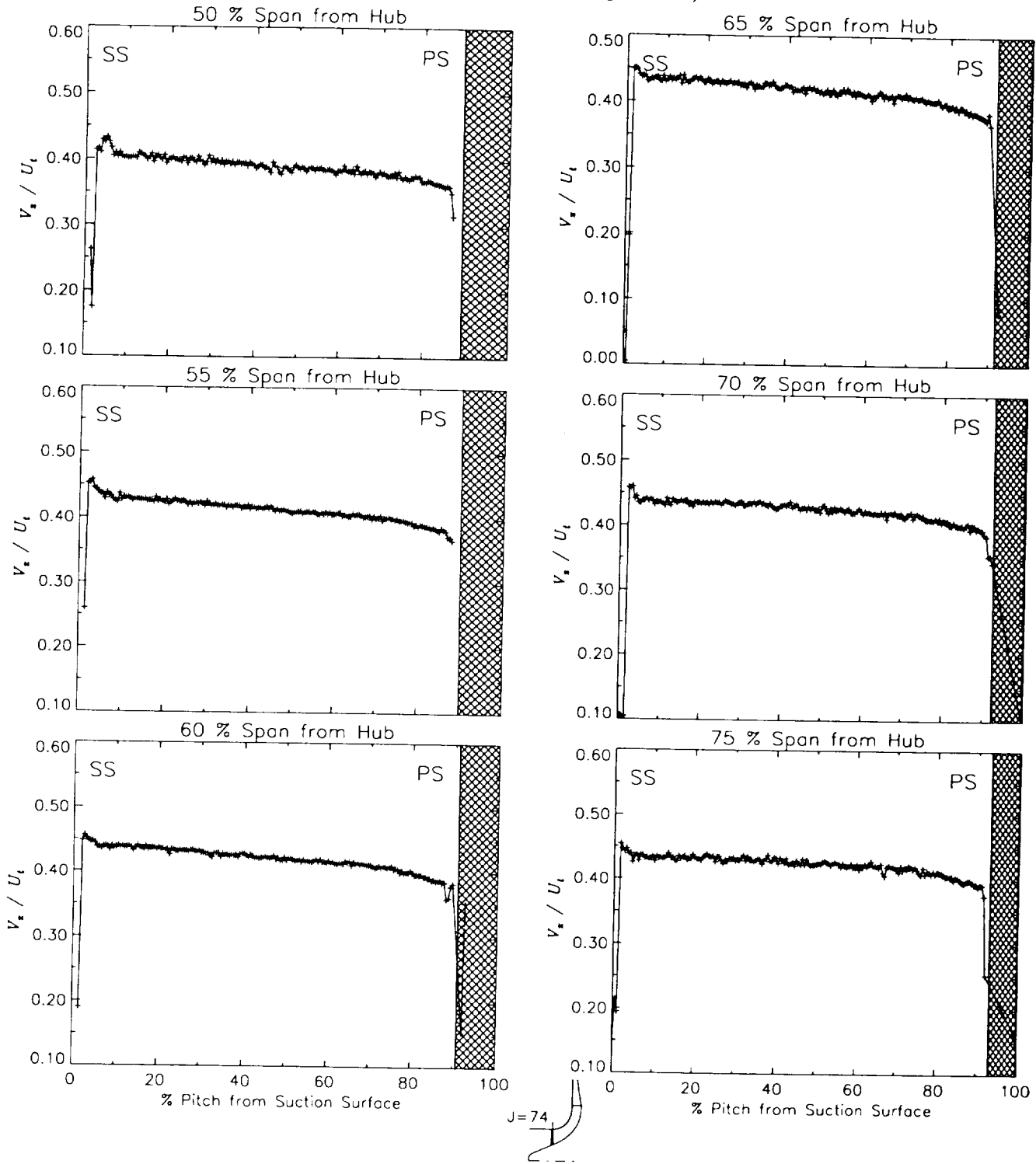
Station J=74, ( $m/m_s=0.040$ )



(b) Relative tangential velocity normalized by impeller tip speed.

Figure 29.-Continued.

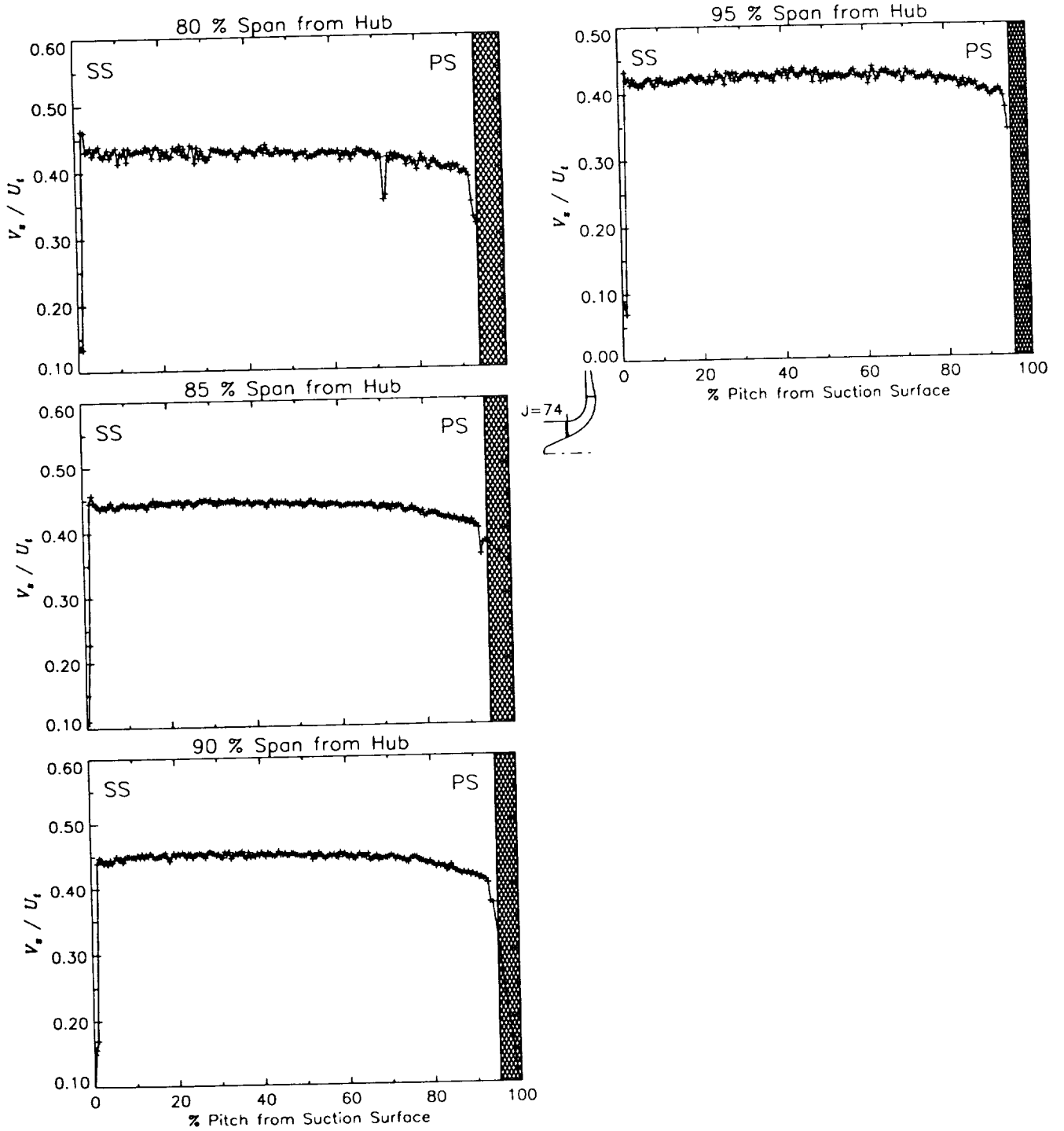
Station J=74, ( $m/m_s=0.040$ )



(c) Axial velocity normalized by impeller tip speed.

Figure 29.-Continued.

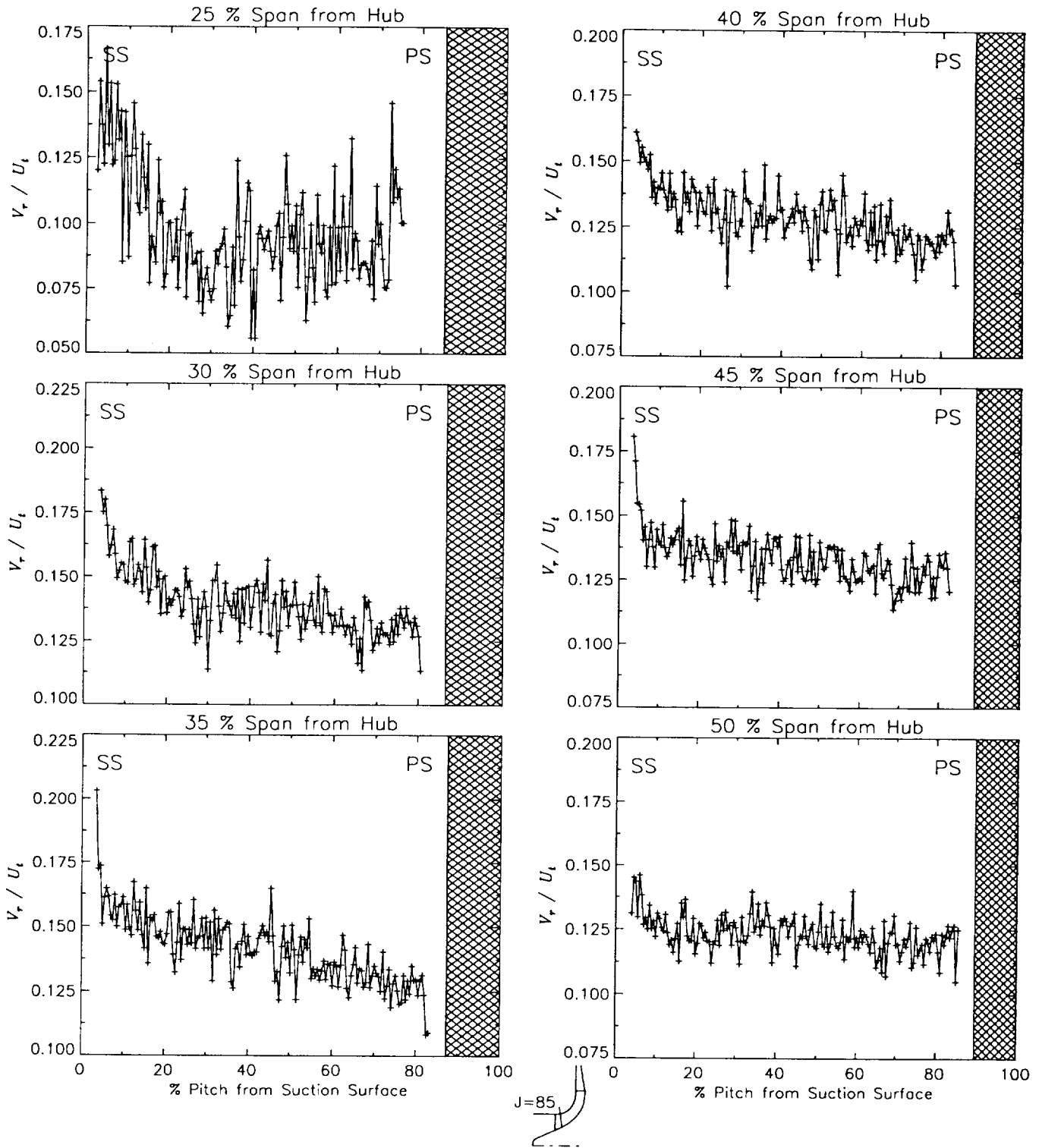
Station J=74, ( $m/m_s=0.040$ )



(c) Axial velocity normalized by impeller tip speed.

Figure 29.—Concluded.

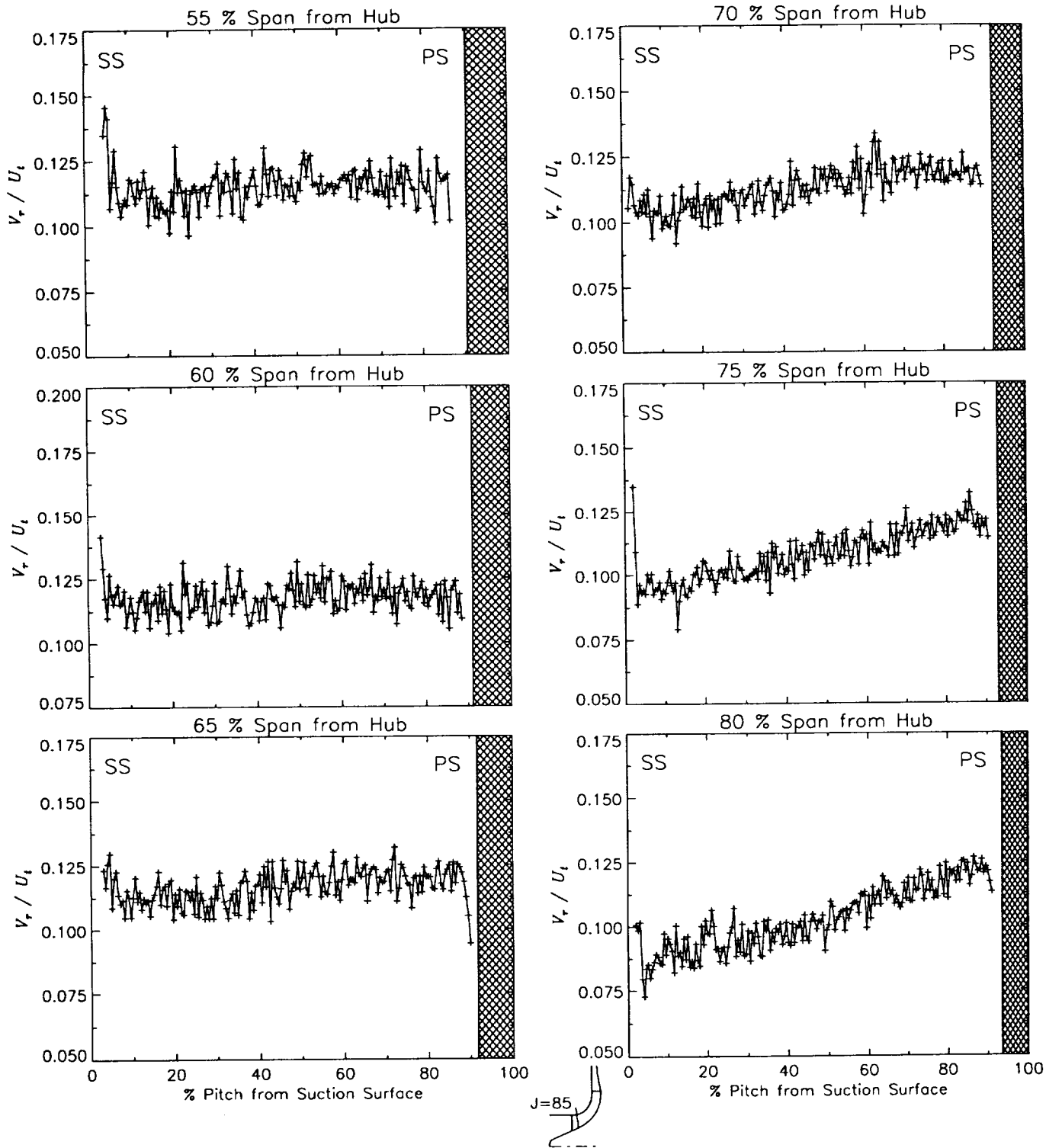
Station J=85, ( $m/m_s=0.149$ )



(a) Radial velocity normalized by impeller tip speed.

Figure 30.—Laser velocimeter results of axial, radial, and relative tangential velocities normalized by impeller tip speed for the design flow condition,  $m_d$ , at station J=85, ( $m/m_s=0.149$ ). The shaded region to the right of each plot represents the physical blade width.

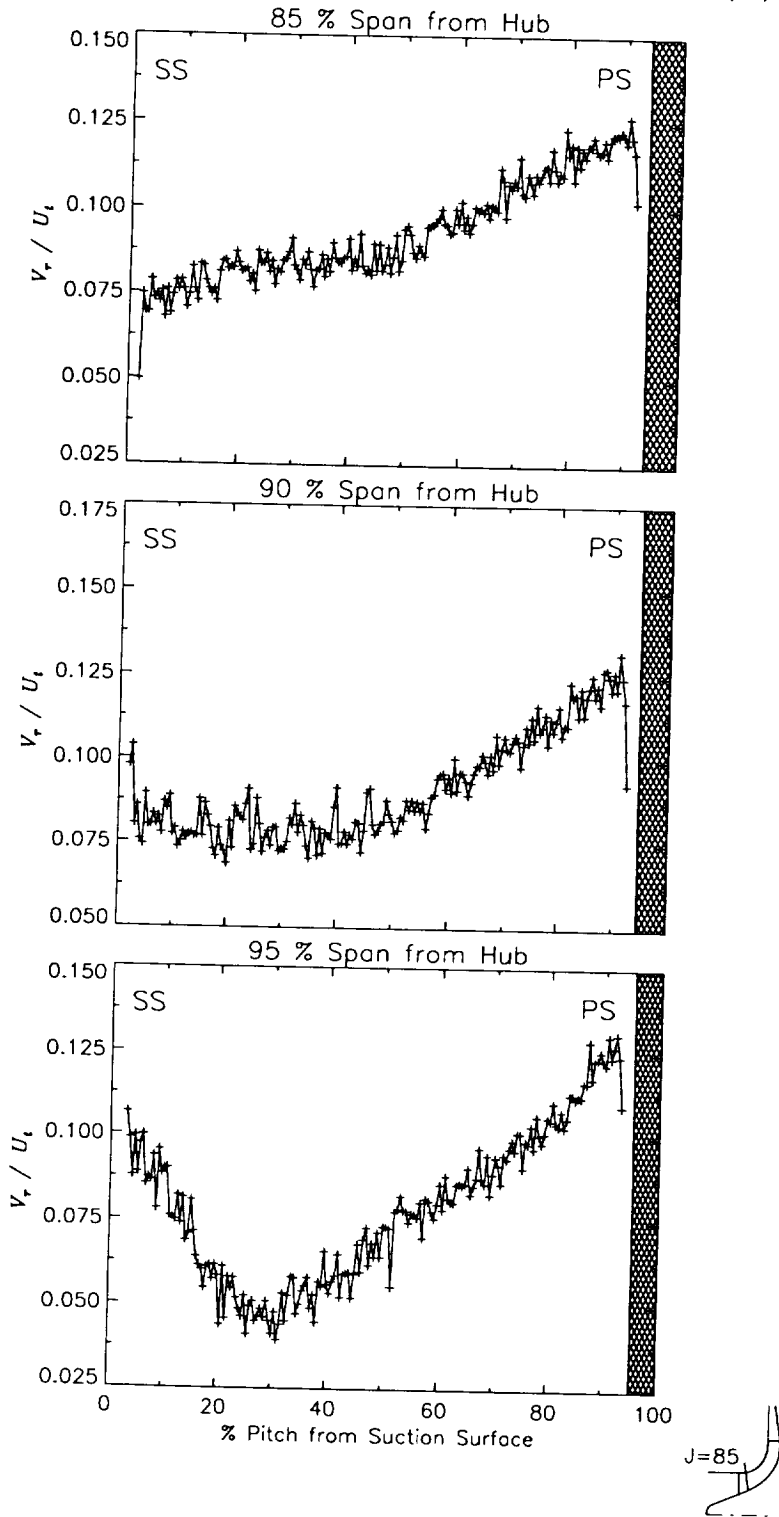
Station J=85, ( $m/m_s=0.149$ )



(a) Radial velocity normalized by impeller tip speed.

Figure 30.—Continued.

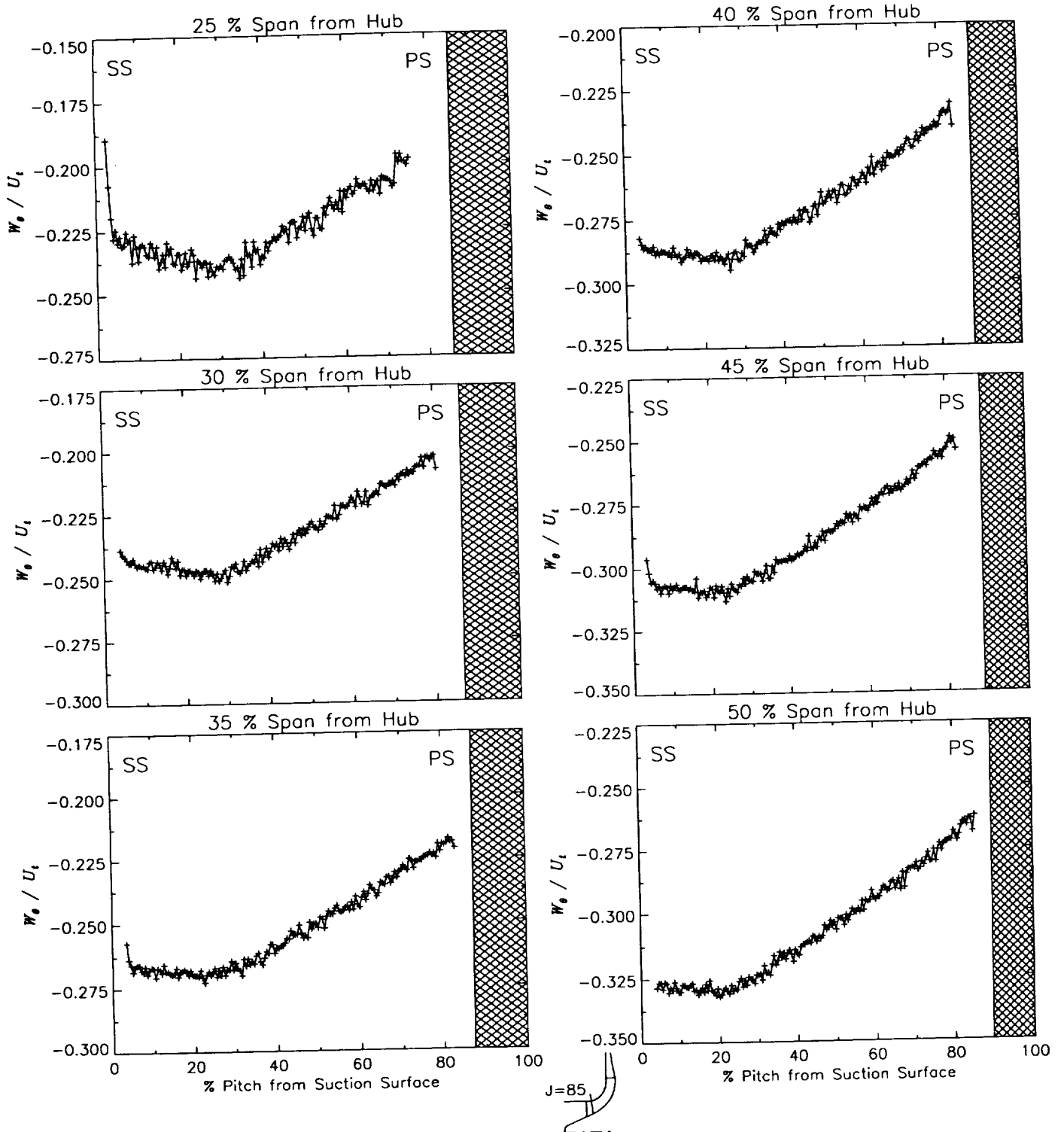
Station J=85, ( $m/m_s=0.149$ )



(a) Radial velocity normalized by impeller tip speed.

Figure 30.—Continued.

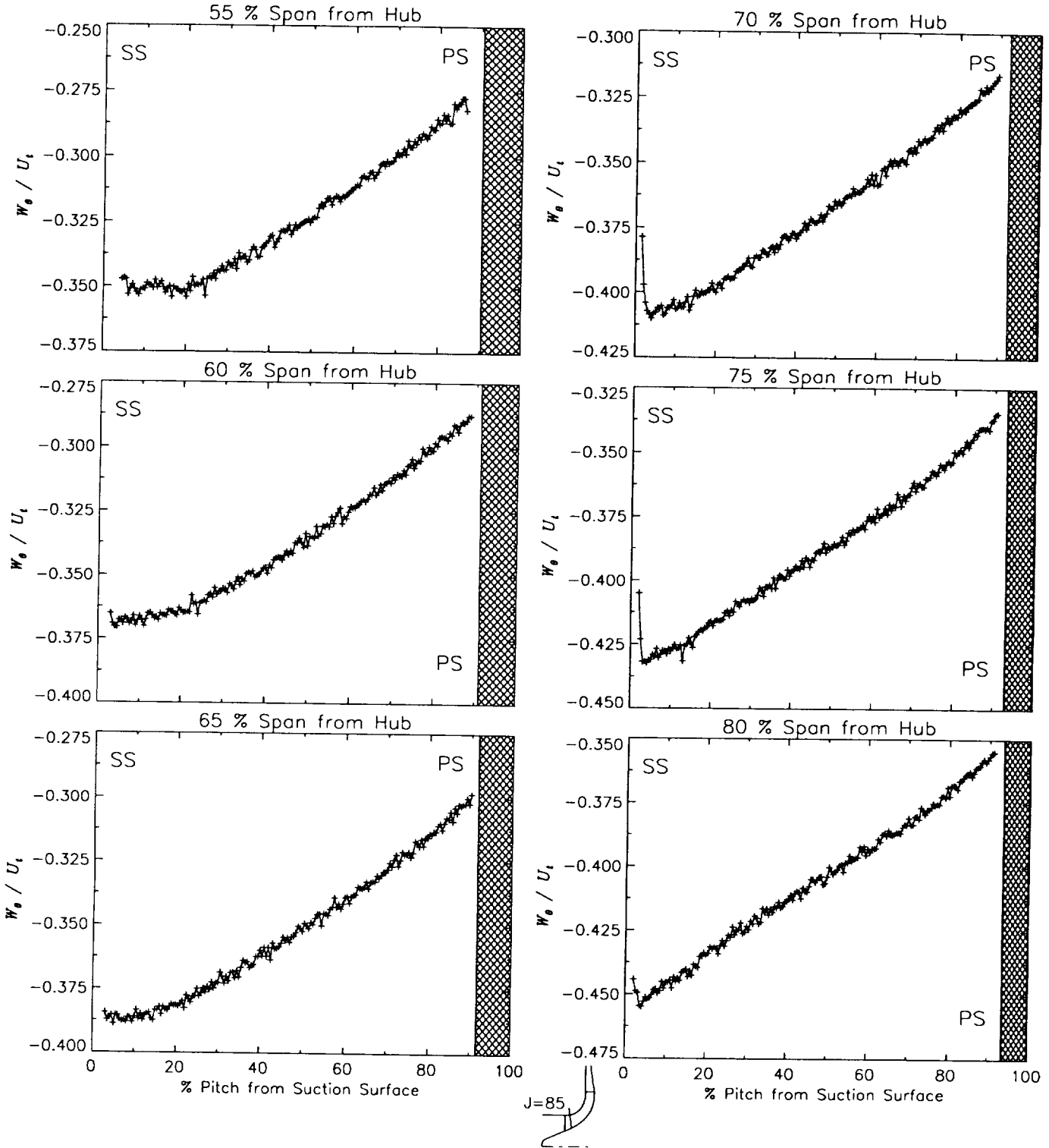
Station J=85, ( $m/m_s=0.149$ )



(b) Relative tangential velocity normalized by impeller tip speed.

Figure 30.-Continued.

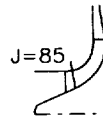
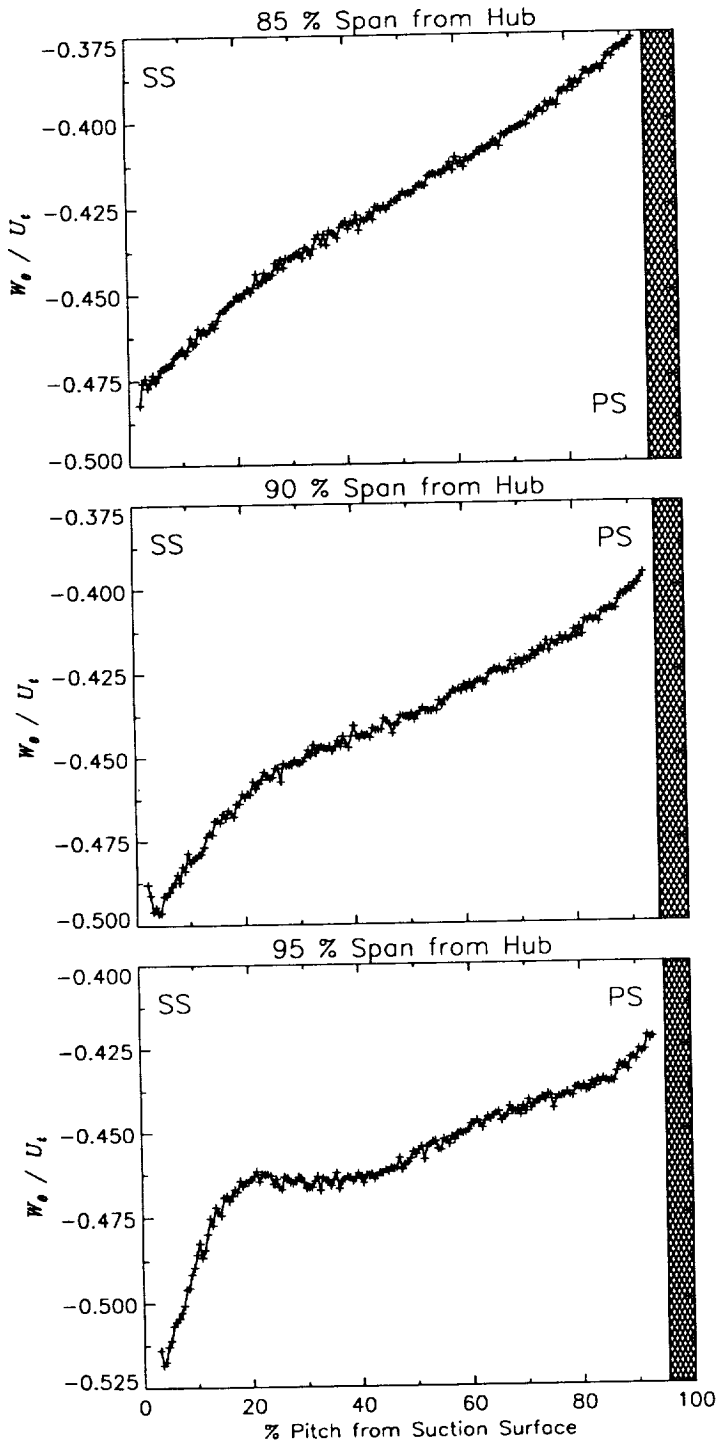
Station J=85, ( $m/m_s=0.149$ )



(b) Relative tangential velocity normalized by impeller tip speed.

Figure 30.-Continued.

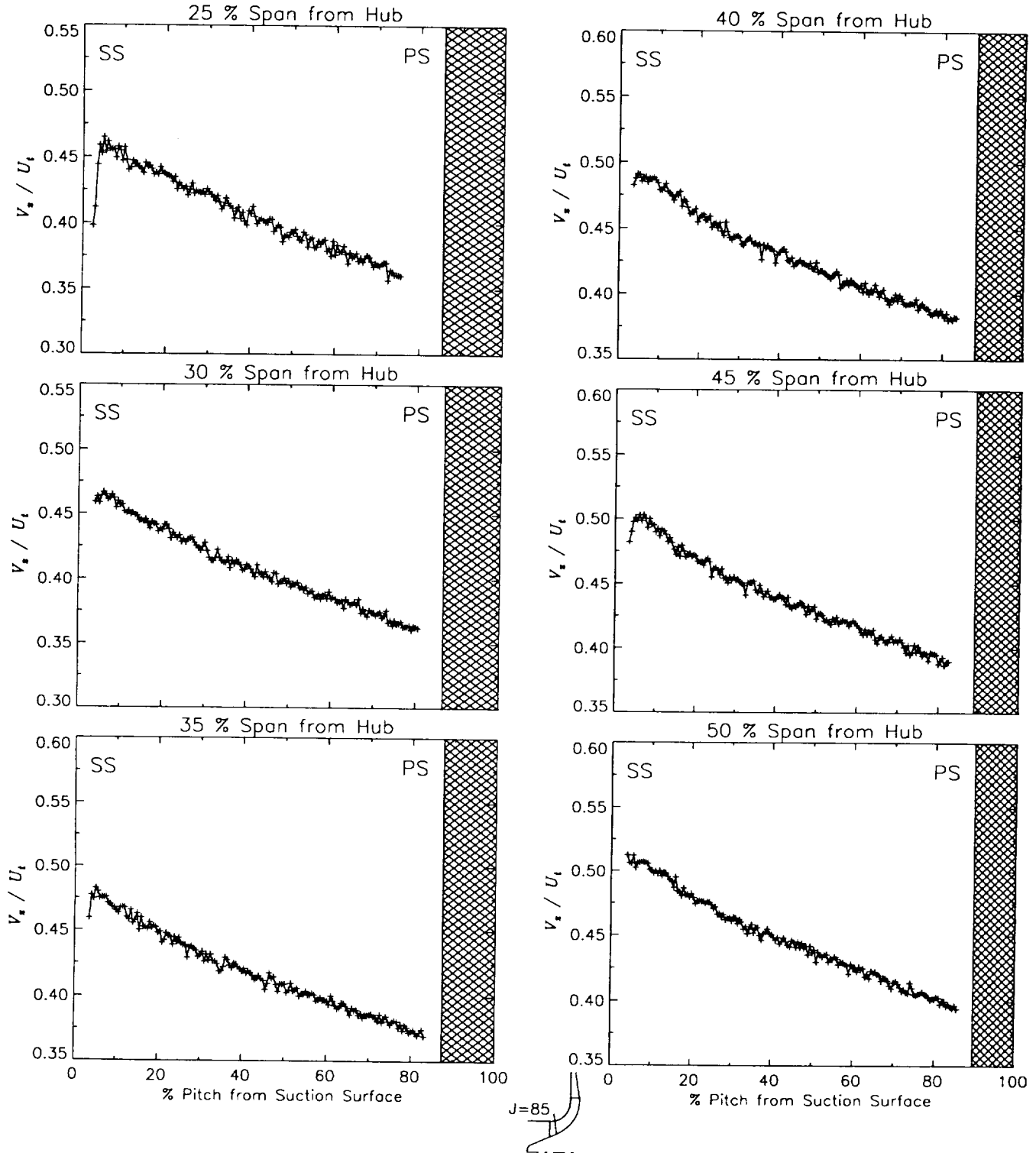
Station J=85, ( $m/m_s=0.149$ )



(b) Relative tangential velocity normalized by impeller tip speed.

Figure 30.-Continued.

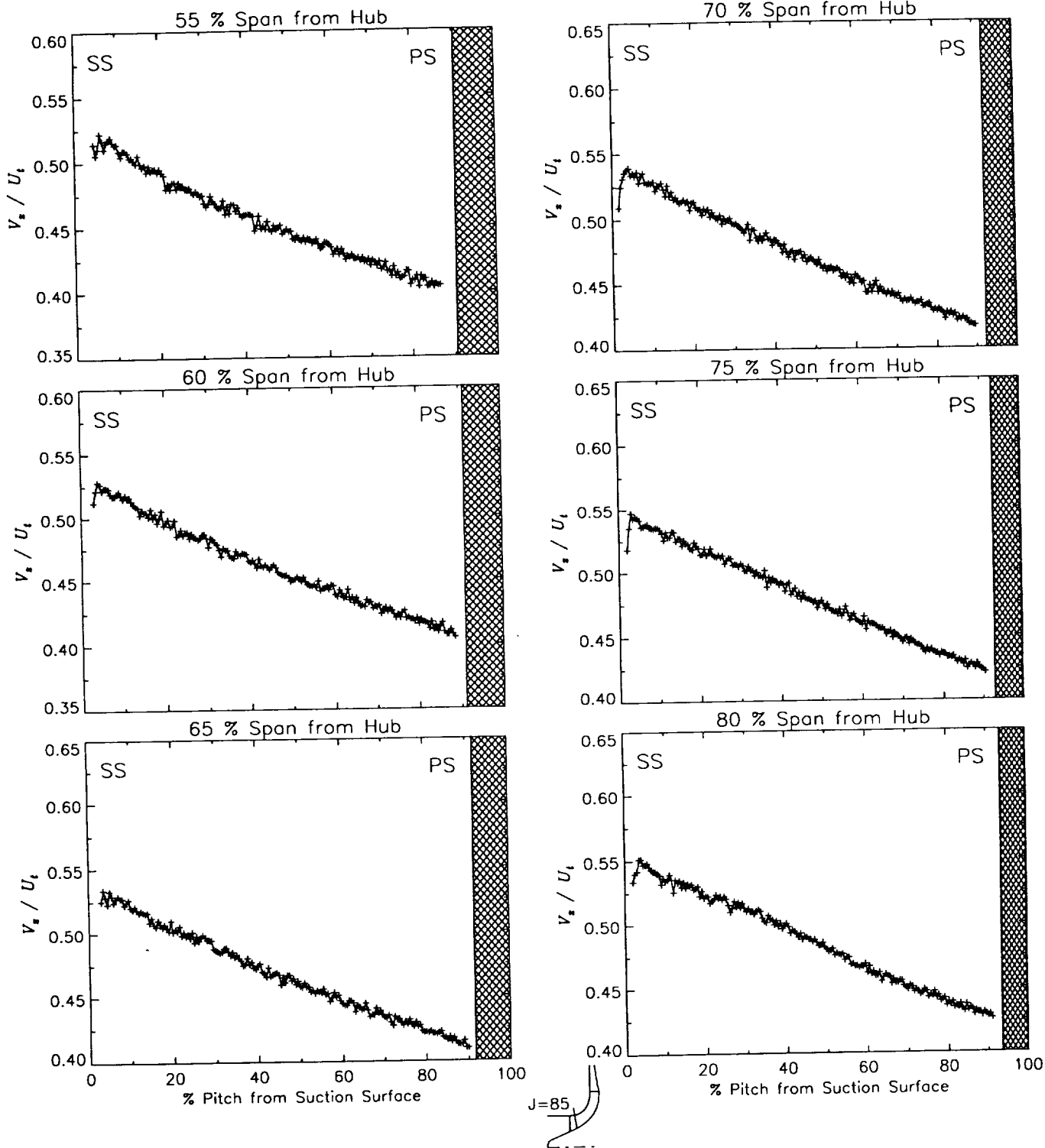
Station J=85, ( $m/m_s=0.149$ )



(c) Axial velocity normalized by impeller tip speed.

Figure 30.-Continued.

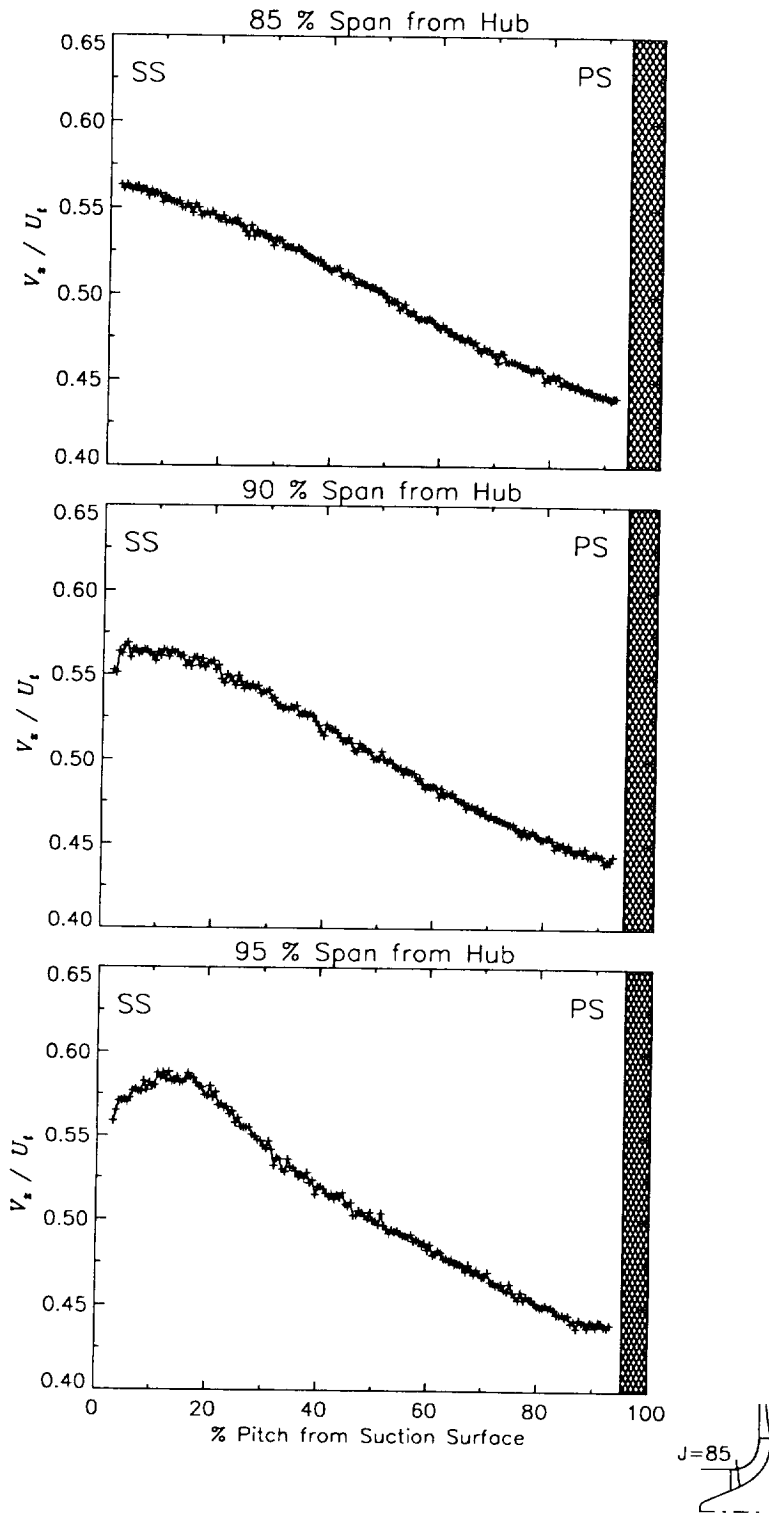
Station J=85, ( $m/m_s=0.149$ )



(c) Axial velocity normalized by impeller tip speed.

Figure 30.—Continued.

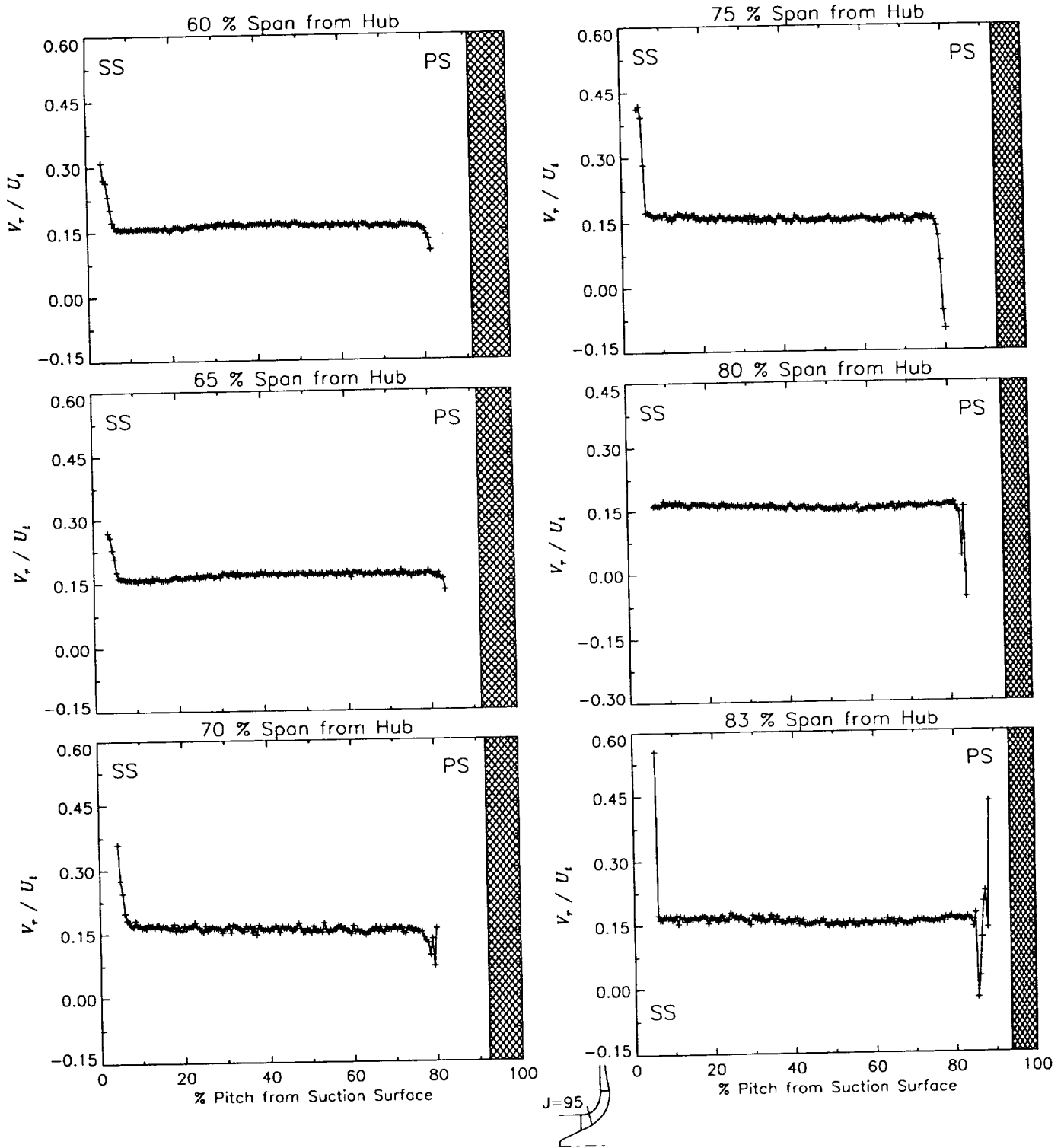
Station J=85, ( $m/m_s=0.149$ )



(c) Axial velocity normalized by impeller tip speed.

Figure 30.-Concluded.

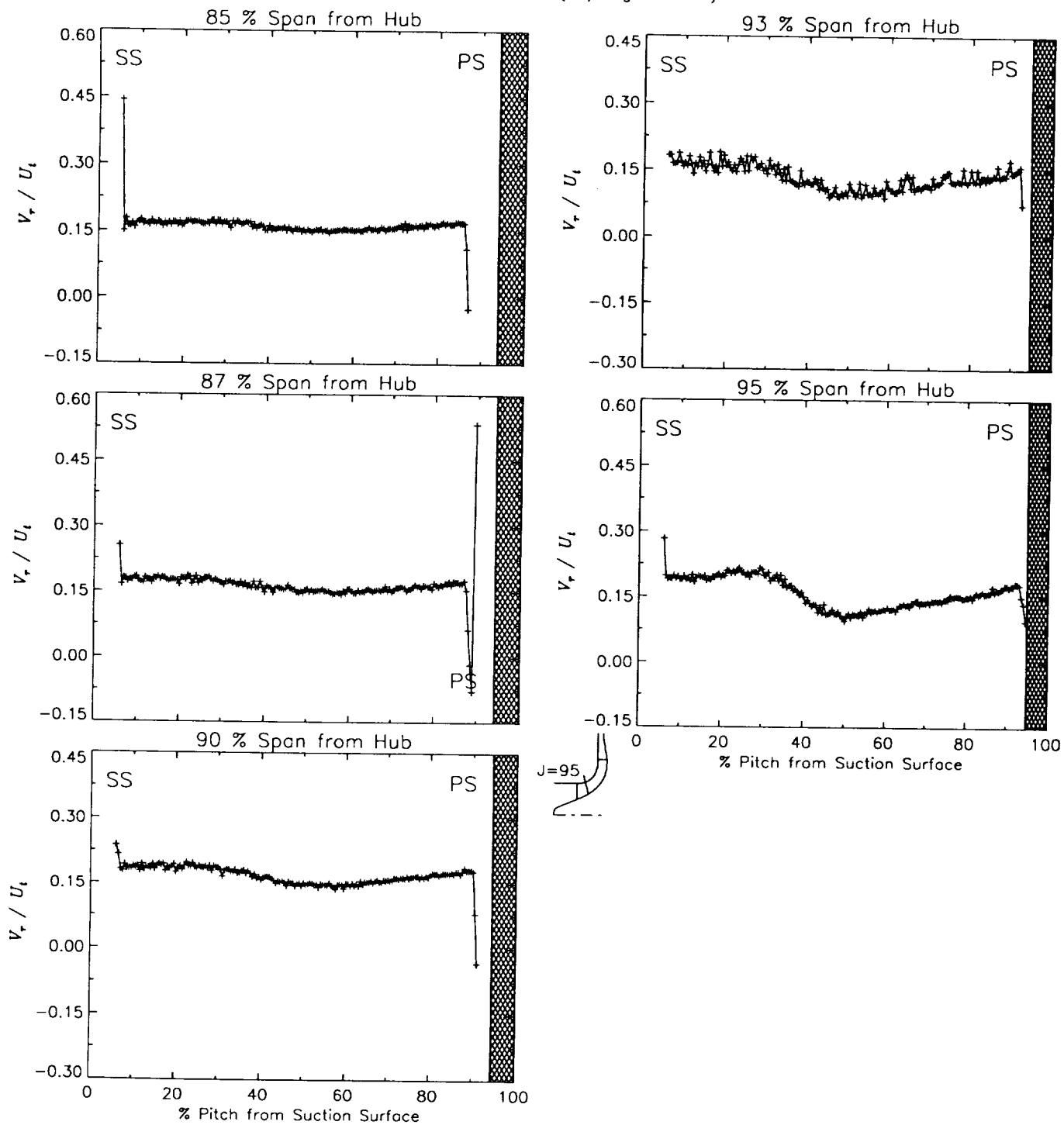
Station J=95, ( $m/m_s=0.248$ )



(a) Radial velocity normalized by impeller tip speed.

Figure 31.—Laser velocimeter results of axial, radial, and relative tangential velocities normalized by impeller tip speed for the design flow condition,  $m_d$ , at station J=95, ( $m/m_s=0.248$ ). The shaded region to the right of each plot represents the physical blade width.

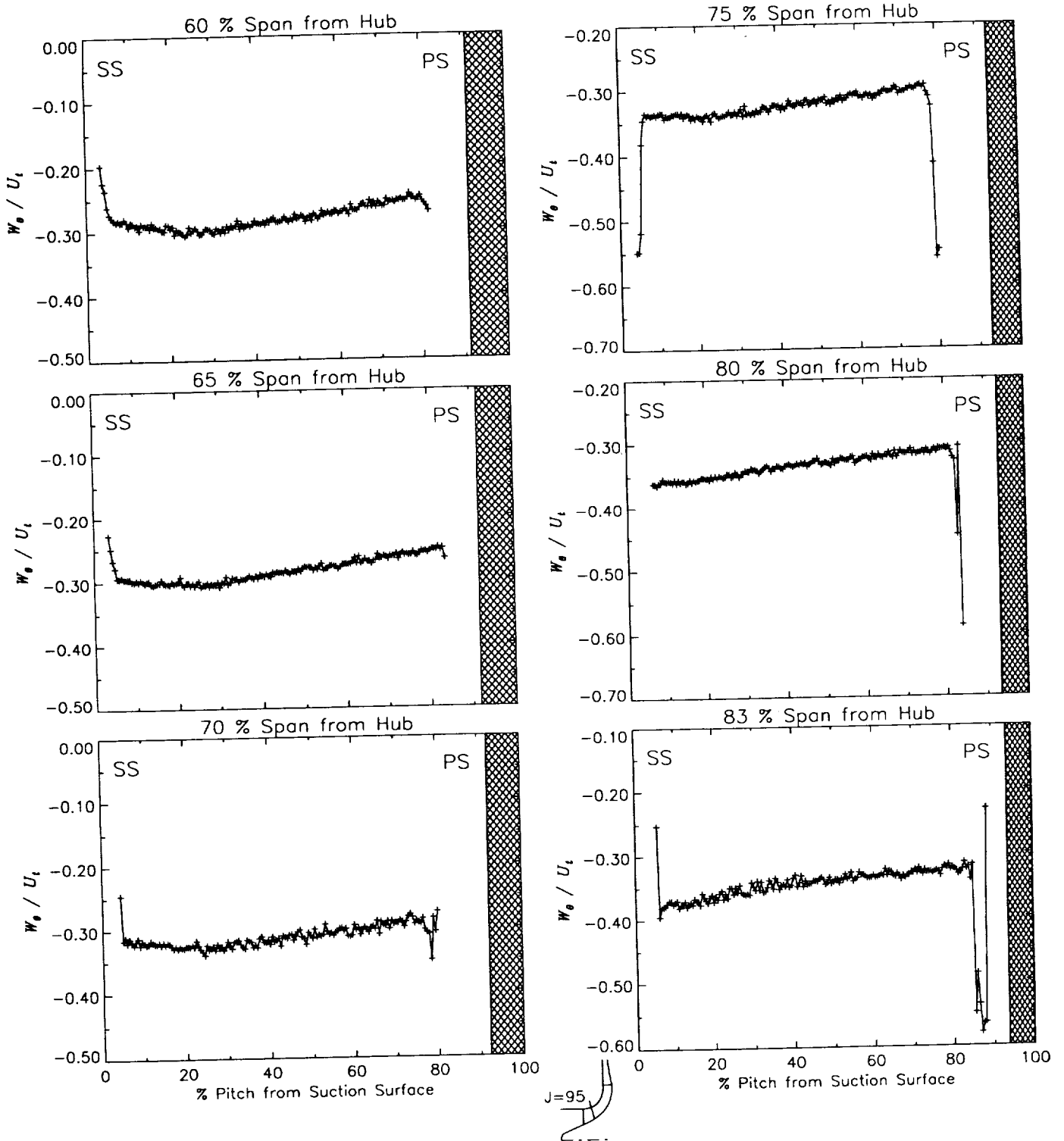
Station  $J=95$ , ( $m/m_s=0.248$ )



(a) Radial velocity normalized by impeller tip speed.

Figure 31.—Continued.

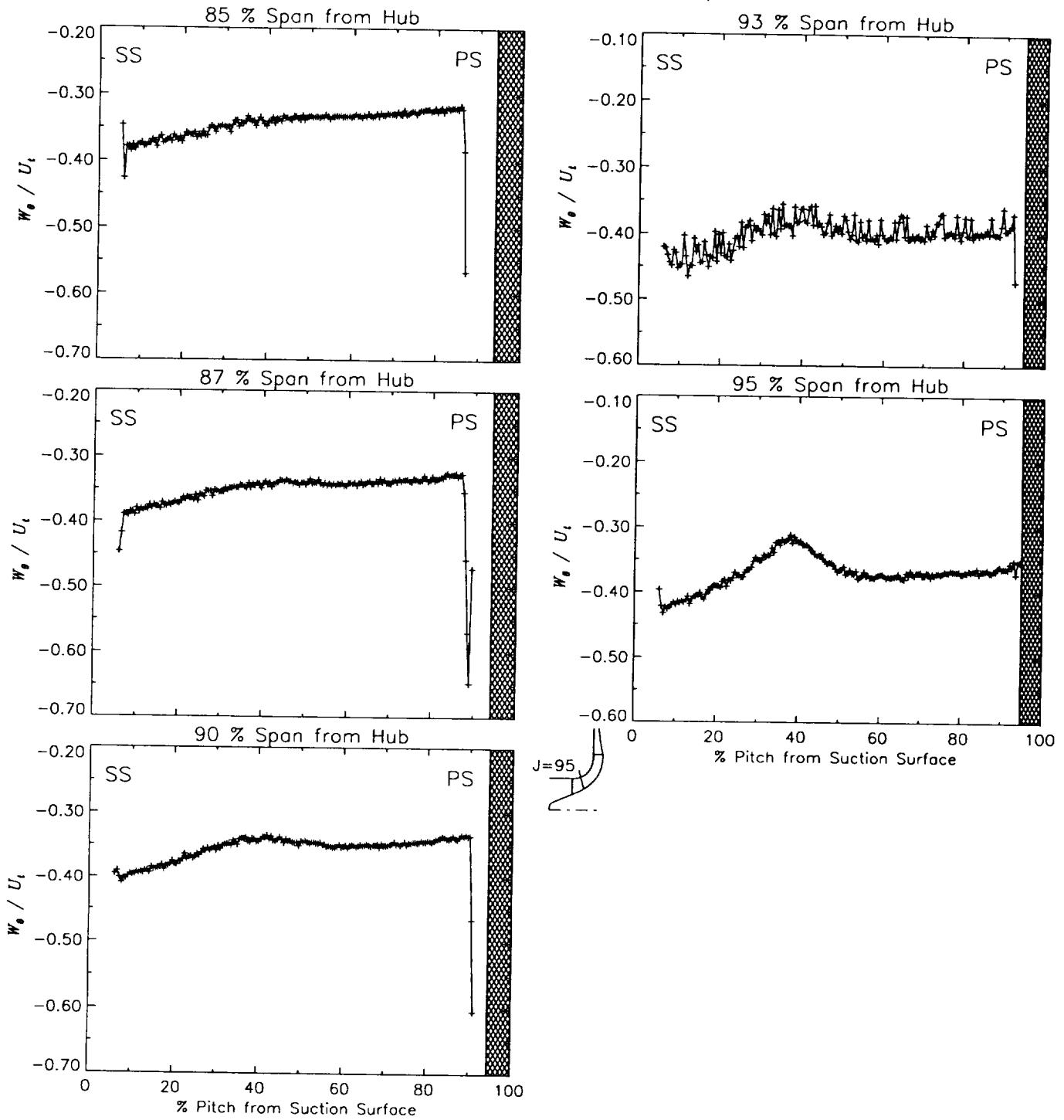
Station J=95, ( $m/m_s=0.248$ )



(b) Relative tangential velocity normalized by impeller tip speed.

Figure 31.-Continued.

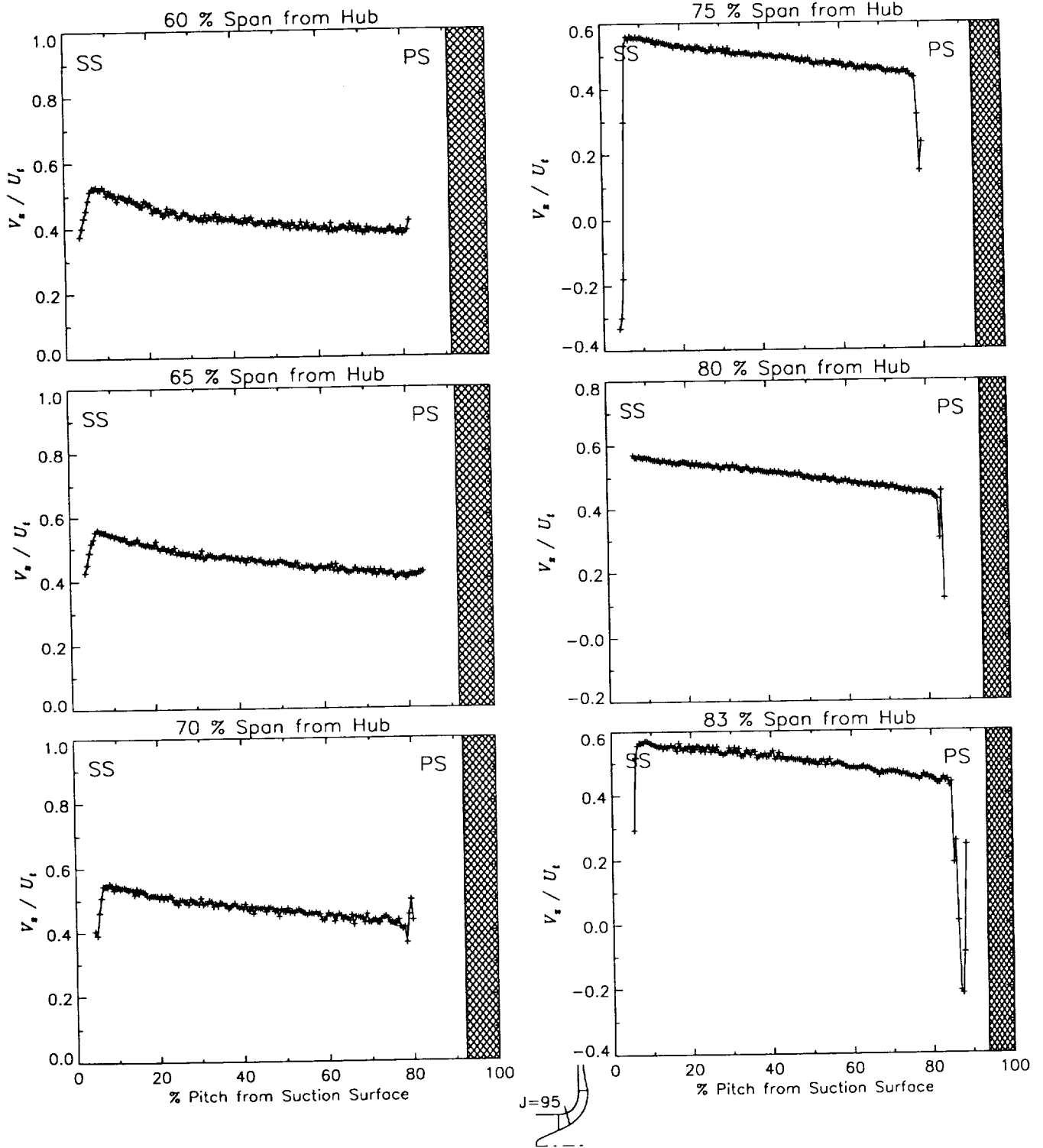
Station J=95, ( $m/m_s=0.248$ )



(b) Relative tangential velocity normalized by impeller tip speed.

Figure 31.-Continued.

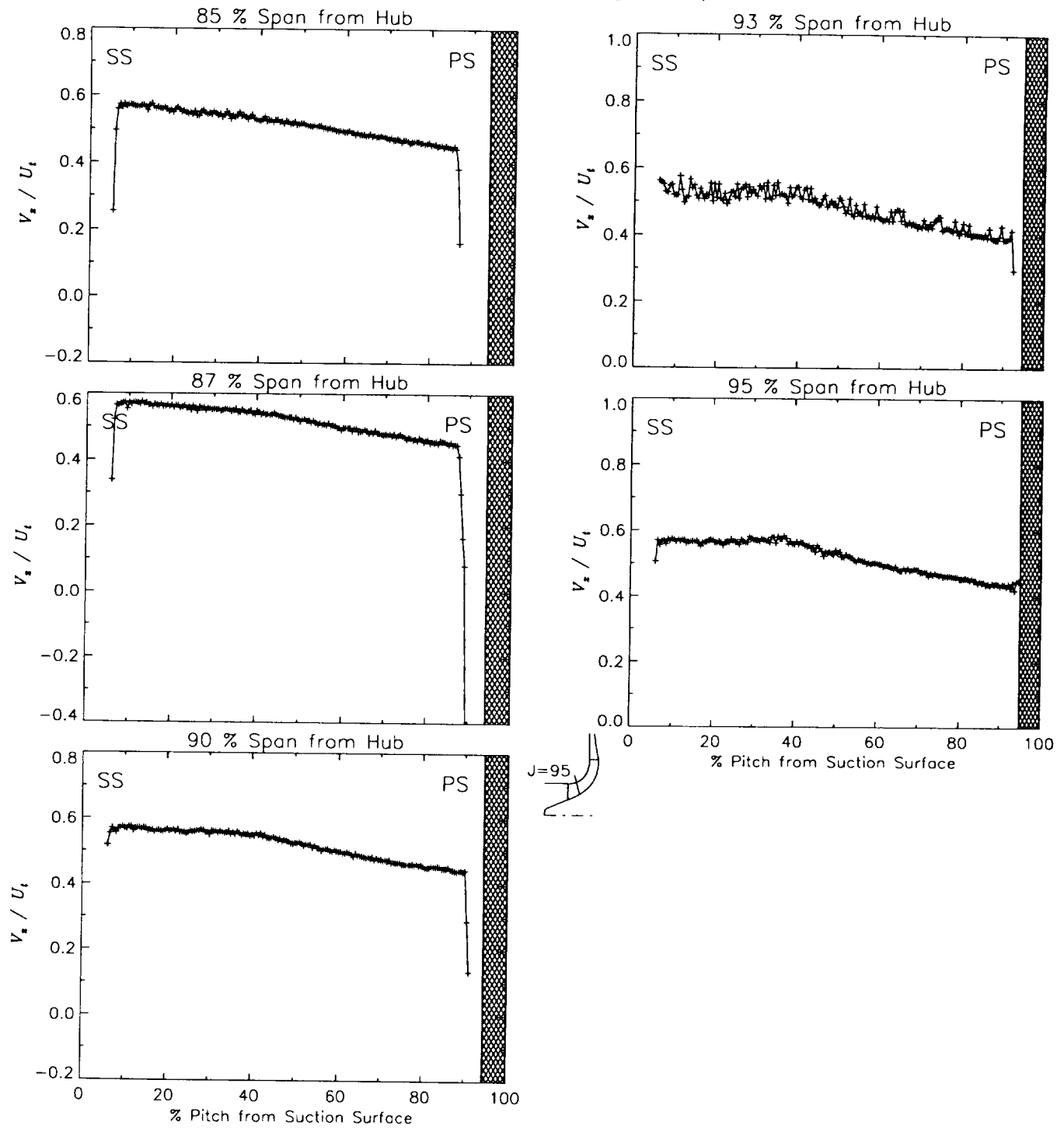
Station J=95, ( $m/m_s=0.248$ )



(c) Axial velocity normalized by impeller tip speed.

Figure 31.-Continued.

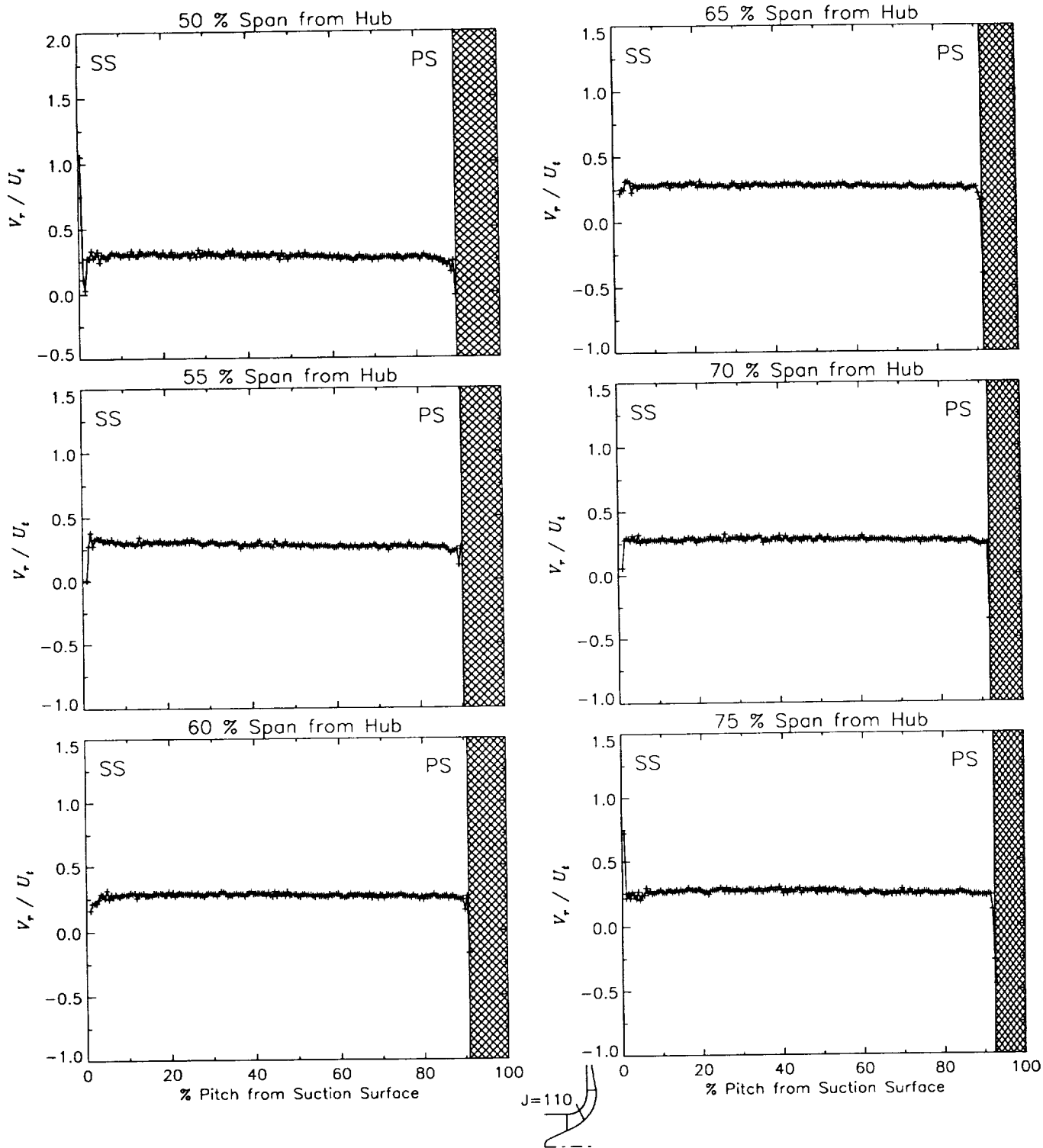
Station J=95, ( $m/m_s=0.248$ )



(c) Axial velocity normalized by impeller tip speed.

Figure 31.—Concluded.

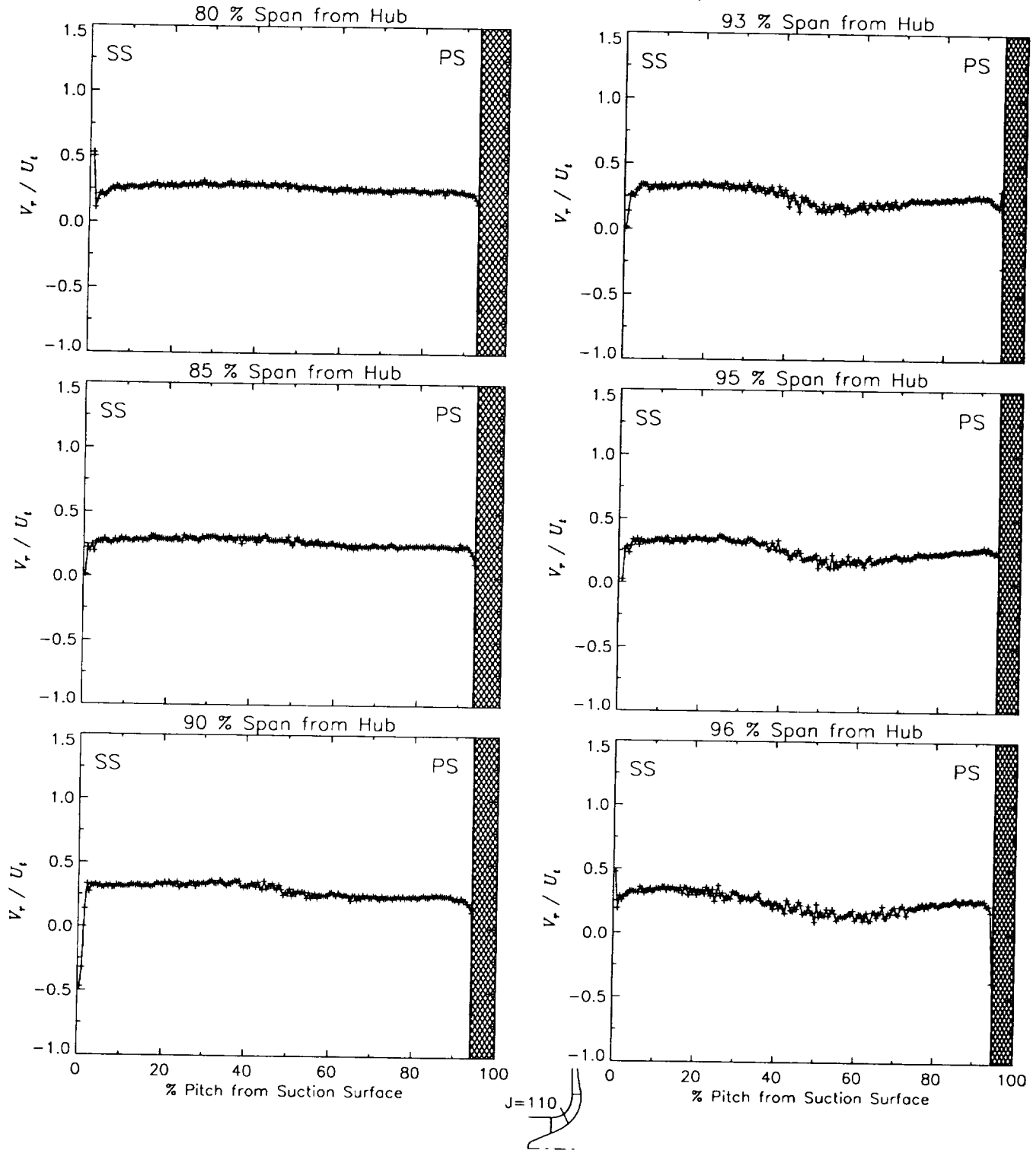
Station J=110, ( $m/m_s=0.396$ )



(a) Radial velocity normalized by impeller tip speed.

Figure 32.—Laser velocimeter results of axial, radial, and relative tangential velocities normalized by impeller tip speed for the design flow condition,  $\dot{m}_d$ , at station J=110, ( $m/m_s=0.396$ ). The shaded region to the right of each plot represents the physical blade width.

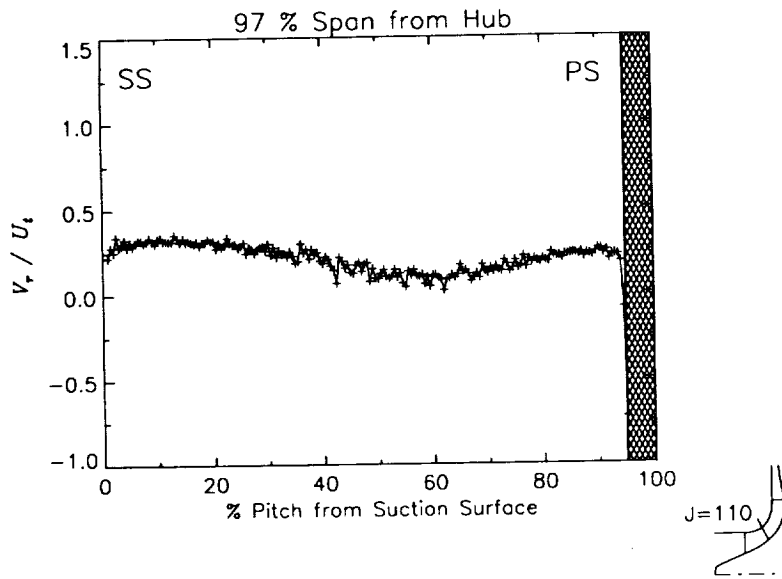
Station J=110, ( $m/m_s=0.396$ )



(a) Radial velocity normalized by impeller tip speed.

Figure 32.-Continued.

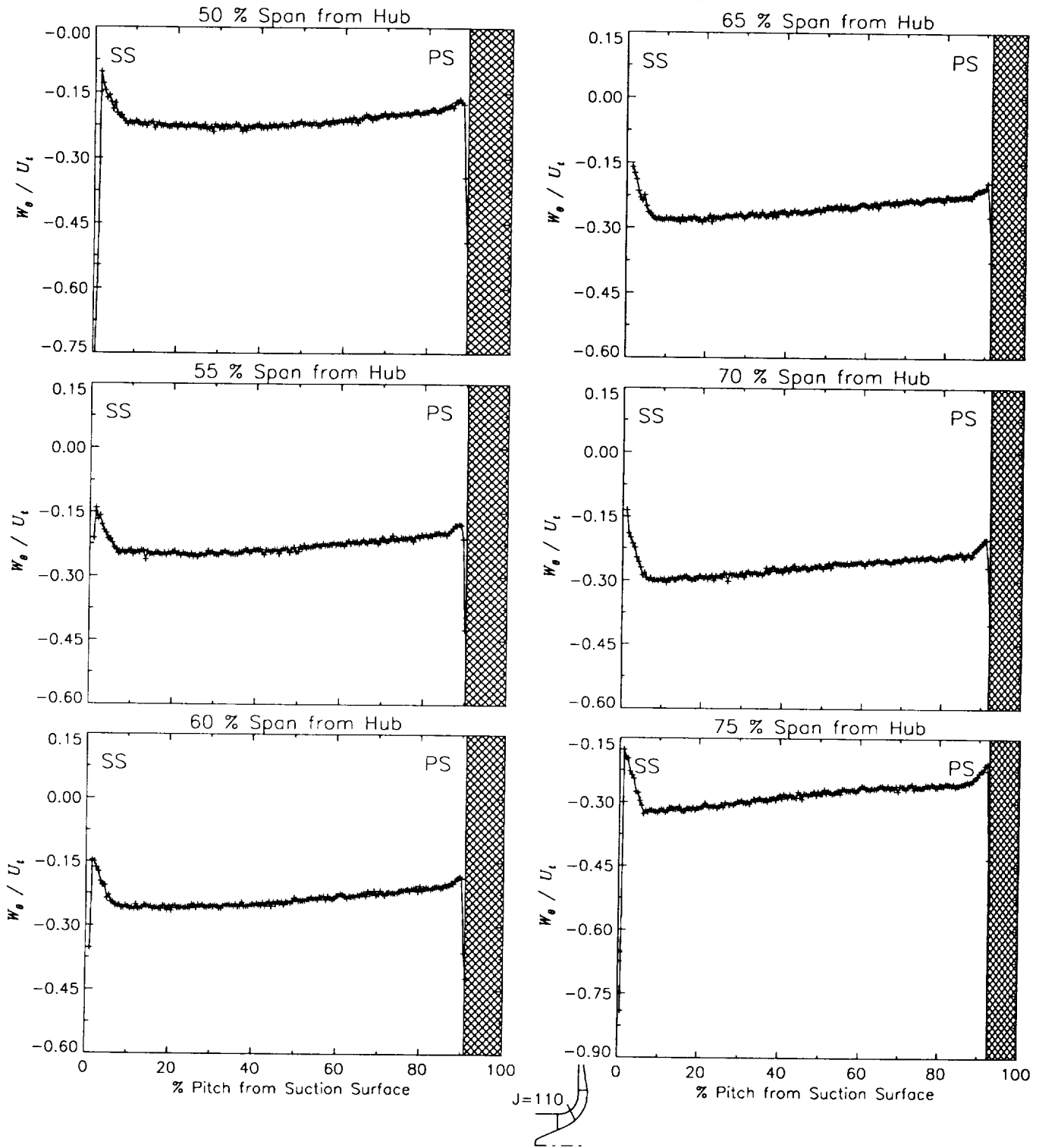
Station J=110, ( $m/m_s=0.396$ )



(a) Radial velocity normalized by impeller tip speed.

Figure 32.-Continued.

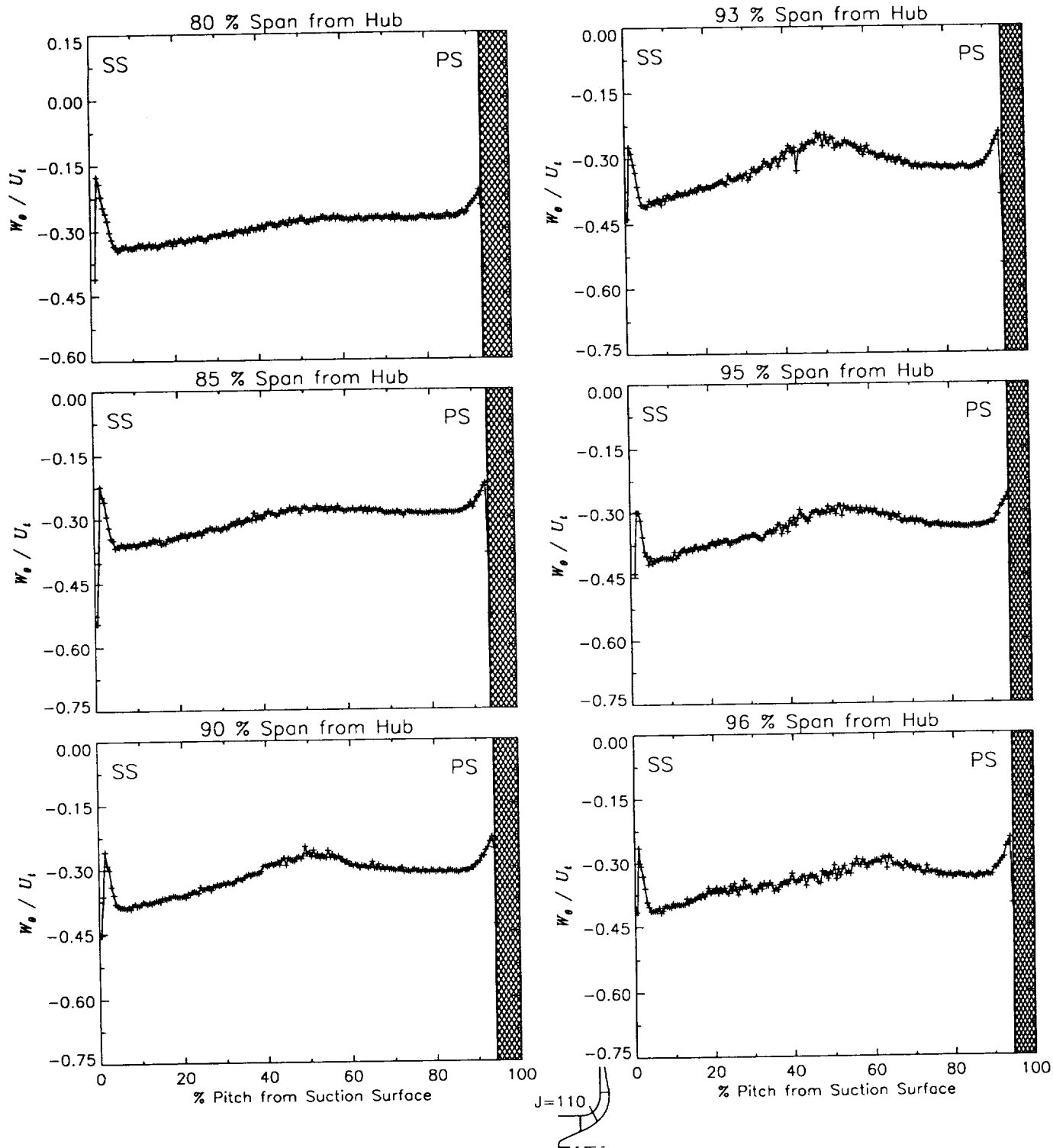
Station J=110, ( $m/m_s=0.396$ )



(b) Relative tangential velocity normalized by impeller tip speed.

Figure 32.—Continued.

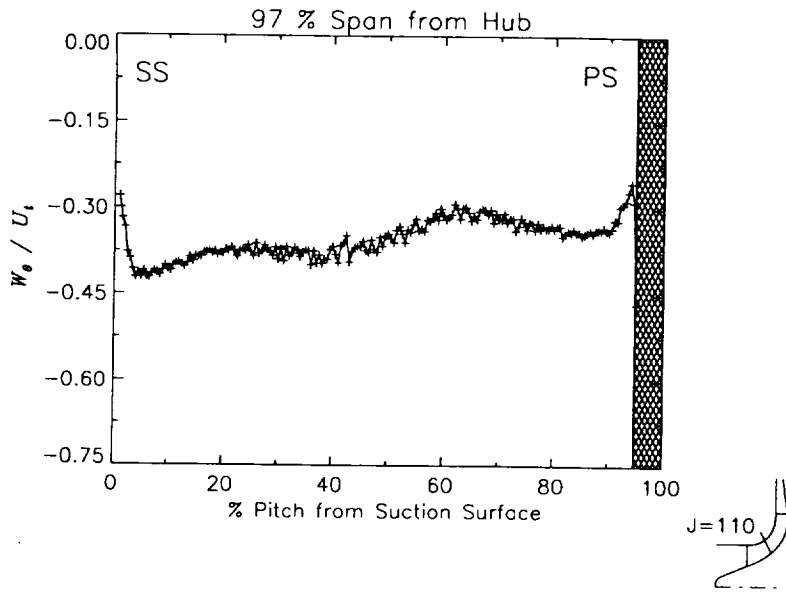
Station J=110, ( $m/m_s=0.396$ )



(b) Relative tangential velocity normalized by impeller tip speed.

Figure 32.—Continued.

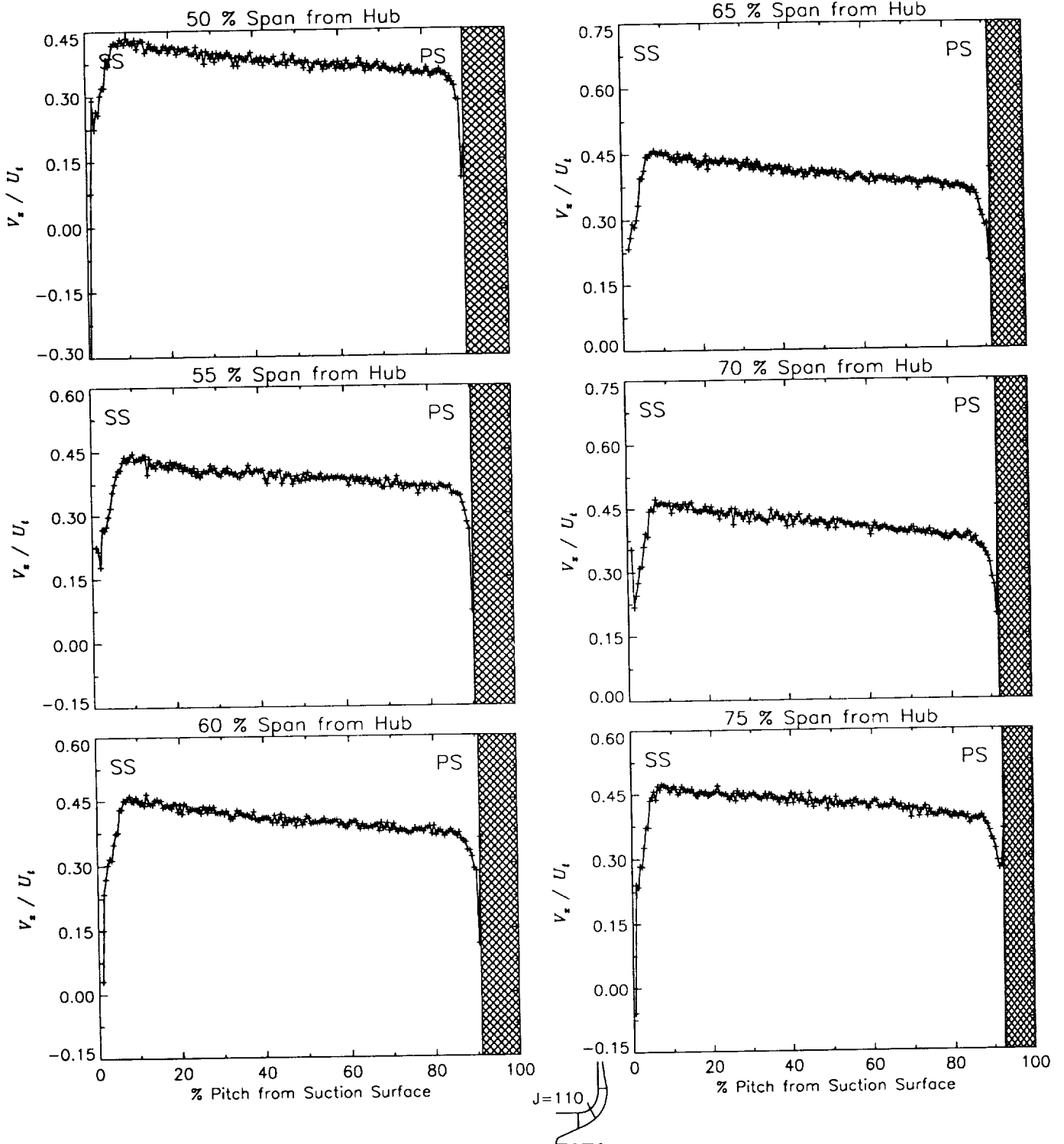
Station J=110, ( $m/m_s=0.396$ )



(b) Relative tangential velocity normalized by impeller tip speed.

Figure 32.-Continued.

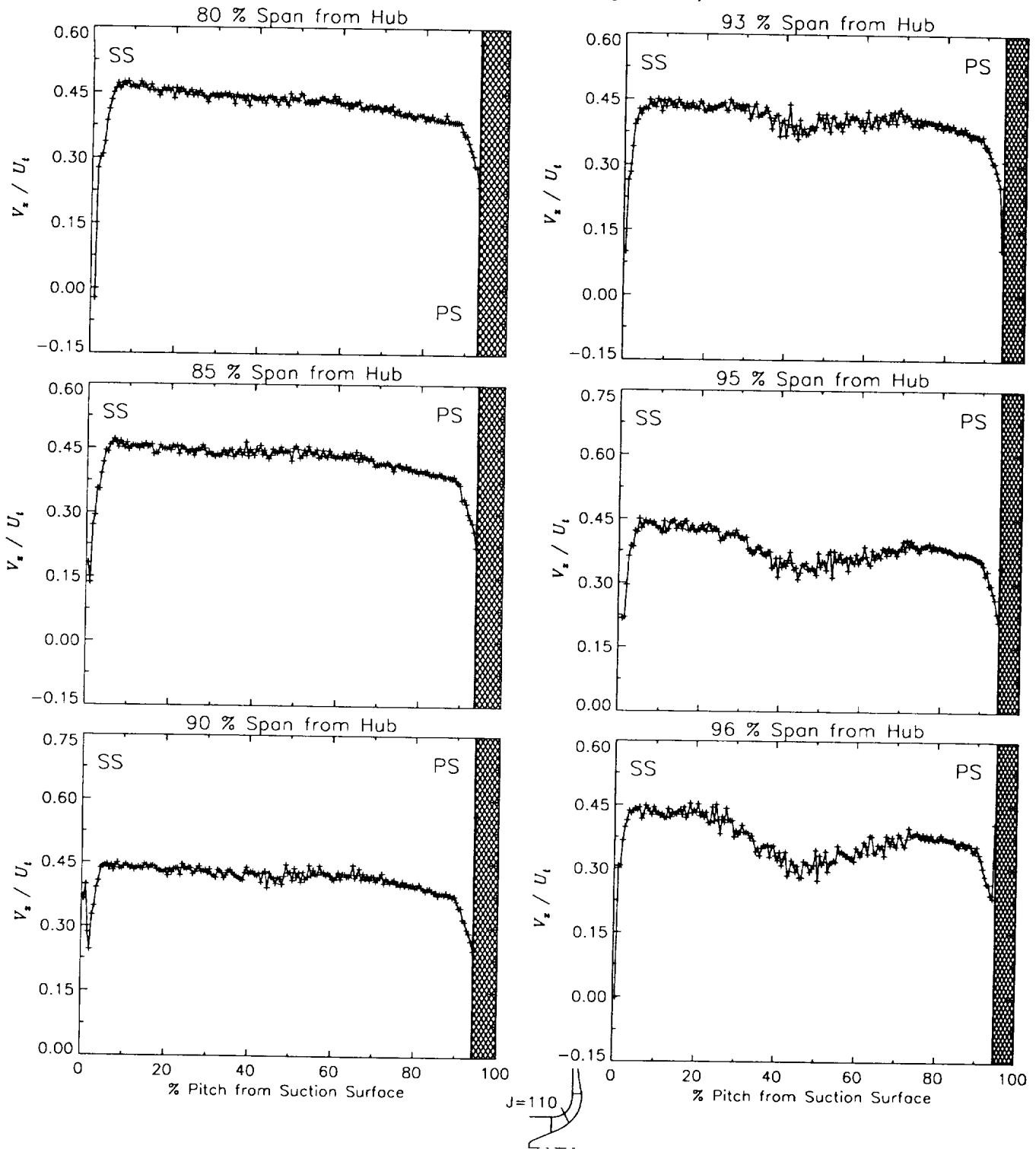
Station J=110, ( $m/m_s=0.396$ )



(c) Axial velocity normalized by impeller tip speed.

Figure 32.-Continued.

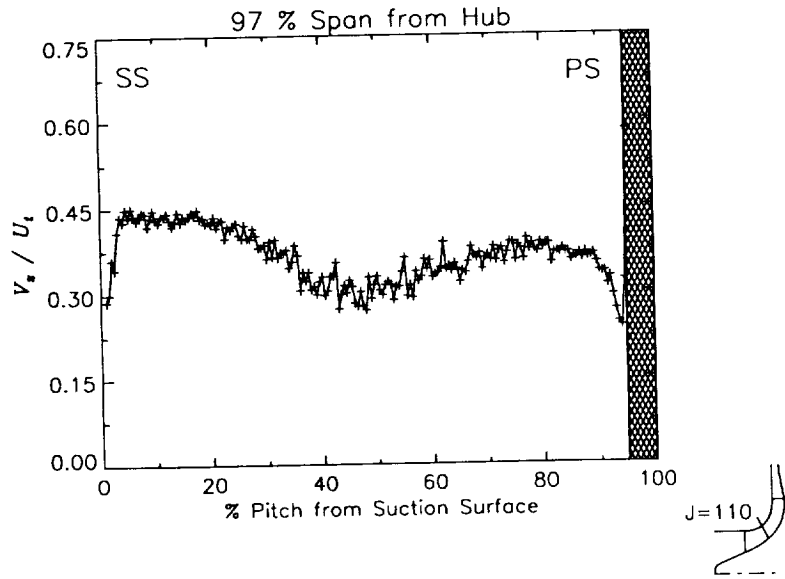
Station J=110, ( $m/m_s=0.396$ )



(c) Axial velocity normalized by impeller tip speed.

Figure 32.-Continued.

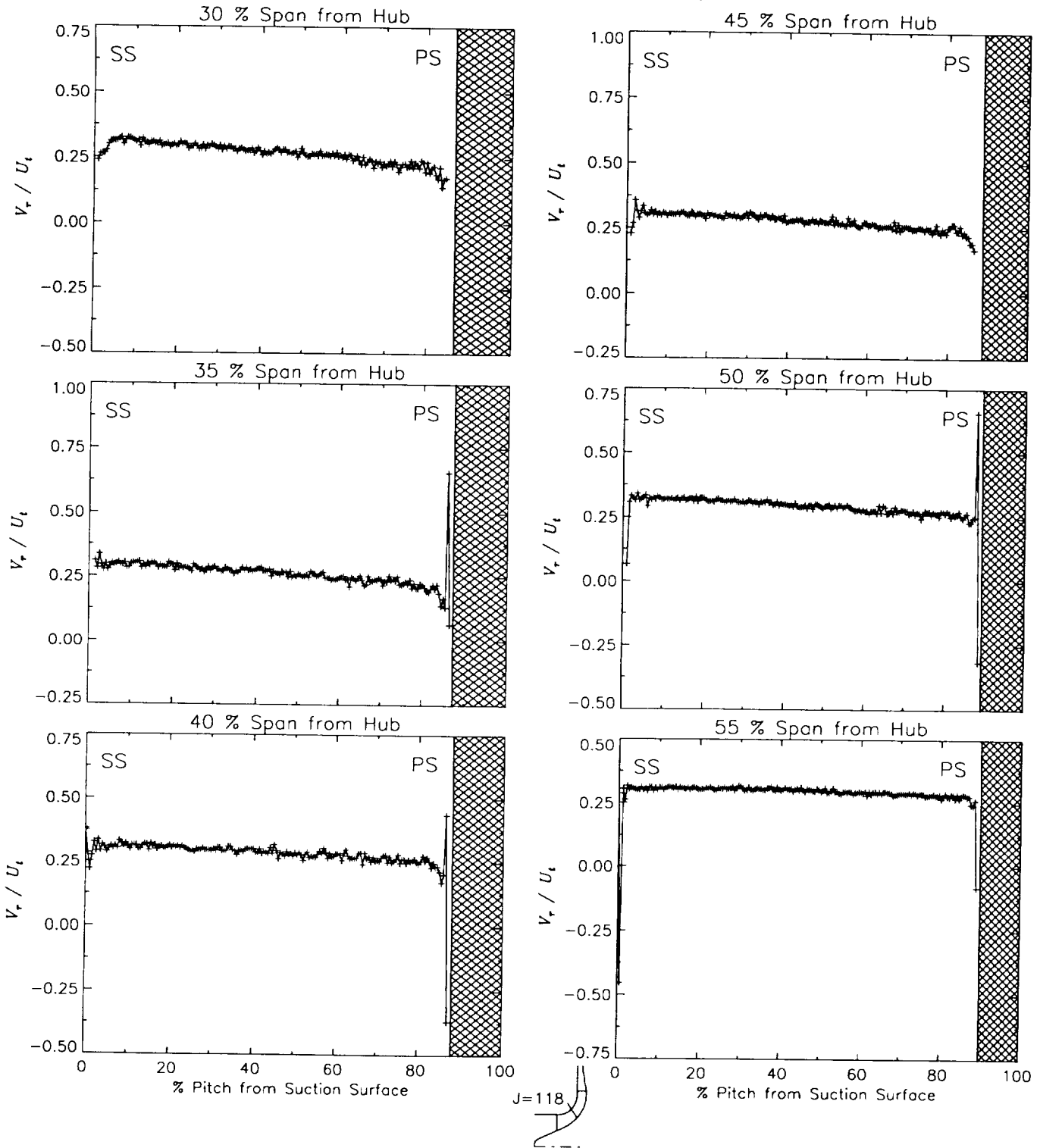
Station J=110, ( $m/m_s=0.396$ )



(c) Axial velocity normalized by impeller tip speed.

Figure 32.—Concluded.

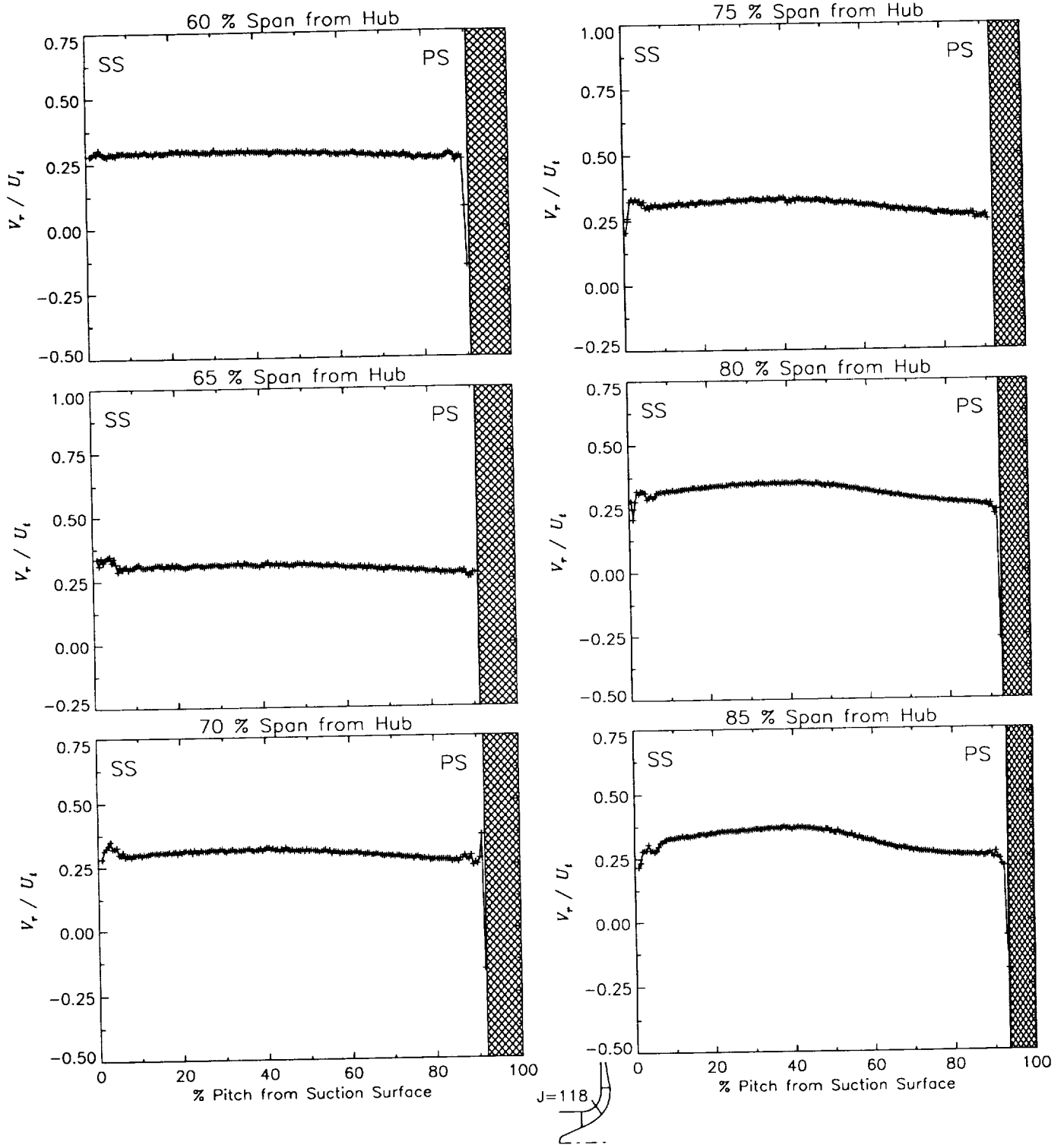
Station J=118, ( $m/m_s=0.475$ )



(a) Radial velocity normalized by impeller tip speed.

Figure 33.-Laser velocimeter results of axial, radial, and relative tangential velocities normalized by impeller tip speed for the design flow condition,  $\dot{m}_d$ , at station J=118, ( $m/m_s=0.475$ ). The shaded region to the right of each plot represents the physical blade width.

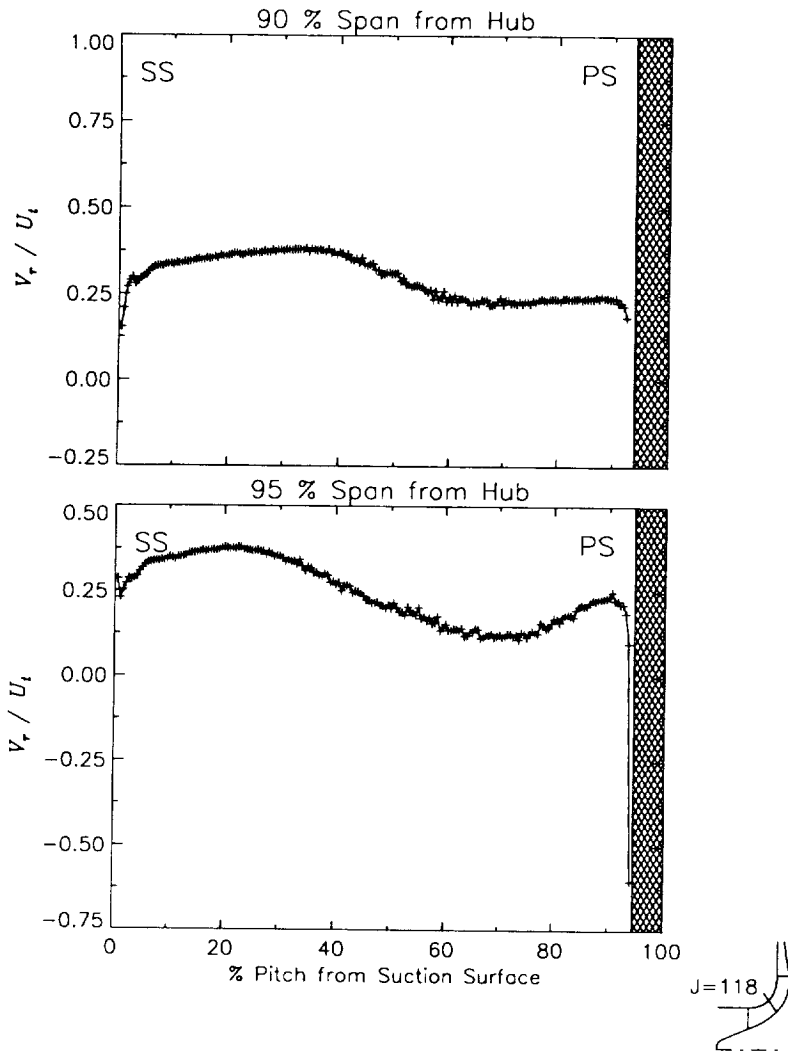
Station J=118, ( $m/m_s=0.475$ )



(a) Radial velocity normalized by impeller tip speed.

Figure 33.-Continued.

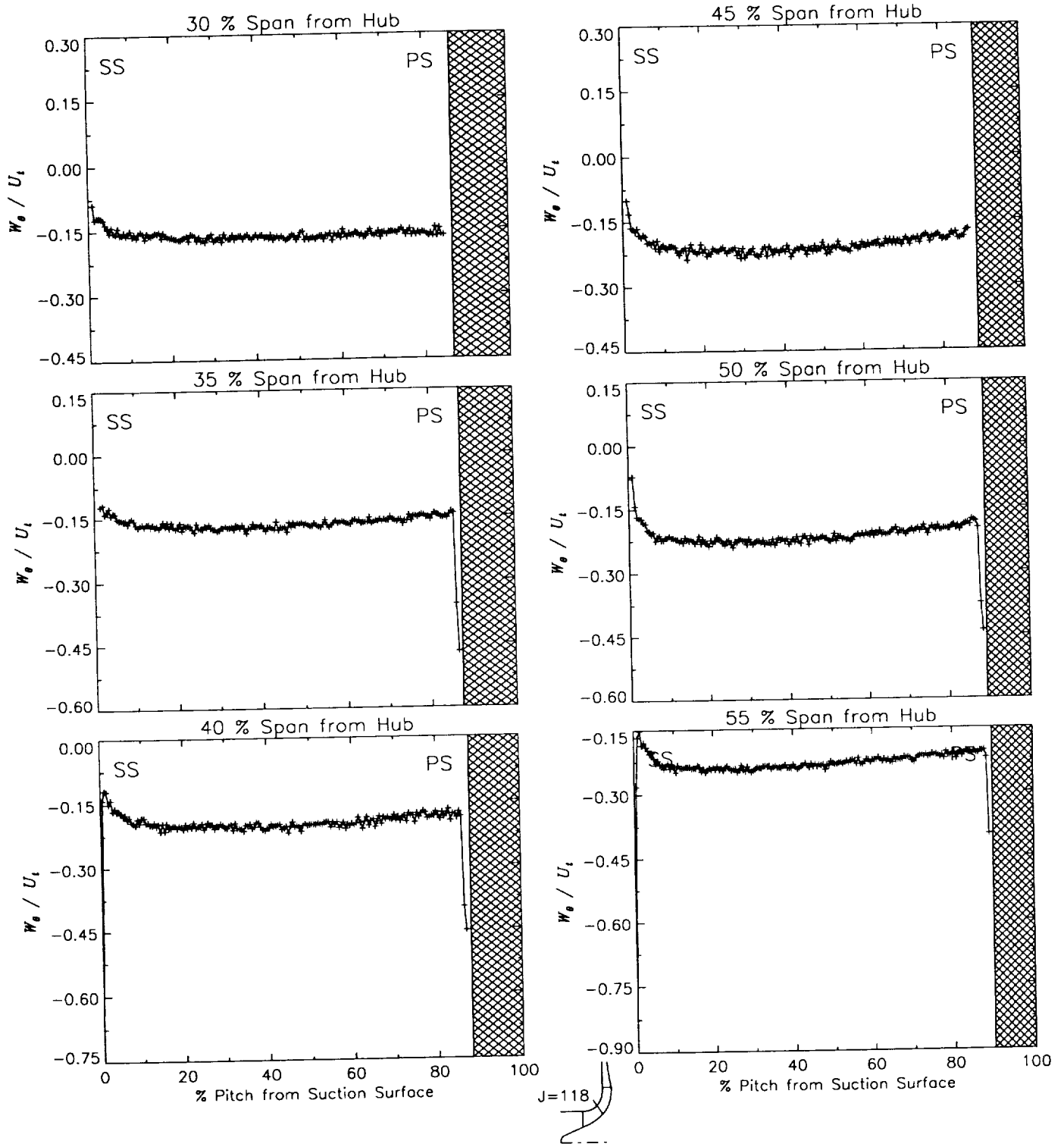
Station J=118, ( $m/m_s=0.475$ )



(a) Radial velocity normalized by impeller tip speed.

Figure 33.—Continued.

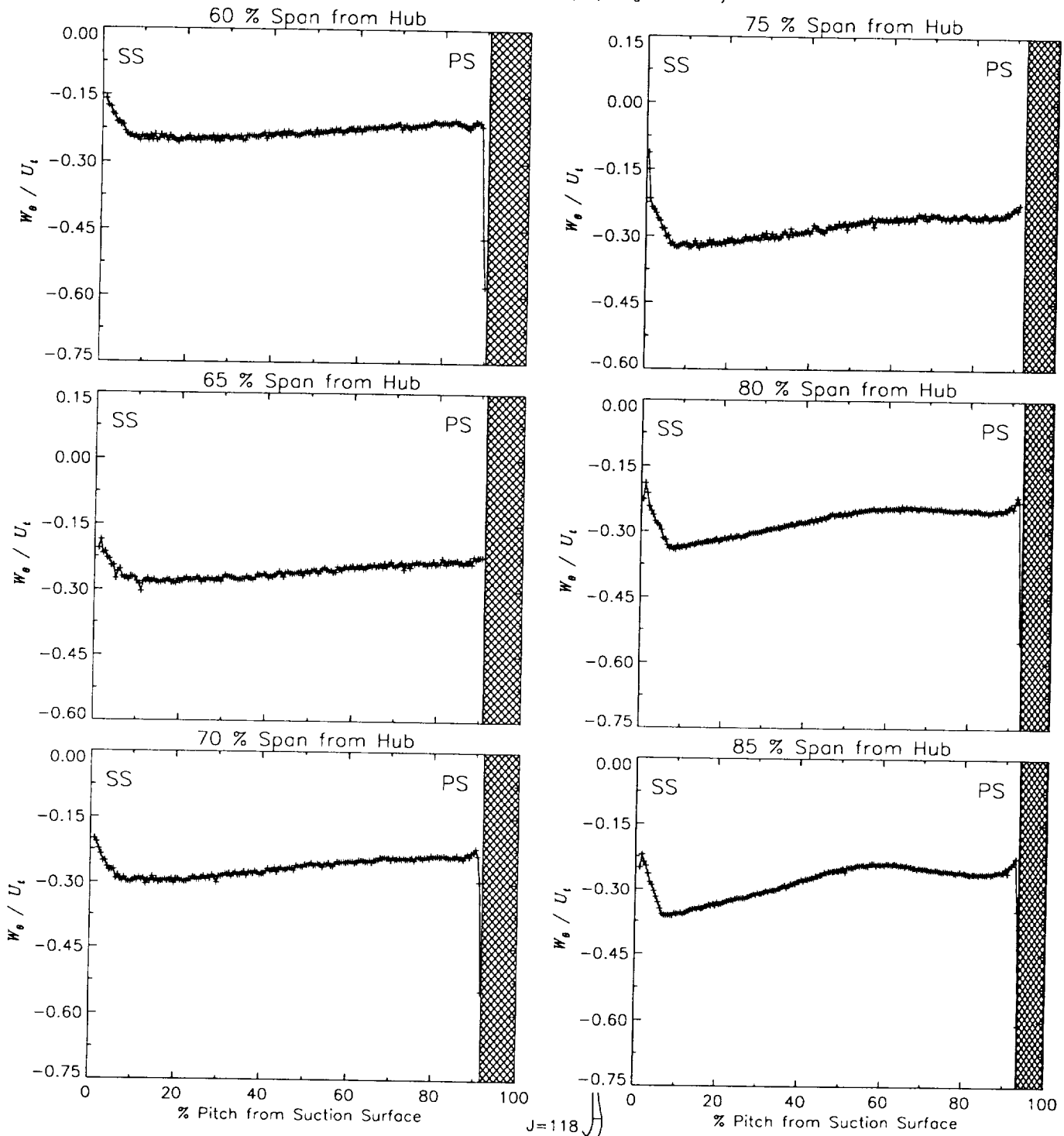
Station J=118, ( $m/m_s=0.475$ )



(b) Relative tangential velocity normalized by impeller tip speed.

Figure 33.-Continued.

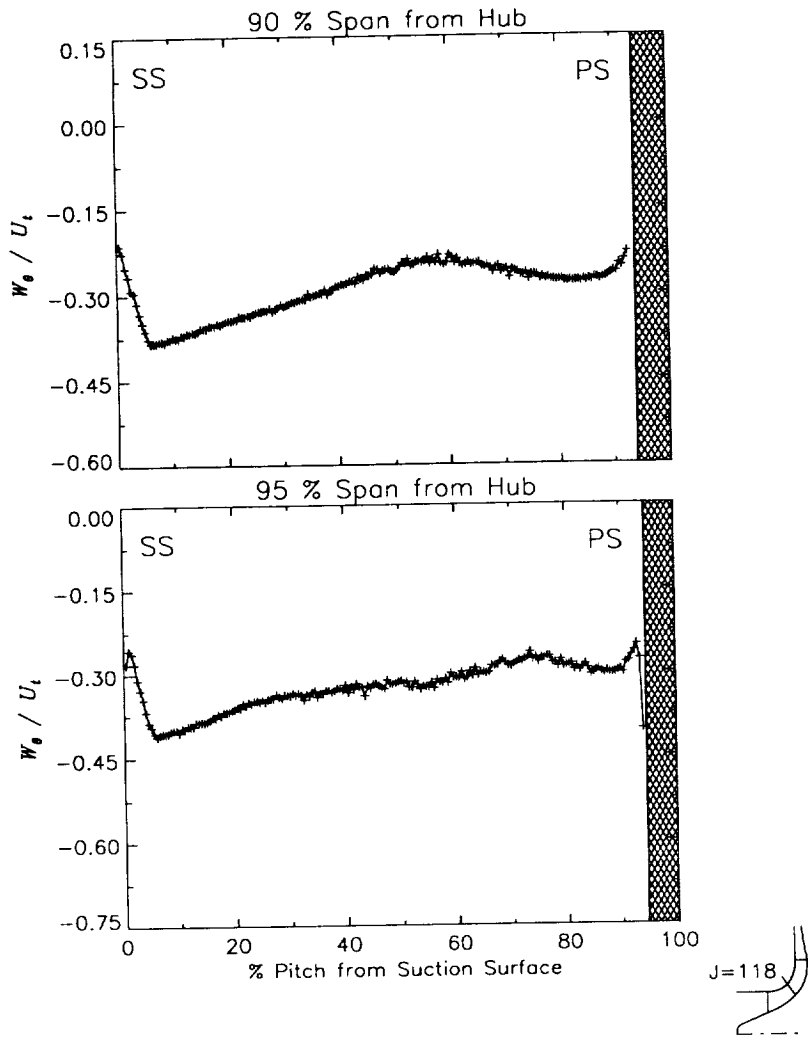
Station J=118, ( $m/m_s=0.475$ )



(b) Relative tangential velocity normalized by impeller tip speed.

Figure 33.-Continued.

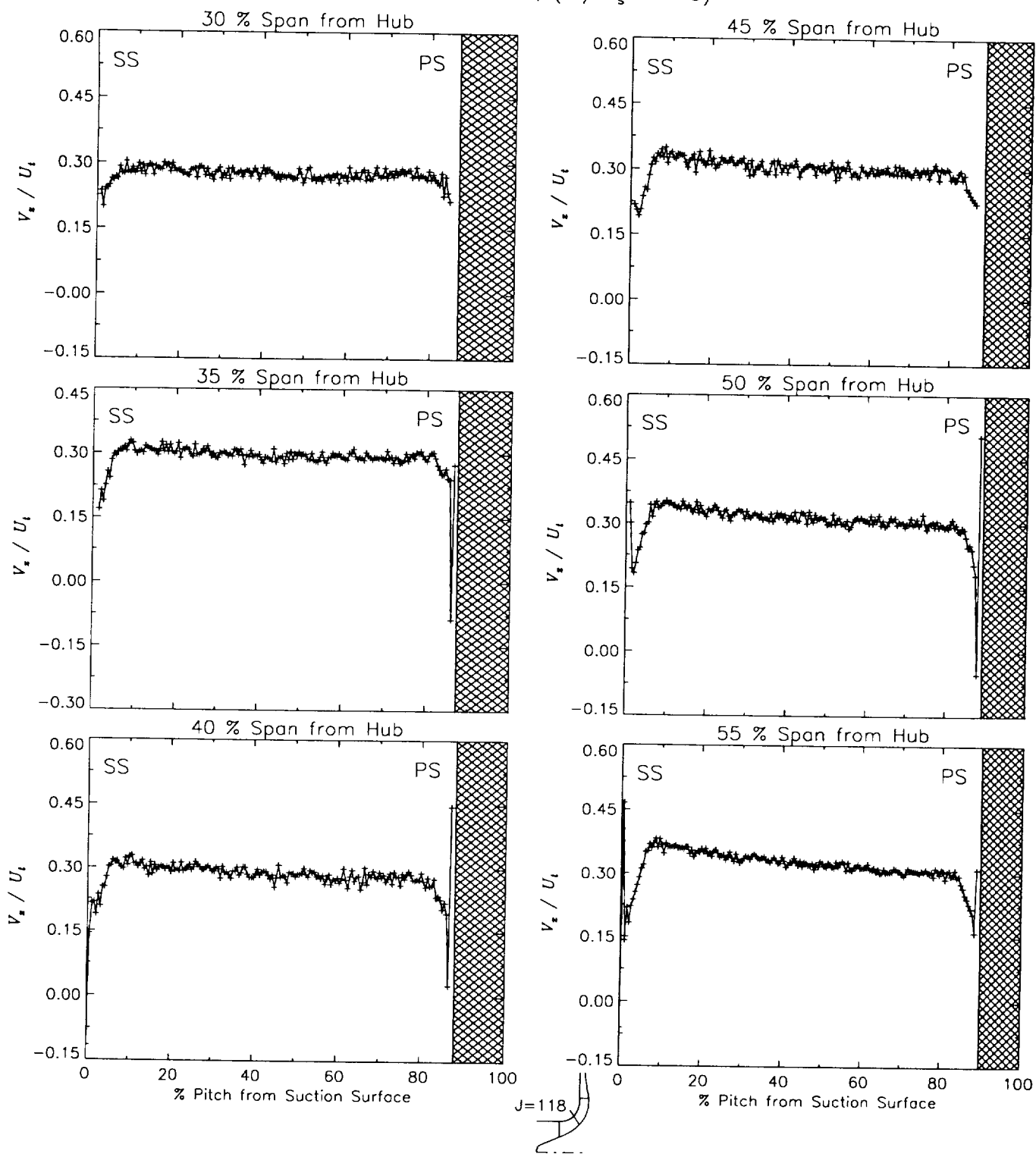
Station J=118, ( $m/m_s=0.475$ )



(b) Relative tangential velocity normalized by impeller tip speed.

Figure 33.-Continued.

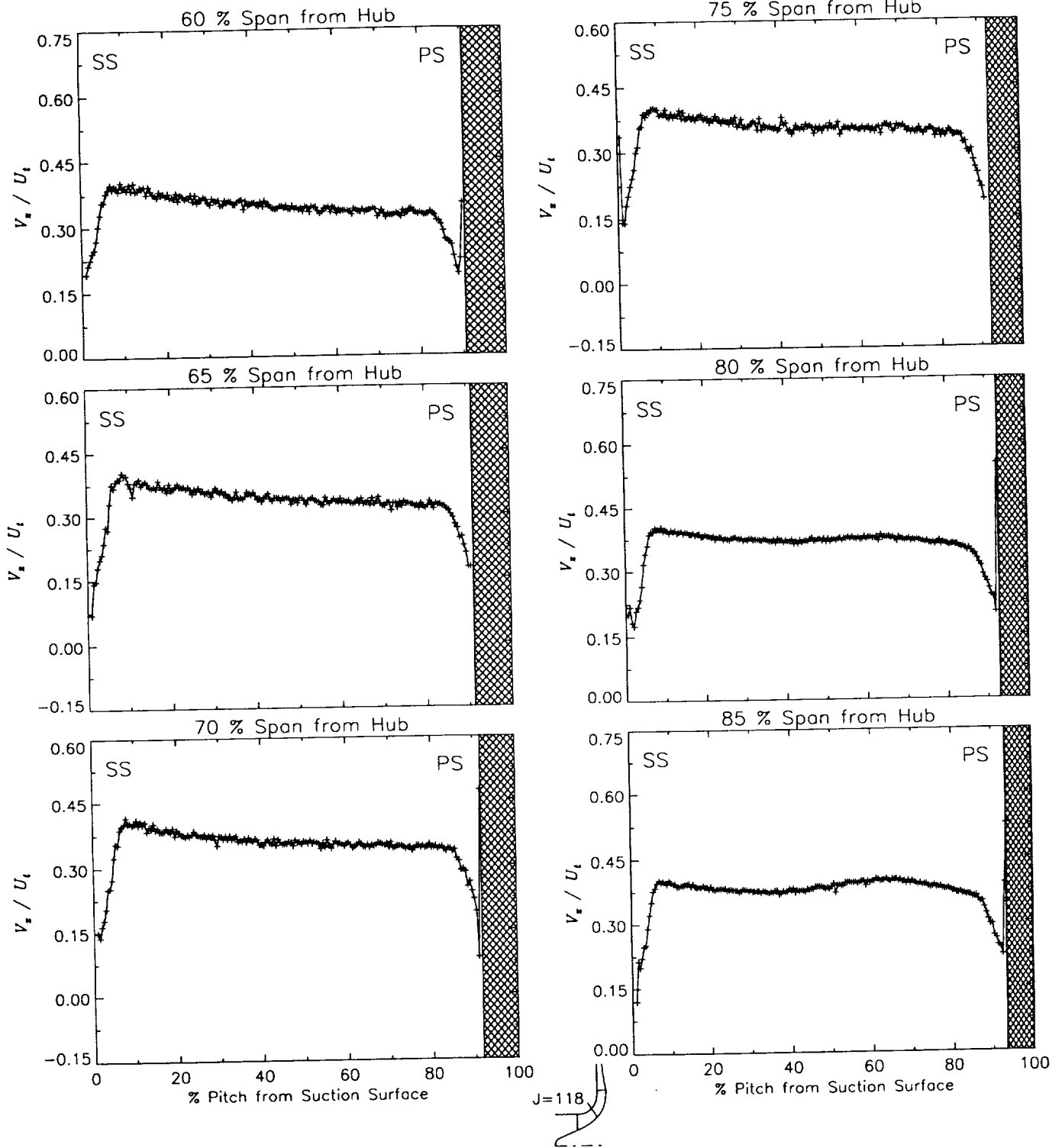
Station J=118, ( $m/m_s=0.475$ )



(c) Axial velocity normalized by impeller tip speed.

Figure 33.-Continued.

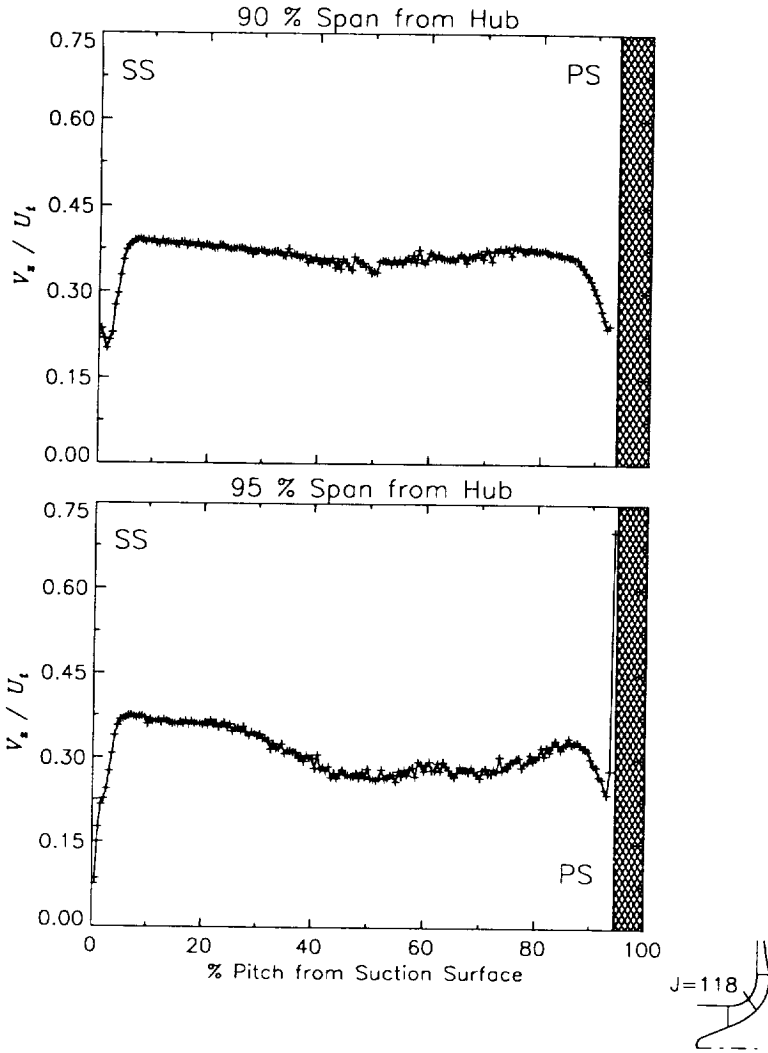
Station J=118, ( $m/m_s=0.475$ )



(c) Axial velocity normalized by impeller tip speed.

Figure 33.-Continued.

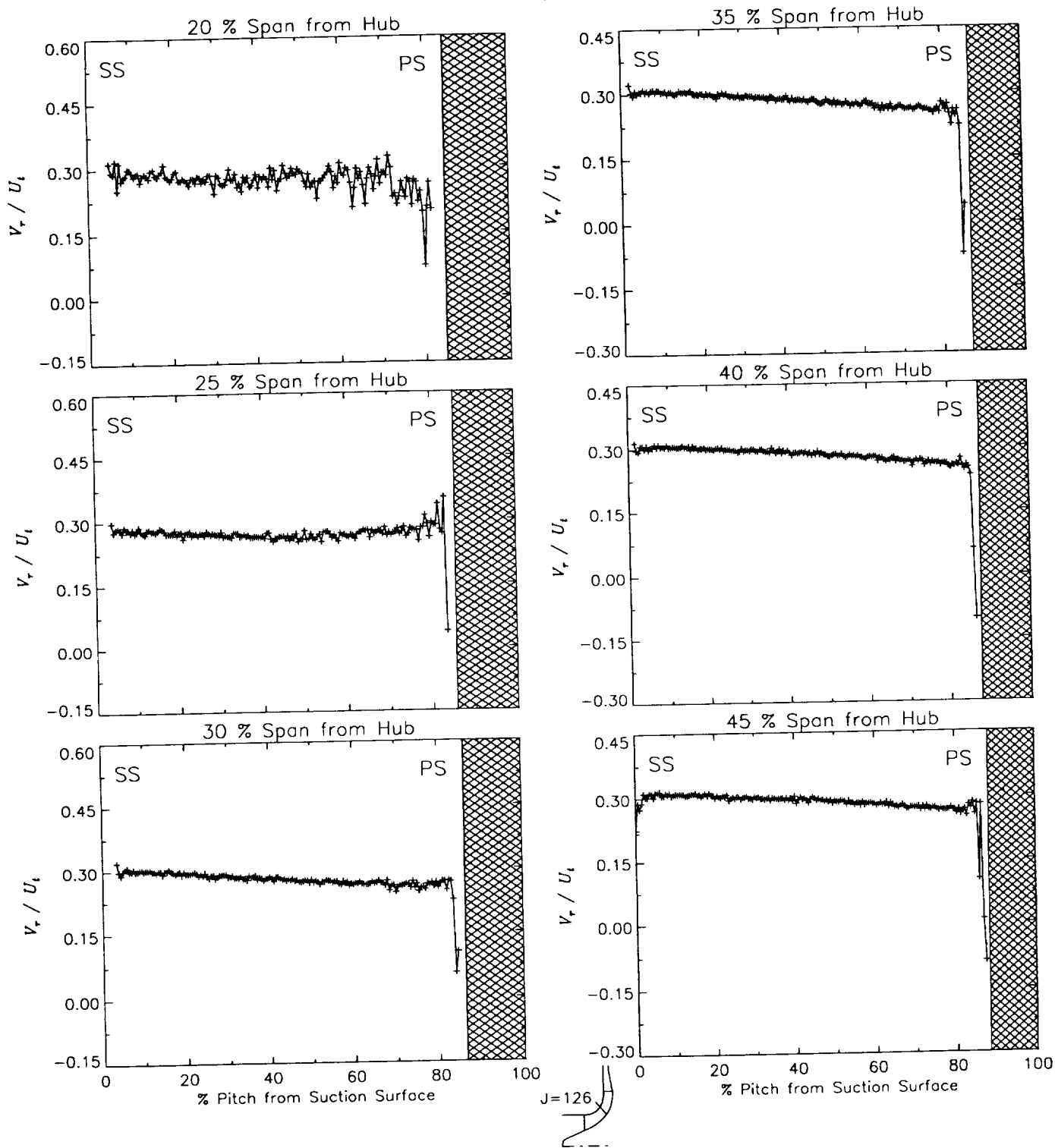
Station J=118, ( $m/m_s=0.475$ )



(c) Axial velocity normalized by impeller tip speed.

Figure 33.—Concluded.

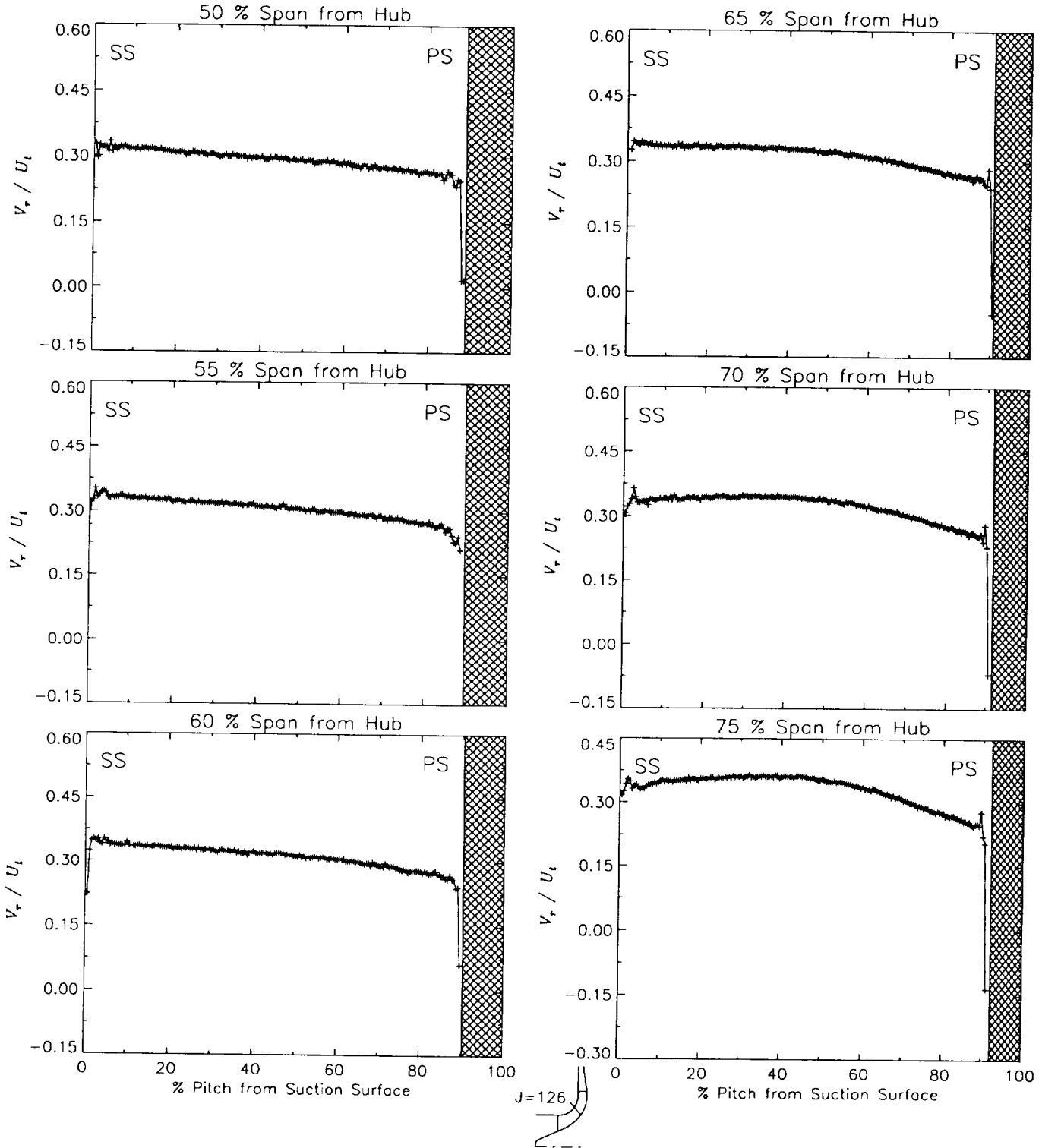
Station J=126, ( $m/m_s=0.555$ )



(a) Radial velocity normalized by impeller tip speed.

Figure 34.—Laser velocimeter results of axial, radial, and relative tangential velocities normalized by impeller tip speed for the design flow condition,  $\dot{m}_d$ , at station J=126, ( $m/m_s=0.555$ ). The shaded region to the right of each plot represents the physical blade width.

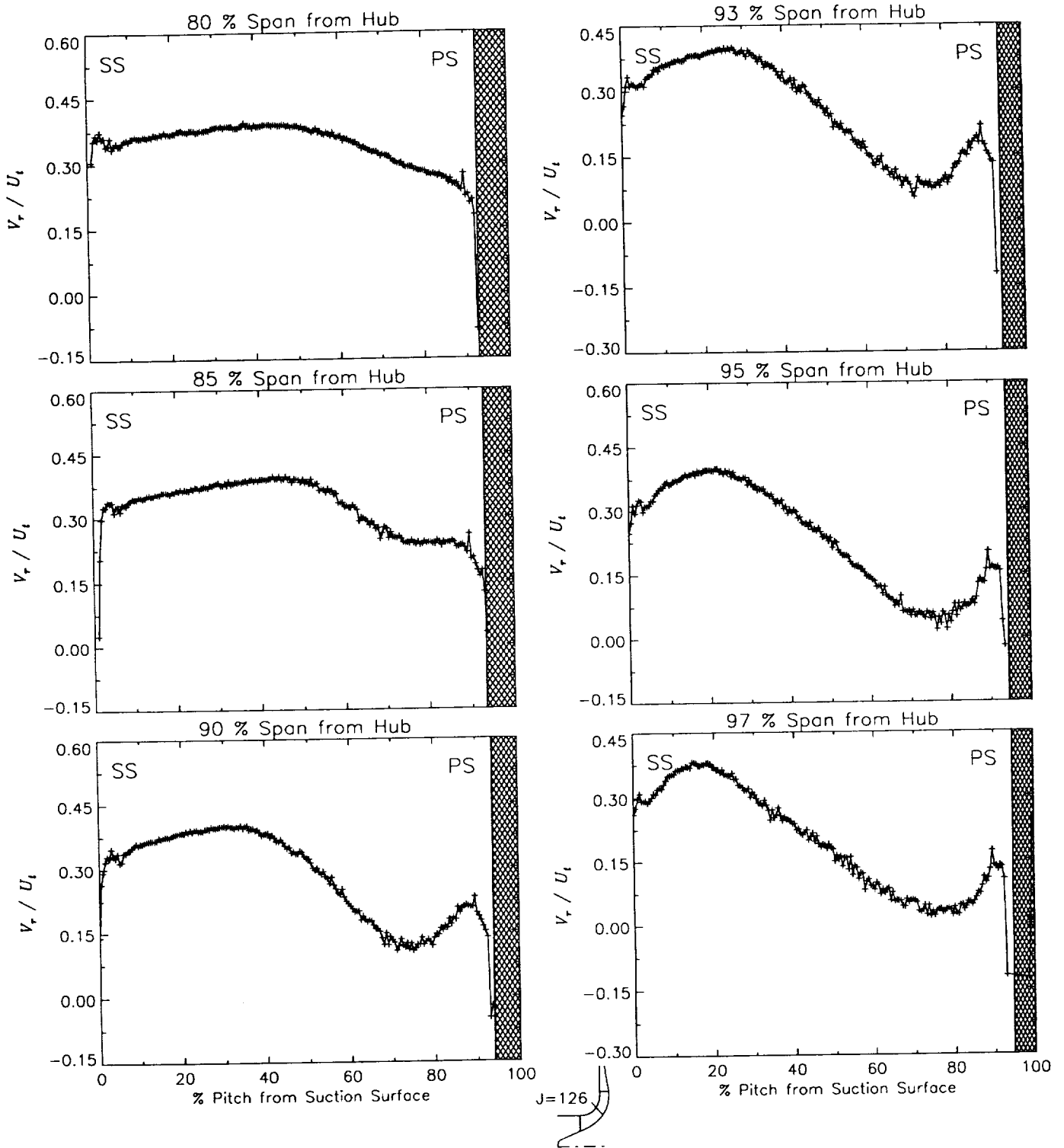
Station J=126, ( $m/m_s=0.555$ )



(a) Radial velocity normalized by impeller tip speed.

Figure 34.-Continued.

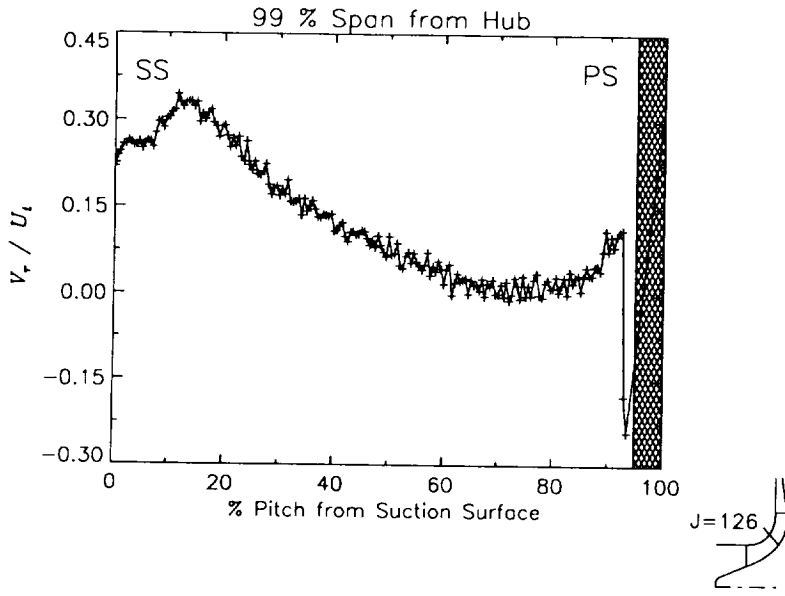
Station J=126, ( $m/m_s=0.555$ )



(a) Radial velocity normalized by impeller tip speed.

Figure 34.-Continued.

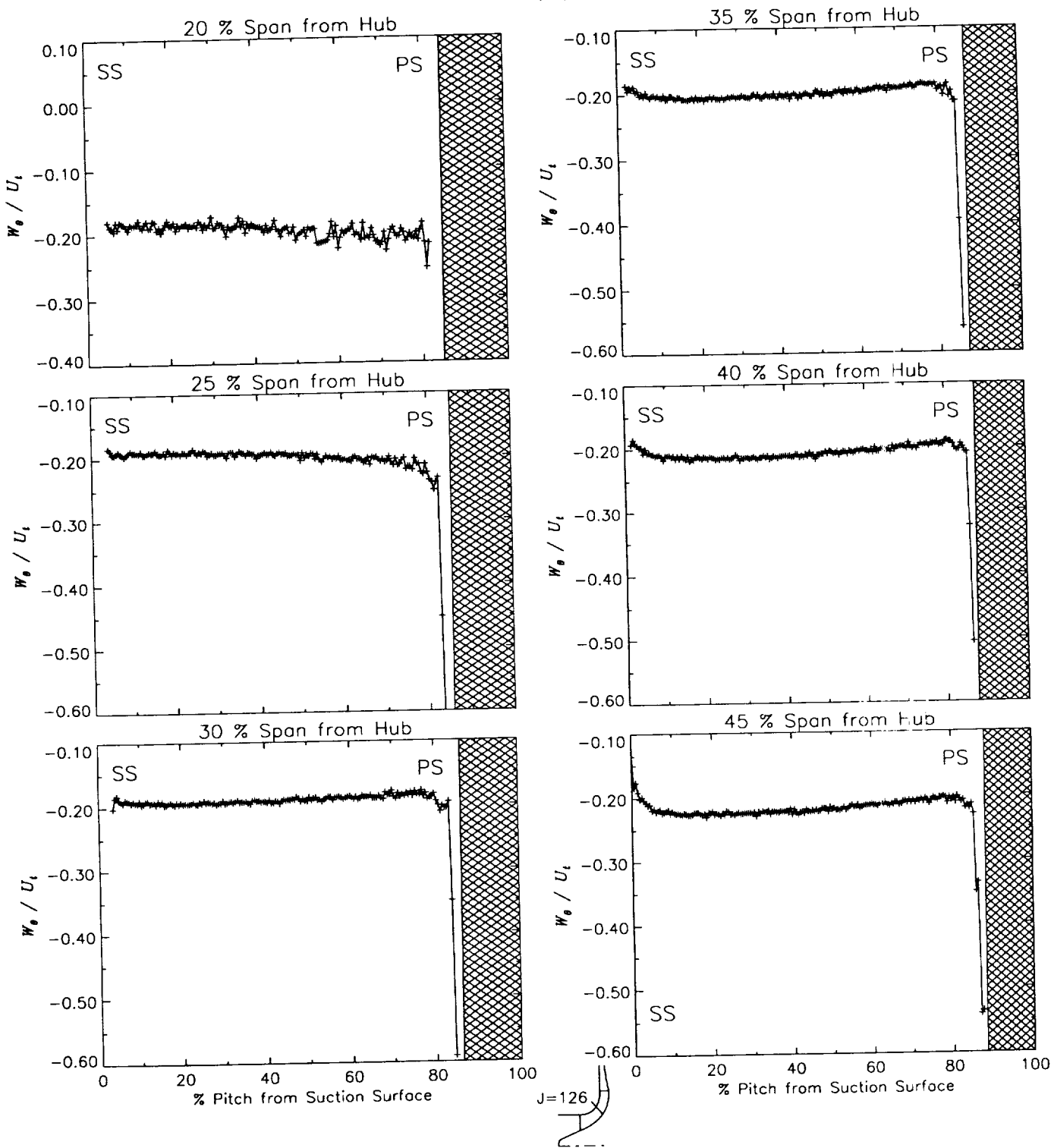
Station J=126, ( $m/m_s=0.555$ )



(a) Radial velocity normalized by impeller tip speed.

Figure 34.—Continued.

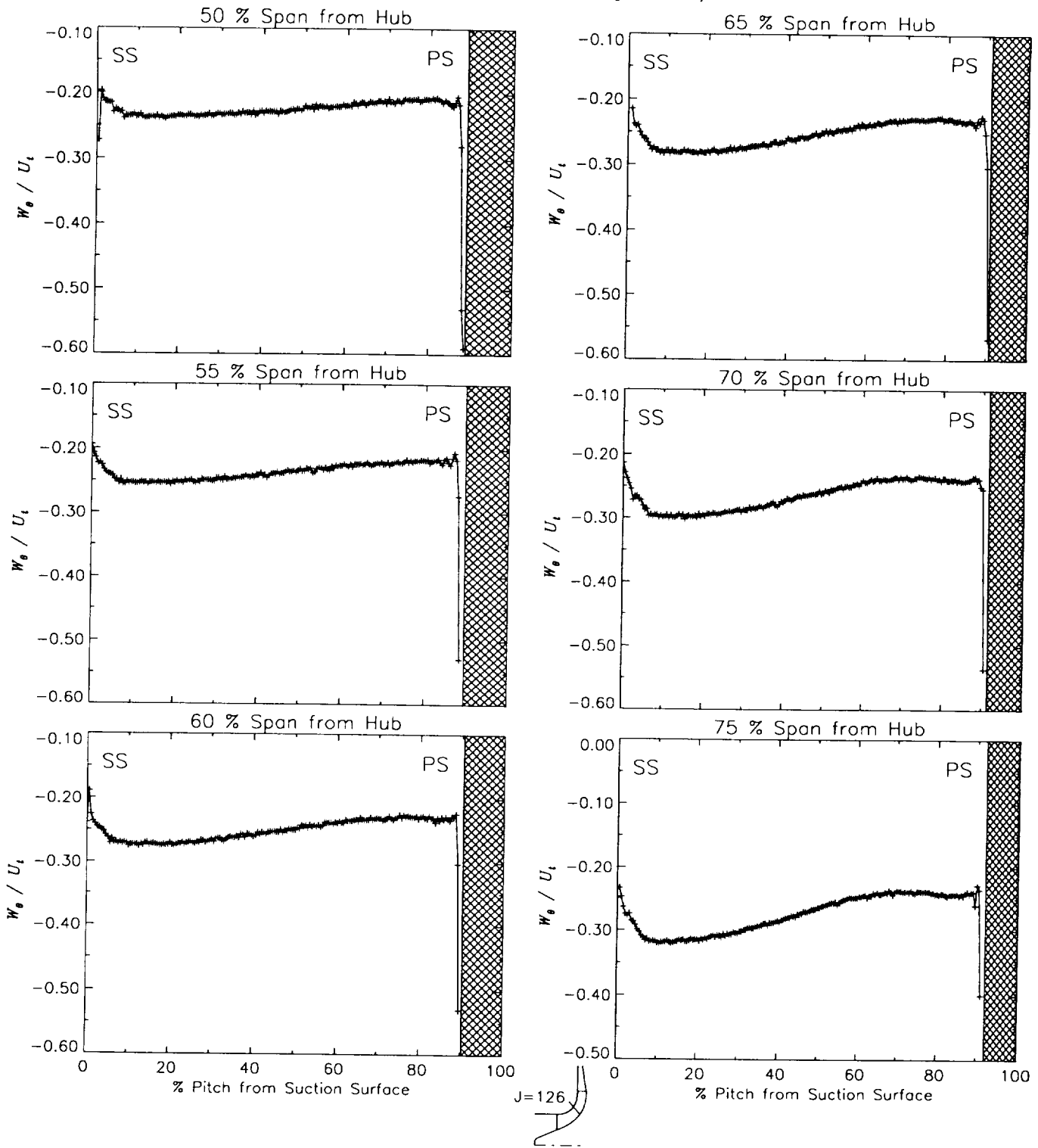
Station J=126, ( $m/m_s=0.555$ )



(b) Relative tangential velocity normalized by impeller tip speed.

Figure 34.-Continued.

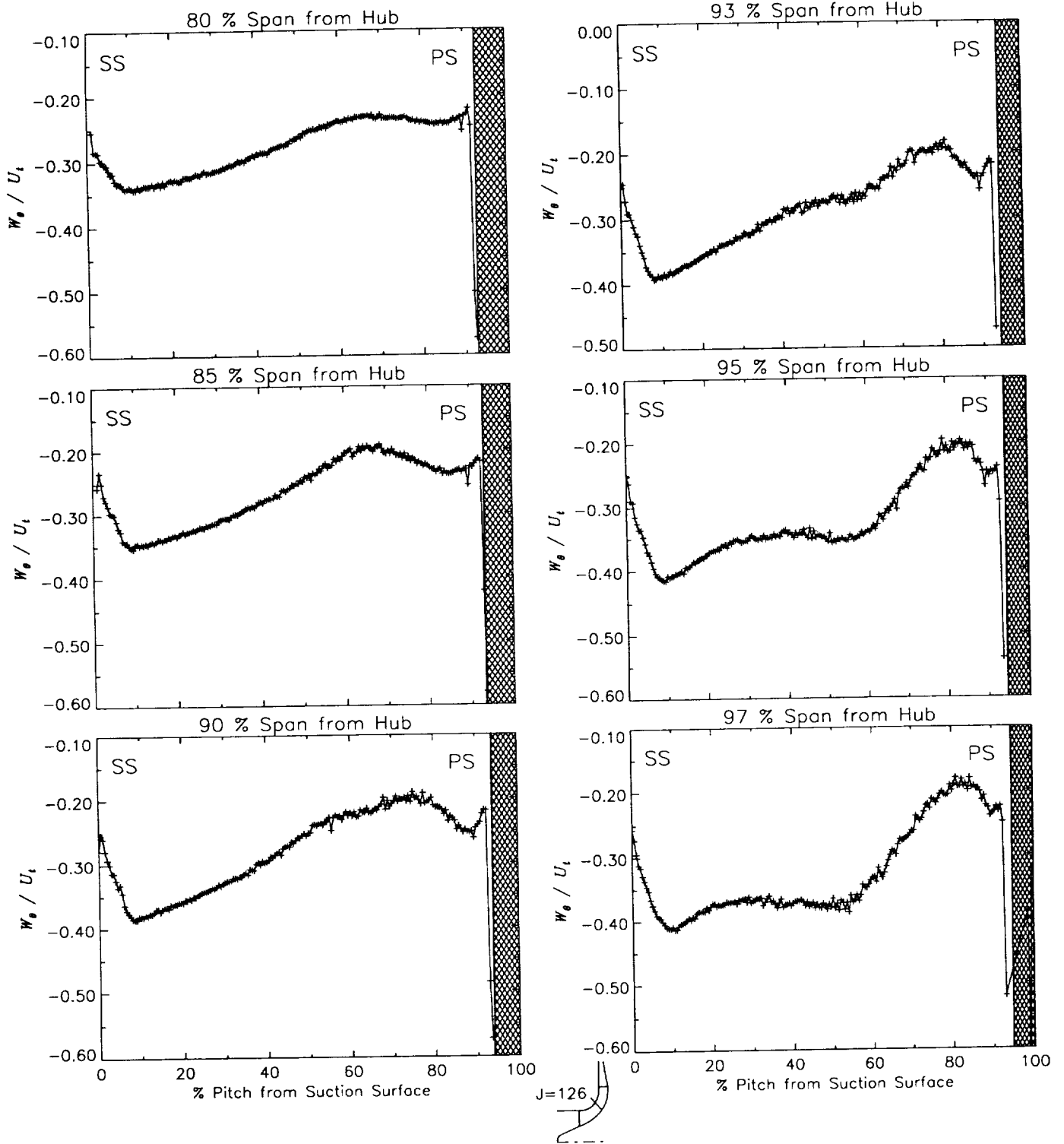
Station J=126, ( $m/m_s=0.555$ )



(b) Relative tangential velocity normalized by impeller tip speed.

Figure 34.-Continued.

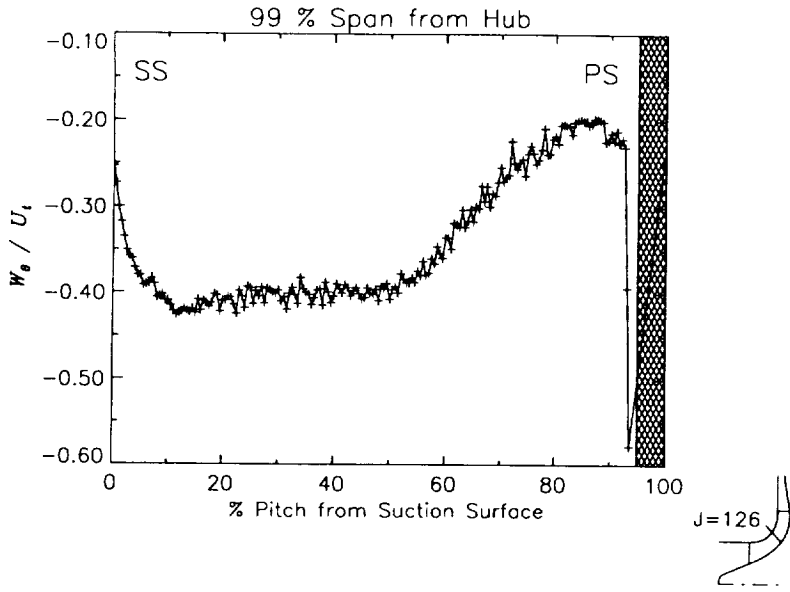
Station J=126, ( $m/m_s=0.555$ )



(b) Relative tangential velocity normalized by impeller tip speed.

Figure 34.-Continued.

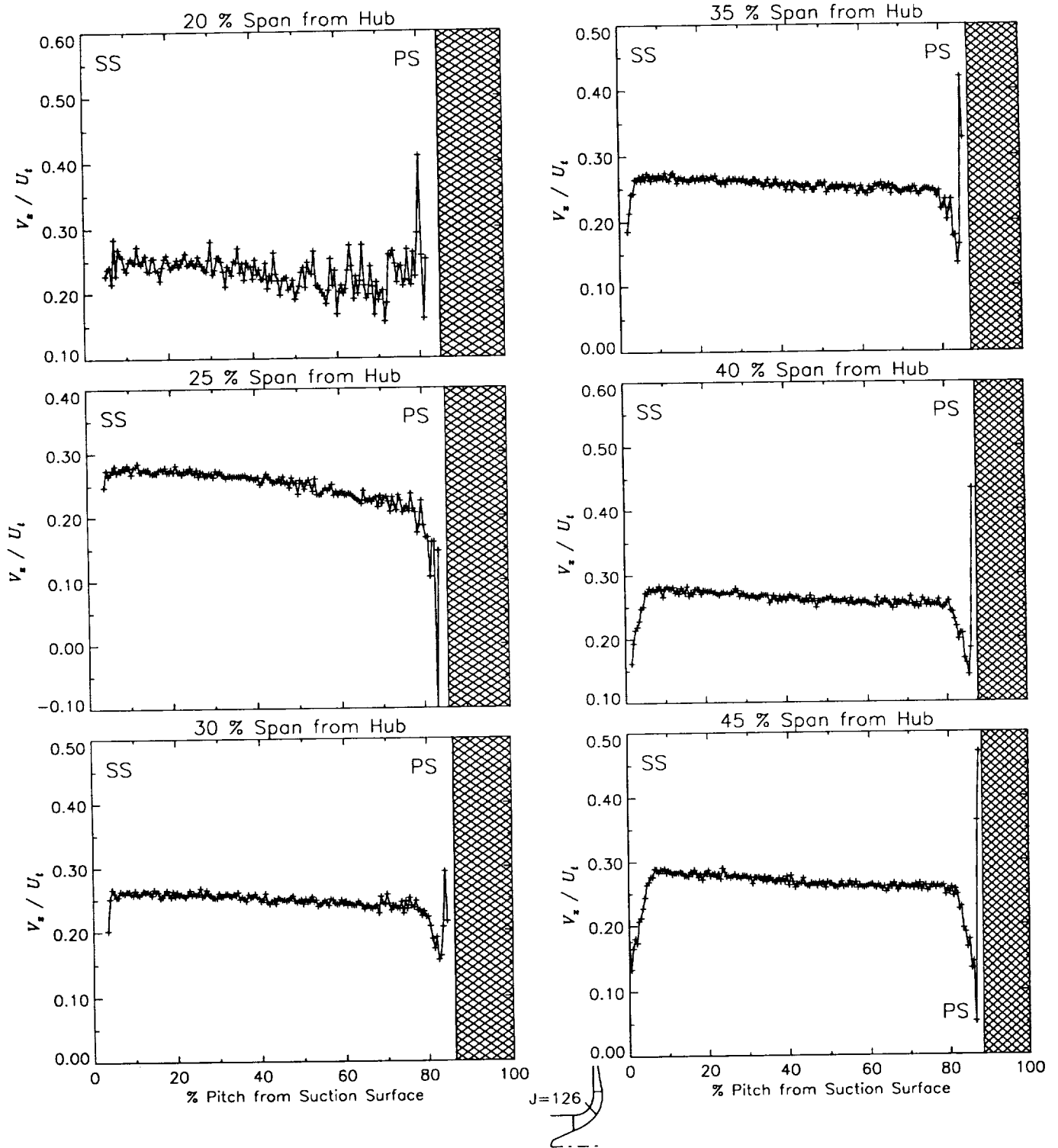
Station J=126, ( $m/m_s=0.555$ )



(b) Relative tangential velocity normalized by impeller tip speed.

Figure 34.-Continued.

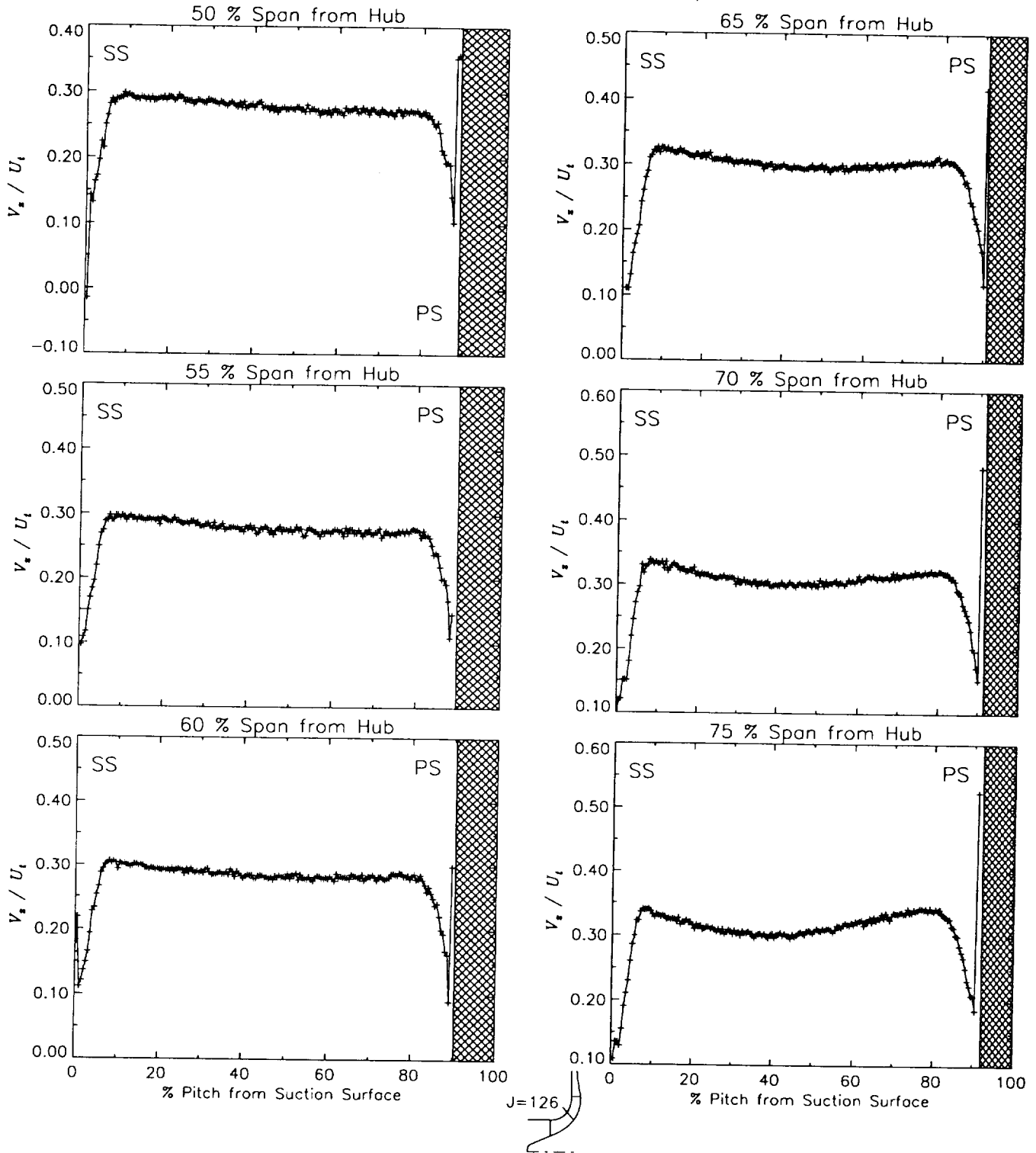
Station J=126, ( $m/m_s=0.555$ )



(c) Axial velocity normalized by impeller tip speed.

Figure 34.—Continued.

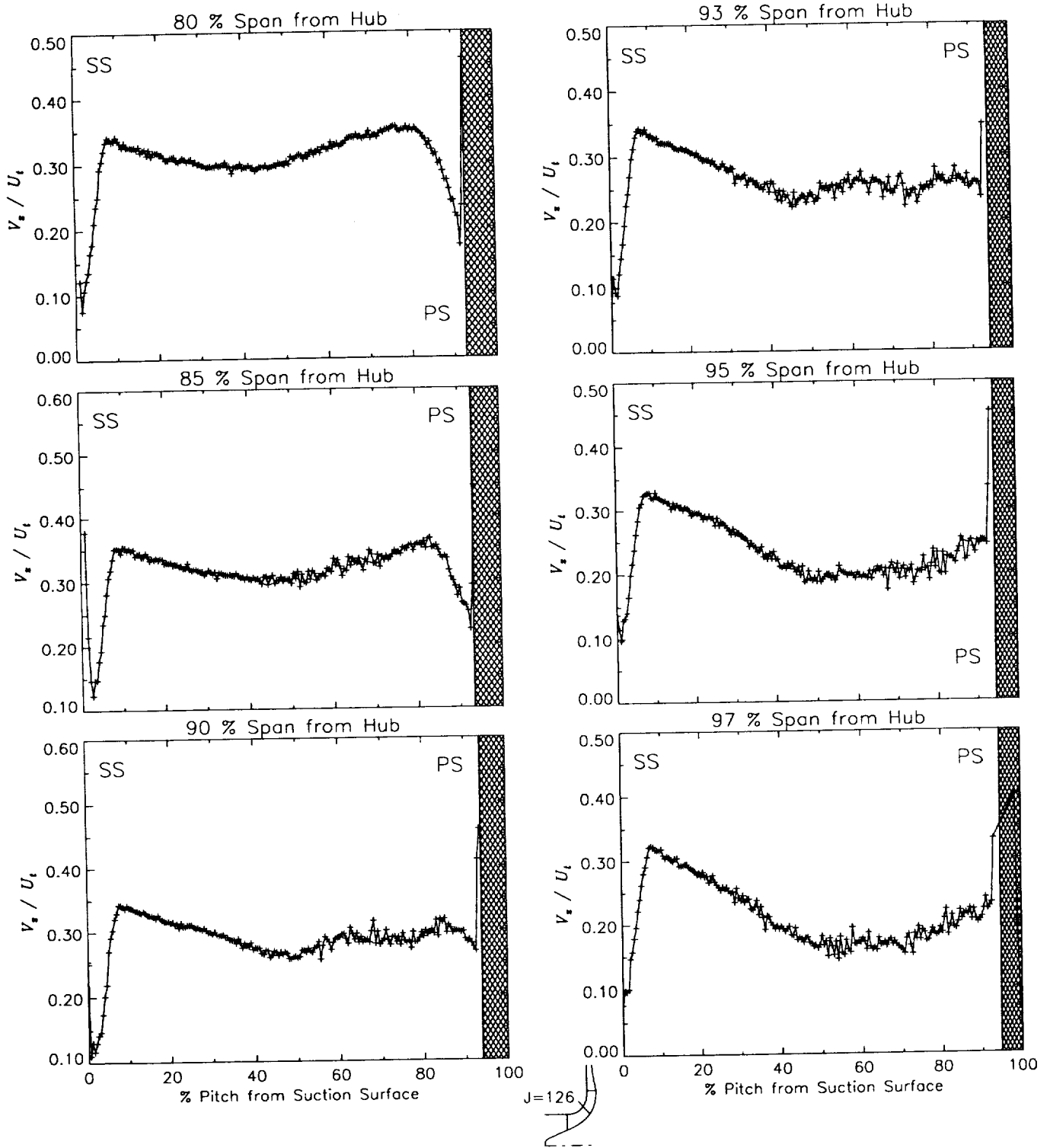
Station J=126, ( $m/m_s=0.555$ )



(c) Axial velocity normalized by impeller tip speed.

Figure 34.—Continued.

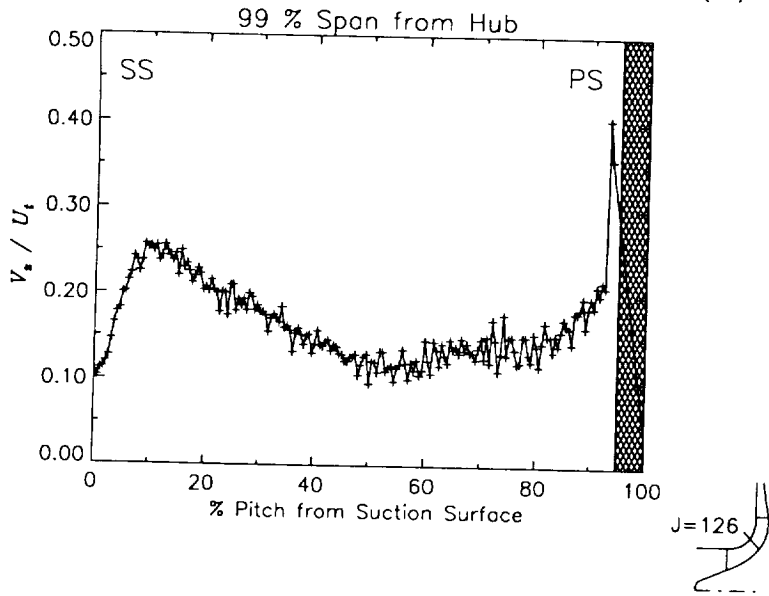
Station J=126, ( $m/m_s=0.555$ )



(c) Axial velocity normalized by impeller tip speed.

Figure 34.-Continued.

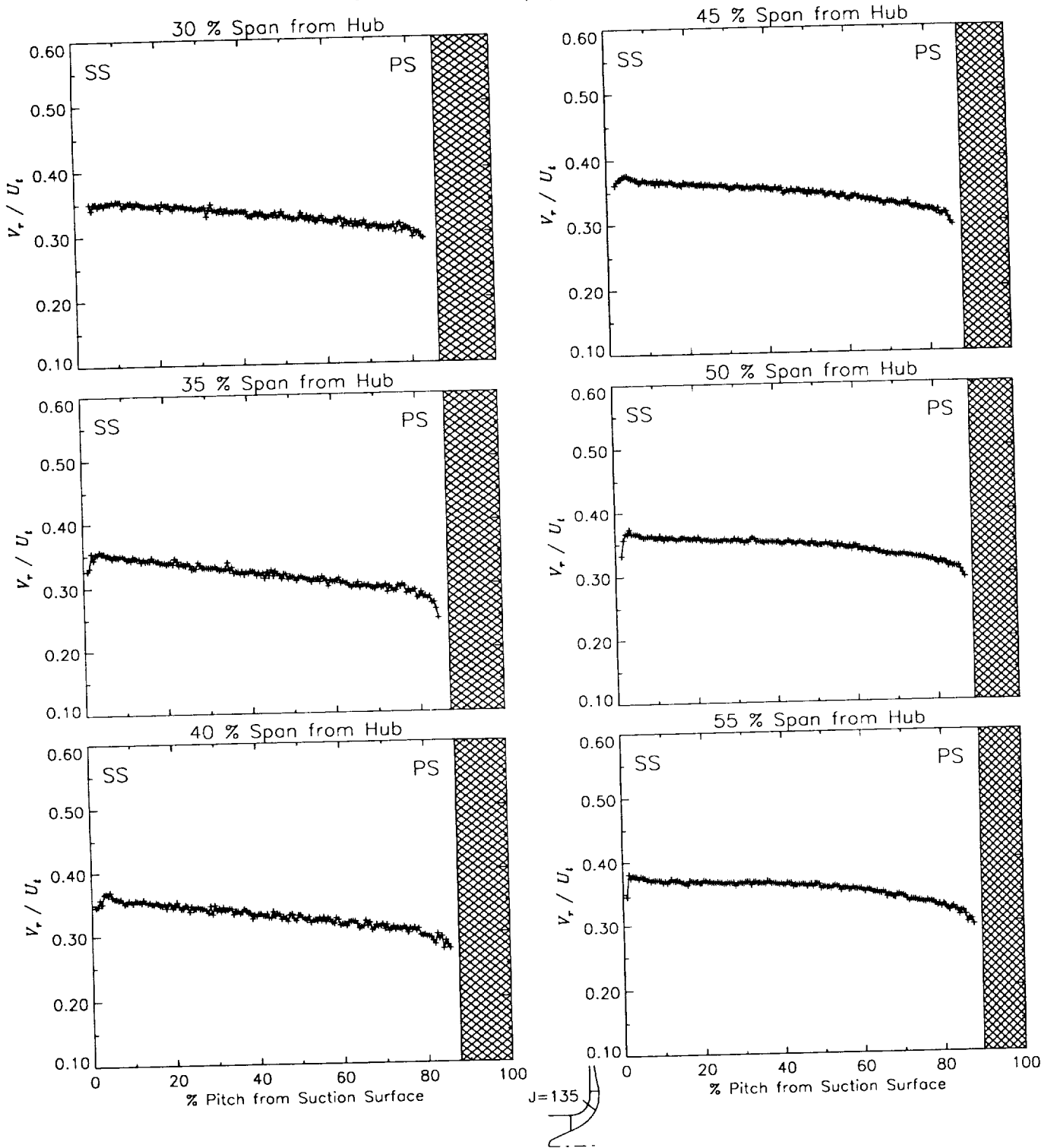
Station J=126, ( $m/m_s=0.555$ )



(c) Axial velocity normalized by impeller tip speed.

Figure 34.—Concluded.

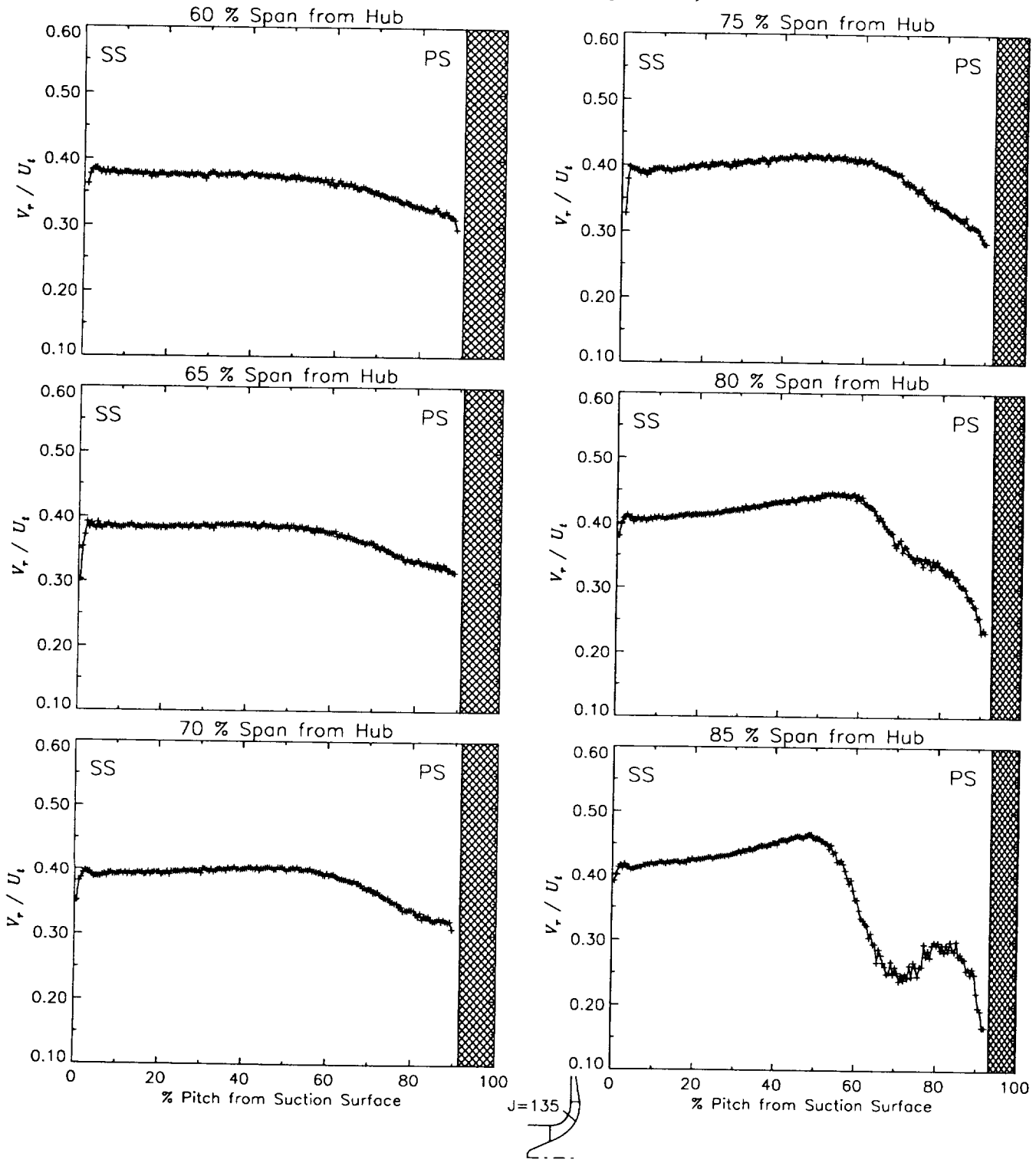
Station J=135, ( $m/m_s=0.644$ )



(a) Radial velocity normalized by impeller tip speed.

Figure 35.—Laser velocimeter results of axial, radial, and relative tangential velocities normalized by impeller tip speed for the design flow condition,  $\dot{m}_d$ , at station J=135, ( $m/m_s=0.644$ ). The shaded region to the right of each plot represents the physical blade width.

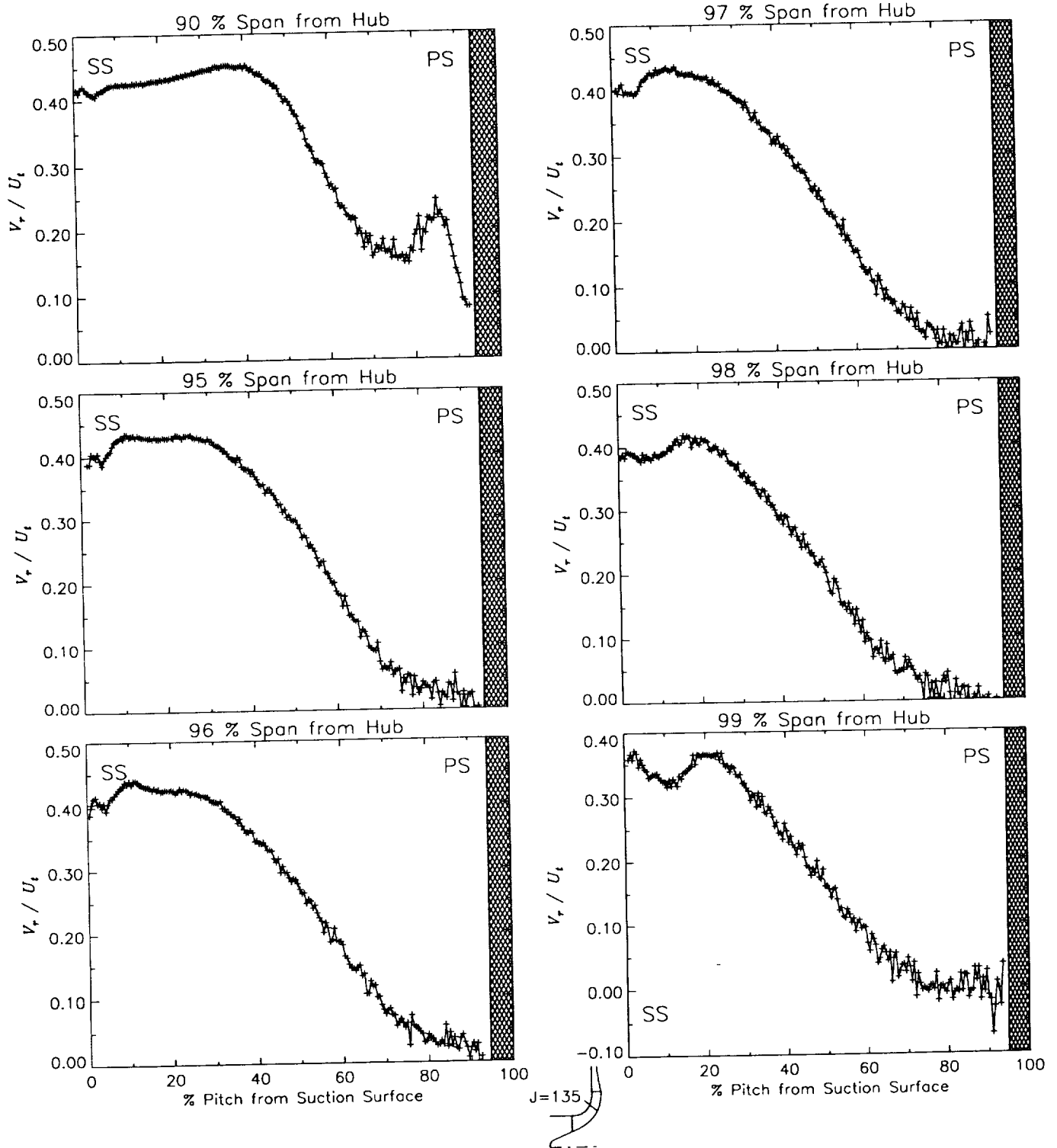
Station J=135, ( $m/m_s=0.644$ )



(a) Radial velocity normalized by impeller tip speed.

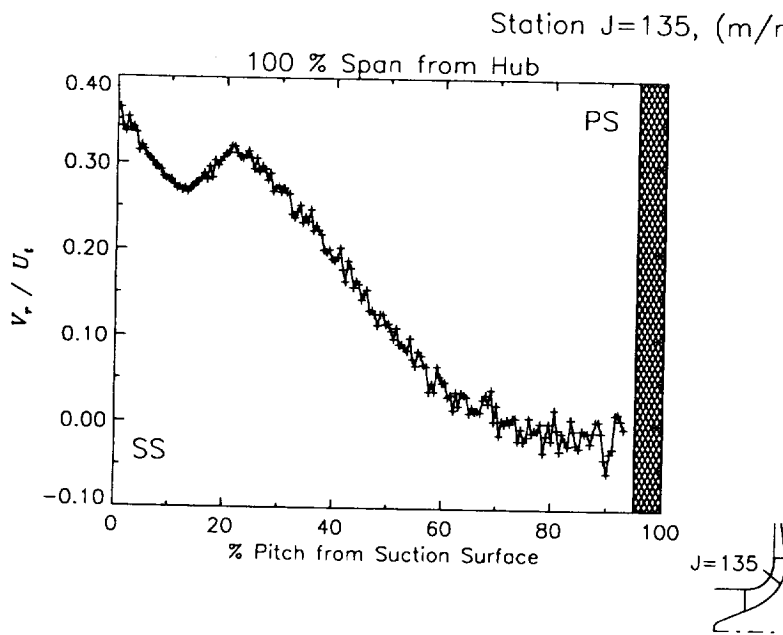
Figure 35.-Continued.

Station J=135, ( $m/m_s=0.644$ )



(a) Radial velocity normalized by impeller tip speed.

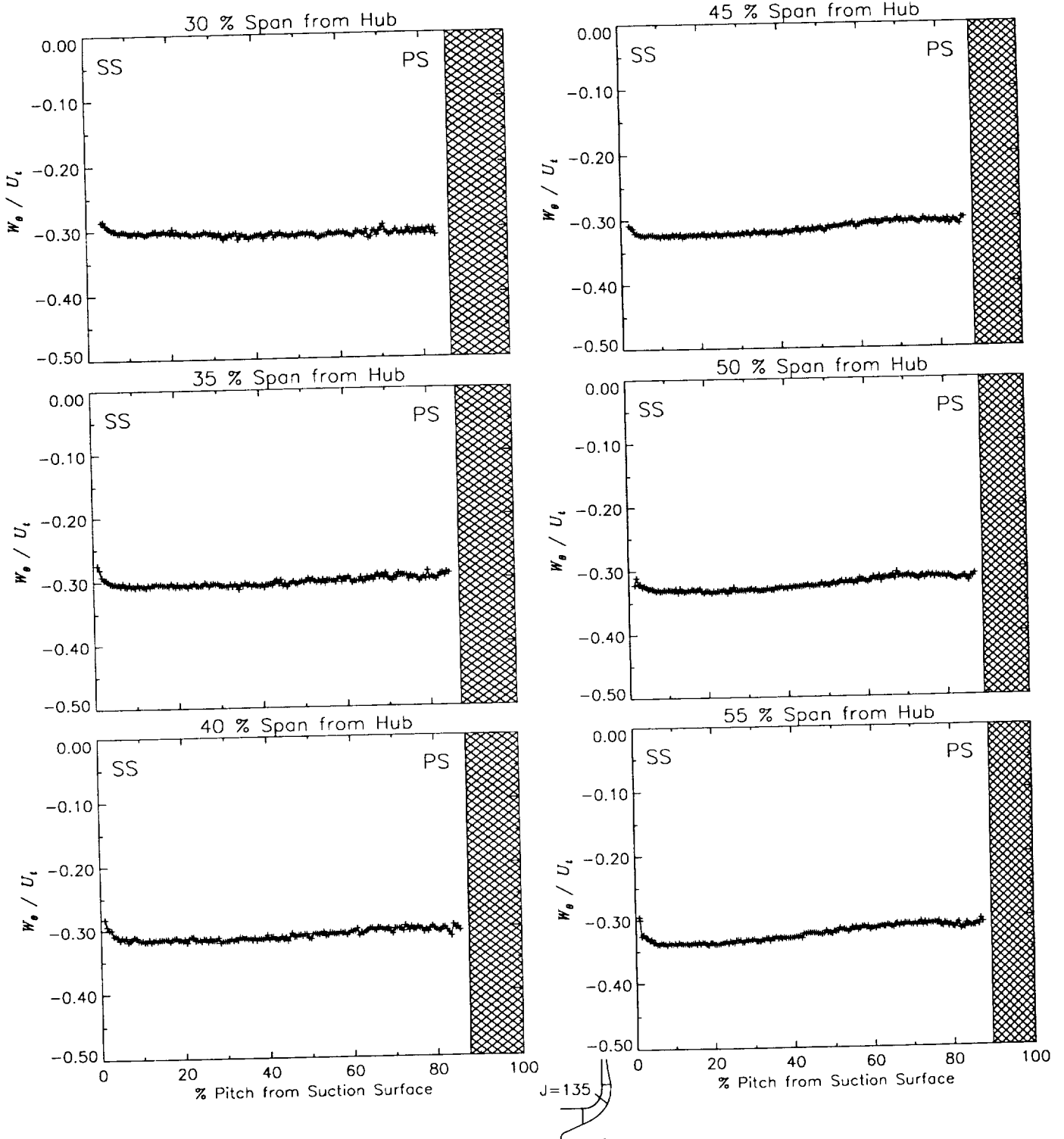
Figure 35.-Continued.



(a) Radial velocity normalized by impeller tip speed.

Figure 35.-Continued.

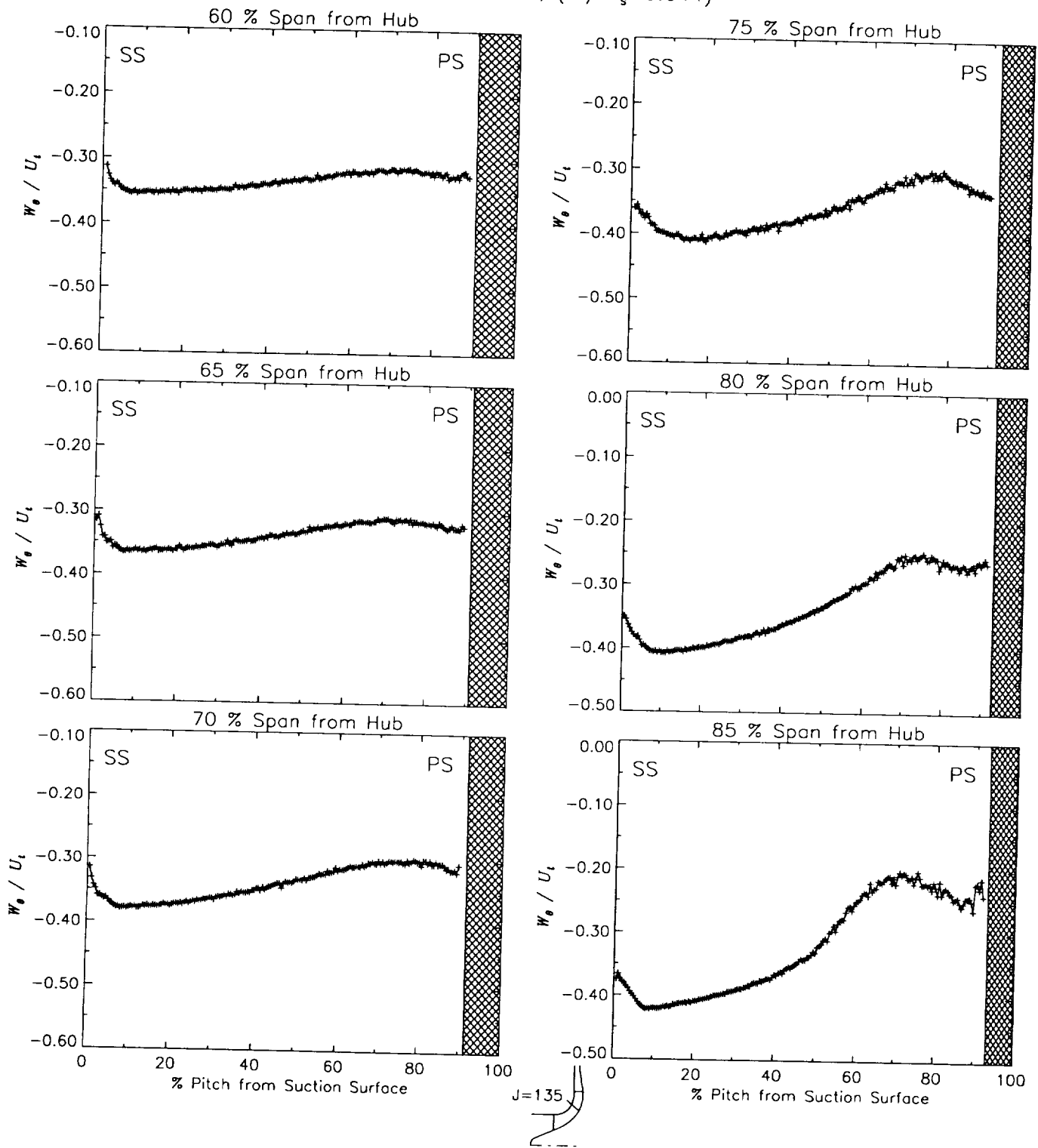
Station J=135, ( $m/m_s=0.644$ )



(b) Relative tangential velocity normalized by impeller tip speed.

Figure 35.-Continued.

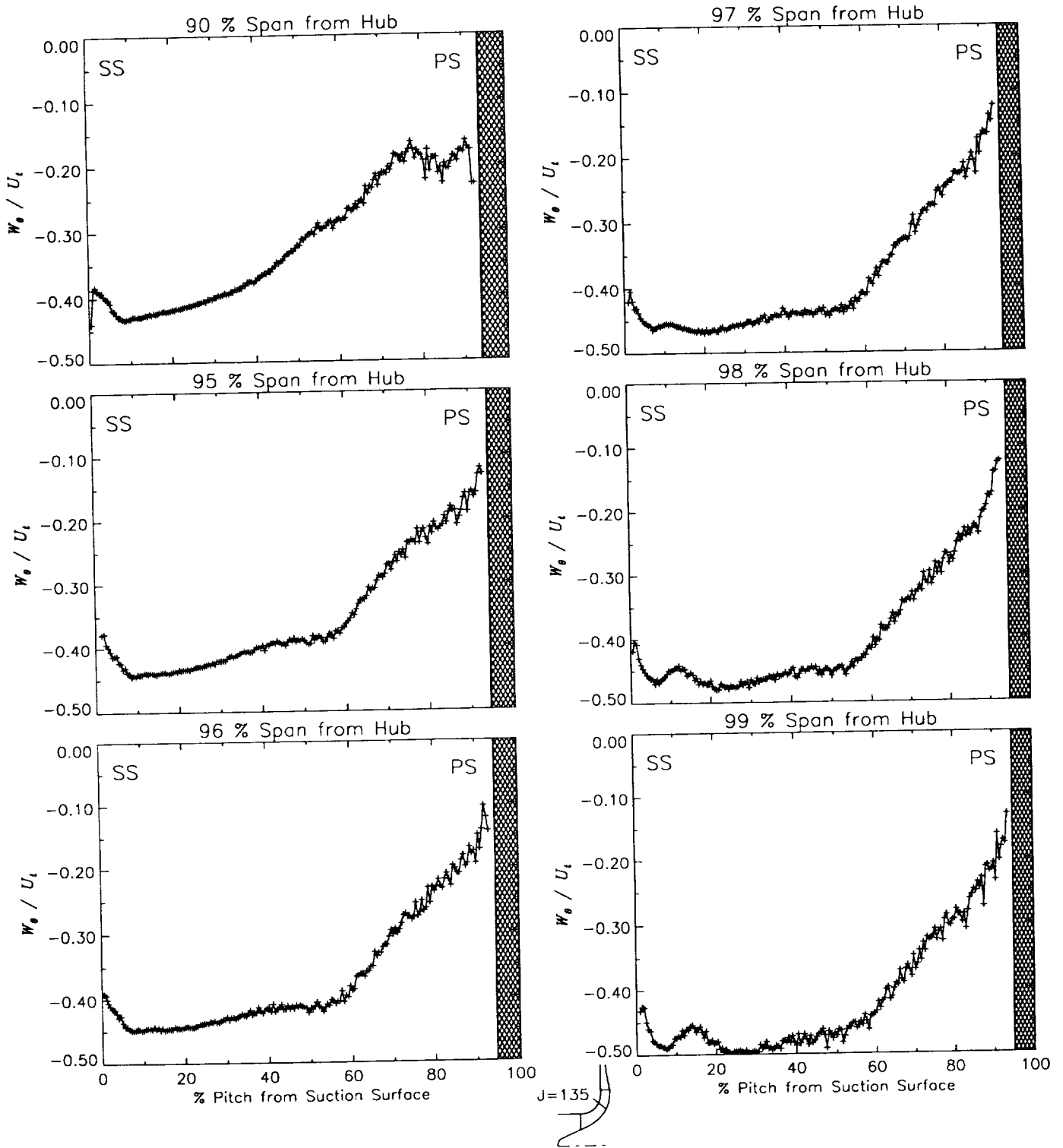
Station J=135, ( $m/m_s=0.644$ )



(b) Relative tangential velocity normalized by impeller tip speed.

Figure 35.—Continued.

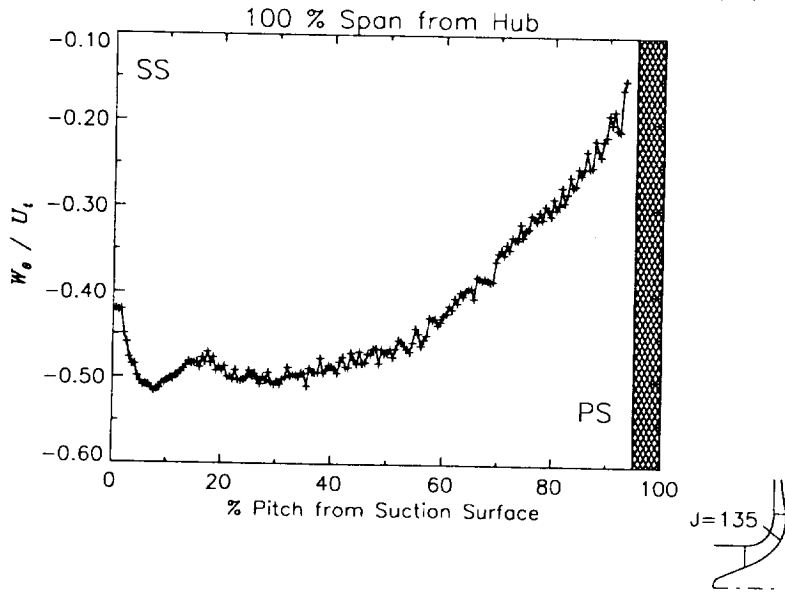
Station J=135, ( $m/m_s=0.644$ )



(b) Relative tangential velocity normalized by impeller tip speed.

Figure 35.—Continued.

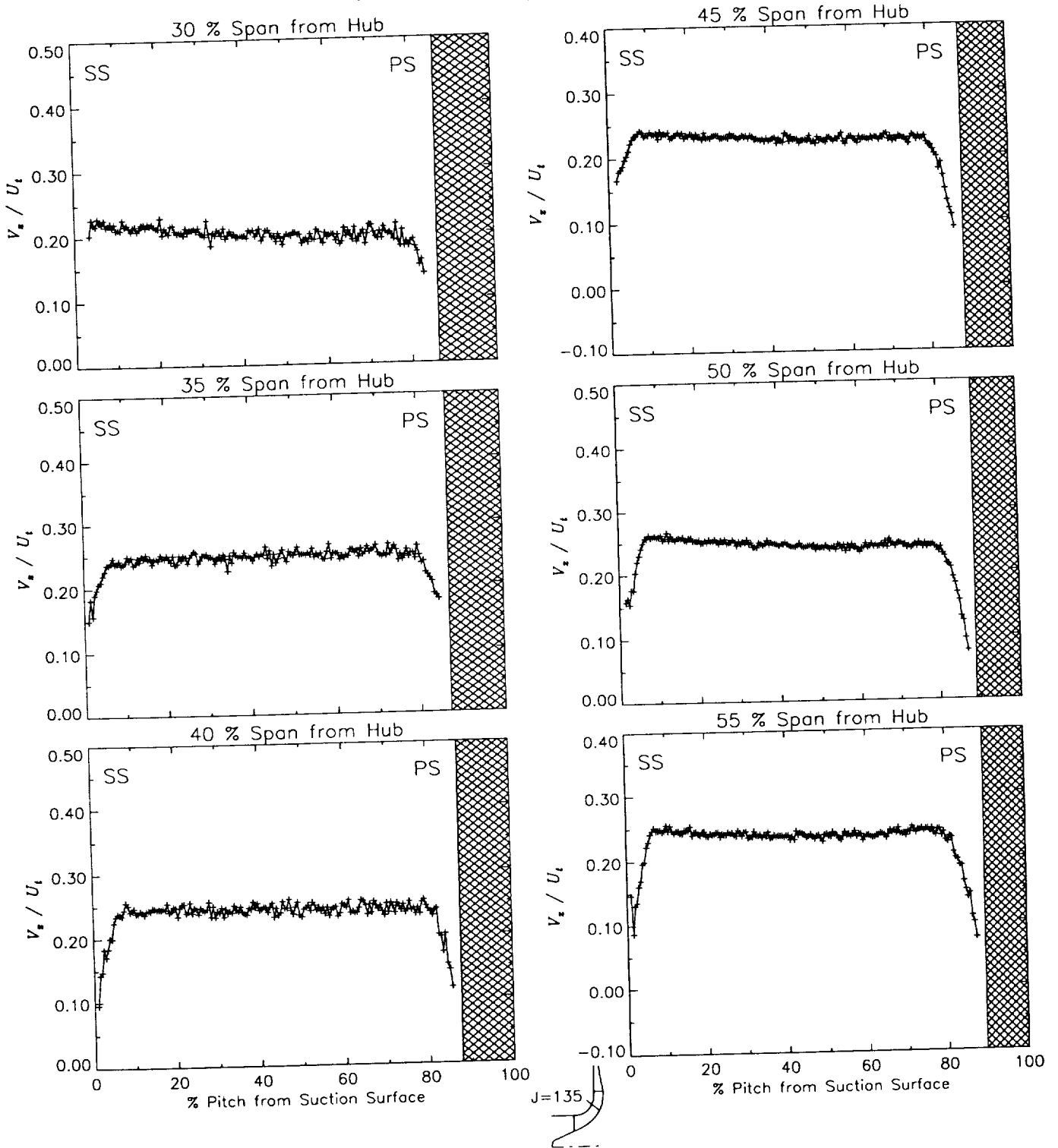
Station J=135, ( $m/m_s=0.644$ )



(b) Relative tangential velocity normalized by impeller tip speed.

Figure 35.-Continued.

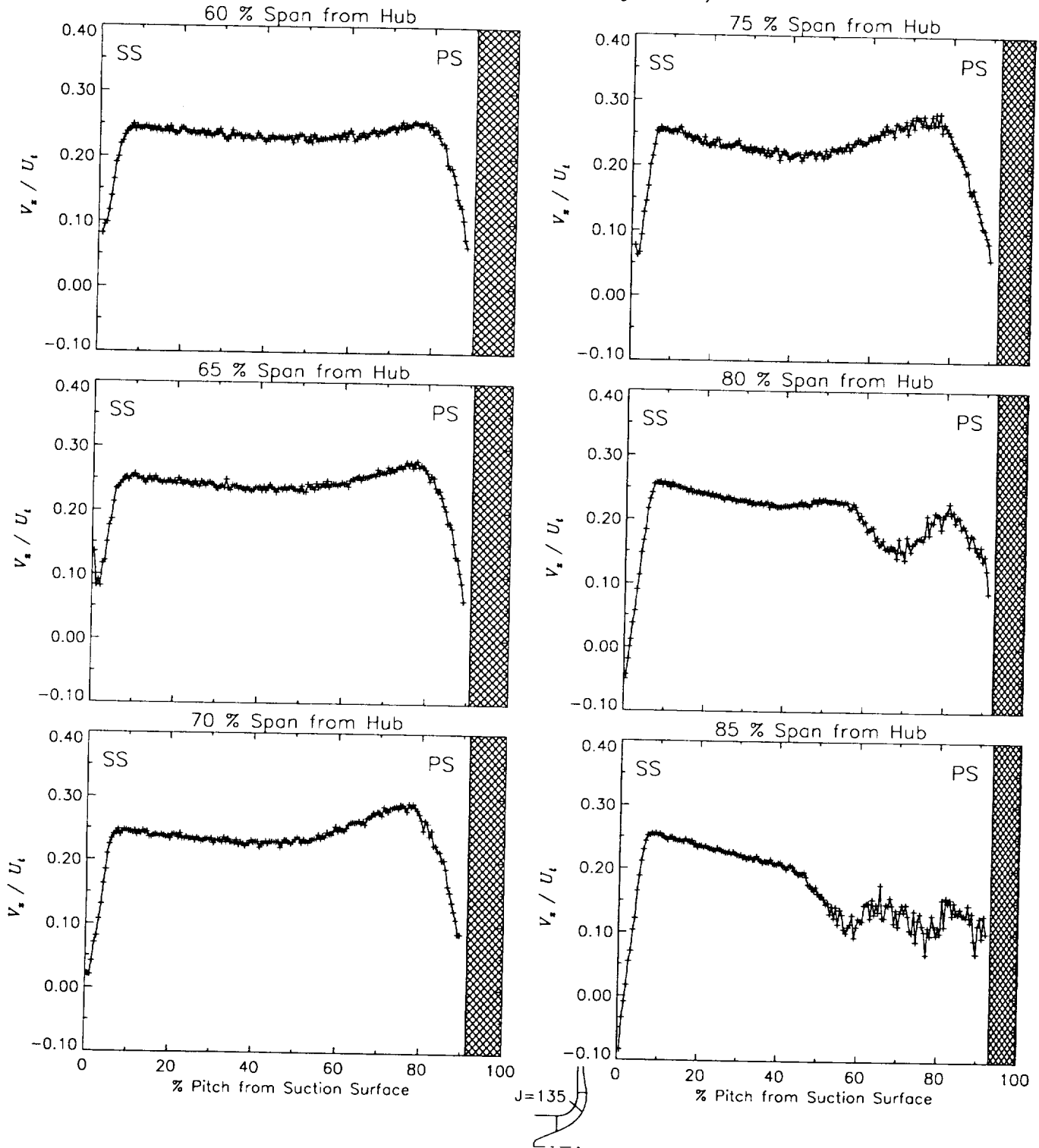
Station J=135, ( $m/m_s=0.644$ )



(c) Axial velocity normalized by impeller tip speed.

Figure 35.-Continued.

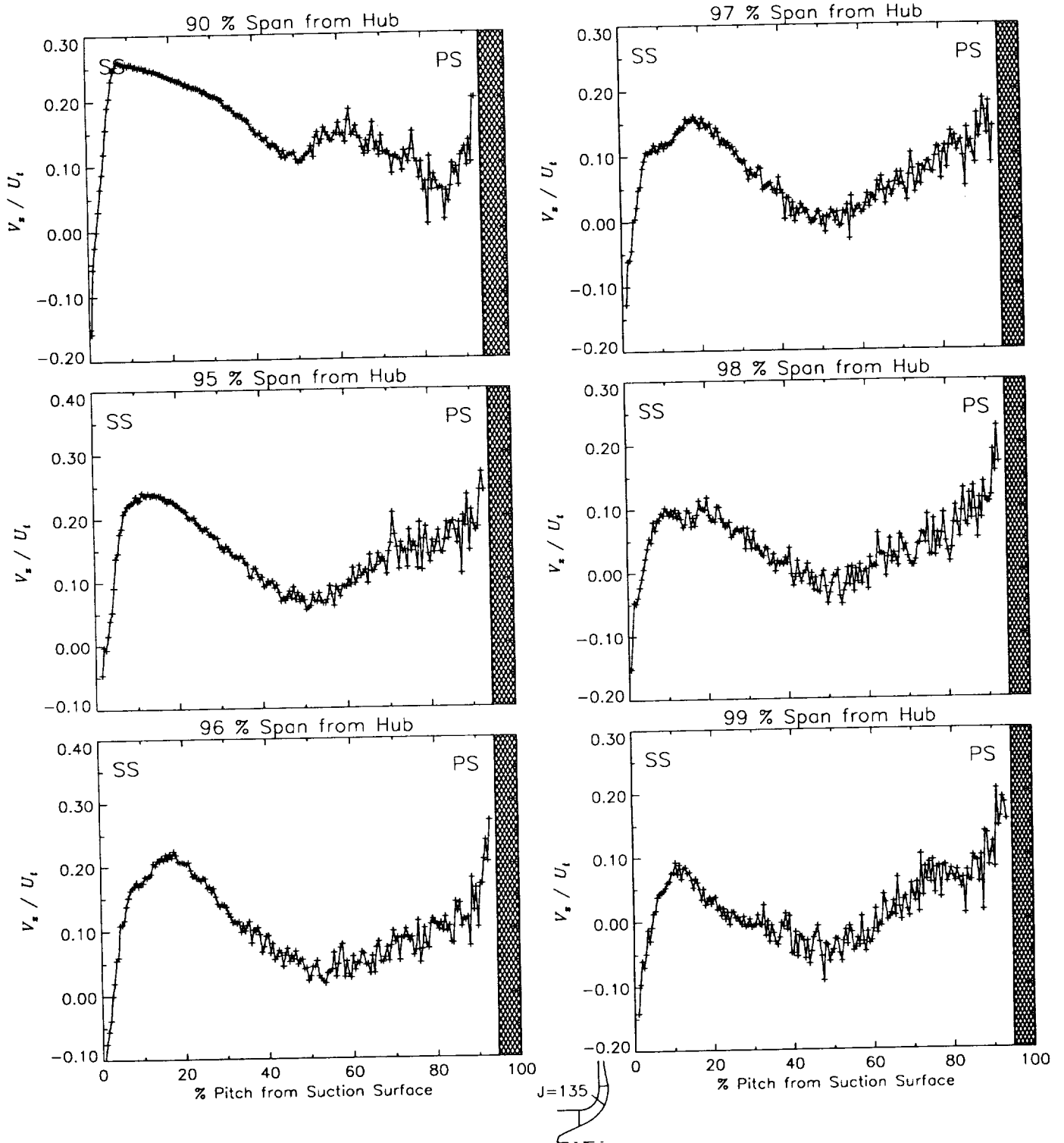
Station J=135, ( $m/m_s=0.644$ )



(c) Axial velocity normalized by impeller tip speed.

Figure 35.-Continued.

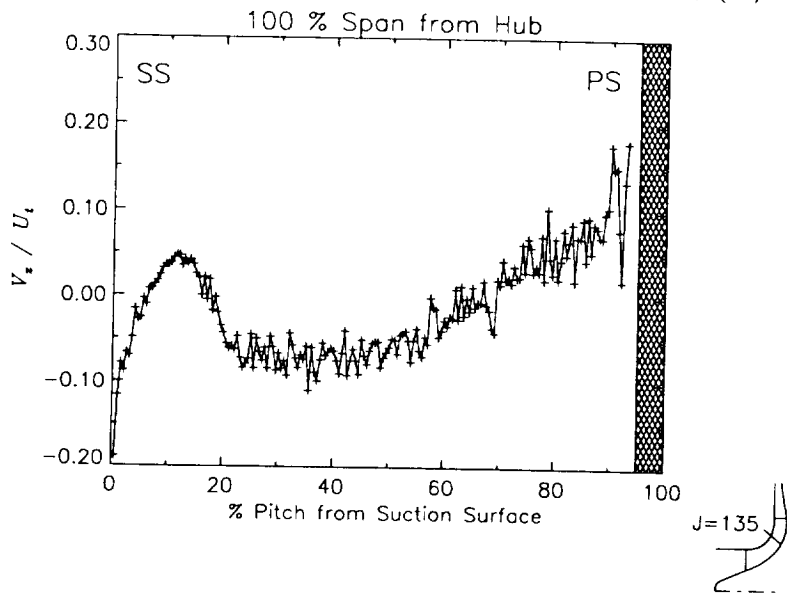
Station J=135, ( $m/m_s=0.644$ )



(c) Axial velocity normalized by impeller tip speed.

Figure 35.—Continued.

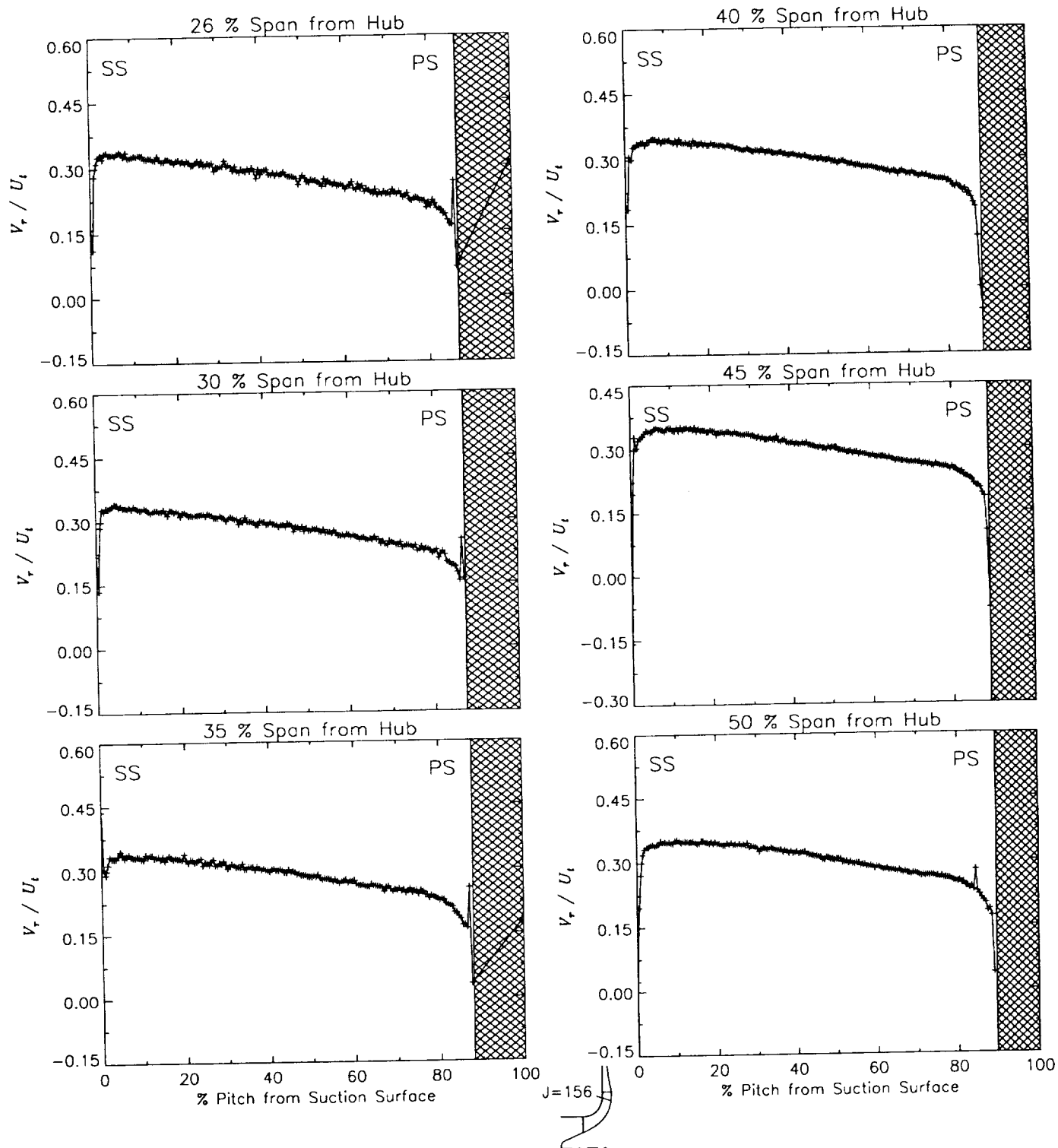
Station J=135, ( $m/m_s=0.644$ )



(c) Axial velocity normalized by impeller tip speed.

Figure 35.—Concluded.

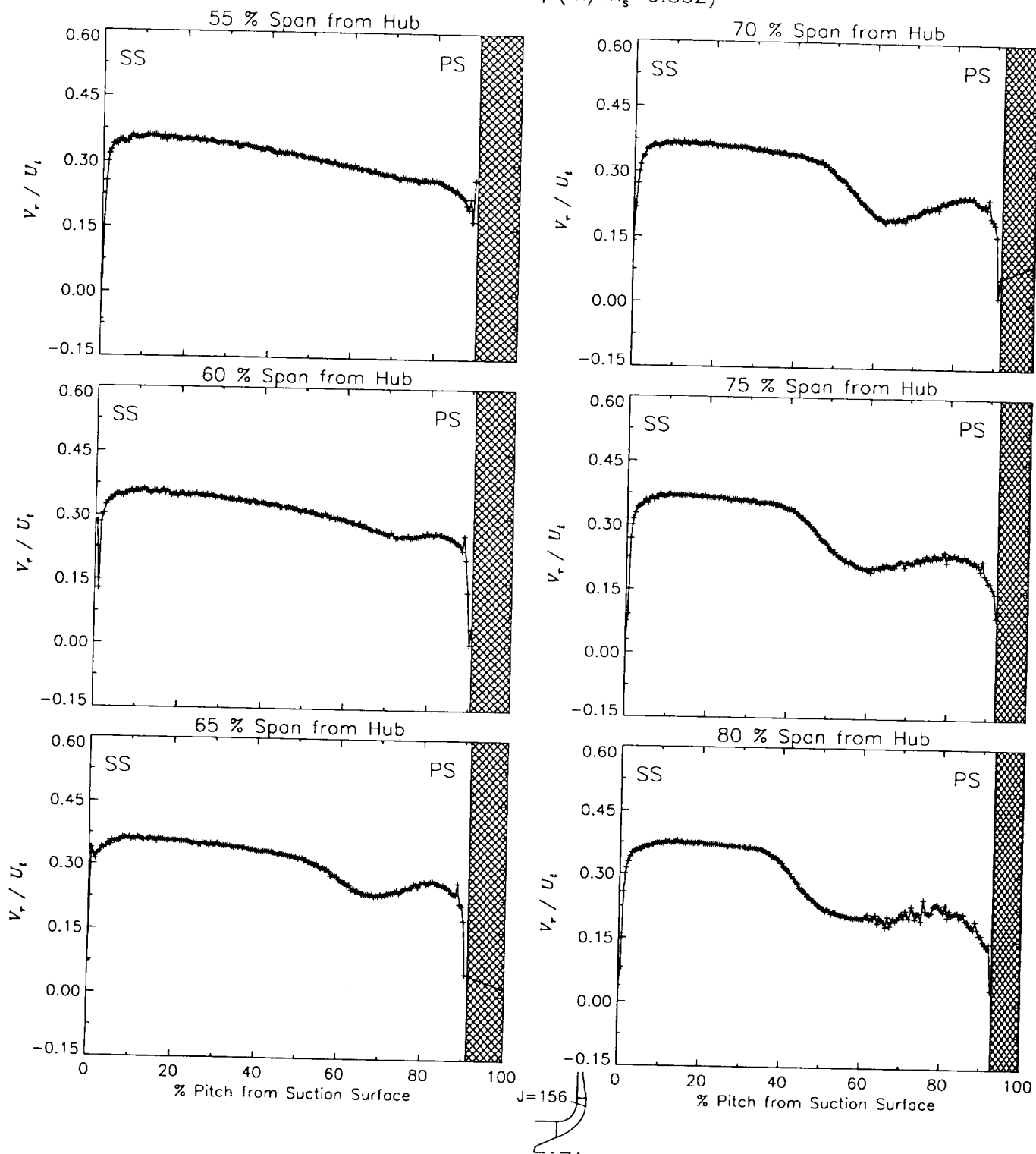
Station J=156, ( $m/m_s=0.852$ )



(a) Radial velocity normalized by impeller tip speed.

Figure 36.-Laser velocimeter results of axial, radial, and relative tangential velocities normalized by impeller tip speed for the design flow condition,  $\dot{m}_d$ , at station J=156, ( $m/m_s=0.852$ ). The shaded region to the right of each plot represents the physical blade width.

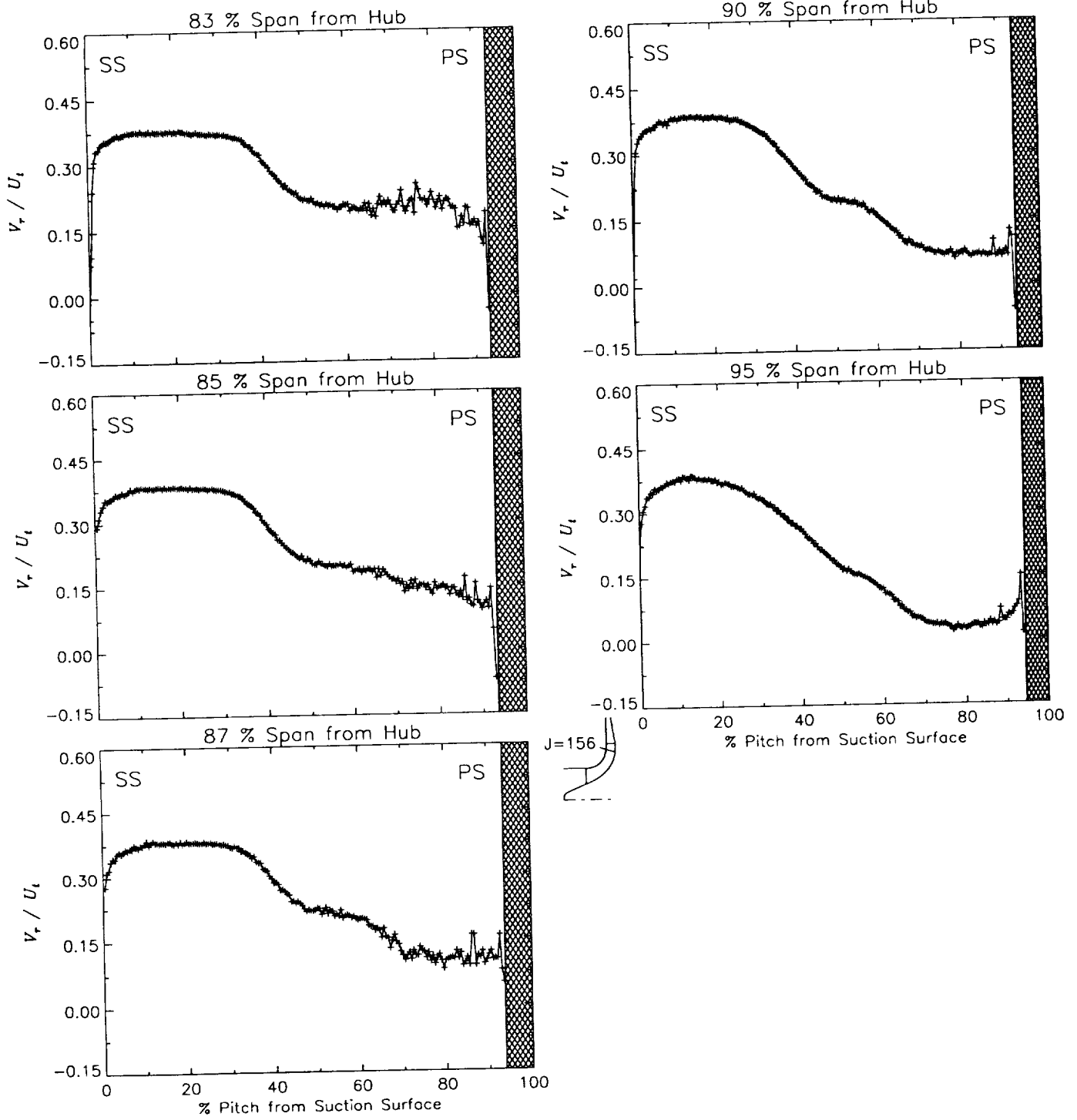
Station J=156, ( $m/m_s=0.852$ )



(a) Radial velocity normalized by impeller tip speed.

Figure 36.—Continued.

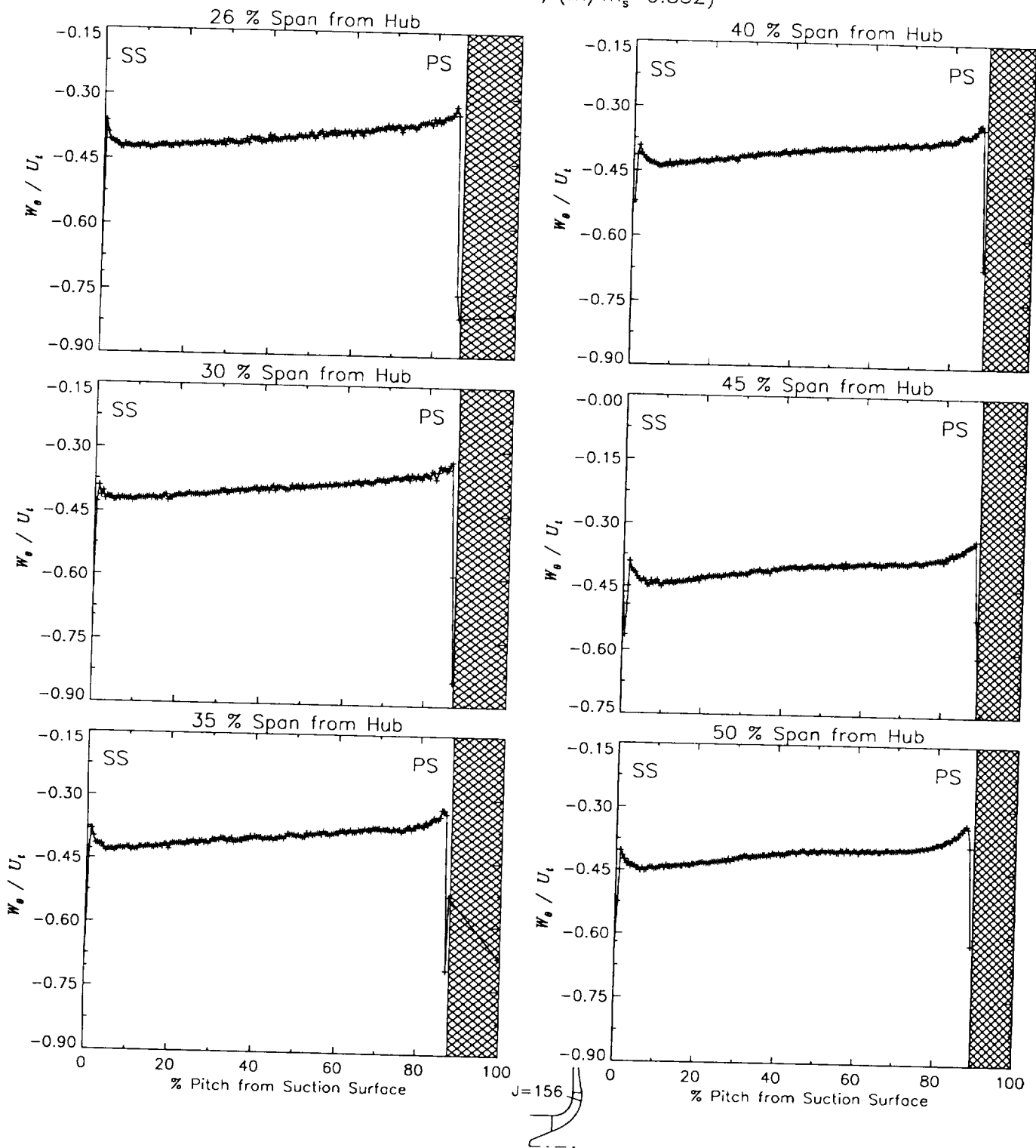
Station J=156, ( $m/m_s=0.852$ )



(a) Radial velocity normalized by impeller tip speed.

Figure 36.—Continued.

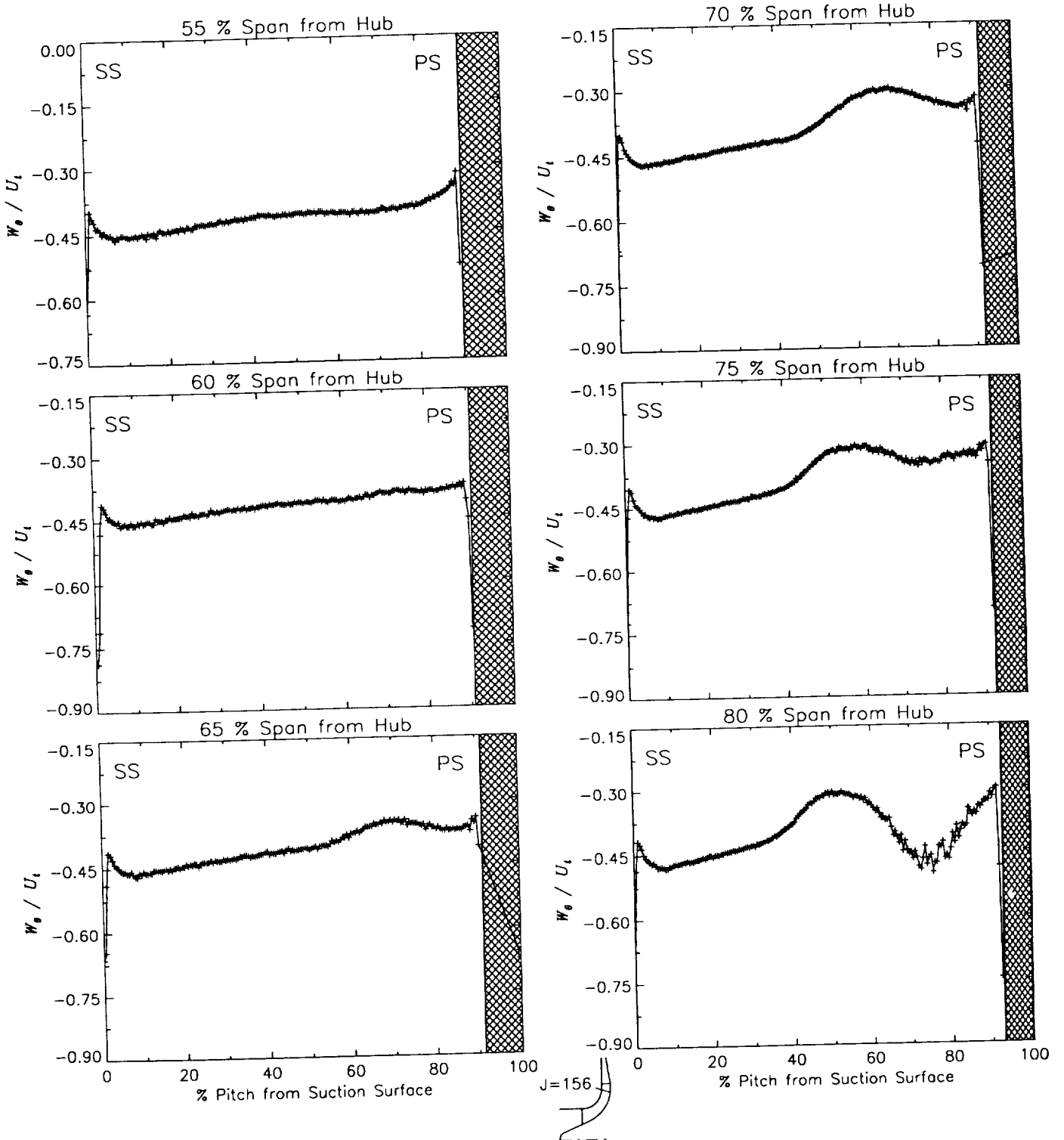
Station J=156, ( $m/m_s=0.852$ )



(b) Relative tangential velocity normalized by impeller tip speed.

Figure 36.-Continued.

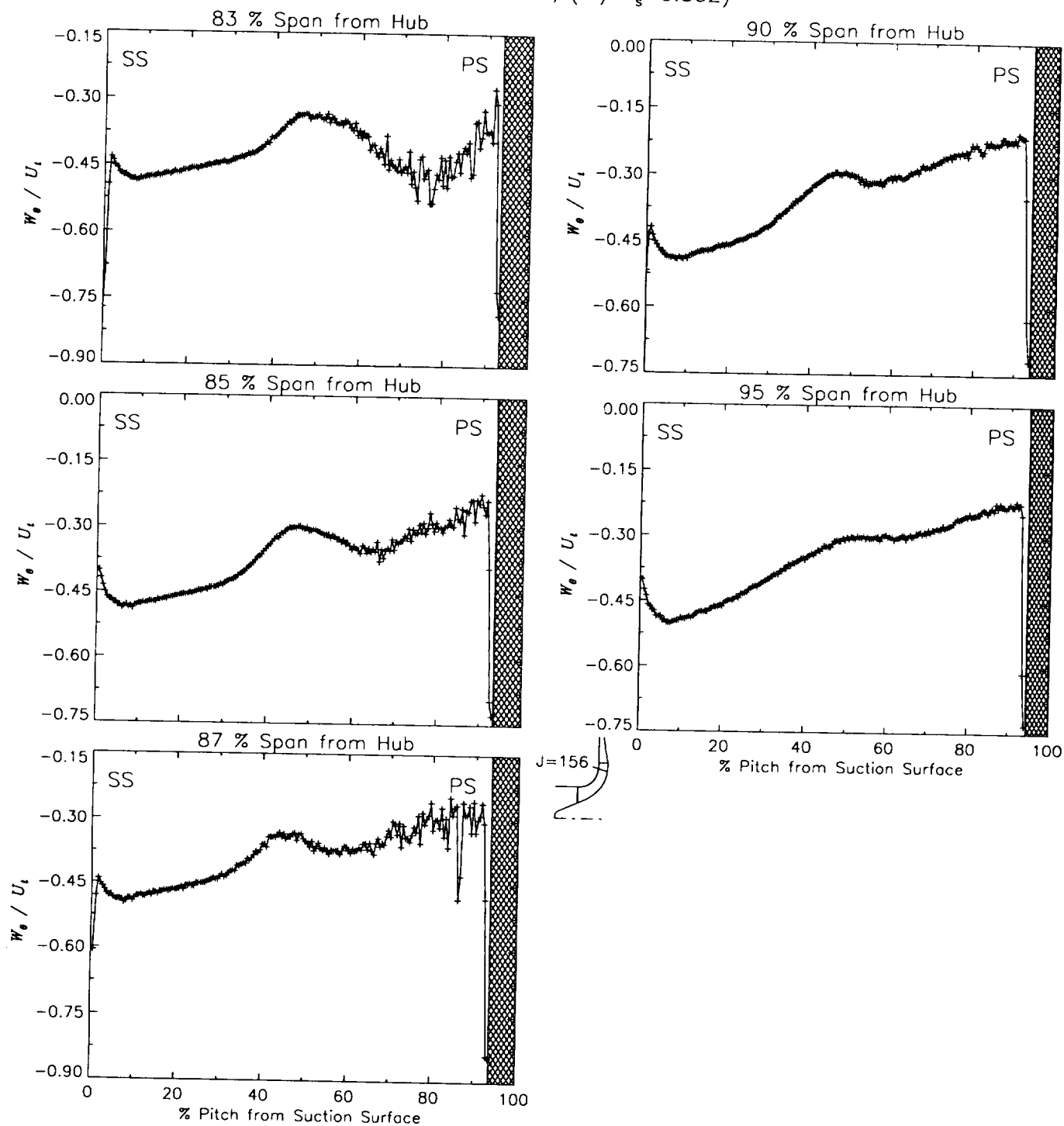
Station J=156, ( $m/m_s=0.852$ )



(b) Relative tangential velocity normalized by impeller tip speed.

Figure 36.—Continued.

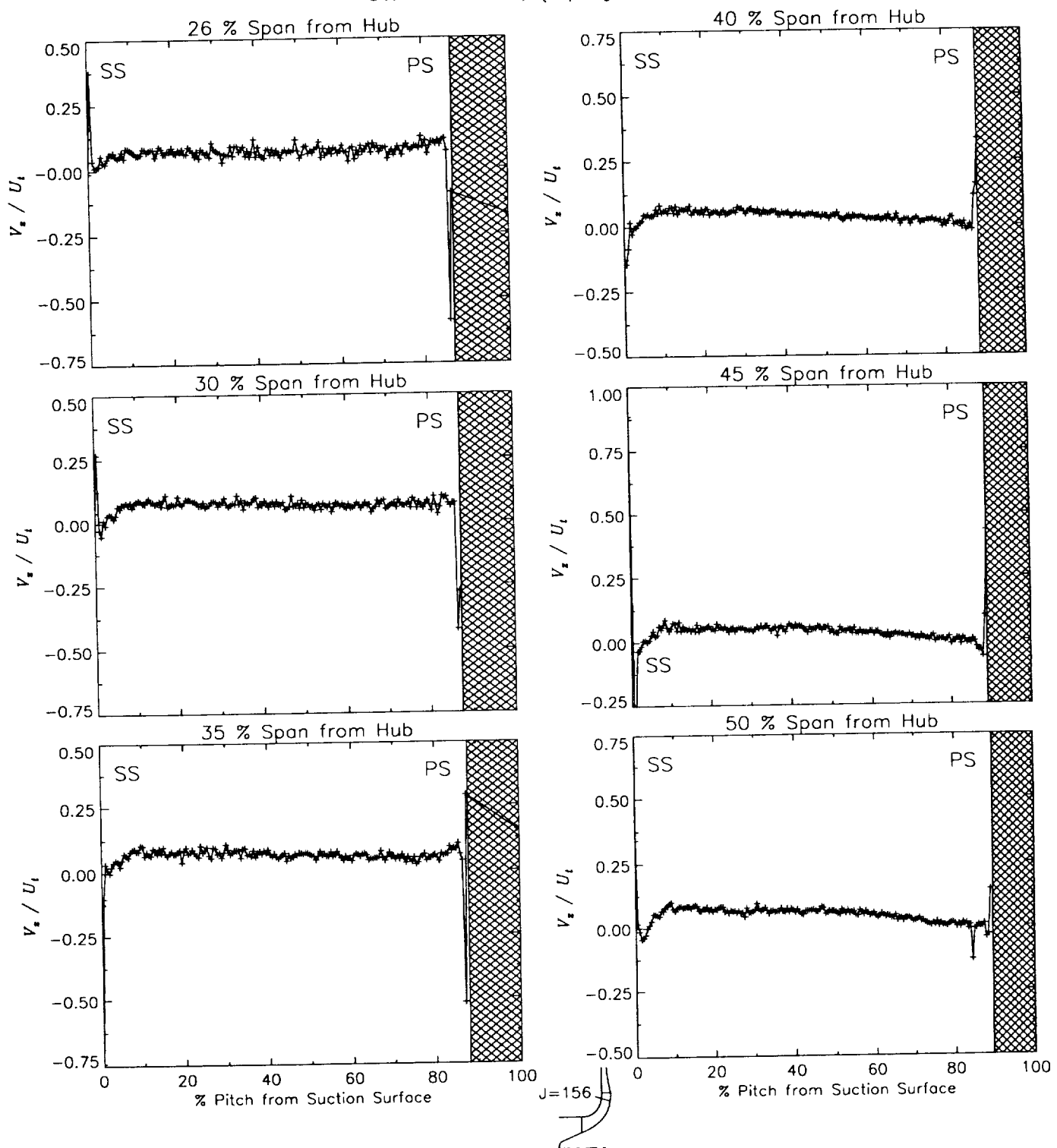
Station J=156, ( $m/m_s=0.852$ )



(b) Relative tangential velocity normalized by impeller tip speed.

Figure 36.—Continued.

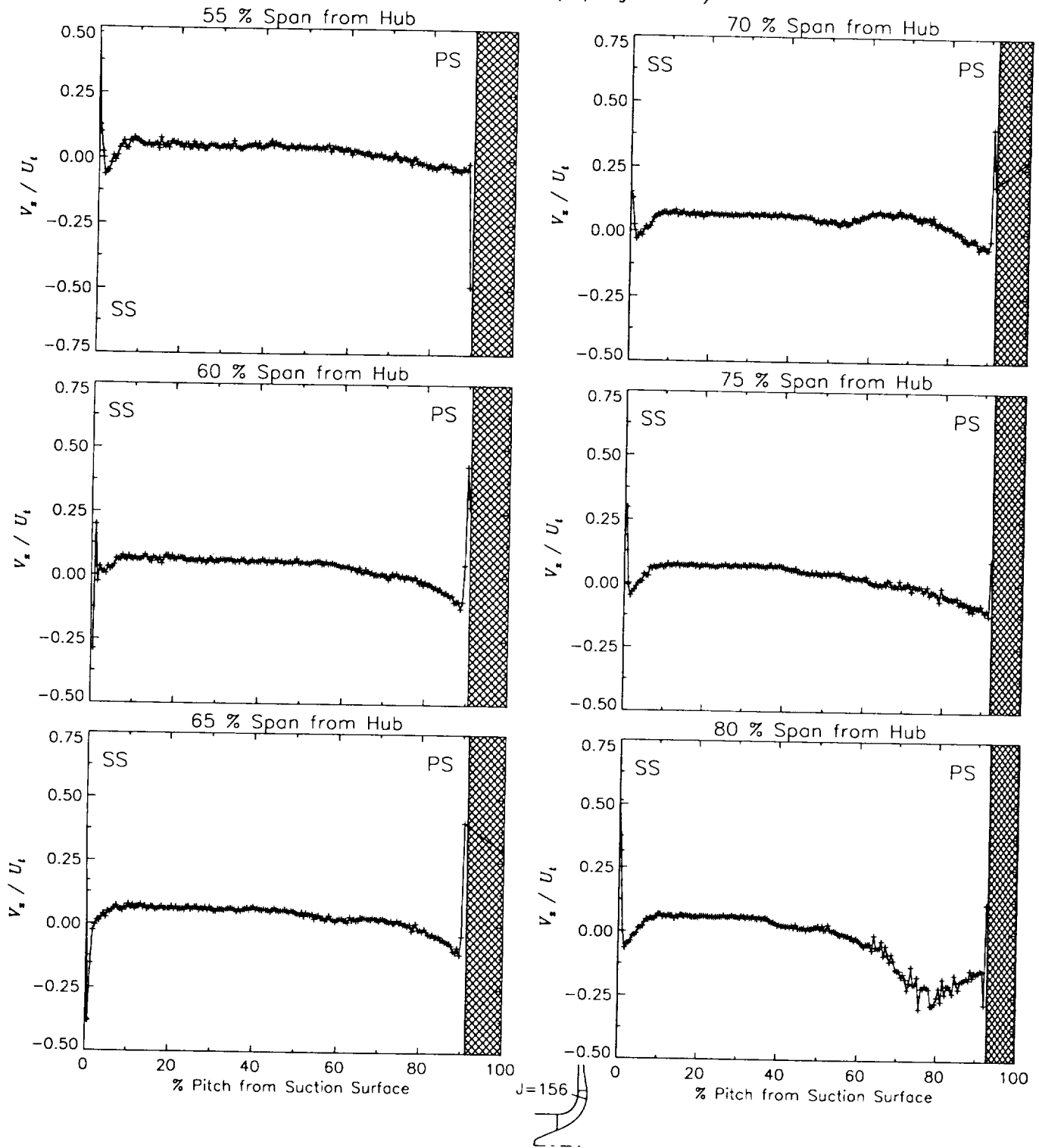
Station J=156, ( $m/m_s=0.852$ )



(c) Axial velocity normalized by impeller tip speed.

Figure 36.-Continued.

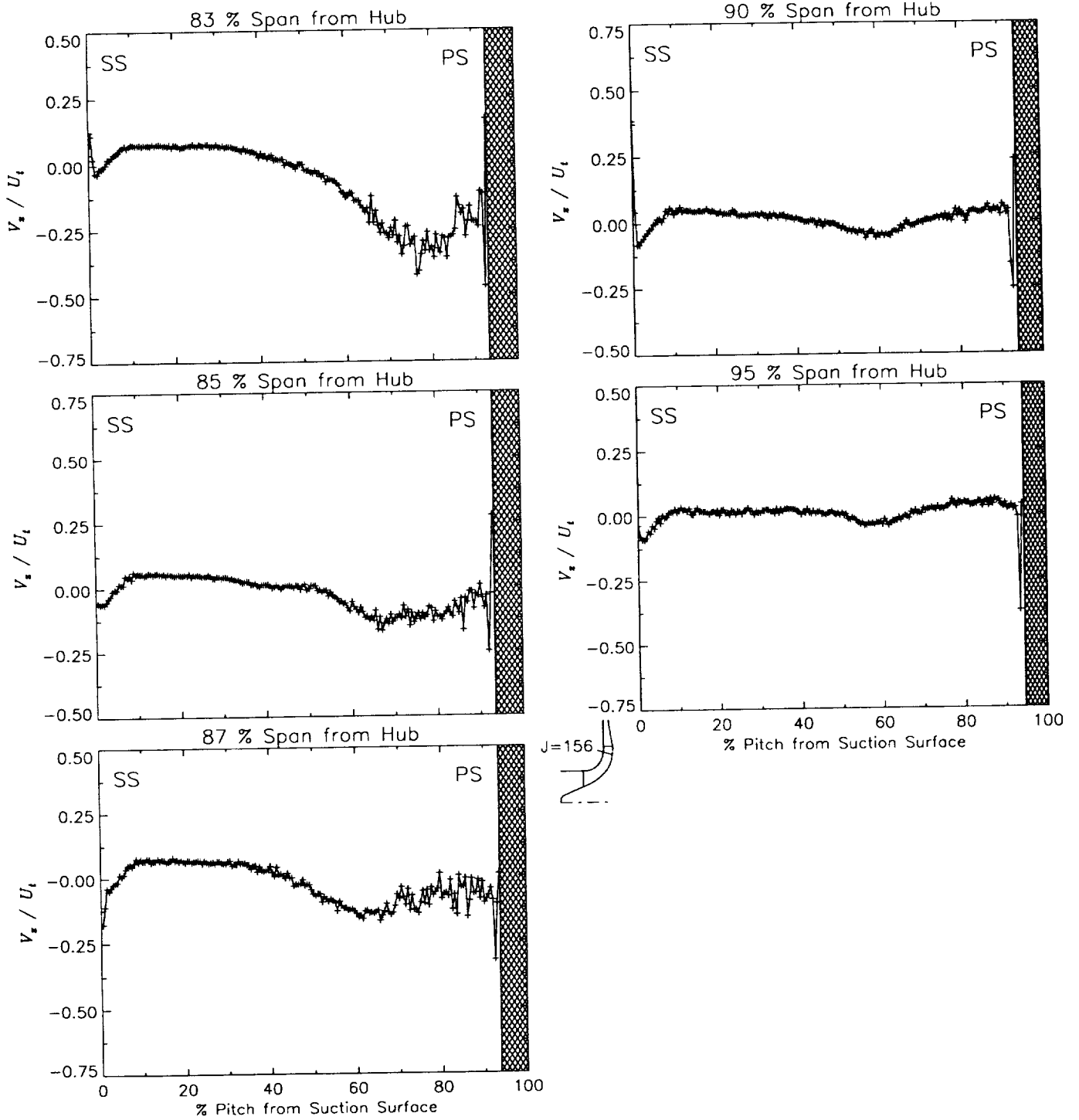
Station J=156, ( $m/m_s=0.852$ )



(c) Axial velocity normalized by impeller tip speed.

Figure 36.-Continued.

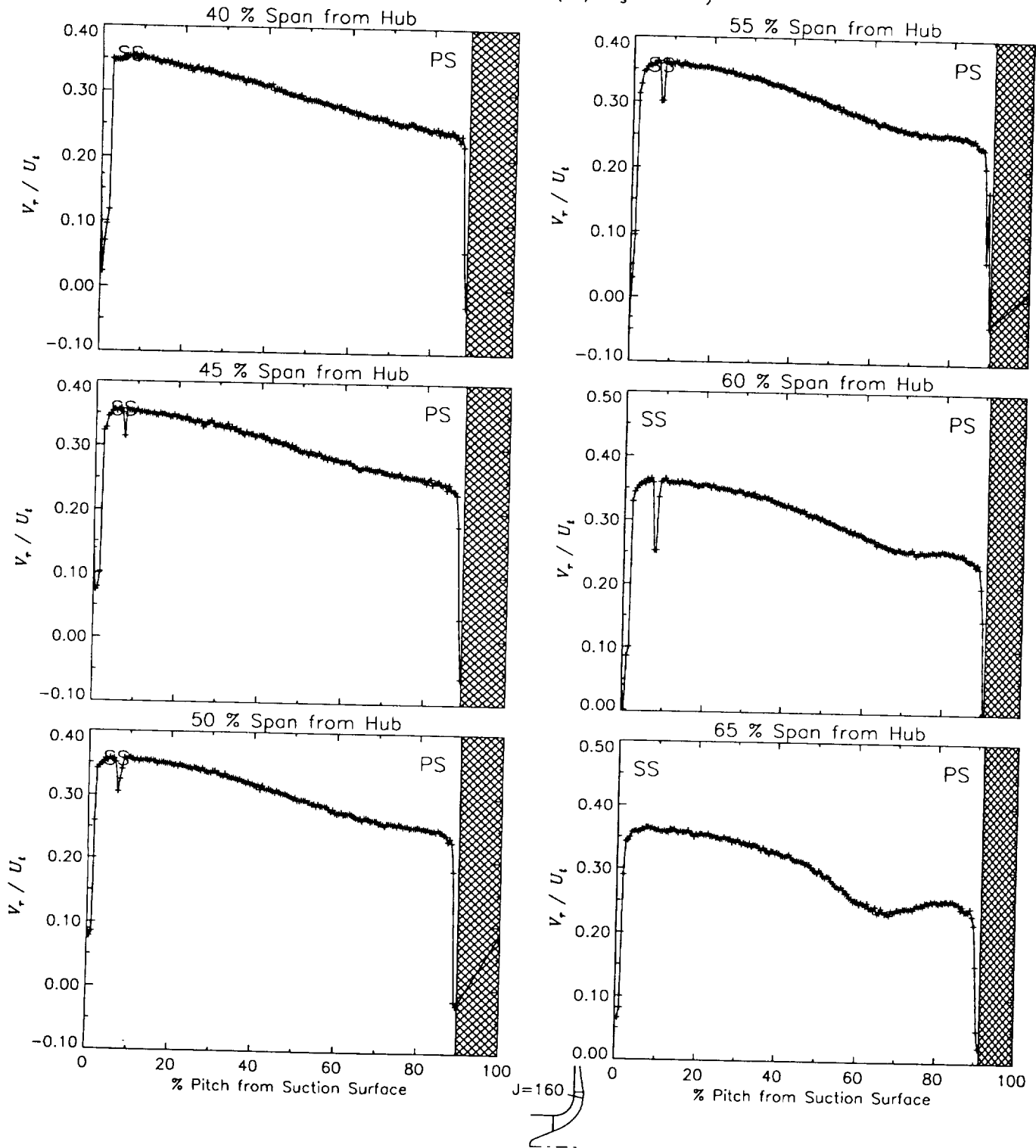
Station J=156, ( $m/m_s=0.852$ )



(c) Axial velocity normalized by impeller tip speed.

Figure 36.—Concluded.

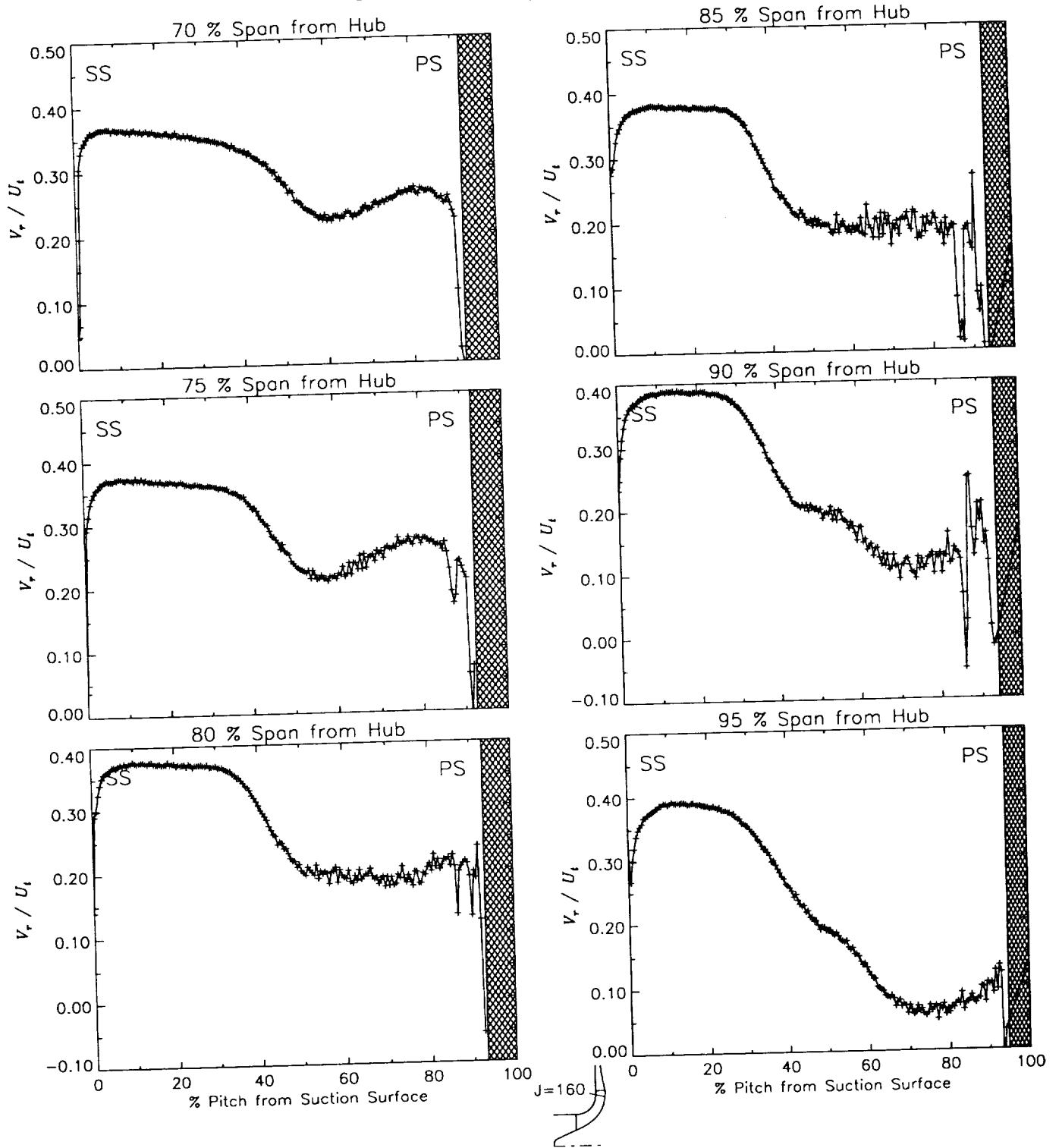
Station J=160, ( $m/m_s=0.891$ )



(a) Radial velocity normalized by impeller tip speed.

Figure 37.—Laser velocimeter results of axial, radial, and relative tangential velocities normalized by impeller tip speed for the design flow condition,  $m_d$ , at station J=160, ( $m/m_s=0.891$ ). The shaded region to the right of each plot represents the physical blade width.

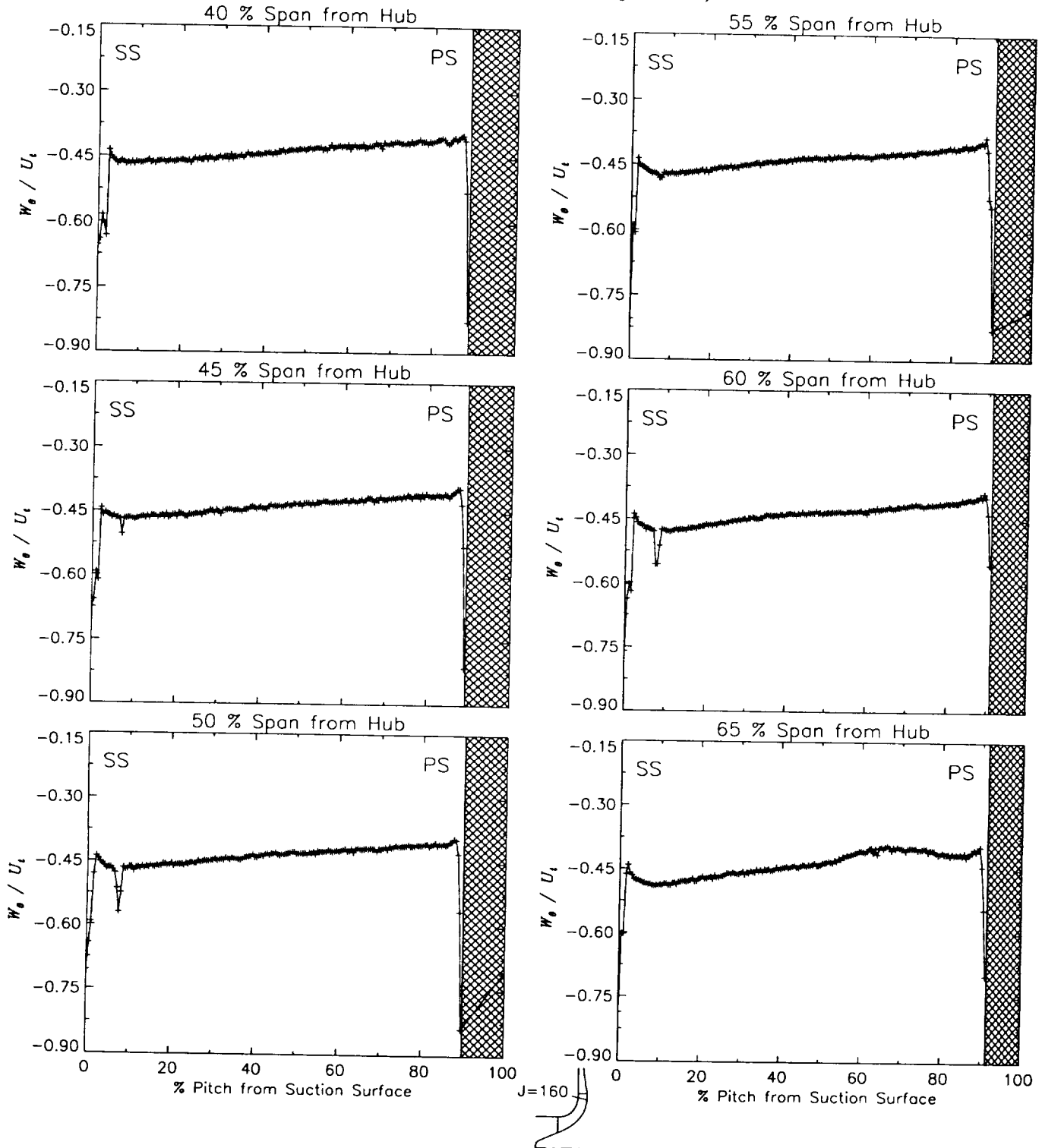
Station J=160, ( $m/m_s=0.891$ )



(a) Radial velocity normalized by impeller tip speed.

Figure 37.-Continued.

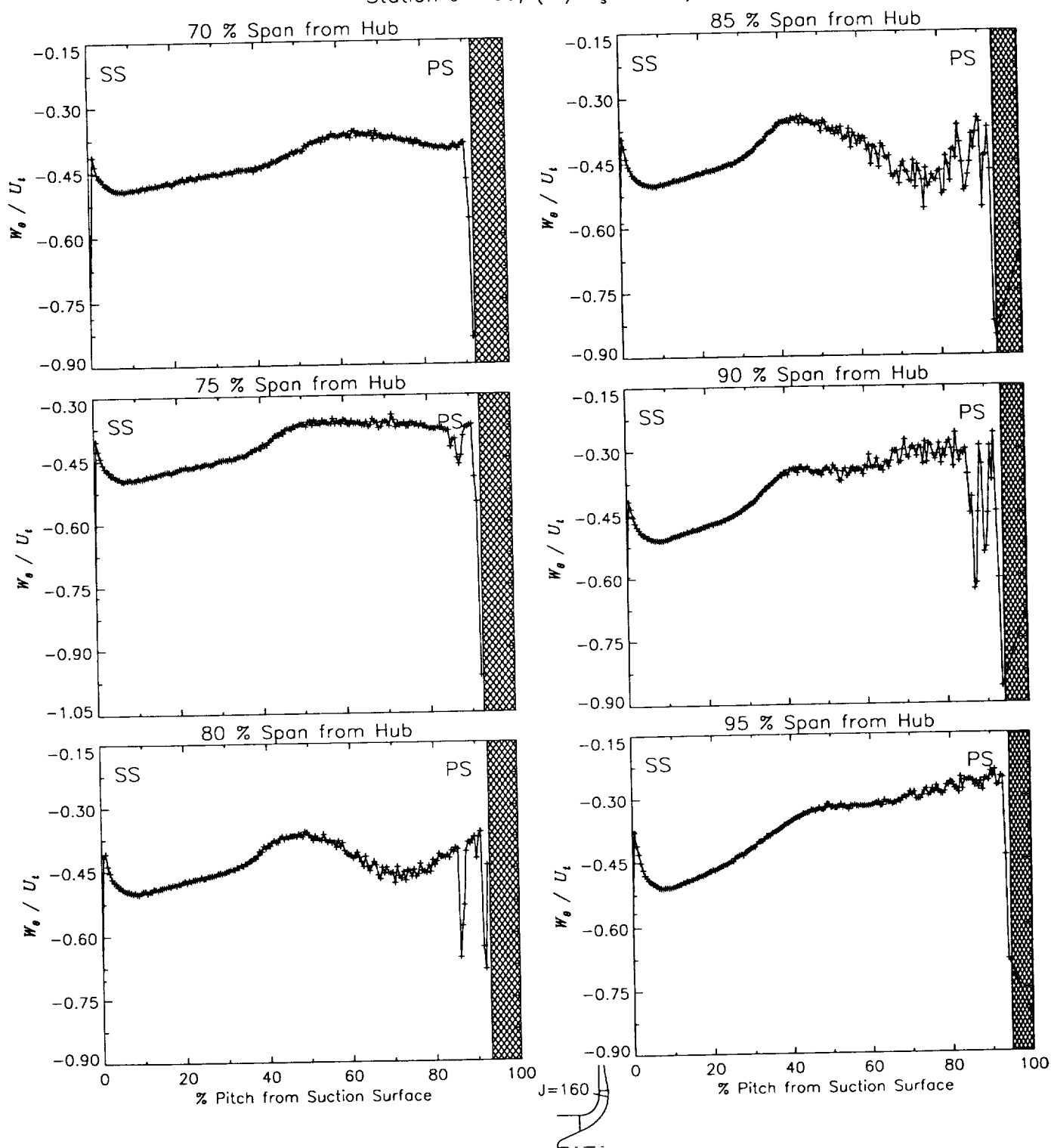
Station J=160, ( $m/m_s=0.891$ )



(b) Relative tangential velocity normalized by impeller tip speed.

Figure 37.-Continued.

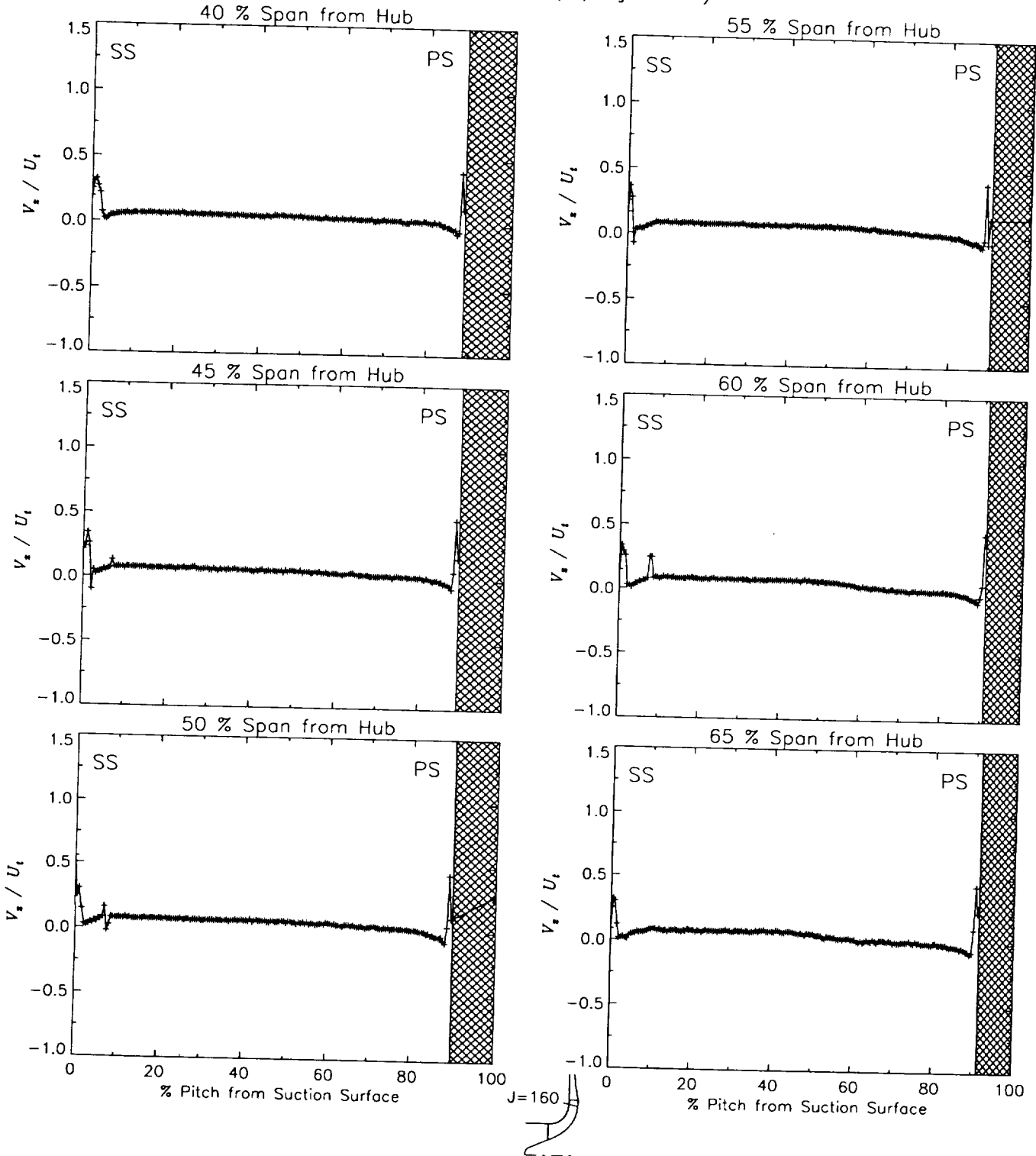
Station J=160, ( $m/m_s=0.891$ )



(b) Relative tangential velocity normalized by impeller tip speed.

Figure 37.-Continued.

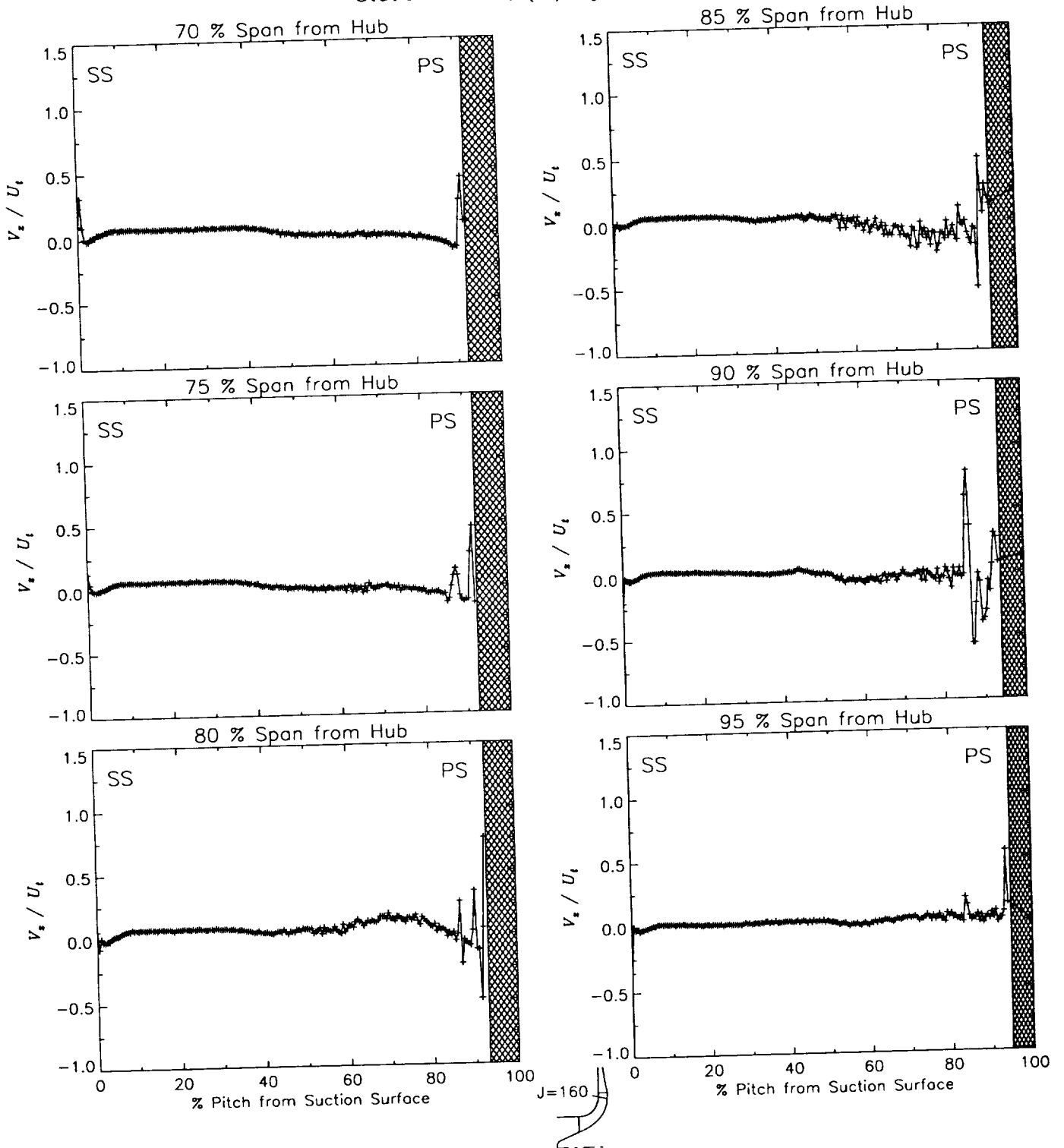
Station J=160, ( $m/m_s=0.891$ )



(c) Axial velocity normalized by impeller tip speed.

Figure 37.-Continued.

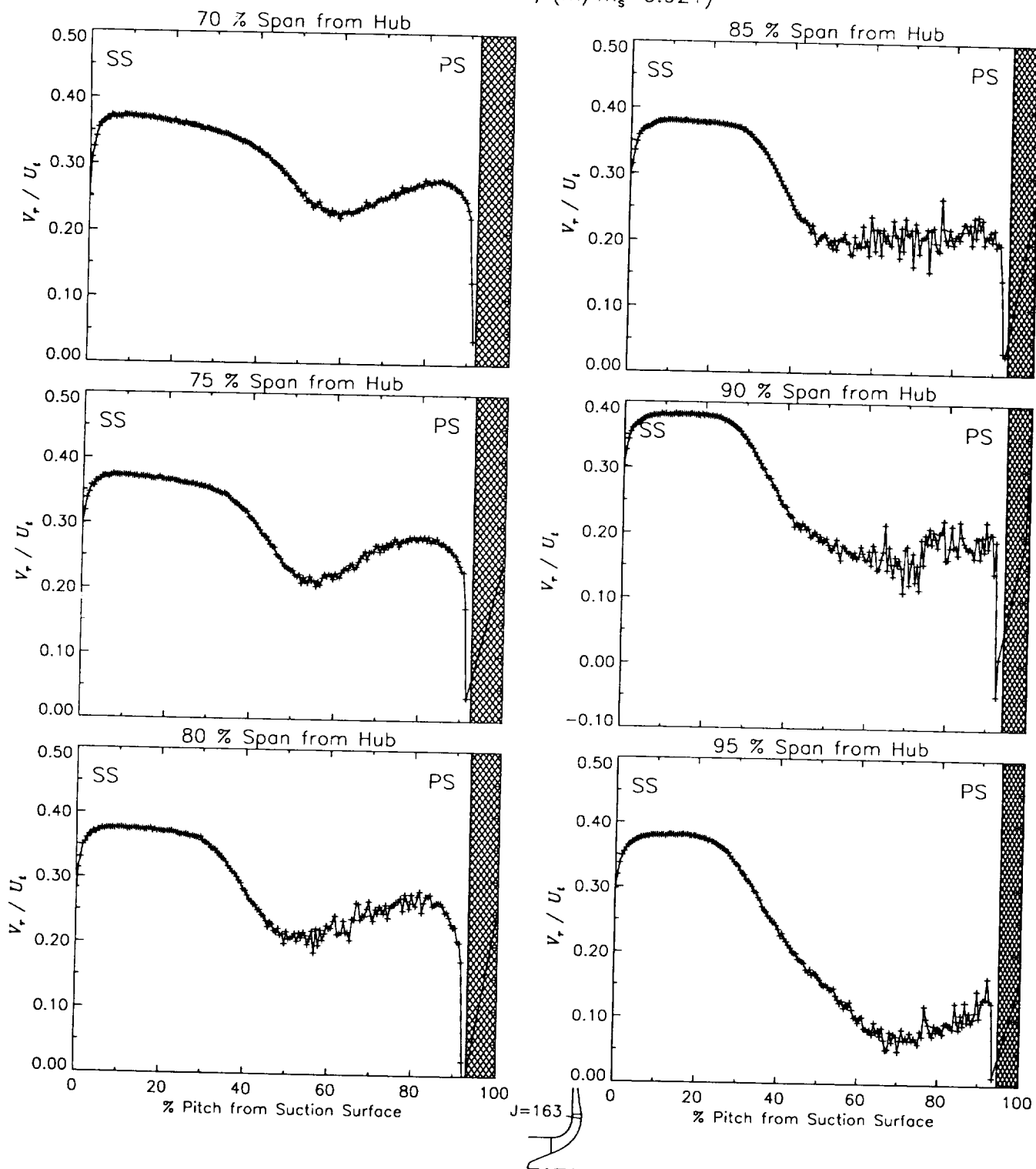
Station J=160, ( $m/m_s=0.891$ )



(c) Axial velocity normalized by impeller tip speed.

Figure 37.-Concluded.

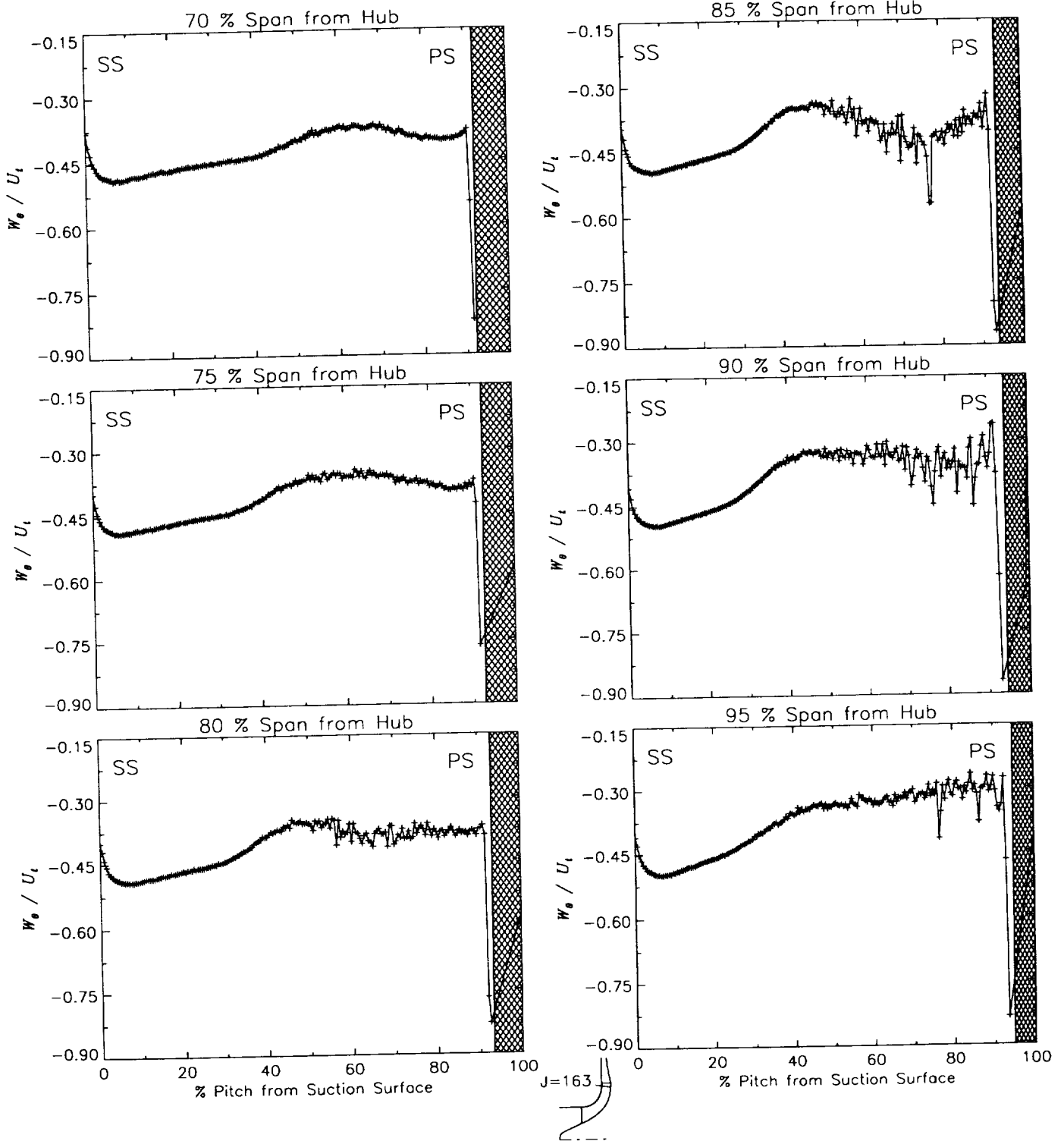
Station J=163, ( $m/m_s=0.921$ )



(a) Radial velocity normalized by impeller tip speed.

Figure 38.—Laser velocimeter results of axial, radial, and relative tangential velocities normalized by impeller tip speed for the design flow condition,  $\dot{m}_d$ , at station J=163, ( $m/m_s=0.921$ ). The shaded region to the right of each plot represents the physical blade width.

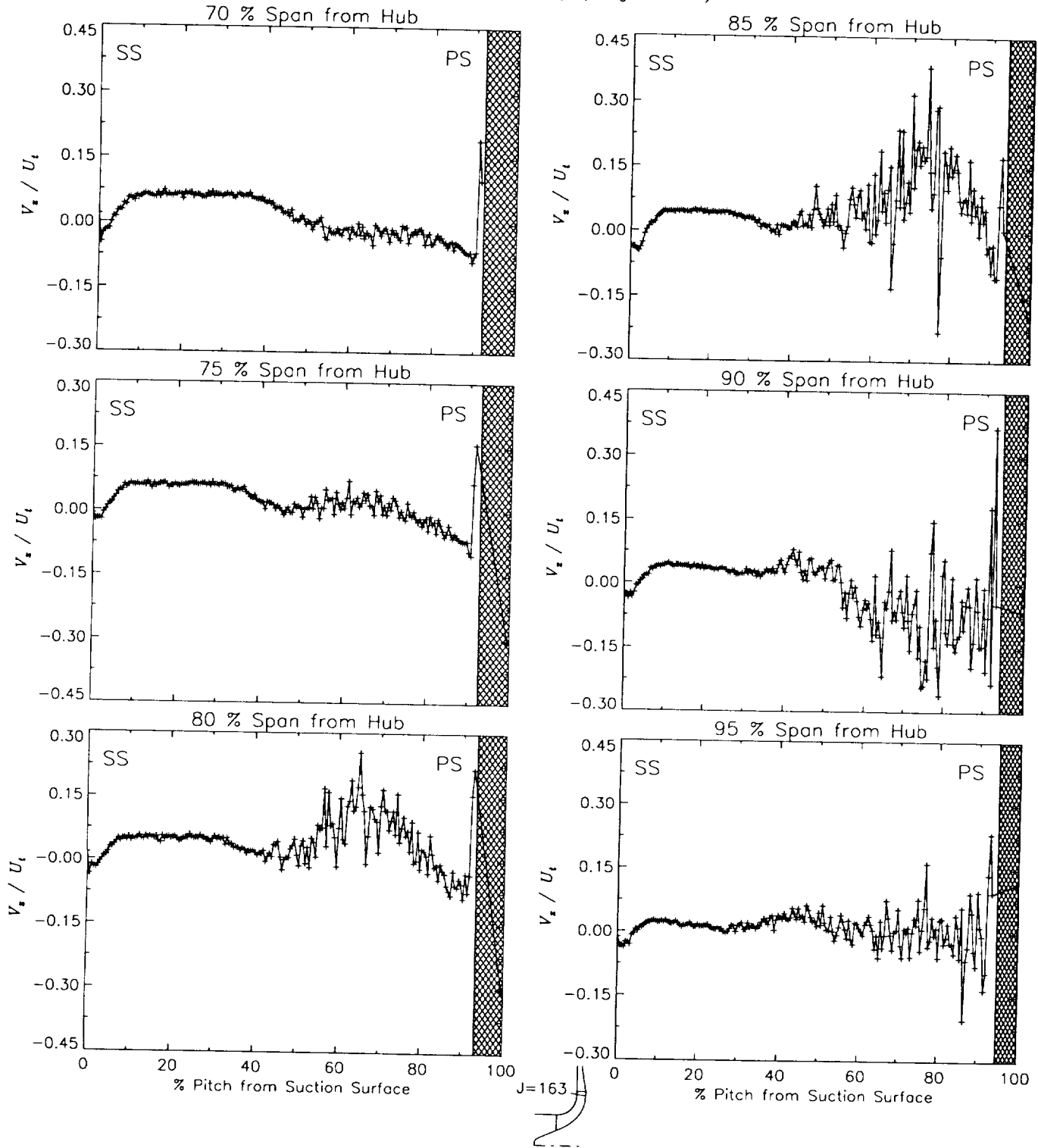
Station J=163, ( $m/m_s=0.921$ )



(b) Relative tangential velocity normalized by impeller tip speed.

Figure 38.—Continued.

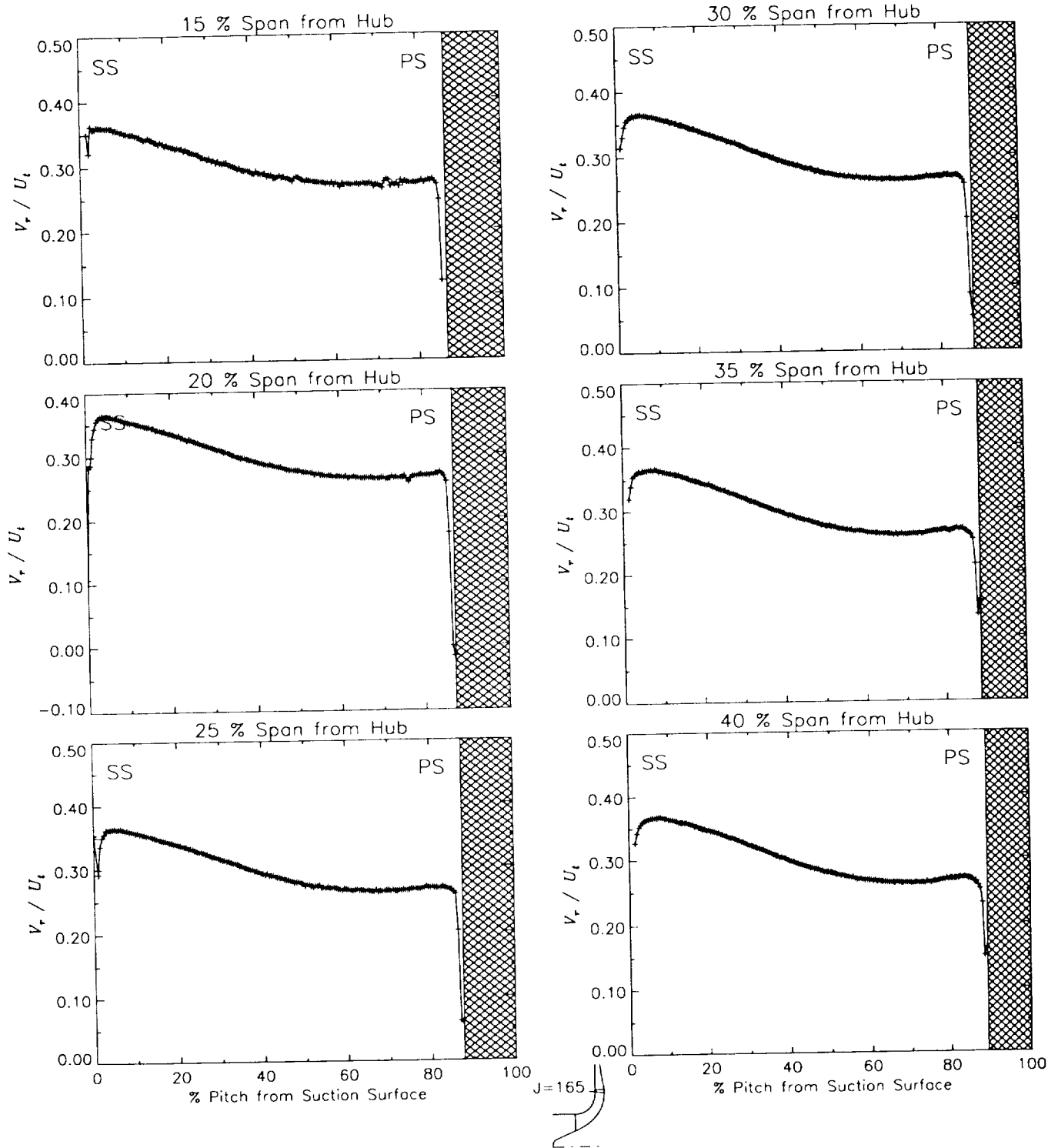
Station J=163, ( $m/m_s=0.921$ )



(c) Axial velocity normalized by impeller tip speed.

Figure 38.—Concluded.

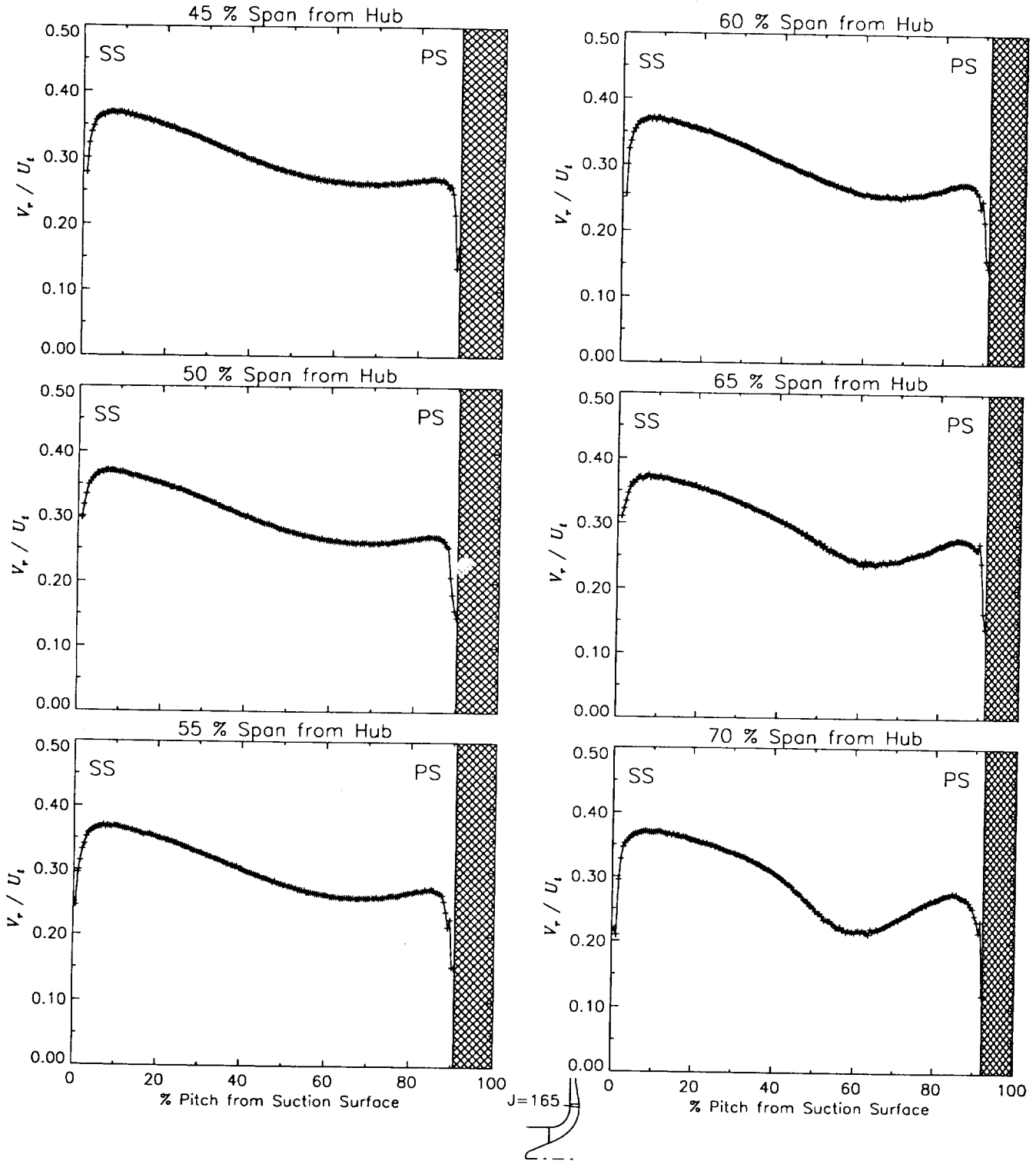
Station J=165, ( $m/m_s=0.941$ )



(a) Radial velocity normalized by impeller tip speed.

Figure 39.—Laser velocimeter results of axial, radial, and relative tangential velocities normalized by impeller tip speed for the design flow condition,  $m_d$ , at station J=165, ( $m/m_s=0.941$ ). The shaded region to the right of each plot represents the physical blade width.

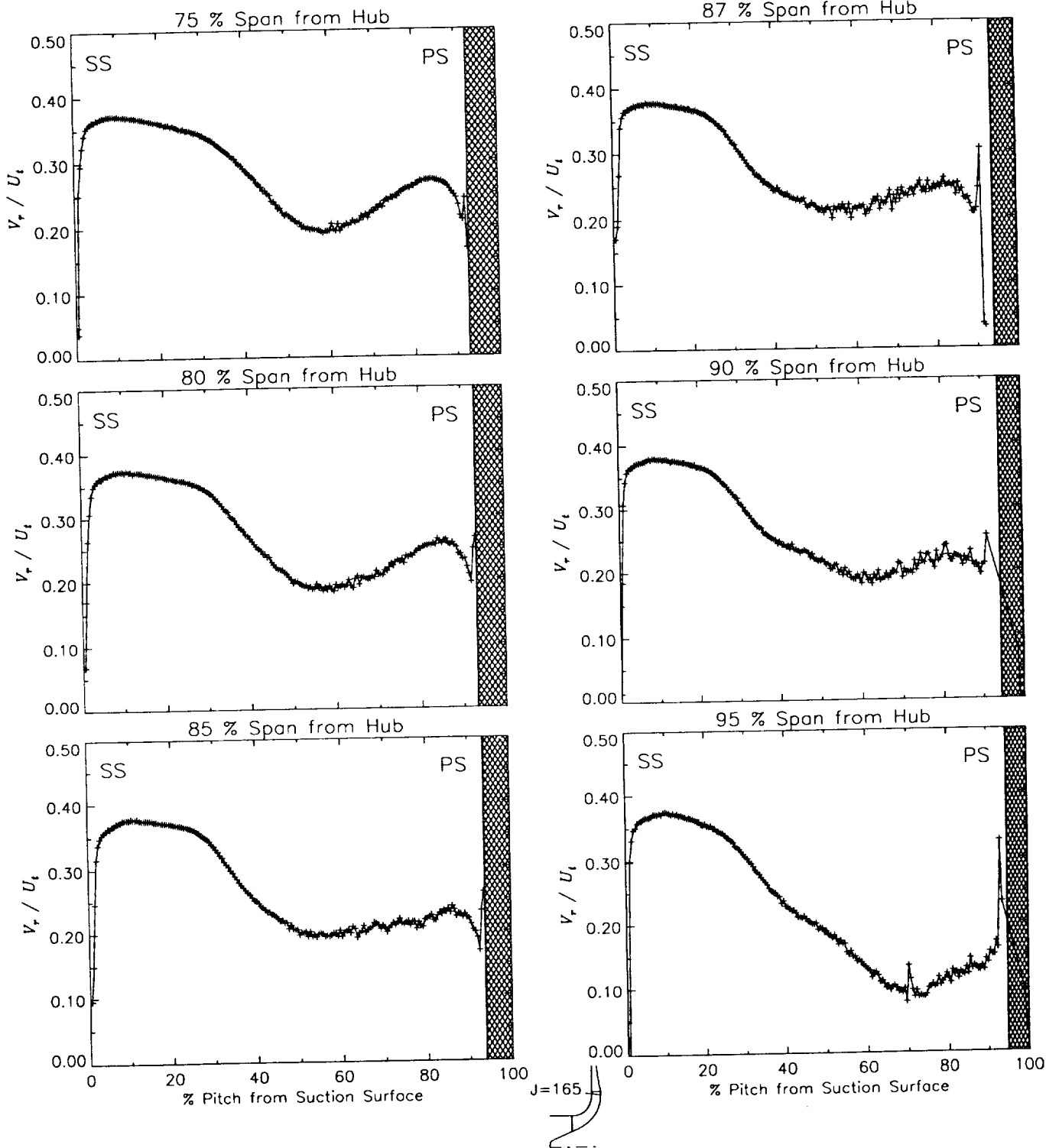
Station J=165, ( $m/m_s=0.941$ )



(a) Radial velocity normalized by impeller tip speed.

Figure 39.—Continued.

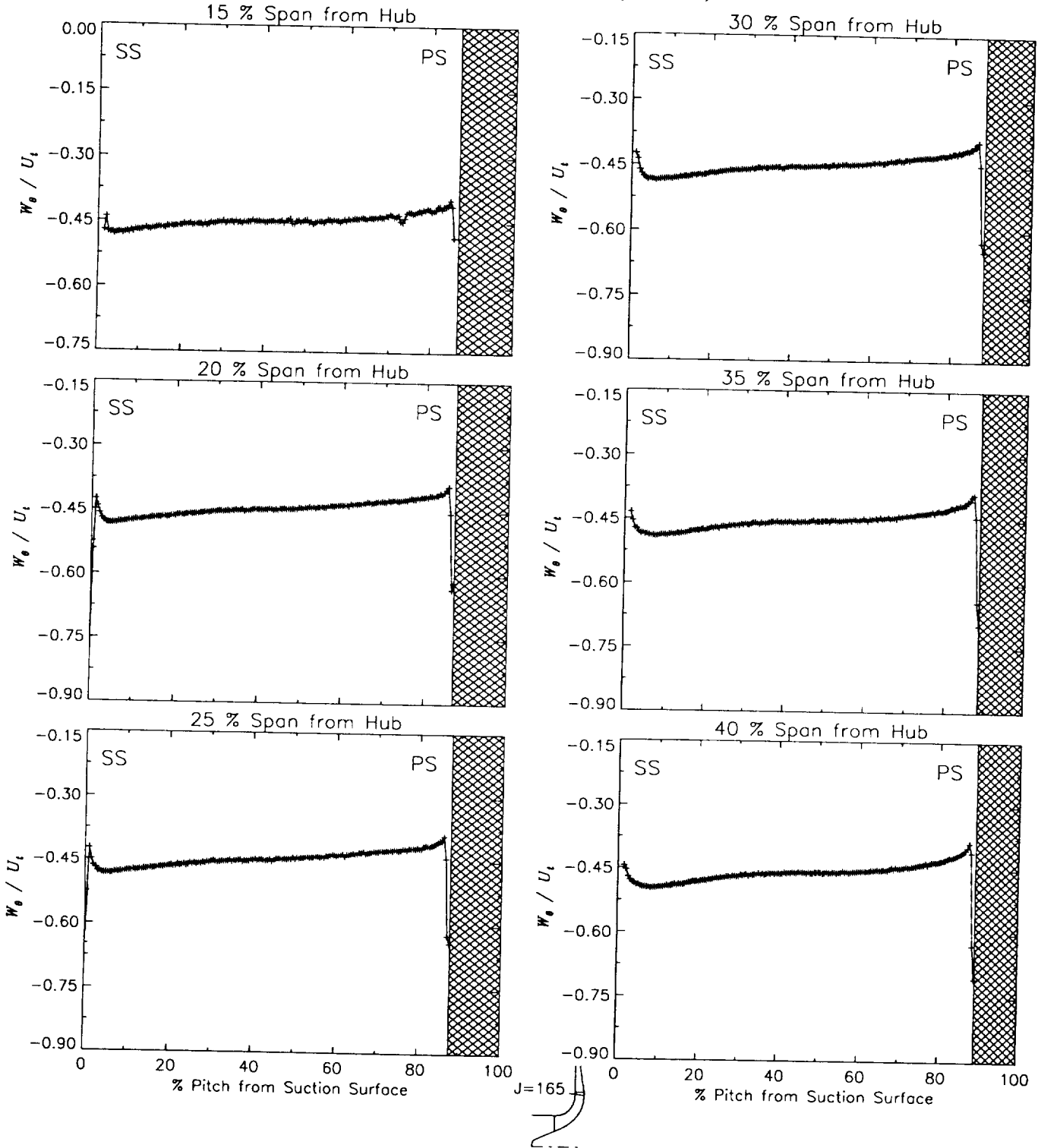
Station J=165, ( $m/m_s=0.941$ )



(a) Radial velocity normalized by impeller tip speed.

Figure 39.—Continued.

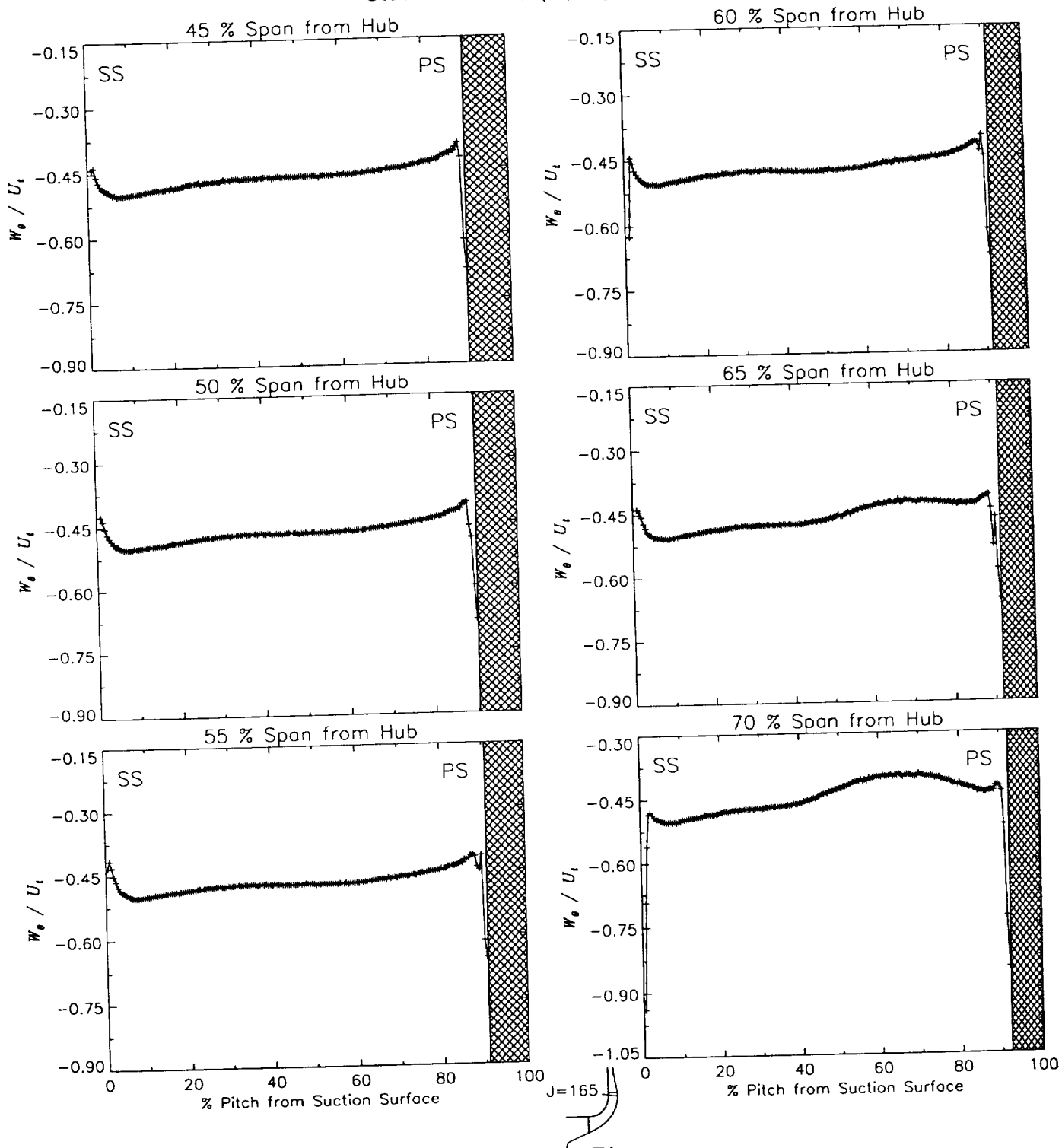
Station J=165, ( $m/m_s=0.941$ )



(b) Relative tangential velocity normalized by impeller tip speed.

Figure 39.—Continued.

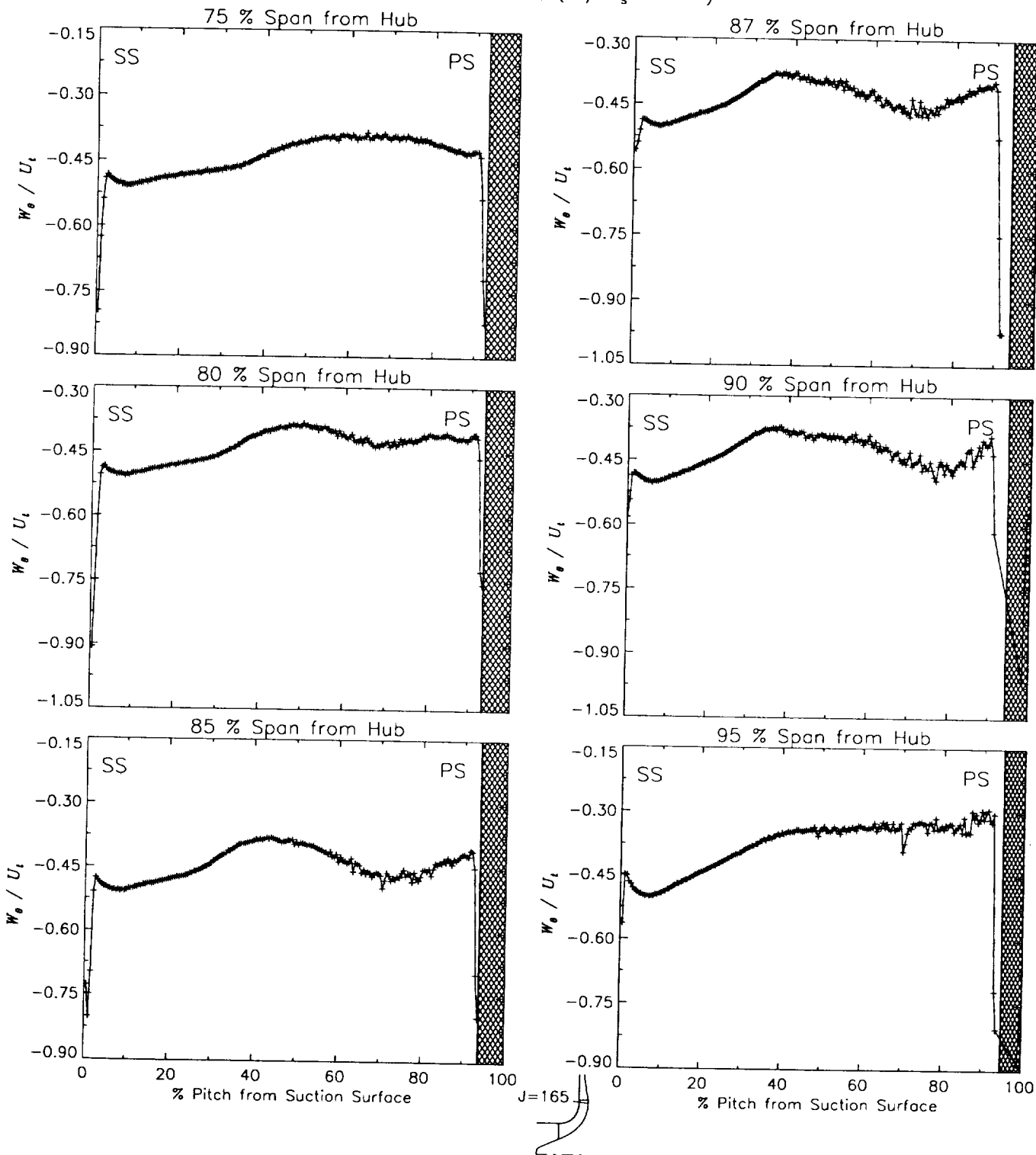
Station J=165, ( $m/m_s=0.941$ )



(b) Relative tangential velocity normalized by impeller tip speed.

Figure 39.-Continued.

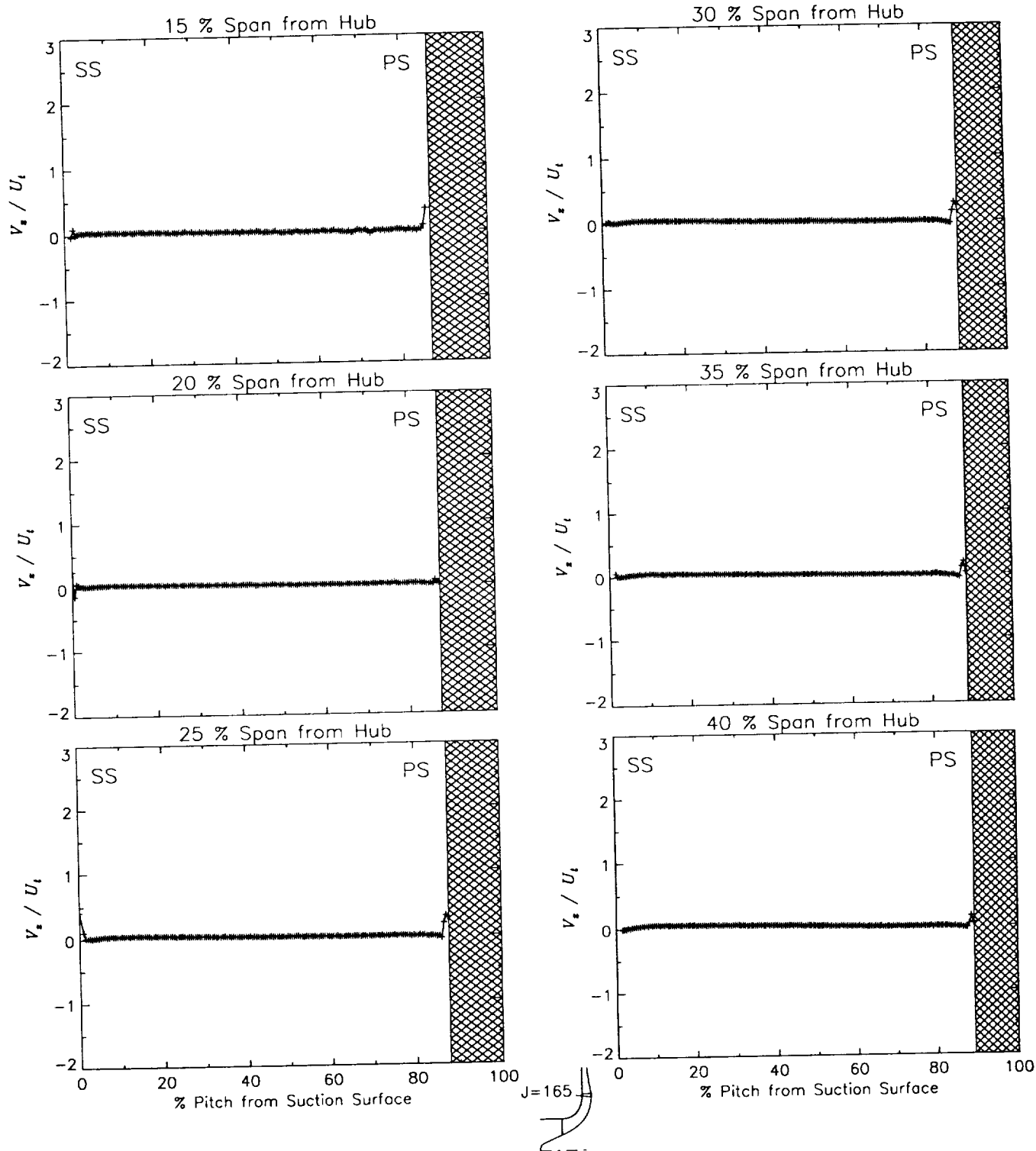
Station J=165, ( $m/m_s=0.941$ )



(b) Relative tangential velocity normalized by impeller tip speed.

Figure 39.-Continued.

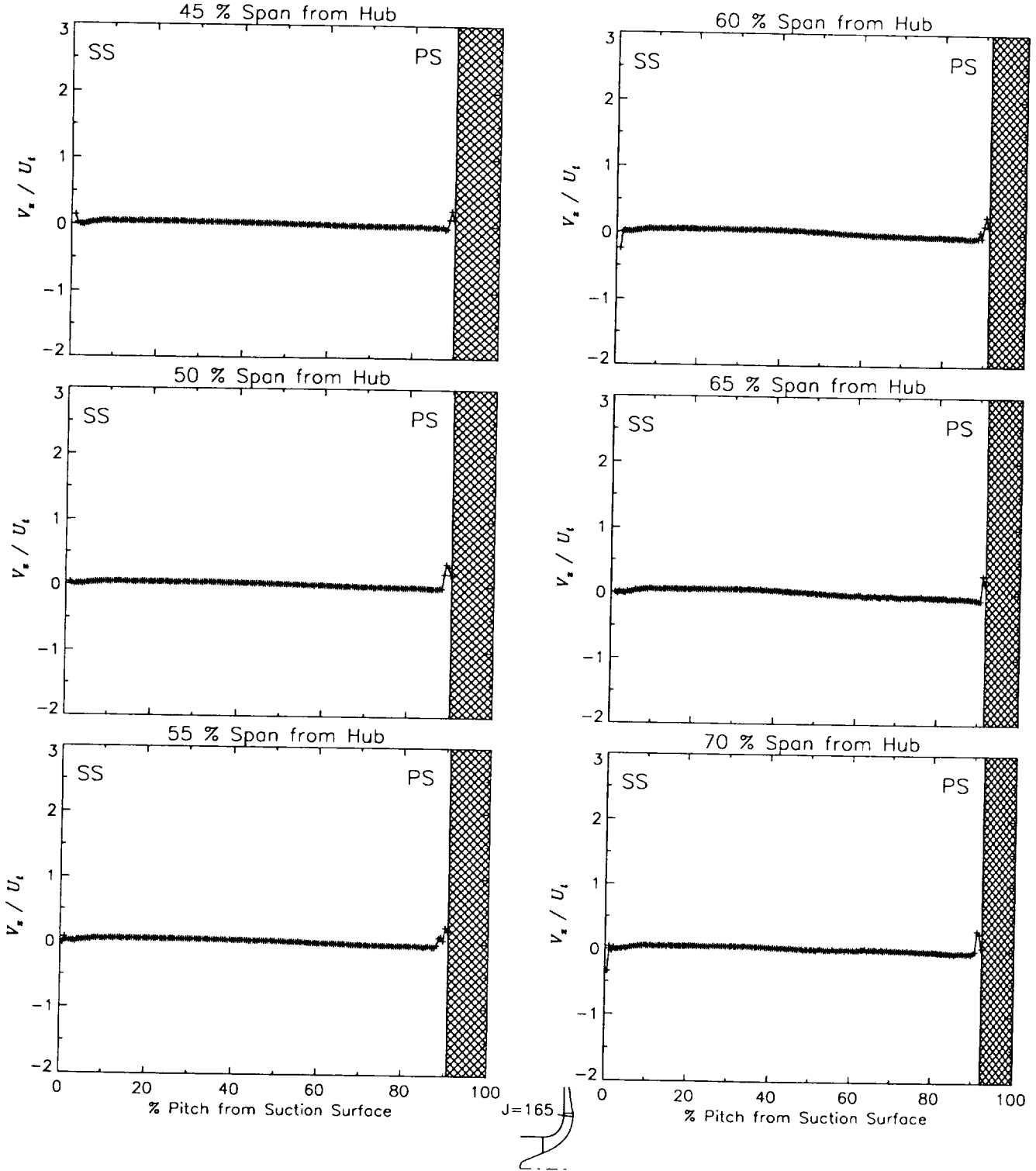
Station J=165, ( $m/m_s=0.941$ )



(c) Axial velocity normalized by impeller tip speed.

Figure 39.—Continued.

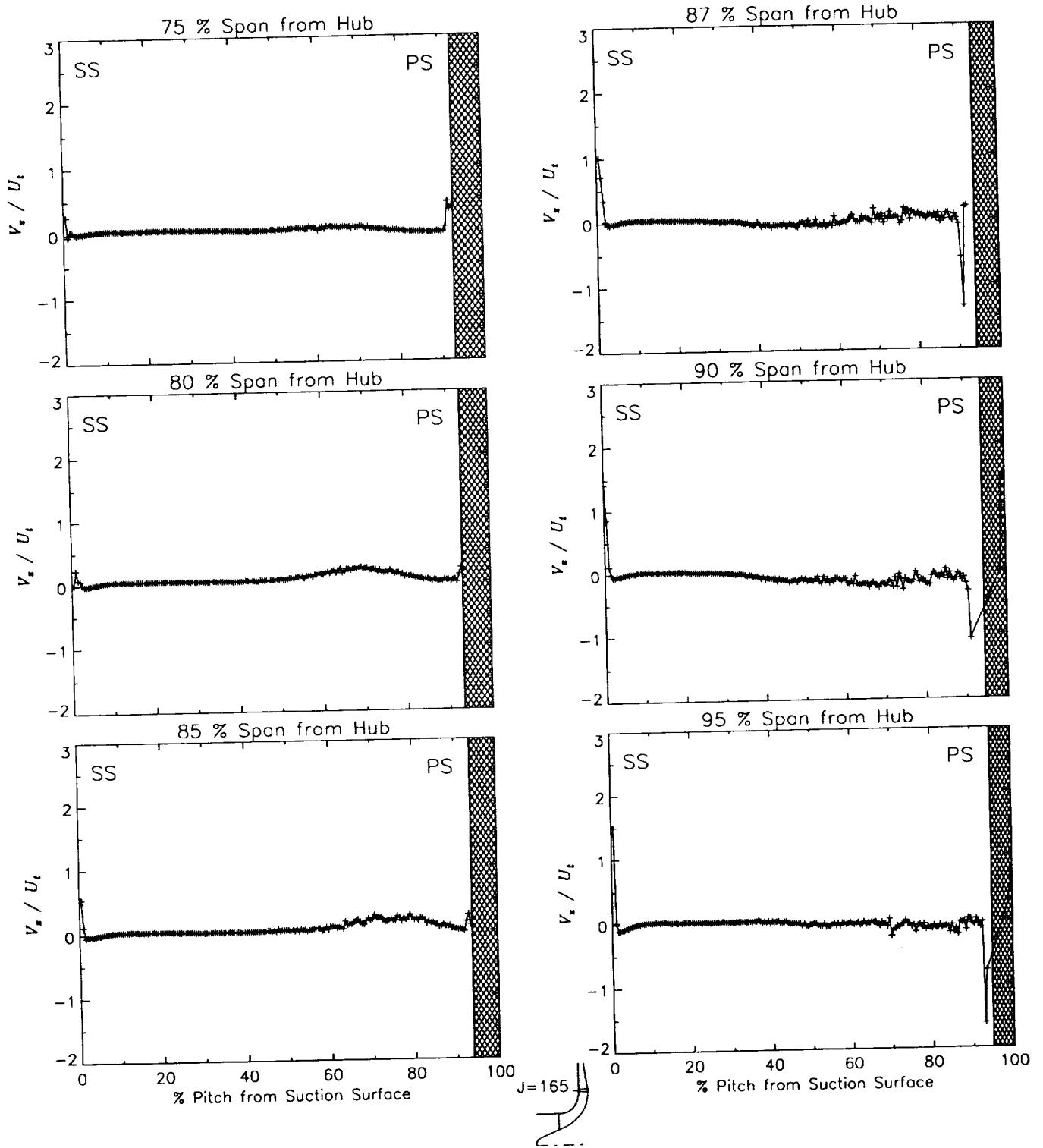
Station J=165, ( $m/m_s=0.941$ )



(c) Axial velocity normalized by impeller tip speed.

Figure 39.-Continued.

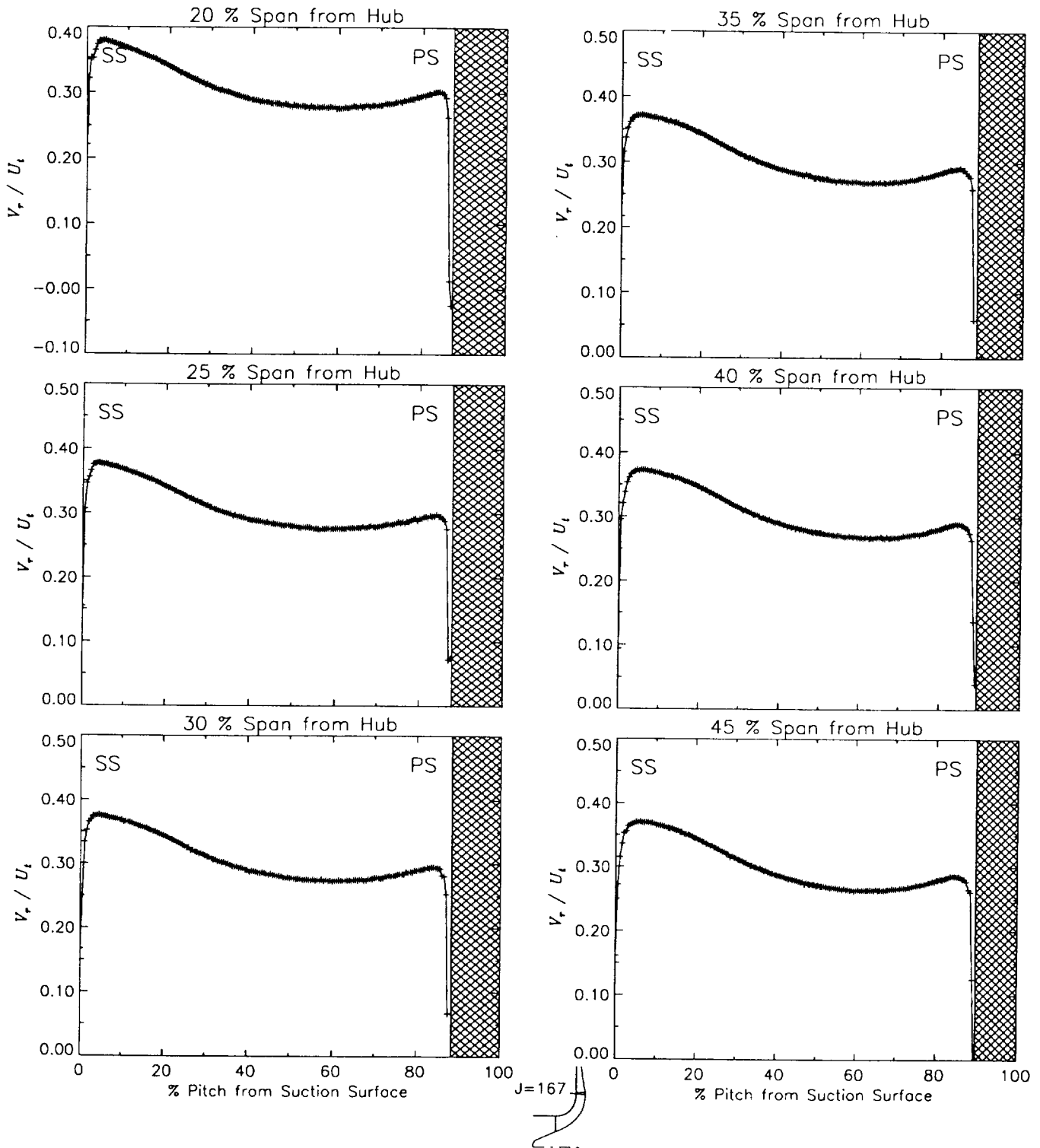
Station J=165, ( $m/m_s=0.941$ )



(c) Axial velocity normalized by impeller tip speed.

Figure 39.-Concluded.

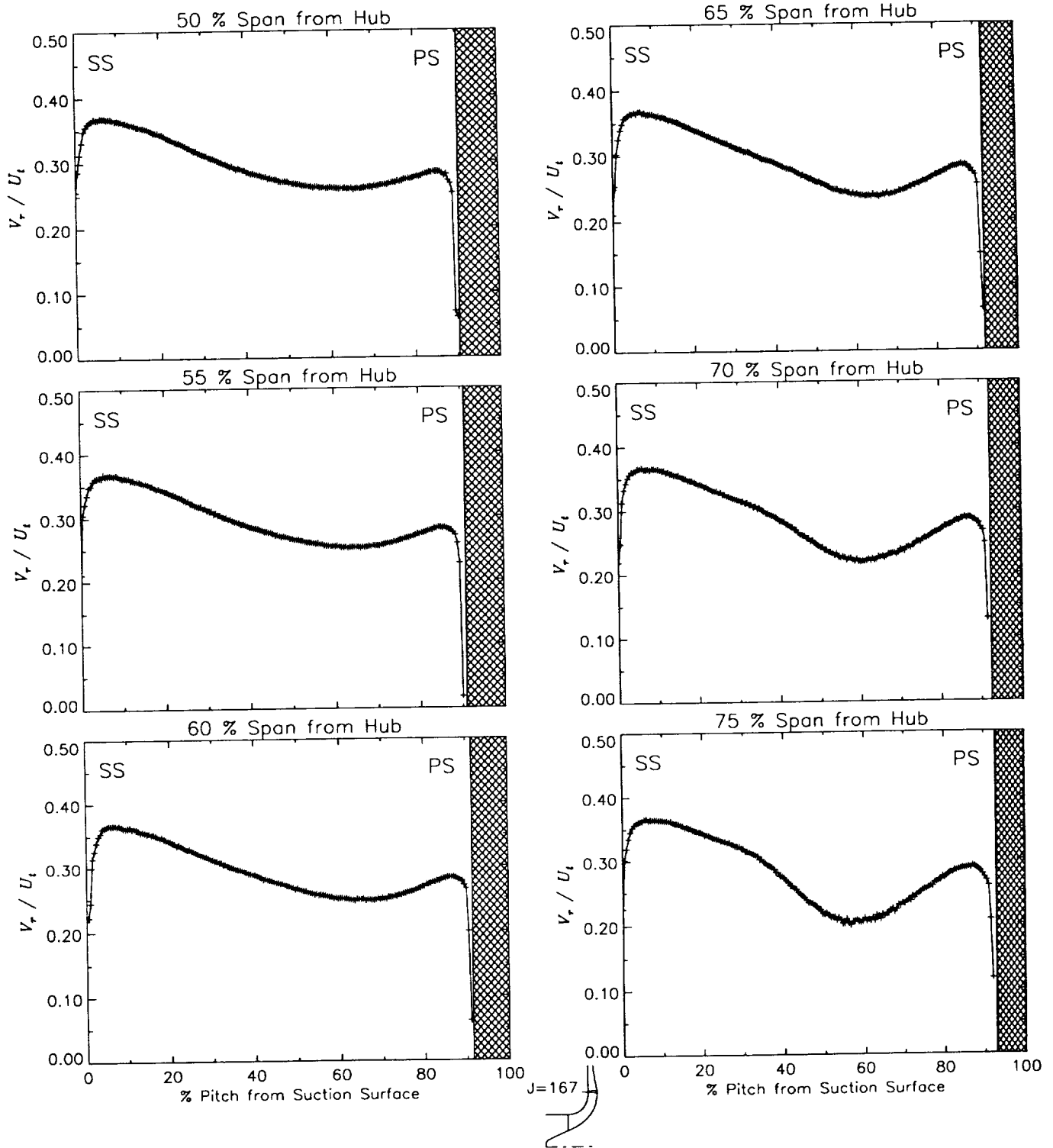
Station J=167, ( $m/m_s=0.960$ )



(a) Radial velocity normalized by impeller tip speed.

Figure 40.-Laser velocimeter results of axial, radial, and relative tangential velocities normalized by impeller tip speed for the design flow condition,  $m_d$ , at station J=167, ( $m/m_s=0.960$ ). The shaded region to the right of each plot represents the physical blade width.

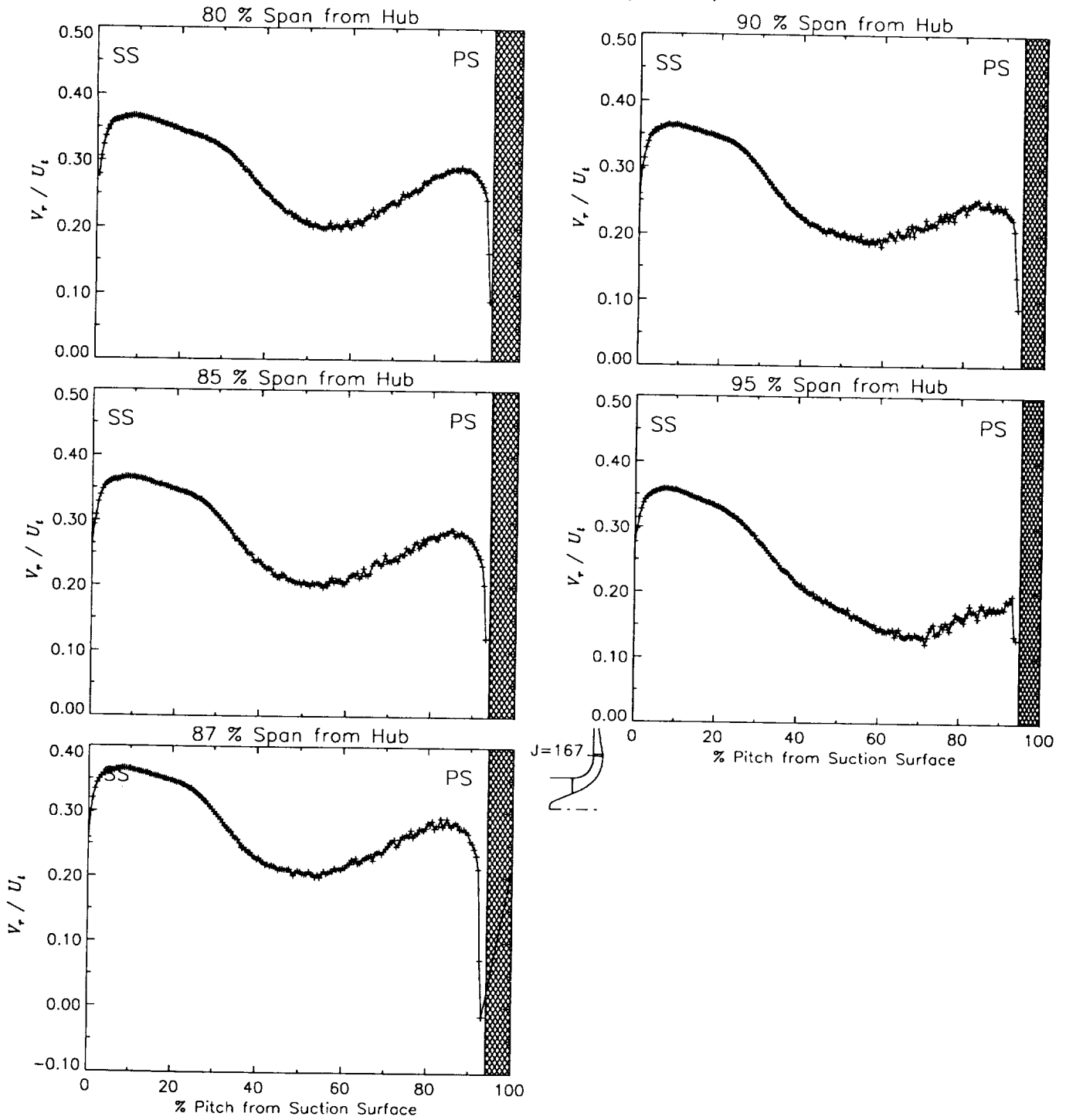
Station J=167, ( $m/m_s=0.960$ )



(a) Radial velocity normalized by impeller tip speed.

Figure 40.—Continued.

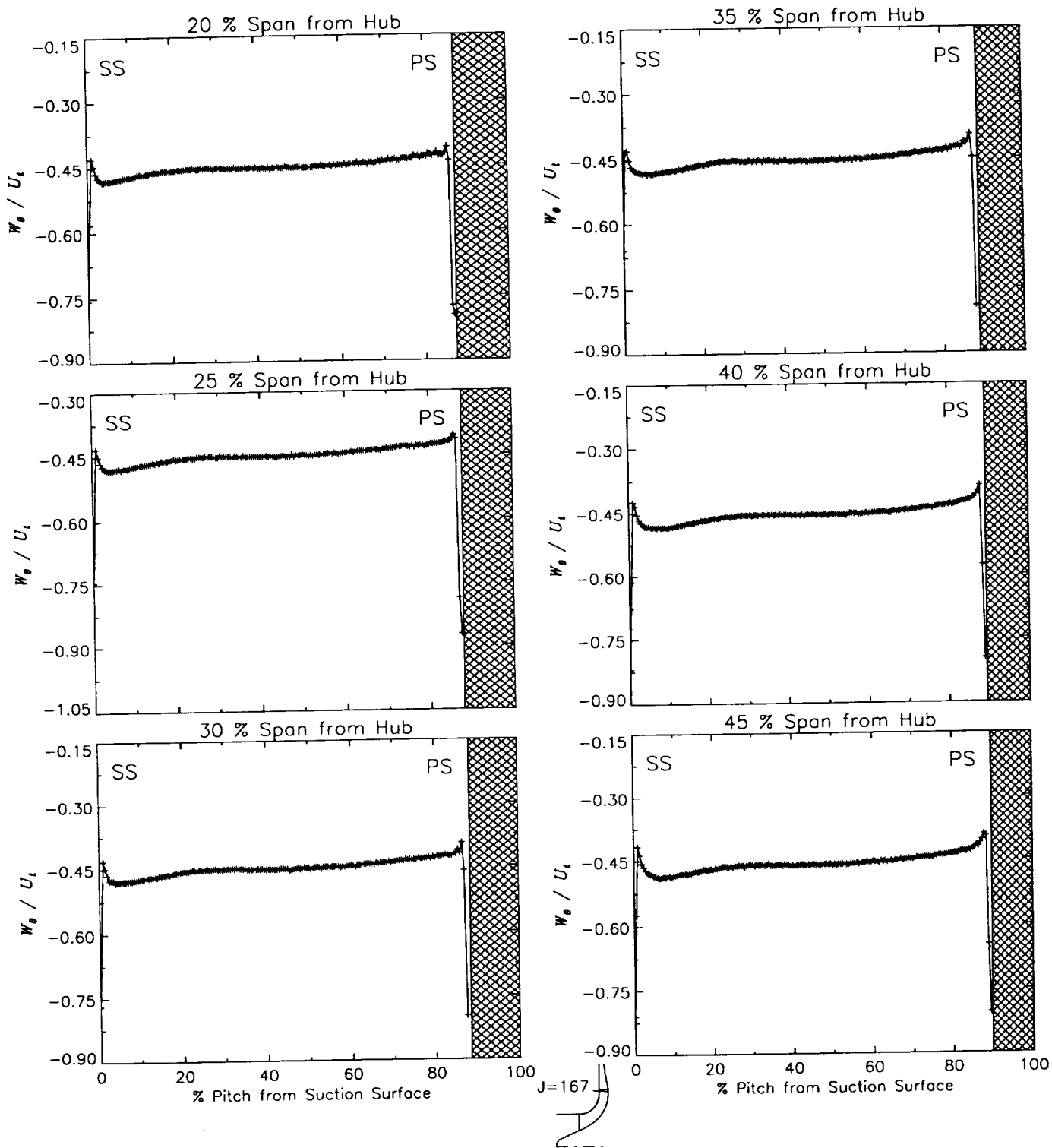
Station J=167, ( $m/m_s=0.960$ )



(a) Radial velocity normalized by impeller tip speed.

Figure 40.—Continued.

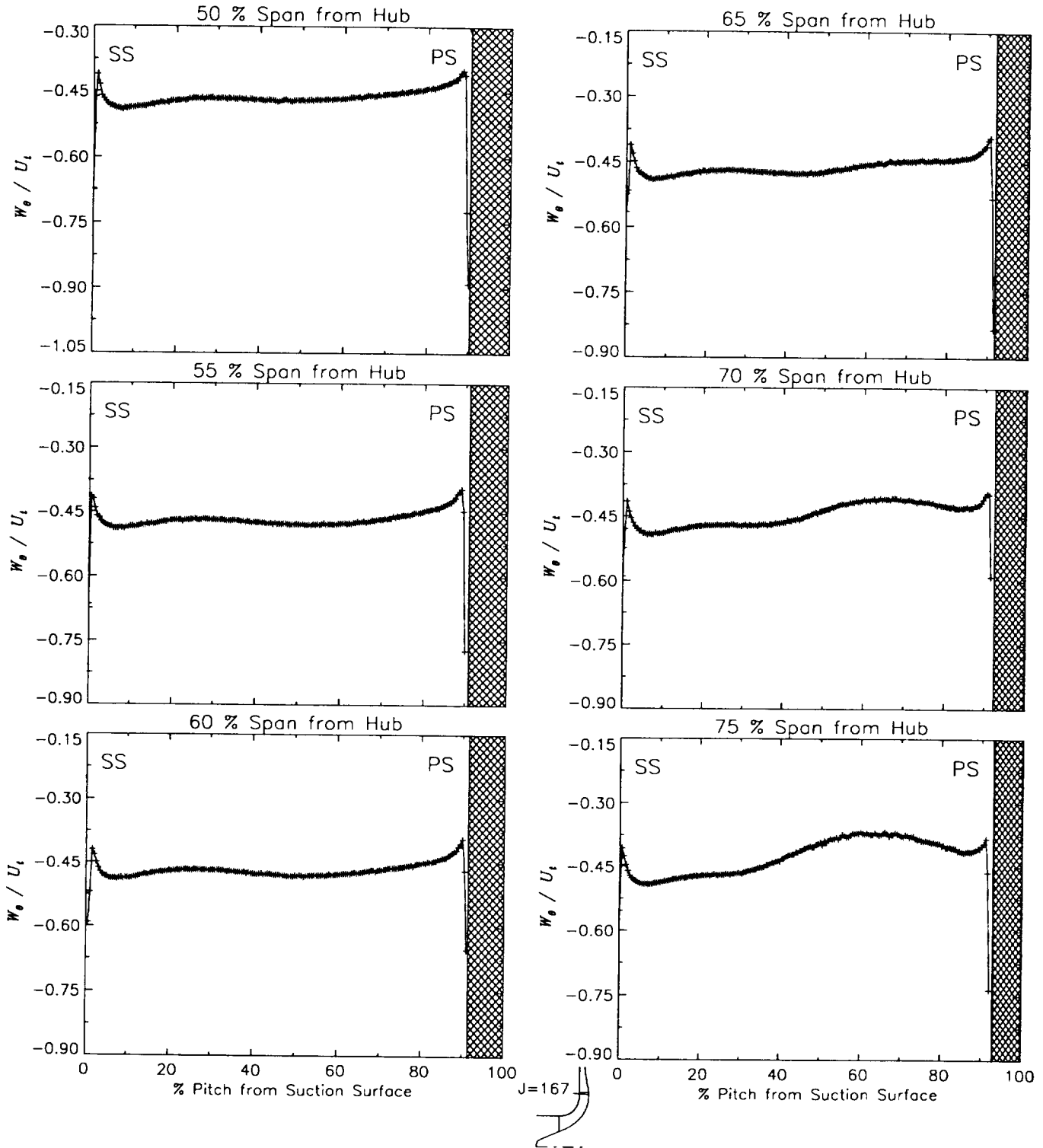
Station J=167, ( $m/m_s=0.960$ )



(b) Relative tangential velocity normalized by impeller tip speed.

Figure 40.-Continued.

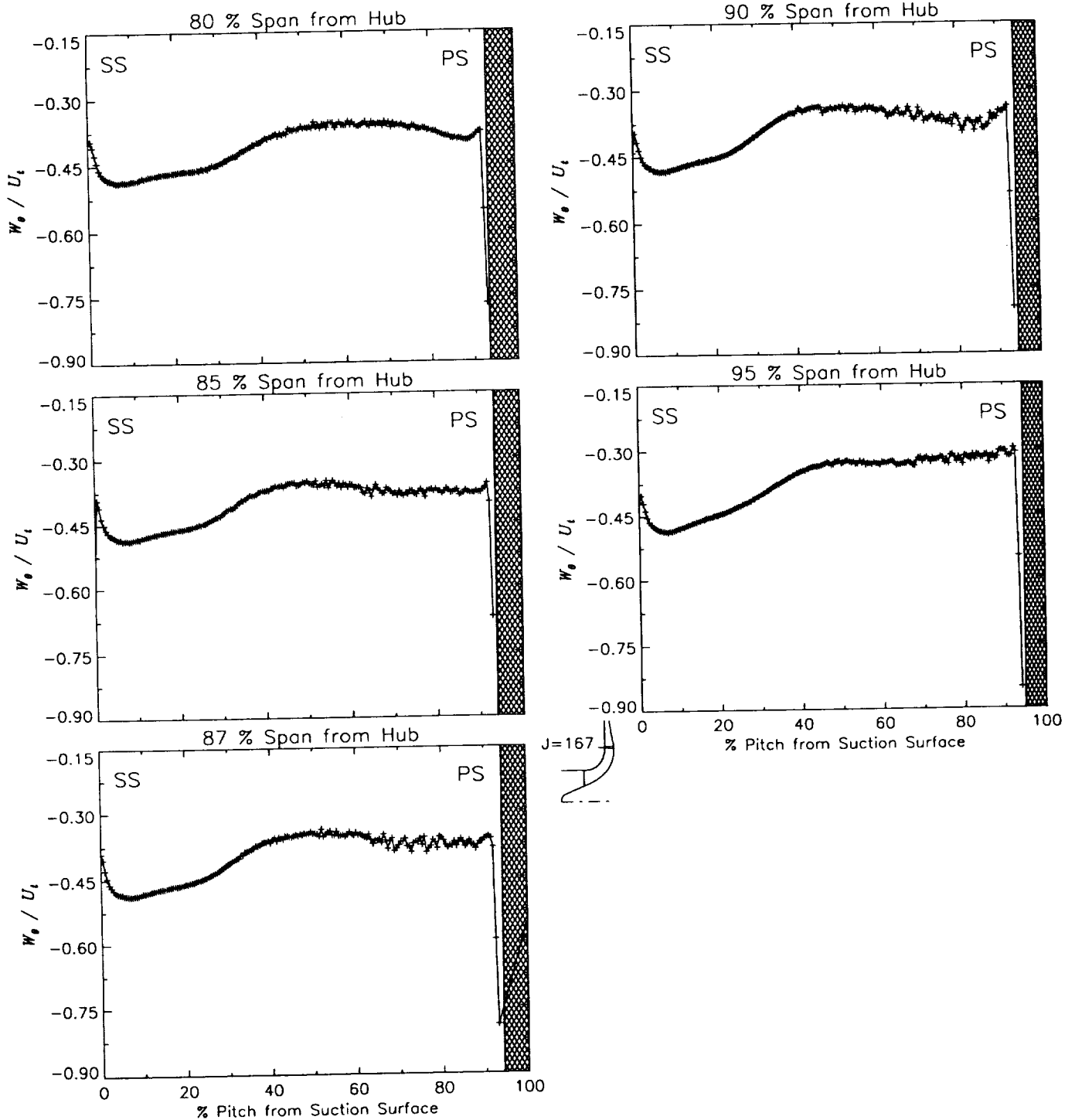
Station J=167, ( $m/m_s=0.960$ )



(b) Relative tangential velocity normalized by impeller tip speed.

Figure 40.-Continued.

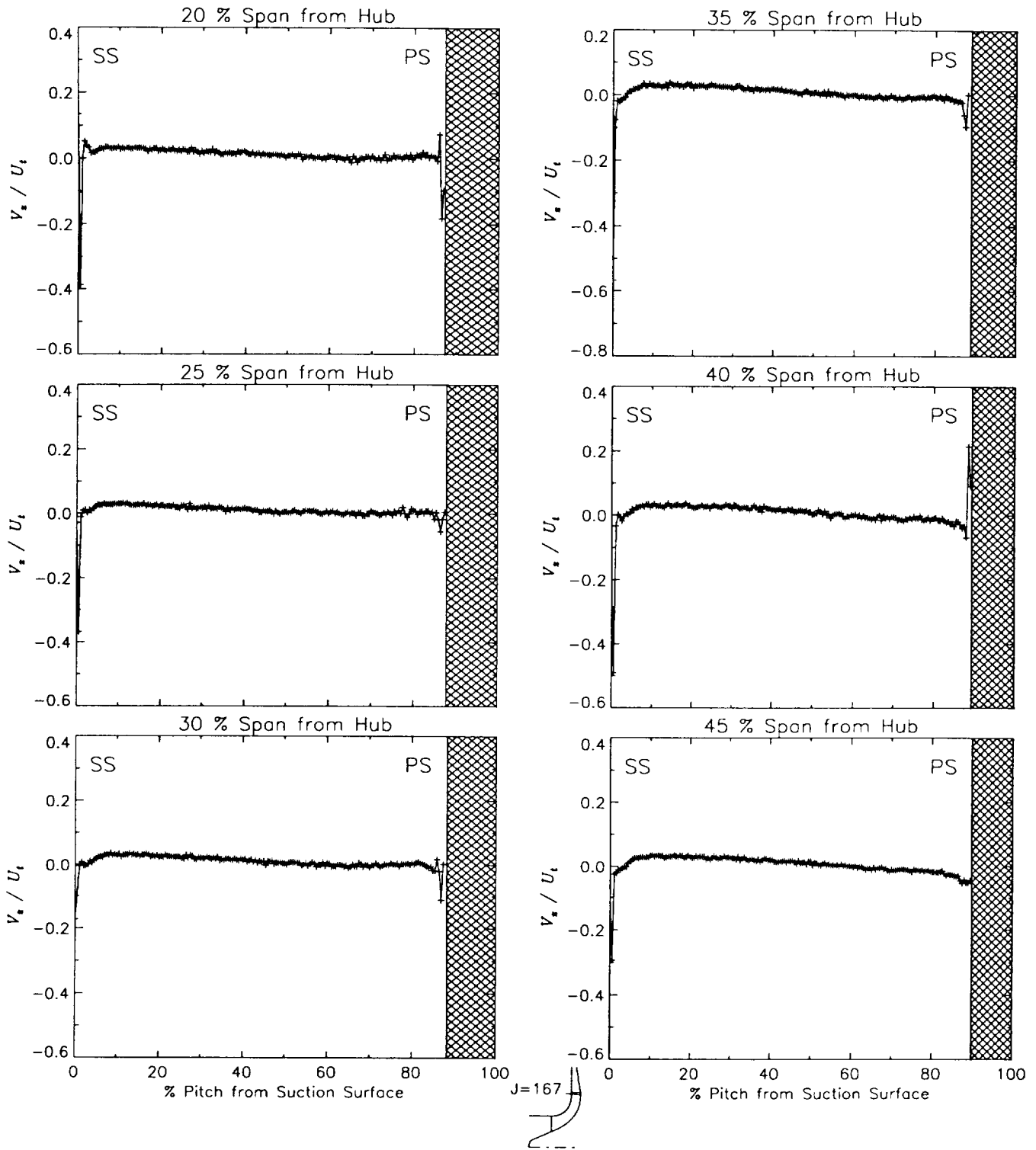
Station J=167, ( $m/m_s=0.960$ )



(b) Relative tangential velocity normalized by impeller tip speed.

Figure 40.-Continued.

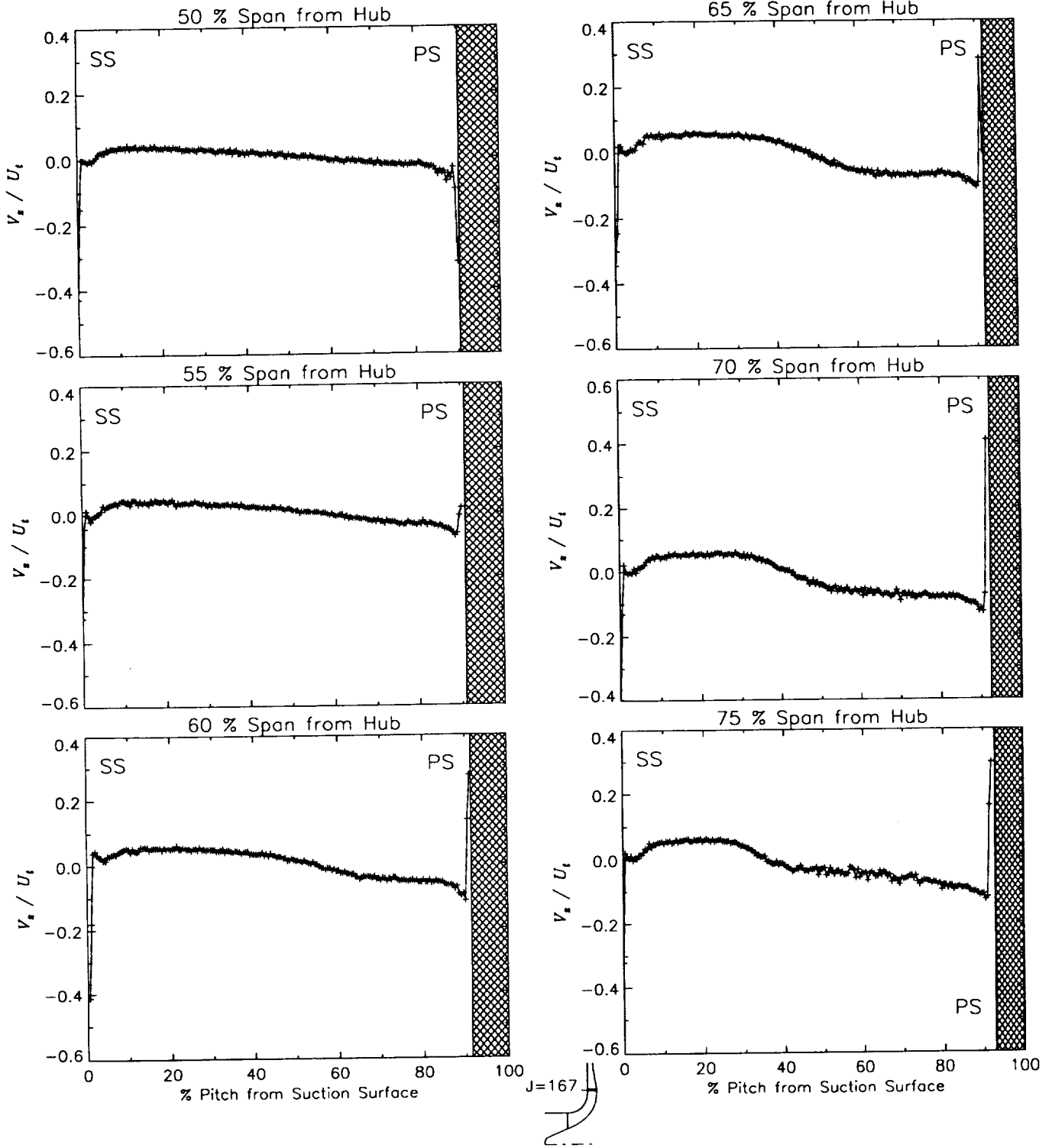
Station J=167, ( $m/m_s=0.960$ )



(c) Axial velocity normalized by impeller tip speed.

Figure 40.—Continued.

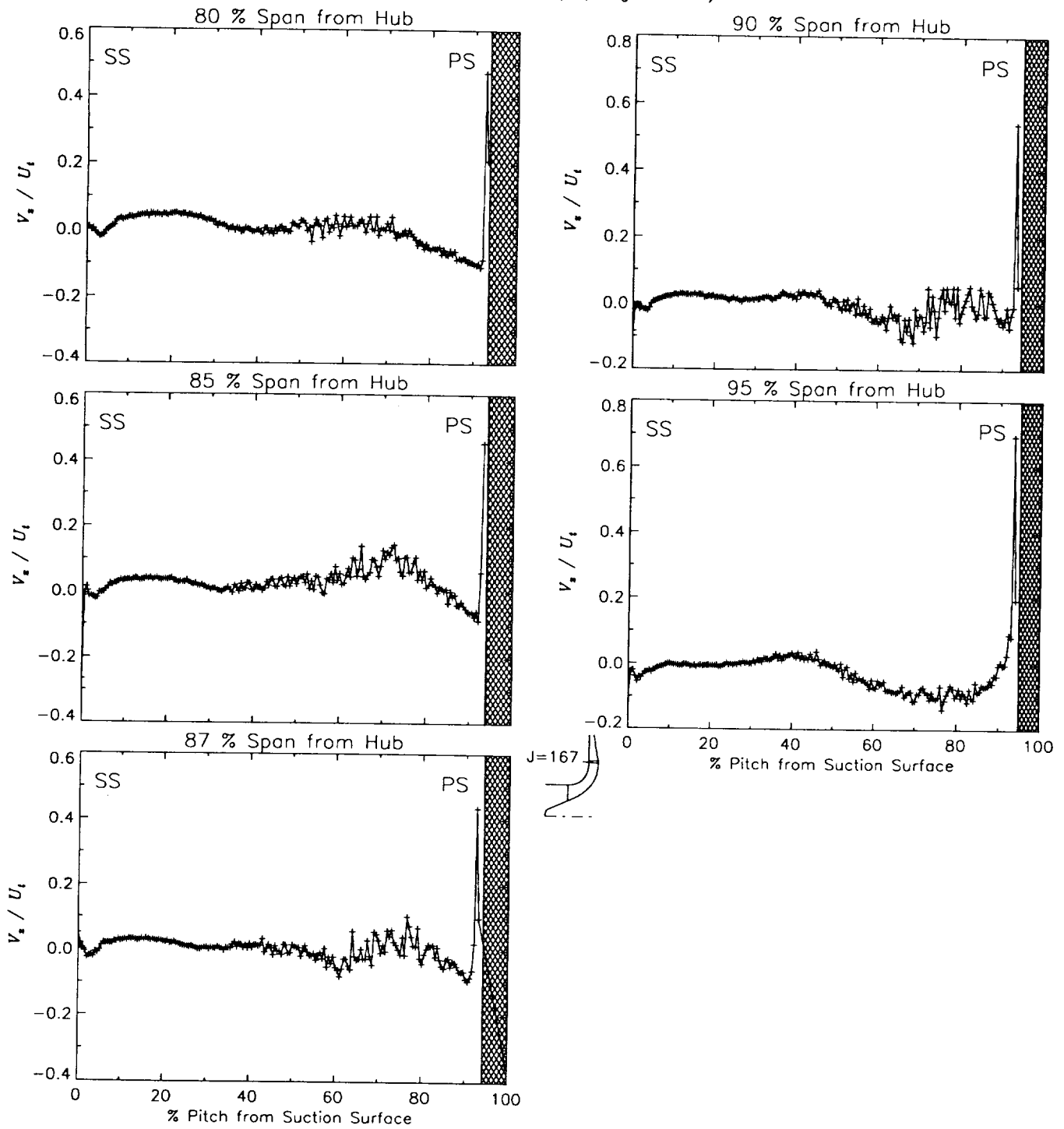
Station J=167, ( $m/m_s=0.960$ )



(c) Axial velocity normalized by impeller tip speed.

Figure 40.-Continued.

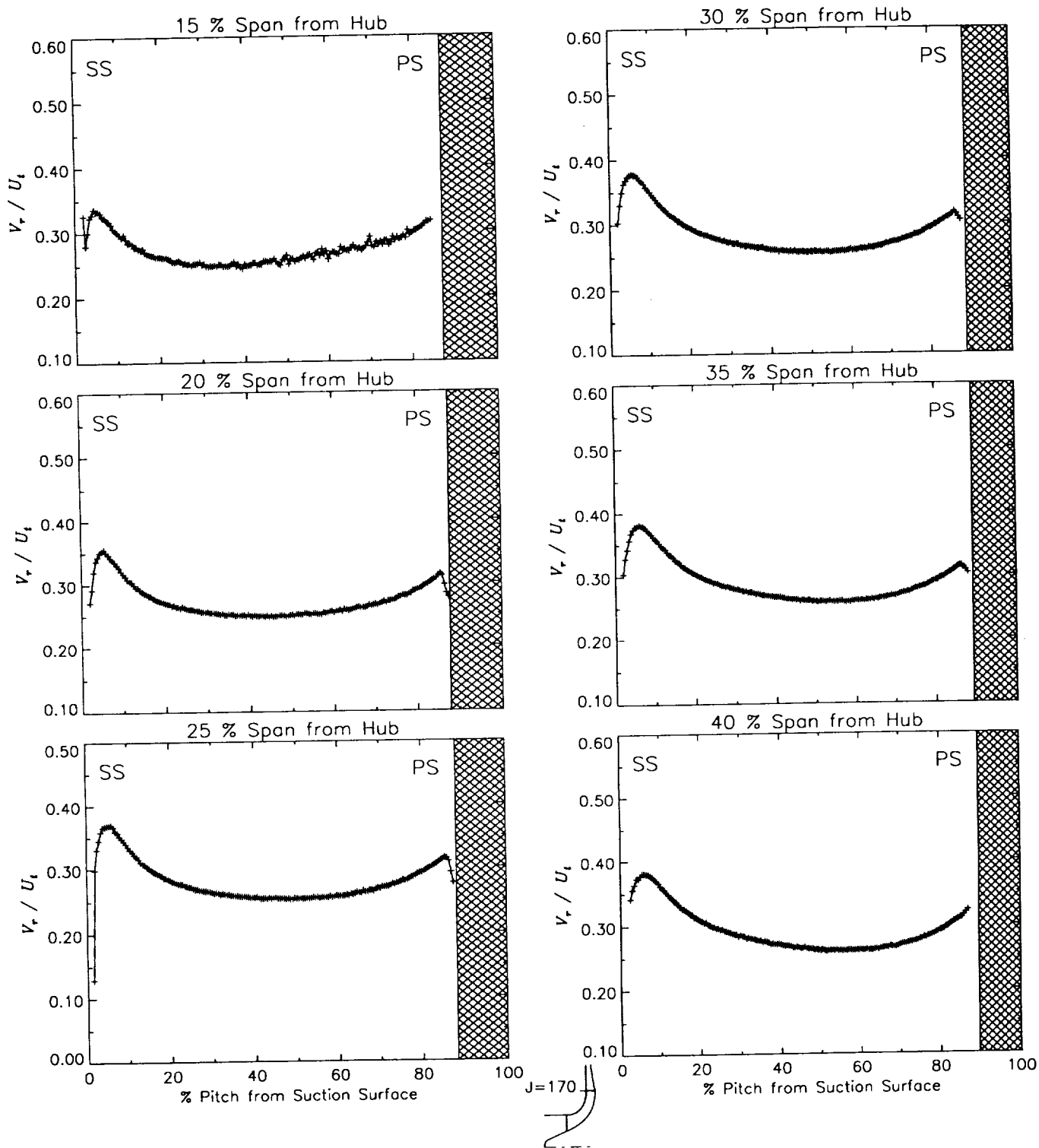
Station J=167, ( $m/m_s=0.960$ )



(c) Axial velocity normalized by impeller tip speed.

Figure 40.—Concluded.

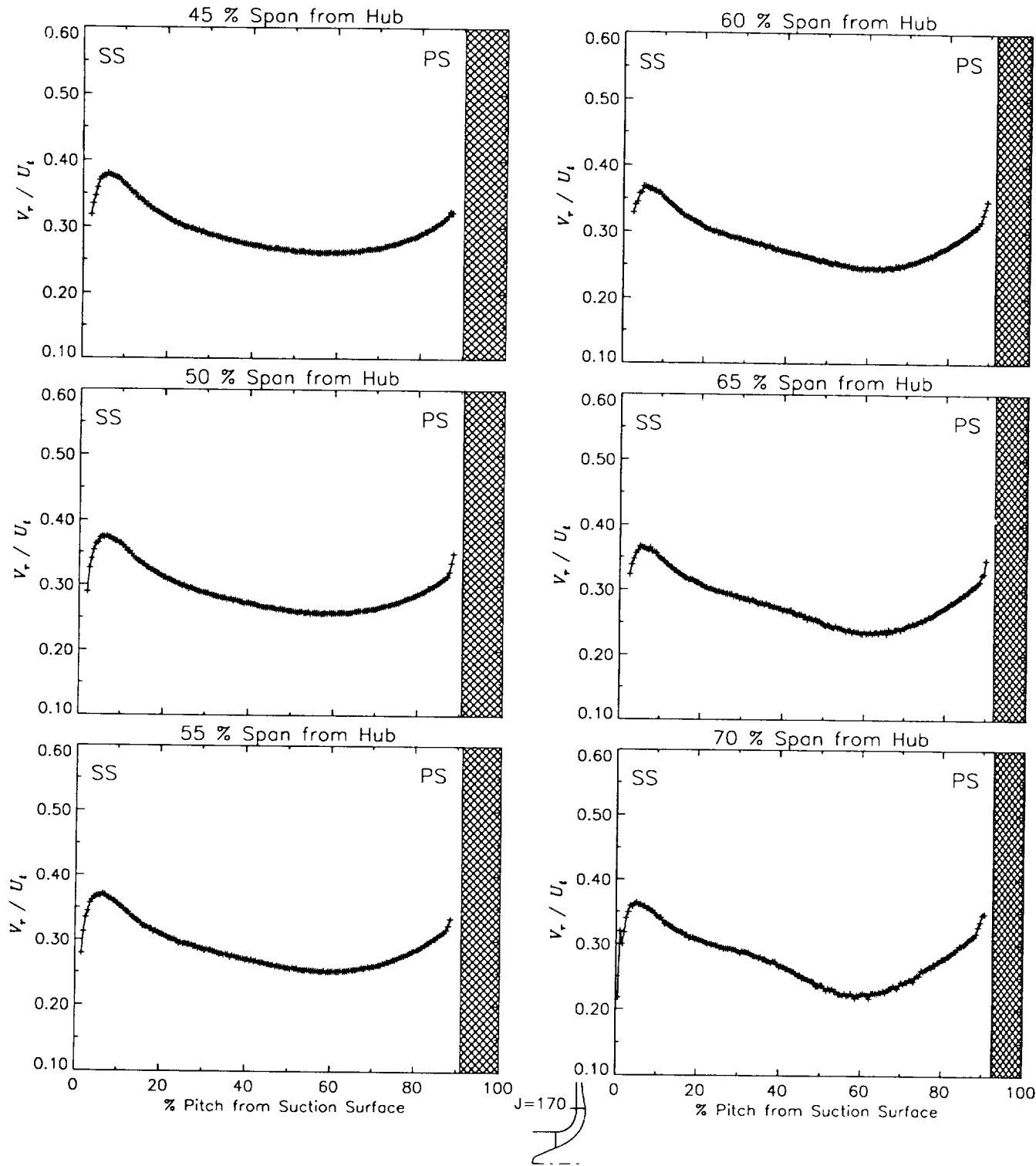
Station J=170, ( $m/m_s=0.990$ )



(a) Radial velocity normalized by impeller tip speed.

Figure 41.—Laser velocimeter results of axial, radial, and relative tangential velocities normalized by impeller tip speed for the design flow condition,  $m_d$ , at station J=170, ( $m/m_s=0.990$ ). The shaded region to the right of each plot represents the physical blade width.

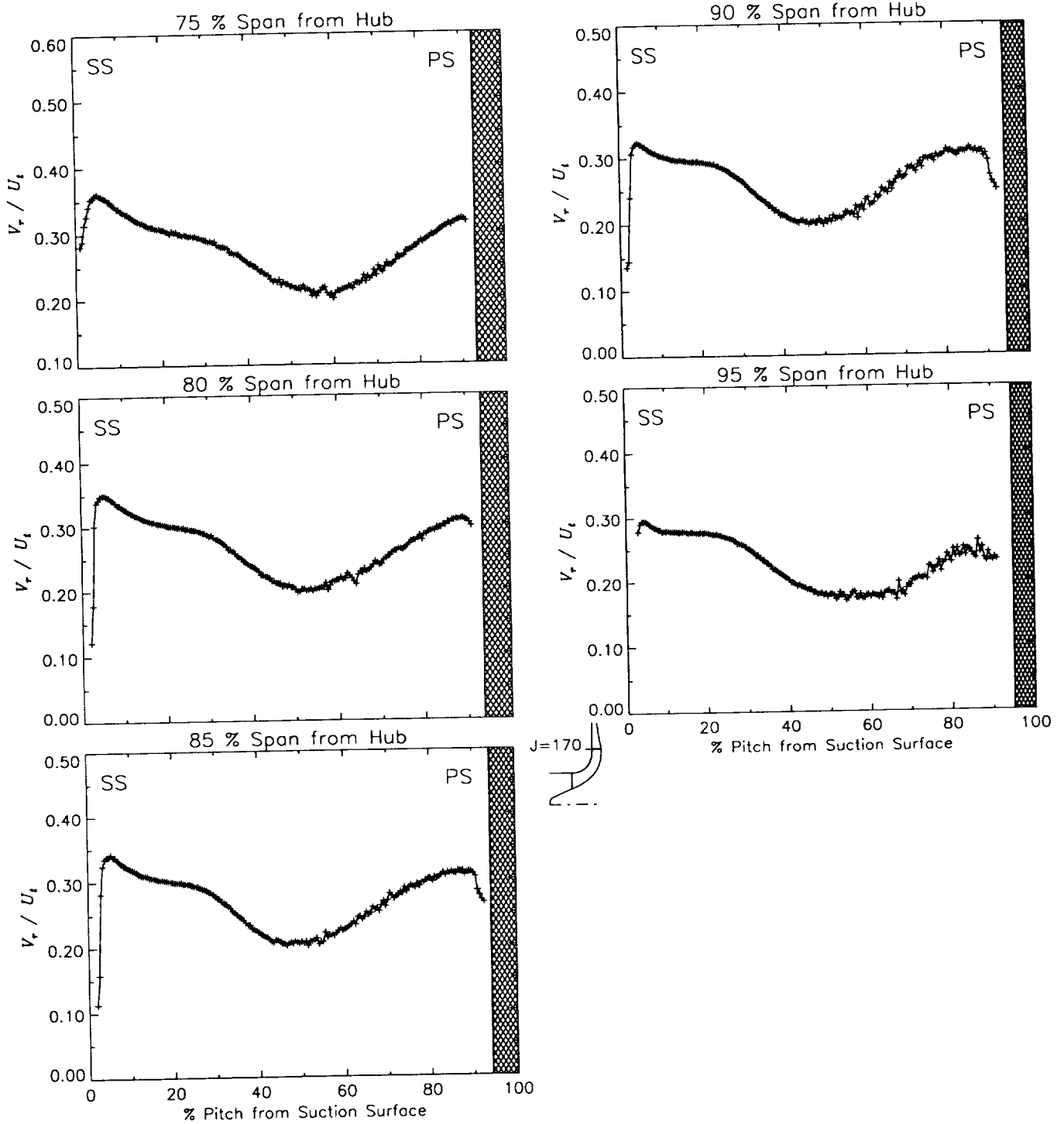
Station J=170, ( $m/m_s=0.990$ )



(a) Radial velocity normalized by impeller tip speed.

Figure 41.-Continued.

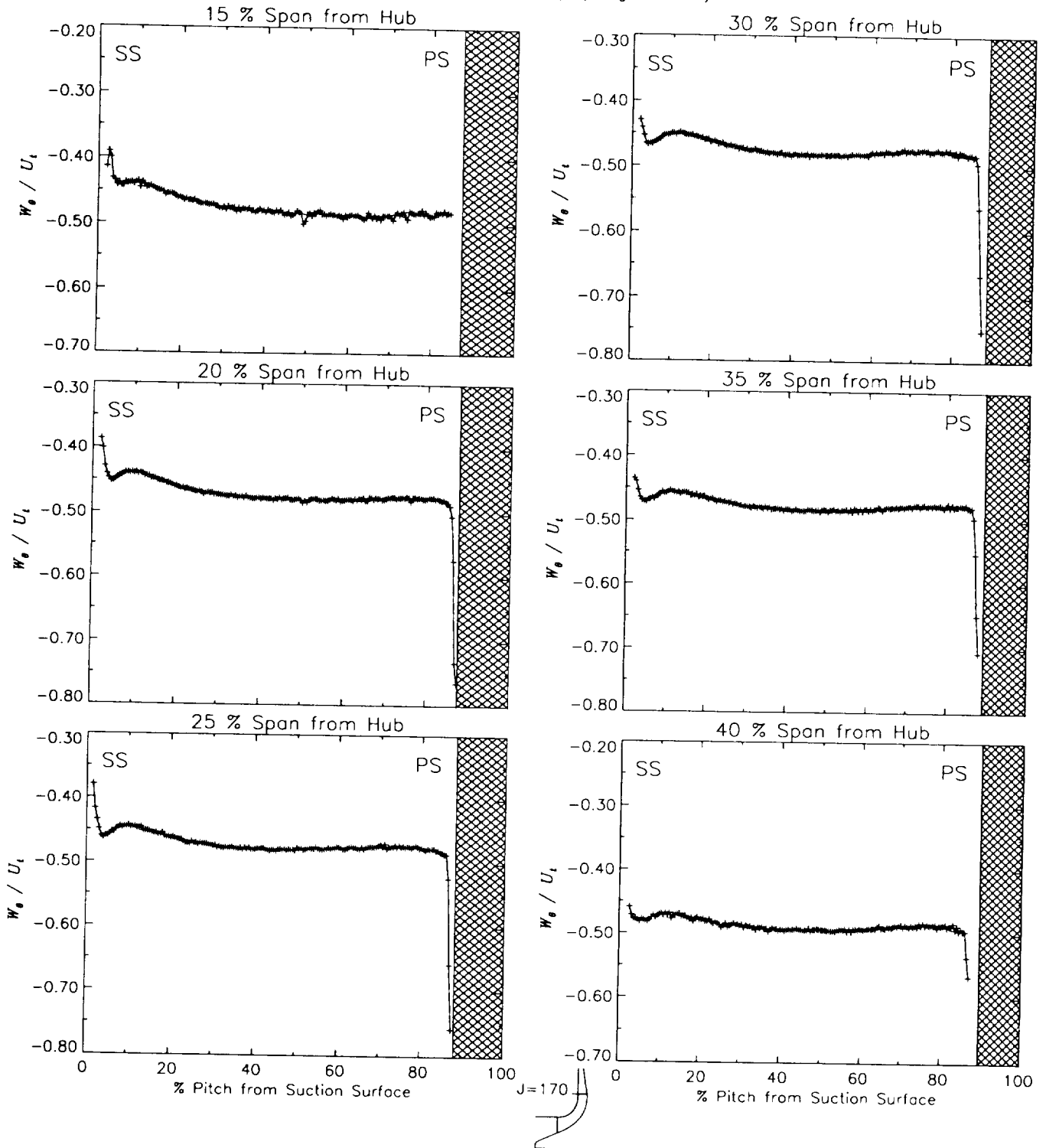
Station J=170, ( $m/m_s=0.990$ )



(a) Radial velocity normalized by impeller tip speed.

Figure 41.—Continued.

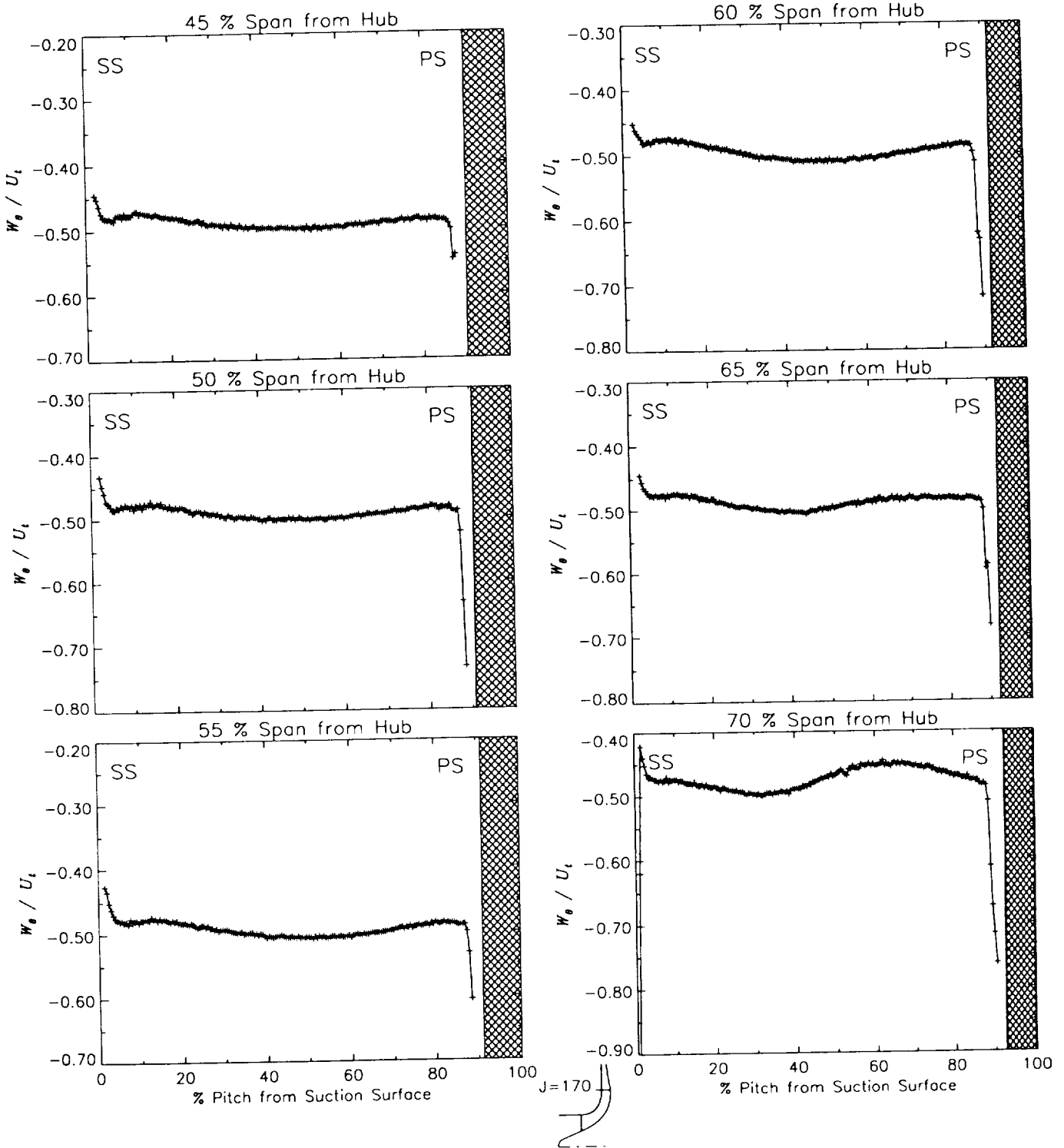
Station J=170, ( $m/m_s=0.990$ )



(b) Relative tangential velocity normalized by impeller tip speed.

Figure 41.-Continued.

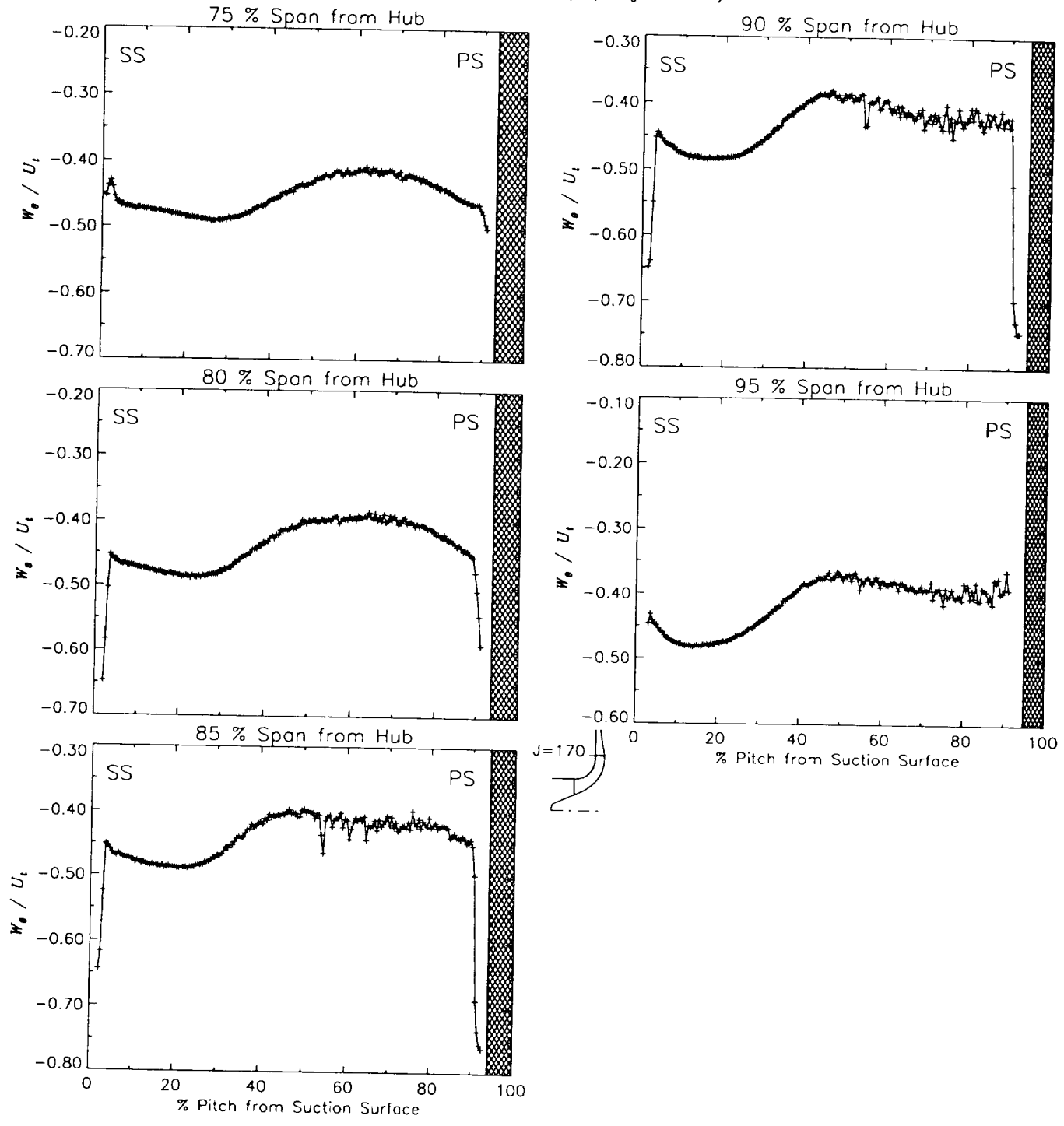
Station J=170, ( $m/m_s=0.990$ )



(b) Relative tangential velocity normalized by impeller tip speed.

Figure 41.-Continued.

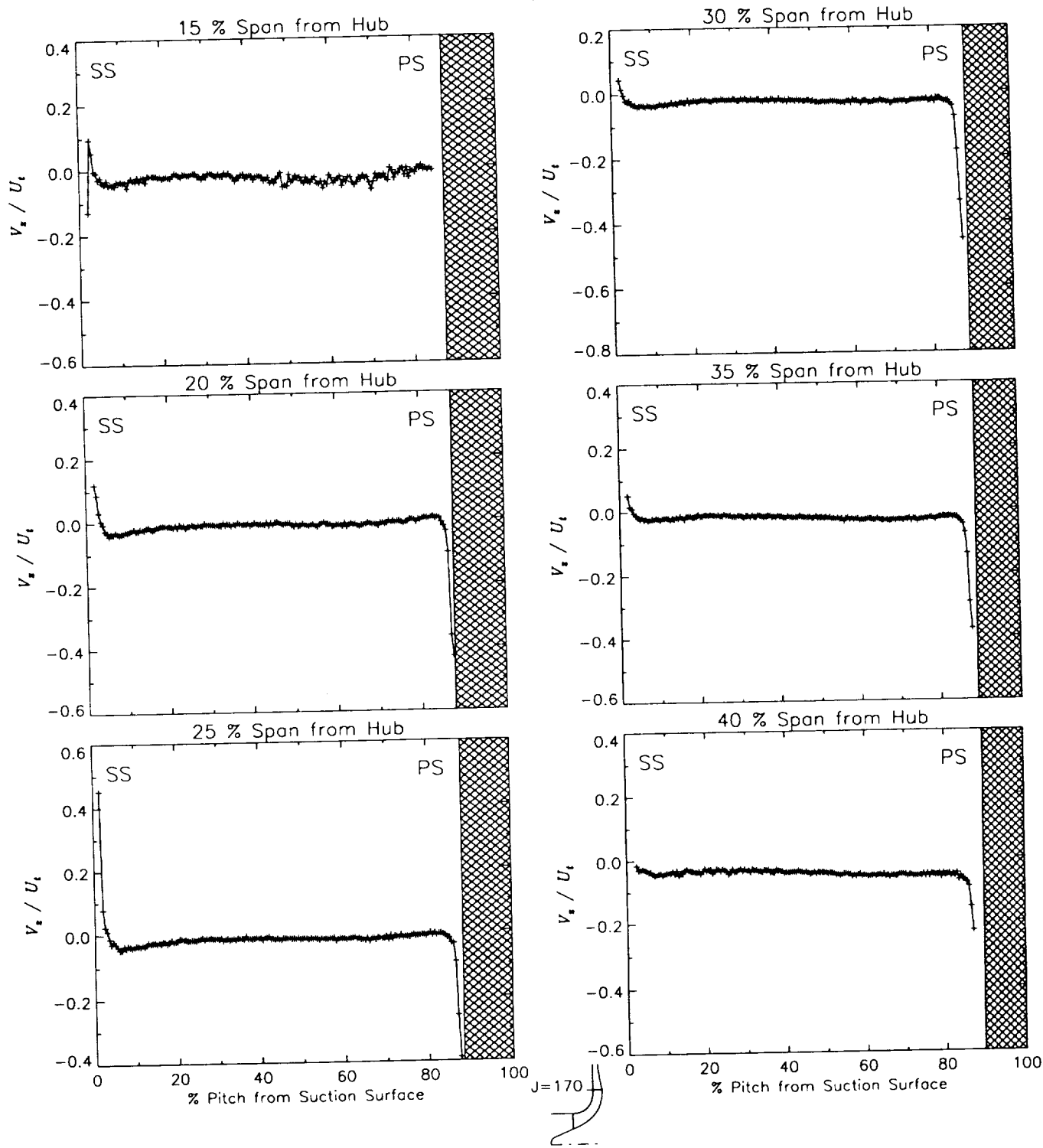
Station J=170, ( $m/m_s=0.990$ )



(b) Relative tangential velocity normalized by impeller tip speed.

Figure 41.-Continued.

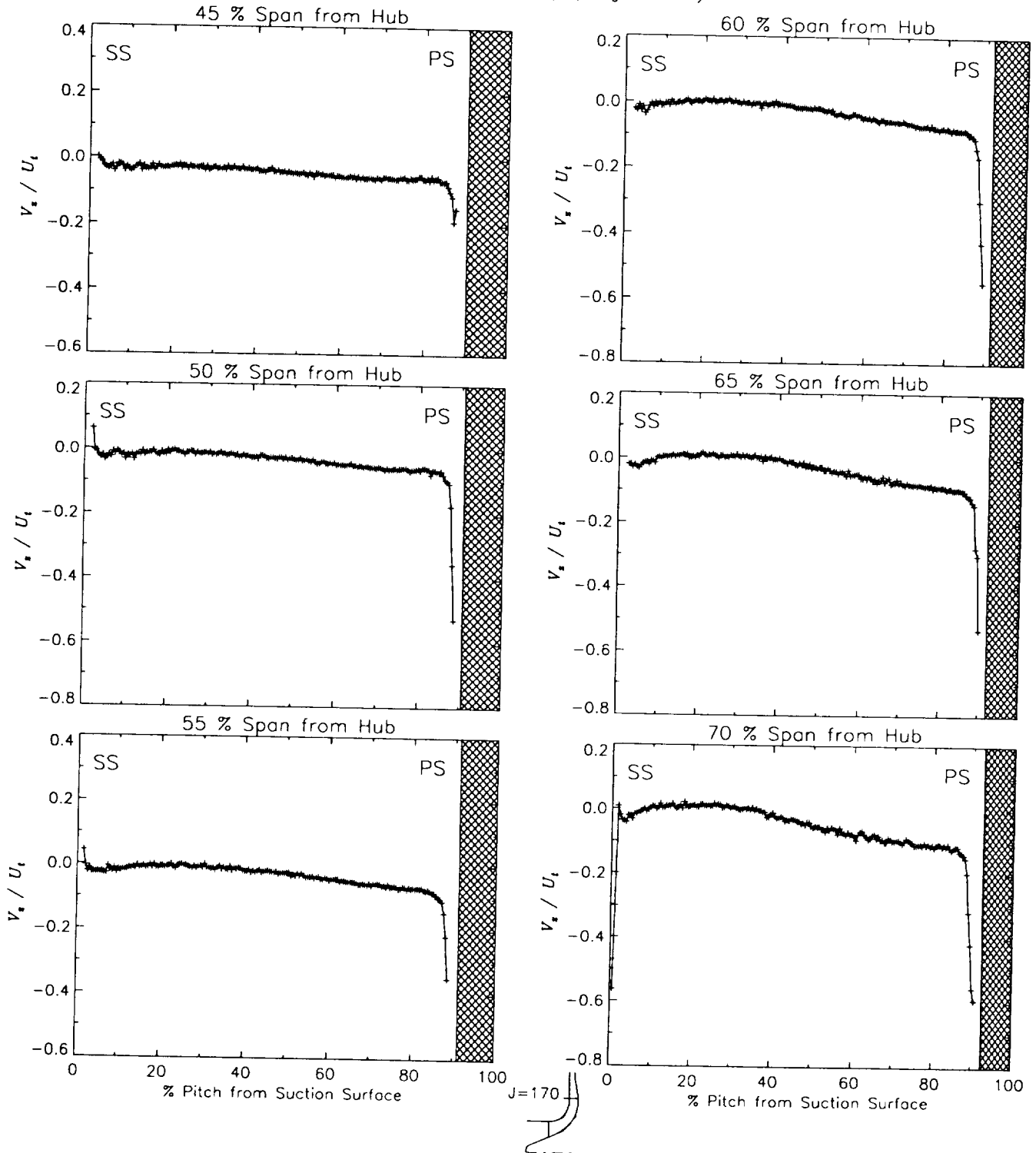
Station J=170, ( $m/m_s=0.990$ )



(c) Axial velocity normalized by impeller tip speed.

Figure 41.-Continued.

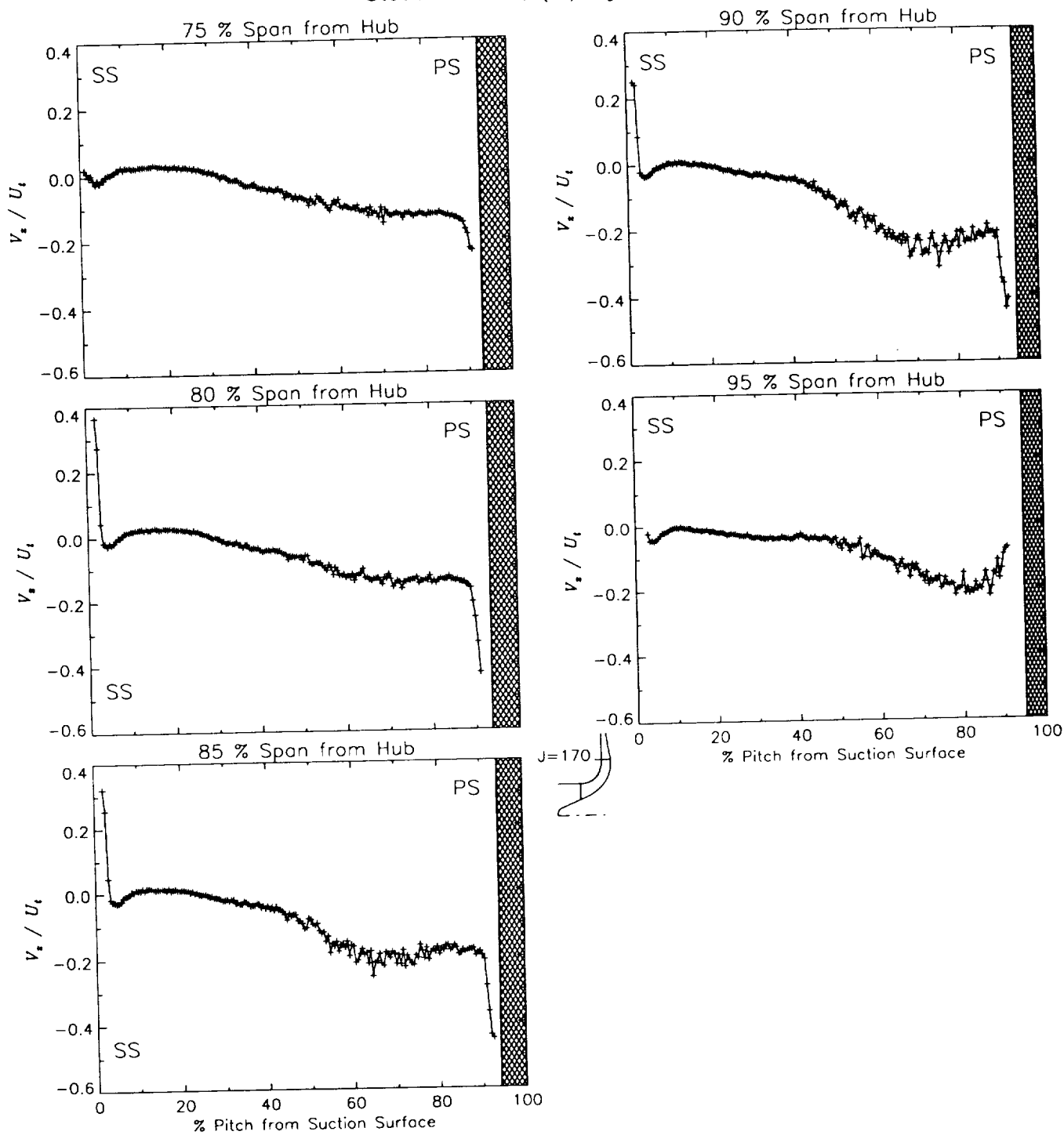
Station J=170, ( $m/m_s=0.990$ )



(c) Axial velocity normalized by impeller tip speed.

Figure 41.-Continued.

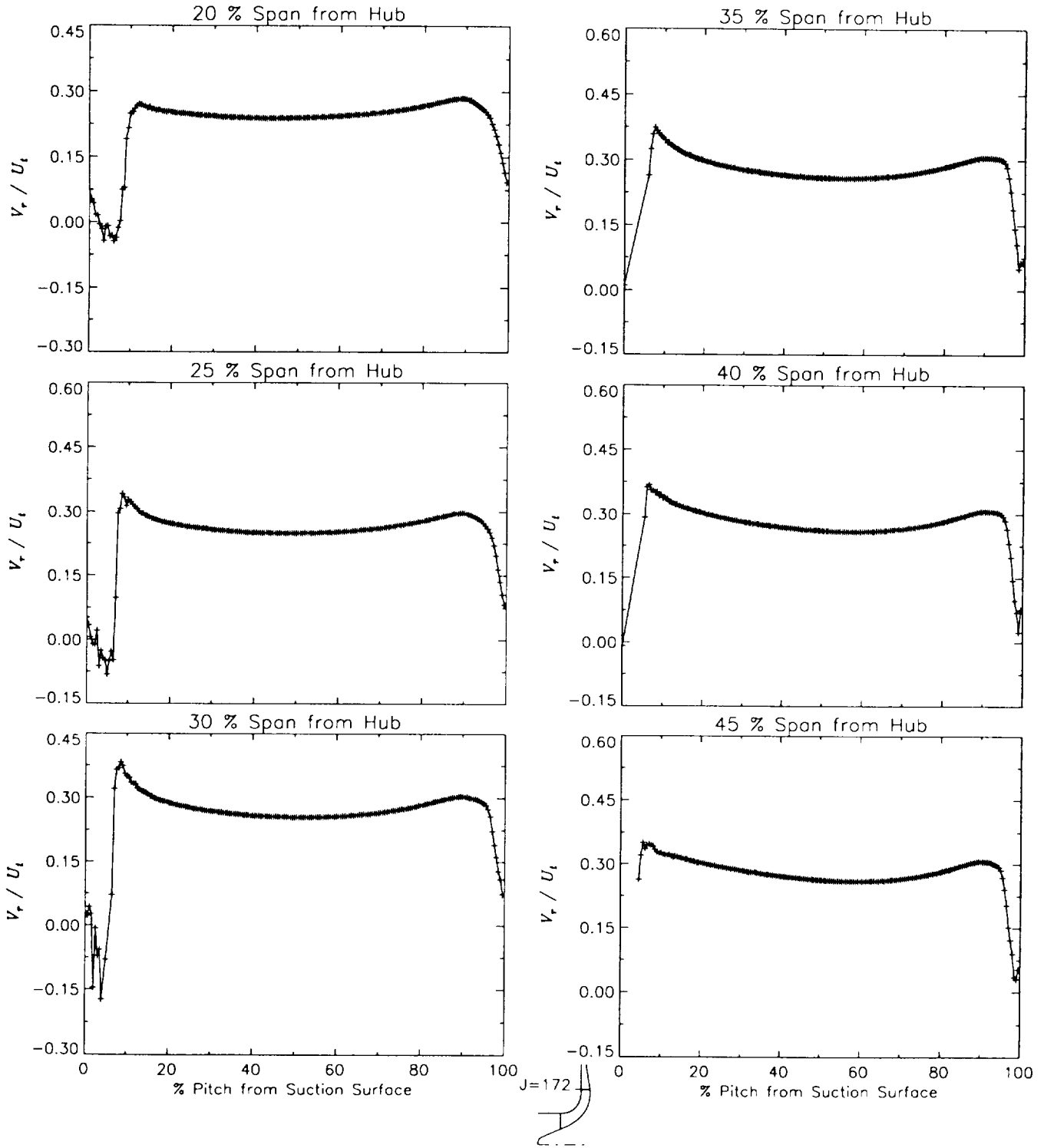
Station J=170, ( $m/m_s=0.990$ )



(c) Axial velocity normalized by impeller tip speed.

Figure 41.-Concluded.

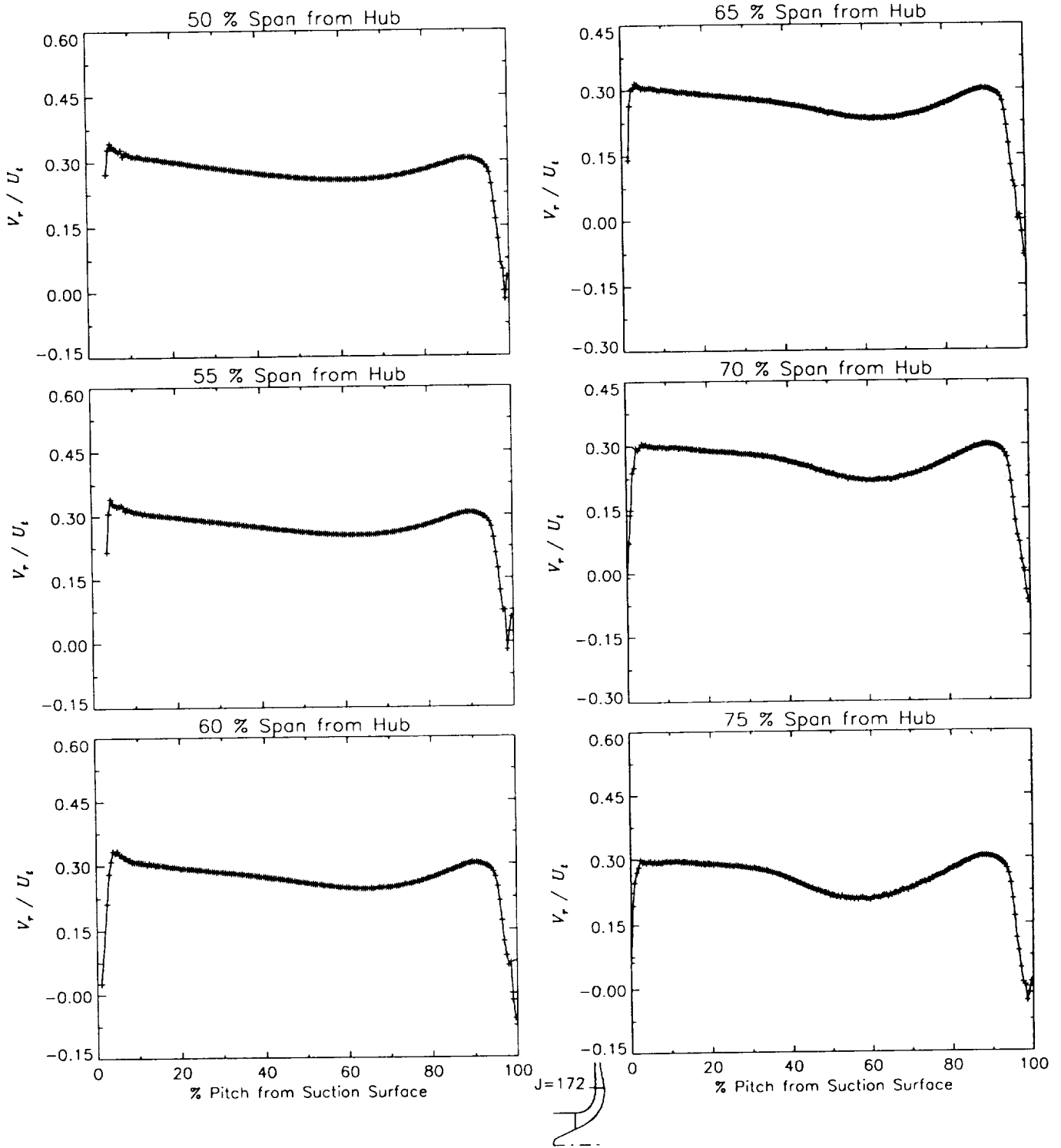
Station J=172, ( $m/m_s=1.014$ )



(a) Radial velocity normalized by impeller tip speed.

Figure 42.—Laser velocimeter results of axial, radial, and relative tangential velocities normalized by impeller tip speed for the design flow condition,  $\dot{m}_d$ , at station J=172, ( $m/m_s=1.014$ ).

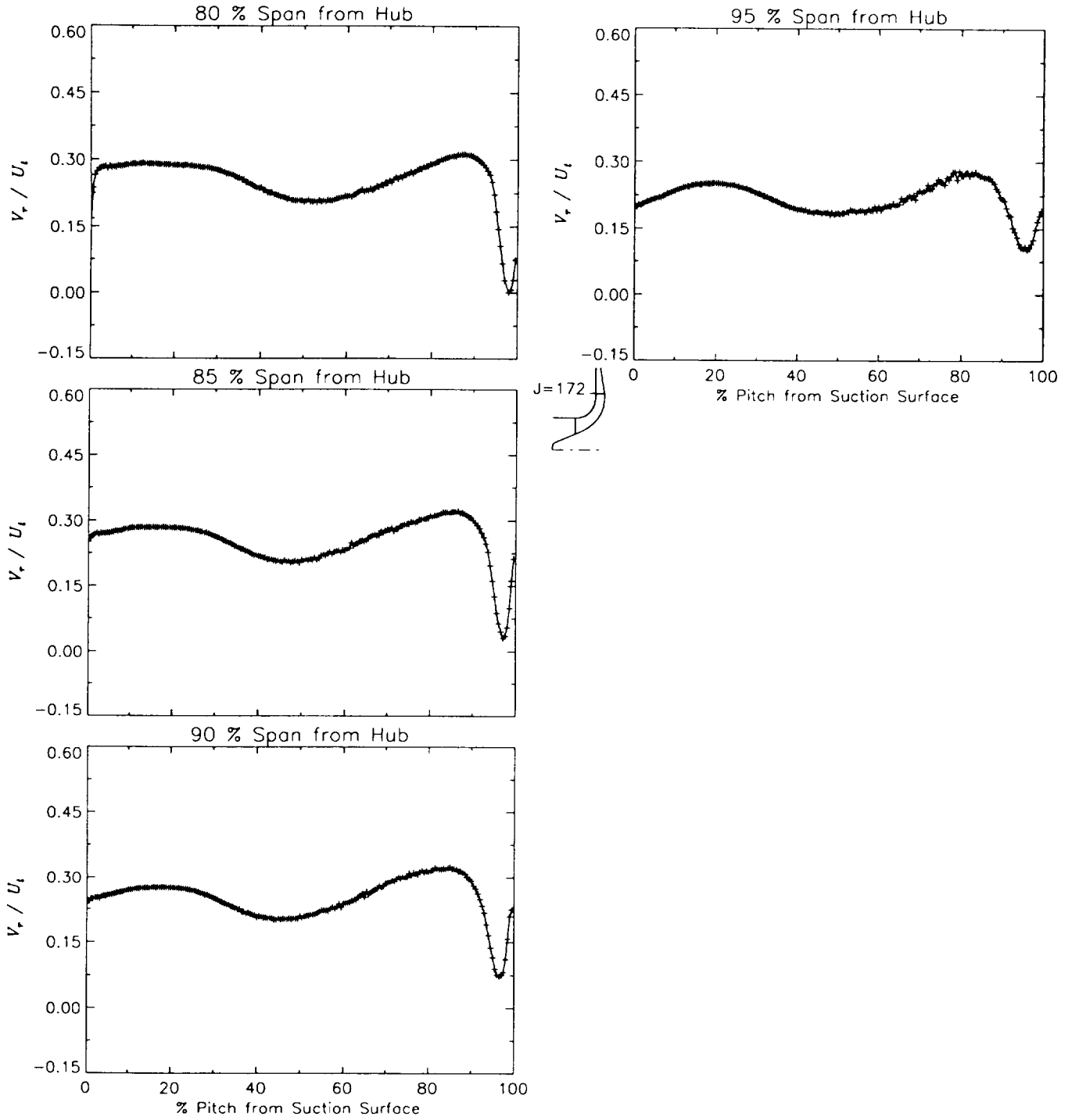
Station J=172, ( $m/m_s=1.014$ )



(a) Radial velocity normalized by impeller tip speed.

Figure 42.-Continued.

Station J=172, ( $m/m_s=1.014$ )

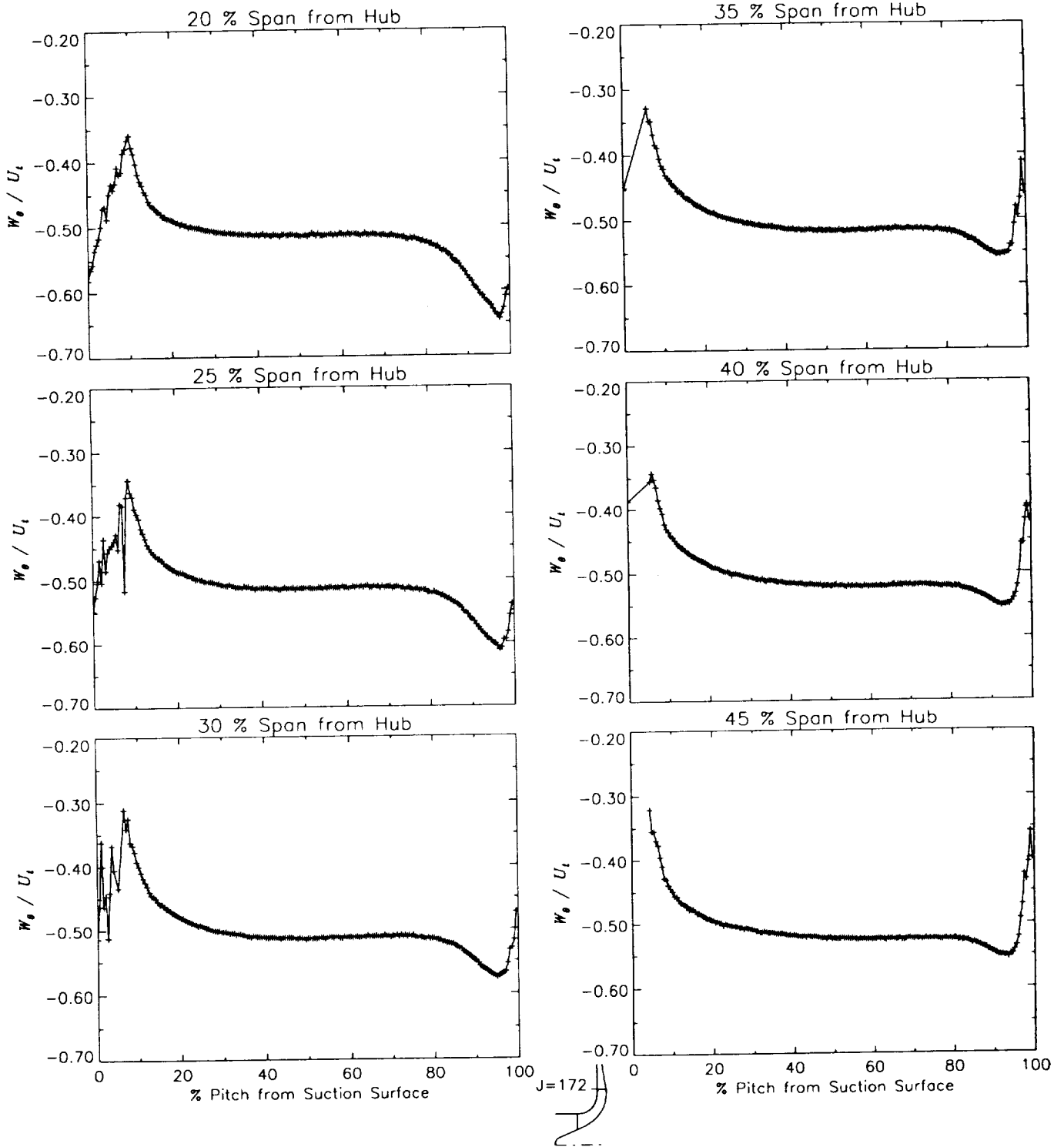


(a) Radial velocity normalized by impeller tip speed.

Figure 42.—Continued.

•

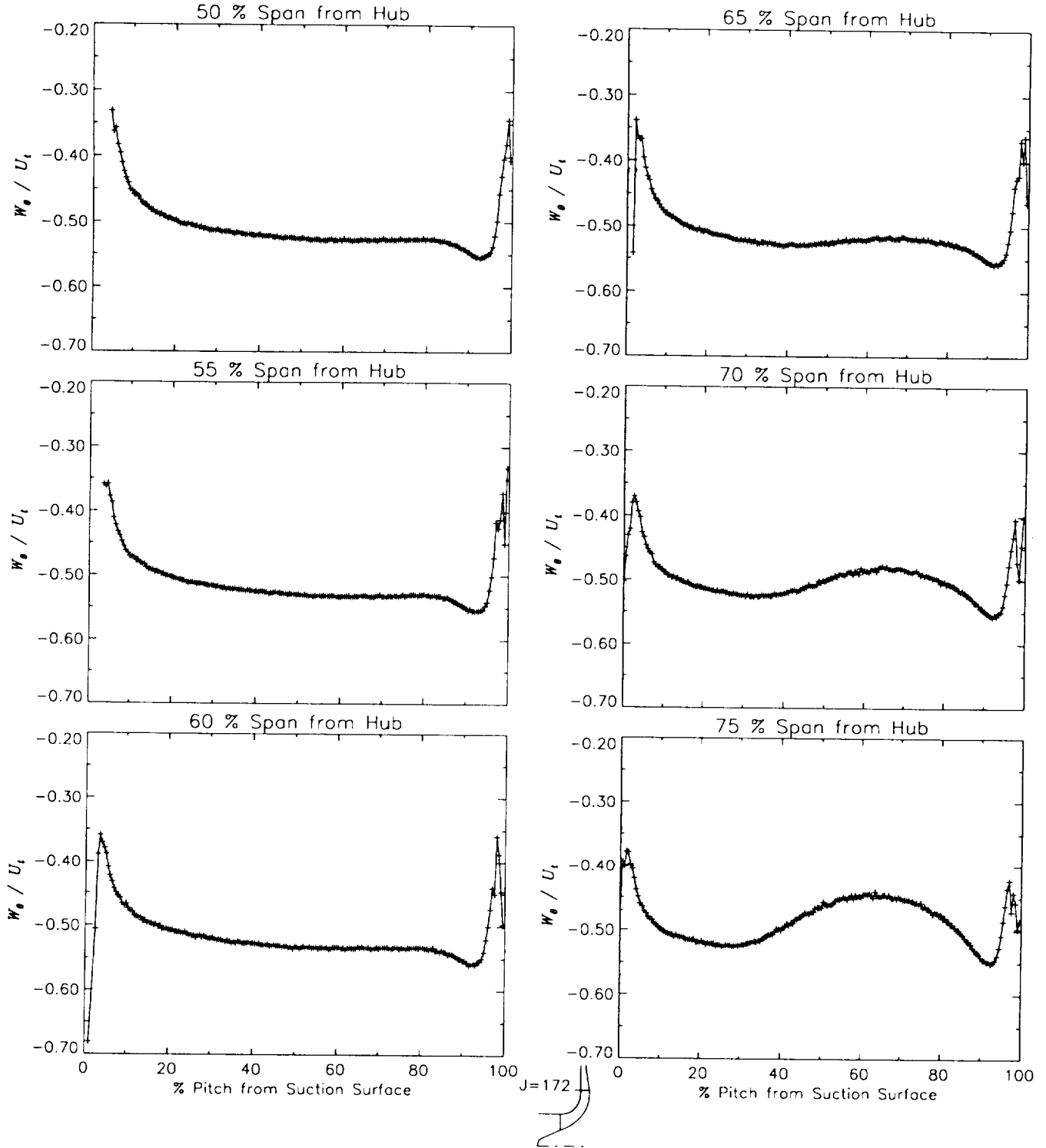
Station J=172, ( $m/m_s=1.014$ )



(b) Relative tangential velocity normalized by impeller tip speed.

Figure 42.—Continued.

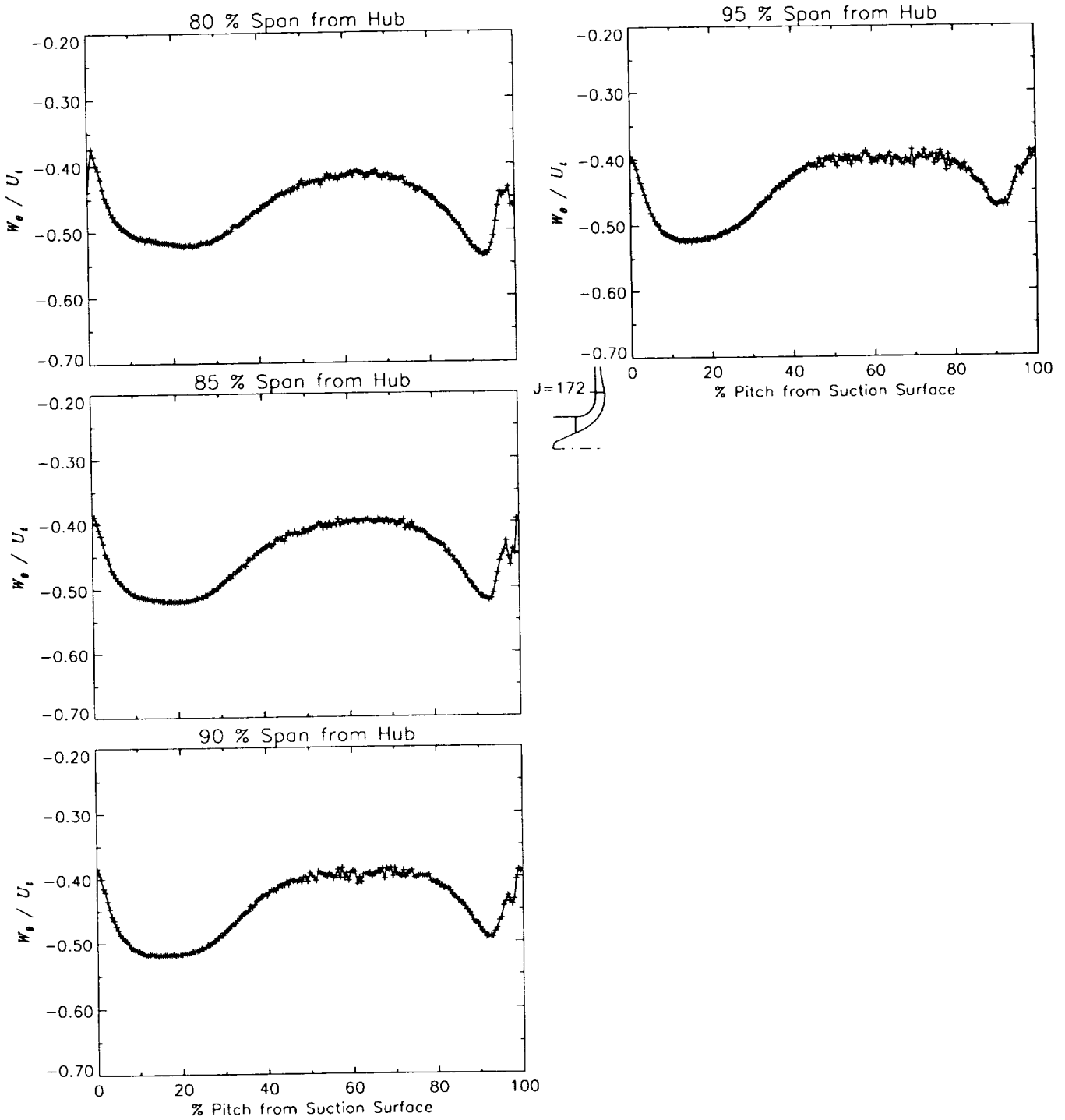
Station J=172, ( $m/m_s=1.014$ )



(b) Relative tangential velocity normalized by impeller tip speed.

Figure 42.—Continued.

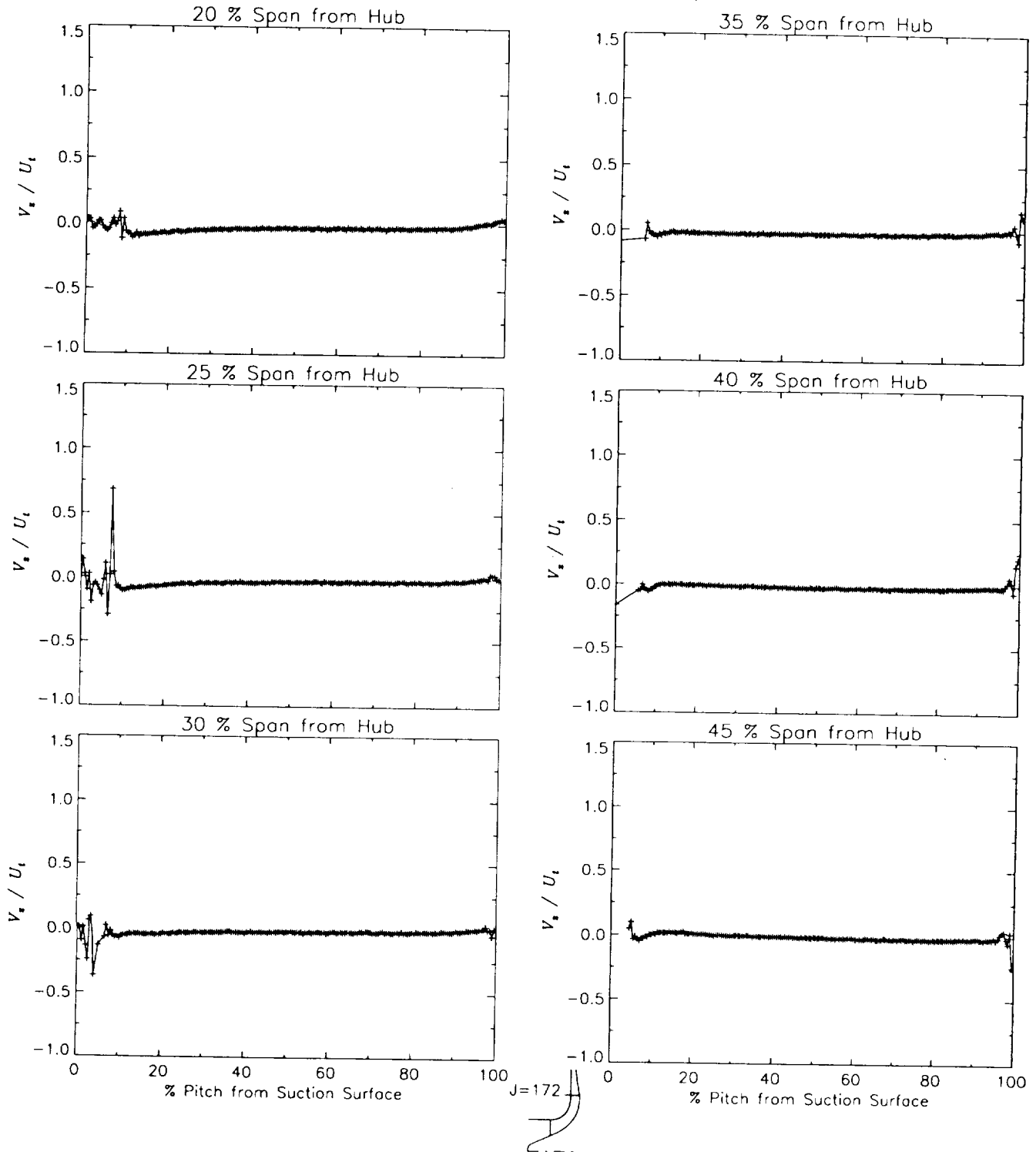
Station J=172, ( $m/m_s=1.014$ )



(b) Relative tangential velocity normalized by impeller tip speed.

Figure 42.--Continued.

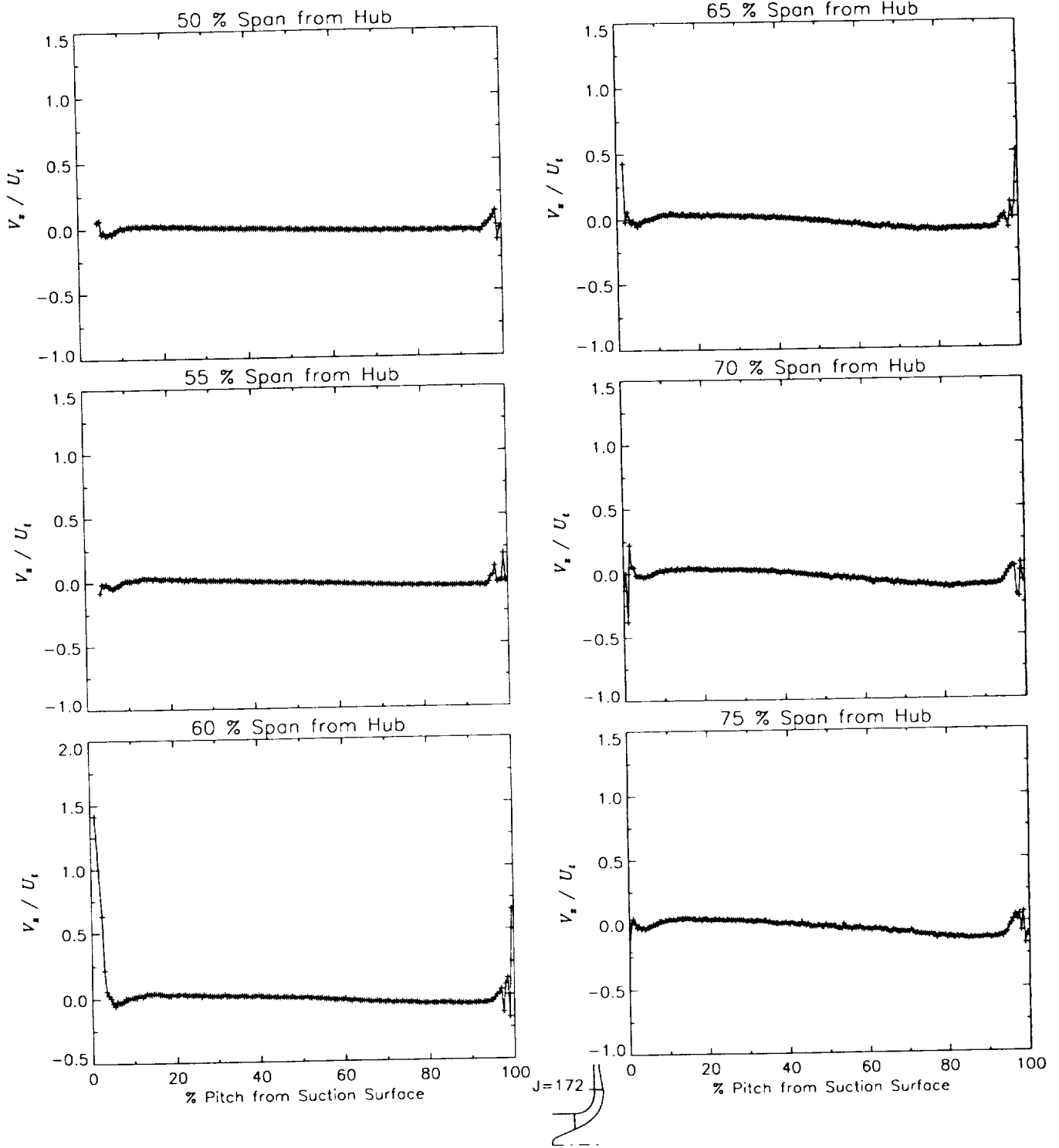
Station J=172, ( $m/m_s=1.014$ )



(c) Axial velocity normalized by impeller tip speed.

Figure 42.—Continued.

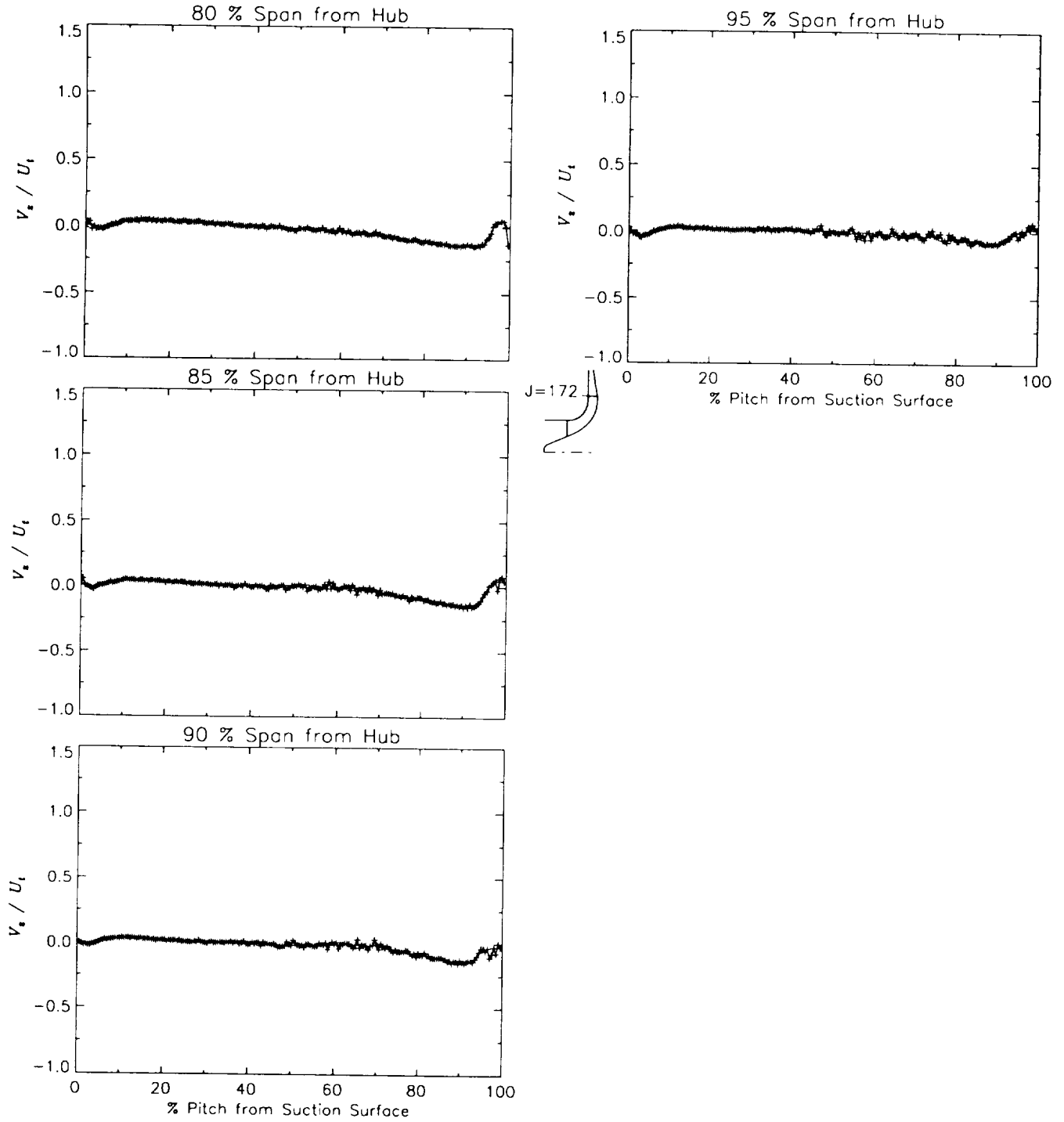
Station J=172, ( $m/m_s=1.014$ )



(c) Axial velocity normalized by impeller tip speed.

Figure 42.-Continued.

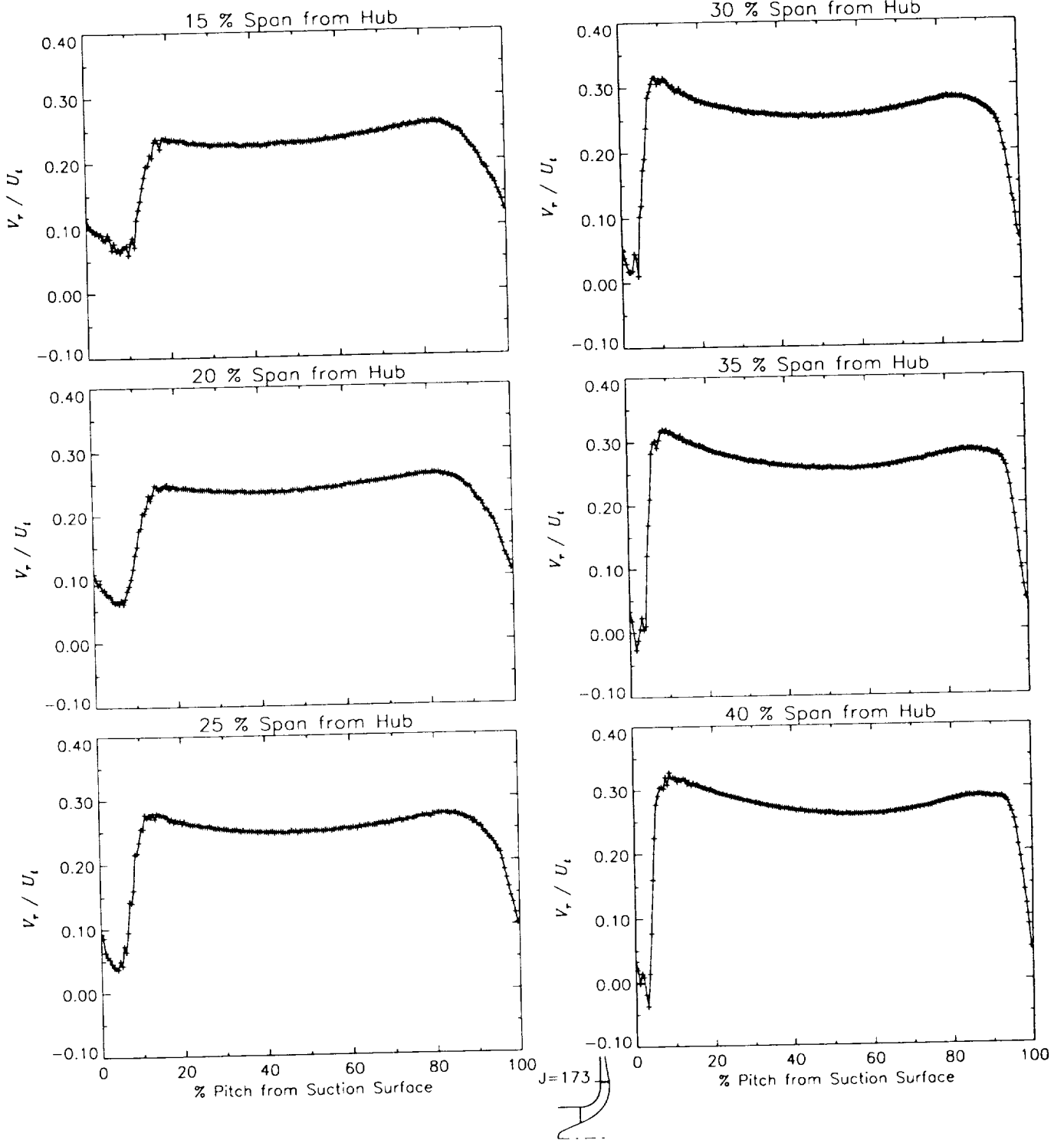
Station J=172, ( $m/m_s=1.014$ )



(c) Axial velocity normalized by impeller tip speed.

Figure 42.-Concluded.

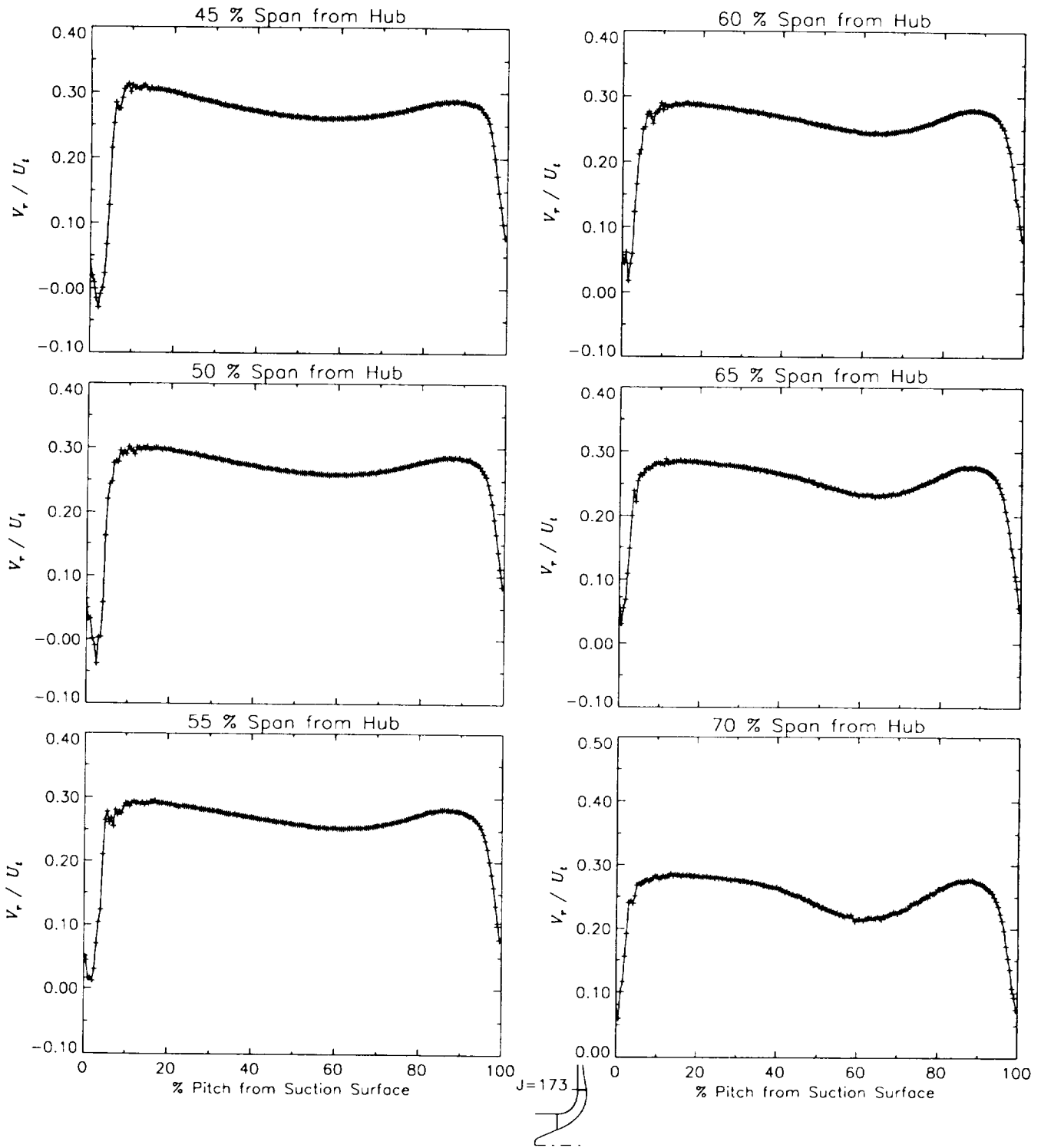
Station J=173, ( $m/m_s=1.027$ )



(a) Radial velocity normalized by impeller tip speed.

Figure 43.—Laser velocimeter results of axial, radial, and relative tangential velocities normalized by impeller tip speed for the design flow condition,  $m_d$ , at station J=173, ( $m/m_s=1.027$ ).

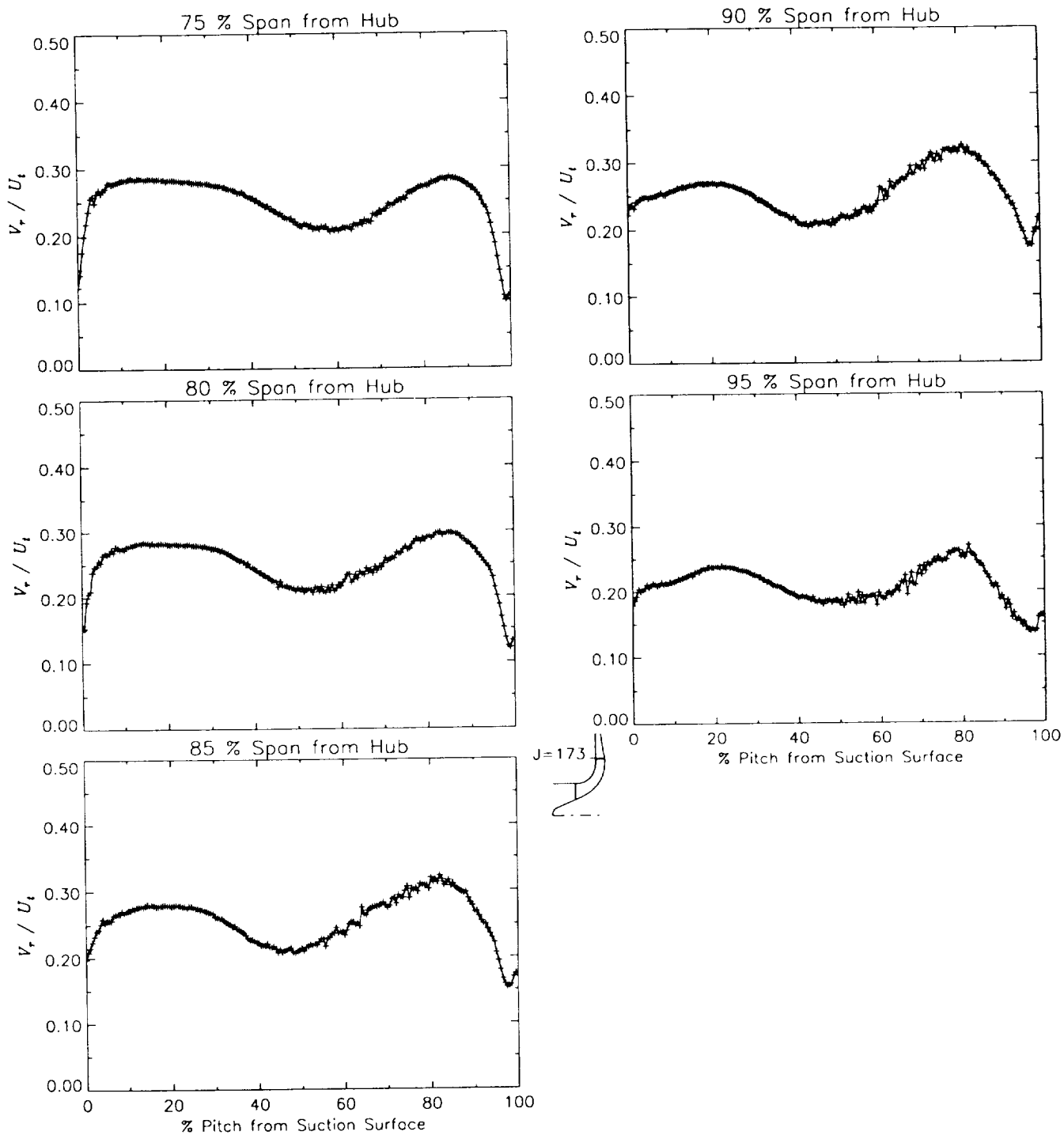
Station J=173, ( $m/m_s=1.027$ )



(a) Radial velocity normalized by impeller tip speed.

Figure 43.—Continued.

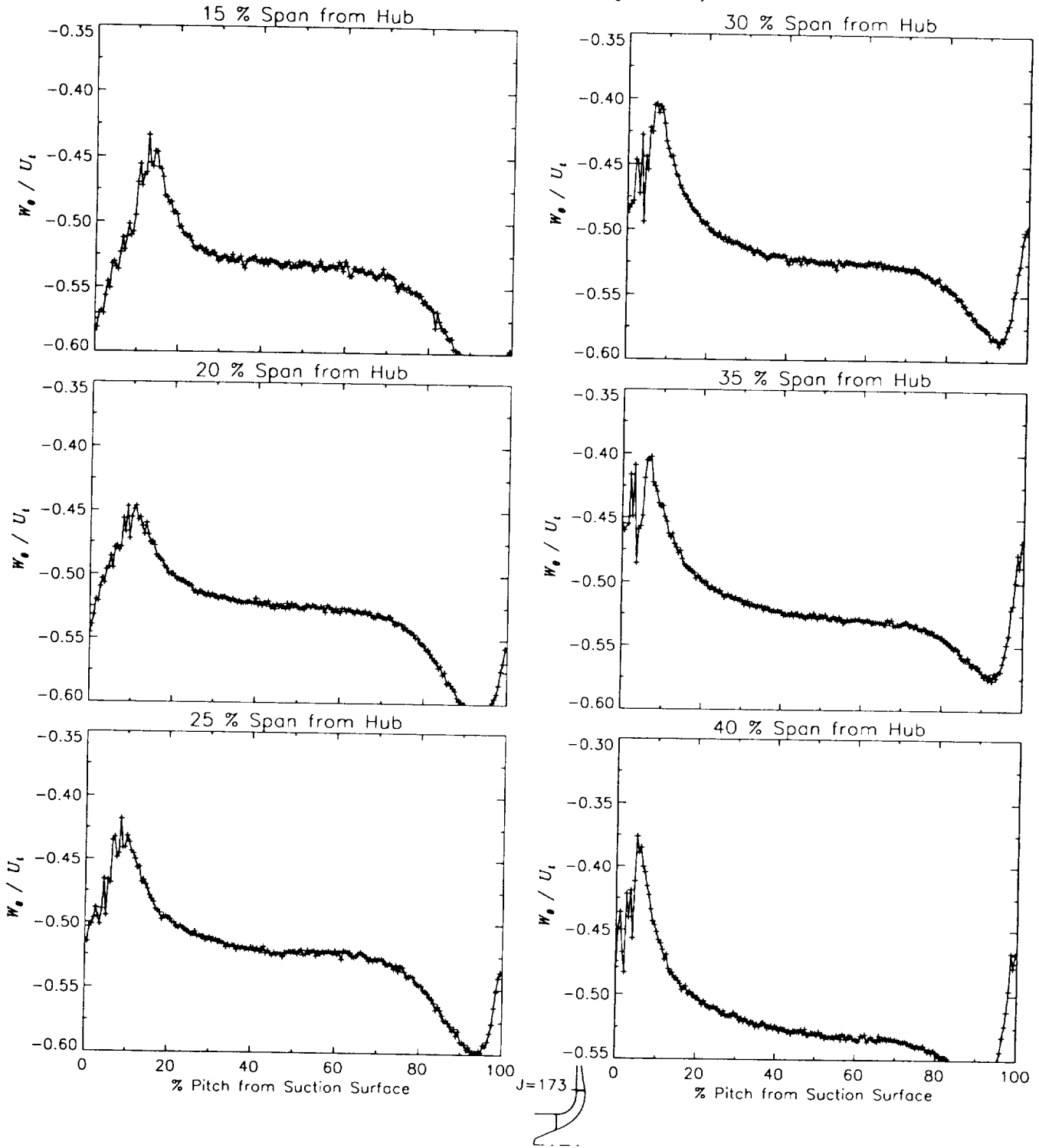
Station J=173, ( $m/m_s=1.027$ )



(a) Radial velocity normalized by impeller tip speed.

Figure 43.—Continued.

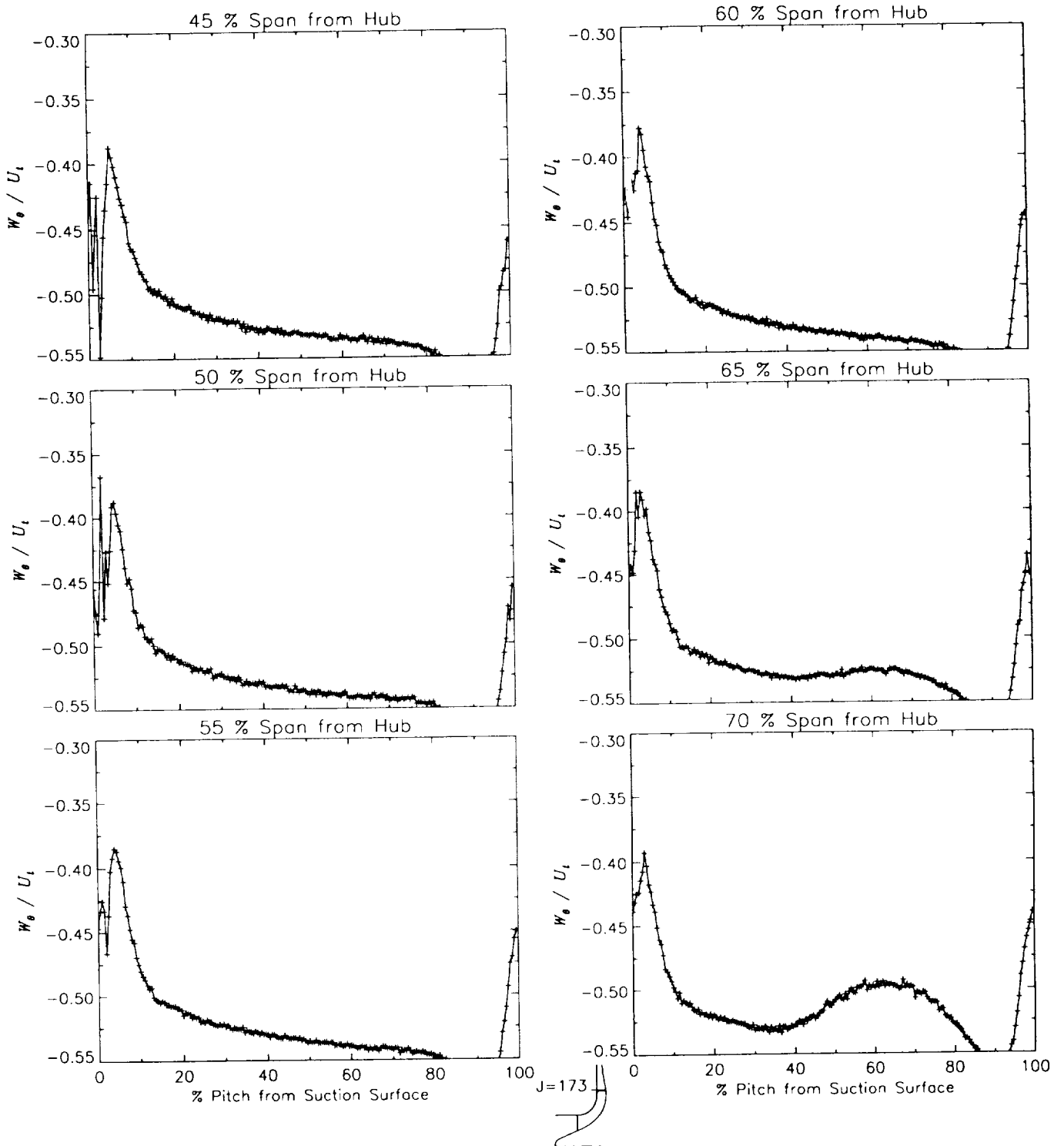
Station J=173, ( $m/m_s=1.027$ )



(b) Relative tangential velocity normalized by impeller tip speed.

Figure 43.-Continued.

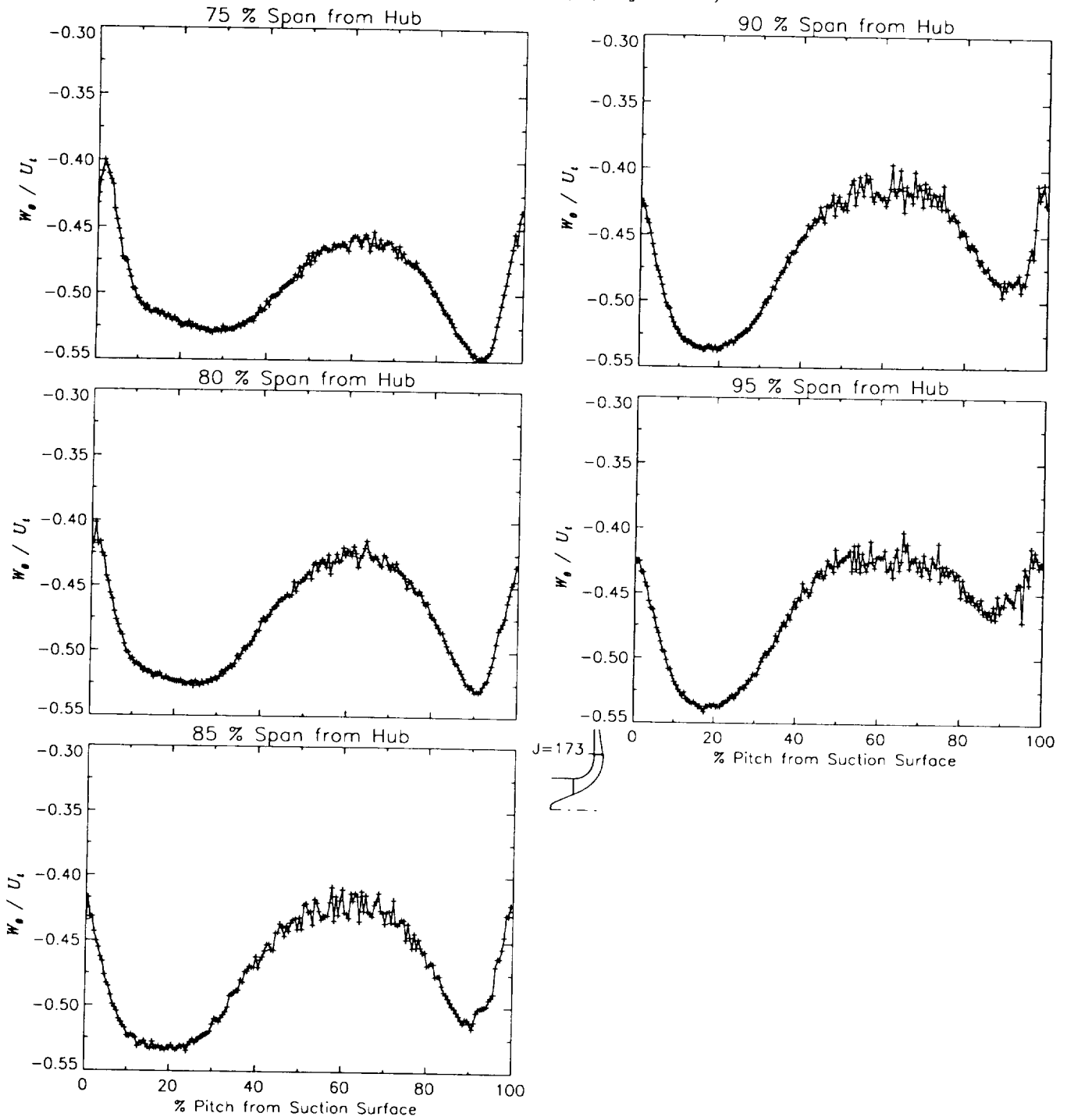
Station J=173, ( $m/m_s=1.027$ )



(b) Relative tangential velocity normalized by impeller tip speed.

Figure 43.—Continued.

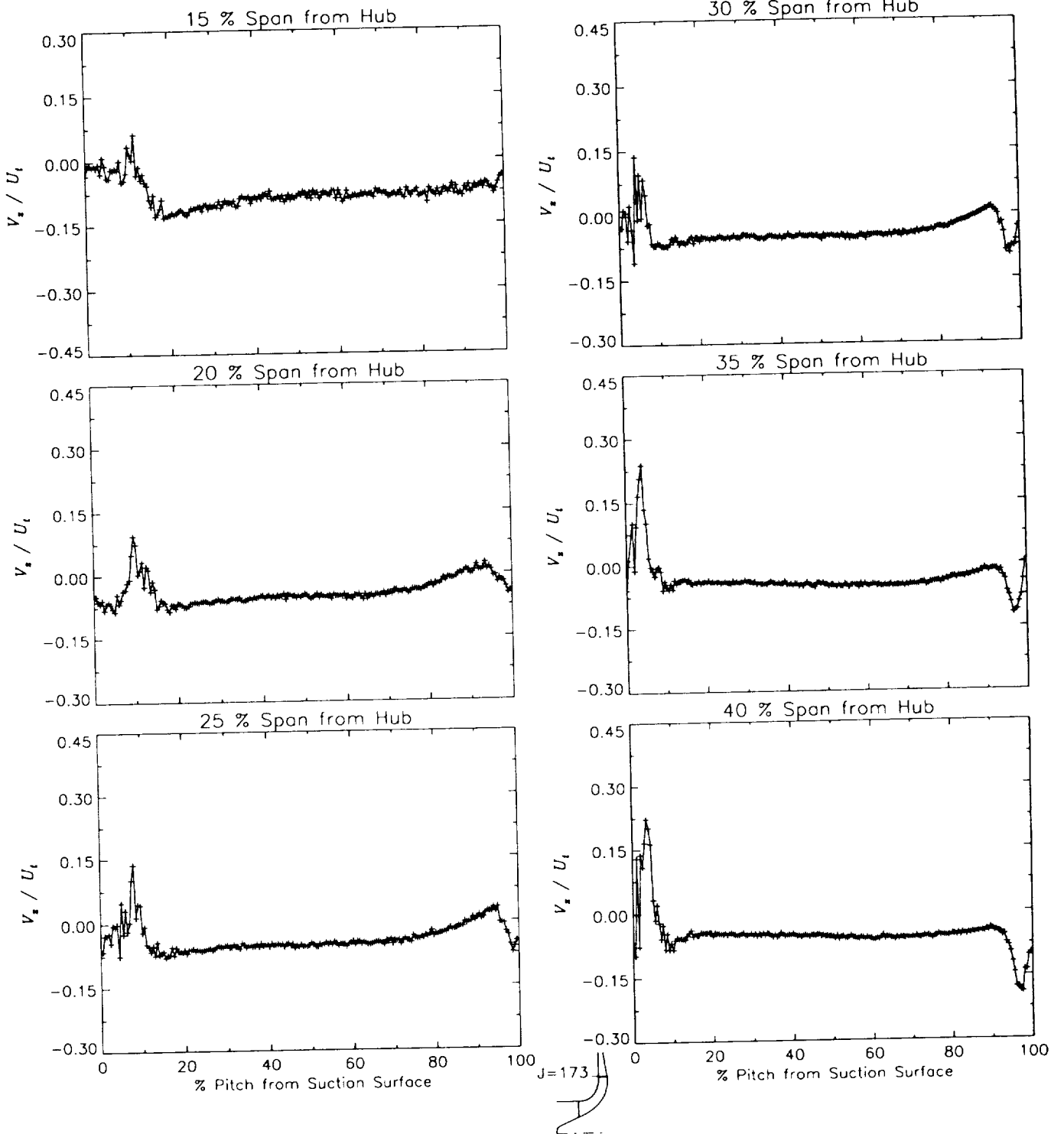
Station J=173, ( $m/m_s=1.027$ )



(b) Relative tangential velocity normalized by impeller tip speed.

Figure 43.-Continued.

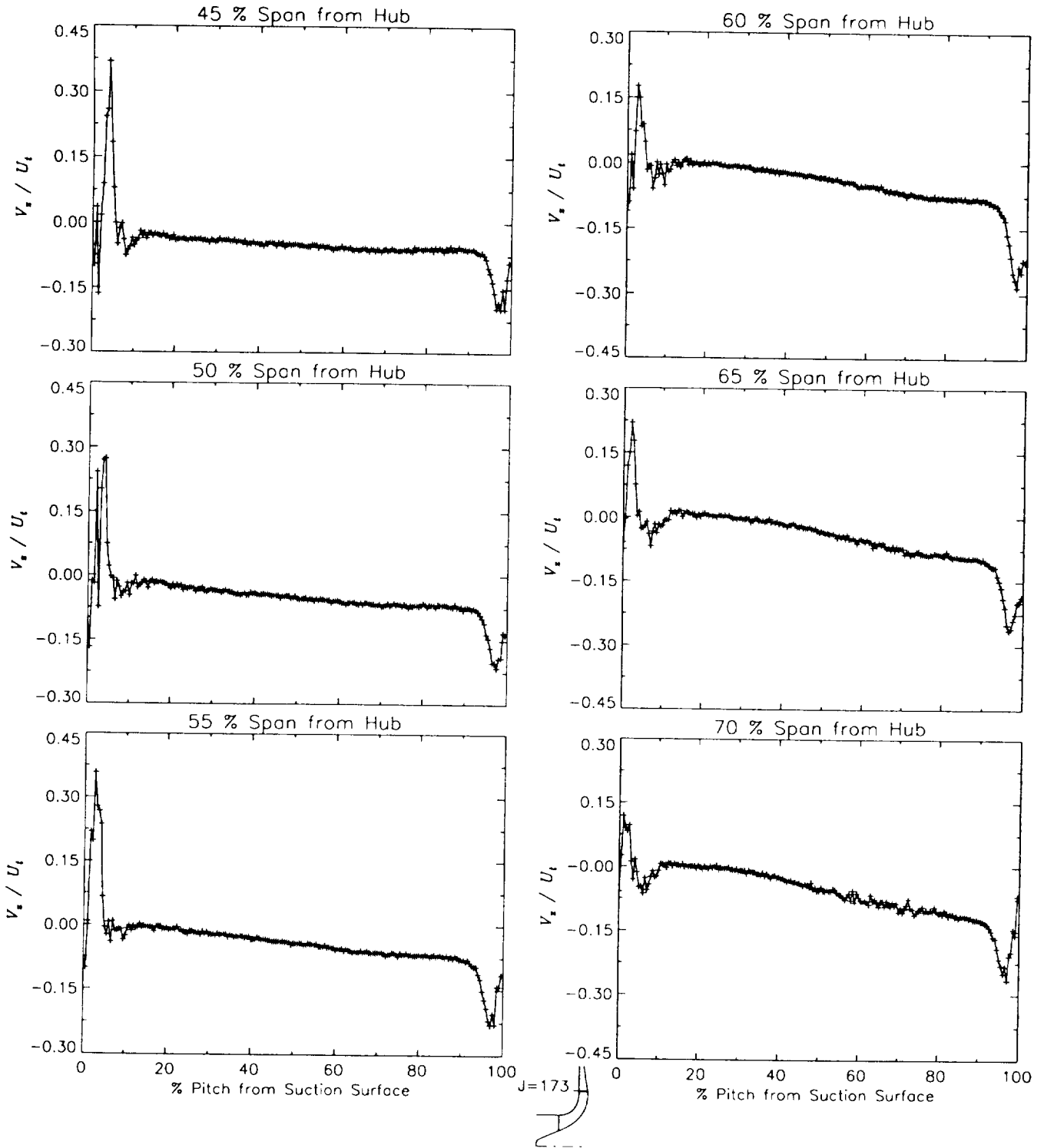
Station J=173, ( $m/m_s=1.027$ )



(c) Axial velocity normalized by impeller tip speed.

Figure 43.—Continued.

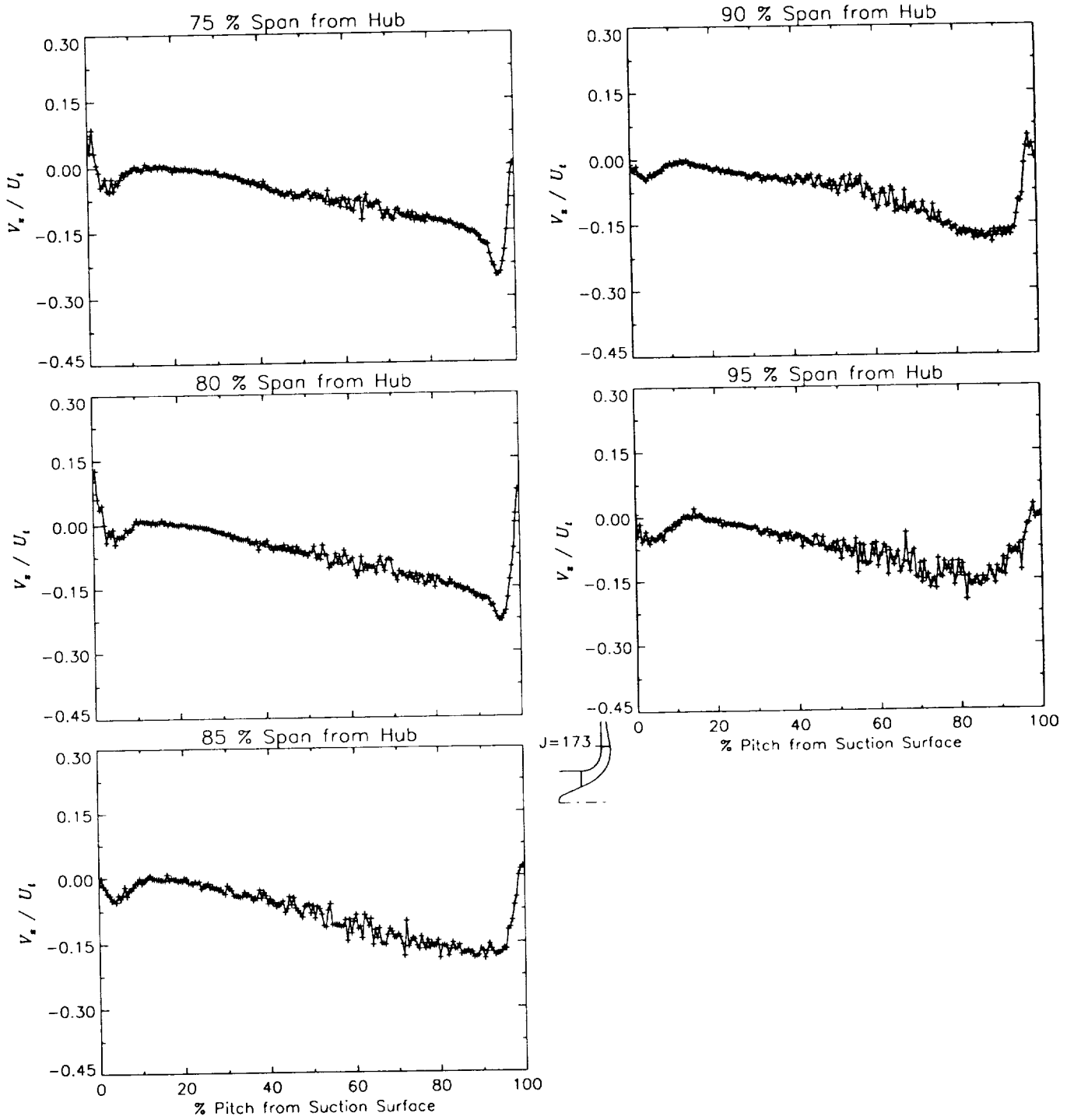
Station J=173, ( $m/m_s=1.027$ )



(c) Axial velocity normalized by impeller tip speed.

Figure 43.-Continued.

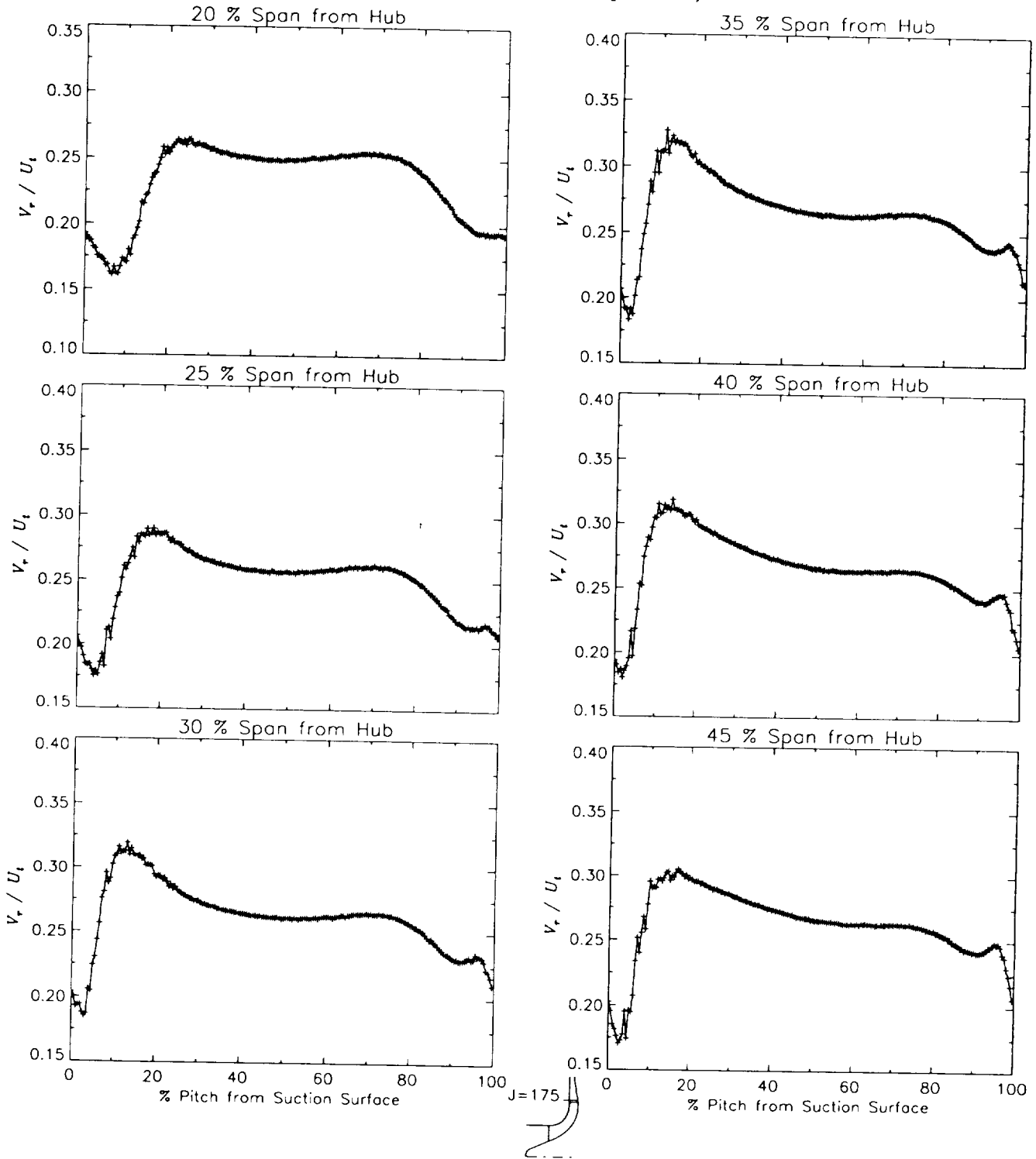
Station J=173, ( $m/m_s=1.027$ )



(c) Axial velocity normalized by impeller tip speed.

Figure 43.—Concluded.

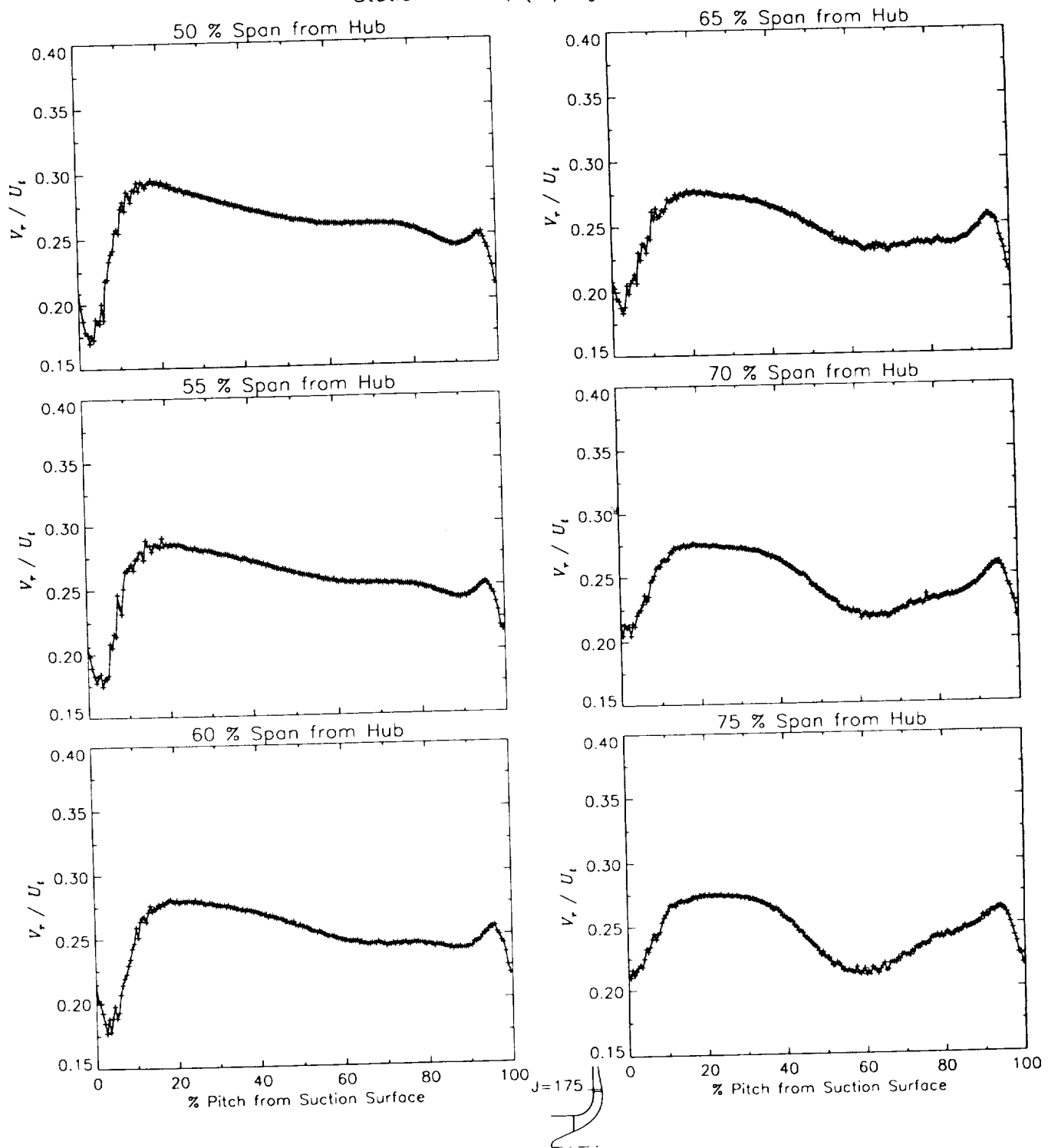
Station J=175, ( $m/m_s=1.054$ )



(a) Radial velocity normalized by impeller tip speed.

Figure 44.-Laser velocimeter results of axial, radial, and relative tangential velocities normalized by impeller tip speed for the design flow condition,  $m_d$ , at station J=175, ( $m/m_s=1.054$ ).

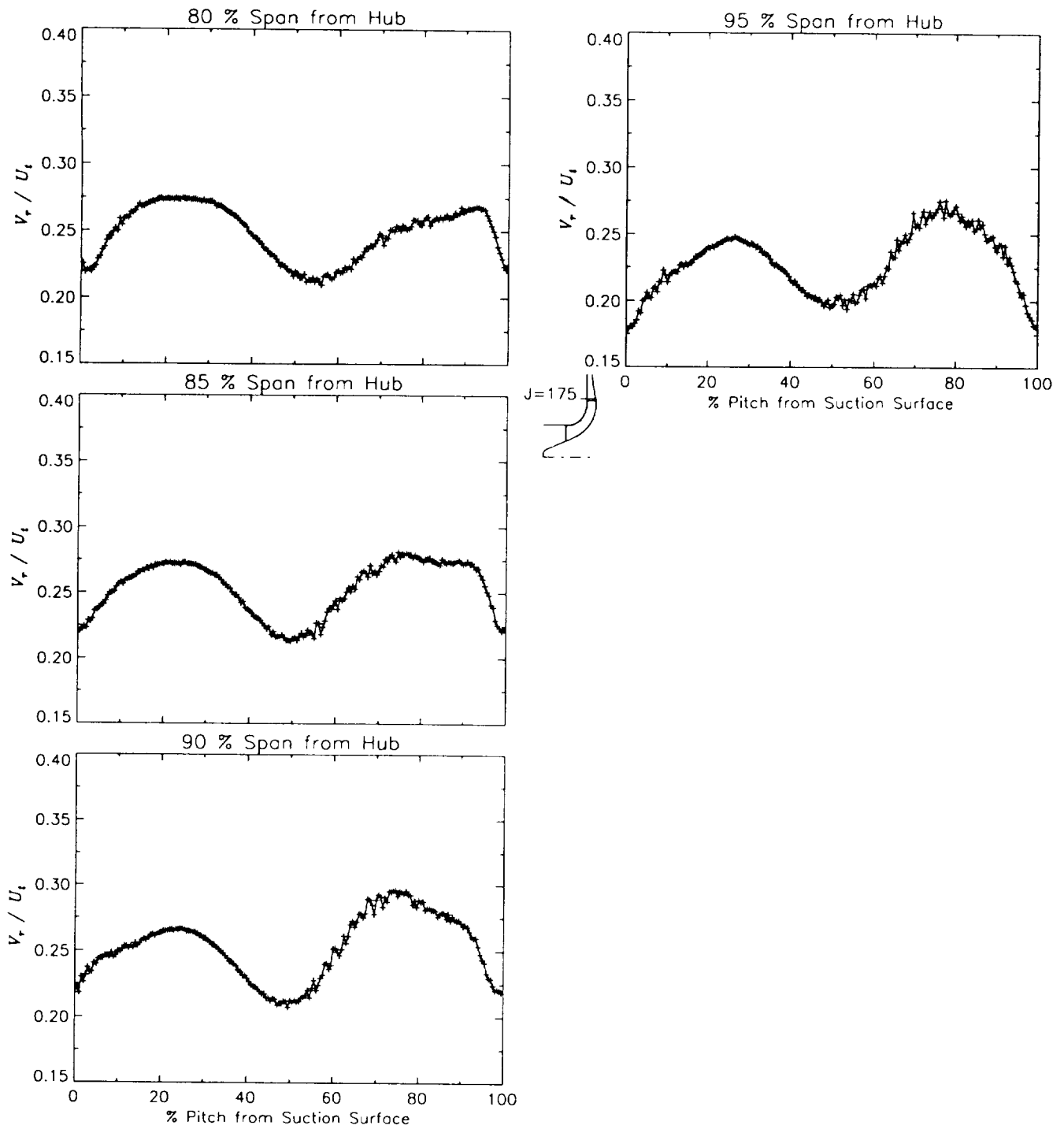
Station J=175, ( $m/m_s=1.054$ )



(a) Radial velocity normalized by impeller tip speed.

Figure 44.-Continued.

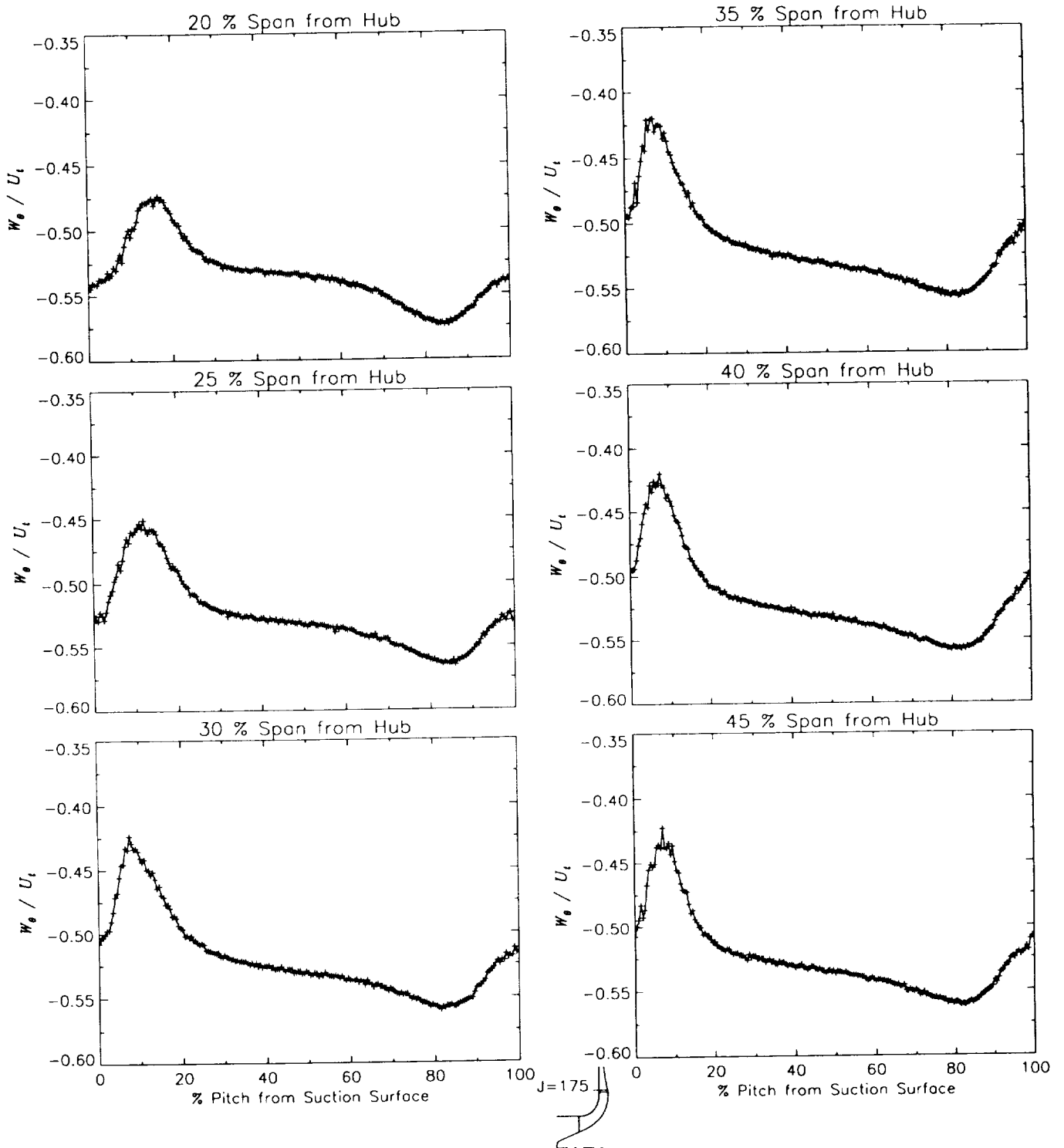
Station J=175, ( $m/m_s=1.054$ )



(a) Radial velocity normalized by impeller tip speed.

Figure 44.-Continued.

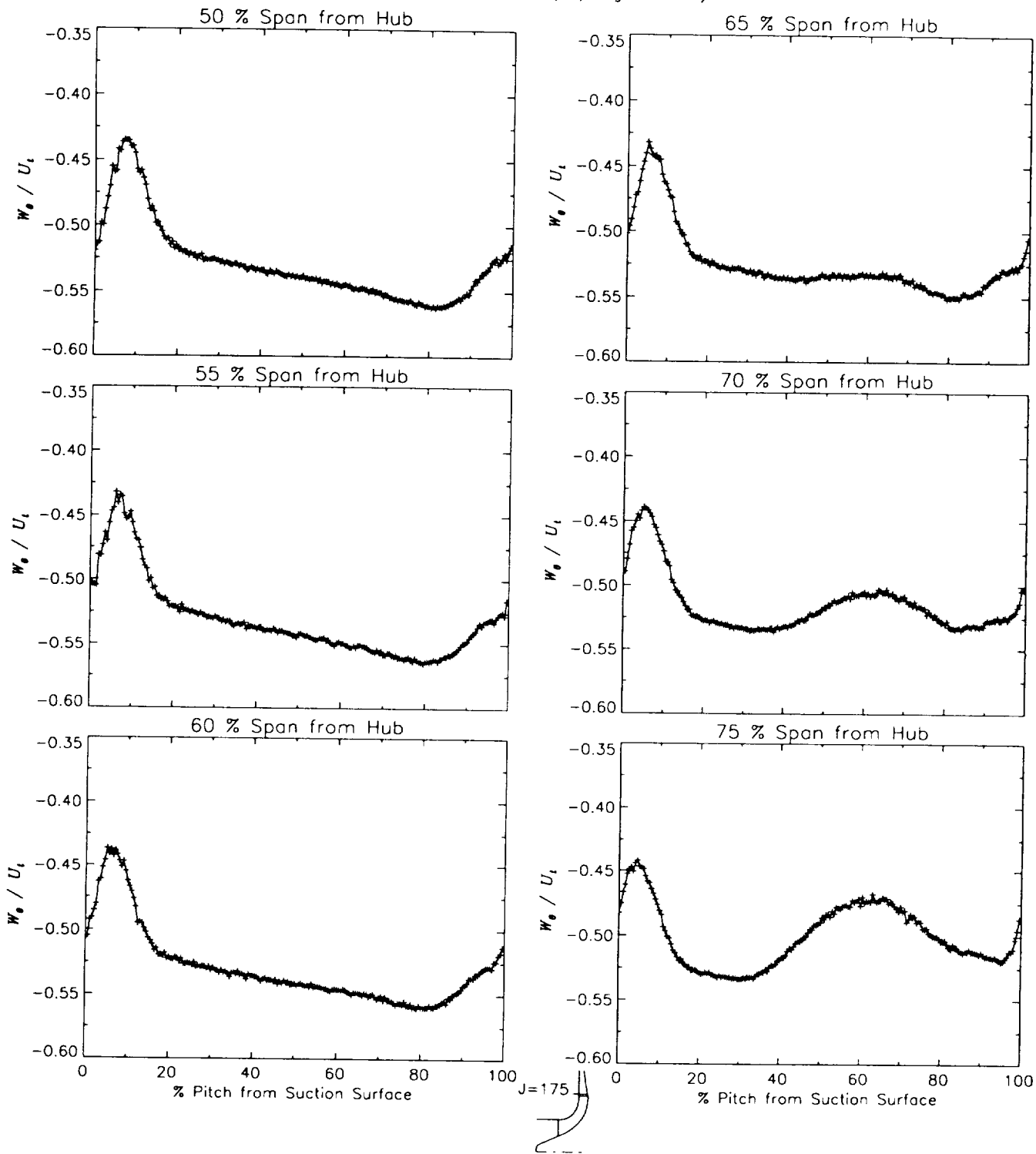
Station J=175, ( $m/m_s=1.054$ )



(b) Relative tangential velocity normalized by impeller tip speed.

Figure 44.-Continued.

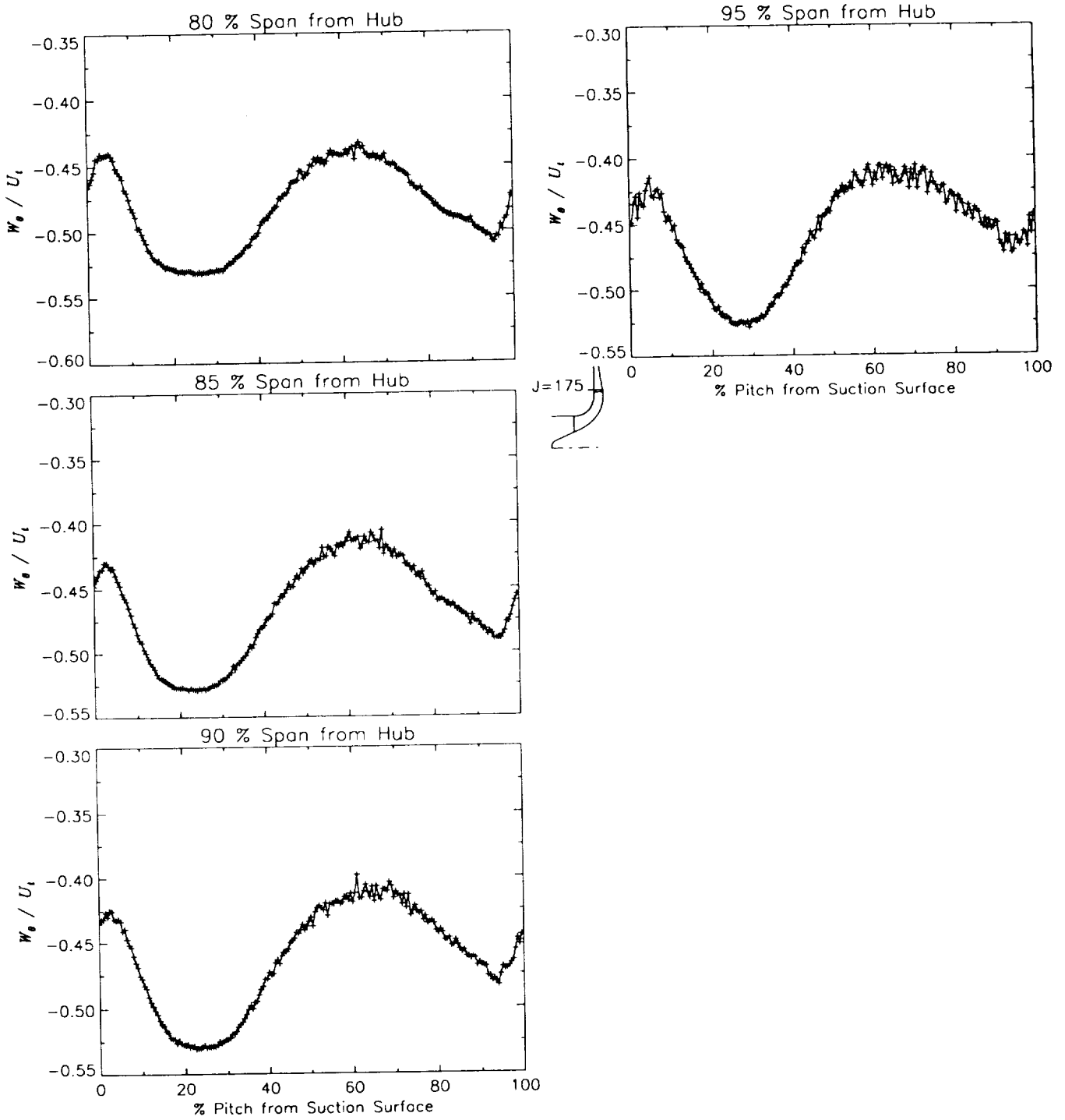
Station J=175, ( $m/m_s=1.054$ )



(b) Relative tangential velocity normalized by impeller tip speed.

Figure 44.-Continued.

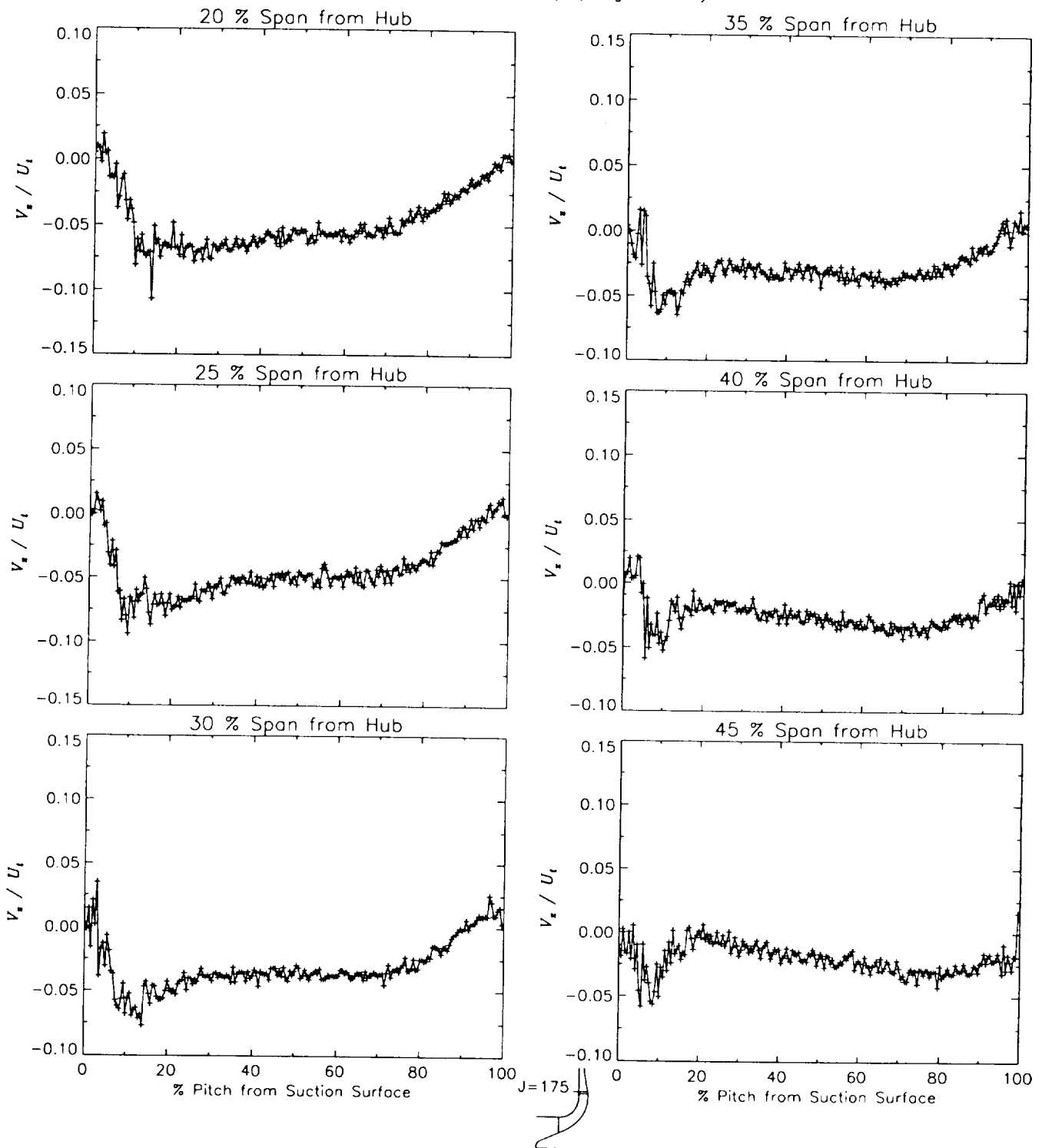
Station J=175, ( $m/m_s=1.054$ )



(b) Relative tangential velocity normalized by impeller tip speed.

Figure 44.-Continued.

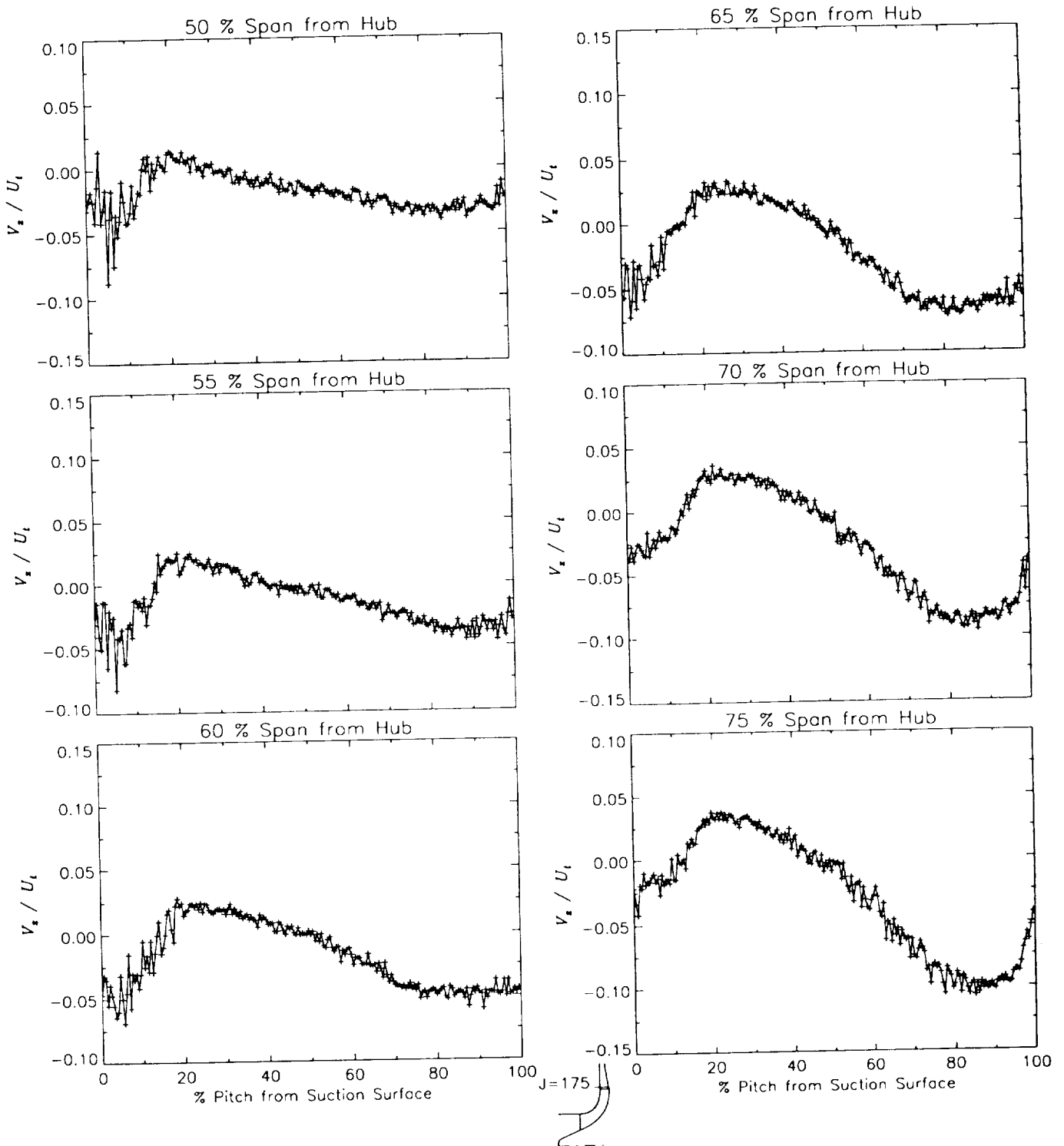
Station J=175, ( $m/m_s=1.054$ )



(c) Axial velocity normalized by impeller tip speed.

Figure 44.—Continued.

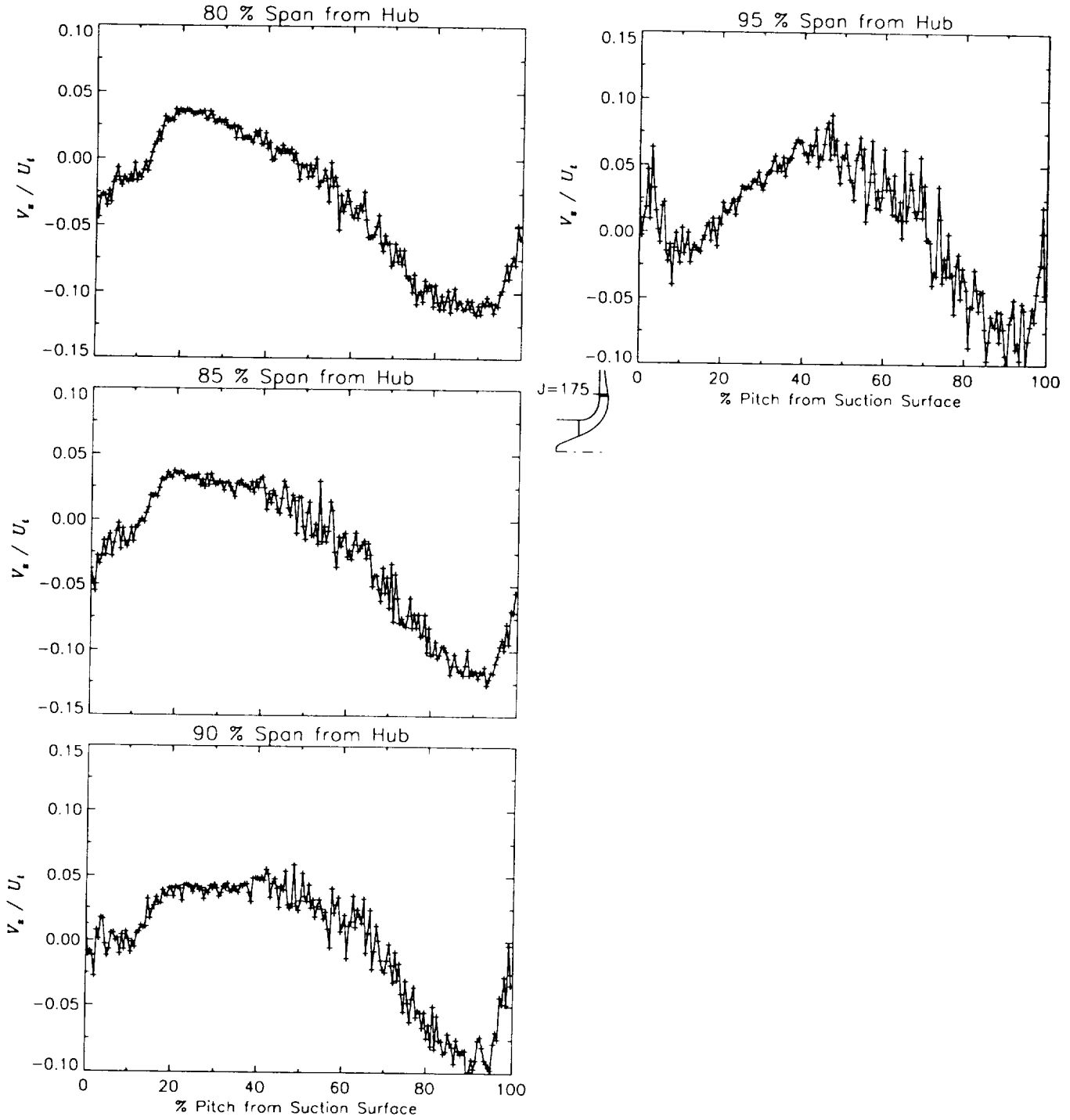
Station J=175, ( $m/m_s=1.054$ )



(c) Axial velocity normalized by impeller tip speed.

Figure 44.-Continued.

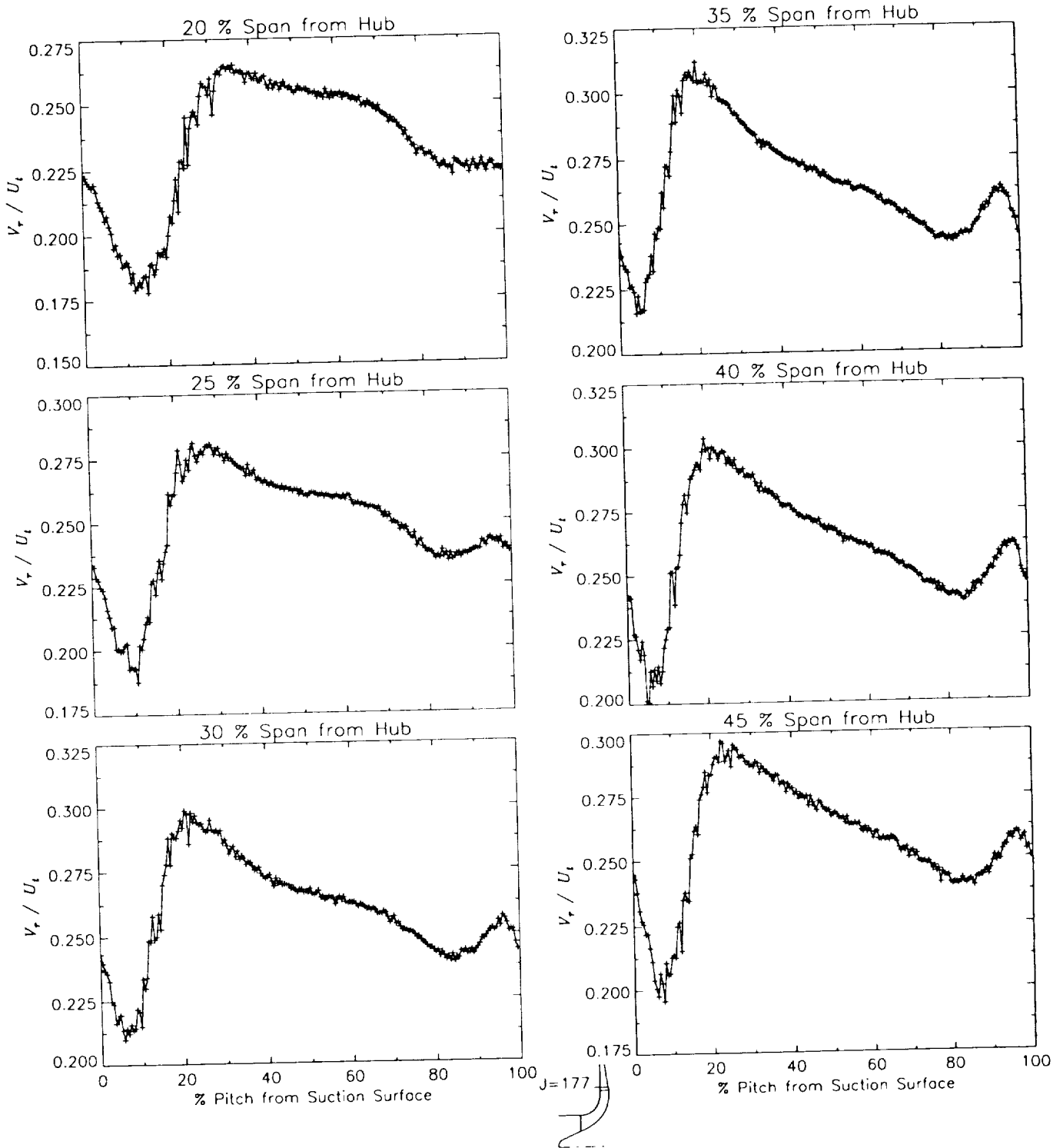
Station J=175, ( $m/m_s=1.054$ )



(c) Axial velocity normalized by impeller tip speed.

Figure 44.—Concluded.

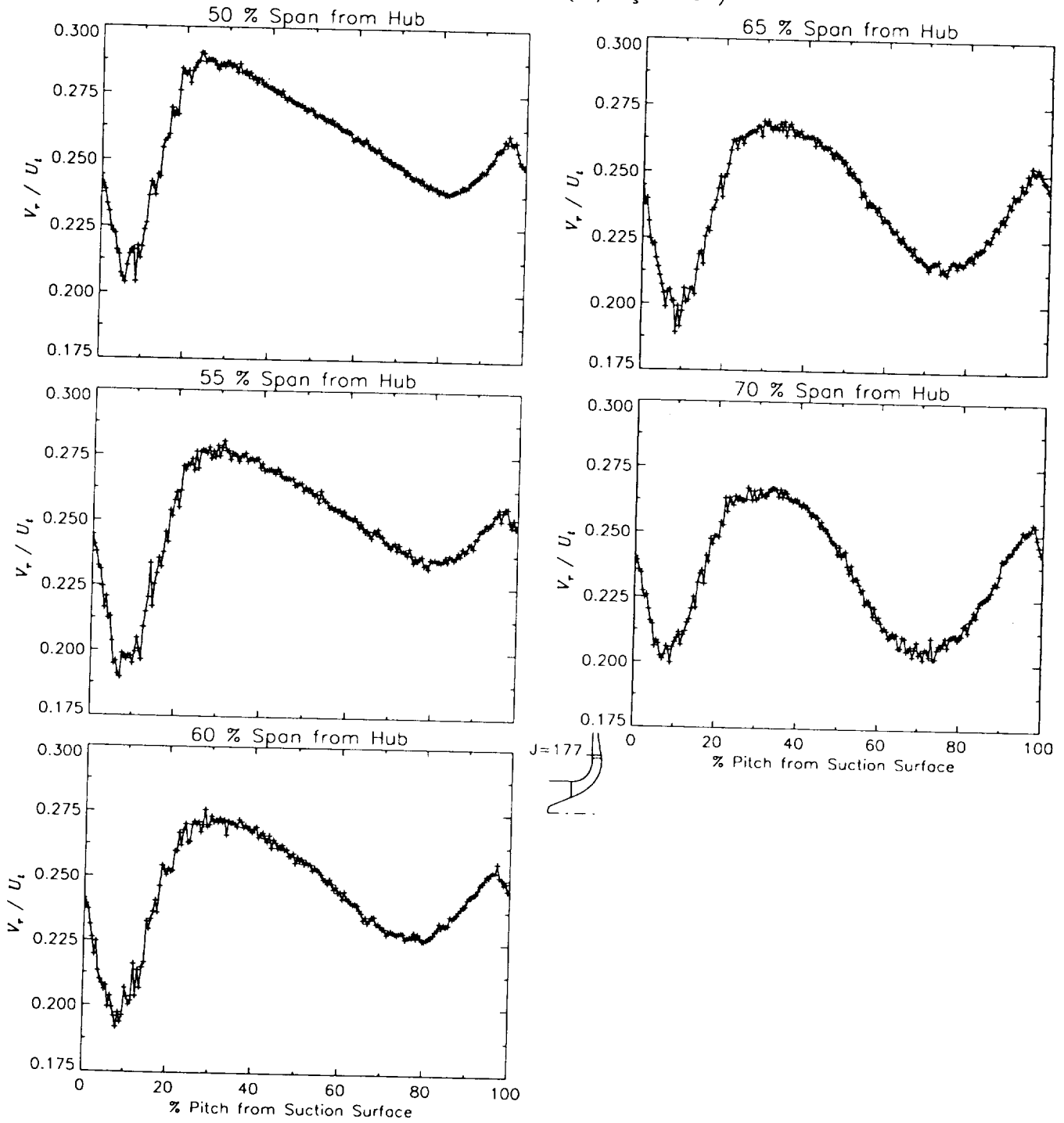
Station J=177, ( $m/m_s=1.081$ )



(a) Radial velocity normalized by impeller tip speed.

Figure 45.-Laser velocimeter results of axial, radial, and relative tangential velocities normalized by impeller tip speed for the design flow condition,  $m_d$ , at station J=177, ( $m/m_s=1.081$ ).

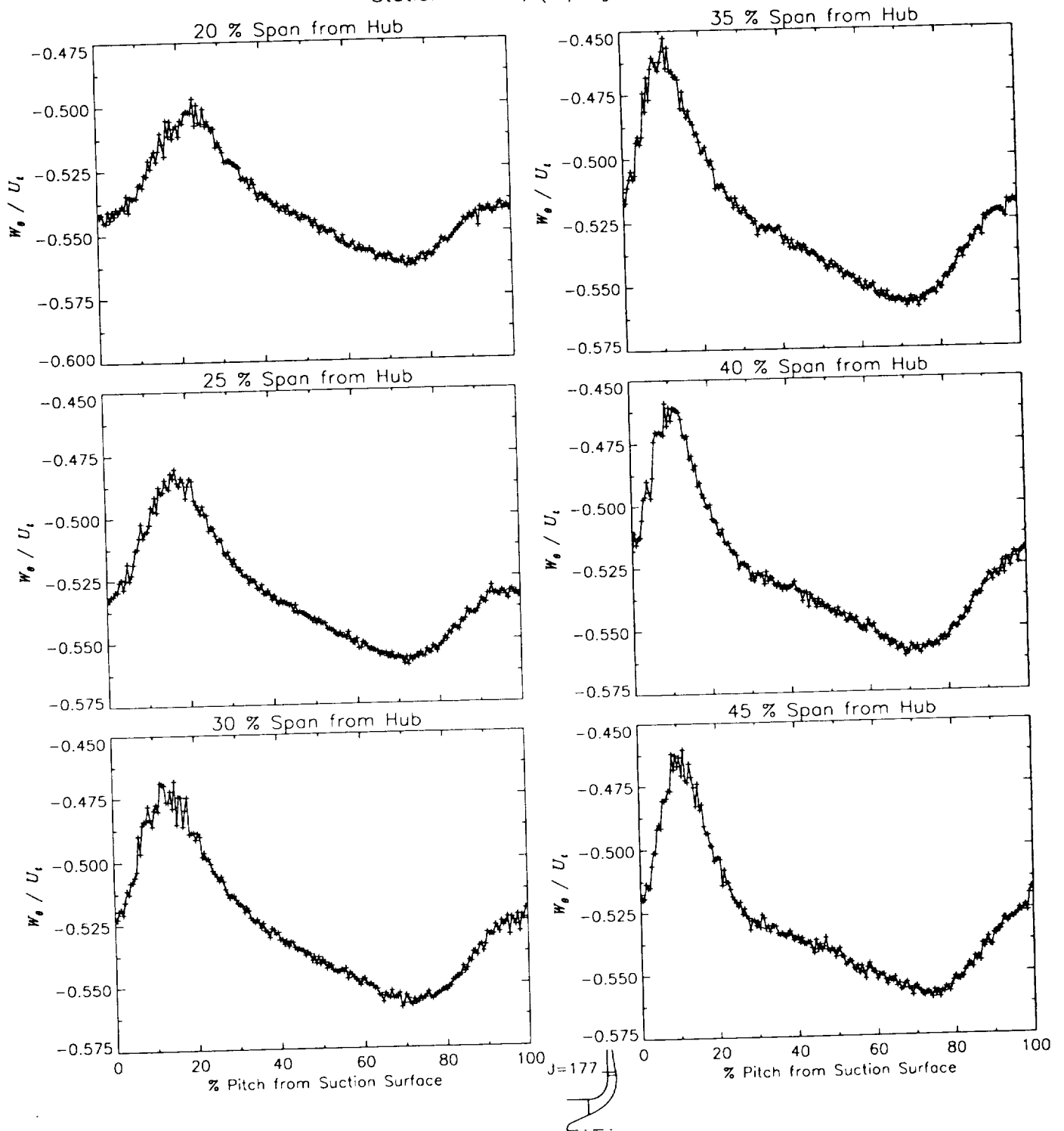
Station J=177, ( $m/m_s=1.081$ )



(a) Radial velocity normalized by impeller tip speed.

Figure 45.-Continued.

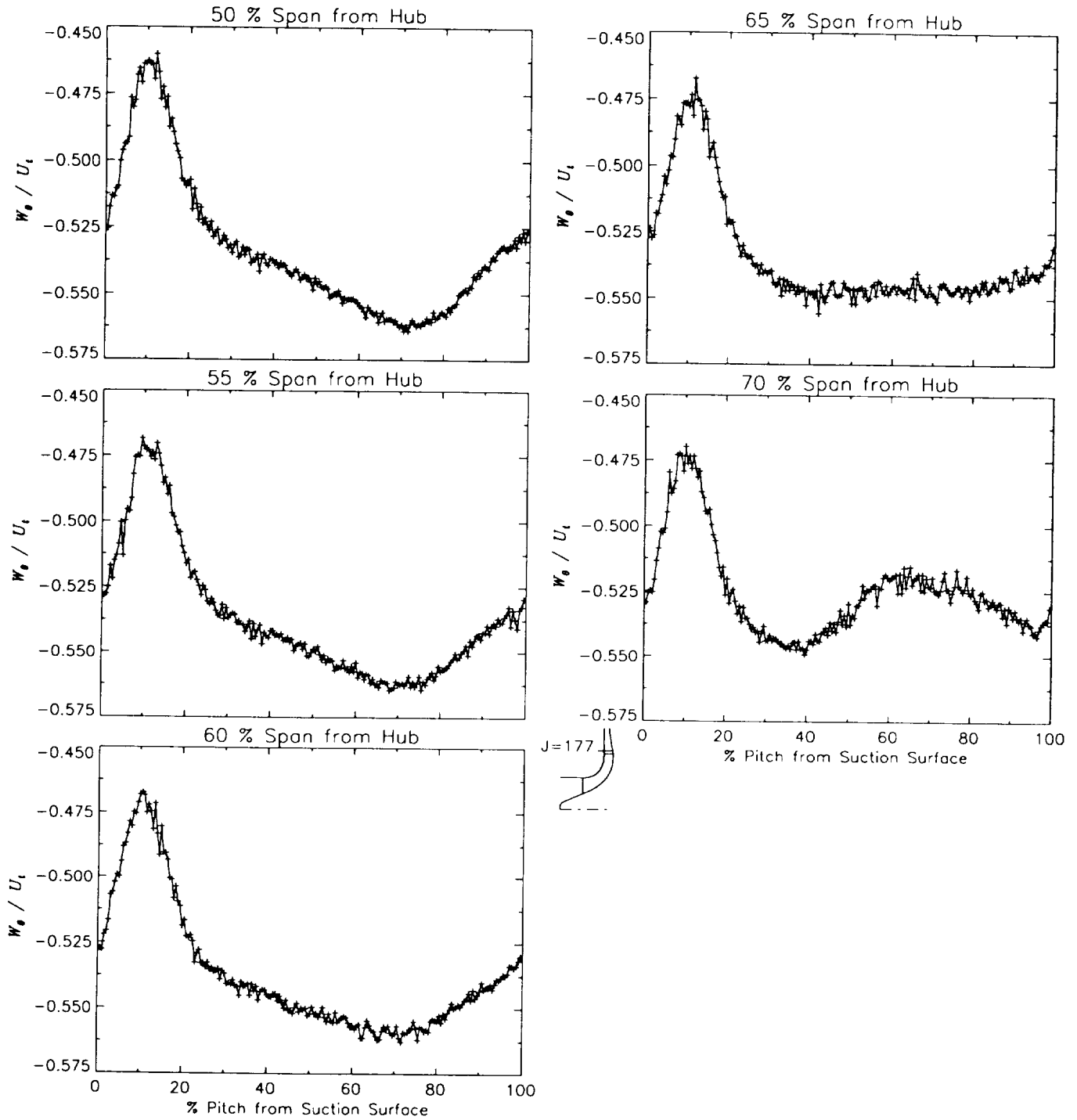
Station J=177, ( $m/m_s=1.081$ )



(b) Relative tangential velocity normalized by impeller tip speed.

Figure 45.-Continued.

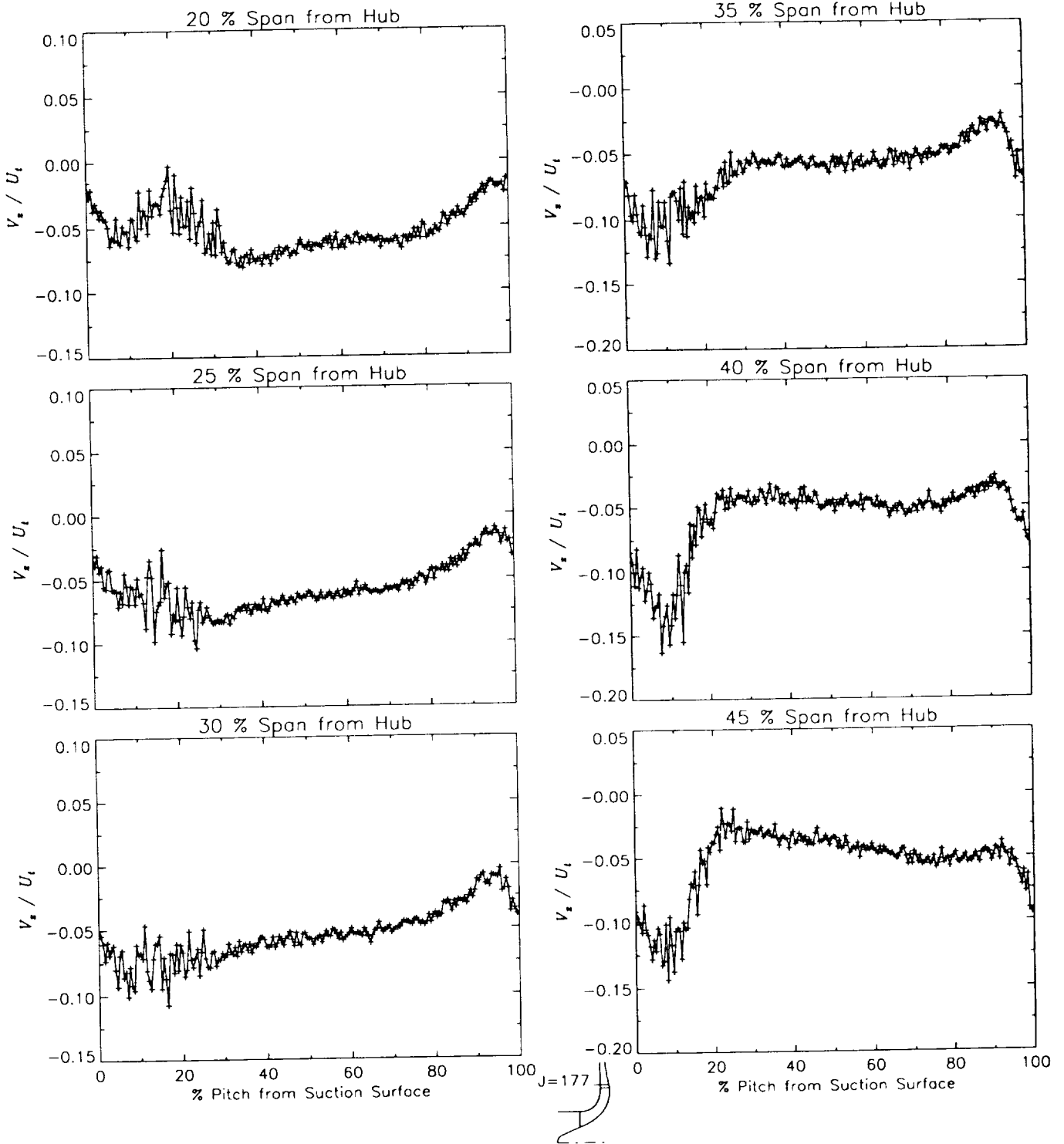
Station J=177, ( $m/m_s=1.081$ )



(b) Relative tangential velocity normalized by impeller tip speed.

Figure 45.-Continued.

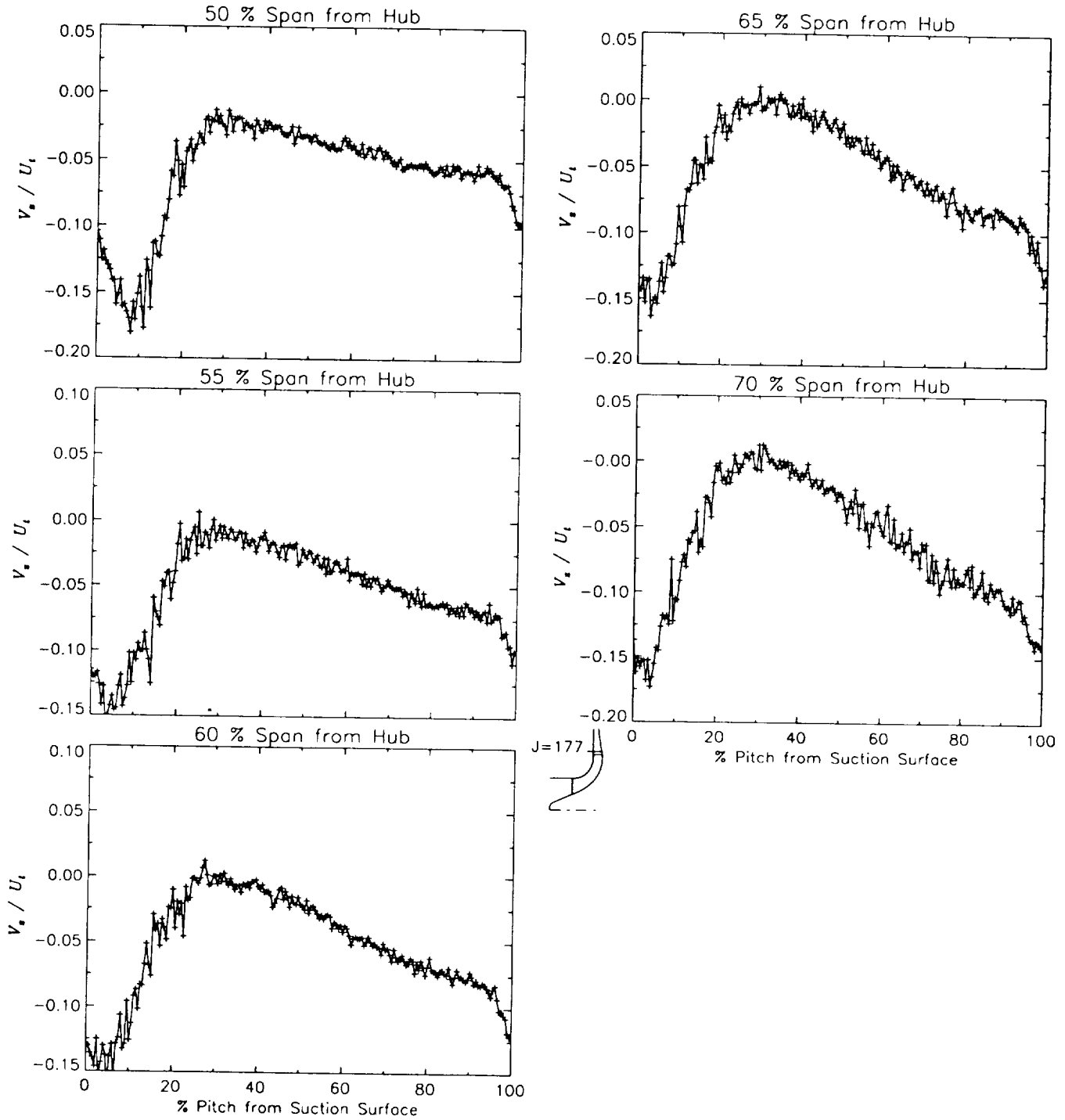
Station J=177, ( $m/m_s=1.081$ )



(c) Axial velocity normalized by impeller tip speed.

Figure 45.--Continued.

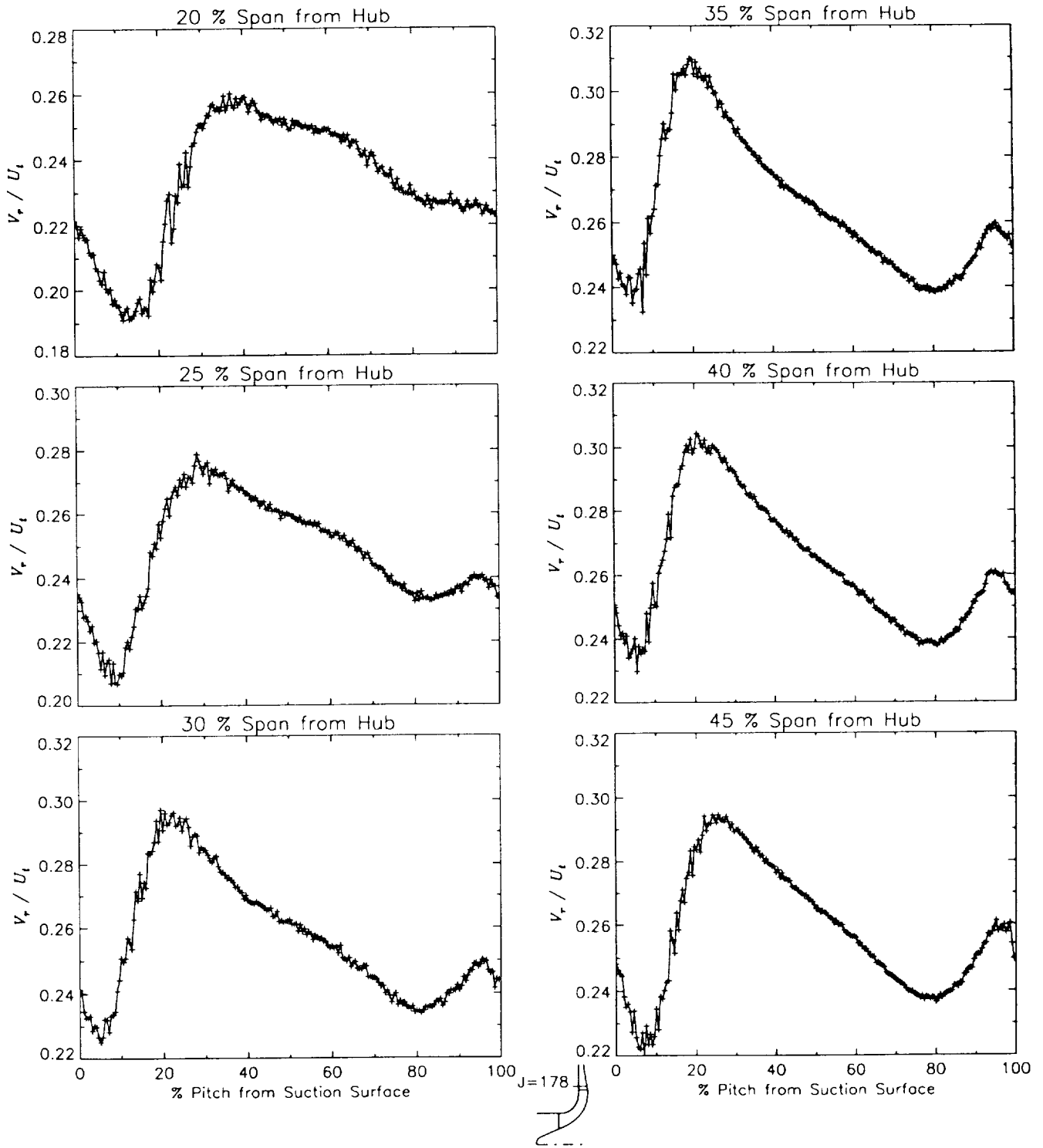
Station J=177, ( $m/m_s=1.081$ )



(c) Axial velocity normalized by impeller tip speed.

Figure 45.—Concluded.

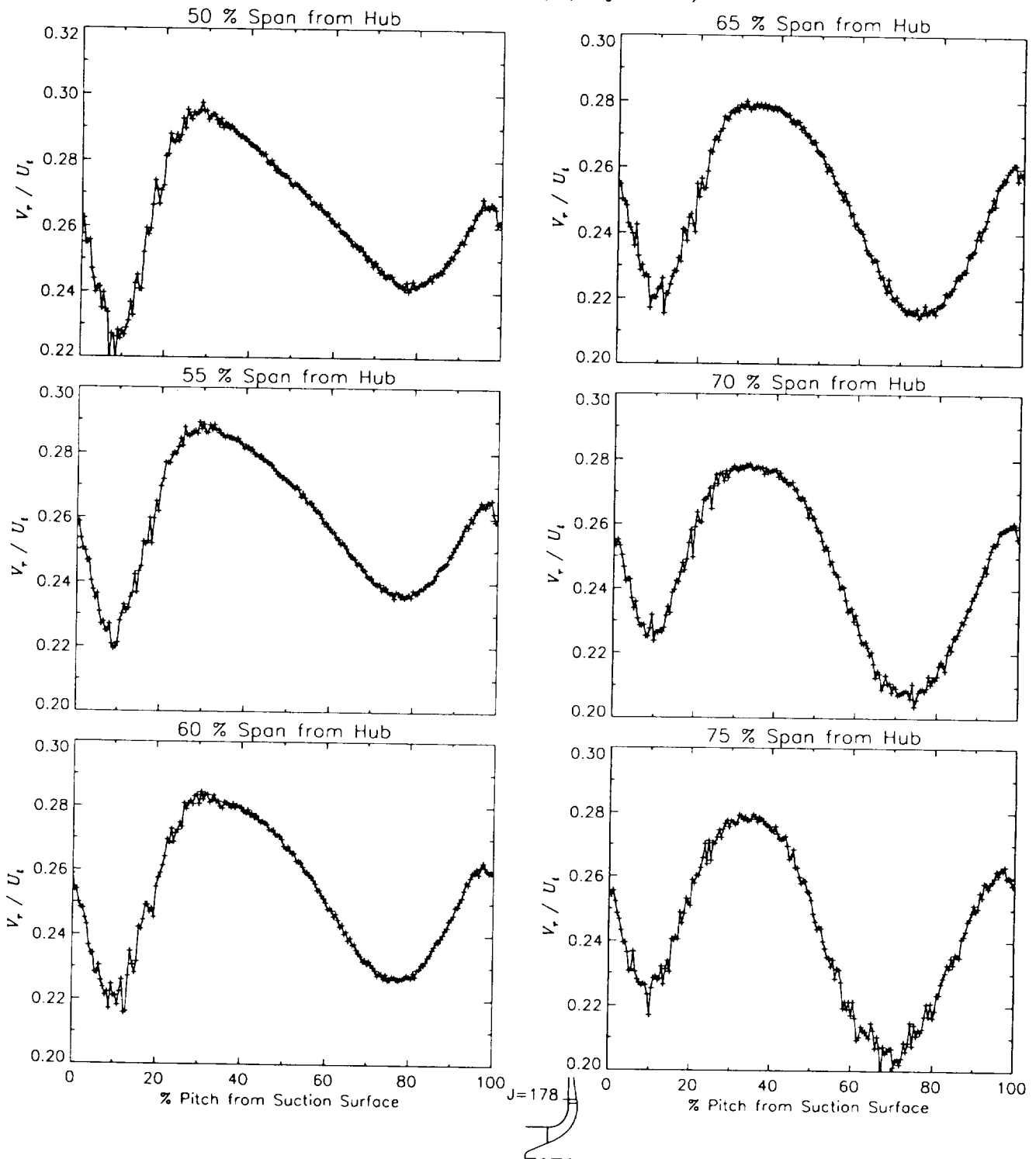
Station J=178, ( $m/m_s=1.094$ )



(a) Radial velocity normalized by impeller tip speed.

Figure 46.-Laser velocimeter results of axial, radial, and relative tangential velocities normalized by impeller tip speed for the design flow condition,  $m_d$ , at station J=178, ( $m/m_s=1.094$ ).

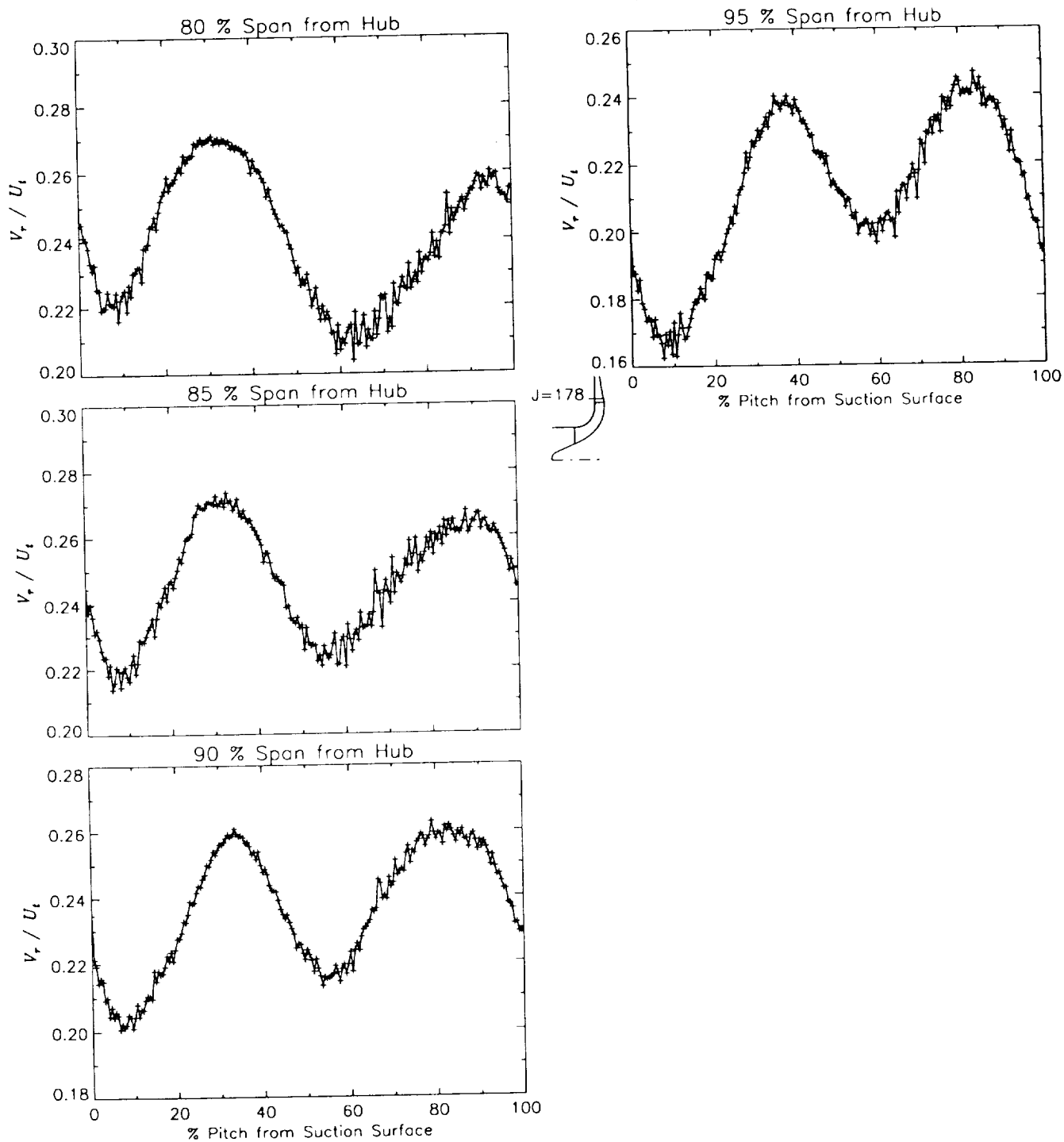
Station J=178, ( $m/m_s=1.094$ )



(a) Radial velocity normalized by impeller tip speed.

Figure 46.-Continued.

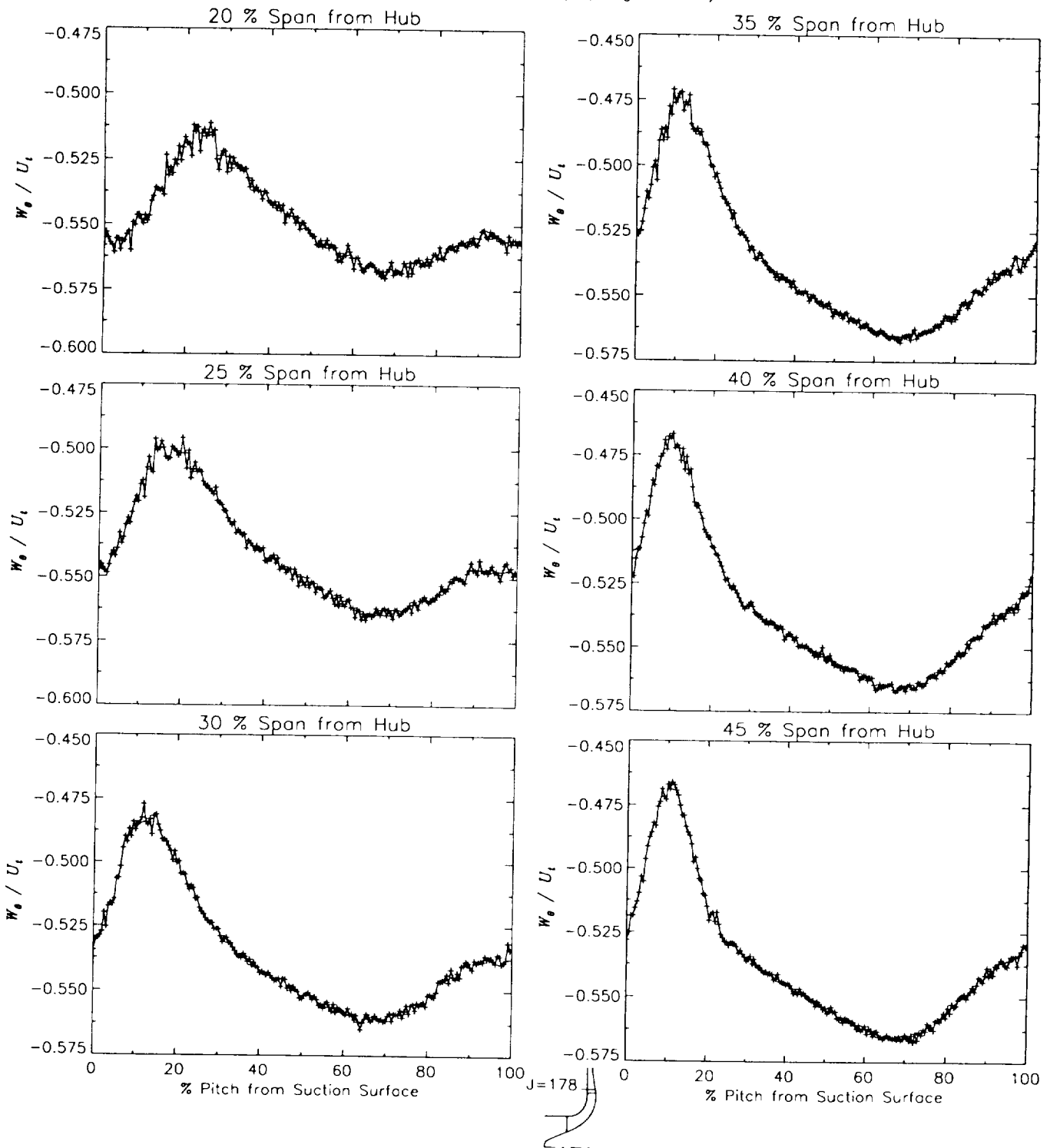
Station J=178, ( $m/m_s=1.094$ )



(a) Radial velocity normalized by impeller tip speed.

Figure 46.-Continued.

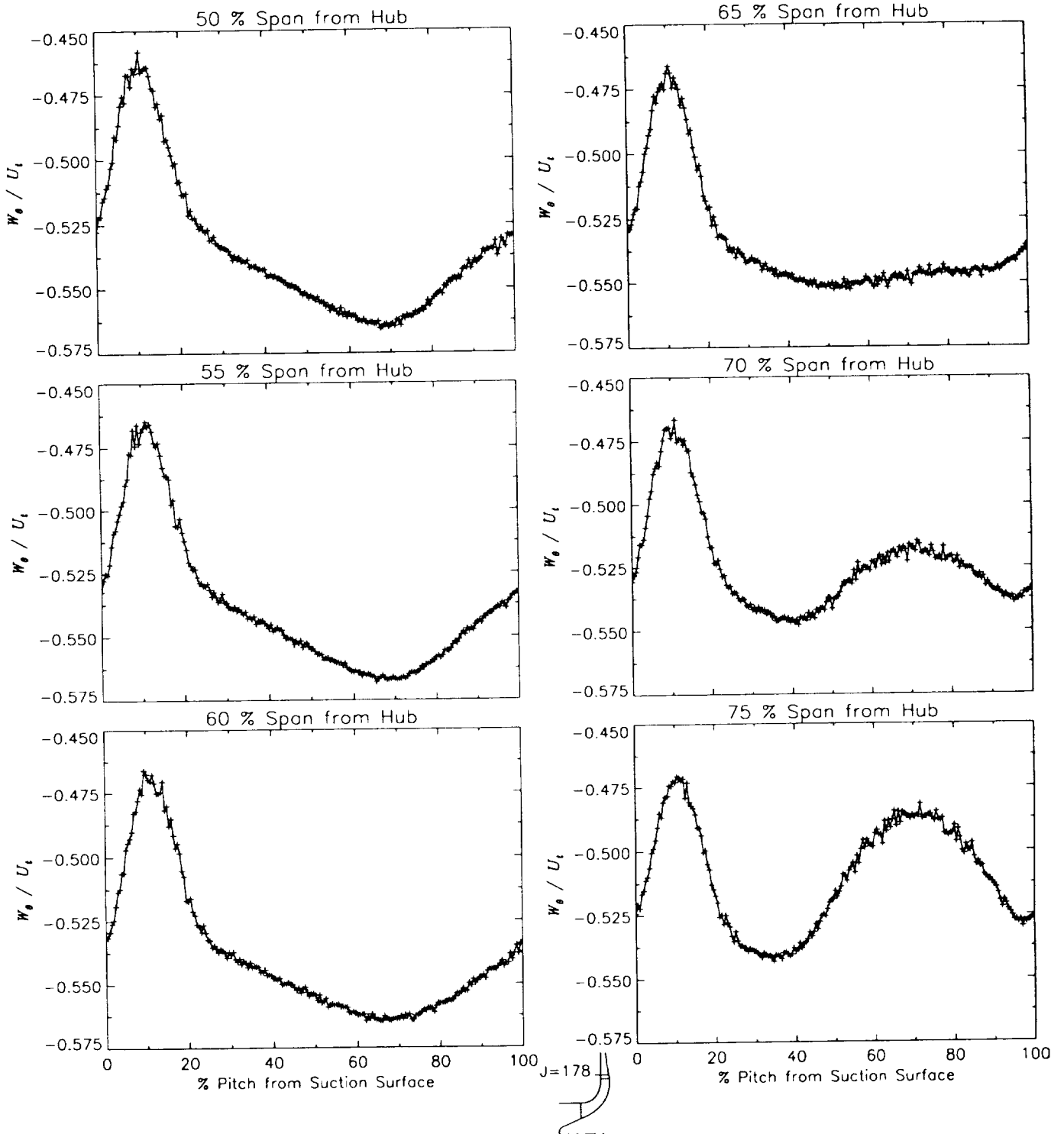
Station J=178, ( $m/m_s=1.094$ )



(b) Relative tangential velocity normalized by impeller tip speed.

Figure 46.-Continued.

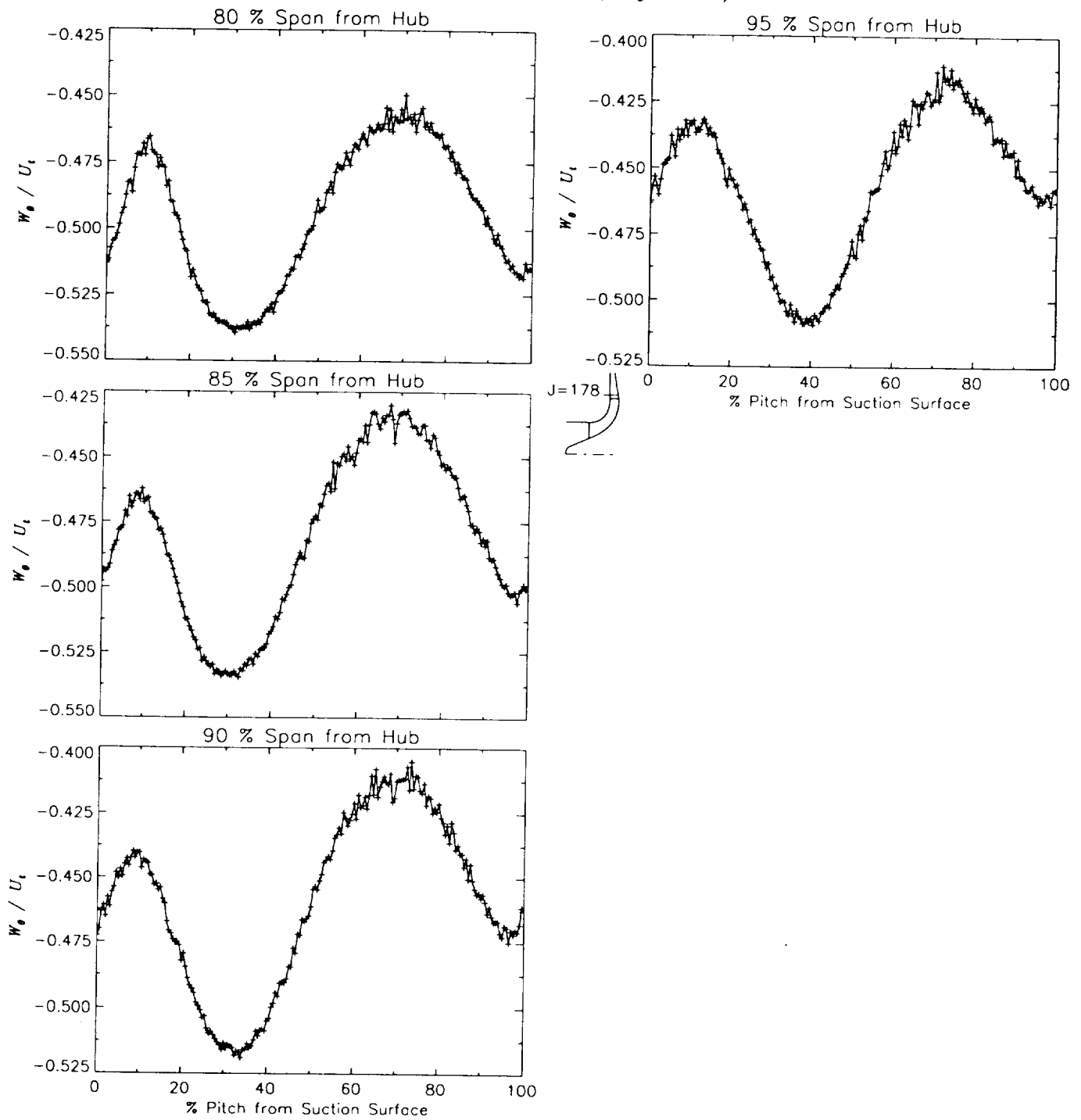
Station J=178, ( $m/m_s=1.094$ )



(b) Relative tangential velocity normalized by impeller tip speed.

Figure 46.-Continued.

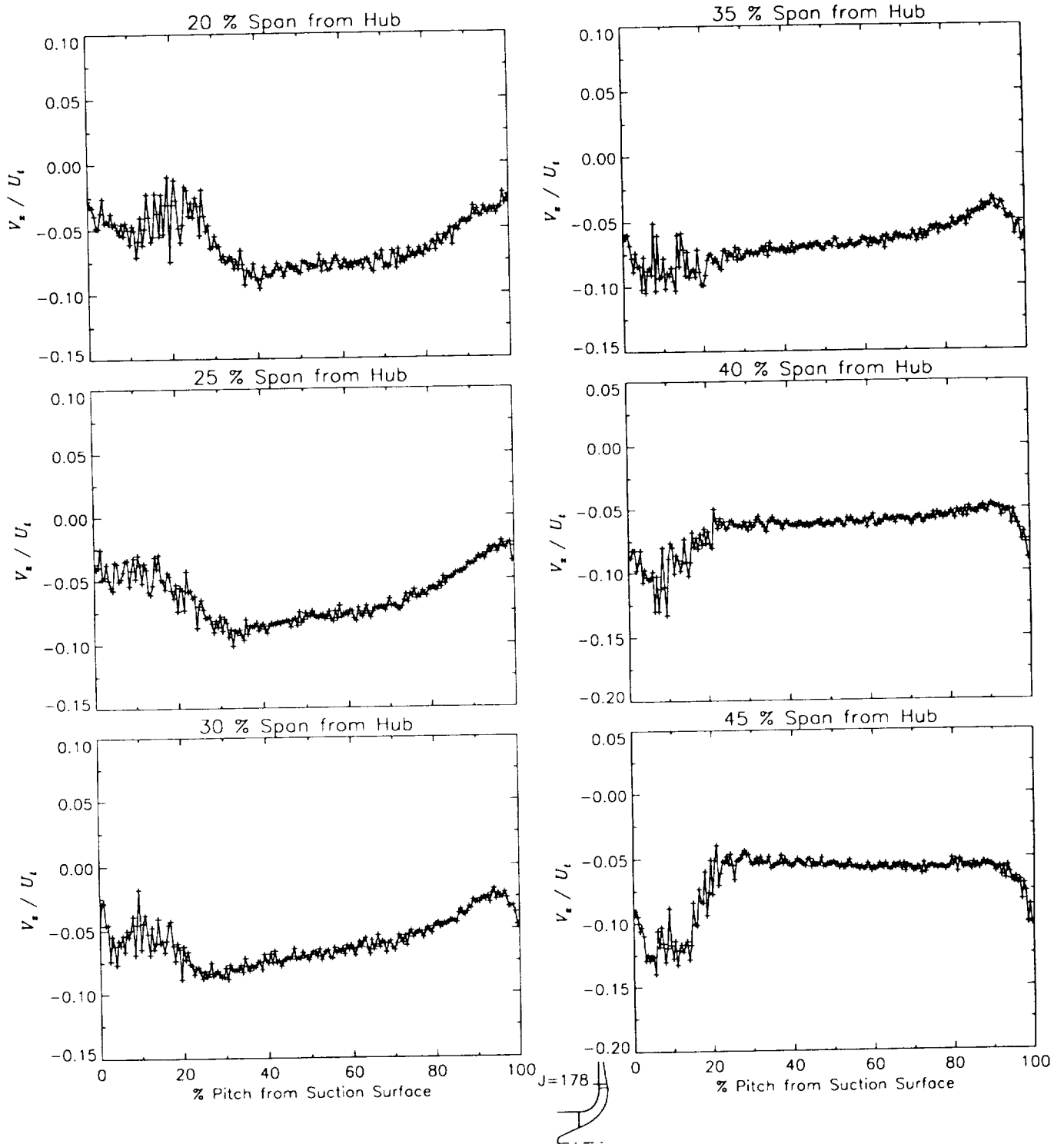
Station J=178, ( $m/m_s=1.094$ )



(b) Relative tangential velocity normalized by impeller tip speed.

Figure 46.-Continued.

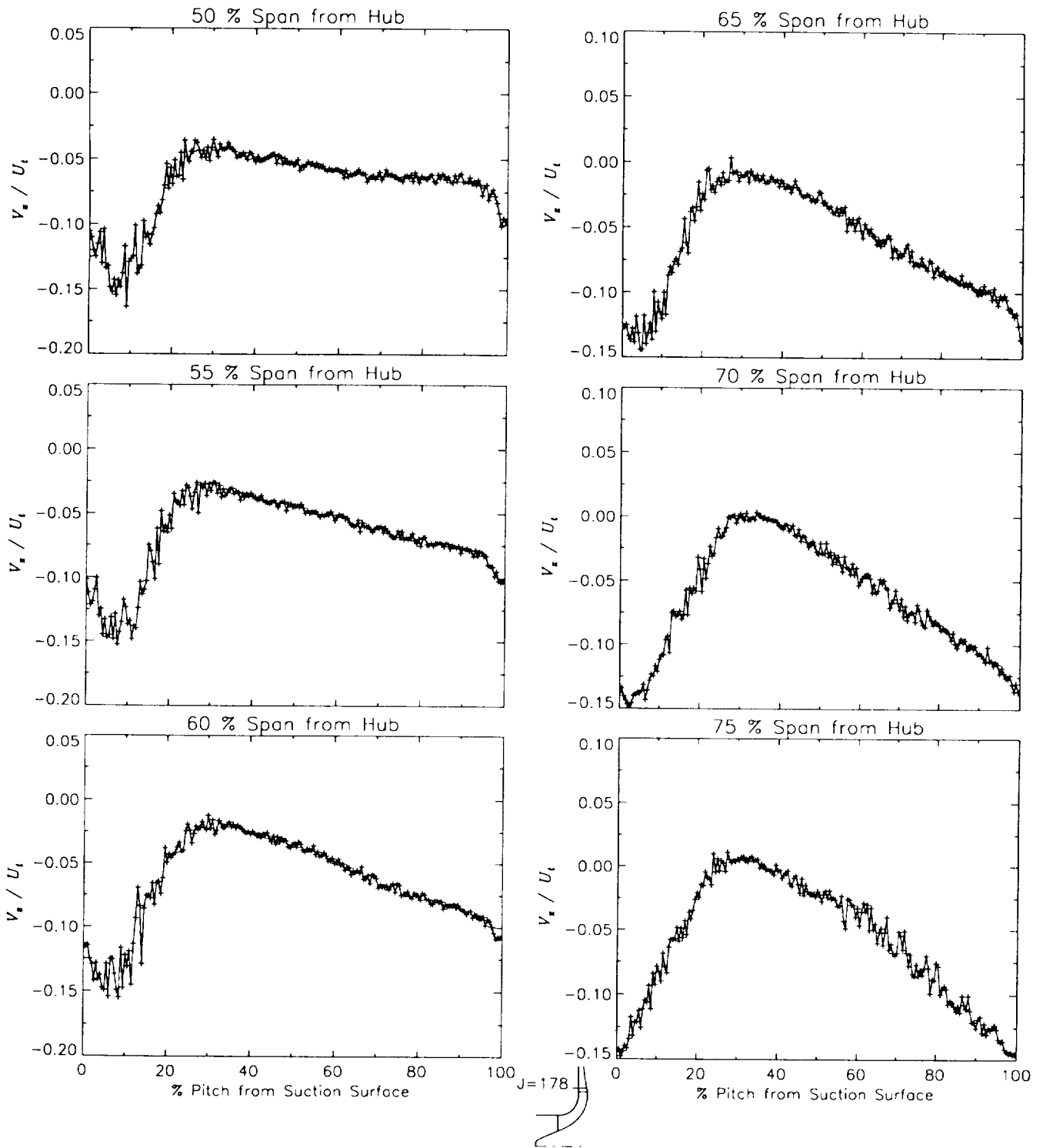
Station J=178, ( $m/m_s=1.094$ )



(c) Axial velocity normalized by impeller tip speed.

Figure 46.-Continued.

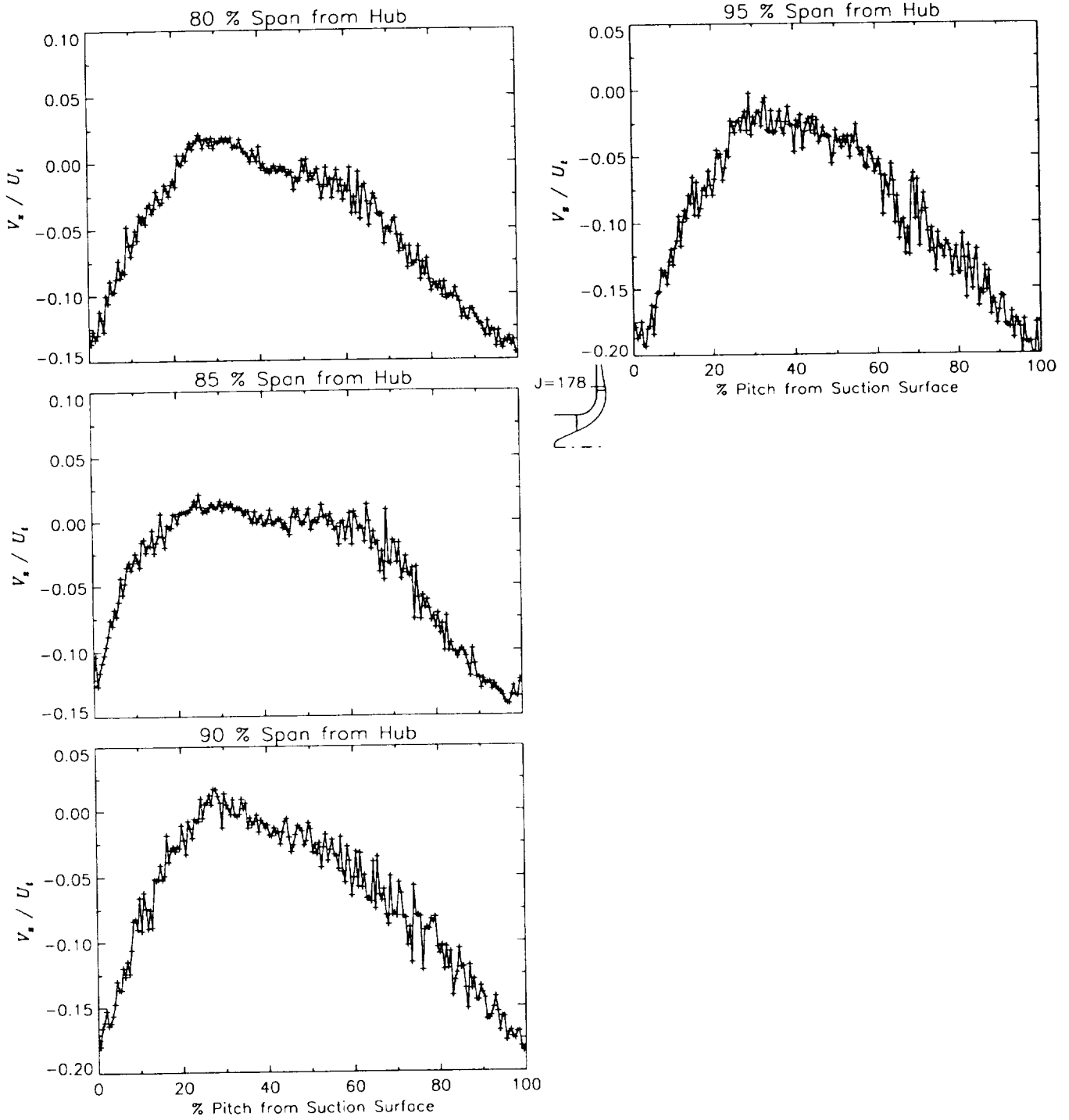
Station J=178, ( $m/m_s=1.094$ )



(c) Axial velocity normalized by impeller tip speed.

Figure 46.-Continued.

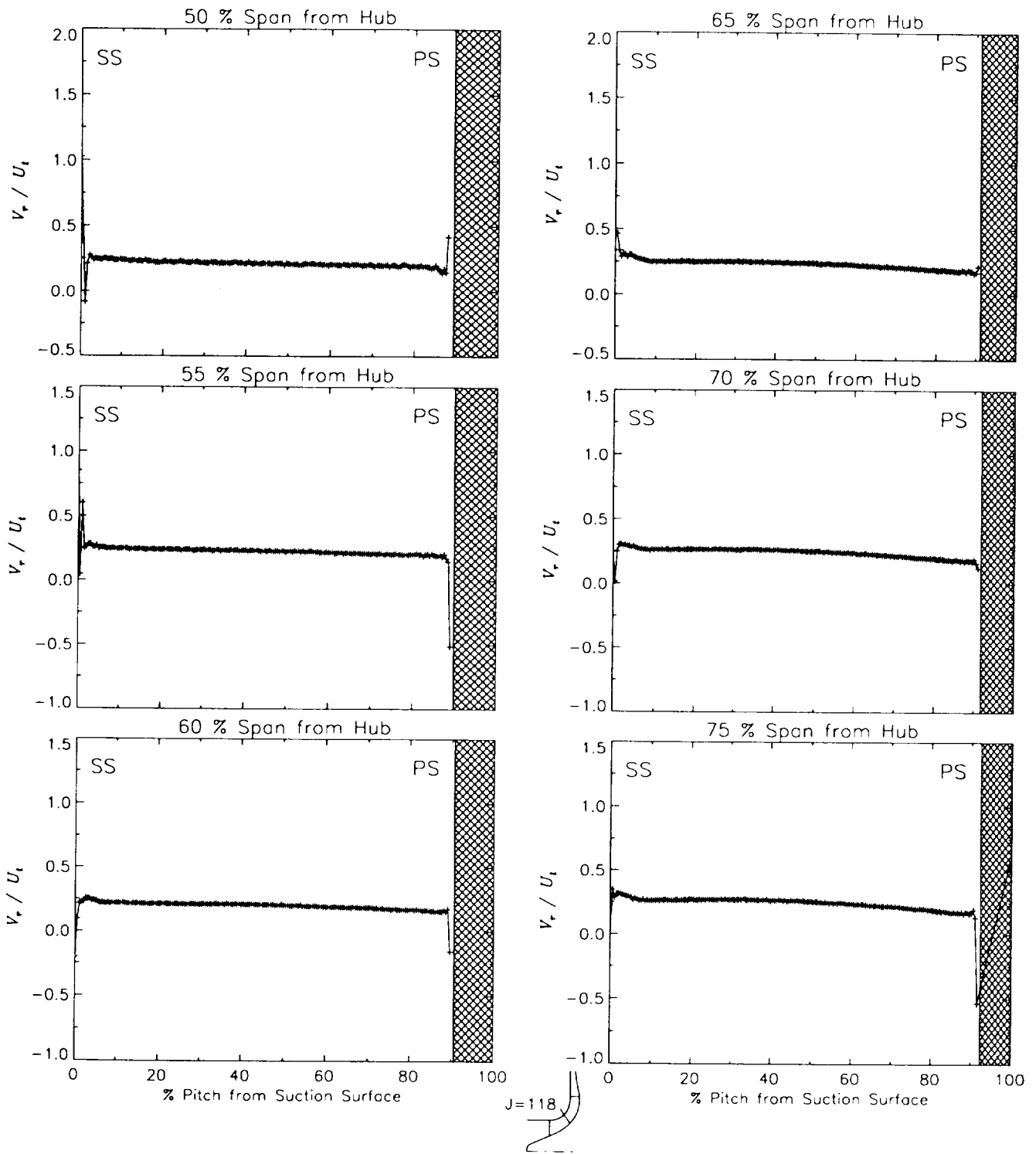
Station J=178, ( $m/m_s=1.094$ )



(c) Axial velocity normalized by impeller tip speed.

Figure 46.—Concluded.

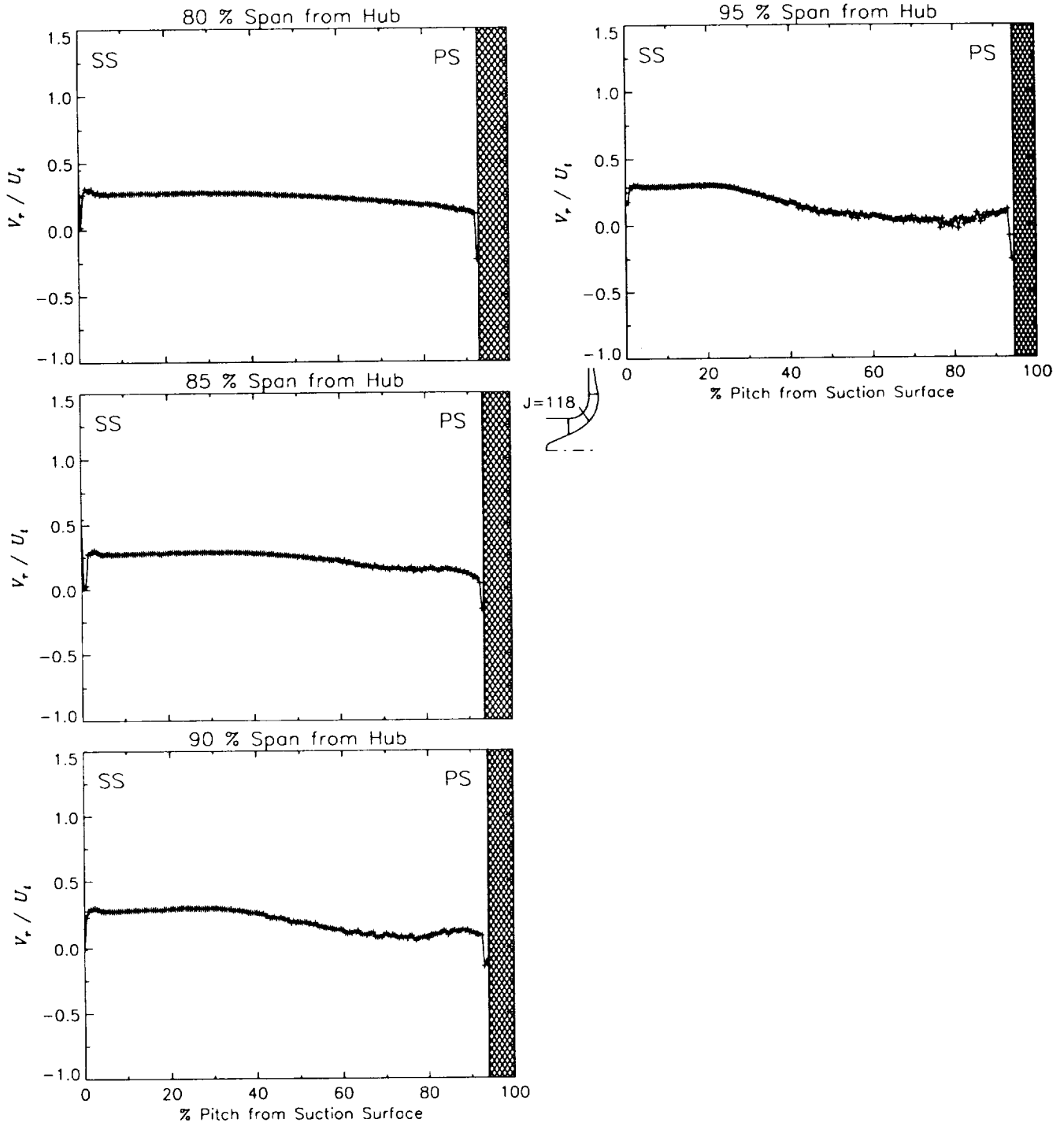
Station J=118, ( $m/m_s=0.475$ )



(a) Radial velocity normalized by impeller tip speed.

Figure 47.-Laser velocimeter results of axial, radial, and relative tangential velocities normalized by impeller tip speed for the off-design flow condition, 78.7%  $\dot{m}_d$ , at station J=118, ( $m/m_s=0.475$ ). The shaded region to the right of each plot represents the physical blade width.

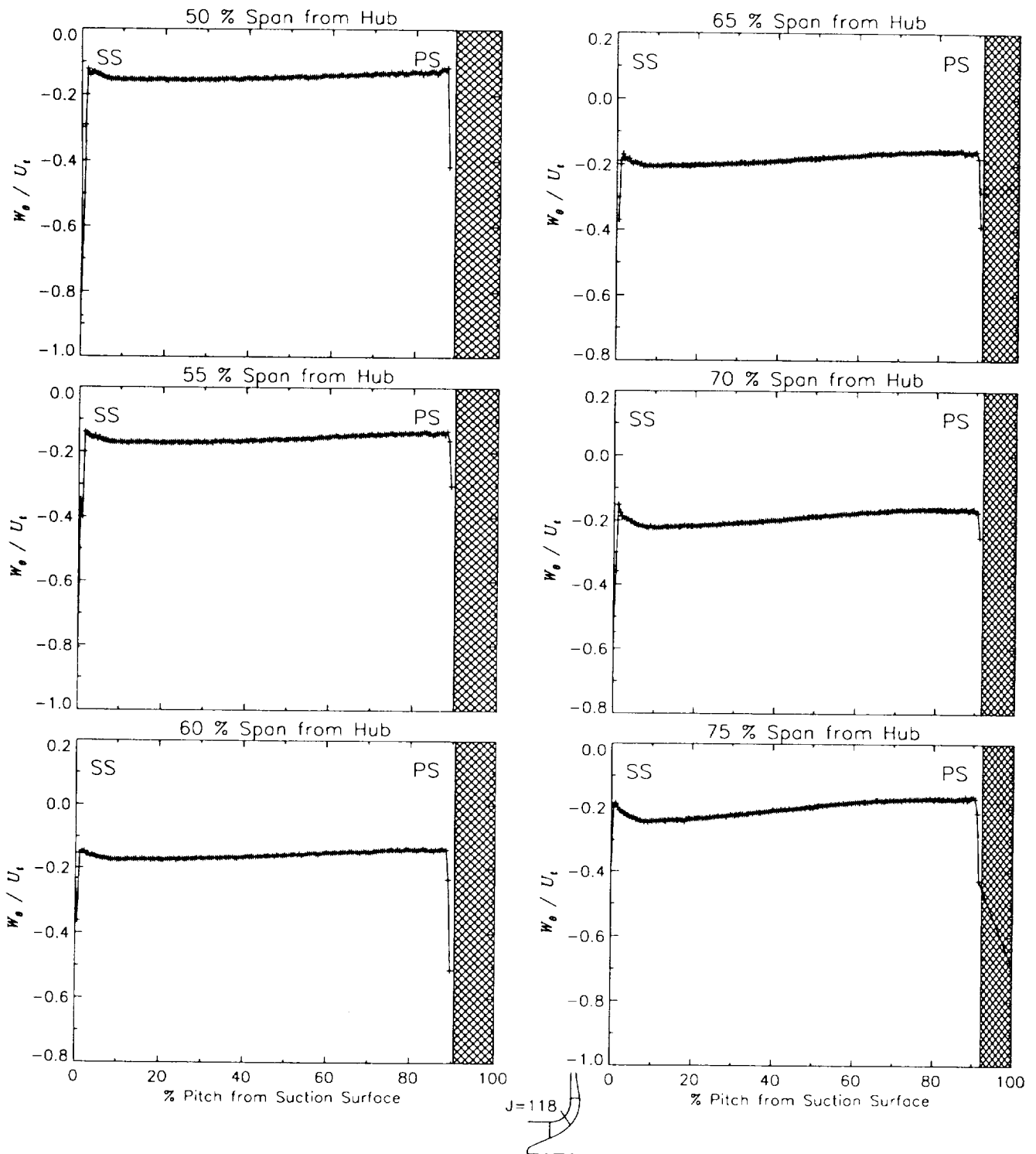
Station J=118, ( $m/m_s=0.475$ )



(a) Radial velocity normalized by impeller tip speed.

Figure 47.-Continued.

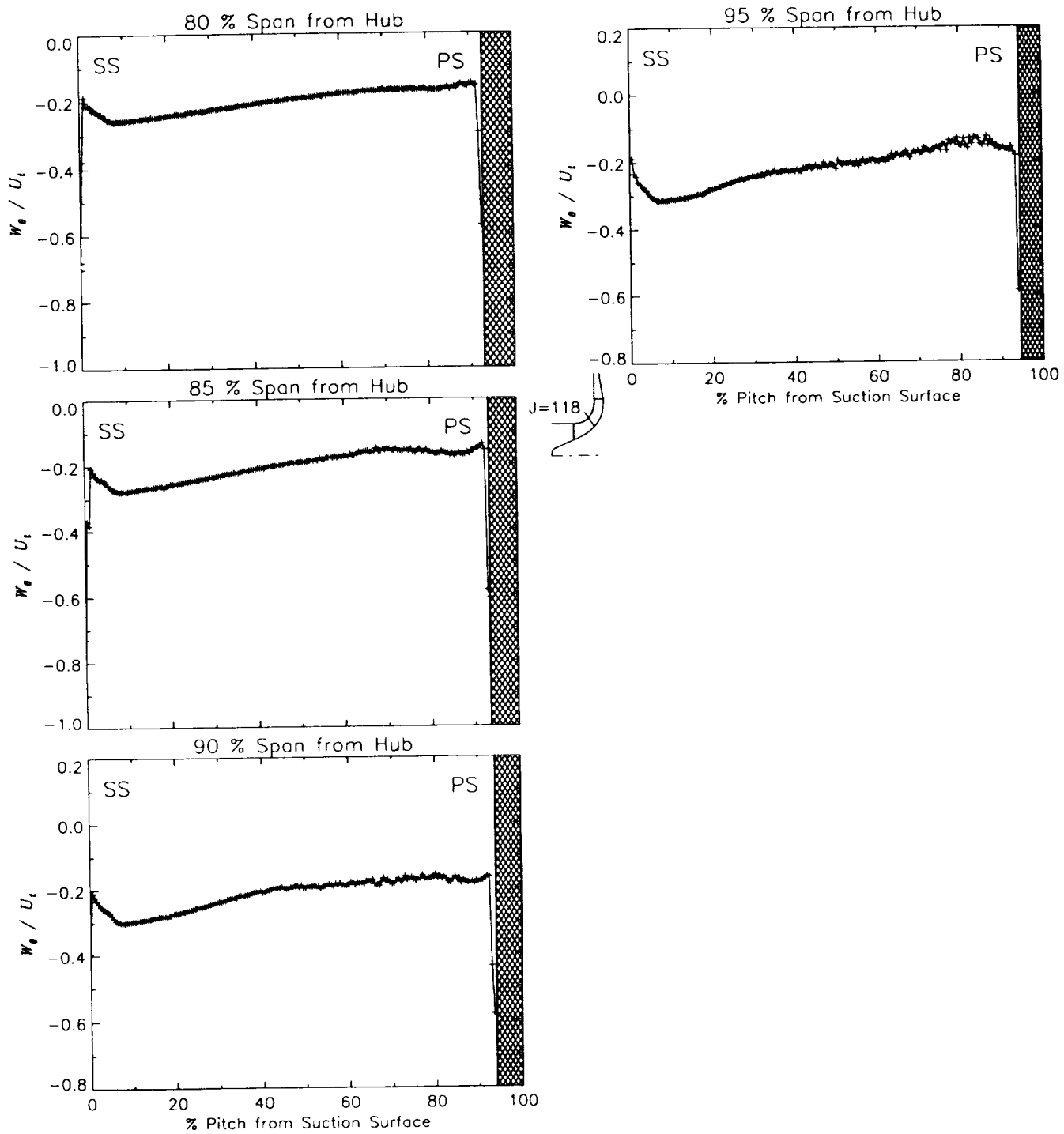
Station J=118, ( $m/m_s=0.475$ )



(b) Relative tangential velocity normalized by impeller tip speed.

Figure 47.—Continued.

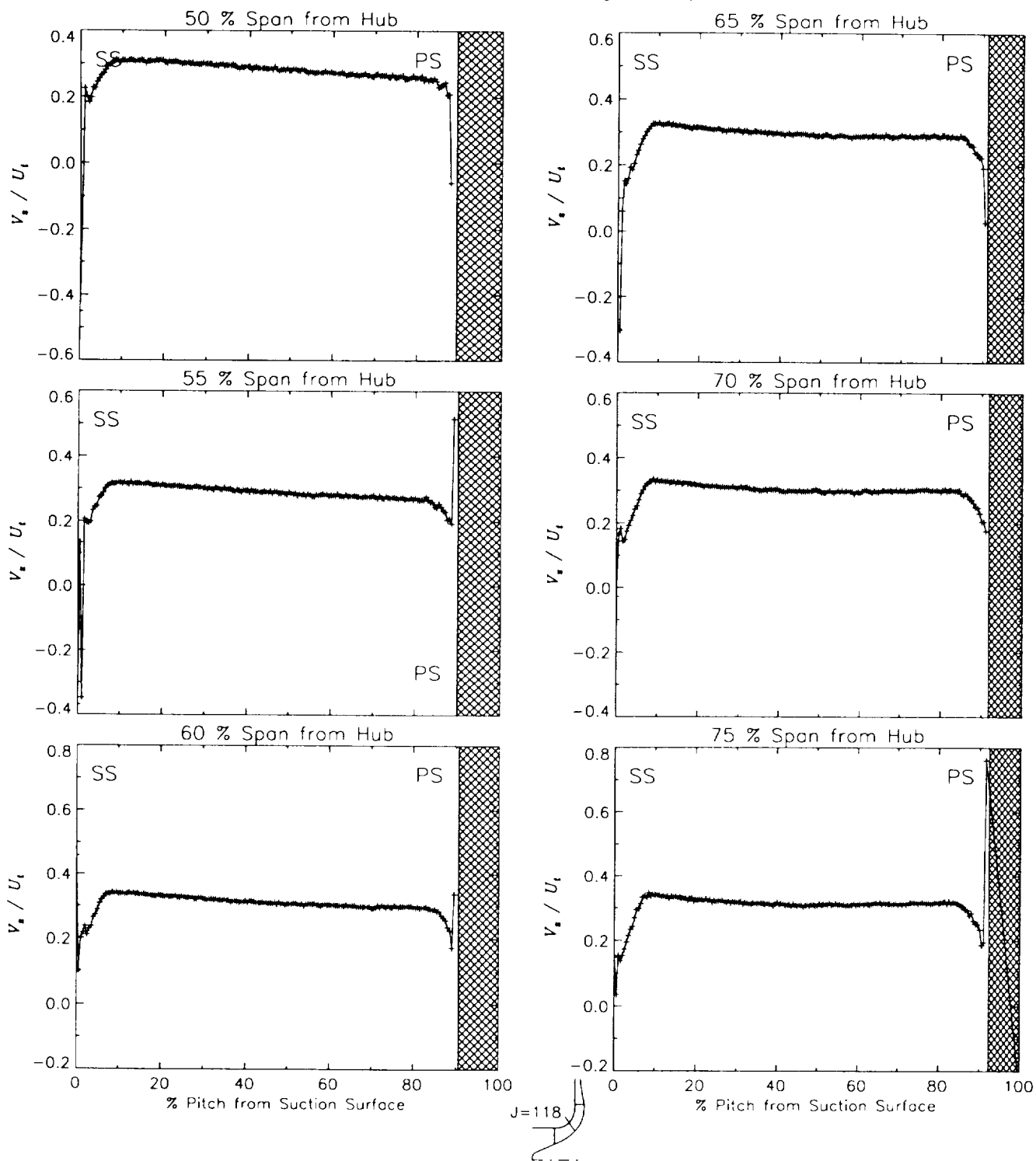
Station J=118, ( $m/m_s=0.475$ )



(b) Relative tangential velocity normalized by impeller tip speed.

Figure 47.-Continued.

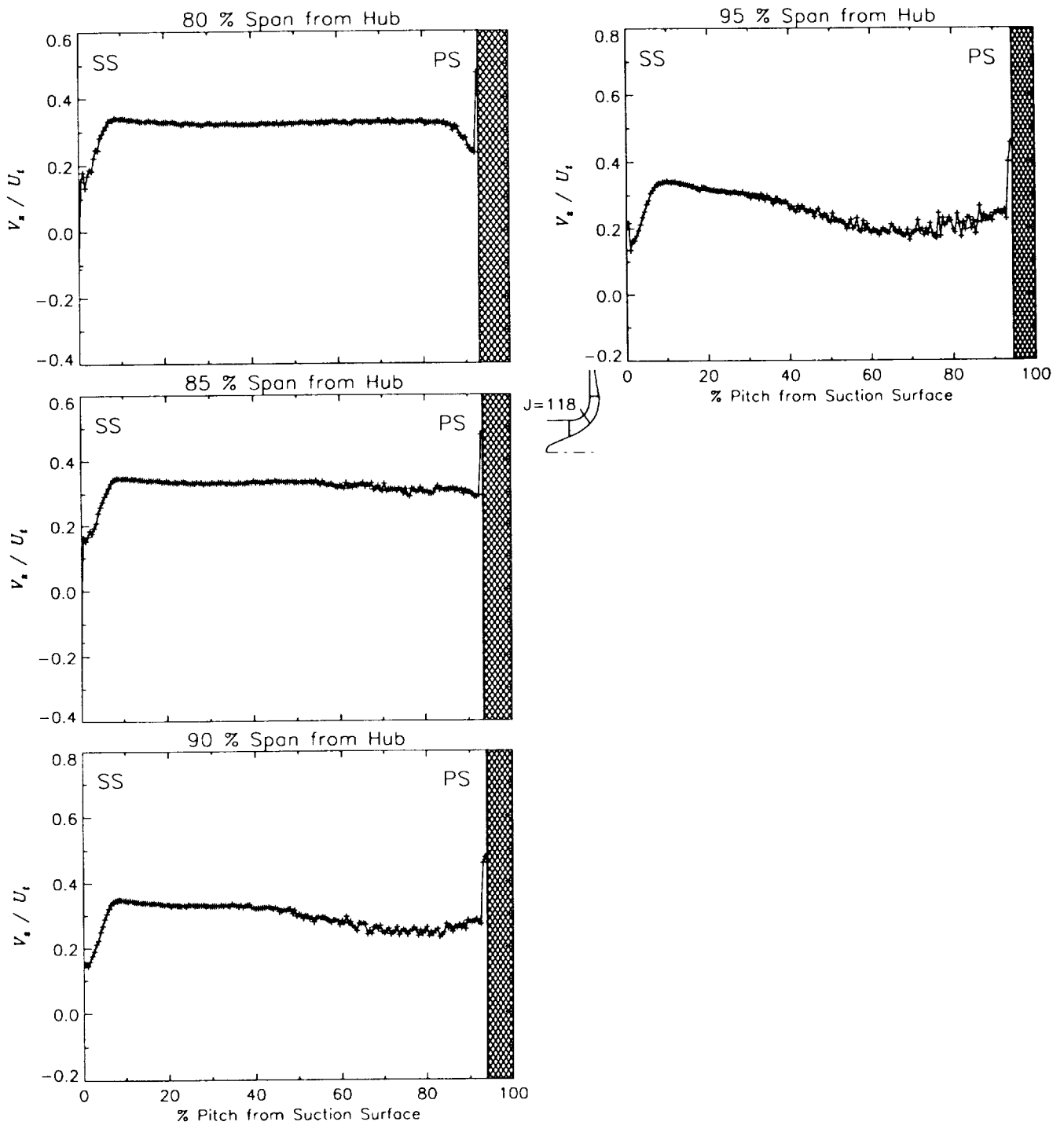
Station J=118, ( $m/m_s=0.475$ )



(c) Axial velocity normalized by impeller tip speed.

Figure 47.-Continued.

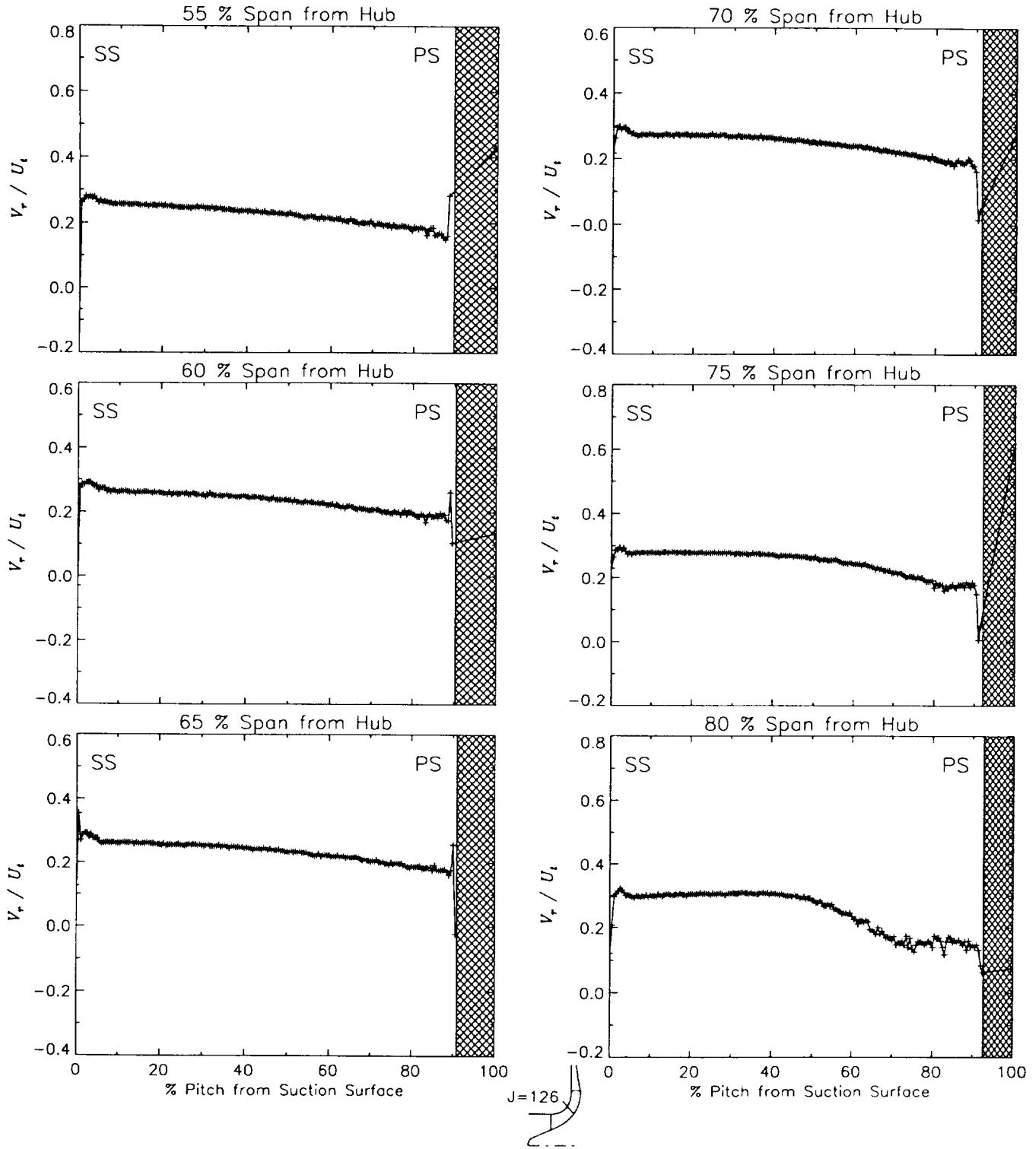
Station J=118, ( $m/m_s=0.475$ )



(c) Axial velocity normalized by impeller tip speed.

Figure 47.-Concluded.

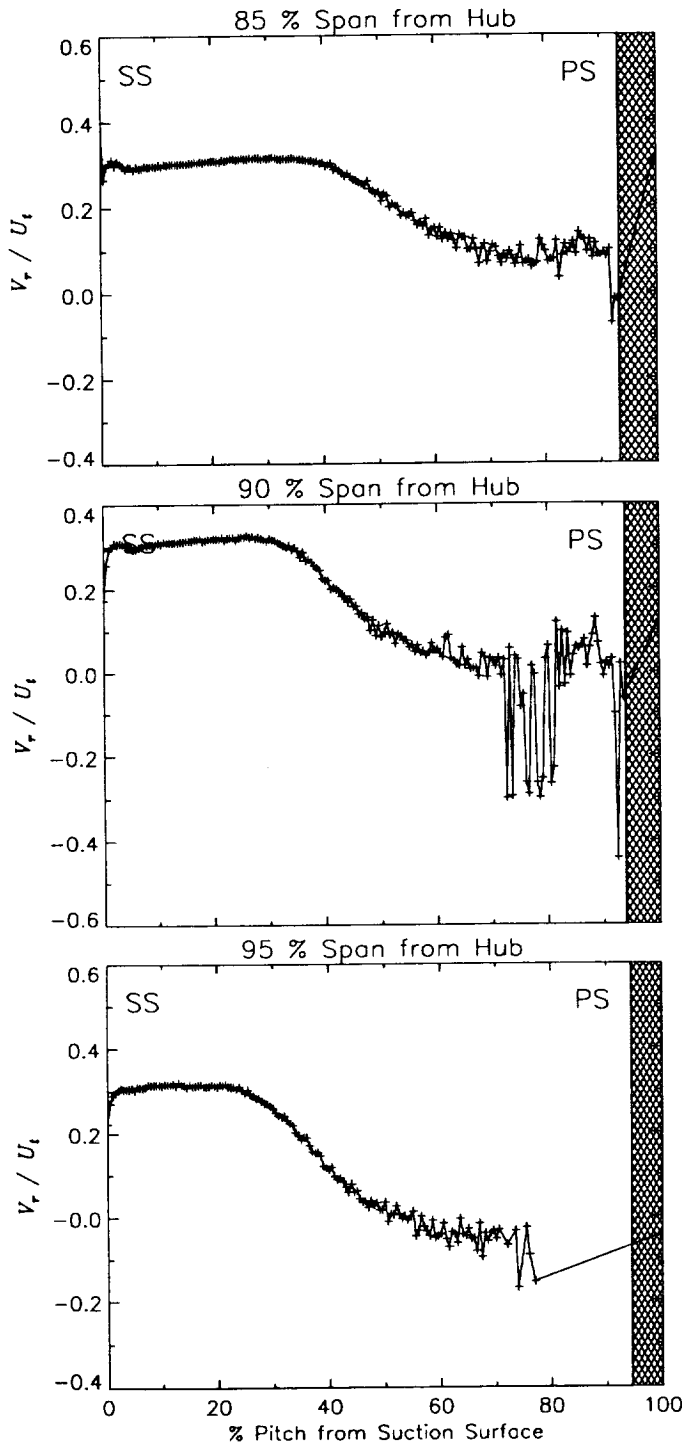
Station J=126, ( $m/m_s=0.555$ )



(a) Radial velocity normalized by impeller tip speed.

Figure 48.—Laser velocimeter results of axial, radial, and relative tangential velocities normalized by impeller tip speed for the off-design flow condition,  $78.7\% \dot{m}_d$ , at station J=126, ( $m/m_s=0.555$ ). The shaded region to the right of each plot represents the physical blade width.

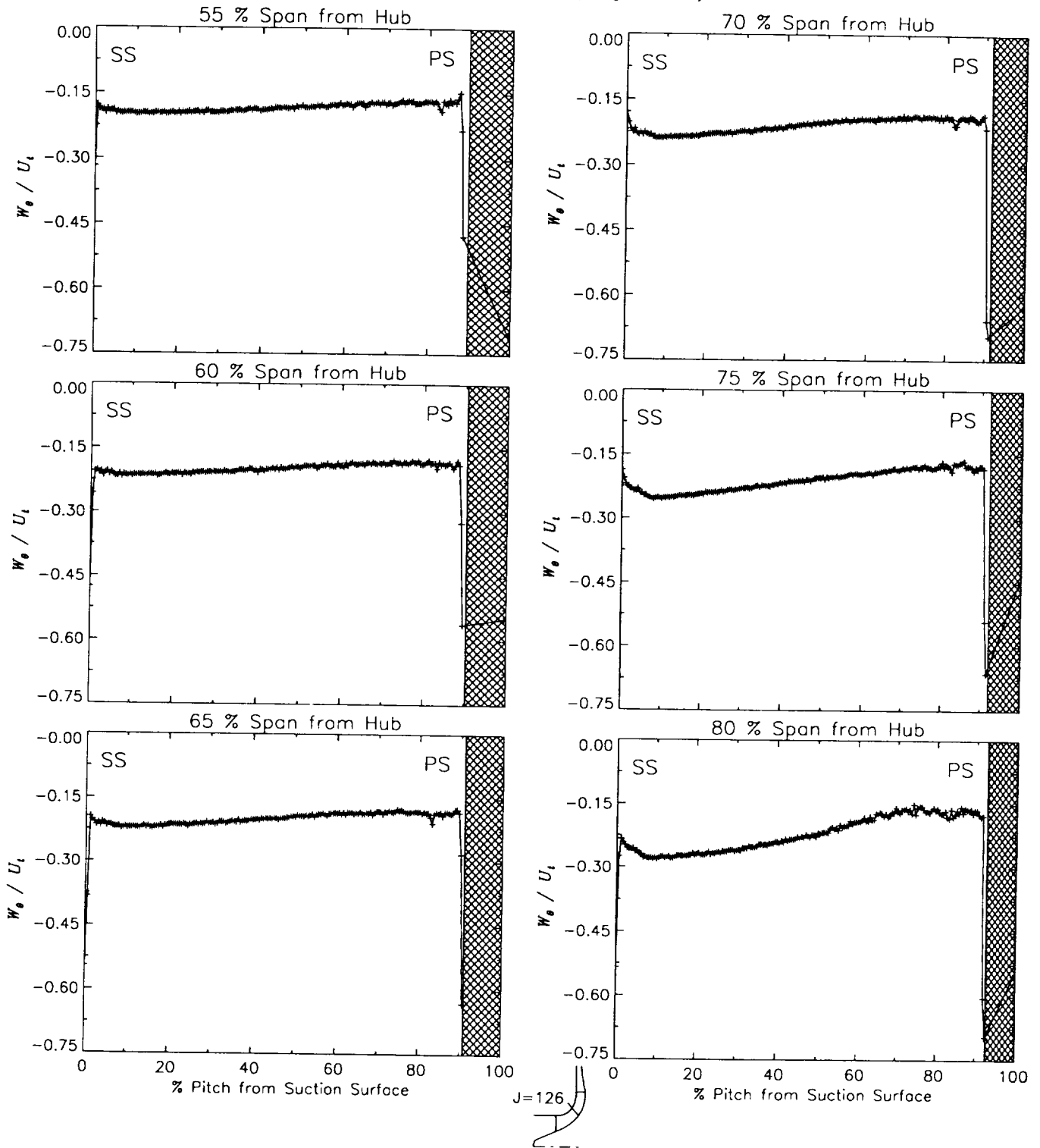
Station J=126, ( $m/m_s=0.555$ )



(a) Radial velocity normalized by impeller tip speed.

Figure 48.-Continued.

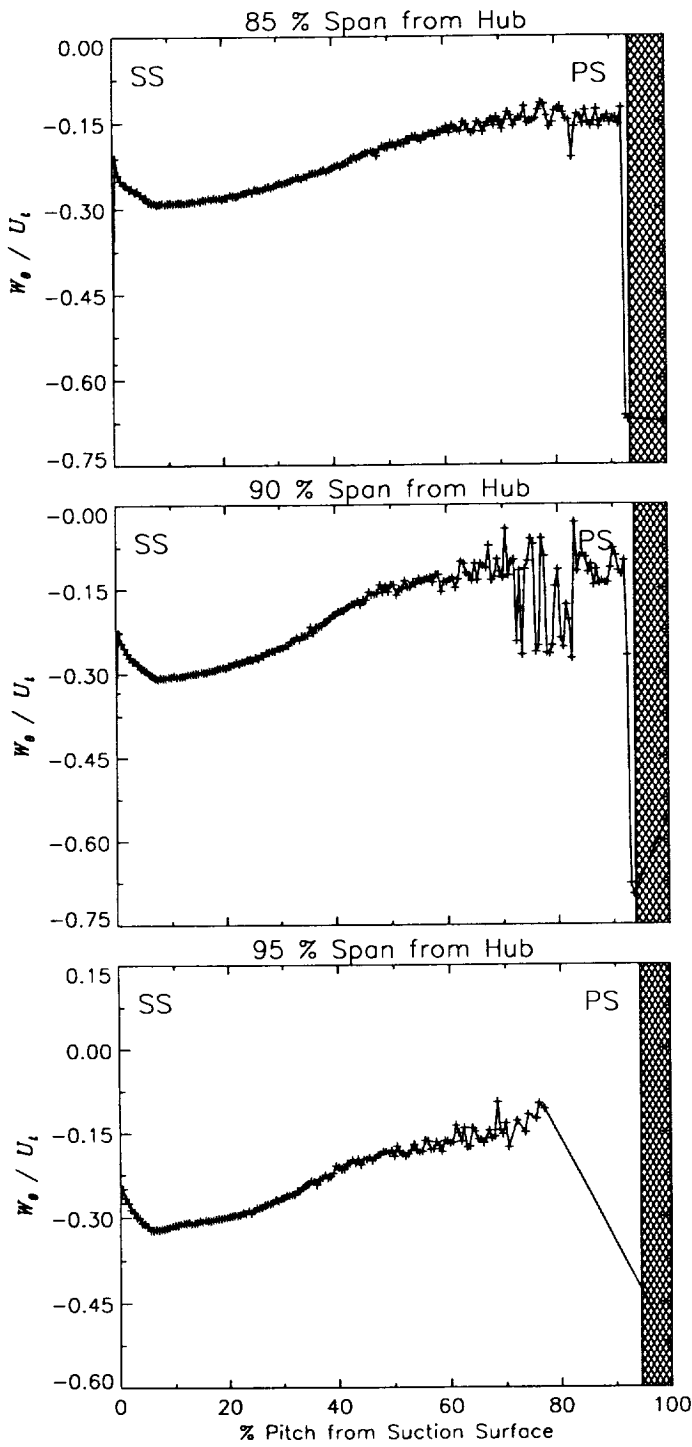
Station J=126, ( $m/m_s=0.555$ )



(b) Relative tangential velocity normalized by impeller tip speed.

Figure 48.—Continued.

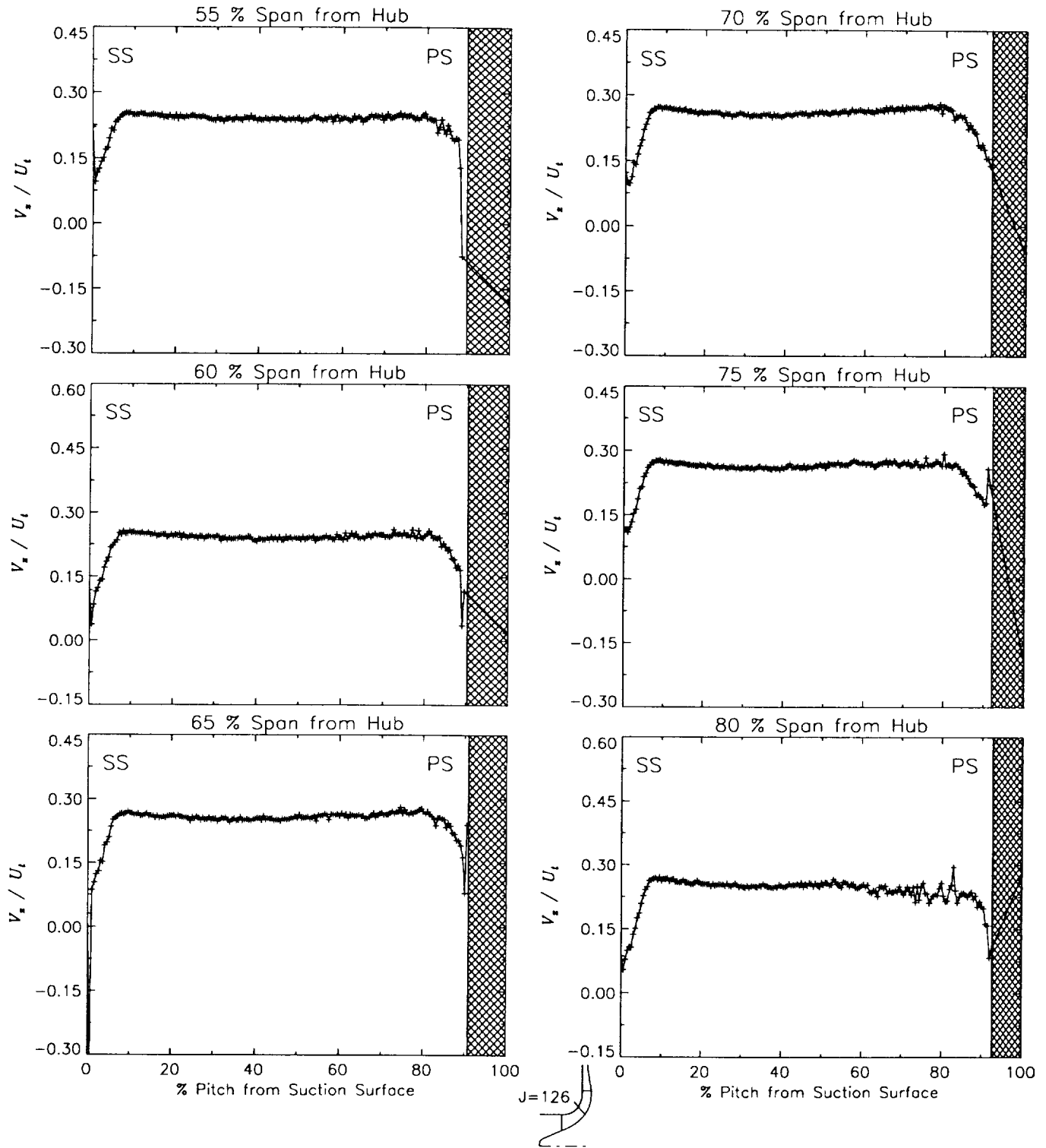
Station J=126, ( $m/m_s=0.555$ )



(b) Relative tangential velocity normalized by impeller tip speed.

Figure 48.-Continued.

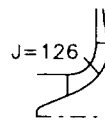
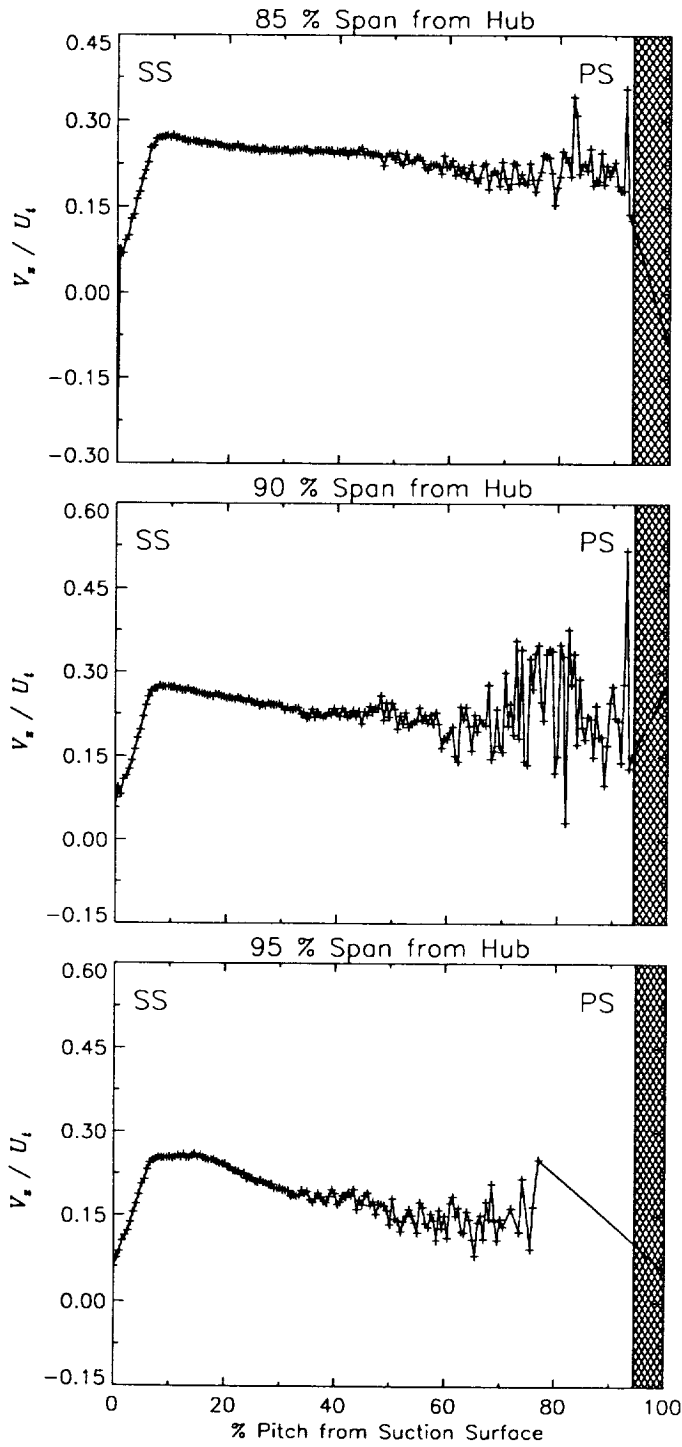
Station J=126, ( $m/m_s=0.555$ )



(c) Axial velocity normalized by impeller tip speed.

Figure 48.—Continued.

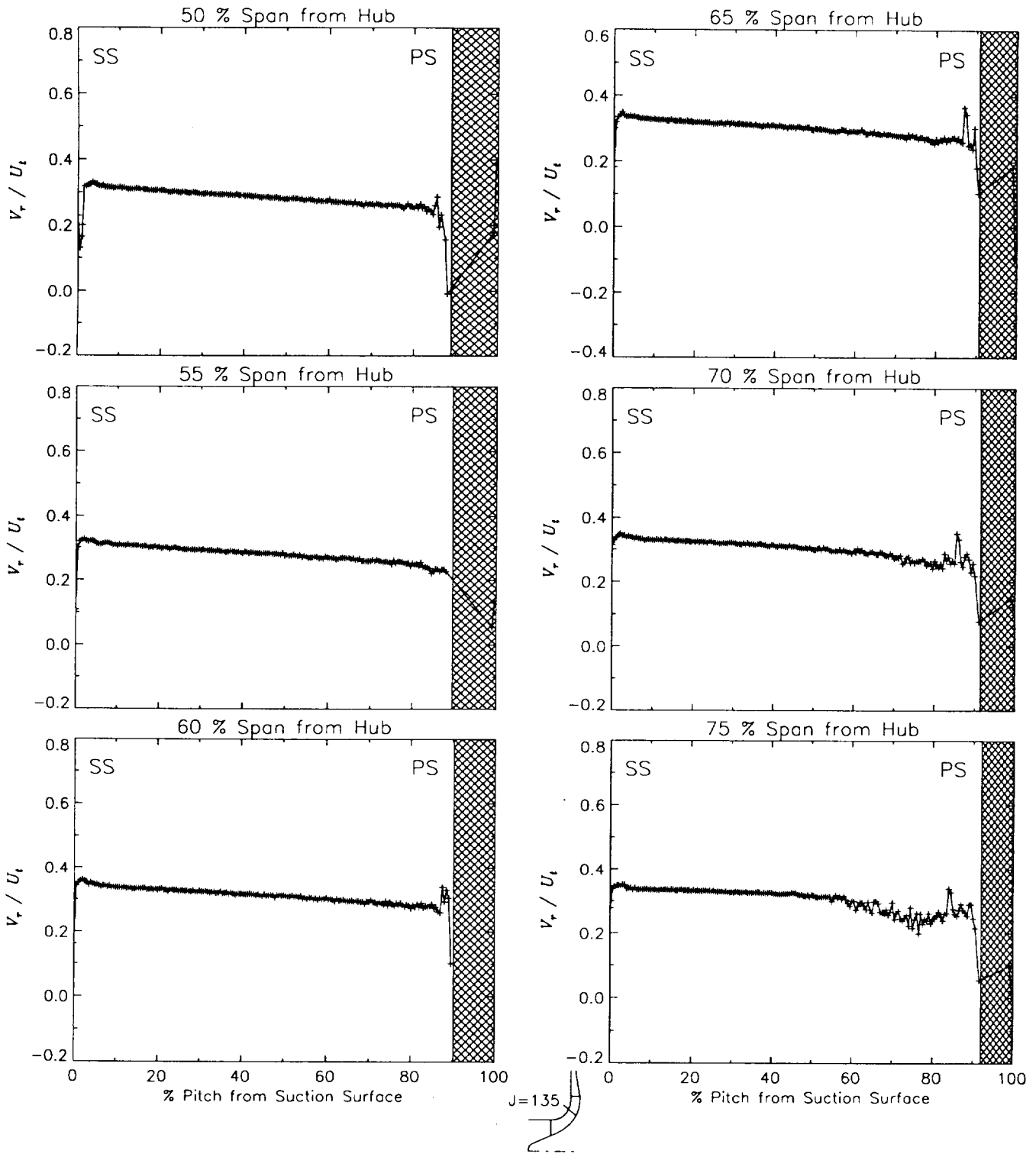
Station J=126, ( $m/m_s=0.555$ )



(c) Axial velocity normalized by impeller tip speed.

Figure 48.—Concluded.

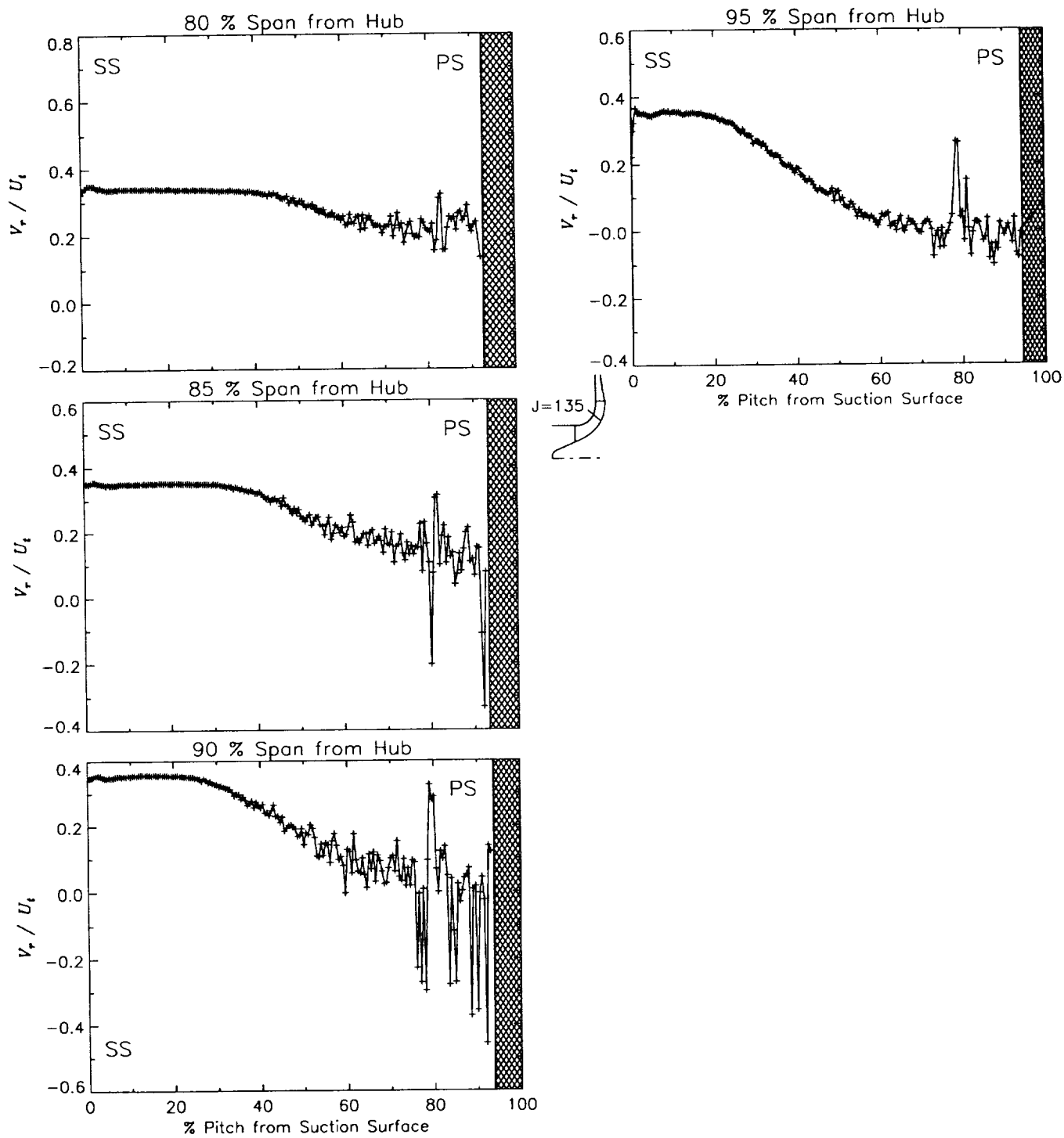
Station J=135, ( $m/m_s=0.644$ )



(a) Radial velocity normalized by impeller tip speed.

Figure 49.—Laser velocimeter results of axial, radial, and relative tangential velocities normalized by impeller tip speed for the off-design flow condition,  $78.7\% \dot{m}_d$ , at station J=135, ( $m/m_s=0.644$ ). The shaded region to the right of each plot represents the physical blade width.

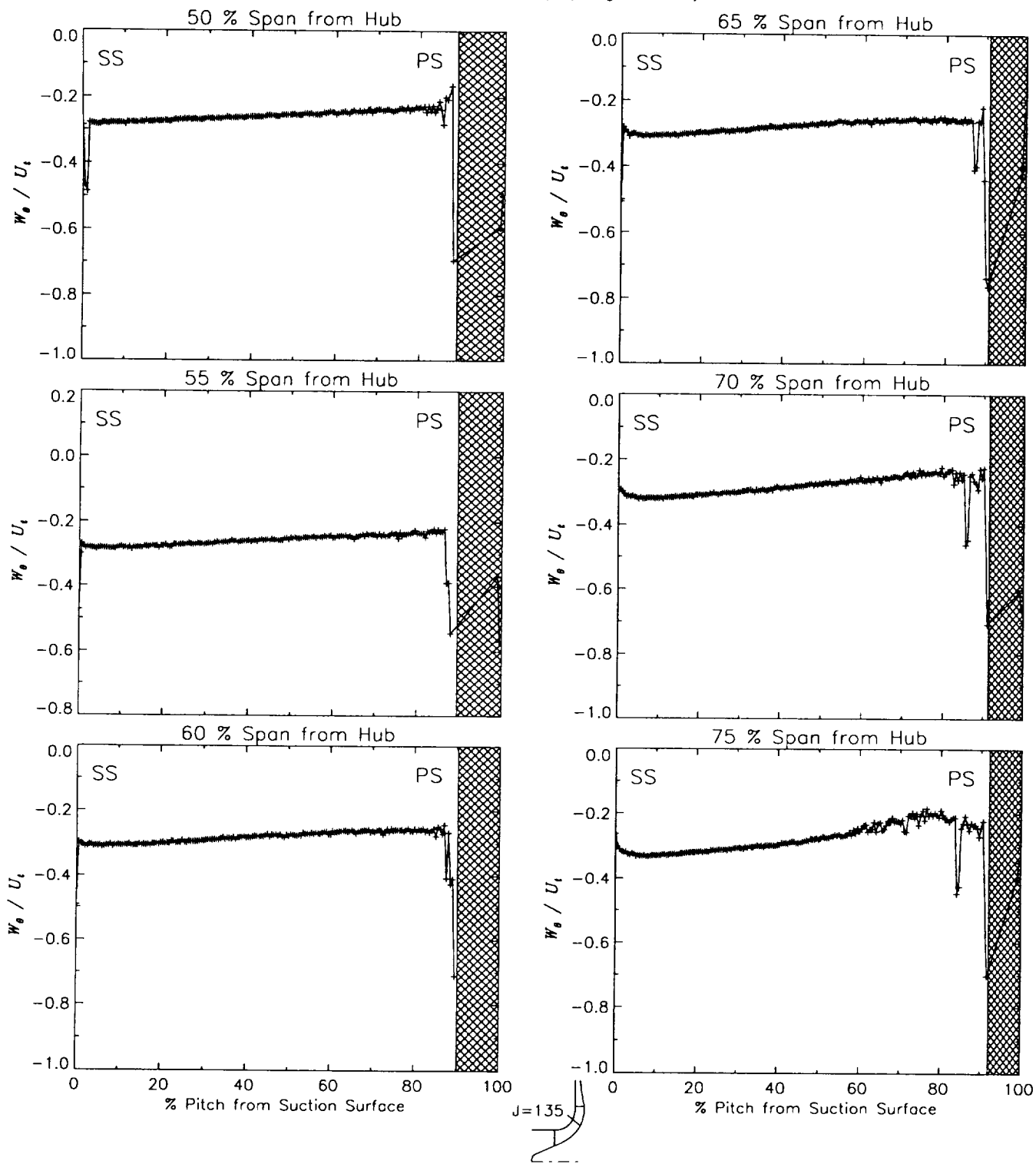
Station J=135, ( $m/m_s=0.644$ )



(a) Radial velocity normalized by impeller tip speed.

Figure 49.—Continued.

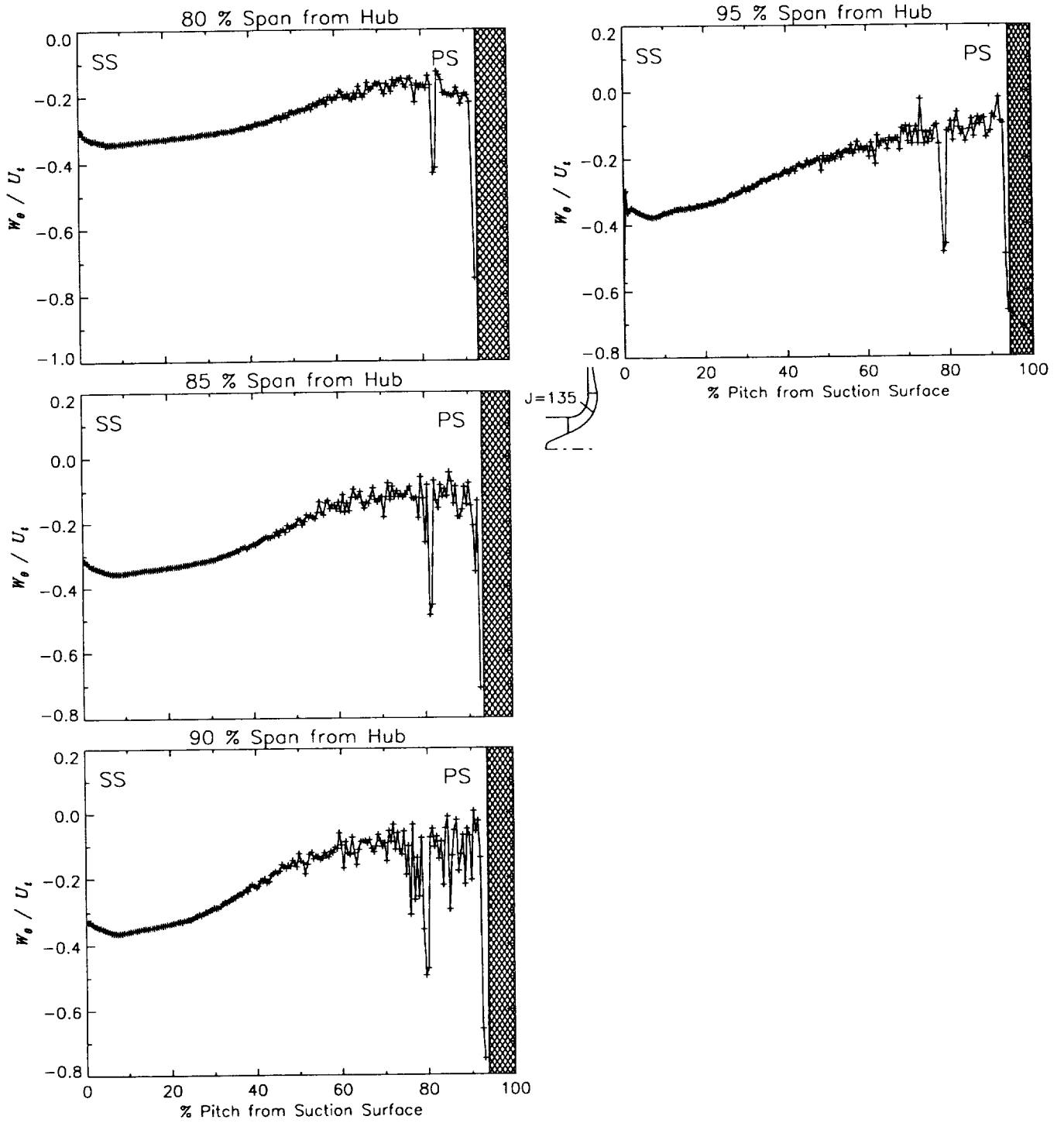
Station J=135, ( $m/m_s=0.644$ )



(b) Relative tangential velocity normalized by impeller tip speed.

Figure 49.-Continued.

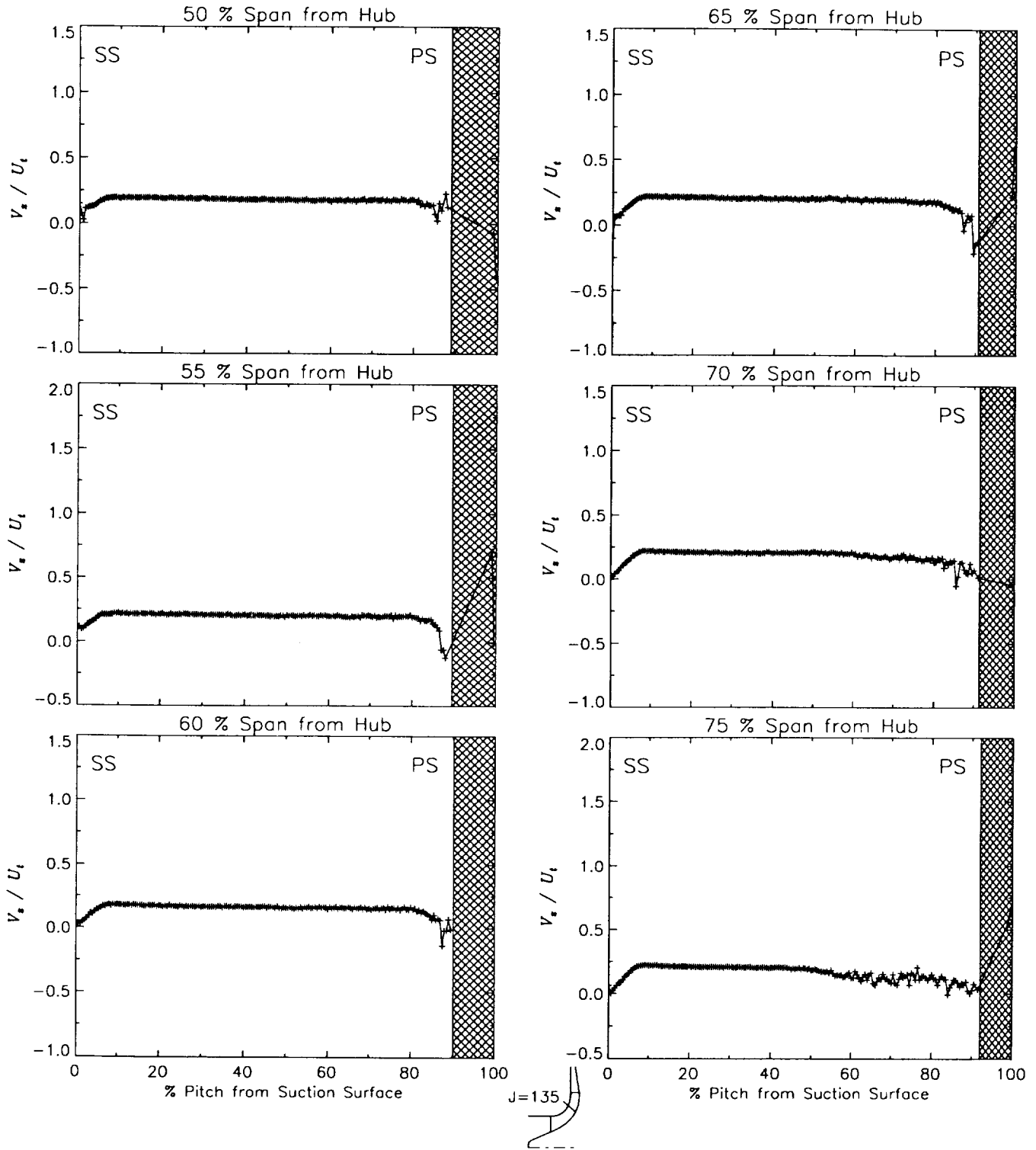
Station J=135, ( $m/m_s=0.644$ )



(b) Relative tangential velocity normalized by impeller tip speed.

Figure 49.-Continued.

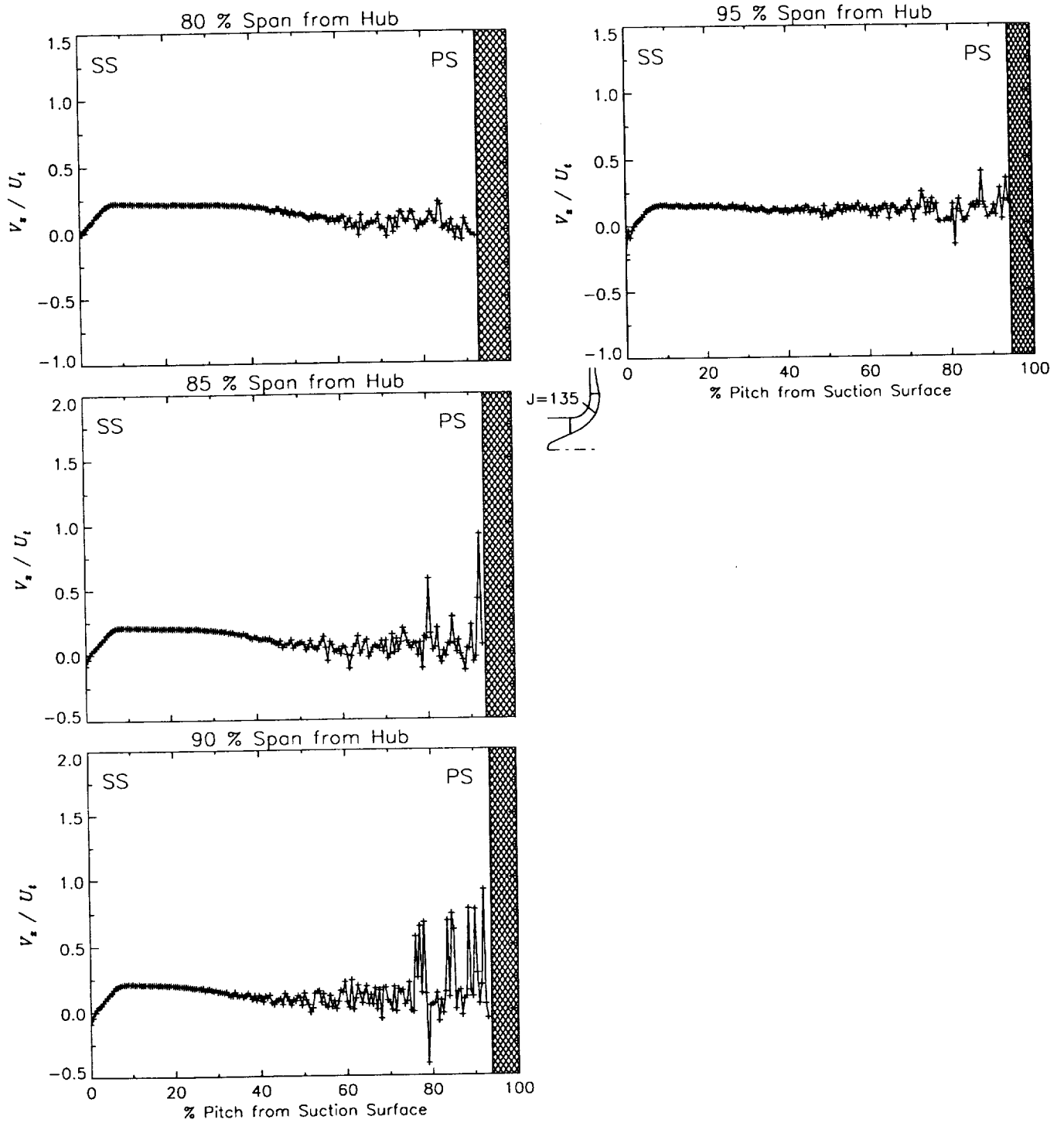
Station J=135, ( $m/m_s=0.644$ )



(c) Axial velocity normalized by impeller tip speed.

Figure 49.—Continued.

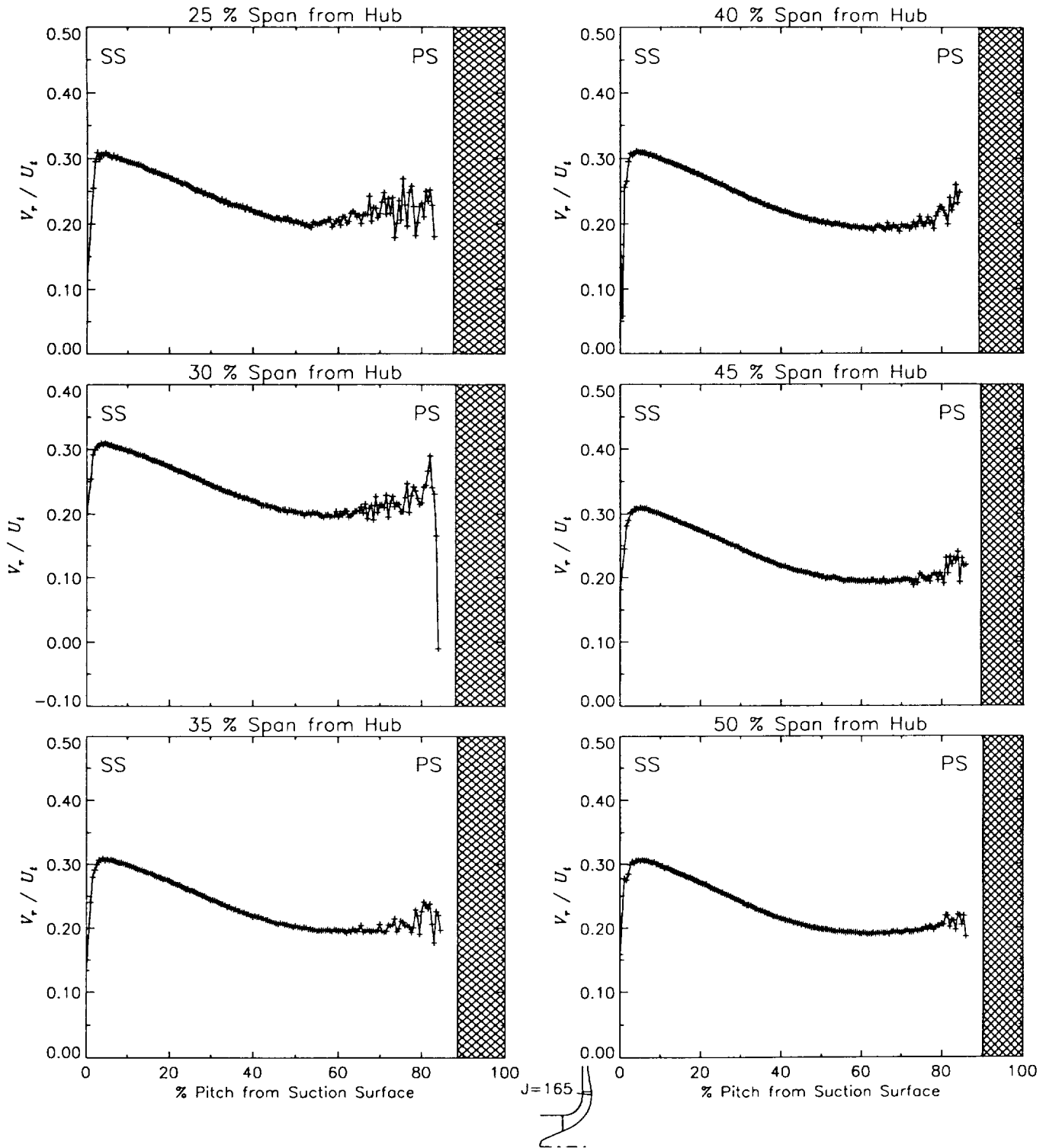
Station J=135, ( $m/m_s=0.644$ )



(c) Axial velocity normalized by impeller tip speed.

Figure 49.—Concluded.

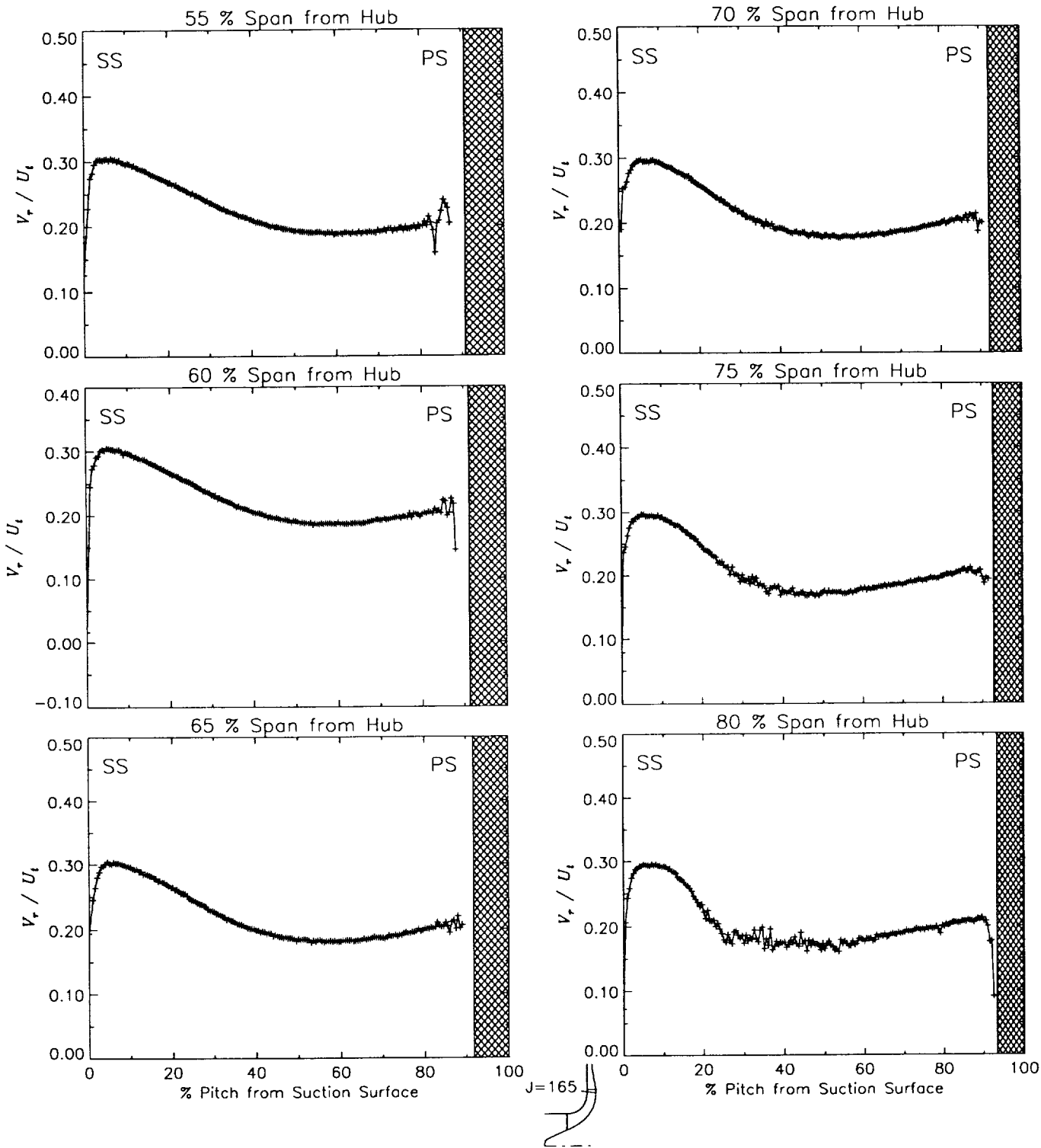
Station J=165, ( $m/m_s=0.941$ )



(a) Radial velocity normalized by impeller tip speed.

Figure 50.—Laser velocimeter results of axial, radial, and relative tangential velocities normalized by impeller tip speed for the off-design flow condition, 78.7%  $\dot{m}_d$ , at station J=165, ( $m/m_s=0.941$ ). The shaded region to the right of each plot represents the physical blade width.

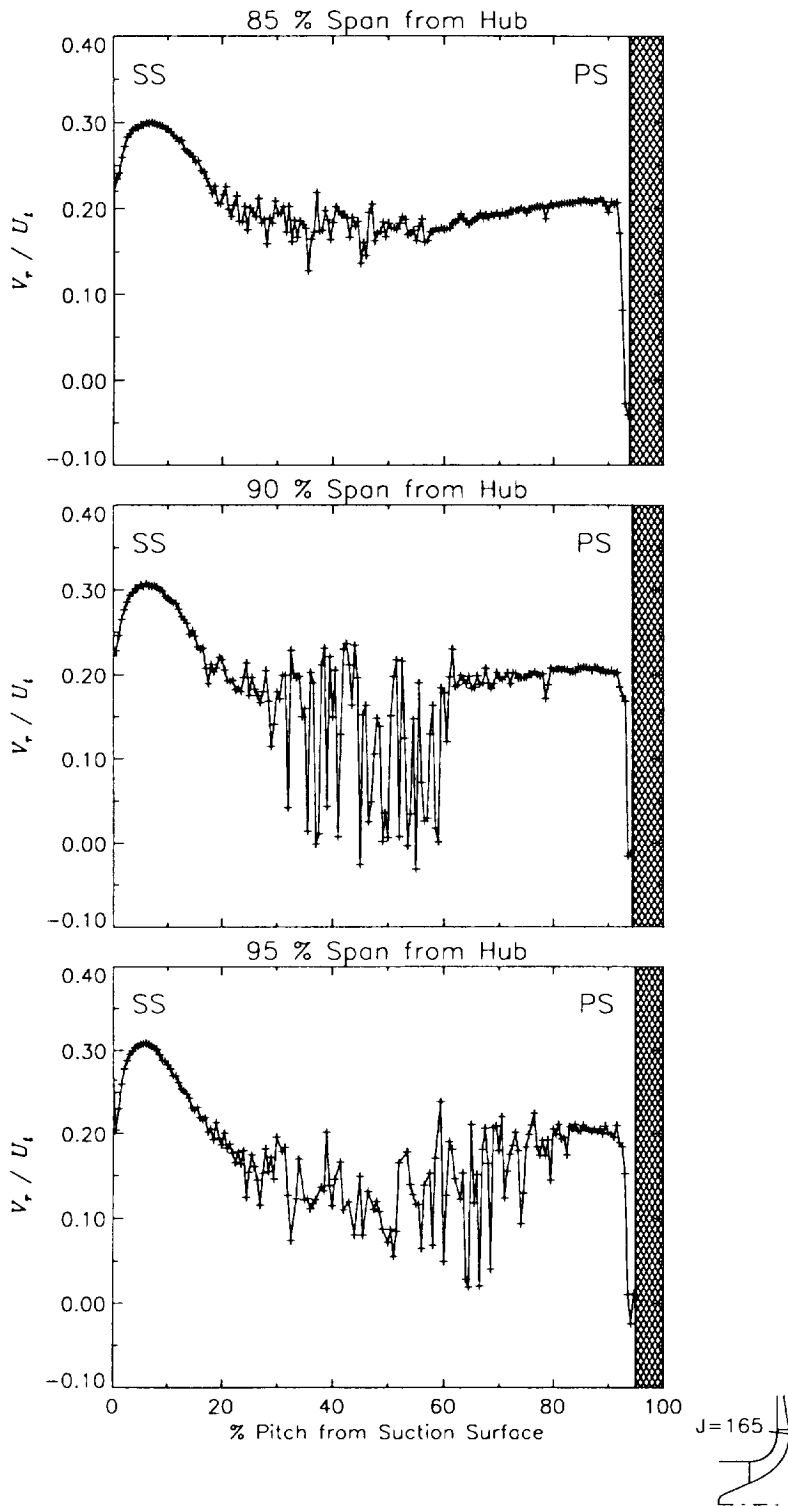
Station J=165, ( $m/m_s=0.941$ )



(a) Radial velocity normalized by impeller tip speed.

Figure 50.—Continued.

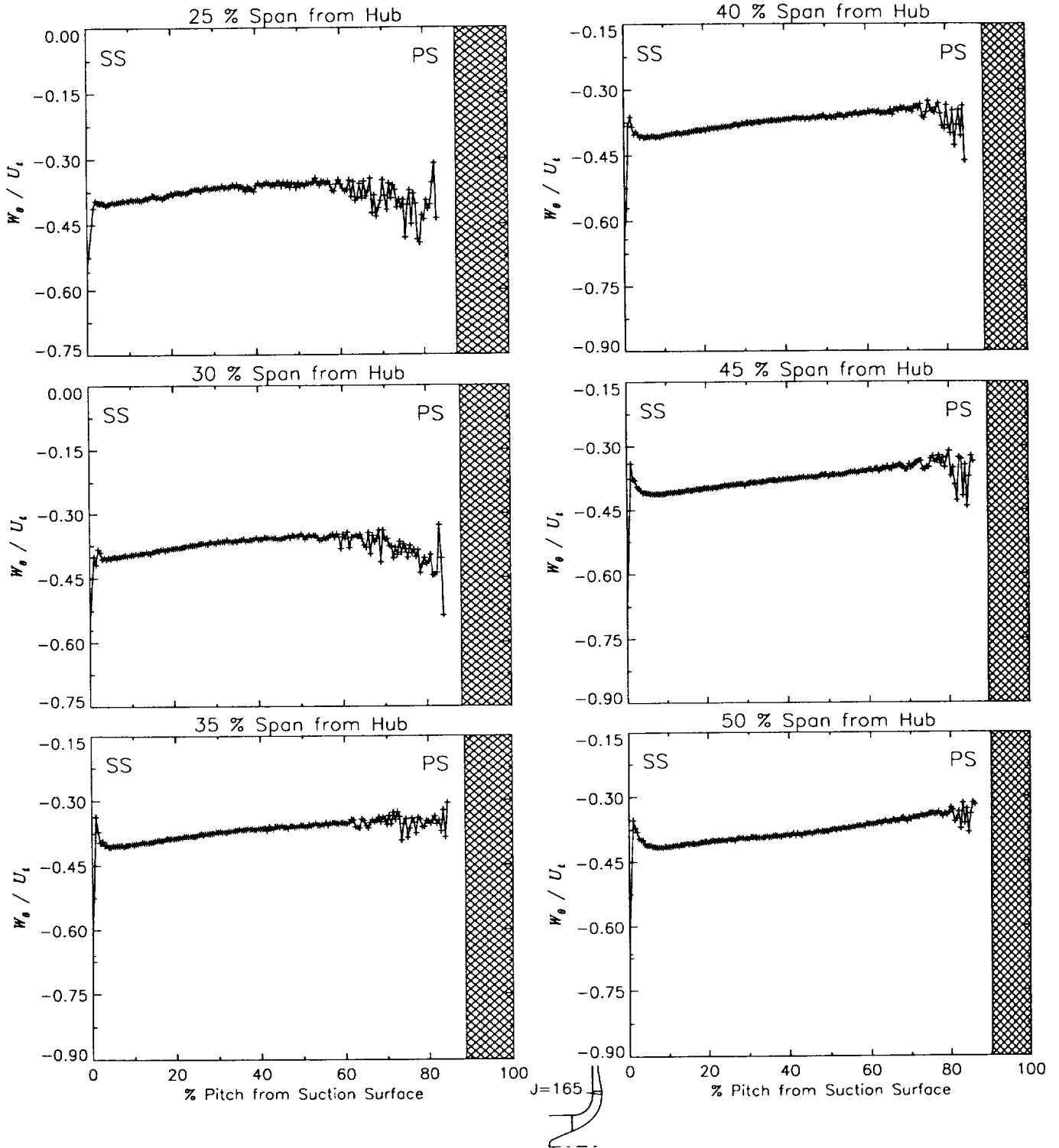
Station J=165, ( $m/m_s=0.941$ )



(a) Radial velocity normalized by impeller tip speed.

Figure 50.—Continued.

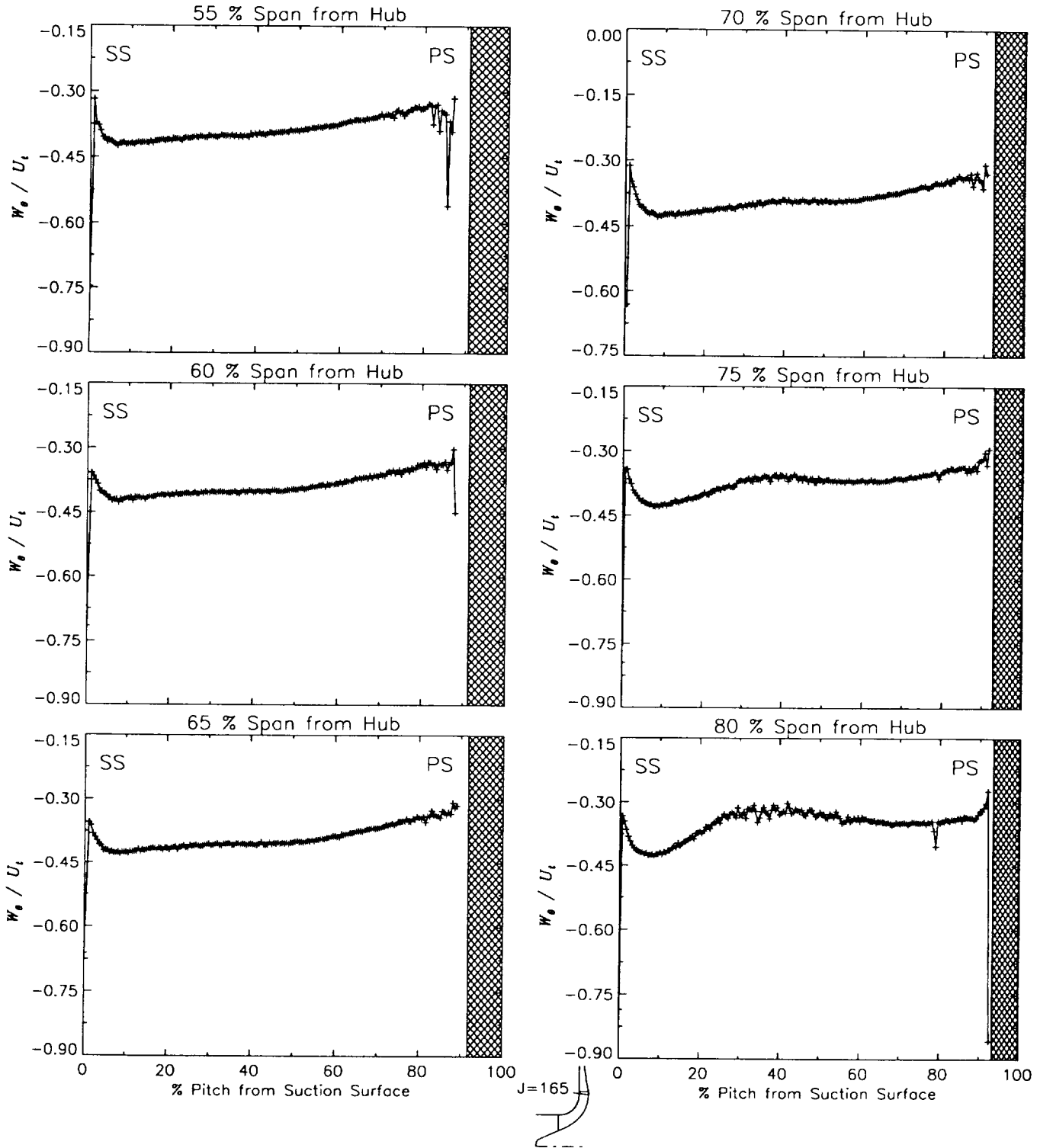
Station J=165, ( $m/m_s=0.941$ )



(b) Relative tangential velocity normalized by impeller tip speed.

Figure 50.-Continued.

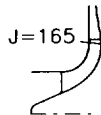
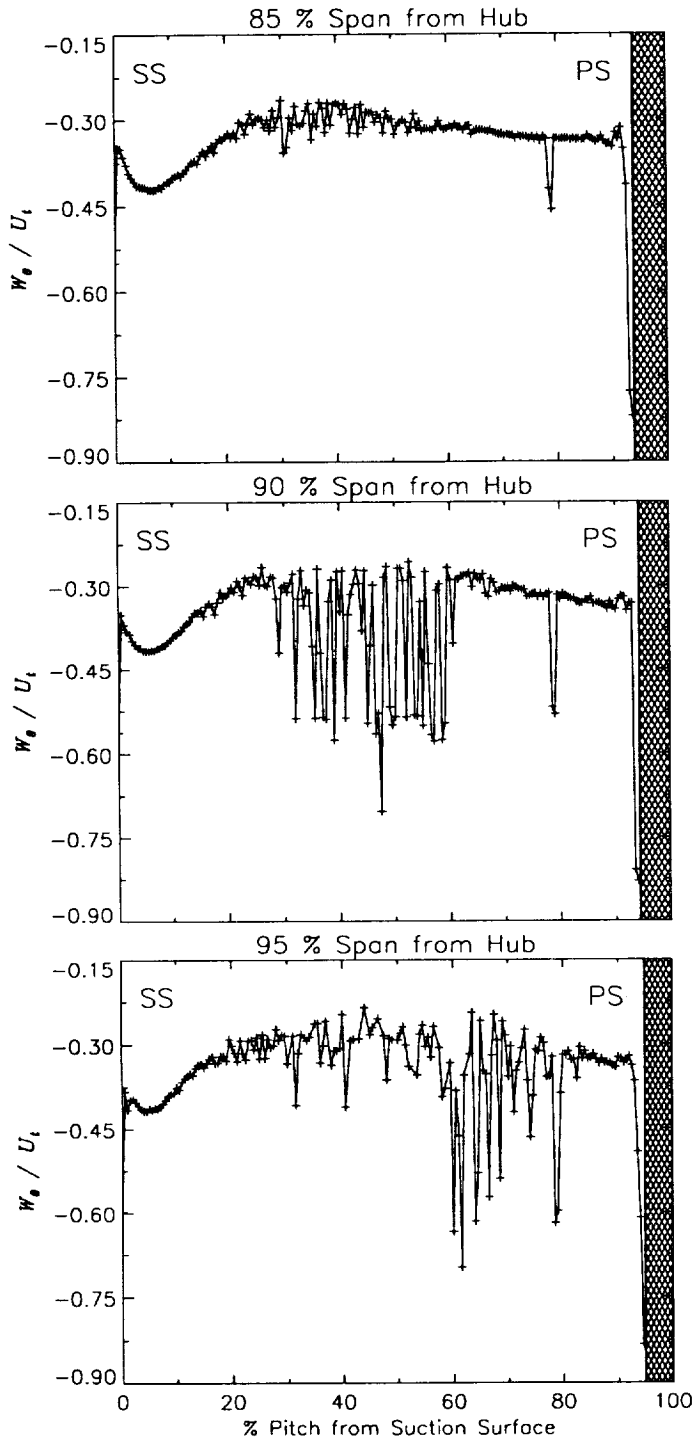
Station J=165, ( $m/m_s=0.941$ )



(b) Relative tangential velocity normalized by impeller tip speed.

Figure 50.—Continued.

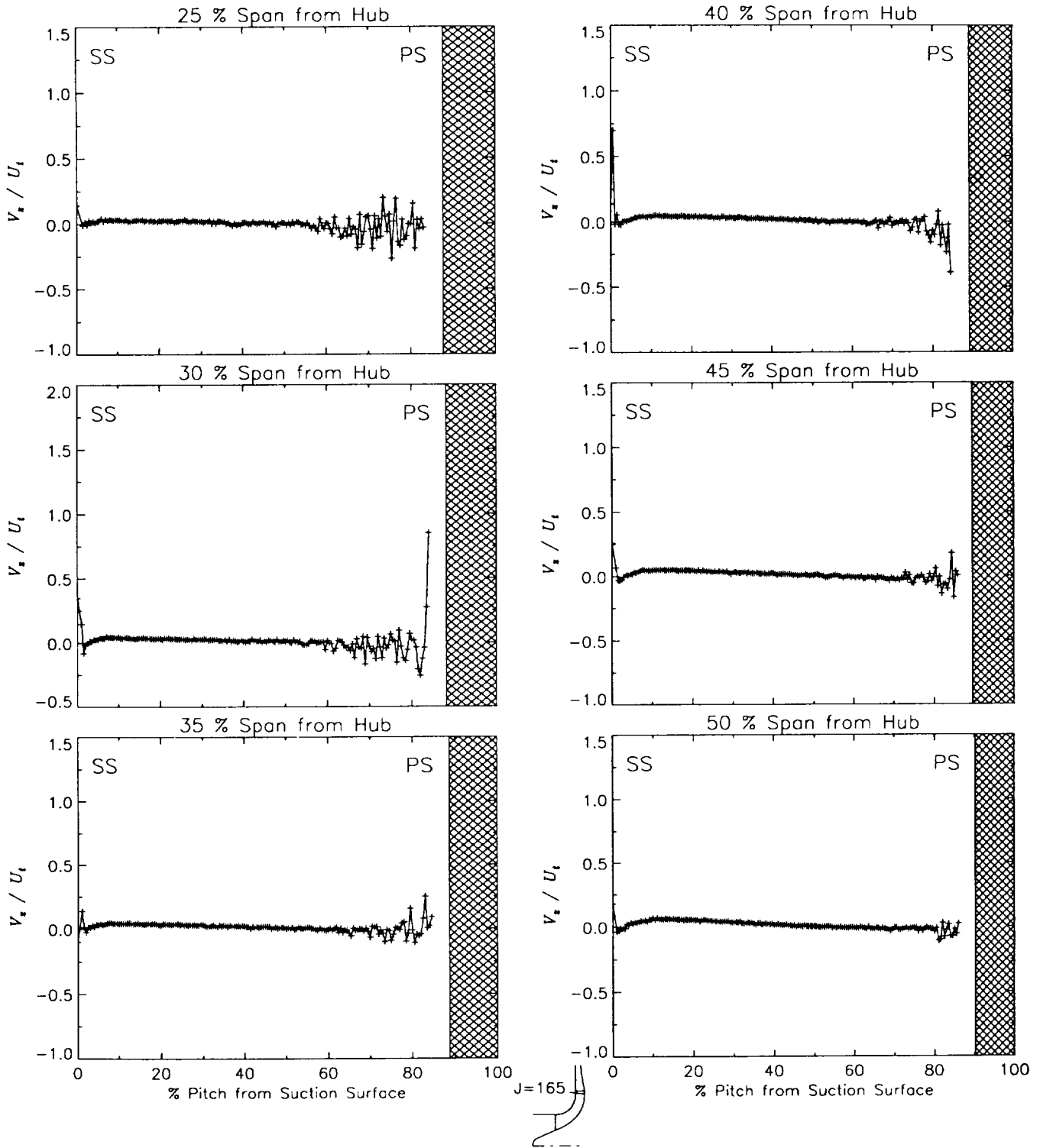
Station J=165, ( $m/m_s=0.941$ )



(b) Relative tangential velocity normalized by impeller tip speed.

Figure 50.-Continued.

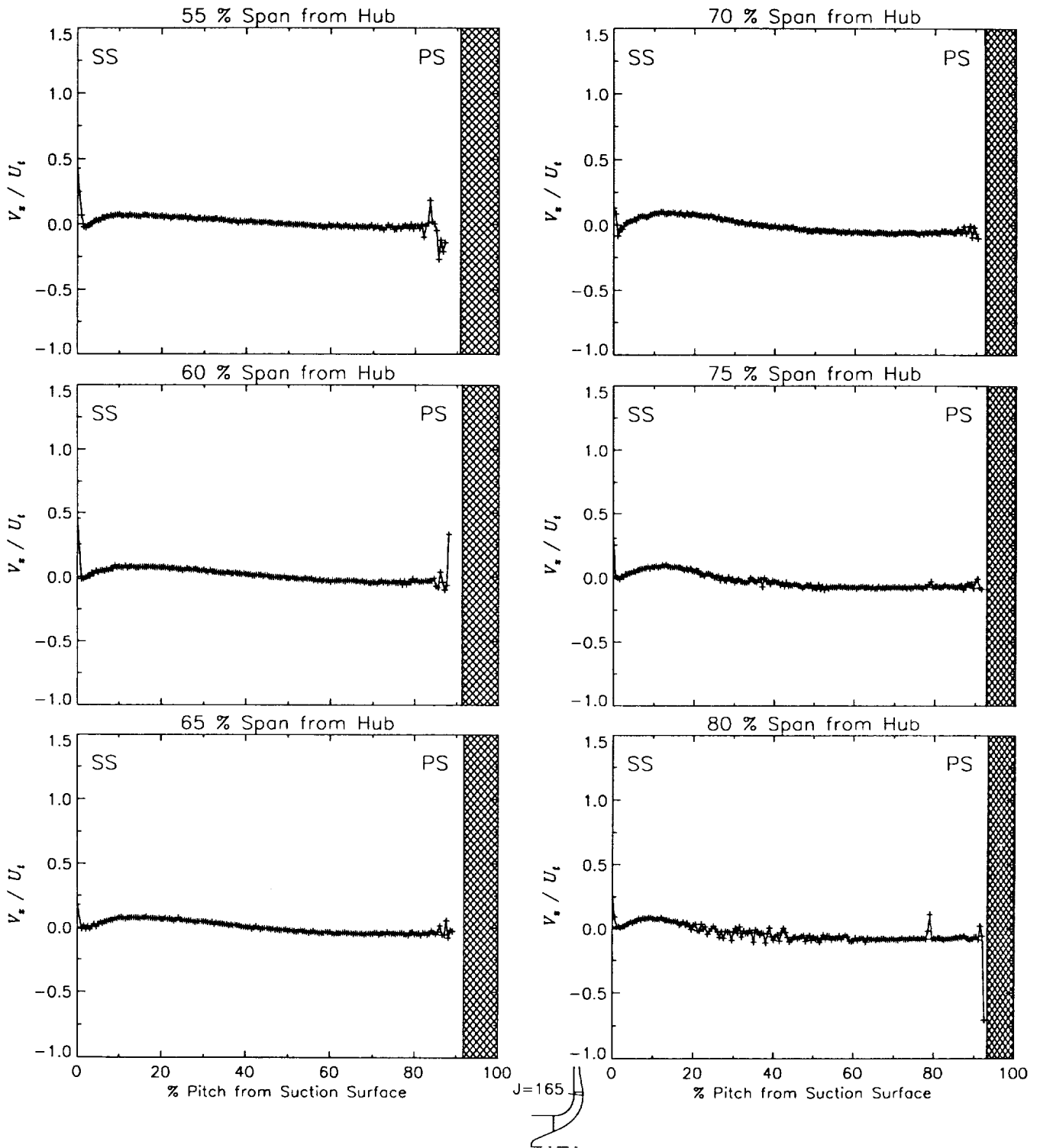
Station J=165, ( $m/m_s=0.941$ )



(c) Axial velocity normalized by impeller tip speed.

Figure 50.-Continued.

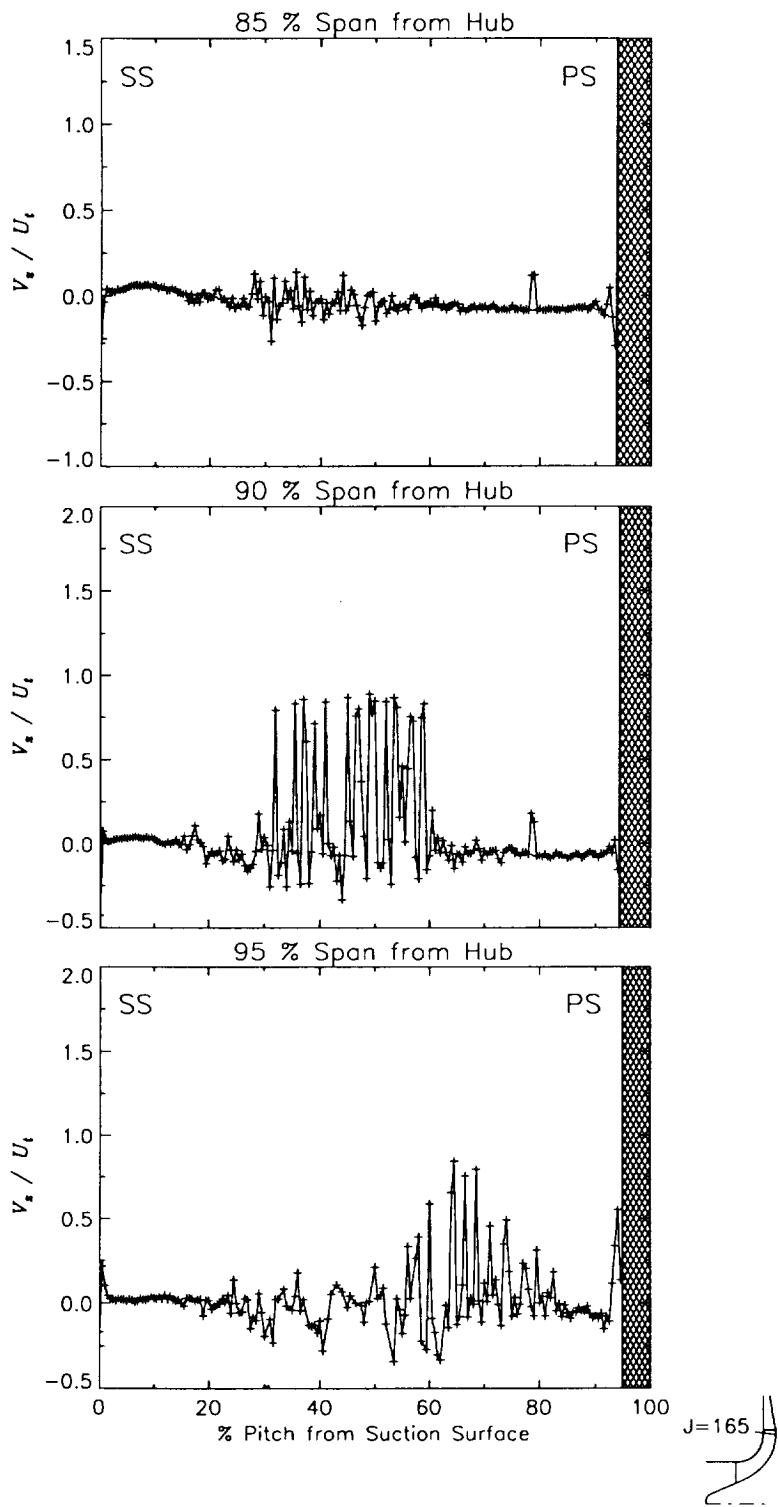
Station J=165, ( $m/m_s=0.941$ )



(c) Axial velocity normalized by impeller tip speed.

Figure 50.-Continued.

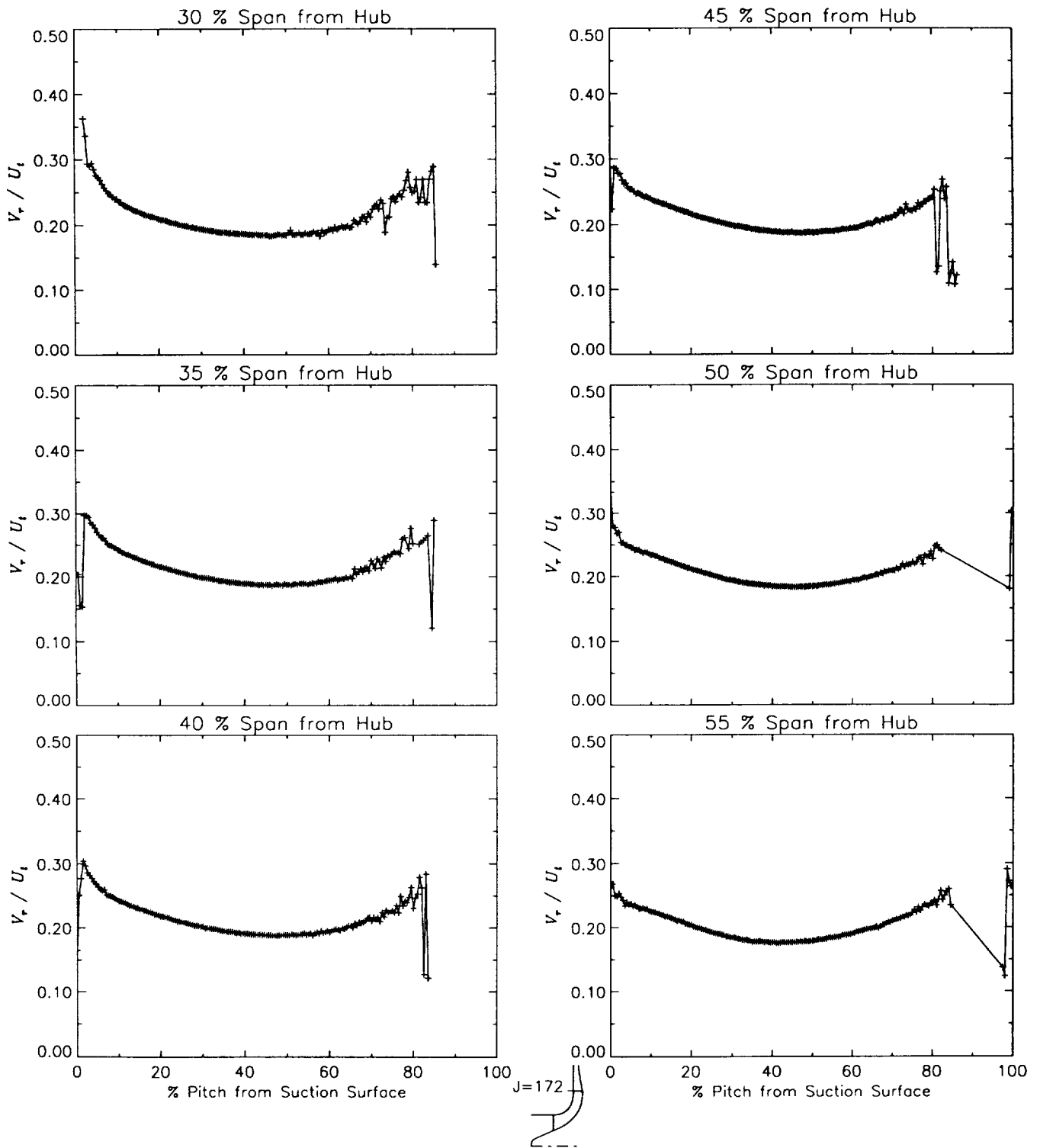
Station J=165, ( $m/m_s=0.941$ )



(c) Axial velocity normalized by impeller tip speed.

Figure 50.—Concluded.

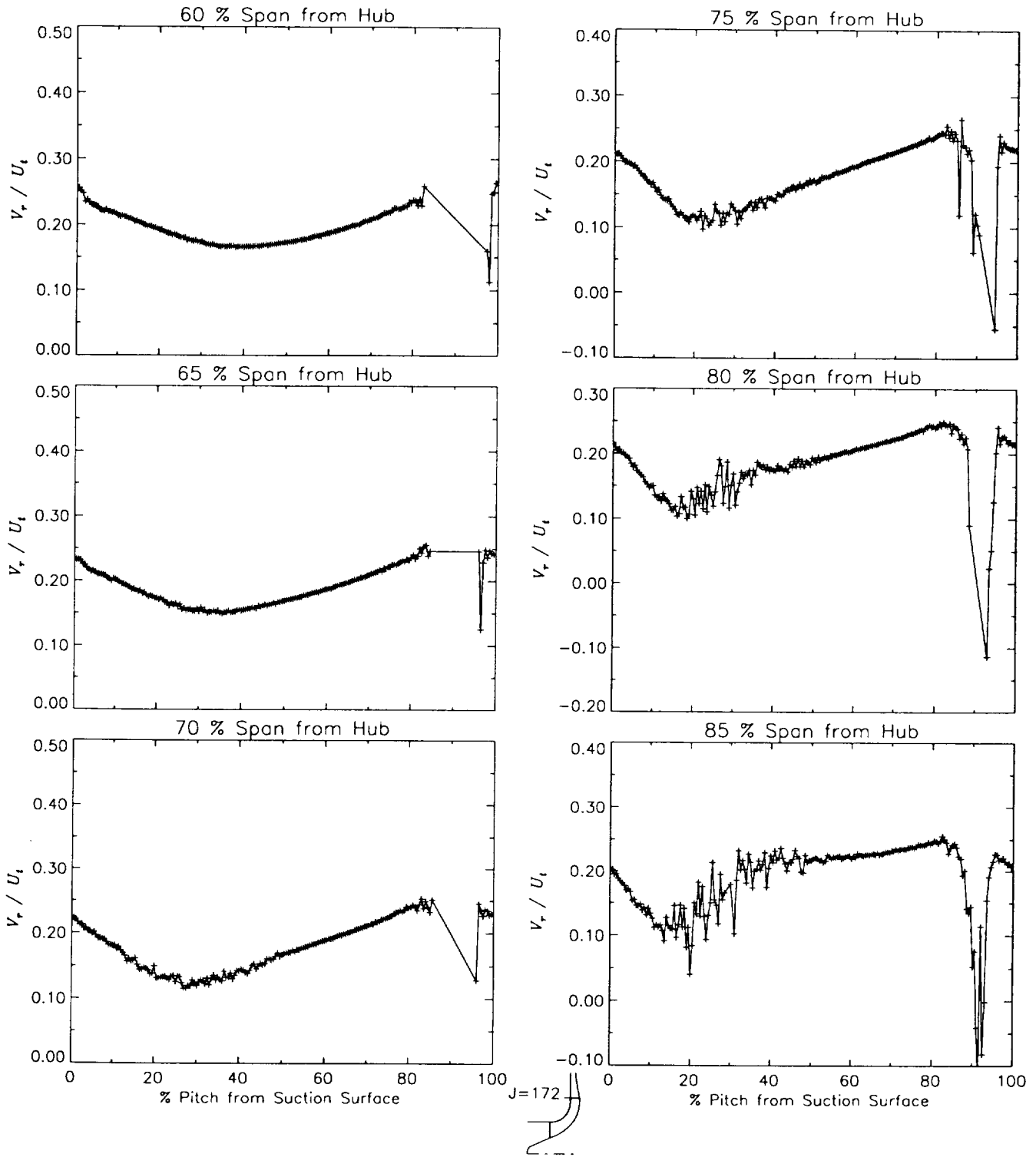
Station J=172, ( $m/m_s=1.014$ )



(a) Radial velocity normalized by impeller tip speed.

Figure 51.—Laser velocimeter results of axial, radial, and relative tangential velocities normalized by impeller tip speed for the off-design flow condition, 78.7%  $\dot{m}_d$ , at station J=172, ( $m/m_s=1.014$ ).

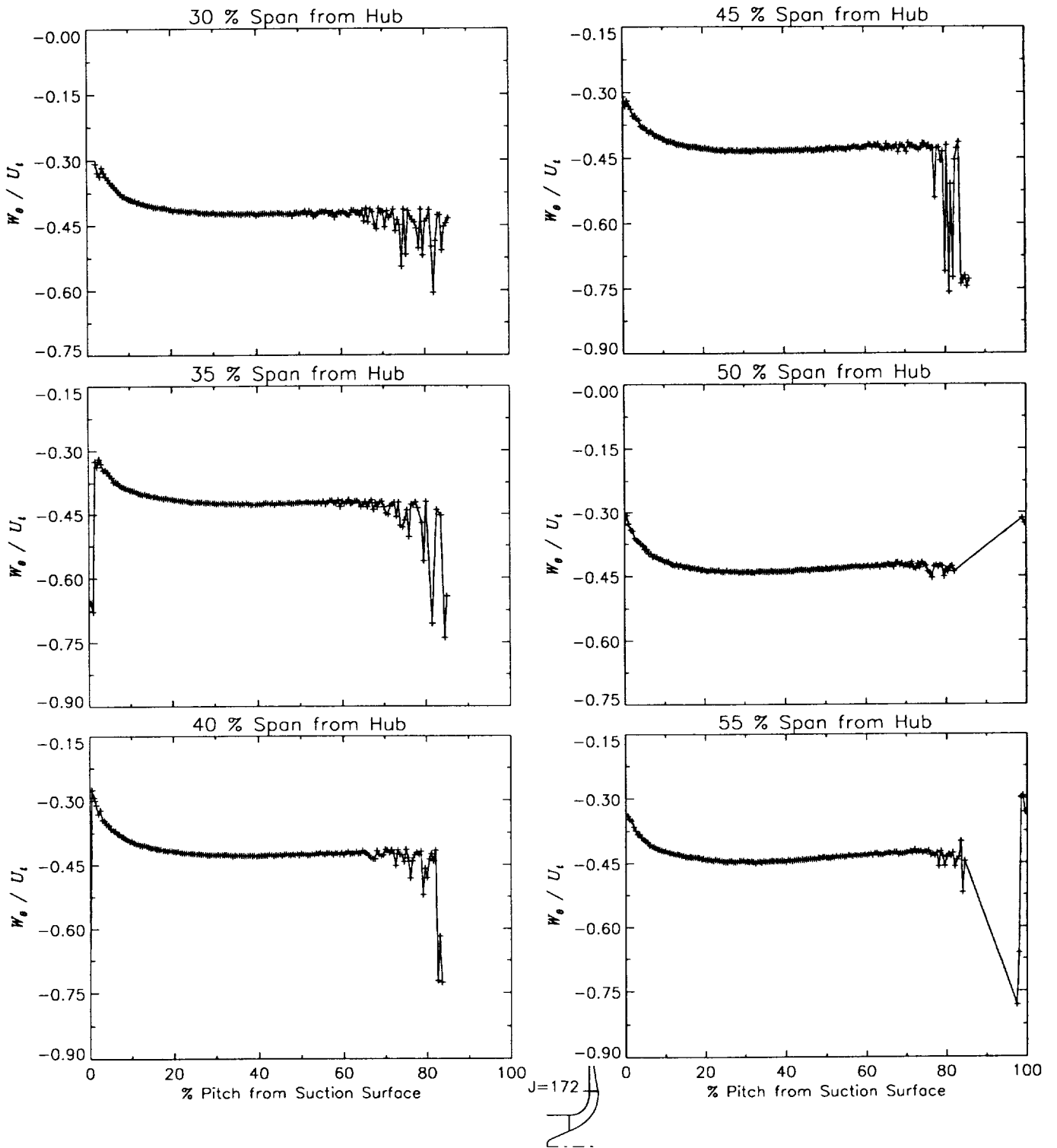
Station J=172, ( $m/m_s=1.014$ )



(a) Radial velocity normalized by impeller tip speed.

Figure 51.—Continued.

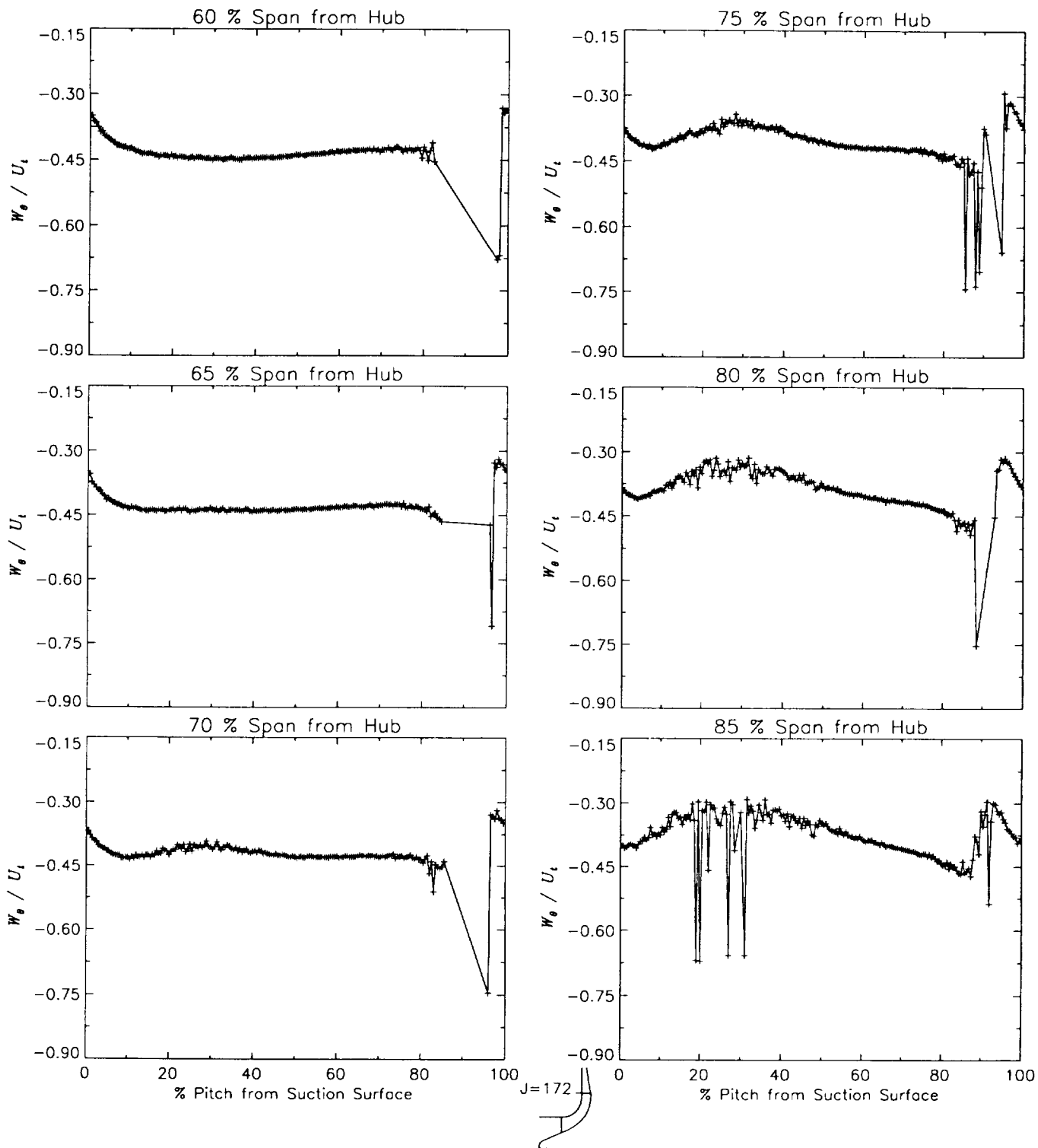
Station J=172, ( $m/m_s=1.014$ )



(b) Relative tangential velocity normalized by impeller tip speed.

Figure 51.-Continued.

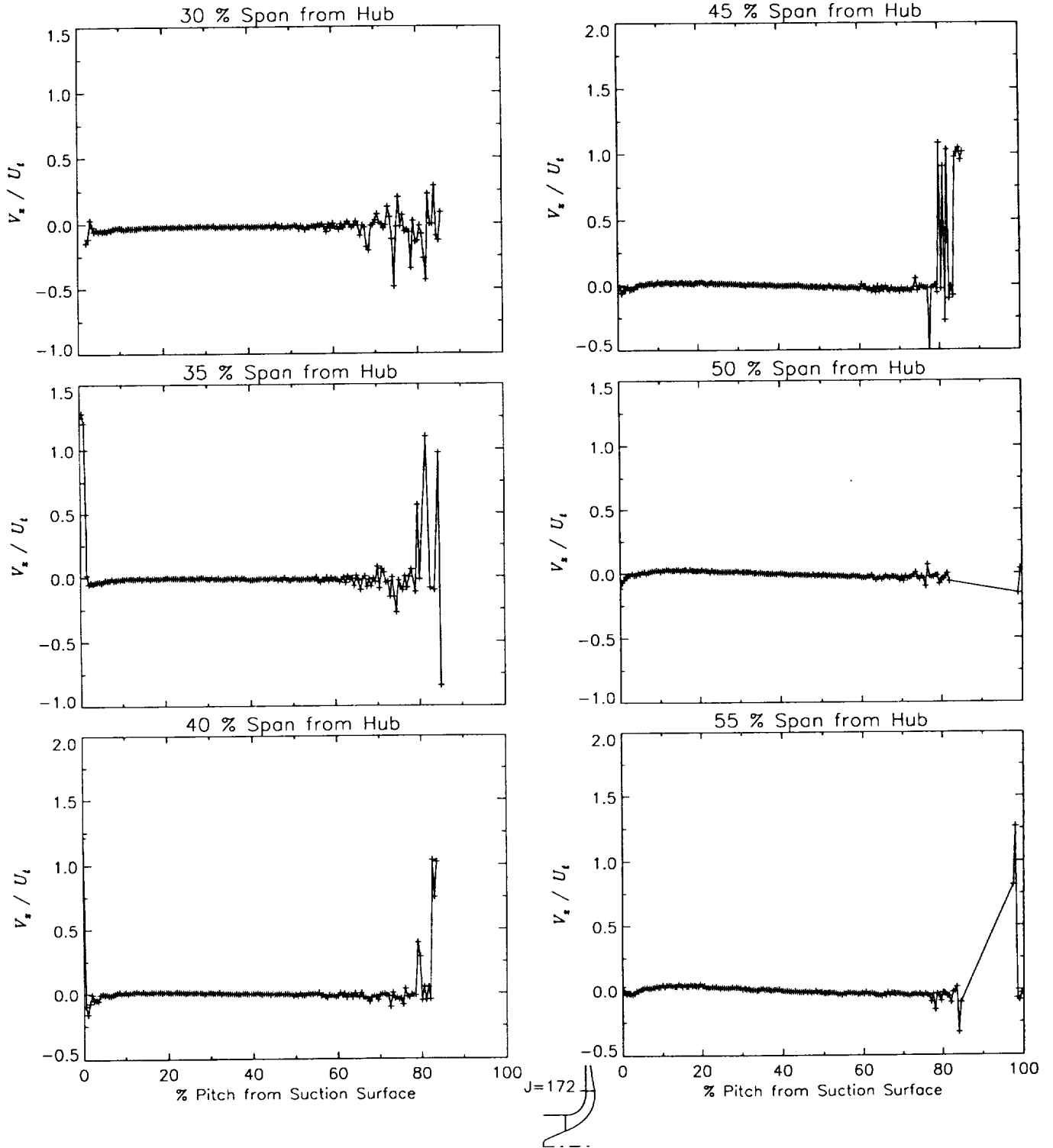
Station J=172, ( $m/m_s=1.014$ )



(b) Relative tangential velocity normalized by impeller tip speed.

Figure 51.-Continued.

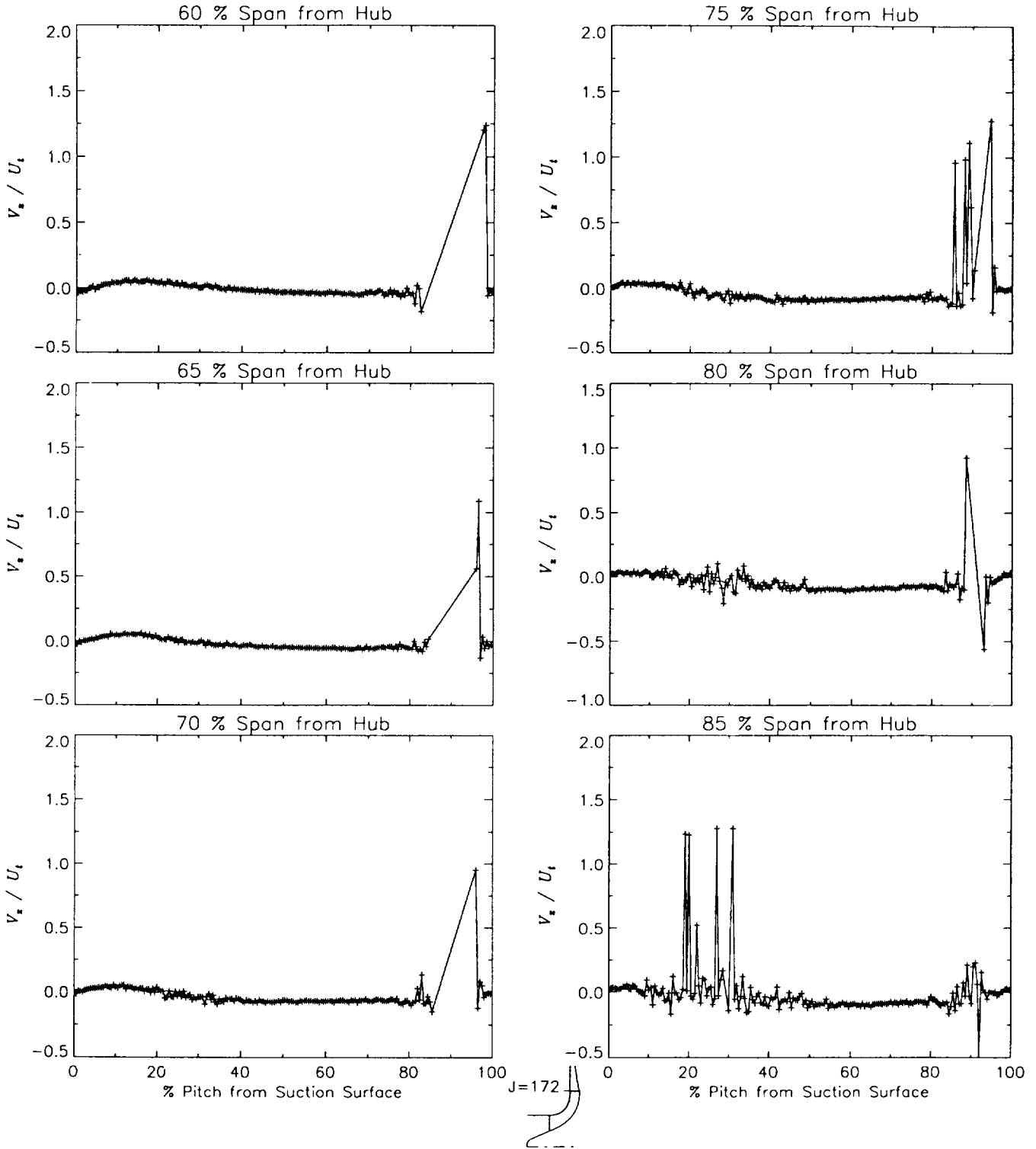
Station J=172, ( $m/m_s=1.014$ )



(c) Axial velocity normalized by impeller tip speed.

Figure 51.—Continued.

Station J=172, ( $m/m_s=1.014$ )



(c) Axial velocity normalized by impeller tip speed.

Figure 51.—Concluded.

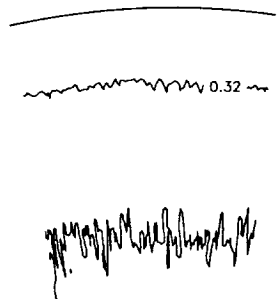


Figure 52 Contour plots of throughflow velocity normalized by impeller tip speed,  $V_T/U_t$ , for the design flow condition,  $\dot{m}_d$  at station 23 ( $m/m_s = -0.397$ ).

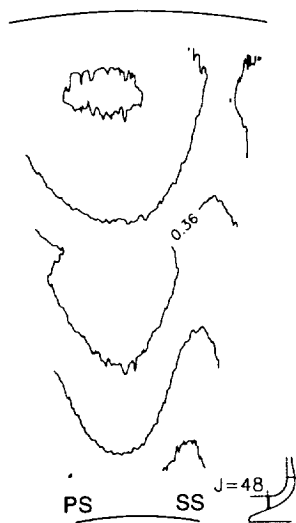


Figure 53 Contour plots of throughflow velocity normalized by impeller tip speed,  $V_T/U_t$ , for the design flow condition,  $\dot{m}_d$  at station 48 ( $m/m_s = -0.038$ ).

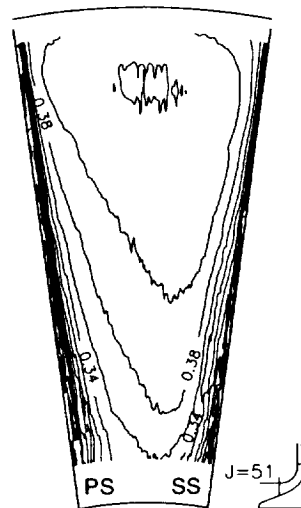


Figure 54 Contour plots of throughflow velocity normalized by impeller tip speed,  $V_T/U_t$ , for the design flow condition,  $\dot{m}_d$  at station 51 ( $m/m_s = 0.000$ ).

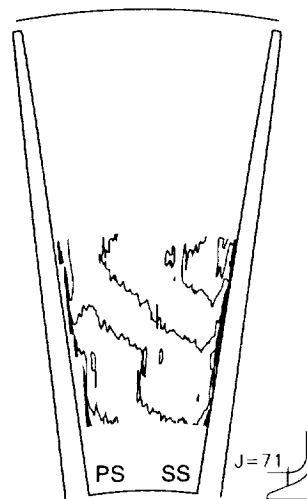


Figure 55 Contour plots of throughflow velocity normalized by impeller tip speed,  $V_T/U_t$ , for the design flow condition,  $\dot{m}_d$  at station 71 ( $m/m_s = 0.010$ ).



Figure 56 Contour plots of throughflow velocity normalized by impeller tip speed,  $V_T/U_t$ , for the design flow condition,  $\dot{m}_d$  at station 73 ( $m/m_s = 0.030$ ).

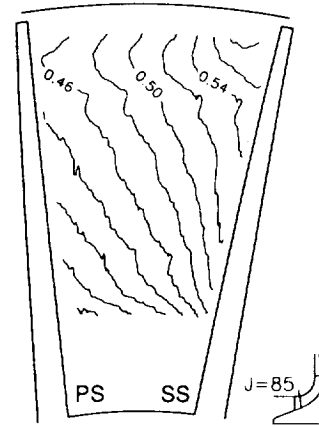


Figure 58 Contour plots of throughflow velocity normalized by impeller tip speed,  $V_T/U_t$ , for the design flow condition,  $\dot{m}_d$  at station 85 ( $m/m_s = 0.149$ ).

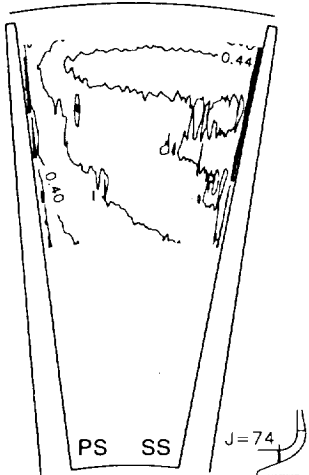


Figure 57 Contour plots of throughflow velocity normalized by impeller tip speed,  $V_T/U_t$ , for the design flow condition,  $\dot{m}_d$  at station 74 ( $m/m_s = 0.040$ ).

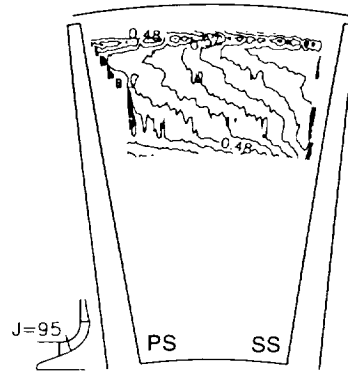


Figure 59 Contour plots of throughflow velocity normalized by impeller tip speed,  $V_T/U_t$ , for the design flow condition,  $\dot{m}_d$  at station 95 ( $m/m_s = 0.248$ ).

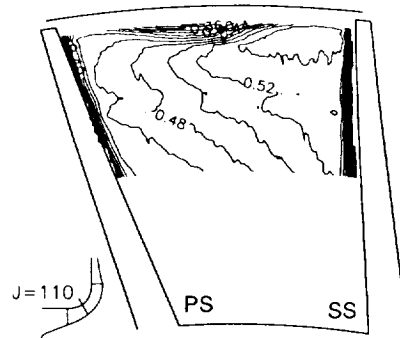


Figure 60 Contour plots of throughflow velocity normalized by impeller tip speed,  $V_T/U_t$ , for the design flow condition,  $\dot{m}_d$  at station 110 ( $m/m_s = 0.396$ ).

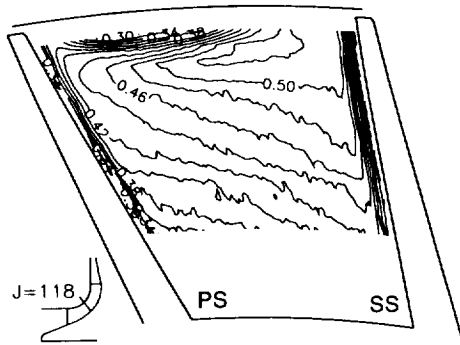


Figure 61 Contour plots of throughflow velocity normalized by impeller tip speed,  $V_T/U_t$ , for the design flow condition,  $\dot{m}_d$  at station 118 ( $m/m_s = 0.475$ ).

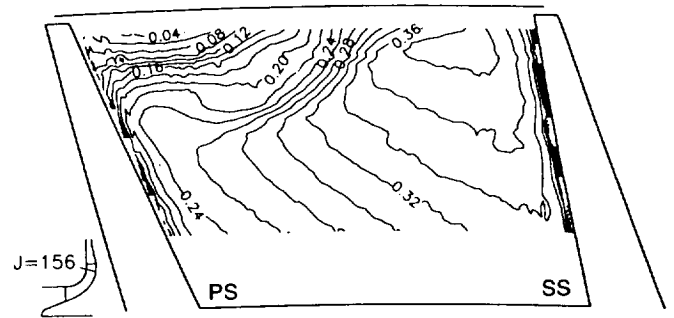


Figure 64 Contour plots of throughflow velocity normalized by impeller tip speed,  $V_T/U_t$ , for the design flow condition,  $\dot{m}_d$  at station 156 ( $m/m_s = 0.852$ ).

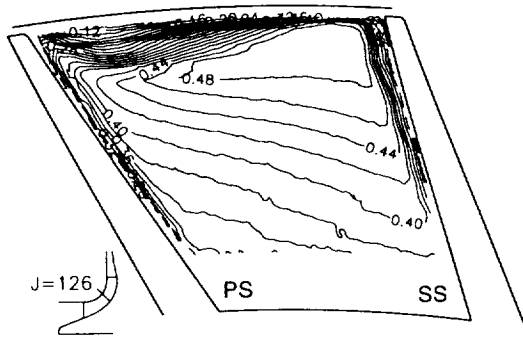


Figure 62 Contour plots of throughflow velocity normalized by impeller tip speed,  $V_T/U_t$ , for the design flow condition,  $\dot{m}_d$  at station 126 ( $m/m_s = 0.555$ ).

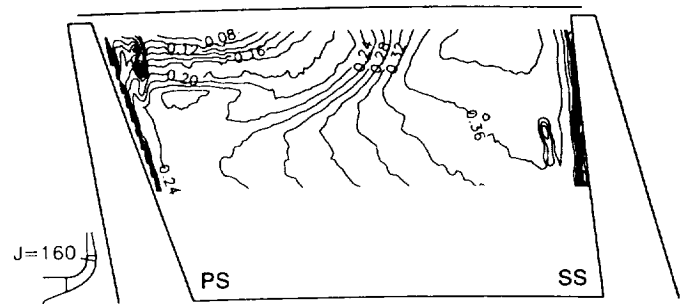


Figure 65 Contour plots of throughflow velocity normalized by impeller tip speed,  $V_T/U_t$ , for the design flow condition,  $\dot{m}_d$  at station 160 ( $m/m_s = 0.891$ ).

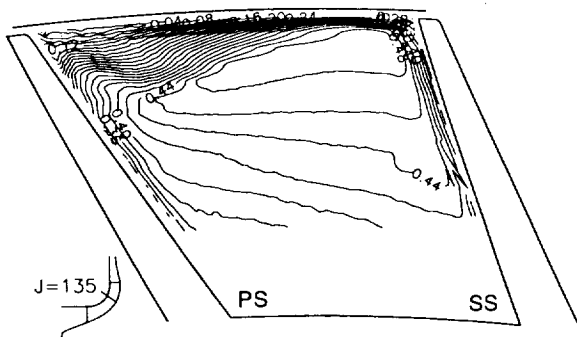


Figure 63 Contour plots of throughflow velocity normalized by impeller tip speed,  $V_T/U_t$ , for the design flow condition,  $\dot{m}_d$  at station 135 ( $m/m_s = 0.644$ ).

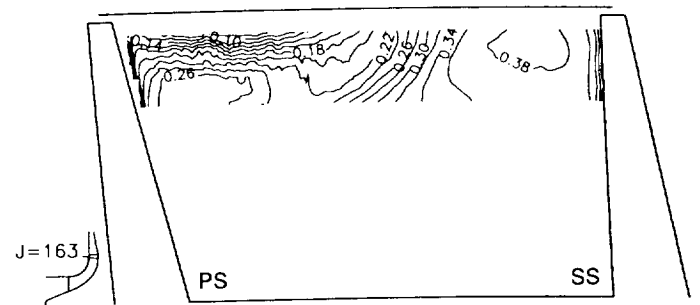


Figure 66 Contour plots of throughflow velocity normalized by impeller tip speed,  $V_T/U_t$ , for the design flow condition,  $\dot{m}_d$  at station 163 ( $m/m_s = 0.921$ ).

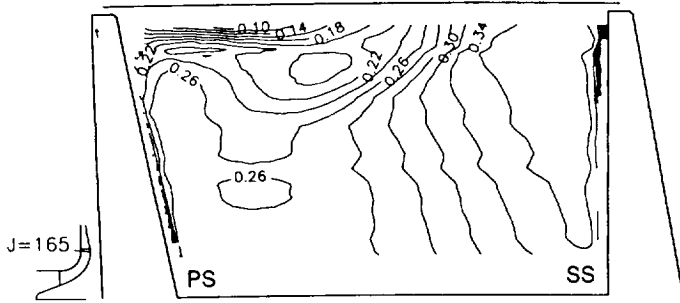


Figure 67 Contour plots of throughflow velocity normalized by impeller tip speed,  $V_T/U_t$ , for the design flow condition,  $\dot{m}_d$  at station 165 ( $m/m_s = 0.941$ ).

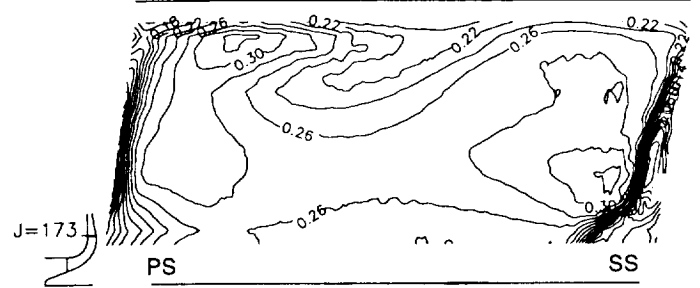


Figure 71 Contour plots of throughflow velocity normalized by impeller tip speed,  $V_T/U_t$ , for the design flow condition,  $\dot{m}_d$  at station 173 ( $m/m_s = 1.027$ ).

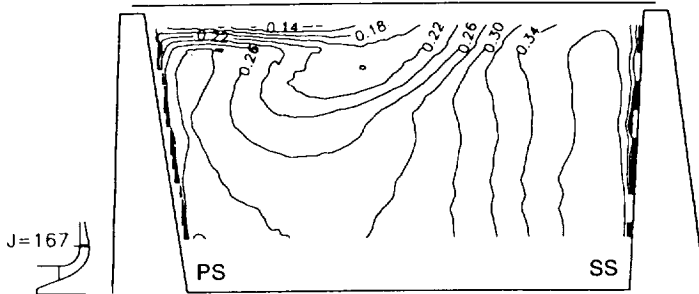


Figure 68 Contour plots of throughflow velocity normalized by impeller tip speed,  $V_T/U_t$ , for the design flow condition,  $\dot{m}_d$  at station 167 ( $m/m_s = 0.960$ ).

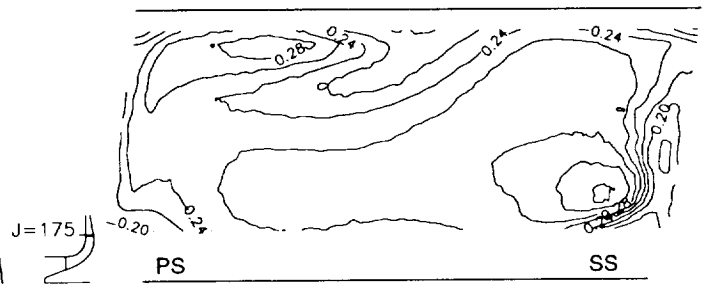


Figure 72 Contour plots of throughflow velocity normalized by impeller tip speed,  $V_T/U_t$ , for the design flow condition,  $\dot{m}_d$  at station 175 ( $m/m_s = 1.054$ ).

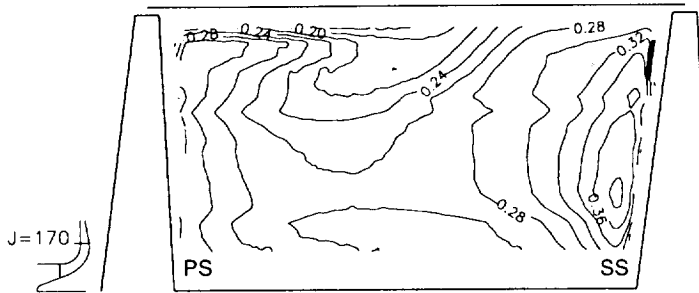


Figure 69 Contour plots of throughflow velocity normalized by impeller tip speed,  $V_T/U_t$ , for the design flow condition,  $\dot{m}_d$  at station 170 ( $m/m_s = 0.990$ ).

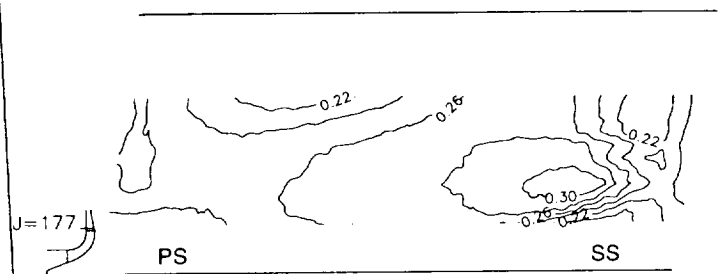


Figure 73 Contour plots of throughflow velocity normalized by impeller tip speed,  $V_T/U_t$ , for the design flow condition,  $\dot{m}_d$  at station 177 ( $m/m_s = 1.081$ ).

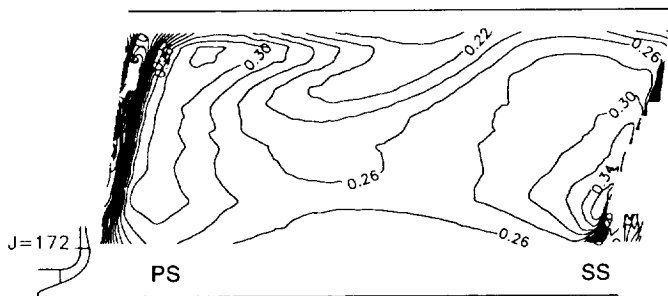


Figure 70 Contour plots of throughflow velocity normalized by impeller tip speed,  $V_T/U_t$ , for the design flow condition,  $\dot{m}_d$  at station 172 ( $m/m_s = 1.014$ ).

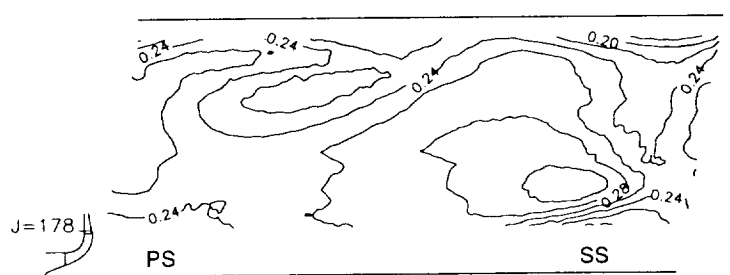


Figure 74 Contour plots of throughflow velocity normalized by impeller tip speed,  $V_T/U_t$ , for the design flow condition,  $\dot{m}_d$  at station 178 ( $m/m_s = 1.094$ ).

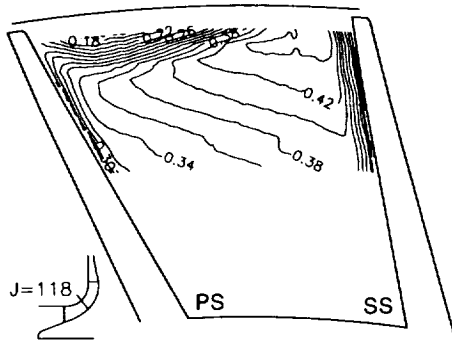


Figure 75 Contour plots of throughflow velocity normalized by impeller tip speed,  $V_T/U_t$ , for the off-design flow condition,  $78.7\% \dot{m}_d$  at station 118 ( $m/m_s = 0.475$ ).

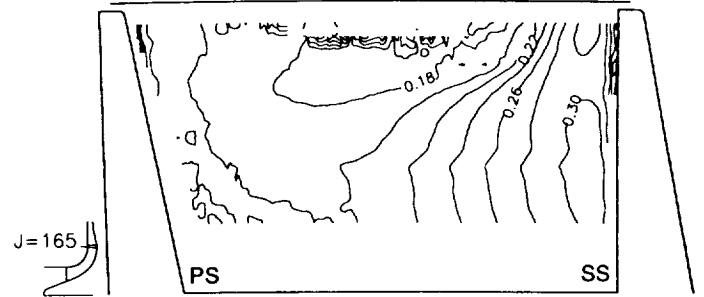


Figure 78 Contour plots of throughflow velocity normalized by impeller tip speed,  $V_T/U_t$ , for the off-design flow condition,  $78.7\% \dot{m}_d$  at station 165 ( $m/m_s = 0.941$ ).

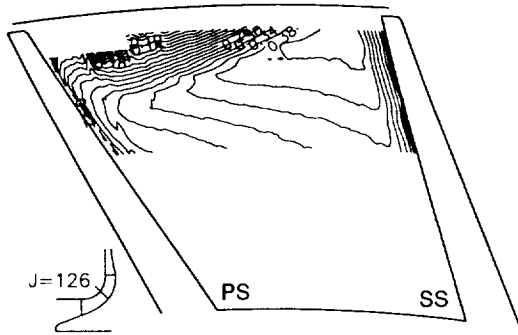


Figure 76 Contour plots of throughflow velocity normalized by impeller tip speed,  $V_T/U_t$ , for the off-design flow condition,  $78.7\% \dot{m}_d$  at station 126 ( $m/m_s = 0.555$ ).

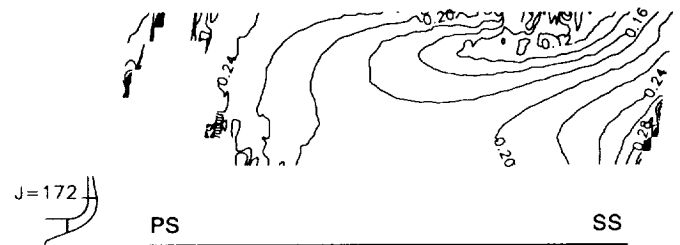


Figure 79 Contour plots of throughflow velocity normalized by impeller tip speed,  $V_T/U_t$ , for the off-design flow condition,  $78.7\% \dot{m}_d$  at station 172 ( $m/m_s = 1.014$ ).

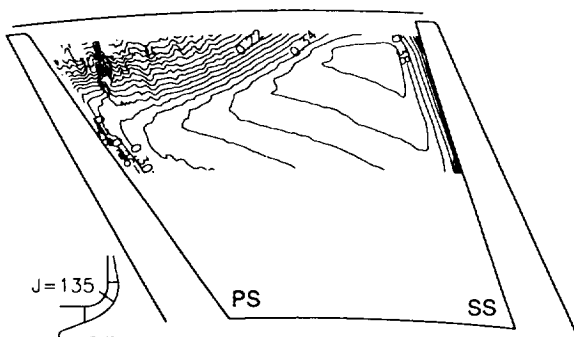


Figure 77 Contour plots of throughflow velocity normalized by impeller tip speed,  $V_T/U_t$ , for the off-design flow condition,  $78.7\% \dot{m}_d$  at station 135 ( $m/m_s = 0.644$ ).

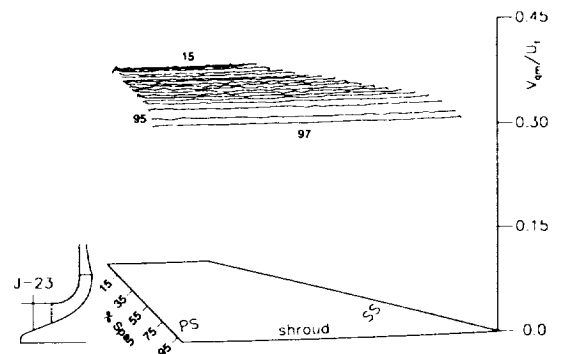


Figure 80 Wire—frame plots of throughflow velocity normalized by impeller tip speed,  $V_T/U_t$ , for the design flow condition,  $\dot{m}_d$  at station 23 ( $m/m_s = -0.397$ ).

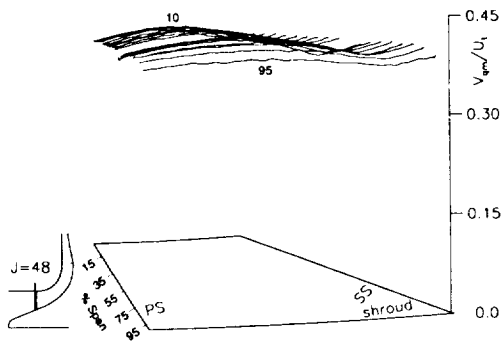


Figure 81 Wire—frame plots of throughflow velocity normalized by impeller tip speed,  $V_T/U_t$ , for the design flow condition,  $\dot{m}_d$  at station 48 ( $m/m_s = -0.038$ ).

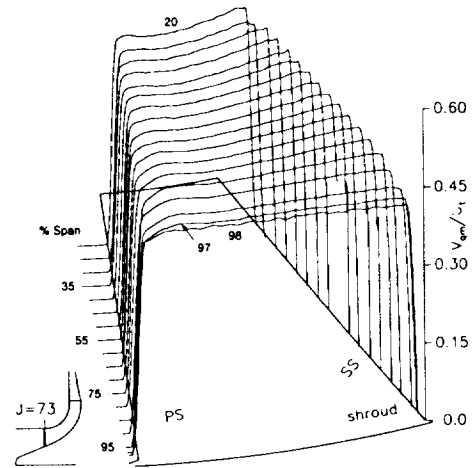


Figure 84 Wire—frame plots of throughflow velocity normalized by impeller tip speed,  $V_T/U_t$ , for the design flow condition,  $\dot{m}_d$  at station 73 ( $m/m_s = 0.030$ ).

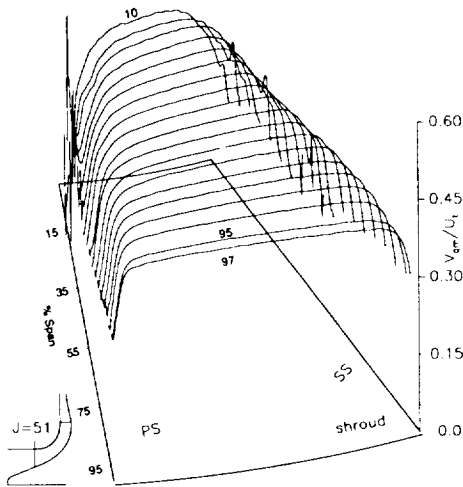


Figure 82 Wire—frame plots of throughflow velocity normalized by impeller tip speed,  $V_T/U_t$ , for the design flow condition,  $\dot{m}_d$  at station 51 ( $m/m_s = 0.000$ ).

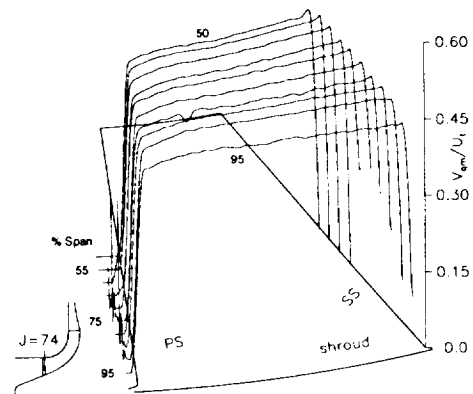


Figure 85 Wire—frame plots of throughflow velocity normalized by impeller tip speed,  $V_T/U_t$ , for the design flow condition,  $\dot{m}_d$  at station 74 ( $m/m_s = 0.040$ ).

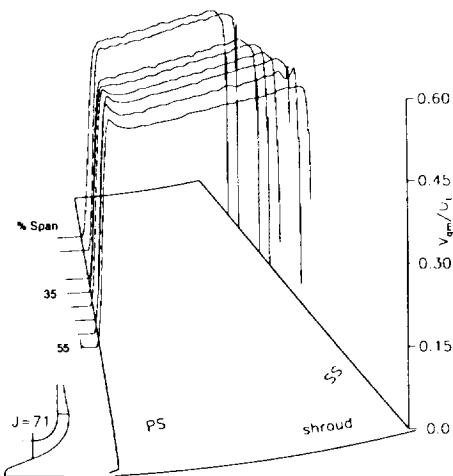


Figure 83 Wire—frame plots of throughflow velocity normalized by impeller tip speed,  $V_T/U_t$ , for the design flow condition,  $\dot{m}_d$  at station 71 ( $m/m_s = 0.010$ ).

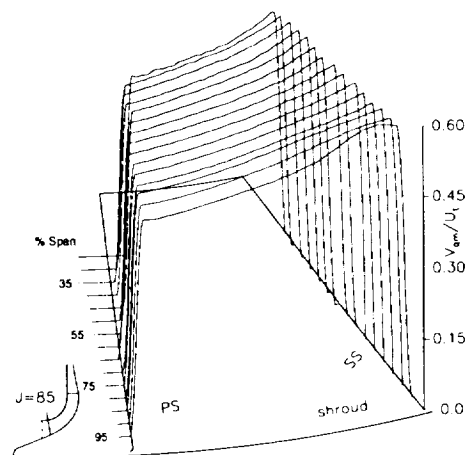


Figure 86 Wire—frame plots of throughflow velocity normalized by impeller tip speed,  $V_T/U_t$ , for the design flow condition,  $\dot{m}_d$  at station 85 ( $m/m_s = 0.149$ ).

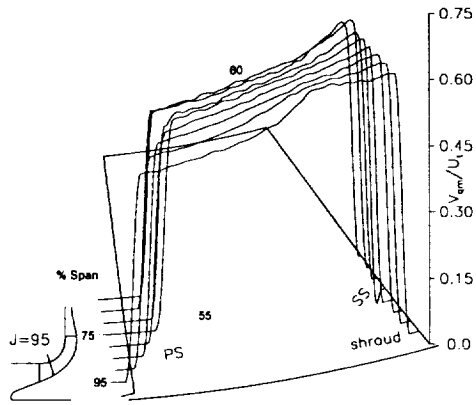


Figure 87 Wire—frame plots of throughflow velocity normalized by impeller tip speed,  $V_T/U_t$ , for the design flow condition,  $\dot{m}_d$  at station 95 ( $m/m_s = 0.248$ ).

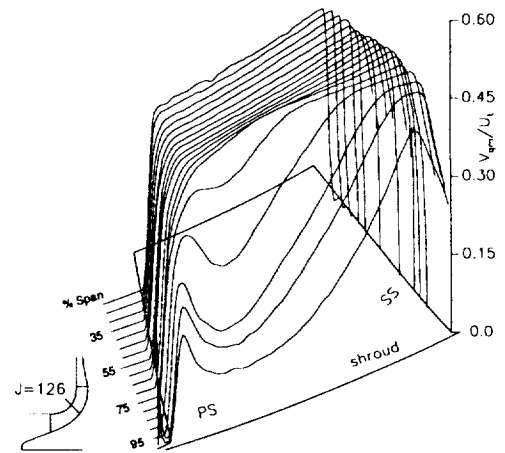


Figure 90 Wire—frame plots of throughflow velocity normalized by impeller tip speed,  $V_T/U_t$ , for the design flow condition,  $\dot{m}_d$  at station 126 ( $m/m_s = 0.555$ ).

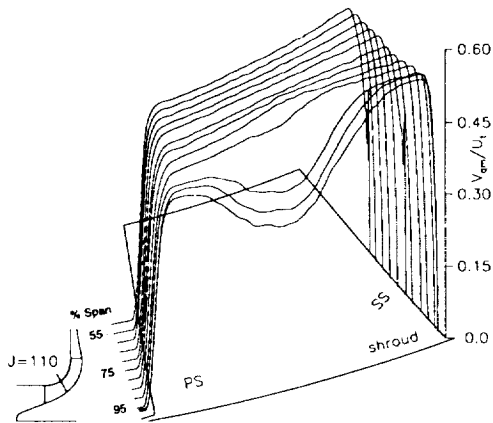


Figure 88 Wire—frame plots of throughflow velocity normalized by impeller tip speed,  $V_T/U_t$ , for the design flow condition,  $\dot{m}_d$  at station 110 ( $m/m_s = 0.396$ ).

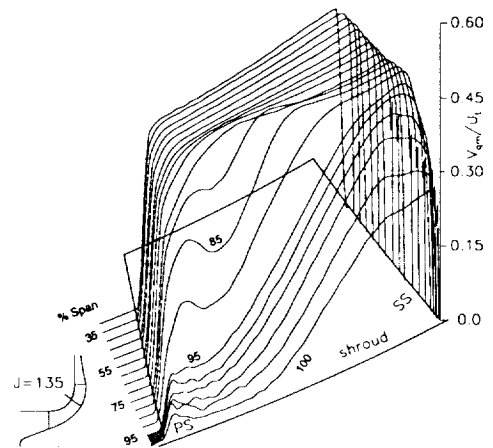


Figure 91 Wire—frame plots of throughflow velocity normalized by impeller tip speed,  $V_T/U_t$ , for the design flow condition,  $\dot{m}_d$  at station 135 ( $m/m_s = 0.644$ ).

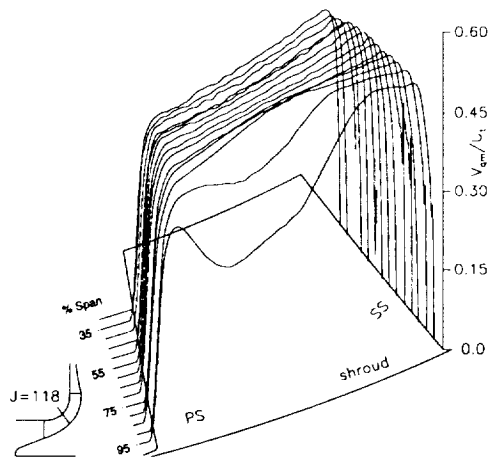


Figure 89 Wire—frame plots of throughflow velocity normalized by impeller tip speed,  $V_T/U_t$ , for the design flow condition,  $\dot{m}_d$  at station 118 ( $m/m_s = 0.475$ ).

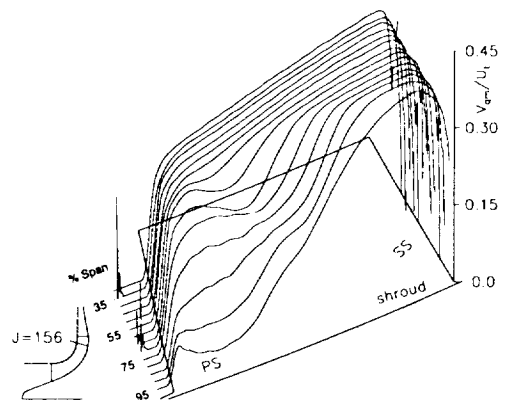


Figure 92 Wire—frame plots of throughflow velocity normalized by impeller tip speed,  $V_T/U_t$ , for the design flow condition,  $\dot{m}_d$  at station 156 ( $m/m_s = 0.852$ ).

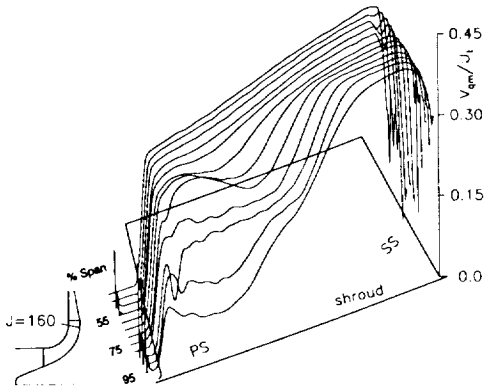


Figure 93 Wire—frame plots of throughflow velocity normalized by impeller tip speed,  $V_T/U_t$ , for the design flow condition,  $\dot{m}_d$  at station 160 ( $m/m_s = 0.891$ ).

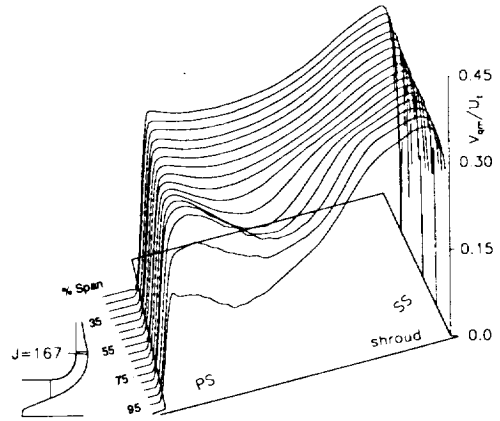


Figure 96 Wire—frame plots of throughflow velocity normalized by impeller tip speed,  $V_T/U_t$ , for the design flow condition,  $\dot{m}_d$  at station 167 ( $m/m_s = 0.960$ ).

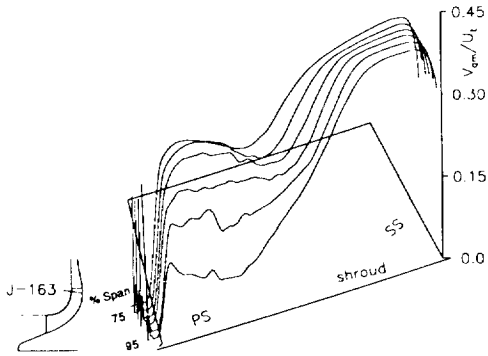


Figure 94 Wire—frame plots of throughflow velocity normalized by impeller tip speed,  $V_T/U_t$ , for the design flow condition,  $\dot{m}_d$  at station 163 ( $m/m_s = 0.921$ ).

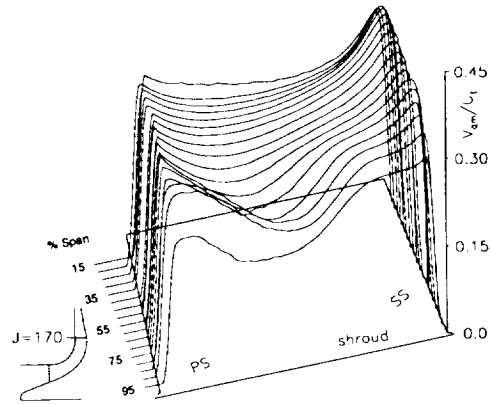


Figure 97 Wire—frame plots of throughflow velocity normalized by impeller tip speed,  $V_T/U_t$ , for the design flow condition,  $\dot{m}_d$  at station 170 ( $m/m_s = 0.990$ ).

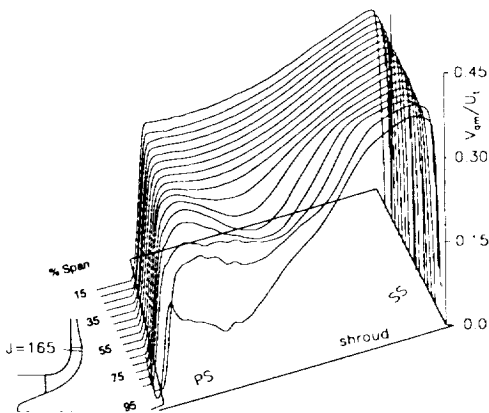


Figure 95 Wire—frame plots of throughflow velocity normalized by impeller tip speed,  $V_T/U_t$ , for the design flow condition,  $\dot{m}_d$  at station 165 ( $m/m_s = 0.941$ ).

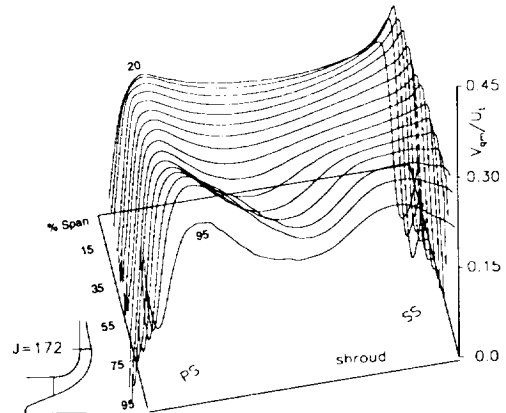


Figure 98 Wire—frame plots of throughflow velocity normalized by impeller tip speed,  $V_T/U_t$ , for the design flow condition,  $\dot{m}_d$  at station 172 ( $m/m_s = 1.014$ ).

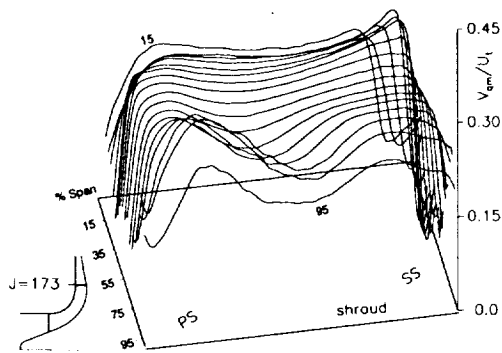


Figure 99 Wire—frame plots of throughflow velocity normalized by impeller tip speed,  $V_T/U_t$ , for the design flow condition,  $\dot{m}_d$  at station 173 ( $m/m_s = 1.027$ ).

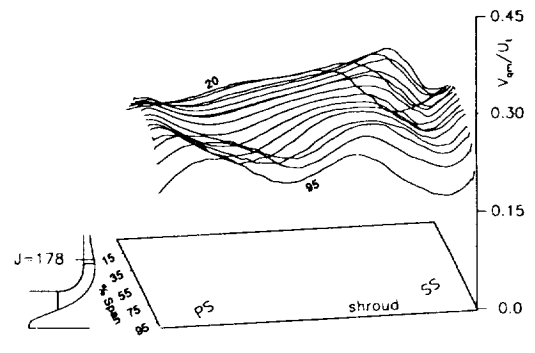


Figure 102 Wire—frame plots of throughflow velocity normalized by impeller tip speed,  $V_T/U_t$ , for the design flow condition,  $\dot{m}_d$  at station 178 ( $m/m_s = 1.094$ ).

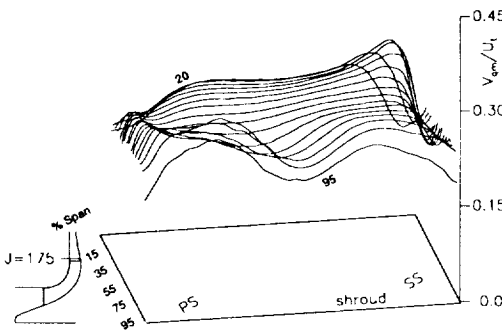


Figure 100 Wire—frame plots of throughflow velocity normalized by impeller tip speed,  $V_T/U_t$ , for the design flow condition,  $\dot{m}_d$  at station 175 ( $m/m_s = 1.054$ ).

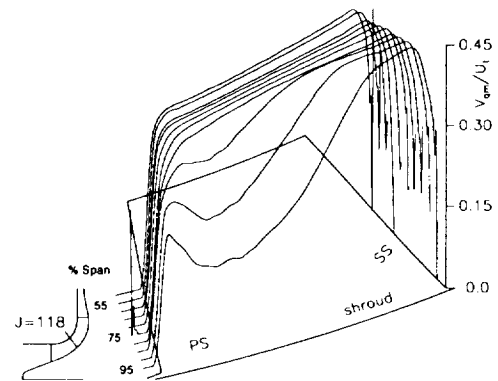


Figure 103 Wire—frame plots of throughflow velocity normalized by impeller tip speed,  $V_T/U_t$ , for the off-design flow condition, 78.7%  $\dot{m}_d$  at station 118 ( $m/m_s = 0.475$ ).

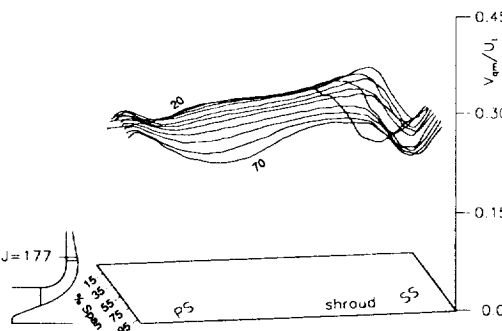


Figure 101 Wire—frame plots of throughflow velocity normalized by impeller tip speed,  $V_T/U_t$ , for the design flow condition,  $\dot{m}_d$  at station 177 ( $m/m_s = 1.081$ ).

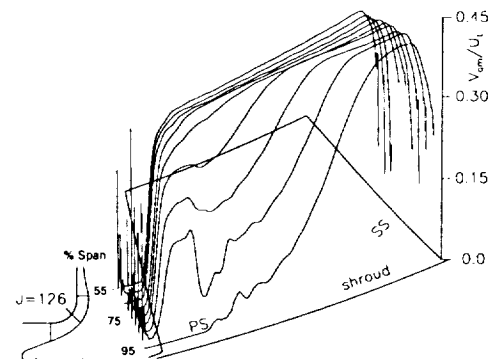


Figure 104 Wire—frame plots of throughflow velocity normalized by impeller tip speed,  $V_T/U_t$ , for the off-design flow condition, 78.7%  $\dot{m}_d$  at station 126 ( $m/m_s = 0.555$ ).

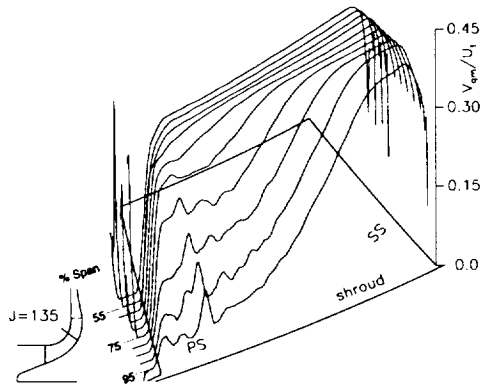


Figure 105 Wire—frame plots of throughflow velocity normalized by impeller tip speed,  $V_T/U_t$ , for the off-design flow condition,  $78.7\% \dot{m}_d$  at station 135 ( $m/m_s = 0.644$ ).

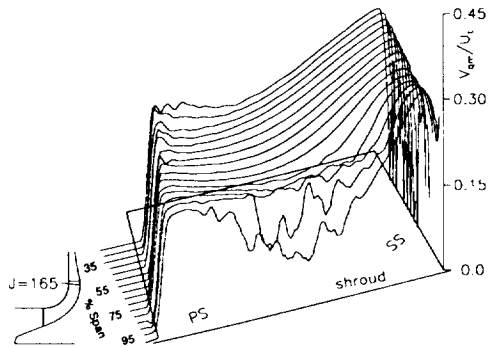


Figure 106 Wire—frame plots of throughflow velocity normalized by impeller tip speed,  $V_T/U_t$ , for the off-design flow condition,  $78.7\% \dot{m}_d$  at station 165 ( $m/m_s = 0.941$ ).

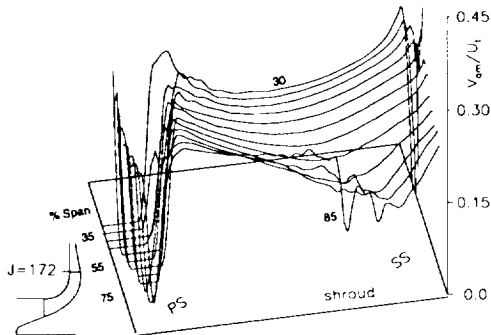


Figure 107 Wire—frame plots of throughflow velocity normalized by impeller tip speed,  $V_T/U_t$ , for the off-design flow condition,  $78.7\% \dot{m}_d$  at station 172 ( $m/m_s = 1.014$ ).

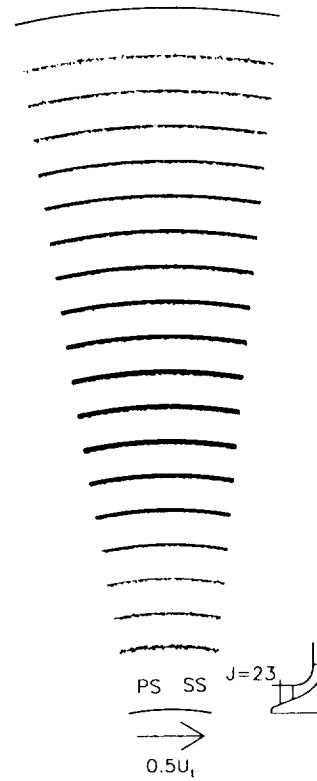


Figure 108 Vector plots of secondary velocity normalized by impeller tip speed,  $\bar{W}_s/U_t$ , for the design flow condition,  $\dot{m}_d$  at station 23 ( $m/m_s = -0.397$ ).

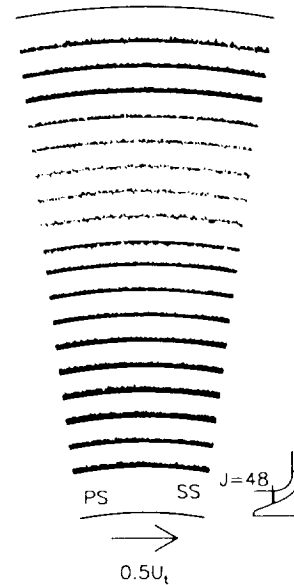


Figure 109 Vector plots of secondary velocity normalized by impeller tip speed,  $\bar{W}_s/U_t$ , for the design flow condition,  $\dot{m}_d$  at station 48 ( $m/m_s = -0.038$ ).

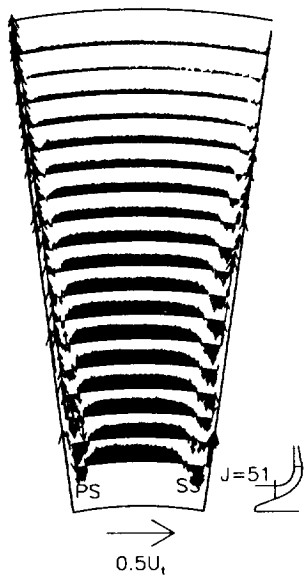


Figure 110 Vector plots of secondary velocity normalized by impeller tip speed,  $\vec{W}_s/U_t$ , for the design flow condition,  $\dot{m}_d$  at station 51 ( $m/m_s = 0.000$ ).

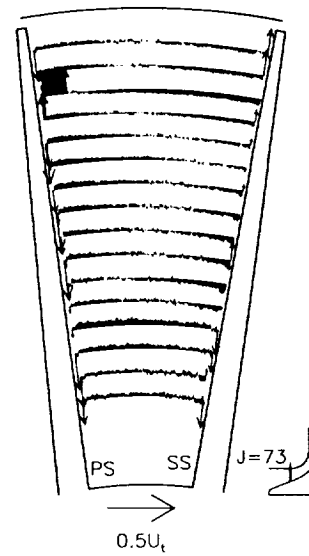


Figure 112 Vector plots of secondary velocity normalized by impeller tip speed,  $\vec{W}_s/U_t$ , for the design flow condition,  $\dot{m}_d$  at station 73 ( $m/m_s = 0.030$ ).

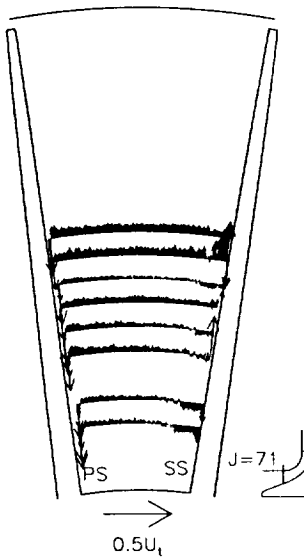


Figure 111 Vector plots of secondary velocity normalized by impeller tip speed,  $\vec{W}_s/U_t$ , for the design flow condition,  $\dot{m}_d$  at station 71 ( $m/m_s = 0.010$ ).

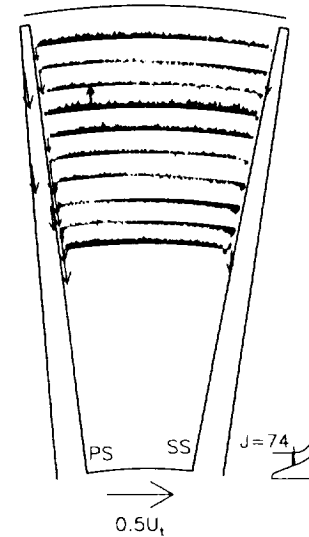


Figure 113 Vector plots of secondary velocity normalized by impeller tip speed,  $\vec{W}_s/U_t$ , for the design flow condition,  $\dot{m}_d$  at station 74 ( $m/m_s = 0.040$ ).

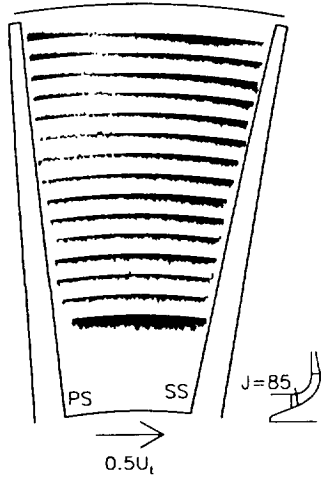


Figure 114 Vector plots of secondary velocity normalized by impeller tip speed,  $\bar{W}_s/U_t$ , for the design flow condition,  $\dot{m}_d$  at station 85 ( $m/m_s = 0.149$ ).

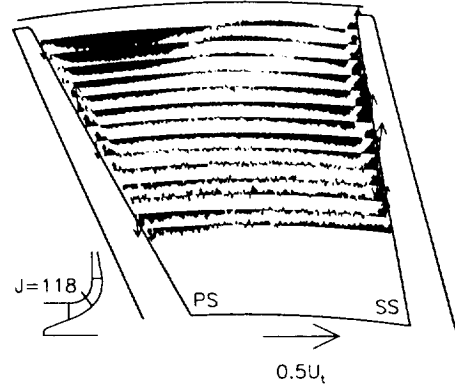


Figure 117 Vector plots of secondary velocity normalized by impeller tip speed,  $\bar{W}_s/U_t$ , for the design flow condition,  $\dot{m}_d$  at station 118 ( $m/m_s = 0.475$ ).

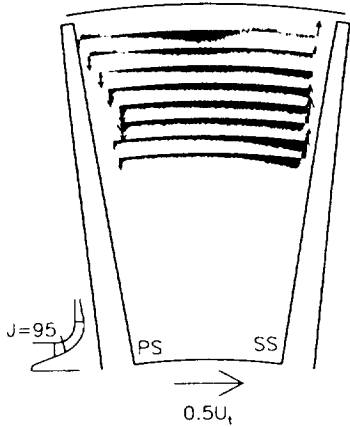


Figure 115 Vector plots of secondary velocity normalized by impeller tip speed,  $\bar{W}_s/U_t$ , for the design flow condition,  $\dot{m}_d$  at station 95 ( $m/m_s = 0.248$ ).

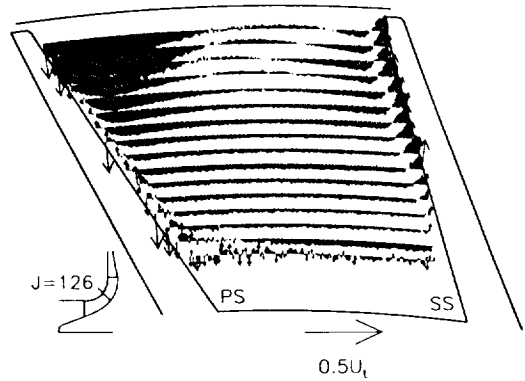


Figure 118 Vector plots of secondary velocity normalized by impeller tip speed,  $\bar{W}_s/U_t$ , for the design flow condition,  $\dot{m}_d$  at station 126 ( $m/m_s = 0.555$ ).

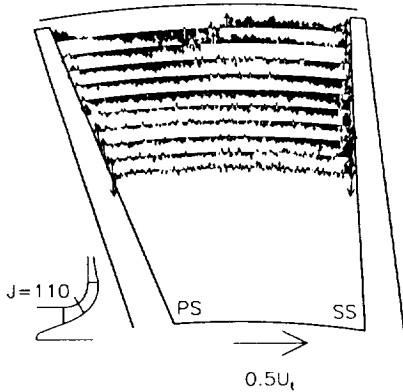


Figure 116 Vector plots of secondary velocity normalized by impeller tip speed,  $\bar{W}_s/U_t$ , for the design flow condition,  $\dot{m}_d$  at station 110 ( $m/m_s = 0.396$ ).

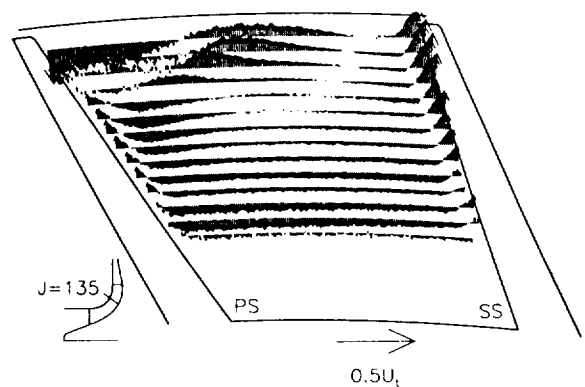


Figure 119 Vector plots of secondary velocity normalized by impeller tip speed,  $\bar{W}_s/U_t$ , for the design flow condition,  $\dot{m}_d$  at station 135 ( $m/m_s = 0.644$ ).

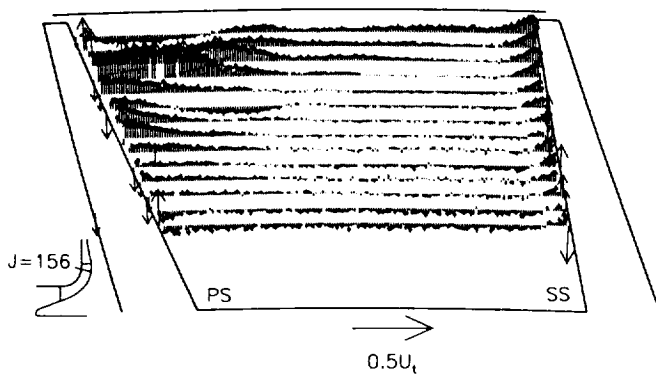


Figure 120 Vector plots of secondary velocity normalized by impeller tip speed,  $\bar{W}_s/U_t$ , for the design flow condition,  $\dot{m}_d$  at station 156 ( $m/m_s = 0.852$ ).

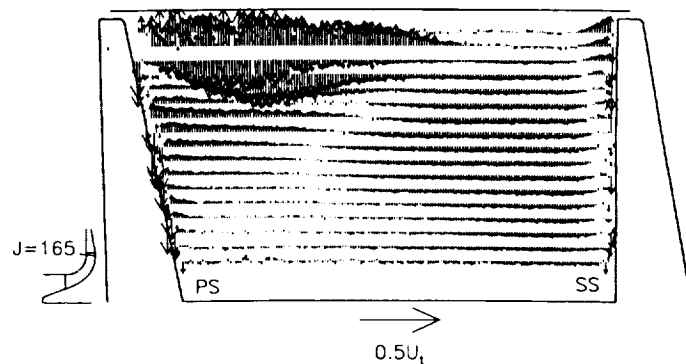


Figure 123 Vector plots of secondary velocity normalized by impeller tip speed,  $\bar{W}_s/U_t$ , for the design flow condition,  $\dot{m}_d$  at station 165 ( $m/m_s = 0.941$ ).

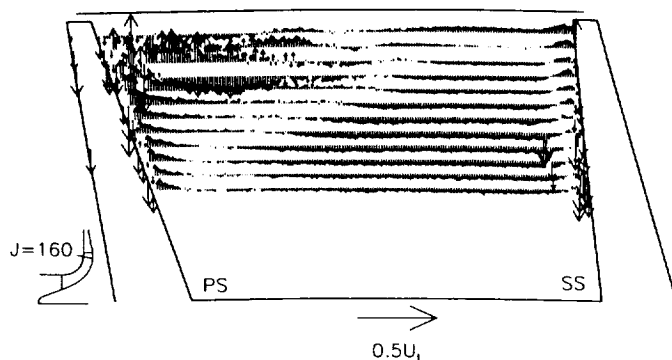


Figure 121 Vector plots of secondary velocity normalized by impeller tip speed,  $\bar{W}_s/U_t$ , for the design flow condition,  $\dot{m}_d$  at station 160 ( $m/m_s = 0.891$ ).

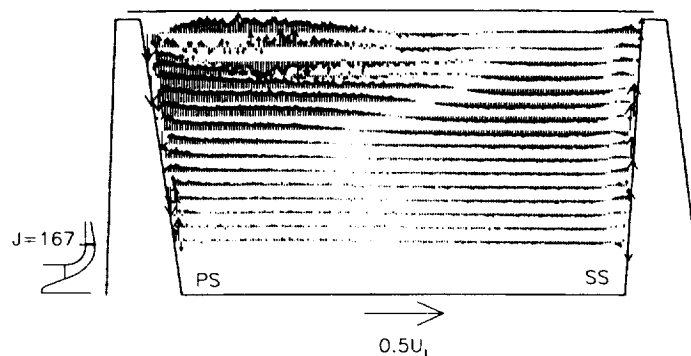


Figure 124 Vector plots of secondary velocity normalized by impeller tip speed,  $\bar{W}_s/U_t$ , for the design flow condition,  $\dot{m}_d$  at station 167 ( $m/m_s = 0.960$ ).

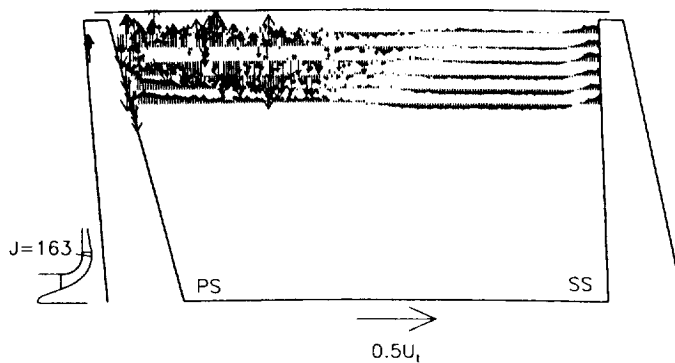


Figure 122 Vector plots of secondary velocity normalized by impeller tip speed,  $\bar{W}_s/U_t$ , for the design flow condition,  $\dot{m}_d$  at station 163 ( $m/m_s = 0.921$ ).

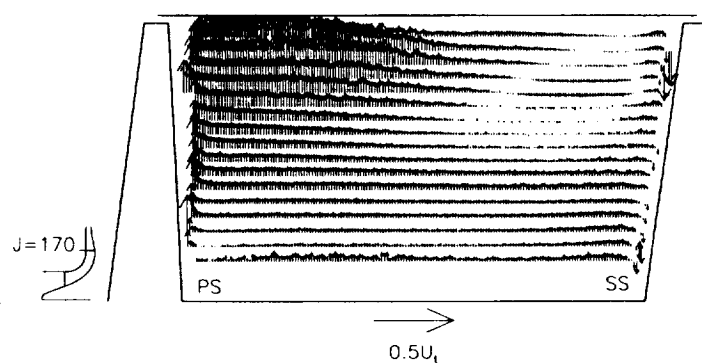


Figure 125 Vector plots of secondary velocity normalized by impeller tip speed,  $\bar{W}_s/U_t$ , for the design flow condition,  $\dot{m}_d$  at station 170 ( $m/m_s = 0.990$ ).

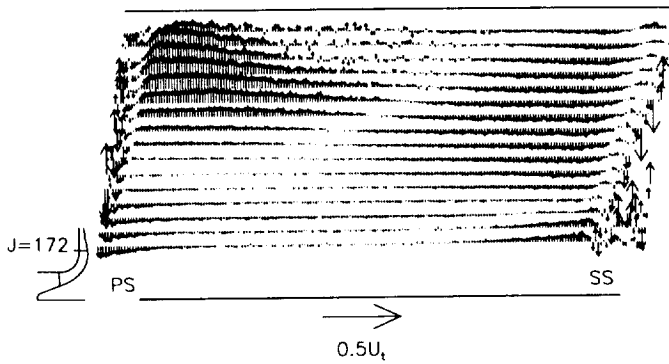


Figure 126 Vector plots of secondary velocity normalized by impeller tip speed,  $\bar{W}_s/U_t$ , for the design flow condition,  $\dot{m}_d$  at station 172 ( $m/m_s = 1.014$ ).

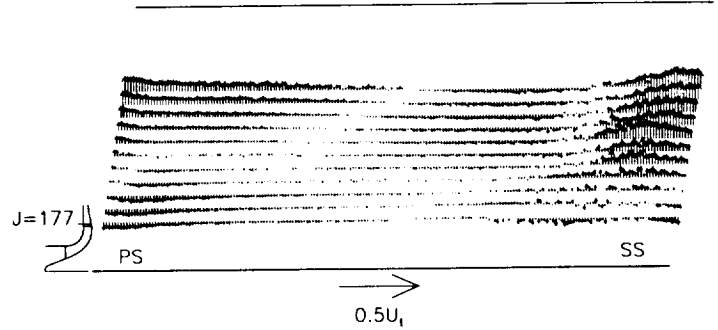


Figure 129 Vector plots of secondary velocity normalized by impeller tip speed,  $\bar{W}_s/U_t$ , for the design flow condition,  $\dot{m}_d$  at station 177 ( $m/m_s = 1.081$ ).

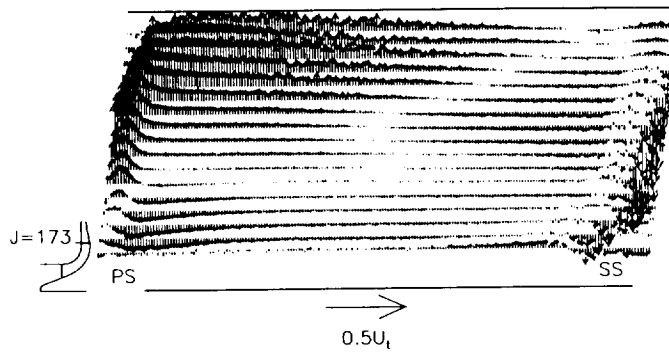


Figure 127 Vector plots of secondary velocity normalized by impeller tip speed,  $\bar{W}_s/U_t$ , for the design flow condition,  $\dot{m}_d$  at station 173 ( $m/m_s = 1.027$ ).

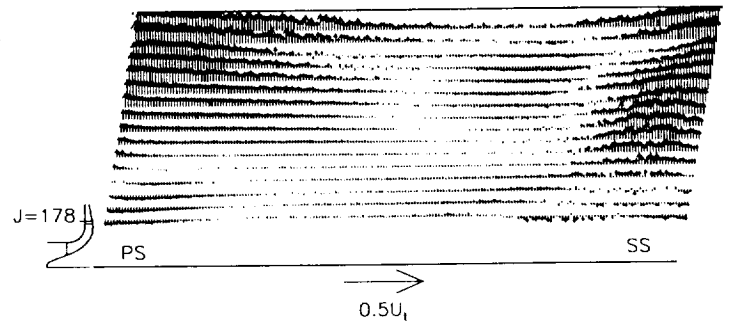


Figure 130 Vector plots of secondary velocity normalized by impeller tip speed,  $\bar{W}_s/U_t$ , for the design flow condition,  $\dot{m}_d$  at station 178 ( $m/m_s = 1.094$ ).

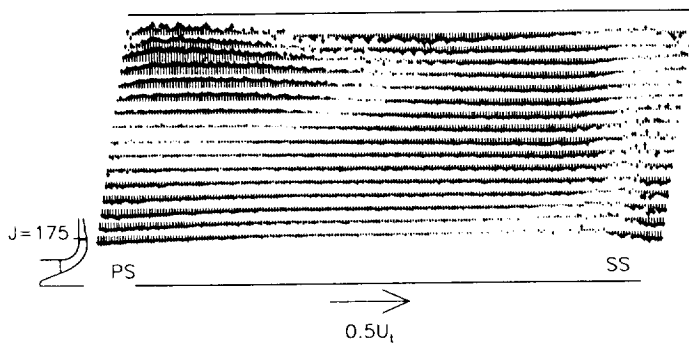


Figure 128 Vector plots of secondary velocity normalized by impeller tip speed,  $\bar{W}_s/U_t$ , for the design flow condition,  $\dot{m}_d$  at station 175 ( $m/m_s = 1.054$ ).

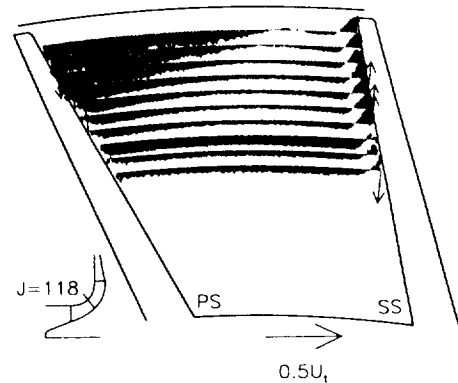


Figure 131 Vector plots of secondary velocity normalized by impeller tip speed,  $\bar{W}_s/U_t$ , for the off-design flow condition, 78.7%  $\dot{m}_d$  at station 118 ( $m/m_s = 0.475$ ).

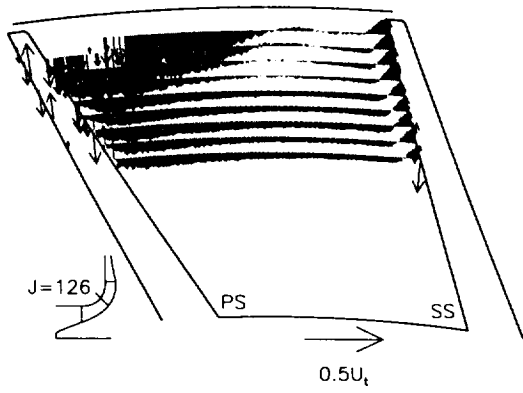


Figure 132 Vector plots of secondary velocity normalized by impeller tip speed,  $\bar{W}_s/U_t$ , for the off-design flow condition, 78.7%  $\dot{m}_d$  at station 126 ( $m/m_s = 0.555$ ).

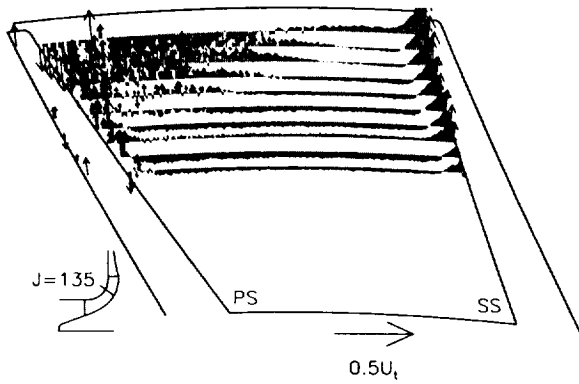


Figure 133 Vector plots of secondary velocity normalized by impeller tip speed,  $\bar{W}_s/U_t$ , for the off-design flow condition, 78.7%  $\dot{m}_d$  at station 135 ( $m/m_s = 0.644$ ).

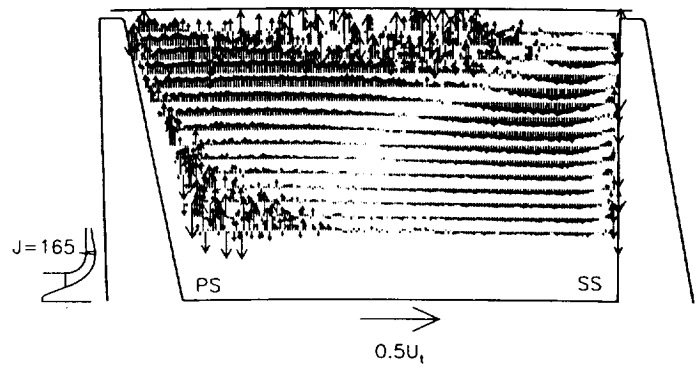


Figure 134 Vector plots of secondary velocity normalized by impeller tip speed,  $\bar{W}_s/U_t$ , for the off-design flow condition, 78.7%  $\dot{m}_d$  at station 165 ( $m/m_s = 0.941$ ).

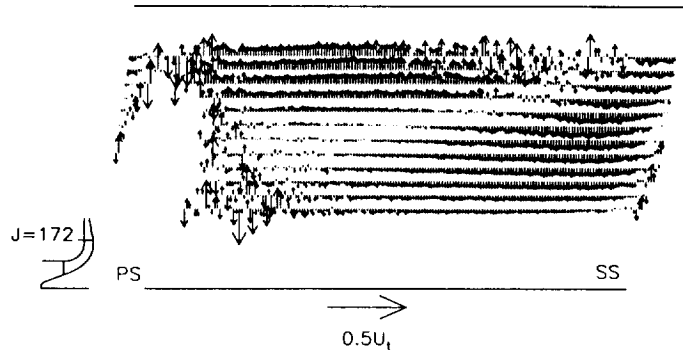


Figure 135 Vector plots of secondary velocity normalized by impeller tip speed,  $\bar{W}_s/U_t$ , for the off-design flow condition, 78.7%  $\dot{m}_d$  at station 172 ( $m/m_s = 1.014$ ).

# REPORT DOCUMENTATION PAGE

Form Approved  
OMB No. 0704-0188

Public reporting burden for this collection of information is estimated to average 1 hour per response, including the time for reviewing instructions, searching existing data sources, gathering and maintaining the data needed, and completing and reviewing the collection of information. Send comments regarding this burden estimate or any other aspect of this collection of information, including suggestions for reducing this burden, to Washington Headquarters Services, Directorate for Information Operations and Reports, 1215 Jefferson Davis Highway, Suite 1204, Arlington, VA 22202-4302, and to the Office of Management and Budget, Paperwork Reduction Project (0704-0188), Washington, DC 20503.

1. AGENCY USE ONLY (Leave blank)	2. REPORT DATE June 1995	3. REPORT TYPE AND DATES COVERED Technical Paper	
4. TITLE AND SUBTITLE  Laser Anemometer Measurements of the Three-Dimensional Rotor Flow Field in the NASA Low-Speed Centrifugal Compressor		5. FUNDING NUMBERS  WU-505-62-52 1L161102AH45	
6. AUTHOR(S)  Michael D. Hathaway, Randall M. Chriss, Anthony J. Strazisar, and Jerry R. Wood		8. PERFORMING ORGANIZATION REPORT NUMBER  E-9390	
7. PERFORMING ORGANIZATION NAME(S) AND ADDRESS(ES) NASA Lewis Research Center Cleveland, Ohio 44135-3191 and Vehicle Propulsion Directorate U.S. Army Research Laboratory Cleveland, Ohio 44135-3191		10. SPONSORING/MONITORING AGENCY REPORT NUMBER  NASA TP-3527 ARL-TR-333	
9. SPONSORING/MONITORING AGENCY NAME(S) AND ADDRESS(ES) National Aeronautics and Space Administration Washington, D.C. 20546-0001 and U.S. Army Research Laboratory Adelphi, Maryland 20783-1145		11. SUPPLEMENTARY NOTES Michael D. Hathaway, Vehicle Propulsion Directorate, U.S. Army Research Laboratory, NASA Lewis Research Center; Randall M. Chriss, Anthony J. Strazisar, and Jerry R. Wood, NASA Lewis Research Center. Responsible person, Michael D. Hathaway, organization code 2640, (216) 433-6250.	
12a. DISTRIBUTION/AVAILABILITY STATEMENT  Unclassified - Unlimited Subject Category 07  This publication is available from the NASA Center for Aerospace Information, (301) 621-0390.		12b. DISTRIBUTION CODE	
13. ABSTRACT (Maximum 200 words)  A laser anemometer system was used to provide detailed surveys of the three-dimensional velocity field within the NASA low-speed centrifugal impeller operating with a vaneless diffuser. Both laser anemometer and aerodynamic performance data were acquired at the design flow rate and at a lower flow rate. Flow path coordinates, detailed blade geometry, and pneumatic probe survey results are presented in tabular form. The laser anemometer data are presented in the form of pitchwise distributions of axial, radial, and relative tangential velocity on blade-to-blade stream surfaces at 5-percent-of-span increments, starting at 95-percent-of-span from the hub. The laser anemometer data are also presented as contour and wire-frame plots of throughflow velocity and vector plots of secondary velocities at all measurement stations through the impeller.			
14. SUBJECT TERMS  Centrifugal; Compressor; Laser velocimetry; Three-dimensional flow field		15. NUMBER OF PAGES 297	16. PRICE CODE A13
17. SECURITY CLASSIFICATION OF REPORT Unclassified	18. SECURITY CLASSIFICATION OF THIS PAGE Unclassified	19. SECURITY CLASSIFICATION OF ABSTRACT Unclassified	20. LIMITATION OF ABSTRACT





**National Aeronautics and  
Space Administration**

**Lewis Research Center  
21000 Brookpark Rd.  
Cleveland, OH 44135-3191**

**Official Business  
Penalty for Private Use \$300**

**POSTMASTER: If Undeliverable — Do Not Return**